

2020

## Proceedings of the 2020 Coal Operators Conference

Naj Aziz

*University of Wollongong, naj@uow.edu.au*

Bob Kininmonth

*Illawarra Outburst Committee*

Follow this and additional works at: <https://ro.uow.edu.au/coal>

---

### Recommended Citation

Aziz, Naj and Kininmonth, Bob, "Proceedings of the 2020 Coal Operators Conference" (2020). *Coal Operators' Conference*. 757.

<https://ro.uow.edu.au/coal/757>



# **PROCEEDINGS OF THE 2020 COAL OPERATORS CONFERENCE**

**UNIVERSITY OF WOLLONGONG, NSW**

**12-14 FEBRUARY 2020**

**PRINCIPAL EDITORS  
NAJ AZIZ AND BOB KININMONTH**

**ORGANISERS  
UNIVERSITY OF WOLLONGONG - MINING ENGINEERING**

**PRINTED IN AUSTRALIA BY  
The University Of Wollongong Printery**

**ISBN (ebook): 978-1-74128-321-1  
ISBN (paperback): 978-1-74128-320-4**

**All papers in these proceedings are peer reviewed**

**Published online: <http://ro.uow.edu.au/coal>  
Or via: <http://www.miningst.com>**

**No paper in these proceedings is to be re-published unless with written permission from the conference organisers and/or the original authors who maintain the copyright for their work.**



## EDITORIAL BOARD

NAJ AZIZ  
JAN NEMCIK  
ISMET CANBULAT  
JASON EMERY

BOB KININMONTH  
ALI MIRZAGHORBANALI  
JOHN HOELLE  
ROGER BYRNES

**Typeset by**  
**Sina Anzanpour**  
**Shahin Aziz**  
**University of Wollongong**

### ADVISORY BOARD

Naj Aziz, University of Wollongong  
Bob Kininmonth, Illawarra Outburst Committee  
Belle Bharat, Anglo American  
Jan Nemcik, University of Wollongong (UOW)  
Basil Beamish, B3 Mining Services, Aust.  
Dennis Black, Pacific MGM, NSW  
David Evans, DSI Australia  
David Cliff, University of Queensland  
Edward Steed, Angloamerican  
Frank Hungerford, University of Wollongong  
Ismet Canbulat, UNSW, Australia  
John Hoelle, Braemar Geotech, Australia  
Martin Watkinson, Simtars Queensland  
Patrycja Sheffield, Centennial Coal  
Russell Frith, Avance Mining  
Stuart MacGregor, SCT Operations

Jacqui Purcell, LDO Group, NSW  
Richard Campbell, Queensland  
Rod Doyle, Hume Coal Pty Limited, NSW  
Kevin Marston- AusIMM –Illawarra Branch  
Paul Hagan, UNSW, Australia  
Robert Hawker, Minova Australia  
Jason Emery, Optimum Geotechnics  
Peter Craig, Jennmar Australia  
Ray Tolhurst, AusIMM Illawarra Branch  
Roger Byrnes, Byrnes Geotechnical Pty ltd  
Terry Medhurst, PDR Engineers  
Ali Mirzaghobanali, USQ  
Ross Seedsman, Australia  
Gavin Lowing, Peabody Energy  
Shahin Aziz, Wollongong

### REVIEWERS

*Naj Aziz, University of Wollongong (UOW)*  
*Bob Kininmonth, Illawarra Outburst Committee*  
*Basil Beamish, B3 Mining Services, Australia*  
*Yvette Heritage, SCT Operations*  
*Jan Nemcik, University of Wollongong*  
*David Cliff, University of Queensland*  
*Ismet Canbulat, UNSW, Australia*

*John Hoelle, Braemar Geotech, Australia*  
*Peter Craig, Jennmar Australia*  
*Jason Emery, Optimum Geotechnics*  
*Ali Mirzaghobanali, University of Southern Queensland*  
*Kevin Marston, AusIMM Illawarra Branch*  
*Patrycja Sheffield, Centennial Coal*  
*Ross Seedsman, Seedsman Geotechnic*

## MESSAGE FROM CONFERENCE CHAIRS

It is with a heavy heart we report the physical cancellation of the Coal Operator's Conference due to the devastating effect of bush fires in Australia and the threatening actions of the climate change activists, who fail to realise that the conference has nothing to do with bushfires. This cancellation has not been easy for us to take, in the light of three decades of holding various conferences, seminars and workshops at the University Of Wollongong.

The aim of the conference, from its inception, has been to promote research and education in mining. Topics covered include ground control, automation, mine gases, mine outburst, mining induced seismic activity, mine geology, mine fires, mining planning, mine closures and rehabilitation, mine management, mine contracts and risk management.

The Coal Operators' Conference has been running since 1998 intermittently and since 2008 it has been held annually. The conference has become the annual cycle of our lives, but it is necessary to halt it for the time being, as the devastating bushfires have further inflamed some members of the community who, it would be fair to say, are placing the blame for this horrendous disaster almost squarely on coal mining and other non-renewable energy sources. It could instead be argued that a number of other factors should also be considered as a cause for climate change.

Let me assure everyone that we are not hanging up our gloves yet, rather we will be wearing new ones, which will energise us and make us more determined to move forward with stronger commitment and resolve for many years to come. However, we need to make a decision either to retain the conference name as it is (i.e., Coal Operators' Conference), or change to a new name, although the main emphasis will remain unchanged.

Obviously this alternative name may not sound fair to potential conference attendees; however it is hoped that attendees will recognise the reason, while remaining focused on our real mission of dealing with mining education and research in innovation technologies and mine safety.

In future the conference may be held mid-year in July, which will be decided upon after consultation with the conference committee and wider interested bodies.

The valuable support coming from delegates, sponsors and exhibitors is immense and has been the backbone of the conference and their logos are retained and published in the proceedings in appreciation of their support.

We would like everybody to maintain their support for many years to come.



**Professor Naj Aziz**

Conference executive chairman



**Mr Robert J Kininmonth**

Conference executive co-chair

## SPONSORS AND EXHIBITORS

### LONG TERM SPONSORS



### SUPPORTERS



# PAST PROCEEDINGS



## TABLE OF CONTENTS

<b>PROCEEDINGS OF THE 2020 COAL OPERATORS CONFERENCE</b> .....	<b>i</b>
<b>EDITORIAL BOARD</b> .....	<b>ii</b>
<b>SPONSORS AND EXHIBITORS</b> .....	<b>iv</b>
<b>PAST PROCEEDINGS</b> .....	<b>v</b>
<b>TABLE OF CONTENTS</b> .....	<b>vi</b>
<b>MEASUREMENT OF IN-SITU COAL CLEAT COMPRESSIBILITY</b> .....	<b>9</b>
Gelber Taco, Alberto Kamenar, Jeff Edgoose	
<b>DETERMINING COAL DIRECTIONAL MECHANICAL PROPERTIES USING TRUE TRIAXIAL TESTING FACILITY</b> .....	<b>23</b>
Zhongwei Chen, Mehdi Serati, Mutaz El-Amin Mohmoud	
<b>SHEAR STRENGTH PROPERTIES OF ARTIFICIAL ROCK JOINTS</b> .....	<b>32</b>
Muhammad Zohaib, Ali Mirzaghobanali, Andreas Helwig, Naj Aziz, Peter Gregor, Ashkan Rastegarmanesh, Kevin McDougall	
<b>FLOOR HEAVE MONITORING USING FLOOR INSTRUMENTATION</b> .....	<b>45</b>
Sungsoon Mo, Peter Yee, Terri O'Sullivan, Hossein Masoumi, Ismet Canbulat, Serkan Saydam	
<b>THE EVOLUTION OF PRIMARY CABLE SUPPORT AT GRASSTREE MINE</b> .....	<b>57</b>
Edward Steed, Jason Emery	
<b>LONGWALL BEHAVIOUR IN MASSIVE STRATA</b> .....	<b>74</b>
Ian Gray, Tim Gibbons	
<b>A ROOF CAVABILITY CLASSIFICATION SYSTEM AND ITS USE FOR ESTIMATION OF MAIN CAVING INTERVAL IN LONGWALL MINING</b> .....	<b>104</b>
Sadjad Mohammadi, Mohammad Ataei, Reza Kakaie, Ali Mirzaghobanali, Zahra Faraji Rad and Naj Aziz	
<b>A REVIEW OF OVERBURDEN FRACTURING AND CHANGES IN HYDRAULIC CHARACTERISTICS DUE TO LONGWALL MINING</b> .....	<b>116</b>
Hadi Nourizadeh, Ismet Canbulat, Joung Oh, Chengguo Zhang, Naj Aziz, Ali Mirzaghobanali, Kevin McDougall	
<b>DESIGN COMBINED SUPPORT UNDER ARBITRARY IMPULSIVE LOADINGG</b> .....	<b>128</b>
Faham Tahmasebinia, Ismet Canbulat, Chengguo Zhang Serkan Saydam, Onur Vardar	
<b>Parametric studies of cable bolts using a modified Short Encapsulation Pull-out Test</b>	<b>138</b>
Danqi Li, Hossein Masoumi	
<b>STATIC AND DYNAMIC TESTING OF TENDONS</b> .....	<b>146</b>
Saman Khaleghparast, Sina Anzanpour, Naj Aziz, Alex Remennikov, Ali Mirzaghobanali	
<b>PERFORMANCE OF BOLTING SYSTEMS IN TENSION AND THE INTEGRITY OF THE PROTECTIVE SLEEVE COATING IN SHEAR</b> .....	<b>155</b>

Naj Aziz, Antoine Schneiderwind, Sina Anzanpour, Saman Khaleghparast, Duncan Best,  
Travis Marshall

**THE EFFECT OF ELEVATED TEMPERATURE ON RESIN-ANCHORED ROCK BOLTS.163**

Kent McTyer

**DEVELOPMENT OF SUPPORT SYSTEMS FOR LONGWALL MINING IN THE BOWEN BASIN,  
CENTRAL QUEENSLAND..... 175**

George Klenowski and Phil McNamara

**APPLICATION OF CONTINUOUS MECHANICAL CUTTING TO COAL OVERBURDEN  
REMOVAL ..... 186**

Isaac Dzakpata, Dihon Tadic, Joji Quidim

**ROLLING DYNAMIC COMPACTION FOR HAUL ROAD CONSTRUCTION AND  
MAINTENANCE – AN UPDATE ..... 198**

Derek Avalle, Brendan Scott and James Miedecke

**DRILL RIG CHARACTERISTICS AND DRILLING TECHNIQUES REQUIRED FOR MAXIMUM  
BOREHOLE DEPTH WITH DIRECTIONAL DRILLING .....207**

Frank Hungerford

**A DISCUSSION ON CAUSATION MECHANISMS FOR OVERBURDEN BUMPS AS DISTINCT  
FROM COAL BURSTS.....219**

Russell Frith, Guy Reed, Martin Mackinnon

**DYNAMIC EVENTS AT LONGWALL FACE, CSM MINE, CZECH REPUBLIC .....233**

Petr Waclawik, Jan Nemcik, Radovan Kukutsch, Libin Gong and Gaetano Venticinque

**THE INFLUENCE OF INTRA-SEAM COAL CHARACTER VARIATION ON OUTBURST RISK  
POTENTIAL.....242**

Patrick Booth, Jan Nemcik, Ting Ren

**DYNAMIC ANALYSIS OF FAULT SLIPS AND THEIR INFLUENCE ON COAL MINE RIB  
STABILITY.....264**

Jan Nemcik, Gaetano Venticinque and Libin Gong

**NUMERICAL MODEL OF DYNAMIC ROCK FRACTURE PROCESS DURING COAL BURST  
.....275**

Gaetano Venticinque and Jan Nemcik

**IMPACT OF CORE SAMPLE RECOVERY TIME ON ACCURACY OF GAS CONTENT  
MEASUREMENT .....281**

Dennis Black

**AN IMPROVED TECHNIQUE FOR MONITORING EXPLOSIBILITY OF GASES .....295**

David Cliff

**GAS MONITORING WHAT WE KNOW SO FAR .....304**

Martin Watkinson, Martin Tsai, Larry Ryan

**OXYGEN DEFICIENCY IN GRAHAM'S RATIO, EVALUATION .....314**

Snezana Bajic, Sean Muller, Mladen Gido

**RECENT CASE STUDIES USING THE REMOTE ROCSIL® FOAM PLUG SYSTEM .....321**

Neil Alston, Jean-Luc Schmitter, Andrew Alcott, Russell Fry

**SELF-HEATING HAZARD INVESTIGATION OF CONVEYOR BELT RUBBER FINES.....331**

Coal Opertors' Conference

Basil Beamish, Jan Theiler

**EVALUATION OF THE RECOVERY OF BLOCK CAVE UNDERBREAK BY SUB LEVEL  
CAVING ..... 340**

Ellie Hawkins and Scott Sheldon

**FIBRE REINFORCEMENT SHOTCRETE IN COAL..... 353**

Barry Sturgeon

**HEALTH MONITORING OF MINING CONVEYOR BELTS ..... 359**

Shuvashis Dey, Omar Salim, Hossein Masoumi, and Nemaï Karmakar

**SAFETY ASPECTS OF DISPOSAL OF A MINE AND ABANDONED UNDERGROUND  
WORKINGS AND RISKS RESULTING FROM THE MINE DISPOSAL..... 367**

Radovan Kukutsch, Petr Waclawik, Jan Nemcik, Libin Gong

**INDEX ..... 378**



# MEASUREMENT OF IN-SITU COAL CLEAT COMPRESSIBILITY

Gelber Taco<sup>1</sup>, Alberto Kamenar<sup>2</sup>, Jeff Edgoose<sup>3</sup>

**ABSTRACT:** This paper presents a new and fast method to measure the *in situ* coal cleat compressibility in a vertical well. Traditional coal cleat compressibility is measured in a lab using small coal samples placed in a cell for its exposure to methane, temperature, pressure and stress representing the *in situ* conditions. This test takes about one year to complete, and coal heterogeneity and fragility make selection of representative samples difficult. While testing coals for permeability, borehole storage coefficients up to 100 times larger than expected were observed. This anomaly suggests a coal cleat compressibility effect and provides a foundation to develop a new method to measure coal cleat compressibility from borehole storage analysis. To assess the reliability of the method, 52 measurements were compared against internationally published lab data. The range of variability considered from both data sets presented a good correlation which validates the results applied from conventional well testing. This is a good result given that coal cleat compressibility changes with depth, coal rank and gas content. This simple method, developed from permeability testing technology, should help engineers understand coal permeability variations with gas drainage, stress, and geomechanical changes.

## INTRODUCTION

Coal Cleat Compressibility (CCC) is a difficult parameter to measure because it requires elaborate lab preparation and the results depend on a variety of environmental and coal properties. For example, Liu, and Harpalani (2014) measured the CCC and the matrix sorption compressibility of a coal from the San Juan Basin, New Mexico, using helium and methane. Helium is used to measure the elastic properties of the coal since it is not adsorbed in coal. Methane is used to assess the adsorption effect on compressibility. The results showed that the total coal compressibility is dominated by the CCC. With helium, the matrix sorption compressibility represents around 0.7 % of the CCC, and with methane, around 1.5 % of the CCC. For this reason, the CCC is also called coal compressibility. Seidle (2011, P 53) states that "coal compressibility values within a factor of two are regarded as excellent agreement". Similarly, coal cleat porosity is also difficult to measure with confidence because of its small value, usually in the order of 0.1% (Liu, et al., 2014).

The method proposed in this paper will simplify the CCC measurement using well testing techniques available in the industry with the advantage of being faster, determined *in situ* and applicable to the whole coal seam intersected by a well.

## TOTAL COAL COMPRESSIBILITY AND CCC

The total compressibility of an in-situ coal seam is a function of the rock matrix and fluids present in the system, Seidle (2011) as shown in equation (1)

$$c_t = S_w c_w + S_g c_g + c_f + c_d \quad (1)$$

---

<sup>1</sup> Principal Reservoir Engineer, Kamenar and Associates Pty Ltd. Email: [gtaco@kamenar.com.au](mailto:gtaco@kamenar.com.au) Tel: +61 (0) 8 9382 2918

<sup>2</sup> Managing Director, Kamenar and Associates Pty Ltd. Email: [alberto@kamenar.com.au](mailto:alberto@kamenar.com.au) Tel: +61 (0) 7 3278 1021

<sup>3</sup> Managing Director, Multiphase Technologies Pty Ltd, Email: [stratatek@bigpond.co](mailto:stratatek@bigpond.co) Tel: +61 (0) 428 571 609



Where:

- $c_t$  = Total system compressibility
- $S_w$  = Water saturation, fraction
- $c_w$  = Water compressibility
- $S_g$  = Gas saturation fraction
- $c_g$  = Gas compressibility
- $c_f$  = Fracture system pore compressibility or the CCC
- $c_d$  = Sorption compressibility (matrix sorption compressibility)

When the coal is under-saturated the cleats and butts contain 100 % water and no free gas, thus  $S_w=1$ , and  $S_g=0$ .

Moreover, the sorption matrix compressibility is very small when compared with the CCC. This is illustrated by the Liu and Harpalani (2014) study of the coal from the San Juan Basin, New Mexico where at 4.0 MPa the sorption compressibility constrained condition is 1.5% of the CCC, thus  $c_d \sim 0$ , and equation (1) becomes:

$$c_t \approx c_w + c_f \quad (2)$$

For the range of temperature and pressure encountered in coal seams, the water compressibility is in the range of  $4.35 \times 10^{-4} \text{ MPa}^{-1}$  ( $3.0 \times 10^{-6} \text{ psi}^{-1}$ ) to  $5.07 \times 10^{-4} \text{ MPa}^{-1}$  ( $3.5 \times 10^{-6} \text{ psi}^{-1}$ ). This is about 100 times smaller than the CCC. Therefore  $c_w \sim 0$  compared with  $c_f$  and equation (1) reduces to:

$$c_t \approx c_f \quad (3)$$

### WELLBORE STORAGE AND COMPRESSIBILITY

In well-testing, the wellbore storage is defined in two ways, Ramey (1965):

- The wellbore storage constant is expressed as a water volume between the isolating packers

$$C = V_u c_w \quad (4)$$

Where:

- $C$  = wellbore storage constant,  $\text{m}^3/\text{MPa}$  (bbl/psi)
- $V_u$  = wellbore water volume between packers,  $\text{m}^3$  (bbl)
- $c_w$  = Water compressibility,  $\text{MPa}^{-1}$  ( $\text{psi}^{-1}$ )

- And the wellbore storage constant is expressed in terms of surface flow rate “q”, time “t” and pressure “p”

$$C = \frac{qB\Delta t}{24\Delta p} \quad (5)$$

Where:

- $q$  = Surface rate  $\text{m}^3/\text{d}$  (bbl/d);  $B$  = Water volumetric factor

$\Delta t, \Delta p$  = Corresponding time - pressure increments, hr, KPa (hr, psi)

Well test interpreters use equation (4) to estimate the wellbore storage constant  $C$  from the linear plot of pressure versus time as shown in Figure 1. The line through the beginning of the shut-in points defines the ratio  $\Delta t/\Delta p$ ; thus, the wellbore storage constant is estimated inserting the flow rate  $q$  and the volumetric factor  $B$  in equation (5).

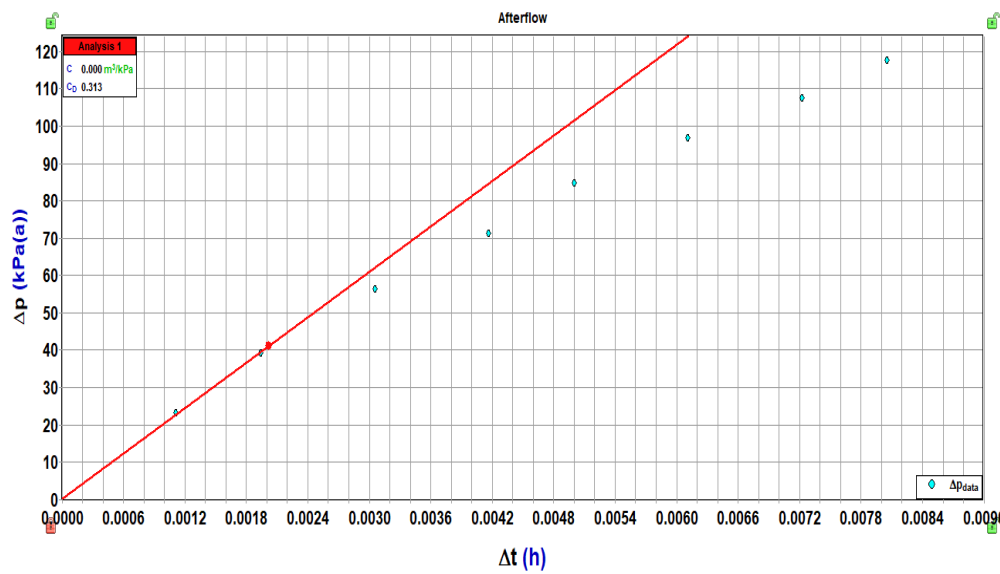


Figure 1: Linear plot of  $\Delta p$  versus  $\Delta t$ .

Another approach widely used in well testing is the use of the log-log plot of pressure versus time. Equation (5) expressed in logarithmic form is:

$$\log \Delta p = \log \Delta t + \log \frac{qB}{24C} \tag{6}$$

This is a classical linear equation of  $\log \Delta p$  versus  $\log \Delta t$  with a slope of 1 and wellbore storage  $C$  included in the intersection with the  $\log \Delta p$  axis. Figure 2 clearly illustrates this slope at the beginning of shut-in where the wellbore storage is dominant. Complete examples of wellbore storage analyses are presented in page 7 of Taco G, Kamenar A and Edgoose J (2012).

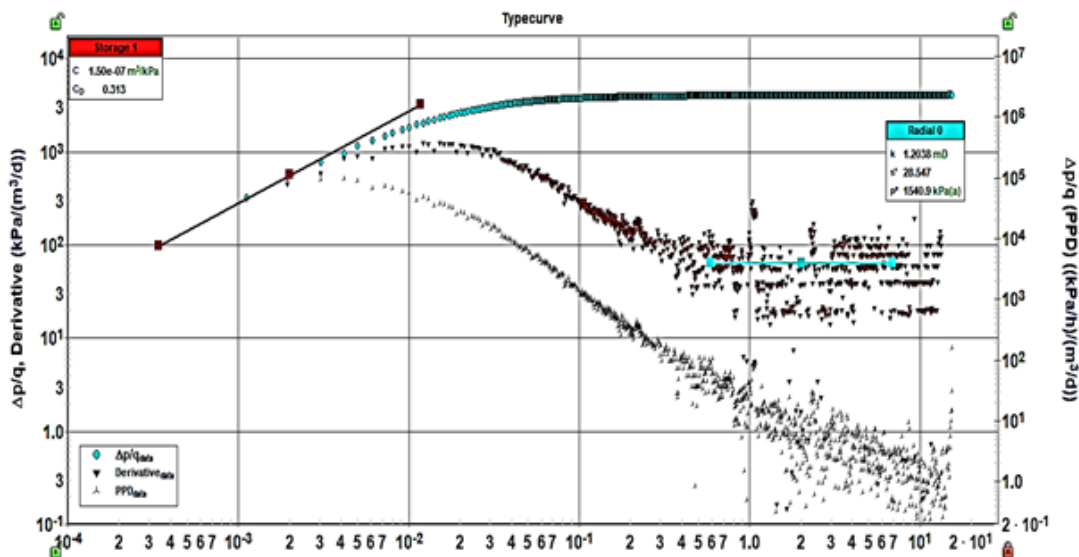


Figure 2: Log-log plot showing the wellbore storage and the radial flow.

**Wellbore storage constant with equations (4) and (5)**

Earlougher (1977) stated that results from equations (4) and (5) should agree fairly well. When this match does not occur, further investigations are required. He also noted that wells highly stimulated or fractured, wells producing at high gas-liquid ratios and wells used for viscous fluid injection often have much larger wellbore storage coefficients from equation (5) than those predicted from equation (4).

It has been consistently observed when testing coal permeability that results from equation (4) are appreciably higher than equation (5) in spite of producing clean water with no gas, having a smooth wellbore in-gauge and prior to any fracture stimulation in the well.

Table 1 shows the wellbore storage results of 26 coal seams where the operator ran sequentially one Drill Stem Test (DST) and one Injection Falloff Test (IFT) in each seam totalling 52 tests in Taco G, Kamenar A and Edgoose J (2012),. Column 5 presents the C results with equation (4) and columns 7 and 9 results derived from equation (5) using DST and IFT data respectively. Figure 3 shows graphically these  $V_u$  results where C values from equation (4) are appreciably higher than that of equation (4).

**Table 1: Wellbore storage and wellbore volumes from DST and IFT**

1	2	3	4	5	6	7	8	9	10
Coal Seam	Packer Spacing (m)	Wellbore Caliper (mm)	Water Comp, $C_w$ (1/MPa)	Wellbore C, Equ 3 ( $m^3/KPa$ )	Wellbore $V_u$ ( $m^3$ )	DST C, Equ 4 ( $m^3/KPa$ )	DST $V_u$ ( $m^3$ )	IFT C, Equ 4 ( $m^3/KPa$ )	IFT $V_u$ ( $m^3$ )
1	7.86	107.4	4.55E-04	3.24E-08	0.07	1.40E-07	0.31	8.50E-07	1.87
2	14.10	116.5	4.50E-04	6.76E-08	0.15	2.53E-06	5.63	4.28E-06	9.50
3	7.86	110.0	4.63E-04	3.46E-08	0.07	2.77E-07	0.60	2.31E-07	0.50
4	7.86	95.5	4.51E-04	2.54E-08	0.06	1.75E-07	0.39	2.15E-07	0.48
5	6.80	116.0	4.51E-04	3.24E-08	0.07	1.18E-06	2.61	5.58E-06	12.37
6	10.55	105.0	4.54E-04	4.15E-08	0.09	1.08E-06	2.38	4.62E-06	10.18
7	10.55	117.0	4.57E-04	5.18E-08	0.11	5.51E-07	1.21	5.77E-07	1.26
8	6.86	100.0	4.54E-04	2.45E-08	0.05	4.29E-06	9.45	7.24E-06	15.94
9	10.86	100.0	4.55E-04	3.88E-08	0.09	3.63E-07	0.80	3.50E-07	0.77
10	13.55	100.0	4.45E-04	4.74E-08	0.11	1.45E-07	0.33	2.03E-07	0.46
11	10.30	135.0	4.49E-04	6.62E-08	0.15	3.69E-07	0.82	1.67E-06	3.73
12	10.30	135.0	4.44E-04	6.55E-08	0.15	5.77E-07	1.30	6.99E-06	15.75
13	10.30	131.0	4.41E-04	6.12E-08	0.14	4.70E-07	1.07	1.54E-06	3.50
14	13.81	132.0	4.50E-04	8.50E-08	0.19	4.44E-07	0.99	9.95E-07	2.21
15	13.81	138.0	4.46E-04	9.21E-08	0.21	5.41E-07	1.21	7.49E-07	1.68
16	10.81	95.5	4.55E-04	3.52E-08	0.08	1.55E-06	3.41	9.86E-07	2.17
17	10.81	96.0	4.50E-04	3.52E-08	0.08	1.44E-06	3.20	4.48E-07	1.00
18	13.81	135.0	4.49E-04	8.88E-08	0.20	3.25E-07	0.72	2.04E-07	0.45
19	15.81	135.0	4.44E-04	1.00E-07	0.23	2.86E-07	0.64	4.40E-07	0.99
20	13.81	135.0	4.42E-04	8.74E-08	0.20	1.82E-07	0.41	2.89E-07	0.65
21	10.55	95.0	4.54E-04	3.39E-08	0.07	1.49E-07	0.33	8.78E-07	1.93
22	10.55	95.0	4.50E-04	3.37E-08	0.07	2.08E-07	0.46	1.17E-06	2.61
23	10.55	95.0	4.54E-04	3.40E-08	0.07	1.34E-06	2.96	2.61E-06	5.75
24	10.55	95.0	4.50E-04	3.37E-08	0.07	1.26E-07	0.28	1.84E-07	0.41
25	7.55	93.0	4.61E-04	2.37E-08	0.05	5.90E-07	1.28	9.48E-07	2.05
26	6.86	98.4	4.66E-04	2.43E-08	0.05	1.48E-06	3.17	4.45E-06	9.42

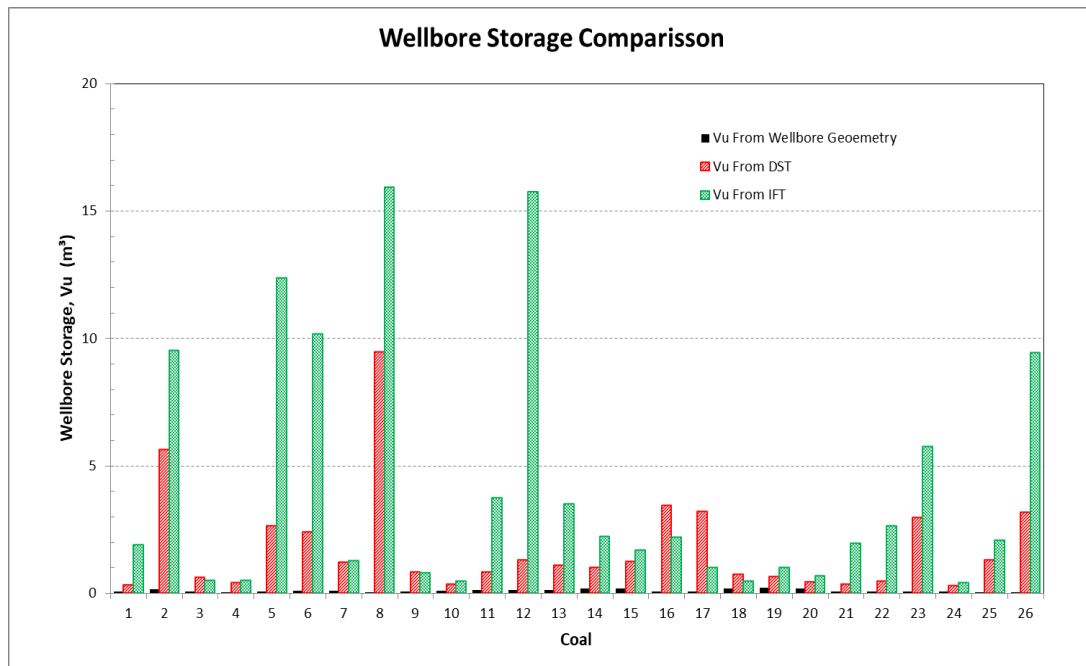


Figure 3: Wellbore storage from: Wellbore Geometry, DST and IFT

**The CCC calculation rationale**

It is likely that the CCC causes results from equation (5) to be higher than equation (4). Accordingly, calculating the *in-situ* CCC of coal seams requires scrutiny of the physics of both equations.

Cleat compressibility is commonly known as pore compressibility Hollup (1992). Reservoir engineers, on the other hand, refer to it as “formation compressibility” which is defined as the ratio of pore volume change caused by pressure change in a determined bulk volume. Based on these concepts, the rationale to calculate CCC from wellbore storage analysis of coal seam well testing follows:

The total coal isothermal compressibility is:

$$c_t = \frac{1}{V_t} \frac{\Delta V_t}{\Delta p} \tag{7}$$

Where:

$V_t$  = Coal bulk volume or volume of reference for compressibility

$c_t$  = Coal bulk volume compressibility

$\Delta V_t$  = Coal volume change caused by applying a  $\Delta p$  pressure

The definition of CCC is:

$$c_f = \frac{1}{\emptyset} \frac{\Delta \emptyset}{\Delta p} \tag{10}$$

Where:

$c_f$  = Fracture system pore compressibility or cleat compressibility

$\emptyset$  = Cleat porosity

From equations (3), (7) and (10) it can be inferred that the total coal compressibility is a good approximation of the CCC as follows:

$$c_t = \frac{1}{V_t} \frac{\Delta V_t}{\Delta p} \approx \frac{1}{\emptyset} \frac{\Delta \emptyset}{\Delta p} = c_f$$

That is:

$$c_f \approx \frac{1}{V_t} \frac{\Delta V_t}{\Delta p} \quad \text{or the CCC.} \quad (11)$$

Equation (11) relates the total coal deformation ( $\Delta V_t$ ) caused in a coal volume ( $V_t$ ) as a result of applying a pressure pulse ( $\Delta p$ ). Therefore, if we know these *in-situ* values, we can calculate the in-situ CCC. The following sections discuss the calculation of the right-hand side variables of equation (11) from well testing data.

### Calculation of $\Delta V_t$

To estimate  $\Delta V_t$  - the total coal volume change caused by the pressure change  $\Delta p$  - a modification of equation (4) is required to include the wellbore volume between packers,  $V_u$ , and the coal deformation,  $\Delta V_t$ , as follows:

$$C = (V_u + \Delta V_t)c_w \quad (12)$$

This equation represents the total equivalent volume of water required to generate the higher wellbore storage calculated with equation (5). The left-hand side of Figure 4 illustrates the concept of  $V_u$  and the right-hand side the  $\Delta V_t$ .

Taking out  $\Delta V_t$ :

$$\Delta V_t = \frac{C}{c_w} - V_u \quad (13)$$

In this equation all the right-hand variables can be measured on conventional borehole testing. To calculate the wellbore volume between packers,  $V_u$ , we use a cylinder volume with a diameter equal to the wellbore calliper, obtained from calliper log, and the height equal to the packer spacing.

For the wellbore storage,  $C$ , the early points of the linear or log-log plots of  $\Delta t$  were used,  $\Delta p$ , values collected during the test as Figure 1 and Figure 2 illustrate. To estimate the water compressibility,  $c_w$ , A correlation of water compressibility was used as a function of temperature, pressure and water salinity. With these values the  $\Delta V_t$  was calculated according to equation (13).

### Calculation of $\Delta p$

Like the  $\Delta V_t$  parameter, the  $\Delta p$  is also obtained from the wellbore storage. It has been observed that at the very early time of wellbore storage the pressure points line up with a straight line that crosses the origin. The slope of this line defines the wellbore storage as illustrated in Figure 1.

After the first few points line up, they start to depart from the straight line. These departing points represent the transition from wellbore storage to radial flow. The points lining up along the line represent the instantaneous coal elastic response to the pressure pulse of shut-in or falloff (DST or IFT respectively). From this departing point, the  $\Delta p$  is taken for the CCC calculation.

This elastic response is a rapid phenomenon, only noticeable when the isolating packers and pressure gauge are very close to the coal seam and the pressure recorder is set to capture high resolution of time steps. In Figure 1, the pressure points departed the red line at 7 secs (0.002 hrs) from commencement of the pressure pulse and when the  $\Delta p$  was 41.37 KPa (6.0 psi).

Figure 5 shows another example where the pressure points depart at 3 secs (0.00083 hrs) with a  $\Delta p$  of 28.96 KPa (4.2 psi)

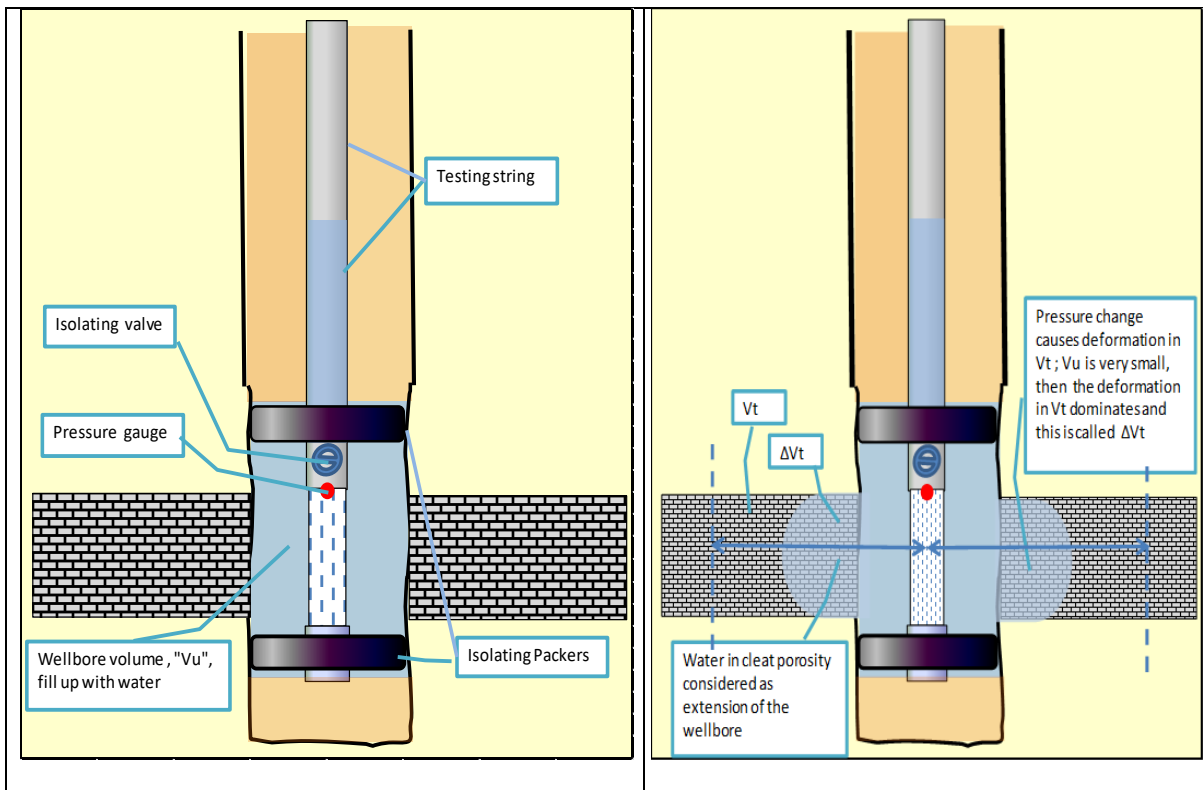


**Figure 4: Water inside the cleat porosity behaves like an extension of the wellbore and communicates pressure constituting the  $\Delta V_t$**

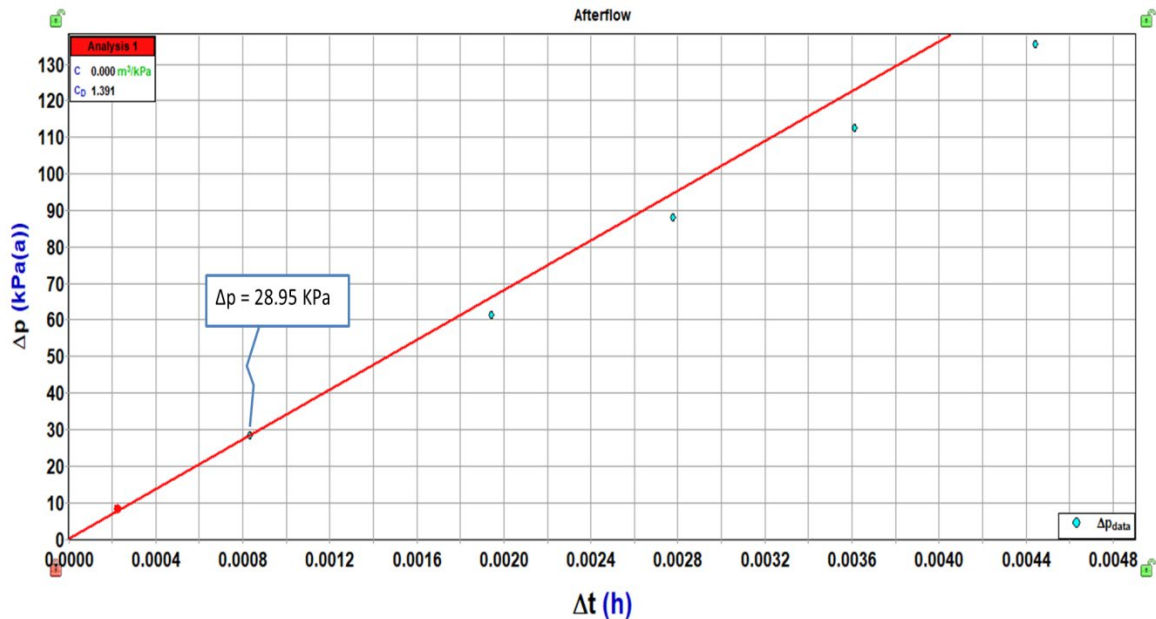


**Figure 5: Linear plot of  $\Delta p$  versus  $\Delta t$  on a DST. The  $\Delta p$  at separation of the line is 4.2 psia**

### Calculation of $V_t$

In the lab, the  $V_t$  of a coal sample is directly measured being the bulk volume. The equivalent bulk volume *in-situ* during well testing would be a large coal annulus cylinder where the inner cylinder represents the borehole and the external cylinder the bulk coal volume affected by the pressure pulse. The left-hand side of Figure 6 shows this concept and the right-hand side its application to a coal seam during a test.

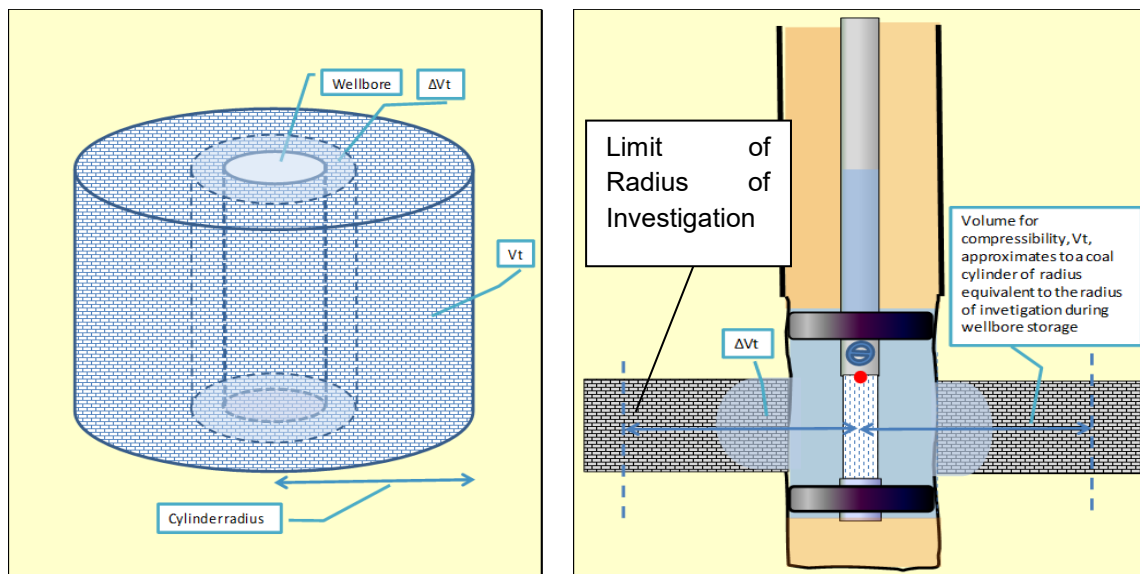


**Figure 6: To estimate the coal volume reference,  $V_t$ , we use a cylinder of coal with radius equivalent to the radius of investigation developed during the wellbore storage.**

From the external cylinder we know the height, which is the coal seam thickness, but we don't know the radial dimension. Intuitively we could calculate this radius invoking proportionality between the wellbore storage duration and the radius of that cylinder, i.e. the larger the cylinder radius the larger the wellbore storage.

The radius of investigation in well testing is a function of permeability and time, the former measured on IFT or DST well tests, the latter calculated at a particular point on the wellbore storage pressure derivative plot.

Figure 7 shows a typical wellbore storage pressure derivative plot and the points to choose for the time calculation of the external cylinder radius for  $V_t$ . The IFT is selected at the maximum of the wellbore storage hump and the DST at 1/3 within that maximum and the beginning of the radial flow as Figure 7 indicates. Thus, with this time and the permeability, the cylinder radius of  $V_t$  is calculated. This approach gives the best calibrated results on the 52 tests.

#### **Justification for the selected times, Figure7**

There are no laboratory measurements of CCC on the coals tested in Table 2 to calibrate the results derived from borehole testing; for this reason, these results are statistically validated with published laboratory values available in the literature.

Seidle (2011) published in his book 13 CCC values from different basins, ages and ranks from around the world. These values range from  $0.0435 \text{ MPa}^{-1}$  to  $0.363 \text{ MPa}^{-1}$  ( $0.0003 \text{ psi}^{-1}$  to  $0.0025 \text{ psi}^{-1}$ ). Figure 8 shows these values in a logarithmic probabilistic grid to assess the sample distribution and are used as the reference to calibrate the values generated with the proposed method.

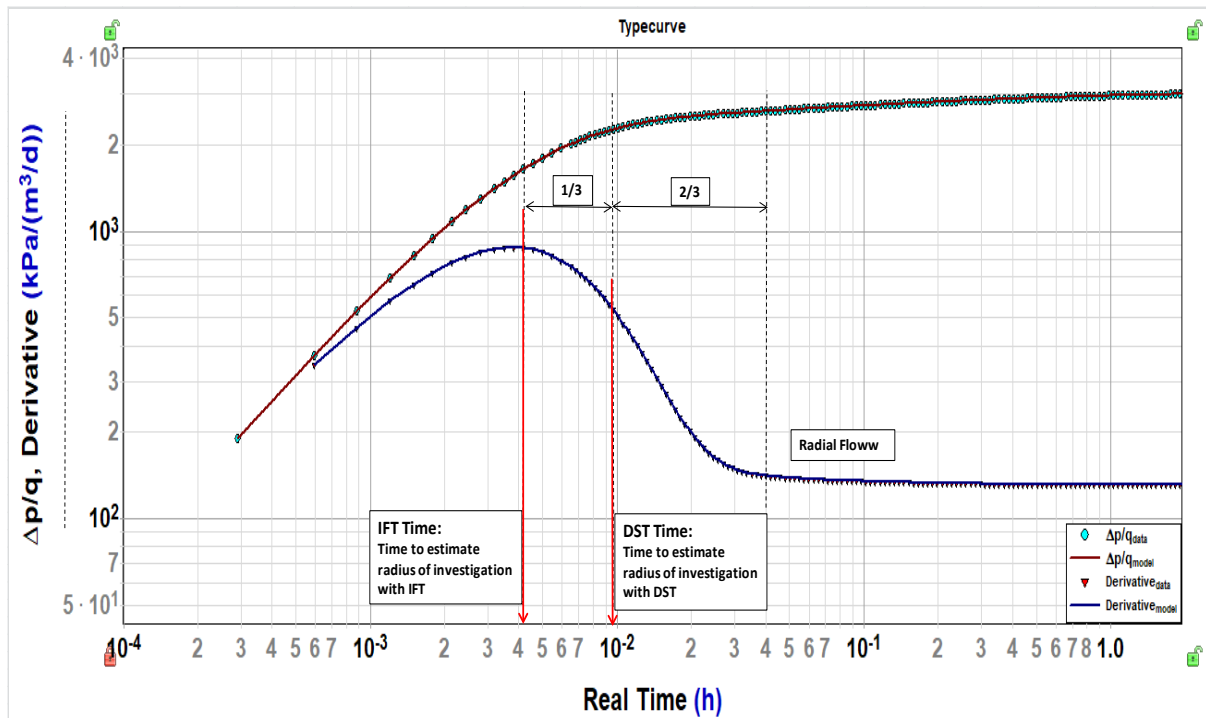


Figure 7: Selected times for the radius of investigation to calculate the cylinder radius for  $V_t$

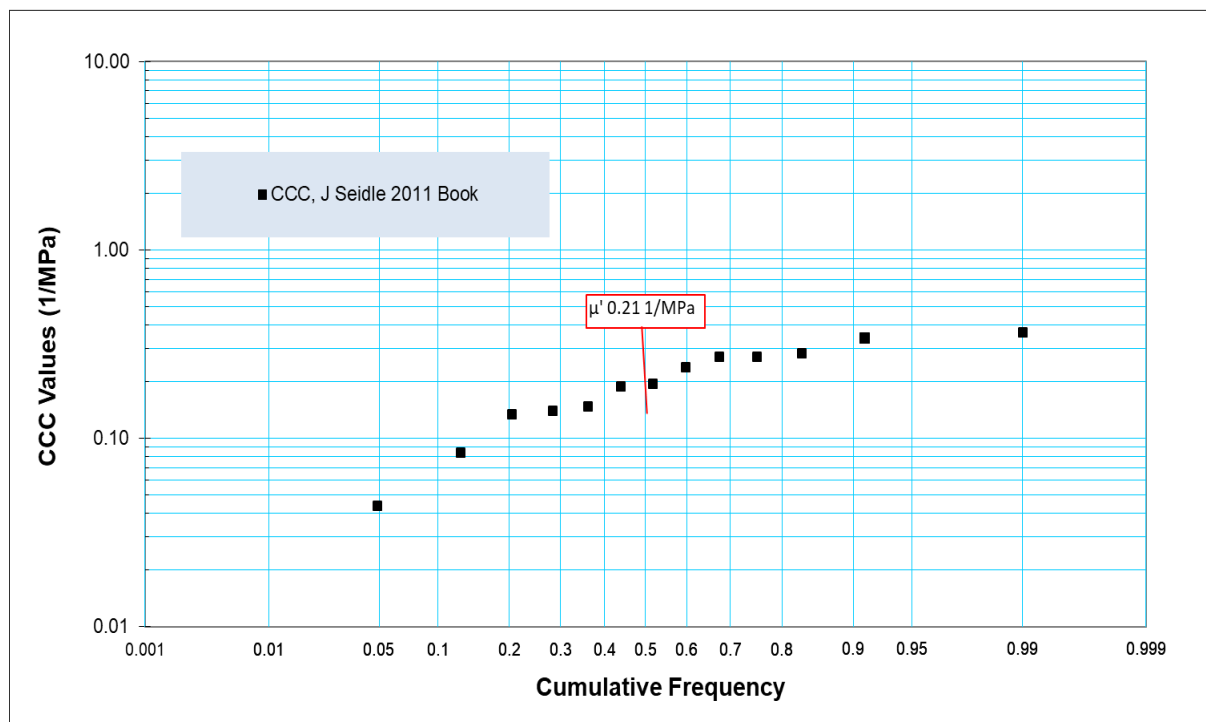


Figure 8: CCC cumulative distribution, Seidle 2011 lab data

Figure 9 shows the CCC data from IFT, DST and Seidle (2011) which matches very well up to a cumulative frequency of 80%. Thus, the values obtained using the proposed method are reasonable as they fall within the expected range of data obtained from lab analyses.



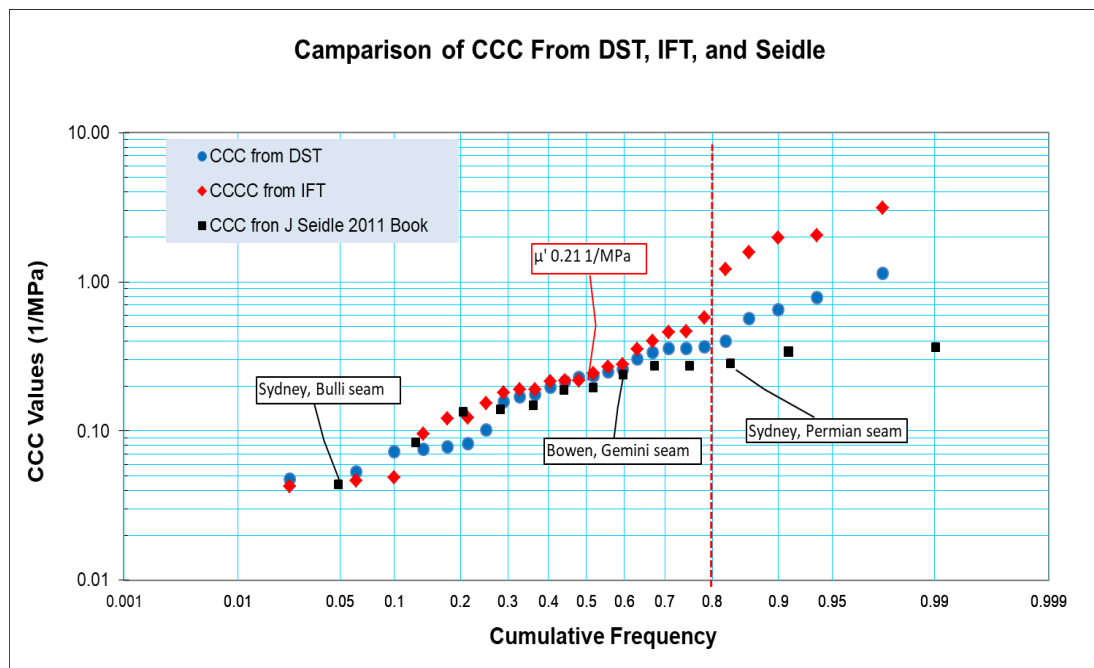


Figure 9: CCC cumulative distribution from DST, IFT and Seidle data

Also note that Seidle's data includes coals from North Queensland and Sydney which are labelled to compare with the other results showing a good match. This is a good outcome given that coal cleat compressibility changes with depth, coal rank and gas content. The reason for different time choices from the pressure derivative for the IFT and DST data is the pressure pulse direction during the tests. The pressure for the IFT is increased in front of the coal face above the reservoir pressure to inject water into the coal seam before the well is shut-in for falloff pressure until the pressure equalises with the reservoir pressure. In contrast, the pressure in the DST is reduced below the reservoir pressure so that water is produced from the coal seam and then is shut-in for built up pressure until pressure equalises with the reservoir pressure. These different pressure actions cause different responses from the coal seam, with different external radius of coal cylinder for each  $V_t$  calculation.

## RESULTS DISCUSSION

The previous sections showed the calculation of  $\Delta V_t$ ,  $V_t$  and  $\Delta p$ . Using these values equation (10) is solved to determine the CCC. This procedure has been applied to 26 DSTs and 26 IFTs run sequentially in 26 coal seams making a total of 52 tests. Table 2 presents the CCC results in columns 7 and 12 from DST and IFT data respectively, and also the  $\Delta V_t$ ,  $V_t$ ,  $\Delta p$  values and the permeability and coal thickness for each test. Figure 10 shows the DST values arranged in increasing order and collated with Seidle (2011) data. Note that the CCC values are in logarithmic scale so that the small values are observed better.

Note that in some cases the DST and IFT are appreciably different. The reason for this is the likelihood of a very small amount of gas being "produced" during the DST test. At the time of the testing operation, the degree of gas saturation of the seams was unknown. It is possible that some wells were tested with the reservoir pressure close to the coal desorption pressure, particularly those wells near a mining operation. These may have released some gas during the DST drawdown affecting the wellbore storage in the IFT falloff and hence the CCC calculation. The tests where gas bubbles were detected during the DST drawdown are labelled in Figure 10.

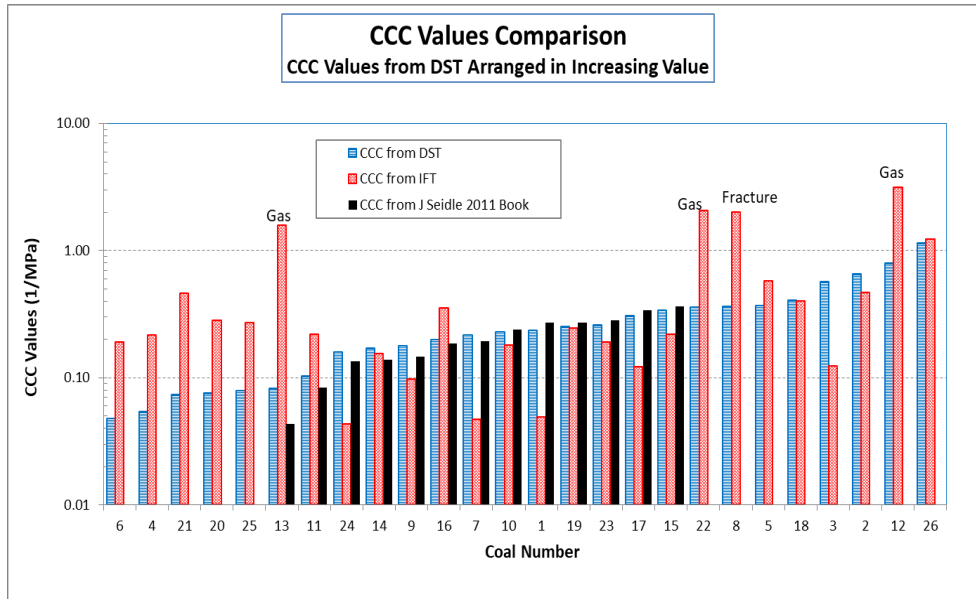


Figure 10: CCC values from DST and IFT with respect to DST increased values collated with J Seidle data

Table 2: Cleat compressibility results from DST and IFT

1	2	3	4	5	6	7	8	9	10	11	12
Coal	Coal	DST					IFT				
Seam	Thick.	Perm	$V_t$	$\Delta V_t$	$\Delta p$	CCC	Perm	$V_t$	$\Delta V_t$	$\Delta p$	CCC
						$C_f$					$C_f$
	(m)	(mD)	(m <sup>3</sup> )	(m <sup>3</sup> )	(KPa)	(1/MPa)	(mD)	(m <sup>3</sup> )	(m <sup>3</sup> )	(KPa)	(1/MPa)
1	4.82	84.56	48.50	0.24	20.69	0.2355	21.81	354.94	1.80	103.43	0.0490
2	9.03	4.95	207.59	5.48	40.67	0.6494	10.75	649.32	9.35	31.03	0.4642
3	4.33	6.45	23.24	0.52	39.65	0.5691	3.65	50.36	0.42	68.95	0.1223
4	5.31	3.06	112.36	0.33	55.16	0.0536	2.24	51.40	0.42	37.92	0.2164
5	4.31	14.48	111.02	2.54	62.06	0.3684	6.56	1287.69	12.30	16.55	0.5772
6	6.29	37.90	316.28	2.28	151.69	0.0476	37.00	3071.75	10.09	17.24	0.1906
7	5.63	14.56	30.65	1.09	165.48	0.2153	12.83	324.51	1.15	75.85	0.0467
8	4.34	9.07	492.58	9.40	53.09	0.3594	4.69	683.34	15.89	11.72	1.9834
9	7.20	6.96	73.10	0.71	55.16	0.1765	0.86	205.90	0.68	34.48	0.0963
10	6.43	0.52	20.73	0.22	46.20	0.2292	0.41	62.70	0.35	31.03	0.1805
11	4.94	3.15	119.68	0.68	55.16	0.1023	3.48	451.10	3.58	36.54	0.2173
12	7.93	2.18	53.03	1.15	27.58	0.7872	0.73	363.05	15.60	13.79	3.1176
13	6.68	1.16	327.27	0.93	34.48	0.0822	0.42	71.71	3.36	29.65	1.5827
14	7.02	4.65	75.45	0.80	62.06	0.1706	2.72	446.30	2.02	29.65	0.1528
15	6.31	4.89	108.34	1.01	27.58	0.3369	2.57	208.92	1.47	32.41	0.2178
16	3.55	36.20	203.66	3.34	82.74	0.1980	25.66	65.92	2.09	89.64	0.3539
17	7.03	16.88	140.30	3.12	73.09	0.3043	2.45	525.18	0.92	14.48	0.1208
18	4.18	9.62	9.96	0.53	131.01	0.4033	5.09	11.86	0.26	55.16	0.3992
19	7.47	2.45	28.51	0.42	58.61	0.2496	1.85	108.52	0.76	28.96	0.2438
20	6.98	1.66	40.90	0.21	68.95	0.0756	1.01	95.02	0.46	17.24	0.2790
21	8.34	1.18	77.26	0.25	44.82	0.0729	0.40	125.51	1.86	32.41	0.4573
22	6.60	0.06	16.96	0.39	64.12	0.3565	0.05	52.85	2.54	23.44	2.0500
23	7.79	4.19	460.41	2.89	24.13	0.2598	3.81	511.92	5.67	58.61	0.1891
24	5.45	0.35	20.94	0.20	62.06	0.1571	0.12	52.71	0.33	148.24	0.0427
25	1.40	75.95	126.69	1.23	124.11	0.0780	50.63	45.20	2.00	165.48	0.2681
26	5.00	5.65	23.34	3.12	117.22	1.1405	2.53	185.27	9.36	41.37	1.2221

Furthermore, it is interesting that both CCC and reservoir permeability present lognormal distributions and this has contributed to the good correlation between DST and IFT result with Seidle data as Figures 9 and 10 illustrate. Also, this confirms the correct time location on the pressure derivative plots, as shown in Figure 7, for the calculation of the radius of investigation.

It was noted that the CCC and other coal properties measured in the lab are sample size dependent, [Massarotto (2002)]. The bigger the core sample the more reliable the results. Furthermore, the coal rank, maturity and tectonic stresses also affect the compressibility. Un-stressed coals have high compressibility, while stressed coals have much lower compressibility. Therefore, the measurement of CCC *in situ* that includes the whole seam will assist the description of other geomechanical parameters at the coal seam scale. The following section illustrates how the CCC can be used to estimate the Young Modulus of a whole coal seam.

### Young and Bulk Modulus calculation from the CCC

Liu and Harpalani (2014) presented an equation that relates the Bulk compressibility and the CCC:

$$C_f = \frac{1}{\phi} [C_b - (1 - \phi)C_s] \quad (14)$$

Where:

- $C_b$  = Bulk compressibility
- $C_f$  = Coal Cleat Compressibility
- $\Phi$  = Cleat porosity (effective porosity)
- $C_s$  = Solid matrix compressibility

Taken out the Bulk compressibility,

$$C_b = \phi(C_f - C_s) + C_s \quad (16)$$

$C_s$  is very small comparing to  $C_f$ , thus  $C_s \sim 0$ , thus:

$$C_b \approx \phi C_f \quad (17)$$

The Bulk compressibility is the reciprocal of Bulk Modulus "K" then

$$c_b = \frac{1}{K} \quad (18)$$

The geomechanical parameters Bulk modulus, Shear modulus and Poisson Ratio are intrinsically related through the equations (18)

$$K = \frac{E}{3(1-2\nu)} \quad (19)$$

Where:

- $K$  = Bulk modulus
- $E$  = Young modulus
- $\nu$  = Poisson Ratio

The cleat porosity  $\Phi$ , is small and difficult to measure; it is often estimated by history matching the water production rates against different values of cleat porosity. Liu and Harpalani (2014) searched the literature for typical values of  $\Phi$  encountering that ranged from 0.05% to 1.0%.

On the other hand, Seidle (2011, P 52) presented values of Young modulus and Poisson Ratio collected also from the literature; with these values and using equation (17) the Bulk Modulus was calculated as Table 3 shows:

Similarly, Bulk Modulus and Young Modulus were evaluated from the CCC obtained from well testing, see Table 2, for which equations (15), (16) and (17) were used assuming Poisson Ratios of  $\nu = 0.3, 0.2$ ; cleat porosity  $\Phi$  of 0.5%, 0.1%, and  $C_s = 0$ . The results together with the values of Table 3 above are

presented in Figure 11. It appears a reasonable match between Seidle laboratory data and the ones derived from CCC data. Note that the majority of well testing data of Table 2 comes from North Queensland coals. Also note that the CCC is derived from field measurements in the whole coal seam column and when using accepted geomechanical equations it provides reasonable and practical results to assess other geomechanical parameters that could be applied to new or existing coal projects.

**Table 3, Bulk Modulus Calculated with equation (17)**

Table 2-11, John Seidle (2011, P 52)					Calculated, Equ, (17)
Basin	Coal	Rank	Young's Module	Poisson's Ratio	Bulk Modulus
			MPa		MPa
na <sup>a</sup>	Na	na	2,689	0.32	2,490
Warrior <sup>b</sup>	Blue Creek		2,758	0.35	3,064
San Juan <sup>c</sup>	Fruitland	med.vol	3,379	0.30	2,815
San Juan <sup>d</sup>	Fruitland	med.vol	5,585	0.35	6,206
WCSB <sup>e</sup>	various	sub.B/Hi-vol.C	2,999	0.30	2,499
na <sup>f</sup>	Na	na	1,000	0.20	555
na <sup>g</sup>	Na	na	13,997	0.4	23,328
San Juan <sup>h</sup>	Fruitland	hi-vol <sup>A</sup>	3,592	0.21	2,065
San Juan <sup>i</sup>	Fruitland	med.vol	4,482	0.32	4,150
Piceane <sup>j</sup>	Cameo	med.vol	2,413	0.31	2,117
WCSB <sup>k</sup>	Na	na	1 - 5,000	0.26 -0.48	

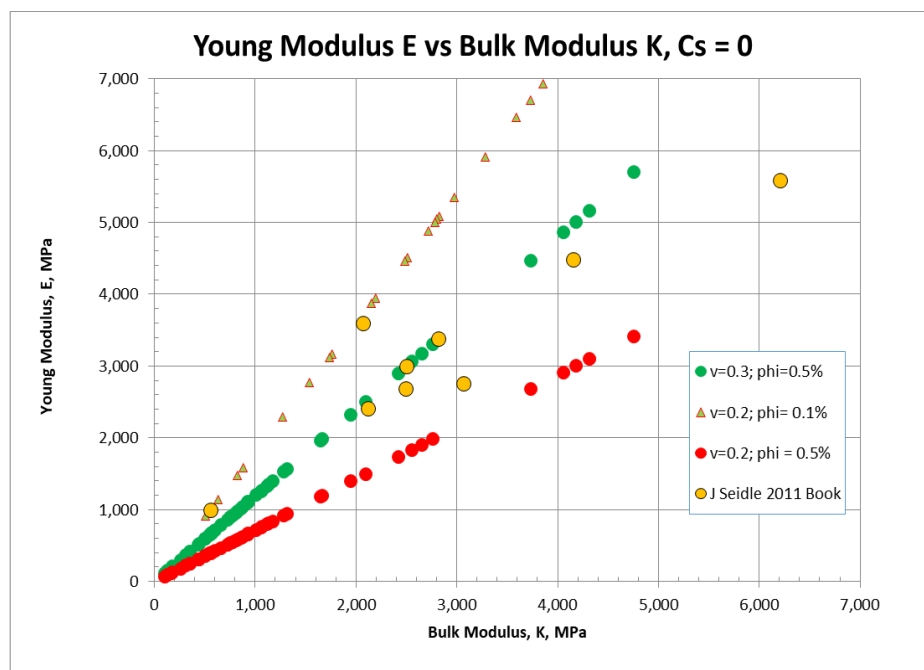


**Figure 11: Young and Bulk Modulus evaluated from CCC from well testing using  $C_s = 0$ . Also, Bulk Modulus calculated from J Seidle Table 3 (2011, P 52)**

### CONCLUSIONS

This practical method, developed from permeability testing technology, should help engineers preparing better simulation models for mine degassing and improve permeability measurements and material balance calculations. Furthermore, it will assist wall and roof stability assessment and fracturing design

by having better geomechanical models. Finally, it is envisaged that the potential application of this method to estimate *in situ* gas desorption pressure to validate Langmuir isotherms.

## REFERENCES

- Ramey, H J, Jr.,1965. Non-Darcy Flow and Wellbore Storage Effects in Pressure Build Up and Drawdown of Gas Wells, J Pet Tech, Feb, Trans, AIME, 234, pp 223 – 233.
- Robert C Earlougher Jr. 1977. Advances in Well Test Analysis. Henry L. Doherty Memorial Fund of AIME, SPE of AIME, Dallas
- Seidle, J, 2011. Fundamentals of Coalbed Methane Reservoir Engineering, Penn Well Corporation Tulsa Oklahoma, USA.
- Taco, G, Kamenar and Associates. Kamenar, A. Kamenar and Associates. Edgoose J., 2010. Multiphase Technologies. "Comparison of Permeabilities and Skin Damages Results from Flow Build-up and Injection Falloff Tests in CBM Reservoirs" Paper SPE 133665-MS,
- Taco, G, Kamenar and Associates. Kamenar, A. Kamenar and Associates. Edgoose J, 2012. Multiphase Technologies Pty Ltd. "Comparison of DFIT, DST and IFT Permeabilities in CBM Reservoirs" Paper SPE 158297 – MS, 7pages.
- Kamal M M, 2009. Transient Well Testing. Henry L. Series, Monograph Volume 23. Society of Petroleum Engineers, Richardson Tx. USA.
- Diamond. W. P, 1987. Underground Observations of Mined -Through Stimulations Treatments of Coalbeds. Quart Review Methane from Coal Seam Tech, Volume 4, Number 4 (Jun).
- Mayerhofer, M.J. Ehlig-Economides, C.A and Economides, M.J. 1995. "Pressure-Transient Analysis of Fracture-Calibration Tests," JPT, March, pp. 229-234.
- Liu Shimin, 2014, Pennsylvania State University; Harpalani Satya, Southern Illinois University, "Compressibility of Sorptive Porous Media: Part 1. Background and Theory", AAPG Bulletin, V 98, No.9, September. PP 1761 -1772.
- Liu Shimin, 2014. Pennsylvania State University; Harpalani Satya, Southern Illinois University, "Compressibility of Sorptive Porous Media: Part 2. Experimental Study on Coal", AAPG Bulletin, V 98, No.9, September, PP 1773 – 1788.
- Kamenar A, Kamenar Associates, Taco G, Kamenar Associates. Edgoose J, Multiphase Technologies Pty Ltd. "How to Plan a Safe and Successful Permeability Test Program in Coal Seams" 17th Coal Operators Conference. University of Wollongong, Australia, 2017.
- Longjun Xu, Chenglun Liu, XuefuXian, Daijun Zhang, 1999. Compressibility of Coal Matter and Coal Pore, Institute of Mining Engineering Physics, Chongqing University, Chongqing 400044, People's Republic of China,
- Massarotto, P, 2002. 4-D Coal Permeability under True Triaxial Stress and Constant Volume Conditions, PhD Thesis, University of Queensland, Australia.
- Hollup, V and Schafer, P., 1992. A guide to coal bed methane operations, Gas Research Institute. GRI Reference No. GRI-94/0397, Pages 4.36, 5.8, 5.9.

# DETERMINING COAL DIRECTIONAL MECHANICAL PROPERTIES USING TRUE TRIAXIAL TESTING FACILITY

Zhongwei Chen<sup>1</sup>, Mehdi Serati<sup>2</sup>, Mutaz El-Amin Mohmoud<sup>3</sup>

**ABSTRACT:** Knowledge of coal mechanical properties and strength is critical in modelling and understanding pillar stability, gateroads stability, gas drainage borehole integrity as well as coal responses to hydraulic fracturing stimulation. However, due to the complexity of coal structures and difficulties in obtaining decent coal specimens, measurements of coal mechanical properties have been limited to the application of traditional triaxial and UCS tests, which in turn has shown adverse influence on the design confidence and reliability in practice. In addition, coal is an anisotropic material and such conventional testing techniques are clearly not capable of directly capturing coal anisotropic features. In this work, a true tri-axial testing facility was used to quantify coal strength and its anisotropic characteristics. Eight 50 mm side cube coal blocks were prepared and three types of tests were implemented. The proposed testing procedure measured successfully the mean values of coal young's moduli in three different x, y and z (vertical) directions as 1,025 MPa, 1,887 MPa, and 2,543 MPa, respectively, which gives the ratio of 1.00: 1.84: 2.48. The mean Poisson's ratio is also measured as 0.098, 0.038, and 0.091 in x, y and z directions. Coal strength follows the Hoek-Brown criterion reasonably well, and the m value is found to be 23.9. These findings suggest that the implementation of true-triaxial testing techniques for coal mechanical properties can effectively capture its anisotropic characteristics, which could enhance analysis confidence for future designs.

## INTRODUCTION

Underground coal mining operations are subjected to a diverse range of tectonic and mine-induced stresses throughout their lifetime (M. Li et al., 2016). Therefore, proper understanding of coal strength over time is critical for the reliable geotechnical design of pillar size, roof and rib support, and gateroads short-term and long-term stability (Bieniawski, 1968; Liu et al., 2019). Coal is characterized as a heterogeneous, anisotropic and porous medium replete with discontinuities, cracks, cleats, bedding plates and faulty zones that control its microstructure (Figure 1). These complex microstructures (mainly with various properties in different directions) determine coal static and time-dependent properties and its ultimate response to stress and excavations (Hudson and Harrison, 1997).

Despite proven and well-known directionally dependent properties in coal, relatively limited efforts have been carried out in the literature to investigate the influence of material heterogeneity on stress-strain redistribution and its impact on coal failure behaviour under uniaxial compressive loading (Zhao et al., 2014). The compressive strength and deformation characteristics of coal have therefore been mainly limited to the application of conventional triaxial apparatus (Barla, Barla, and Debernardi, 2010; Perera, Ranjith, and Choi, 2013; Ranjith and Perera, 2011; Somerton, Söylemezoğlu, and Dudley, 1975), but with a few recent exemption studies (Dexing et al., 2018; Li, et al., 2019). In addition, due to the anisotropic nature of the coal, the traditional triaxial and UCS testing methods are no longer capable of directly capturing the mechanical parameters of coal. Moreover, the effect of the intermediate principal stress on the coal deformational analysis is ignored under the conventional triaxial apparatus. With

---

1. Senior Lecturer, The University of Queensland. Email: [zhongwei.chen@uq.edu.au](mailto:zhongwei.chen@uq.edu.au) Tel: +61 7 3365 3742

2. Lecturer, The University of Queensland. Email: [m.serati@uq.edu.au](mailto:m.serati@uq.edu.au) Tel: +61 7 3365 3911

3. PhD Student, The University of Queensland. Email: [m.mahmoud@uq.net.au](mailto:m.mahmoud@uq.net.au) Tel: +61 7 3365 3742

these motivations in mind, this study aims to symmetrically quantify coal triaxial strength and its directional mechanical properties using true triaxial testing procedures.

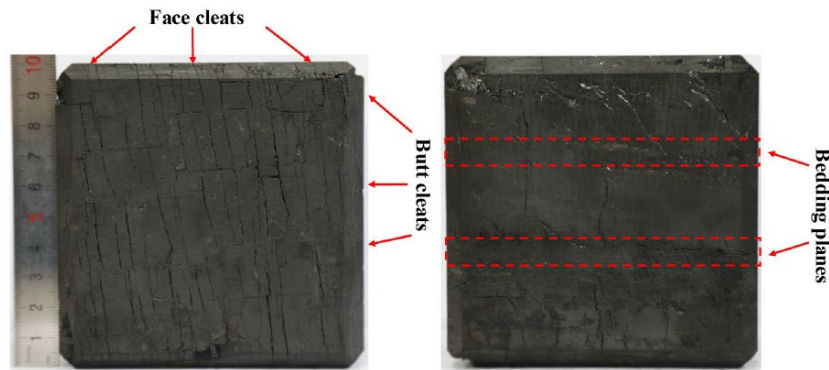


Figure 1: Cleats and bedding plates in coal (After Yubing et al, 2019)

## EXPERIMENTAL DESIGN AND SETUP

### Experimental design

For this work, eight coal cubed samples were prepared using high-quality bituminous coal samples collected from Dongda Coal Mine, Ordos basin in China (Figure 2). Three types of laboratory measurements were designed: Uniaxial Compressive Strength (UCS), step-compression (SC), and true triaxial strength (TTS) tests. The step-compression tests, in particular, were designed to gain coal directional mechanical properties (i.e., Young's modulus and Poisson's ratio) as described below in detail. The UCS and true triaxial strength measurements were further aimed to obtain coal triaxial strength data. The numbering of each sample and the corresponding type of measurement are summarized in Table 1. It is to be noted that Sample 3 was not tested due to the existence of extensive visible cleats/fractures presented in the sample, which were expected to reduce the sample strength significantly and thus unable to provide comparable results.

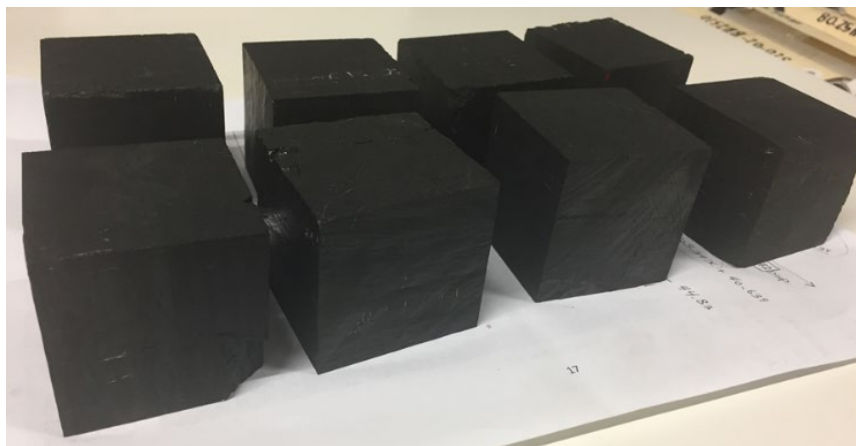


Figure 2: Coal cubic samples

Table 1: Sample specification and the corresponding testing

Sample Label	Proposed Testing	Sample Dimension (mm)		
		L1 direction	L2 direction	L3 direction
S1	UCS	50.75	49.20	49.31
S2	UCS	49.26	48.31	48.51
S3	Not tested due to major cracks	49.04	49.29	49.47
S4	SC TTS	49.64	47.11	49.35
S5	SC TTS	49.26	49.98	48.15
S6	SC TTS	49.38	49.96	50.62
S7	SC TTS	49.98	50.23	48.19
S8	SC TTS	49.36	49.50	47.44

For the step-compression measurements, each sample is tested following the sequence below:

1. Step loading: Nine loading steps, starting from 2 MPa in all three directions, and gradually increasing the stress in different orders (as illustrated in Table 2) until reaching 8 MPa in all three directions.
2. Unloading the sample to 2 MPa; and then
3. Conducting true-triaxial strength testing: the two horizontal principal stresses are loaded to the designed value, and then the vertical load increases gradually until failure.

Table 2: Loading sequence for the true triaxial testing

Loading Step	Sigma x (MPa)	Sigma y (MPa)	Sigma z (vertical) (MPa)
1	2	4	2
2	2	4	4
3	4	4	4
4	4	4	6
5	6	4	6
6	6	6	6
7	8	6	6
8	8	8	6
9	8	8	8
True-triaxial Strength Testing			
Sample 5	2	2	To fail
Samples 4 and 7	4	4	To fail
Sample 6	6	6	To fail
Sample 8	8	8	To fail

### True Triaxial Testing Facility

The True Triaxial Testing system used in this study is located at the Geotechnical Engineering Centre (GEC) within the School of Civil Engineering at the University of Queensland (UQ). The GEC is equipped with a number of cutting-edge rock testing facilities, unique in Australia, such as True Triaxial Testing System and a Biaxial Testing System, supported by a stereo (3D) ultra-high-speed and high-resolution camera system capable of running at up to 1,000,000 frames per second, a Stereo Digital Image Correlation (DIC) software platform, and Hoek triaxial cells of various diameters, as well as rock preparation equipment including coring, cutting and grinding machines. The true triaxial testing rig at the UQ Civil is capable of applying up to 340 MPa on 50 mm cubed specimens in three orthogonal directions (or up to 21 MPa stress on 200 mm cubic specimens). It is equipped with temperature (up to 100° C) and relative humidity control, has the capability for testing under saturated and unsaturated conditions (see Figure 3 below). The system is also capable of performing hydraulic fracturing at up to 51 MPa injection pressure and rock permeability tests at water pressure up to 10 MPa.



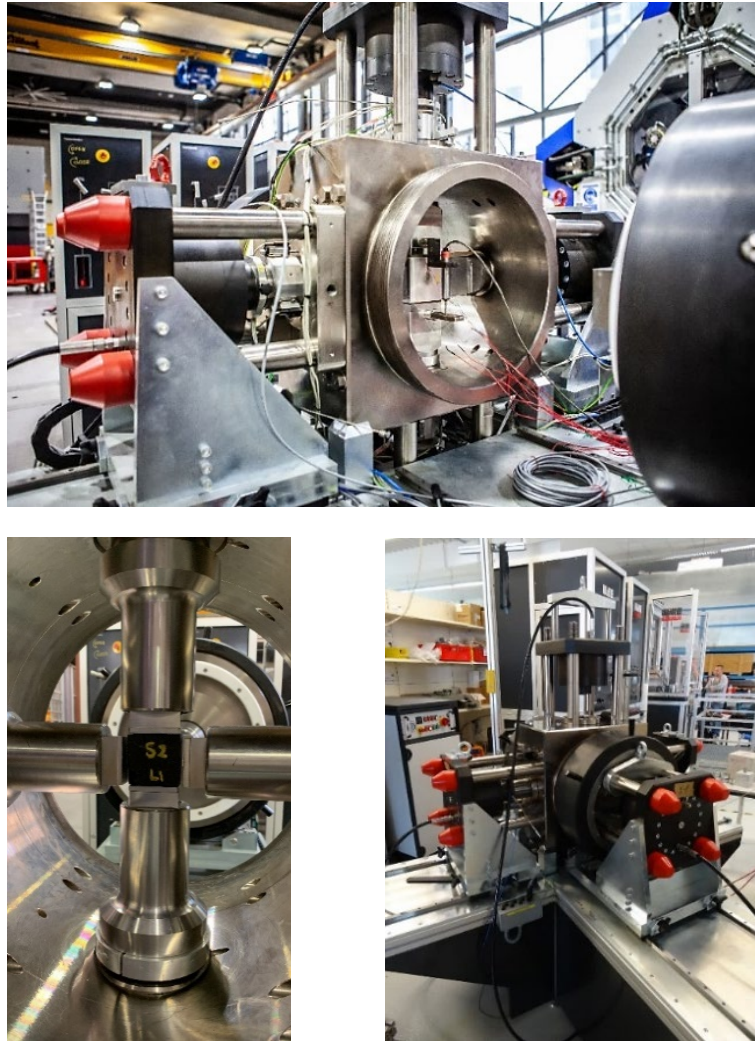


Figure 3: The true triaxial testing facility at UQ Geotechnical Engineering Centre

## RESULTS AND ANALYSIS

### UCS and true triaxial strength measurements

A loading rate of 10 kN/ min was applied to satisfy the ISRM standard recommendations. The time taken for S1 and S2 to fail is 437 s and 195 s, respectively. The maximum compressive strains at failure for two samples are 2.59% and 0.927%, respectively. As the samples are cubes rather than cylinders, the comparison with traditional UCS measurements was not conducted, but based on the existing literature (CAPRARO and MEDEIROS, 2019), the difference is generally within the range of 20%, with greater values from cubic samples.

The UCS values for samples 1 and 2 are 26.77 MPa and 10.57 MPa. The calculated E values are 1,404 MPa and 611 MPa, respectively. The result for Sample 2 is apparently not presentive due to the existence of fractures. The measured values are consistent with existing work done on cylindrical samples from the same basin, which show an average of E and UCS values of 2,171 MPa and 26.71 MPa (Cao, Kang and Deng, 2019). It is worth mentioning that the displacement data from the rig does not subtract the contribution of the loading cell to the total deformation, which means that the actual deformation should be less and thus the E values are expected to be slightly higher.

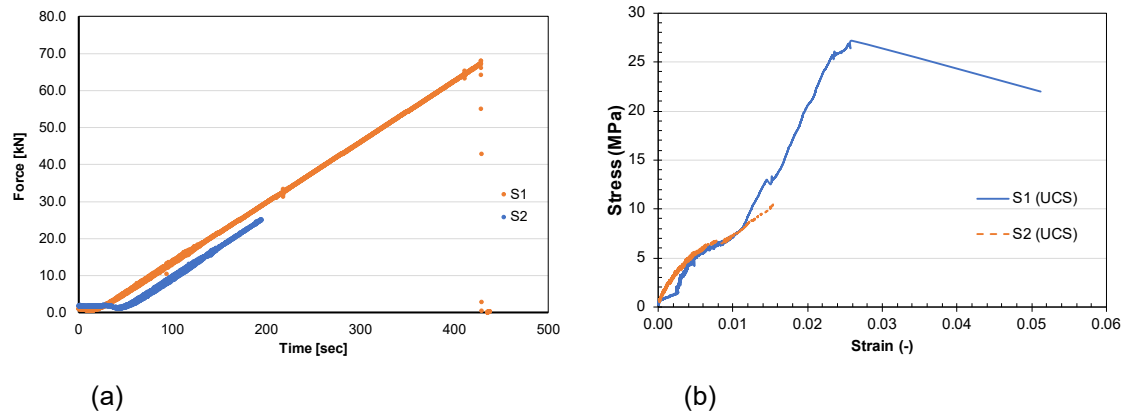


Figure 4: Loading path (a) and stress-strain curves (b) for S1 and S2 samples

### Step-compression testing

Coal is generally more anisotropic than most other types of rocks. For an anisotropic material, in general, its compliances/stiffness matrix can have 36 different properties, but the number reduces to 21 independent constants due to symmetry. In this work, we do not aim to determine all these independent constants, instead, we assume that the properties are the same in three orthogonal planes of microstructural symmetry (i.e. coal samples are treated as an orthotropic body with properties that differ along three mutually-orthogonal axes of rotational symmetry at a particular point). The number of properties, therefore, reduces to 9 accordingly which includes 3 Young's moduli and 6 Poisson's ratios. To directly calculate each of the mechanical properties, the loading step was particularly designed as illustrated in Table 2.

The stress-strain relationship under 3D stress conditions can be represented through the compliance matrix as shown in Equation 1:

$$\begin{cases} \varepsilon_x = \frac{1}{E_x} \sigma_x - \frac{\nu_{yx}}{E_y} \sigma_y - \frac{\nu_{zx}}{E_z} \sigma_z \\ \varepsilon_y = \frac{1}{E_y} \sigma_y - \frac{\nu_{xy}}{E_x} \sigma_x - \frac{\nu_{zy}}{E_z} \sigma_z \\ \varepsilon_z = \frac{1}{E_z} \sigma_z - \frac{\nu_{xz}}{E_x} \sigma_x - \frac{\nu_{yz}}{E_y} \sigma_y \end{cases} \quad (1)$$

When only  $\sigma_x$  changes during the test, e.g., increasing from  $\sigma_{x2}$  to  $\sigma_{x1}$ , Equation 1 can be re-arranged into:

$$\begin{cases} \Delta\varepsilon_x = \varepsilon_{x2} - \varepsilon_{x1} = \frac{1}{E_x} (\sigma_{x2} - \sigma_{x1}) = \frac{1}{E_x} \Delta\sigma_x \\ \Delta\varepsilon_y = \varepsilon_{y2} - \varepsilon_{y1} = -\frac{\nu_{xy}}{E_x} \Delta\sigma_x \\ \Delta\varepsilon_z = \varepsilon_{z2} - \varepsilon_{z1} = -\frac{\nu_{xz}}{E_x} \Delta\sigma_x \end{cases} \quad (2)$$

Therefore, the following three properties can be determined from the stress-strain data in the three principal directions.

$$\begin{cases} E_x = \frac{\Delta\sigma_x}{\Delta\varepsilon_x} \\ v_{xy} = -\frac{\Delta\varepsilon_y}{\Delta\sigma_x} \times E_x \\ v_{xz} = -\frac{\Delta\varepsilon_z}{\Delta\sigma_x} \times E_x \end{cases} \quad (3)$$

Similarly, when varying  $\sigma_y$  and  $\sigma_z$ , the following correlations stay true.

$$\begin{cases} E_y = \frac{\Delta\sigma_y}{\Delta\varepsilon_y} \\ v_{yx} = -\frac{\Delta\varepsilon_x}{\Delta\sigma_y} \times E_y \\ v_{yz} = -\frac{\Delta\varepsilon_z}{\Delta\sigma_y} \times E_y \end{cases} \quad (4)$$

$$\begin{cases} E_z = \frac{\Delta\sigma_z}{\Delta\varepsilon_z} \\ v_{xy} = -\frac{\Delta\varepsilon_y}{\Delta\sigma_z} \times E_z \\ v_{xz} = -\frac{\Delta\varepsilon_z}{\Delta\sigma_z} \times E_z \end{cases} \quad (5)$$

In this work, Equations 3-5 are combined to determine the nominated 9 properties shown in Equation 1. Theoretically, they can be determined by changing the loading of each direction once, but to minimize data uncertainty the 9 steps (3 steps in each direction) in total are implemented.

There is a large amount of data recorded during the tests. Due to space limitations, only the data for sample 5 was presented in detail here as an example. The loading history and the calculated results of the sample are plotted in Figure 5 and Equation 6, respectively.

Figure 6 summarizes the results of the directional E of the four samples (S5-S8). A significant difference in E values along different orientations was observed. The mean E values in x, y and z directions are 1,025 MPa, 1,887 MPa, and 2,543 MPa, which gives the ratio of 1.00: 1.84: 2.48. The difference in E values is considerable. The prediction of gateroads deformation could be quite different when different E values are used, and this uncertainty should be beard in mind when conducting a geotechnical analysis.

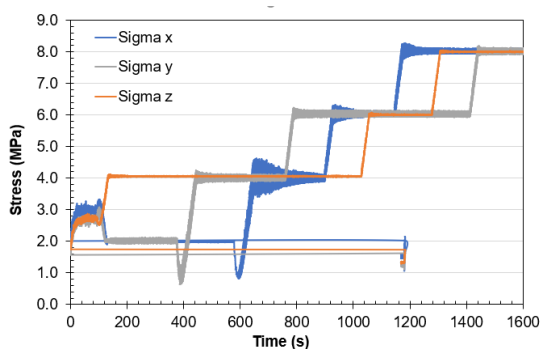


Figure 5: Loading history of Sample 5

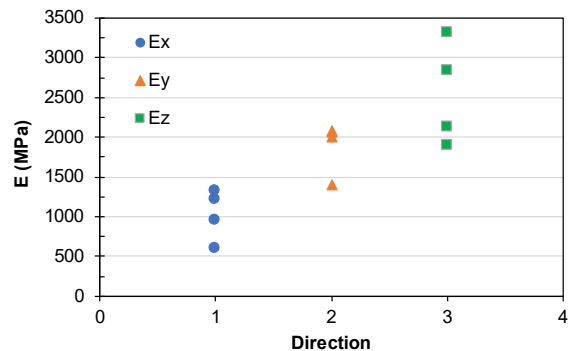


Figure 6: Results of directional Young's moduli

The results of Poisson's ratio are a bit messy as illustrated in Figure 7, and do not show a particular trend. The mean Poisson's ratio values are 0.098, 0.038, and 0.091 respectively (x, y and z directions), which gives the ratio of 1.00: 0.38: 0.93. The majority are significantly smaller than representative values for coal, which varies from 0.26 to 0.43 (Szabo, 1981).

A good potential reason could be associated with the stiffness of the loading plates of the true triaxial rig. The stiffness of coal is typically one or two orders of magnitude lower than hard rocks (e.g., 1.5 GPa for coal vs 10 GPa for sandstone vs 30 GPa for granite). This means that during coal compression testing, the Poisson's effect will not generate adequate forces in the two orthogonal directions to push the loading plates away to maintain designed constant pressure. Essentially the loading condition of coal changes from stress-controlled by design to uniaxial strain equivalent conditions. This could result in minimal detection of coal lateral deformation, thus obtain much smaller values of Poisson's ratio from the calculation.

$$\begin{bmatrix} E_x & \nu_{xy} & \nu_{xz} \\ \nu_{yx} & E_y & \nu_{yz} \\ \nu_{zx} & \nu_{zy} & E_z \end{bmatrix} = \begin{bmatrix} 1,210 & 0.04 & 0.05 \\ 0.20 & 2,068 & 0.16 \\ 0.10 & 0.02 & 2,841 \end{bmatrix} \quad (6)$$

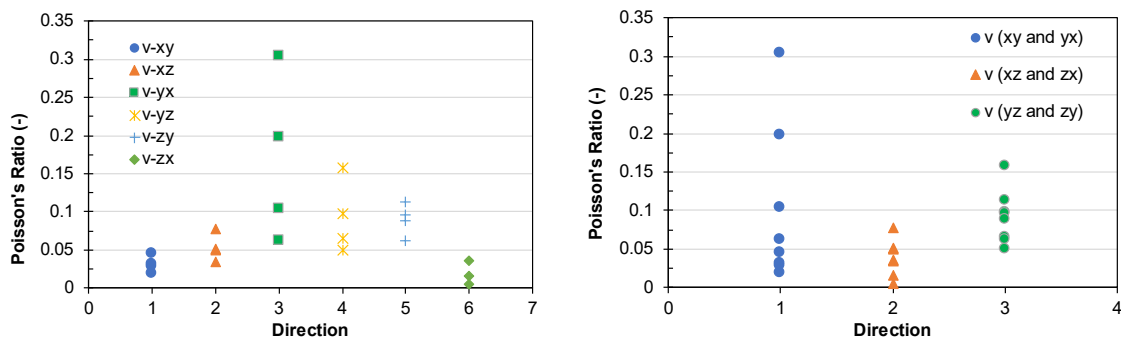


Figure 7: Result of directional Poisson's ratio

### Coal triaxial strength

Samples 5-8 were used for conducting step-compression and the subsequent strength measurements, and the failure modes are provided in Figure 8. No noticeable difference in failure modes is observed for the four samples and it is consistently seen that the shear surface occurs along the gaps between loading plates.

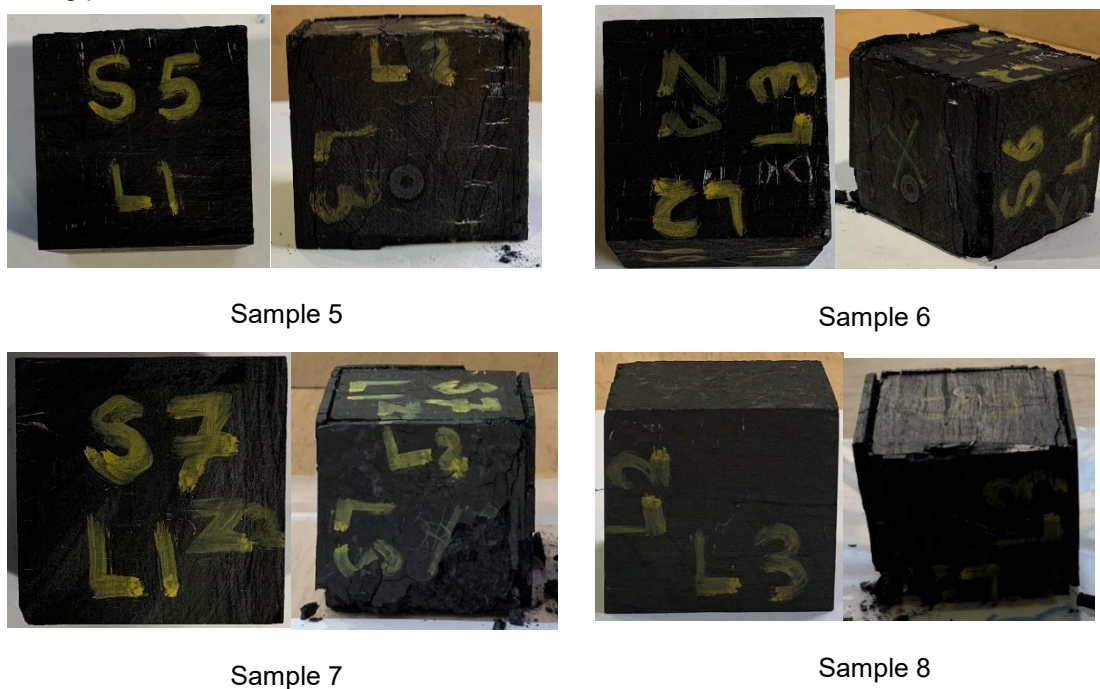


Figure 8: Coal samples before and after true triaxial tests

To calculate coal triaxial strength, two probably most widely used criteria can be applied: Mohr-Coulomb and Hoek-Brown. The latter is used for this work due to its more suitable feature for rock-like materials. The expression of Hoek-Brown criterion can be defined as (Eberhardt, 2012):

$$\sigma_1' = \sigma_3' + \sigma_{ci} \left( m \frac{\sigma_2'}{\sigma_{ci}} + s \right)^{0.5} \quad (7)$$

where  $\sigma_1'$  and  $\sigma_3'$  are the major and minor principal effective stresses at failure,  $m$  and  $s$  are constants for the target material ( $s$  is normally taken as 1.0 for intact samples), and  $\sigma_{ci}$  is the UCS strength of intact coals. The experimental results of triaxial compression tests are plotted in Figure 9. The data point in red is from sample S4, and seems a bit off the trend. The  $m$  value is 23.9 for all data and  $m = 22.3$  if the red dot point is excluded in the fitting. The difference seems minimal for coal mining at shallow depth (e.g. < 500m).

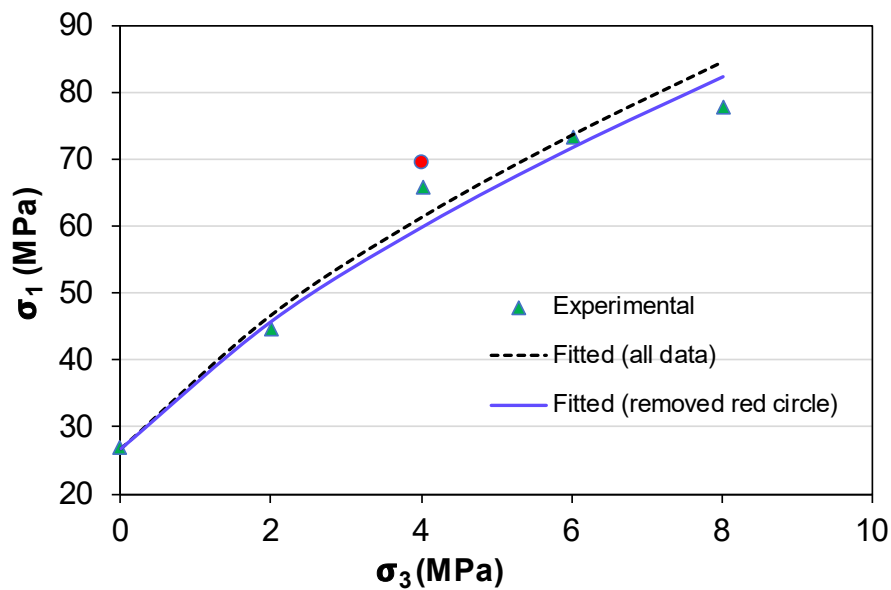


Figure 9: Coal Strength Based on Hoek-Brown Criterion

### CONCLUSIONS

In this work, a series of tests were conducted to determine coal strength and directional mechanical properties using a true triaxial testing rig. Three types of tests were designed on seven coal samples. The key findings from this work are:

- E values along different orientations are quite different. The mean E values in x, y and z directions are 1,025 MPa, 1,887 MPa, and 2,543 MPa, which gives the ratio of 1.00: 1.84: 2.48.
- The results of Poisson's ratio do not show obvious trend in different directions. The mean Poisson's ratio values are 0.098, 0.038, and 0.091 respectively (x, y and z directions), which gives the ratio of 1.00: 0.38: 0.93.
- Coal strength follows the Hoek-Brown criterion reasonably well. The  $m$  value is 23.9 for all data and  $m = 22.3$  if the red dot point is excluded in the fitting from Figure 9.

The results show that coal anisotropic feature is quite strong, and should be considered when conducting the relevant geotechnical analysis. Coal mechanical properties need to be probably tested and used to enhance analysis confidence.

REFERENCES

- Barla, G., Barla, M., Debernardi, D., 2010. New Triaxial Apparatus for Rocks. *Rock Mechanics and Rock Engineering*, 43(2), 225-230. doi:10.1007/s00603-009-0076-7
- Bieniawski, Z. T., 1968. In situ strength and deformation characteristics of coal. *Engineering Geology*, 2(5), 325-340. doi:https://doi.org/10.1016/0013-7952(68)90011-2
- Cao, M., Kang, Y., Deng, Z., 2019. Influence of coal rank and tectonic stress intensity on mechanical properties of coal rock. *Coal Science and Technology*, 47(12), 45-55. doi:doi:10.13199/j.cnki.cst.2019.12.007
- CAPRARO, D. F. A., CAPRARO, A. P. B., ARGENTA, M. A., MEDEIROS, M. H. F., 2019. Experimental and numerical evaluation of mortar specimens shape and size influence on compression tests. *Revista IBRACON de Estruturas e Materiais*, 12, 429-444. Retrieved from [http://www.scielo.br/scielo.php?script=sci\\_arttextpid=S1983-41952019000200429nrm=iso](http://www.scielo.br/scielo.php?script=sci_arttextpid=S1983-41952019000200429nrm=iso)
- Dexing, L., Enyuan, W., Xiangguo, K., Xiaoran, W., Chong, Z., Haishan, J., Jifa, Q., 2018. Fractal characteristics of acoustic emissions from coal under multi-stage true-triaxial compression. *Journal of Geophysics and Engineering*, 15(5), 2021-2032. doi:10.1088/1742-2140/aac31a
- Eberhardt, E., 2012. The Hoek–Brown Failure Criterion. *Rock Mechanics and Rock Engineering*, 45(6), 981-988. doi:10.1007/s00603-012-0276-4
- Li, M., Yin, G., Xu, J., Li, W., Song, Z., Jiang, C., 2016). A Novel True Triaxial Apparatus to Study the Geomechanical and Fluid Flow Aspects of Energy Exploitations in Geological Formations. *Rock Mechanics and Rock Engineering*, 49(12), 4647-4659. doi:10.1007/s00603-016-1060-7
- Li, Z., Wang, L., Lu, Y., Li, W., Wang, K., Fan, H., 2019. Experimental investigation on True Triaxial Deformation and Progressive Damage Behaviour of Sandstone. *Scientific Reports*, 9(1), 3386. doi:10.1038/s41598-019-39816-9
- Liu, Y., Yin, G., Li, M., Zhang, D., Huang, G., Liu, P., Yu, B., 2019. Mechanical Properties and Failure Behavior of Dry and Water-Saturated Anisotropic Coal Under True-Triaxial Loading Conditions. *Rock Mechanics and Rock Engineering*. doi:10.1007/s00603-019-02035-9
- Perera, M. S. A., Ranjith, P. G., Choi, S. K., 2013. Coal cleat permeability for gas movement under triaxial, non-zero lateral strain condition: A theoretical and experimental study. *Fuel*, 109, 389-399. doi:https://doi.org/10.1016/j.fuel.2013.02.066
- Ranjith, P. G., Perera, M. S. A., 2011. A new triaxial apparatus to study the mechanical and fluid flow aspects of carbon dioxide sequestration in geological formations. *Fuel*, 90(8), 2751-2759. doi:https://doi.org/10.1016/j.fuel.2011.04.004
- Somerton, W. H., Söylemezoğlu, I. M., Dudley, R. C., 1975. Effect of stress on permeability of coal. *International Journal of Rock Mechanics and Mining Sciences Geomechanics Abstracts*, 12(5), 129-145. doi:https://doi.org/10.1016/0148-9062(75)91244-9
- Szabo, T. L., 1981. A representative poisson's ratio for coal. *International Journal of Rock Mechanics and Mining Sciences Geomechanics Abstracts*, 18(6), 531-533. doi:https://doi.org/10.1016/0148-9062(81)90517-9
- Zhao, Y., Liu, S., Zhao, G.-F., Elsworth, D., Jiang, Y., Han, J., 2014) Failure mechanisms in coal: Dependence on strain rate and microstructure. *Journal of Geophysical Research: Solid Earth*, 119(9), 6924-6935. doi:10.1002/2014jb011198



# SHEAR STRENGTH PROPERTIES OF ARTIFICIAL ROCK JOINTS

**Muhammad Zohaib<sup>1</sup>, Ali Mirzaghobanali<sup>1,2</sup>, Andreas Helwig<sup>3</sup>, Naj Aziz<sup>1,2</sup>, Peter Gregor<sup>1</sup>, Ashkan Rastegarmanesh<sup>1</sup>, Kevin McDougall<sup>1</sup>**

*Abstract:* The shear strength property of artificial rock joints with triangular and sinusoidal roughness was investigated in the laboratory by the aid of direct shear test machine. In particular, this paper includes literature review of past studies on shear strength properties of unfilled and infilled rock joints, experimental studies on shear strength properties of artificial rock joints with triangular, sinusoidal and plain roughness under various normal load and comparison between shear behaviour of these rock joints having different roughness patterns. This research presents the concepts development essential to envision the shear behaviour of rock slopes aided by artificial rock joints. It was concluded that the shear behaviour of rock joints is a function of normal stress, roughness value and pattern of asperity.

## INTRODUCTION

Joints impact on the deformation and shear strength behaviour of rocks. The mechanical properties of rock mass are identical to that of joints in hard rocks (Lama, 1978). If the rock dilates while shearing, then the normal stress increases significantly and the shearing behaviour of rock becomes a function of the normal stiffness rather than the normal stress (Haque, A., 1999). The unfilled joint testing, through studies undertaken in past, can be categorised as joint testing of medium to hard rock joints or medium to soft rock joints, under constant normal stiffness. The key factors that affect the shear actions of infilled joints are summarized to be the type of joint, type of infill material, rate of shearing displacement, externally applied stiffness, horizontal confinement of specimen and characteristics of consolidation. Because of such a broad range of influence factors, in particular the shear behaviour of infilled joints with constant normal stiffness factors is very crucial to examine, since almost all previous tests under constant normal load were carried out. In this research study the shear strength of artificial rock joints, with different types of surface asperities, was investigated under low normal stress under unfilled and infilled joint conditions. The concepts developed in this research are valid for and applicable to the analysis of rock slopes.

## METHODOLOGY

In this research, the shear behaviour of artificial rock joints was investigated. In order to cast artificial rock joints, the moulds were prepared at first. The specimens were prepared by incorporating five distinctive surfaces roughness. Each surface was comprised of different asperity height. The moulds were initially designed by the aid of Tinker CAD online 3D designing software, where each design was developed with the surface roughness that was required for casting corresponding specimen. Tinker CAD is an online application that allows designing and printing of 3D objects. It allows the use of distinctive tools including guides, references, grid lines and a number of hollow and solid 3D shapes. In this application, by combining and modifying the basic 3D shapes, the design of complex objects is

---

<sup>1</sup> School of Civil Engineering and Surveying, University of Southern Queensland, Email: [ali.mirzaghobanali@usq.edu.au](mailto:ali.mirzaghobanali@usq.edu.au) Tel: +61 7 4631 2919

<sup>2</sup> School of Civil, Mining and Environmental Engineering, University of Wollongong. Email: [naj@uow.edu.au](mailto:naj@uow.edu.au)

<sup>3</sup> School of Electrical and Mechanical Engineering, University of Southern Queensland

developed. Figure 1 shows typical design that was developed using this application, where the final object after 3D printing can be seen. A total of four surfaces were designed and printed with different asperity patterns and roughness sizes. However, the plain surface did not need any design as for the purpose the plain board was used underneath PVC forms while casting plain surface.

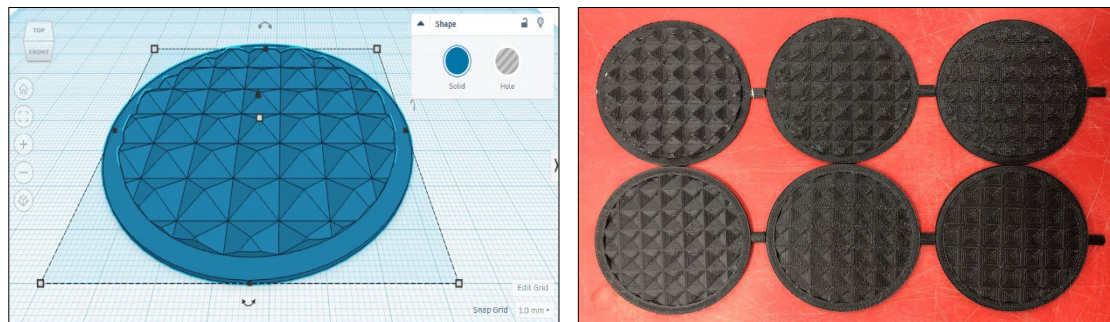


**Figure 1: Design of typical asperity shape and 3D printed moulds**

The diameter of specimen was 63.5 mm. The asperity height in each sample was different. For triangular asperities the asperity height of first specimen is 0.84 mm, in second specimen the height is 1.67 mm and in the third specimen the height of tooth is 2.5 mm. The angles of internal friction are 9.5, 18.5 and 26.5 degrees correspondingly. Moreover, the asperity height in sinusoidal mould (blue mould shown in Figure 2) is 1.67 mm and angle of internal friction is 18.5 degrees. In order to cast the specimen, the PVC tubes having 63.5 mm internal diameter were used. These tubes were used as forms for specimen. To obtain the required surface roughness and to attain the required shape of samples, the 3D printed moulds were attached at the bottom of PVC tube with the aid of general-purpose duct tape. Figure 3 presents the forms prepared for casting the samples.

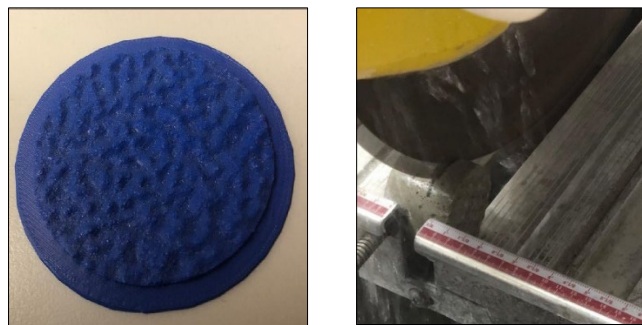


**Figure 2: Sample preparation**

Prior to filling PVC tubes with grout, the formwork release agent (shuttering oil) was applied to internal surface of PVC tubes to facilitate removal of specimen after hardening. Subsequently, the tubes were filled with grout prepared consisting of cement (0.6 kg), sand (2.004 kg) and water (0.432 kg), with yielding strength of 40 MPa. To cast the specimen, first the cement and sand were mixed in dry state, followed with water. The binding material used was ordinary Portland cement. The tubes were then filled before the initial setting time of cement. Each cylinder required 0.1 kg of cement, 0.334 kg of sand and 0.072 kg of water to yield 40 MPa strength sample.

The samples were removed from forms after 24 hours, they were placed in the curing room for proper hydration and strength development. The samples were marked for proper surface alignment upon form removal, so as to mitigate error during the shearing of specimen.





**Figure 3: PVC forms**

The specimens were subsequently trimmed to the required height in order to fit in the apparatus. For the purpose a concrete cutter was used and the sample was made ready to testing in direct shear testing machine.

### TESTING RESULTS

In order to perform testing the ShearTrac-II direct shear testing machine was used. ShearTrac-II operates as an intelligent loading system. Its operations are based on the response received from horizontal and vertical force transducers and horizontal and vertical displacement transducers. It's hardware includes five major components consisting of a loading frame, test accessories, computer, keyboard and mouse and a display unit. The horizontal displacement limit of ShearTrac-II was 20 mm. The overall height was 560 mm; however, the cabinet height was 228 mm. The length of ShearTrac-II was 762 mm and the depth was 368 mm. The machine weighs of was 63 kg and consumes power of 110 volts. The ShearTrac-II direct shear testing machine is shown in Figure 4.

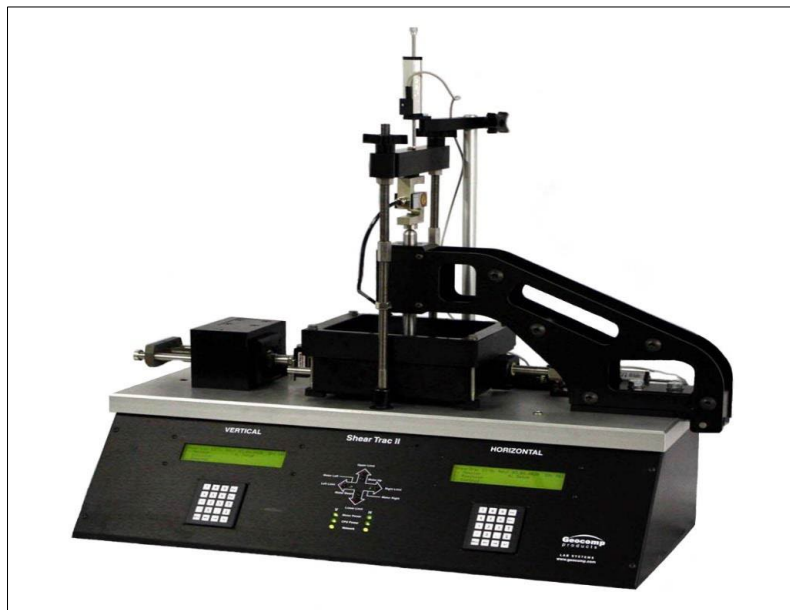


**Figure 4: Shear Trac – II, Direct shear testing machine**

In order to conduct the experimentation, the specimen was placed in a relatively flat box. Under the application of normal loading the box was split horizontally into two parts, where half box was held restrained while the other half was pushed with sufficient force and specimen experienced shear failure. Figure 5 shows the testing of a few samples. A total of five specimens with different types of asperity and surface roughness parameters were tested. These parameters are listed in Table 1.



Figure 5: Direct shear test

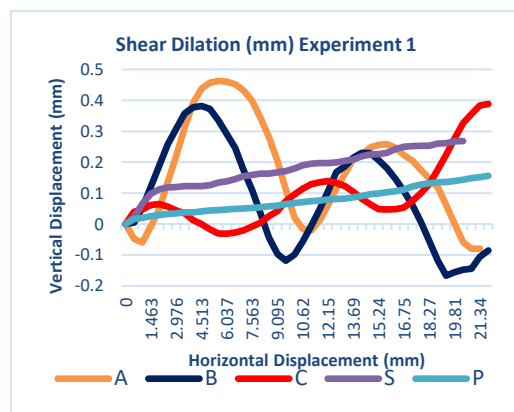
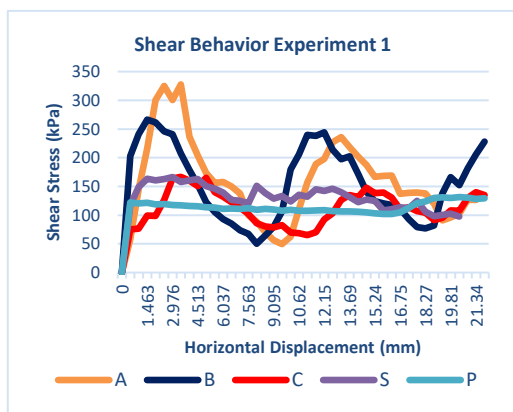
**RESULTS AND ANALYSIS**

All samples were cast using 40 MPa strength mortar. The samples were tested having 28 days strength of curing. Table 1 shows the specification of samples used for unfilled and infilled experiments. In infilled joints, as infill material kiln dried especially graded fine sand was used. The water content for infill was 10 %t compared with the weight of infill material, where 10 gm of water was mixed with 100 gm of sand infill material preparation.

**Table 1: Specimen specifications for unfilled and infilled tests**

Sr. No	Specimen	Asperity Height (mm)	Angle of Internal Friction (Degree)	Strength (MPa)	Diameter (mm)
1	A- (Triangular-Prismatic)	2.5	26.5	40	63.5
2	B- (Triangular-Prismatic)	1.67	18.5	40	63.5
3	C- (Triangular-Prismatic)	0.84	9.5	40	63.5
4	S- Sinusoidal Surface	1.67	18.5	40	63.5
5	P- Plain Surface	0	0	40	63.5

The shear behaviour and dilation of unfilled and infilled tests are shown in Figure 6 and Figure 7.



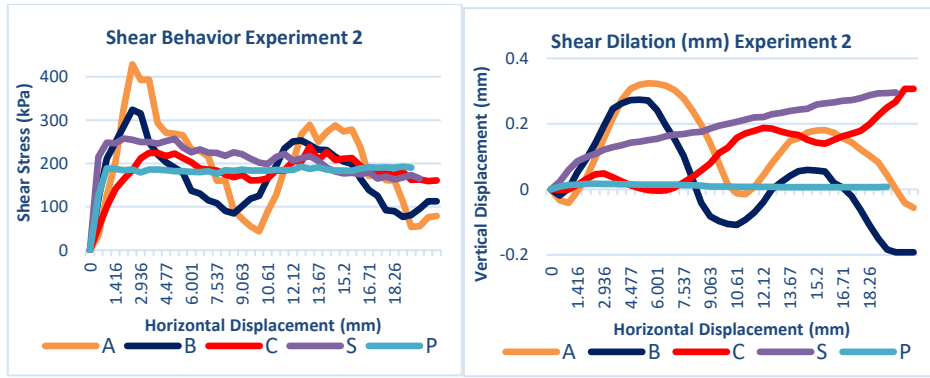


Figure 6: Shear behaviour and shear dilation of unfilled joints

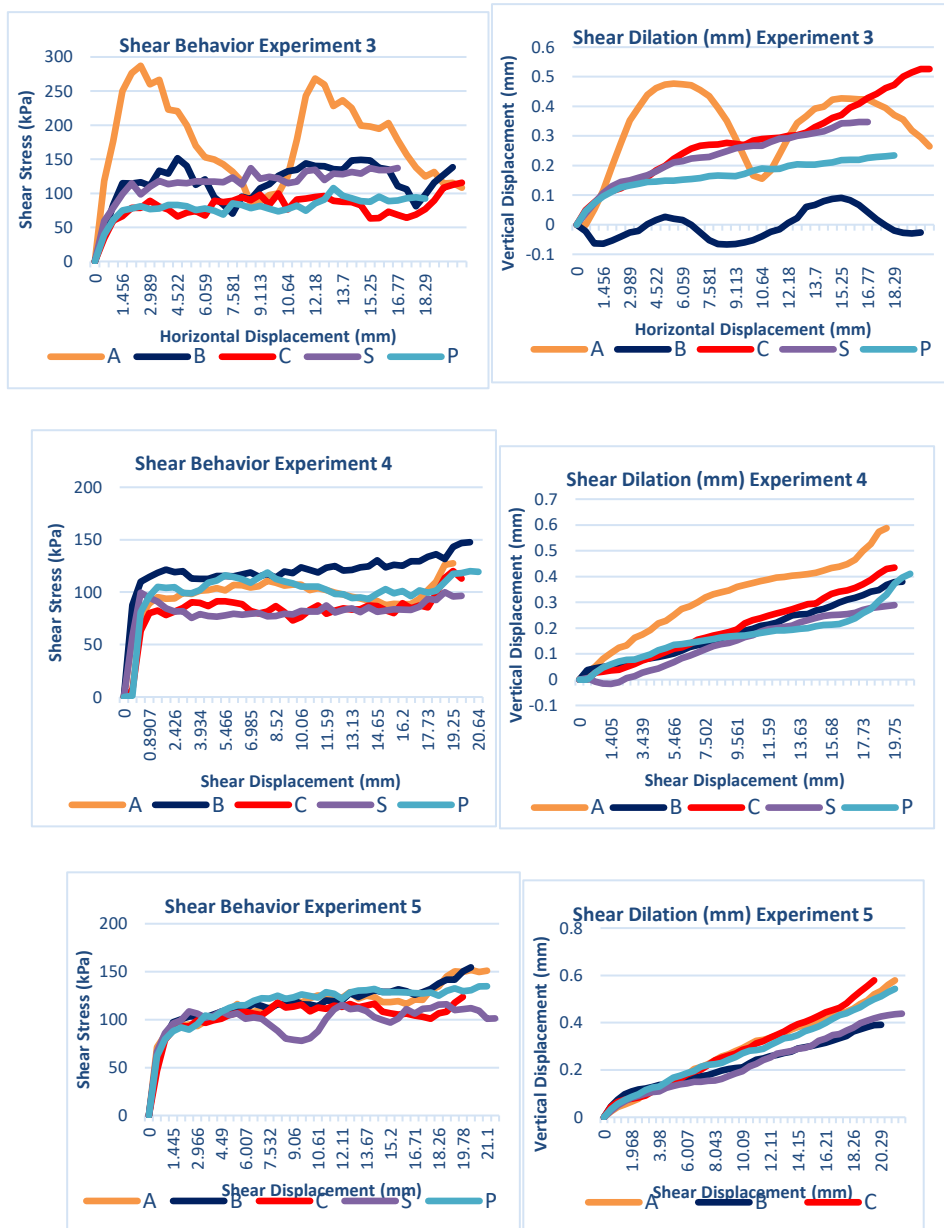
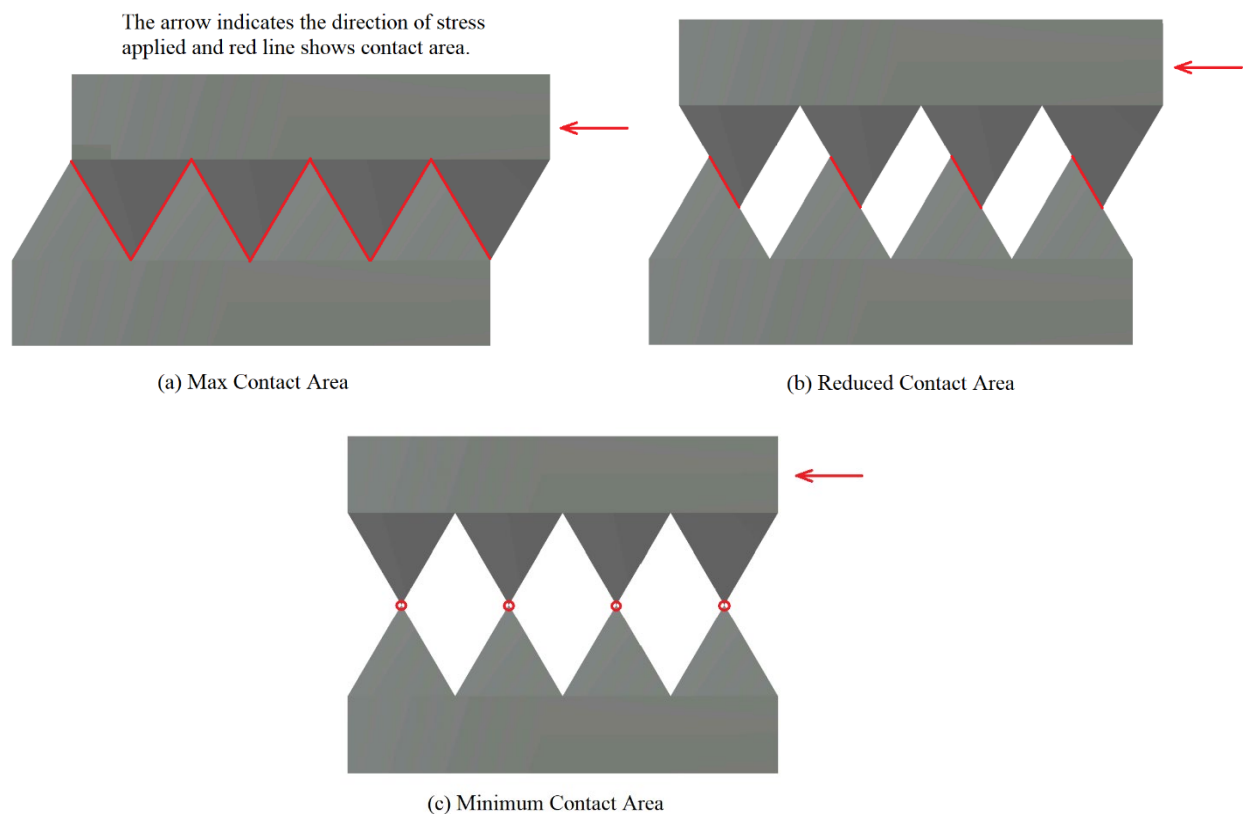


Figure 7: Shear behaviour and shear dilation of infilled joints

### Experiment 1

Experiment 1 was conducted on unfilled rock joints under constant normal stress of 237 kPa and the corresponding normal load was 750 N. The asperity pattern of specimen A was triangular (prismatic) with asperity height of 2.5 mm. It was observed that the shear stress increased initially in a linear manner reaching the maximum value of 327.6 kPa at the horizontal displacement of 3.512 mm. The minimum value of shear stress was 49.82 kPa at the horizontal displacement of 9.68 mm. Throughout the test, the shear stress varied consistently due to the variation in interlocking of asperities developed due to surface roughness between shearing surfaces. Due to this variation in interlocking of asperities, the value of friction between the surfaces also varied and hence the shear stress varied consistently throughout the test. The maximum shear stress was achieved when the top and bottom surfaces were entirely interlocked and the area of interaction was maximum as shown in Figure 8 (a). The shear stress changes between maximum and minimum value, was induced due to the variation in surface friction between minimum and maximum interaction area. This effect can be seen in the Figure 8 (b). At the minimum shear stress value the interlocking between the top and bottom surfaces was minimum as shown in Figure 8 (c).



**Figure 8: Interlocking of surfaces, designed in AutoCAD**

Therefore, it is concluded that, as the interlocking of surfaces due to asperity height is increased the shear stress increases and as the interlocking decreases the shear stress decreases. Figure 6 shows the dilation behaviour of experiment 1, which that the pattern of dilation is to some extent identical to the shape of asperity. The negative values in the graph shows the compression due to normal stress; the positive value shows the amount of dilation that took place during shearing. The amount of dilation was greatest when the first asperity of bottom surface slid against the first asperity of top surface, however, it reduced in the sliding stage of subsequent asperities. The reason behind this behaviour is the surface damage while shearing, which reduced the amount of dilation. However, the damage of surface was not significant.

The asperity pattern of specimen B was triangular (prismatic) with asperity height of 1.67 mm. The shear behaviour of sample B was almost identical to the shear behaviour of sample A, where the stress increased initially in a linear manner and reaching the maximum value of 266.4 kPa at the horizontal displacement of 1.413 mm. The minimum value of shear stress was 50.39 kPa at the horizontal displacement of 8.111 mm. However, the asperity height and angle of internal friction of sample B was less compared with sample A. This due to the fact that the maximum shear stress of sample B was less than the maximum shear stress of sample A.

The asperity pattern of specimen C was also triangular (prismatic) with asperity height of 0.84 mm. It was observed that the shear behaviour of sample C was also nearly similar to the shear behaviour of samples A and B, where the stress increased initially in a linear manner reaching the maximum value of 166.7 kPa at the horizontal displacement of 3.482 mm and the minimum value of shear stress was 65.42 kPa at the horizontal displacement of 11.16 mm. This behaviour in sample C is also similar to sample A and B. However, the asperity height and the angle of internal friction of sample C was further reduced compared with the sample A and B. This was attributed to the fact that the maximum shear stress of sample C is less compared with the shear stress of both samples A and B.

The asperity height of specimen C was 0.84 mm. The dilation graph of experiment 1 in Figure 6 shows the maximum value of dilation of 0.064 mm at 1.976 mm of horizontal displacement, where there was no significant damage to the surface due to shearing. The value of dilation increased up to 0.1392 mm at 12.16 mm of horizontal displacement. Also, the dilation reached a value of 0.388 mm in the end of test at a horizontal displacement of 21.37 mm. The reason behind this dilation behaviour is that as the test progressed, the surface began to get damaged, due to the accumulation of damaged particles between the shearing surfaces. As the test progressed further, the accumulation of particles also increased between the shearing surfaces. These accumulated particles resulted in the incremental dilation as the accumulation increased. This effect can be seen in Figure 9.



**Figure 9: Increment in dilation of unfilled joint due to damaged surface particles, designed in AutoCAD**

The shear behaviour of sinusoidal "S" joint and plain "P" joint shows linear increment in shear stress at first and reached the peak. It varied consistently and reduced as the shear displacement progressed. The minimum shear stress of sinusoidal joint was 97.762 kPa at 20.31 mm of shear displacement. The reason behind this depression in the shear graph was caused by the consistent reduction in the shear strength of the rock joint due to the consistent damage of the surface. The plain surfaces do not interlock as the asperity height was negligible because of less friction between surfaces. This is the reason why the plain surface has the minimum shear strength compared with other asperities. Moreover, the broken

surface particles were also a reason of reduction of shear strength, as these particles assisted in the sliding of surfaces and acts as infill in clean joint after some shear displacement.

The dilation behaviour of sinusoidal and plain joint shows steady increment in the value of dilation compared to the initial to final dilation. This is due to the consistent breaking of the surface due to shear and accumulation of broken particles between the shearing surfaces of rock joints. At the initial stage the dilation was minimum because of the minimal the damaged particles. However, the accumulation of broken particles increased as shearing progressed. This behaviour was identical to the one shown in Figure 9. These broken particles were also the reason of reduction in shear strength, as these particles assisted in the sliding of surfaces and acted as infill in clean joint.

## **Experiment 2**

Experiment 2 was performed under unfilled joint condition and constant normal loading. The normal stress applied was 295 kPa and results of experiment 2 can be seen in Figure 6. The behaviour of each type of surface was analysed and explained in detail in experiment 1. Therefore, those points will not be repeated in the subsequent experiments. The only behaviours that are different, compared with the behaviours shown in experiment 1, are analysed and are explained in detail subsequently.

In experiment 2, the individual behaviour of each specimen was identical to the corresponding sample with similar surface asperity in experiment 1. The shear stress of samples A and B reached to the maximum value in linear manner. The interlocking of surfaces was maximum at maximum shear stress and it reduced in similar way as for samples A and B in experiment 1. However, the values of maximum shear stress were noted to be 428.6 kPa for sample A and 324 kPa for sample B. This stress was significantly higher compared to the maximum stress obtained of samples A and B in experiment 1. Similarly, the maximum shearing stress for samples C, S and P was higher than the one of samples C, S and P in experiment 1. This rise of maximum shear stress was the result of application of additional 58 kPa of normal stress to the specimens in experiment 2. This additional normal stress imposed more pressure between the shearing surfaces. This additional pressure induced higher friction between the sliding surfaces. To slide surfaces with lower surface friction requires less force compared to the surfaces with higher friction. Therefore, due to this increment in friction a higher shearing stress was required to slide the joint surfaces.

## **Experiment 3**

In experiment 3, the constant normal stress was 237 kPa and joint was sheared with infill having thickness of 0.5 times asperity height. Height of infill used in experiment 3 for corresponding samples is given in Table 2.

In this test, the shear behaviour of asperities is changed compared with the results of experiment 1. The reason of this change in shear behaviour is the infill material between the shearing surfaces. The shearing material assists the surfaces to slip at lower shear stress even if the angle of internal friction is greater. The existence of infill material (in this case, non – cohesive) between surfaces mitigates the friction between surfaces. The shear strength of the joint was reduced compared with the shear strength of joint without infill material. In this case where the joint is infilled, some of the shear strength is controlled by the infill material and some is controlled by the sharp asperity. Figure 10 shows the shear behaviour of experiment 3. The shear behaviour of sample A shows maximum shear strength compared to other samples. It is noted that the maximum shear stress induced in sample A while shearing is 284 kPa at 2.493 mm of shear displacement. The maximum shear stress of specimen A in experiment 3 is less compared with the maximum shear stress of specimen A in experiment 1, even the specimen specifications are same, it is because the joint tested in experiment 1 is unfilled joint, however, the joint tested in experiment 3 is infilled joint and it is the infill material that has reduced the maximum shearing strength in experiment 3. The maximum shearing strength of other specimens in experiment 3 is also quite low compared with the rest of specimens in experiment 1, and it is also reduced due to the infill

material. Whereas the normal stress in both experiments was equal and constant. Therefore, it is evident that the shear strength of rock joint decreases due to infill material. Figure 7 shows the dilation behaviour of experiment 3. It shows that the dilation of samples A and B in experiment 3 is quite similar to the dilation behaviour of samples A and B in experiment 1 and 2. There is no significant change in the behaviour of vertical displacement of samples A and B in experiment 3, because the shape of asperity is uniform and the height of asperity is large enough, also the thickness of infill layer is not sufficient to alter the dilation behaviour of samples A and B. The dilation behaviour of samples A and B show that the shearing is controlled by both the sharp asperities and the infill material. However, the behaviour of vertical displacement of sample C was influenced by the infill material and it can be noted that the dilation pattern of sample C in experiment 3 did not vary as it varied in experiment 1 and 2, instead it is identical to the behaviour of plain surface. It is because the angle of internal friction is quite low as height of asperity is not enough and the thickness of infill layer is higher and the dilation graph shows that the shear behaviour of sample C is mostly controlled by infill material compared with the asperities. The samples S and P have shown the similar behaviour as in experiment 1 and 2. It is because infill thickness has no significant effect on dilation behaviour of the surfaces due to the low internal friction angle. In summation, the shear graph shows consistent variation in shear stress of all asperities except plain surface. Therefore, it is evident that still the shear behaviour, to some extent, is controlled by sharp asperities.

**Table 2: Infill specification**

Infill height in experiment 3					
Sr. No	Sample/Asperity	Unfilled Asperity Height (mm)	Infill Height (mm)	Total Height (mm)	Asperity Shape
			0.5*H of Asperity		
1	A	2.5	1.25	3.75	Triangular
2	B	1.67	0.835	2.505	Triangular
3	C	0.84	0.42	1.26	Triangular
4	S	1.67	0.835	2.505	Sinusoidal
5	P	0	1	1	Plain
Infill height in experiment 4					
Sr. No	Sample/Asperity	Unfilled Asperity Height (mm)	Infill Height (mm)	Total Height (mm)	Asperity Shape
			1*H of Asperity		
1	A	2.5	2.5	5	Triangular
2	B	1.67	1.67	3.34	Triangular
3	C	0.84	0.84	1.68	Triangular
4	S	1.67	1.67	3.34	Sinusoidal
5	P	0	2	2	Plain
Infill height in experiment 5					
Sr. No	Sample/Asperity	Unfilled Asperity Height (mm)	Infill Height (mm)	Total Height (mm)	Asperity Shape
			1.5*H of Asperity		
1	A	2.5	3.75	6.25	Triangular
2	B	1.67	2.505	4.175	Triangular
3	C	0.84	1.26	2.1	Triangular
4	S	1.67	2.505	4.175	Sinusoidal
5	P	0	3	3	Plain

**Experiment 4**

In experiment 4 the constant normal stress was 237 kPa and joint was sheared with infill having thickness equal to asperity height. Height of infill used in experiment 4 for corresponding samples is given in Table 2.



In this test, the shear behaviour of asperities was changed compared with the results of experiment 3. The maximum shear strength of all samples in experiment 4 was reduced significantly, as shown in Figure 7. In the shear behaviour graph of experiment 4, the pattern of shearing stress for all the specimen was no longer varying as was varied in experiments 1, 2 and 3. However, the variation was very little, which has very less influence of the asperity pattern. Instead this variation was mainly the function of internal friction of infill material. The dilation graph of experiment 4 in Figure 7 shows that the dilation of sample A was greater compared to other specimens and occurred due to the highest asperity height and over laying and accumulation of infill material. As the thickness of infill was greater, there was minimal contact of sharp asperities and there was minimal damage to the asperities. The increment in dilation at the end of test was significant and it was not because of the accumulation of damaged particles but instead occurred due to the over-riding of infill particles. This behaviour is shown in Figure 10. Moreover, the infill material interlocked partially with the top surface and partially with the bottom surface, leaving minimal damage to the interacting surfaces of rock joints. The normal stress was not significant, however, if greater normal stress was applied that could damage the surfaces as well. In this case with infill between shearing surfaces the normal stress required to shear the surfaces would be significantly large. From the discussion above, it is concluded that as the thickness of infill layer increases the shear behaviour becomes the function of the shear parameters of infill material rather than the asperities.



**Figure 10: Sample A with infill height equal to asperity height**

### **Experiment 5**

In experiment 5 the constant normal stress was 237 kPa and joint was sheared with infill having thickness equal to 1.5 times the asperity height. Height of infill used in experiment 5 for corresponding samples is given in Table 2.

The shear behaviour of experiment 5 in Figure 7 shows identical maximum shear stress for all samples, where the thickness of infill layer was greater than the asperity height. As the surface asperities did not interact with each other, so the shear strength of these samples was the function of infill material rather than that of joint surface asperities. Hence, the maximum shear strength of each specimen in experiment 5 was significantly low compared with the shear strength of specimens tested in experiment 1, where the applied normal stress was exactly same. Therefore, it was concluded that the shear strength of rock joint reduces as the depth of infill material increases and a point reaches where the shear strength of joint becomes the function of infill material entirely and the shear strength of surfaces becomes negligible in joint strength.



## CONCLUSIONS

Interlocking of joint surface plays vital role in increment or reduction of shear strength in rock joints. As roughness height and angle of internal friction in sample B is less than the one in sample A, therefore, the maximum shearing stress was less than the maximum shear stress of sample A in experiments 1 and 2. Therefore, it is concluded that the asperity height and angle of internal friction have significant influences on the shear strength of the rock joint. The greater is the surface roughness the greater is the shear strength. This only applies in case of uniform interaction between shearing surfaces and joint being unfilled. In case of non-uniform interlocking between shearing surfaces and high roughness, the shear strength will be significantly reduced, which is clearly been demonstrated in Figure 7 (c) where there is minimum interlocking and interaction area between shearing surfaces. Moreover, it is also concluded that, the joint remains unfilled until the surfaces are damaged. The evidence can be seen in the Figure 8. Furthermore, it is determined that the shear resistance is greatly influenced by asperity height, angle of internal friction and interlocking of shearing surfaces. Additionally, the joint dilation increases due to shearing of surfaces and accumulation of damaged particles. Therefore, it is concluded that the maximum dilation might be greater than the maximum height of infill layer. The greater the asperity height the greater the dilation occurs in uniform asperity patterns; however, this is not the case where the pattern of asperities is irregular.

The experiments conducted on infilled joints revealed that the shear strength of rock joint decreases due to infill material. The shear behaviour depends on the thickness of infill material, if the thickness of infill layer is high then the shear is controlled by infill. However, if the thickness of the infill is less and the asperity height is greater, then the shear strength is mainly controlled by sharp asperities of the joint surface. As the thickness of infill layer increases, then the increment of infill height increases and the shear behaviour becomes the function of shear parameters of infill material. The shear strength of rock joint reduces as the depth of infill material increases and a point reaches where the shear strength of joint becomes the function of infill material entirely and the shear strength of joint surfaces become negligible in joint strength.

## REFERENCES

- Bandis, S., Lumsden, A.C. and Barton, N.R., 1981, February. Experimental studies of scale effects on the shear behaviour of rock joints. In *International journal of rock mechanics and mining sciences geomechanics abstracts* (Vol. 18, No. 1, pp. 1-21). Pergamon press.
- Barla, G., Forlati, F. and Zaninetti, A., 1985, September. Shear behaviour of filled discontinuities. In *Proceedings of the international symposium on fundamentals of rock joints, Bjorkliden* (pp. 163-172).
- Barton, N.R., 1986. Deformation phenomena in jointed rock. *Geotechnique*, 36(2), pp.147-167.
- Barton, N., 1973. Review of a new shear-strength criterion for rock joints. *Engineering geology*, 7(4), pp.287-332.
- Barton, N., 1976, September. The shear strength of rock and rock joints. In *International Journal of rock mechanics and mining sciences Geomechanics abstracts* (Vol. 13, No. 9, pp. 255-279). Pergamon.
- Benmokrane, B. and Ballivy, G., 1989, January. Laboratory study of shear behaviour of rock joints under constant normal stiffness conditions. In *The 30th US Symposium on Rock Mechanics (USRMS)*. American Rock Mechanics Association.
- Crawford, A.M. and Curran, J.H., 1981, December. The influence of shear velocity on the frictional resistance of rock discontinuities. In *International Journal of Rock Mechanics and Mining Sciences Geomechanics Abstracts* (Vol. 18, No. 6, pp. 505-515). Pergamon.

- Curran, J.H. and Leong, P.K., 1983, January. Influence of shear velocity on rock joint strength. In 5th ISRM Congress. International Society for Rock Mechanics and Rock Engineering.
- De Toledo, P.E., De Freitas, M.H. and CGcol, 1993. Laboratory testing and parameters controlling the shear strength of filled rock joints. *Geotechnique*, 43(1), pp.1-19.
- Eurenius, J. and Fagerstrom, H., 1969. Sampling and testing of soft rock with weak layers. *Géotechnique*, 19(1), pp.133-139.
- Goodman, R.E., 1970. The deformability of joints. In Determination of the in situ Modulus of Deformation of Rock. ASTM International.
- Goodman, R.E., 1976. Methods of geological engineering in discontinuous rocks, West publishing, St. Paul, Minn. USA.
- Haberfield, C.M. and Seidel, J.P., 1999. Some recent advances in the modelling of soft rock joints in direct shear. *Geotechnical Geological Engineering*, 17(3-4), pp.177-195.
- Haque, A., 1999. Shear behaviour of soft rock joints under constant normal stiffness. PhD thesis, University of Wolongong, Australia, P.271
- Hencher, S.R., 1989. Laboratory direct shear testing of rock discontinuities. *Ground Engineering*, pp.24-31.
- Hoek, E. and Brown, E.T., 1980. Underground excavations in rock. CRC Press.
- Hoek, E., 1990, June. Estimating Mohr-Coulomb friction and cohesion values from the Hoek-Brown failure criterion. In *Intl. J. Rock Mech. Mining Sci. Geomechanics Abstracts* (Vol. 12, No. 3, pp. 227-229).
- Hoek, E., 1977, March. Rock mechanics laboratory testing in the context of a consulting engineering organization. In *International Journal of Rock Mechanics and Mining Sciences Geomechanics Abstracts* (Vol. 14, No. 2, pp. 93-101). Pergamon.
- INDRARATNA, B., 1993. Experimental Study of Shear Behaviour of Rock Joints Under Constant Normal Stiffness. *Int. J. Rock Mech. Min. Sci. Geomech. Abstr.*, 34(3), p.534.
- Kanji, M.A., 1974, September. Unconventional laboratory tests for the determination of the shear strength of soil-rock contacts. In *Proc. 3rd Congr. Int. Soc. Rock Mech.*, Denver (Vol. 2, pp. 241-247).
- Kodikara, J.K. and Johnston, I.W., 1994, August. Shear behaviour of irregular triangular rock-concrete joints. In *International journal of rock mechanics and mining sciences geomechanics abstracts* (Vol. 31, No. 4, pp. 313-322). Pergamon.
- Kulatilake, P.H.S.W., Wathugala, D.N. and Stephansson, O., 1993, October. Joint network modelling with a validation exercise in Stripa Mine, Sweden. In *International Journal of Rock Mechanics and Mining Sciences Geomechanics Abstracts* (Vol. 30, No. 5, pp. 503-526). Pergamon.
- Kulatilake, P.H.S.W., Shou, G., Huang, T.H. and Morgan, R.M., 1995, October. New peak shear strength criteria for anisotropic rock joints. In *International Journal of Rock Mechanics and Mining Sciences Geomechanics Abstracts* (Vol. 32, No. 7, pp. 673-697). Pergamon.
- Kutter, H.K. and Rautenberg, A., 1979, January. The residual shear strength of filled joints in rock. In 4th ISRM Congress. International Society for Rock Mechanics and Rock Engineering.

- Ladanyi, B. and Archambault, G., 1977, July. Shear strength and deformability of filled indented joints. In Proc International Symposium on the Geotechnics of Structurally Complex Formations. Capri (Vol. 1, No. 1, pp. 317-326).
- Ladanyi, B. and Archambault, G., 1969, January. Simulation of shear behavior of a jointed rock mass. In The 11th US Symposium on Rock Mechanics (USRMS). American Rock Mechanics Association.
- Lam, T.S. and Johnston, I.W., 1989. Shear behavior of regular triangular concrete/rock jointsevaluation. Journal of geotechnical engineering, 115(5), pp.728-740.
- Lama, R.D., 1978. Influence of clay fillings on shear behaviour of joints. In: Division of Applied Geomechanics, editor/s. Proceedings III International Congress I.A.E.G.; Sep 4-8, 1978; 1978. 27-34. <http://hdl.handle.net/102.100.100/299705?index=1>
- Leichnetz, W., 1985, October. Mechanical properties of rock joints. In International Journal of Rock Mechanics and Mining Sciences Geomechanics Abstracts (Vol. 22, No. 5, pp. 313-321). Pergamon.
- Mirzaghobanali, A., Nemcik, J. and Aziz, N., 2014. Effects of shear rate on cyclic loading shear behaviour of rock joints under constant normal stiffness conditions. Rock mechanics and rock engineering, 47(5), pp.1931-1938.
- Obert, L., Brady, B.T. and Schmechel, F.W., 1976. The effect of normal stiffness on the shear resistance of rock. Rock mechanics, 8(2), pp.57-72.
- Ohnishi, Y. and Dharmaratne, P.G.R., 1990. Shear behaviour of physical models of rock joints under constant normal stiffness conditions. Rock Joints, Balkema, Rotterdam, pp.267-273.
- Papaliangas, T., Hencher, S.R., Lumsden, A.C. and Manolopoulou, S., 1993, April. The effect of frictional fill thickness on the shear strength of rock discontinuities. In International Journal of Rock Mechanics and Mining Sciences Geomechanics Abstracts (Vol. 30, No. 2, pp. 81-91). Pergamon.
- Paulino Pereira, J., 1990. Mechanics of filled discontinuities. In International conference on mechanics of jointed and faulted rock (pp. 375-380).
- Pereira, J.P., 1990. Shear strength of filled discontinuities. Rock Joints. Balkema, Rotterdam, pp.283-287.
- Phien-Wej, N., Shrestha, U.B. and Rantucci, G., 1990. Effect of infill thickness on shear behaviour of rock joints. Rock joints, pp.289-294.
- Saeb, S. and Amadei, B., 1992, May. Modelling rock joints under shear and normal loading. In International journal of rock mechanics and mining sciences geomechanics abstracts (Vol. 29, No. 3, pp. 267-278). Pergamon.
- Tulinov, R. and Molokov, L., 1971, September. Role of joint filling material in shear strength of rocks. In International Society of Rock Mechanics, Symposium on Rock Fracture, Nancy (Vol. 2, p. 13).
- Van Sint Jan, M.L., 1990. Shear tests of model rock joints under stiff normal loading. Rock joints. Balkema, Rotterdam, pp.323-327.
- Xu, S., 1989. The relationship between stress and displacement for rock surfaces in shear (Doctoral dissertation, Imperial College London (University of London)).

# FLOOR HEAVE MONITORING USING FLOOR INSTRUMENTATION

Sungsoon Mo<sup>1</sup>, Peter Yee<sup>2</sup>, Terri O'Sullivan<sup>3</sup>, Hossein Masoumi<sup>4</sup>, Ismet Canbulat<sup>5</sup>, Serkan Saydam<sup>6</sup>

**ABSTRACT:** Several underground coal mines in Australia have recently reported and anticipated significant floor heave in gateroads during longwall retreat. Floor heave on longwall retreat is typically attributed to a stress notch. To further understand the mechanisms of floor heave, *in situ* floor heave monitoring was conducted using floor instrumentation at two coal mines. This paper provides the field monitoring results along with the process of selecting the instruments and monitoring sites. To grasp the whole picture of the deformation of floor strata, the instruments for both the vertical and horizontal movements of floor units were considered. For the horizontal floor deformation, the strain gauged shear strips were used in both mines. For the vertical displacement of floor units, a remote reading tell-tale (RRTT) was chosen in Mine A, while a GEL extensometer specifically designed for this floor monitoring was selected in Mine B. As Mine A had negligible floor heave at the monitoring sites, no significant movement of the floor was captured. Although the level of floor deformation was minimal, there were indications of bedding separations as the longwall face approached the sites. In Mine B, minor floor heave was observed at the monitoring location. The data from the instruments showed that the horizontal movement of the floor strata occurred greater than approximately 4 m below the floor surface which may suggest the depth of floor failure. While several practical issues were identified from the field studies, the field monitoring results facilitated better understanding of the failure mechanisms.

## INTRODUCTION

Several underground coal mines have recently reported significant floor heave in gateroads. Although the phenomenon is well-known in the mining industry, research on floor heave has been relatively limited. The Australian Coal Association Research Program (ACARP) project C26064 was initiated to better understand the floor failure mechanisms and controlling factors.

As part of the project, *in situ* floor heave monitoring was carried out using floor instrumentation at two underground coal mines in Australia. Since floor instrumentation is not a common practice, discussions on the selection of instruments and monitoring locations were held many times with the mine sites. The process of selecting the instruments and monitoring sites is detailed, followed by the monitoring results and discussion on the results.

- 
1. PhD Student, UNSW Sydney. Email: [sungsoon.mo@unsw.edu.au](mailto:sungsoon.mo@unsw.edu.au)
  2. Geotechnical Engineer, Anglo American. Email: [peter.yee@angloamerican.com](mailto:peter.yee@angloamerican.com)
  3. Senior Geotechnical Engineer, Centennial Coal. Email: [terri.osullivan@centennialcoal.com.au](mailto:terri.osullivan@centennialcoal.com.au)
  4. Senior Lecturer, Monash University. Email: [hossein.masoumi@monash.edu](mailto:hossein.masoumi@monash.edu)
  5. Professor, UNSW Sydney. Email: [i.canbulat@unsw.edu.au](mailto:i.canbulat@unsw.edu.au)
  6. Professor, UNSW Sydney. Email: [s.saydam@unsw.edu.au](mailto:s.saydam@unsw.edu.au)

## PREPARATION FOR FLOOR INSTRUMENTATION

### Review on types of field monitoring

Various field monitoring techniques were reviewed and compared for the fieldwork. Many displacement monitoring devices including borescope, convergence rod and various types of extensometers have been used (Spearing and Hyett, 2014; Sweeney, 2015; Galvin, 2016). The term 'tell-tale' is commonly used in the mining industry for extensometers that have visual indicators of vertical strata movement (Bigby, *et al.*, 2010). The strain gauged shear strip is widely used to monitor the roof and rib in the Australian coal mining industry (Nemcik, 2003; Tarrant, 2005; Heritage, 2018). Several stress measurement techniques also exist while the ANZI cell and CSIRO cell are typically used in Australian coal mines for stress measurements (Worotnicki, 1993; Sweeney, 2015; Galvin, 2016; Mills and Puller, 2018).

Apart from the displacement and stress monitoring, there are other types of instrumentation. Tiltmeters, also known as inclinometers, measuring changes in tilt or slope, have been used to monitor ground movements (Logan, 2008; Mills, 2011; Spearing and Hyett, 2014). Time Domain Reflectometry (TDR) can also detect the movement of rock mass by interpreting cable deformation (Dowding *et al.*, 1989; Dowding and Huang, 1995; Dussud, 2002). Laser scanning technologies and photogrammetry have been trialled to monitor the deformation of roadways in underground mines (Kukutsch, *et al.*, 2016; Slaker and Mohamed, 2017; Vazaios *et al.*, 2017; Raval, *et al.*, 2019).

When it comes to floor monitoring, floor instrumentation including the extensometer, inclinometer, stress cell and strain gauged shear strip has been used (Speck, 1979; Kumar, 1990; Seedsman and Gordon, 1992; Wuest, 1992; Wang, 1996; Nemcik, 2003; Kang, *et al.*, 2014; Zhu, *et al.*, 2014). Convergence rods were used to measure the clearance between the roof and floor and subsequently to identify the movement of the floor (Vasundhara, 1999; Unal, *et al.*, 2001). In a rare case, a test pit was created so that the cross-section of the floor could be seen (Whiteley, *et al.*, 2005). Eventually, displacement monitoring was selected to provide a complete view of the deformation of floor strata. Equipment for both the vertical and horizontal movements of floor units was considered.

### Selection of instruments and monitoring locations

Two typical types of extensometers include the sonic probe extensometer and roadway deformation indicators also known as tell-tales (Sweeney, 2015). The sonic extensometer allows more detailed monitoring with a greater number of anchors compared to the tell-tales (Corbett and Payne, 1995; Bigby and DeMarco, 2001; Nemcik, 2003). However, the sonic extensometer is vulnerable to damage and more expensive; thus, the tell-tales were chosen over the sonic probe extensometer to monitor the vertical displacement of the floor. In Mine A, the remote reading tell-tale was used (Bigby and DeMarco, 2001; Bigby, *et al.*, 2010; Buddery, *et al.*, 2018). In Mine B, the GEL extensometer (Shen, *et al.*, 2006; Sweeney, 2015) particularly designed for floor monitoring was used with a higher travel range of 400 mm. For the lateral floor displacement in both mines, the strain gauged shear strip was chosen.

Also, the specific locations for monitoring were chosen where floor heave was expected and traffic could be avoided as much as possible. In Mine A, it was hypothesised that the interburden thickness between the coal seam being mined and the lower coal seam would affect the occurrence of floor heave. Thus, four locations along the roadways in LW603 were selected as shown in Figure 10. In Mine B, significant floor heave was frequently observed around the areas near the longwall finish lines. Therefore, one location around the finish line of LW425 was selected as shown in Figure 11a.

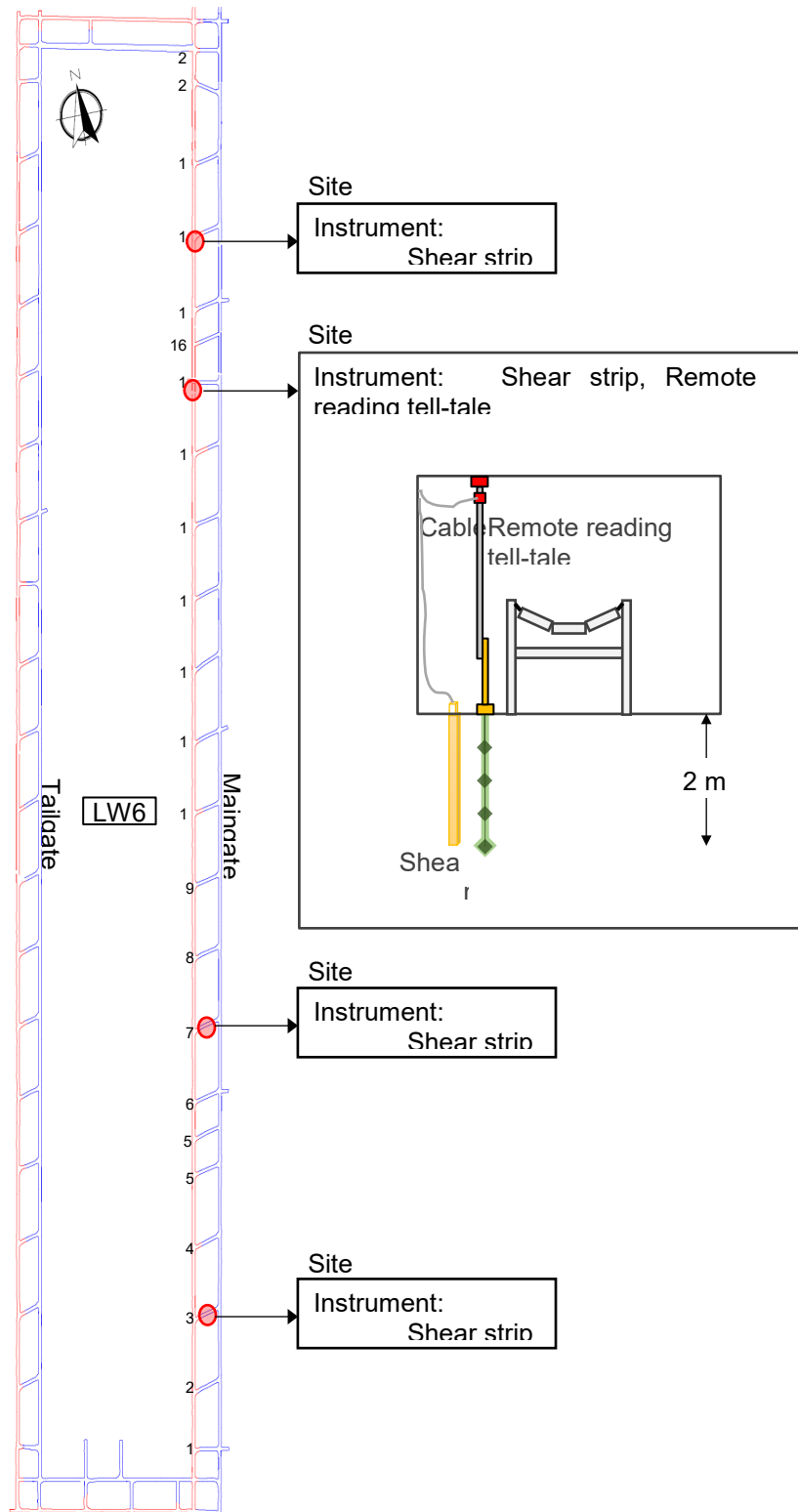


**Figure 10: Monitoring locations in Mine A with types of instrument and interburden thickness between the coal seam being mined and lower coal seam**

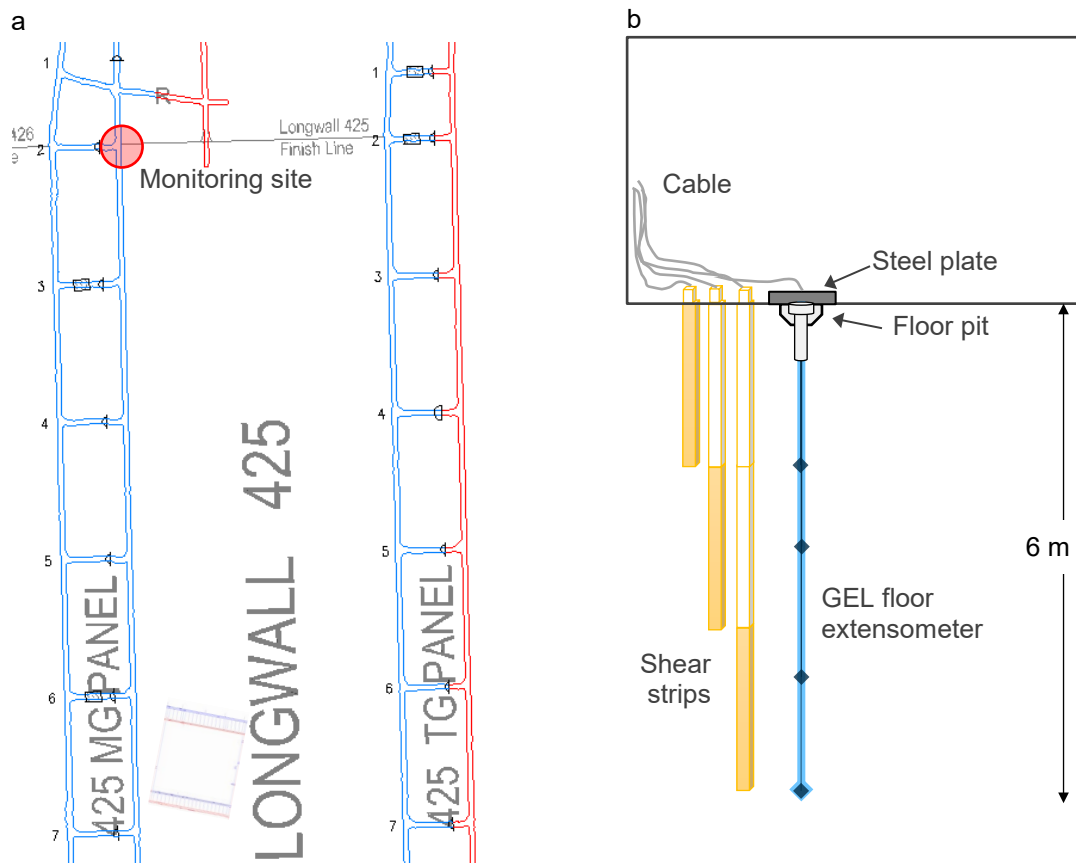


**Figure 11: Floor instrumentation at Mine B (a: monitoring location, and b: types of instrument)**

Different approaches to gathering data in terms of depth of floor failure were used for each mine. In Mine A, a monitoring depth of 2 m into the floor was targeted since the impact of the immediate floor units was considered critical. Hence, four strain gauged shear strips were arranged for each monitoring location and a 2-m-long remote reading tell-tale with four anchors located every 0.5 m in the 2 m floor horizon were added to one of the monitoring sites as shown in Figure 10. In Mine B, the greatest movement of the floor strata was expected at around 4 m below the floor surface due to the location of the soft clay matrix. Therefore, a monitoring depth of 6 m into the floor was considered to cover the deformation of the soft material. As a typical length of the strain gauged shear strip is 2 m, three strain gauged shear strips were prepared to cover the 6 m floor horizon. In addition, a 6-m-long GEL floor extensometer with four anchors was prepared as shown in Figure 11b. The anchor depths of the GEL extensometer were 2 m, 3 m, 4.5 m and 6 m.

### Installation

After the monitoring locations and types of instruments were determined, the equipment was installed. Figure 12 shows the site where the shear strip and remote reading tell-tale were installed together adjacent to the conveyor belt in Mine A. As described in Figure 10, only one shear strip was installed at the other three locations in the mine.

To install the GEL floor extensometer in Mine B, an auger hole with a diameter of 500 mm and a depth of 250 mm was produced to recess the instrument (Figure 13a). Then the extensometer was installed into the hole (Figure 13b), followed by placing a steel plate with a thickness of 6 mm to protect the head of the extensometer from excessive groundwater (Figure 13c). Three sets of shear strips were also installed close to the GEL extensometer. Finally, the instrumented site was barricaded to protect it from traffic and to limit access to the instruments.

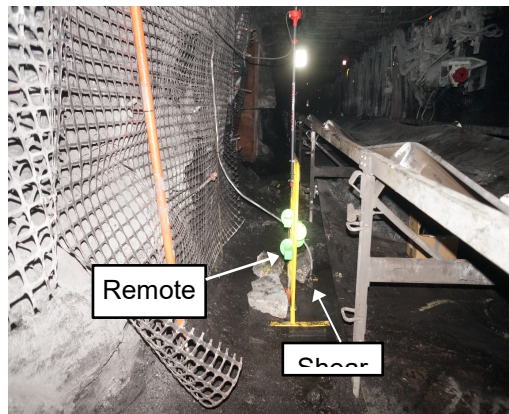


Figure 12: Shear strip and remote reading tell-tale installed in Mine A



Figure 13: Installation of GEL floor extensometer (a: top of the hole reamed using auger, b: GEL extensometer placed into the hole, and c: steel plate covering the instrument)



## RESULTS

The effect of longwall retreat on floor heave was monitored as Mine A anticipated floor heave and Mine B experienced significant floor heave on longwall retreat.

### Mine A

During the monitoring period from June 2018 to December 2018 as LW603 retreated, Mine A rarely experienced floor heave in the maingate where a stress notch was present. Consequently, the data obtained from the floor instrumentation did not capture significant movement of the floor. Figure 14 illustrates the results from one of the strain gauged shear strips. Many shear planes appeared to exist such as around 0.25 m, 0.35 m, 0.6 m, 0.85 m, 0.95 m and 1.15 m below the floor surface. The biggest movement was captured around 0.6 m below the surface. As the uppermost floor unit of Mine A is coal with a thickness of approximately 0.5 m, the shearing may indicate that a bedding plane exists between the coal floor and the underlying floor unit. While the magnitudes of the shear displacement were not significant, the shearing seemed to accelerate where the longwall face was 60 m inbye the monitoring location. The data showed the maximum displacement of shearing where the longwall face was 24 m away.

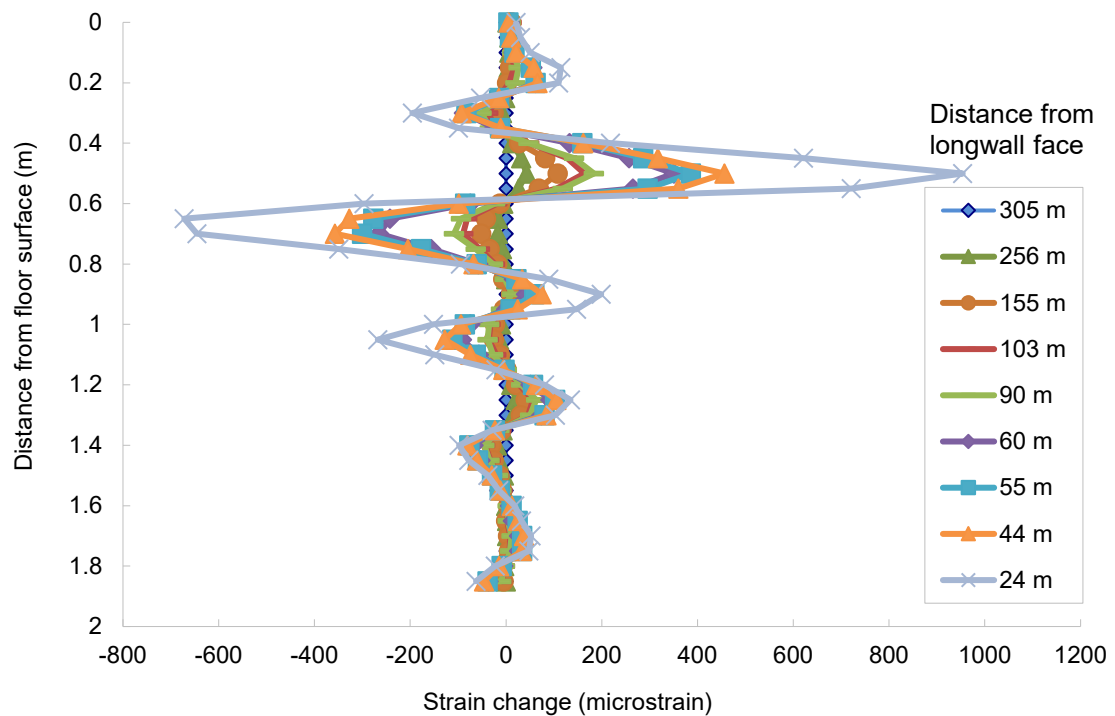


**Figure 14: Strain change data from shear strip at Site 1 in Mine A**

Figure 15 illustrates the monitoring data from the remote reading tell-tale. As floor heave at the monitoring location was negligible, it appeared that erroneous results were obtained from the instrument. The spikes on 28 July and 19 August 2018 were thought to be caused by the impact of some materials off the conveyor belt. The distances from the longwall face were approximately 500 m on 28 July and 260 m on 19 August. The fluctuation of the displacement data was possibly due to vibrations caused by the belt structure right next to the instrument.

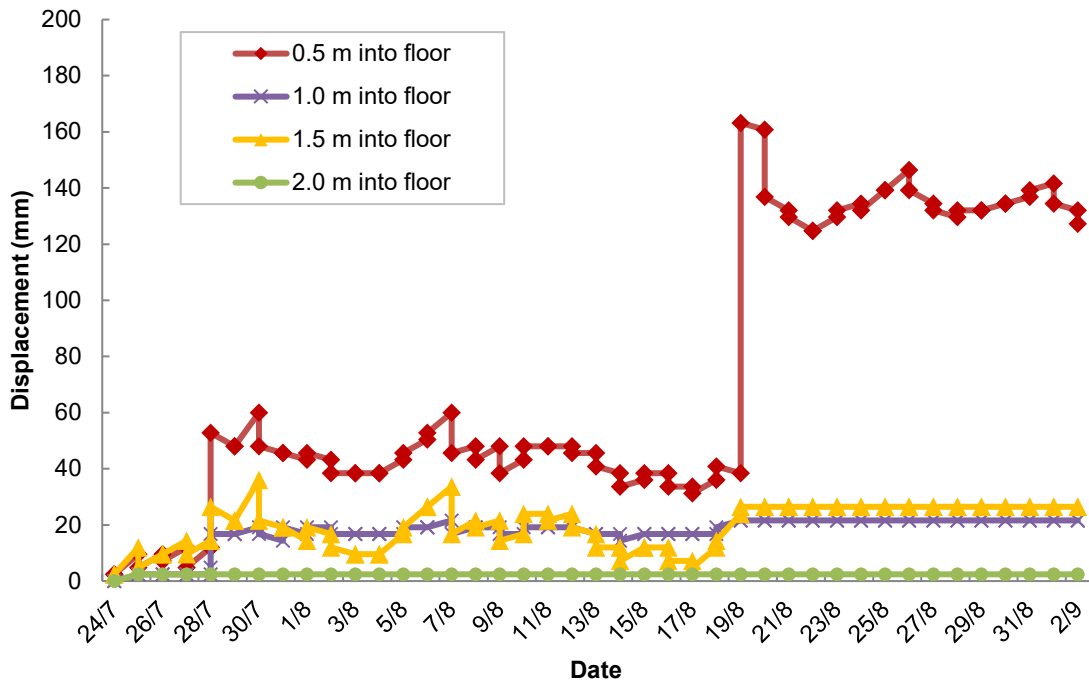


Figure 15: Displacement data from remote reading tell-tale at Site 2 in Mine A

**Mine B**

Mine B showed minor floor heave around the location of floor instrumentation during the monitoring period from March 2019 to August 2019. Figure 16 shows the results from the shear strips installed in the mine, with a predominant shear plane 3.8 m below the floor surface. It was difficult to drill beyond the 4 m floor horizon, which indicated a strong floor unit. The predominant shear plane possibly indicates a bedding plane between the soft clay matrix and the underlying strong unit.

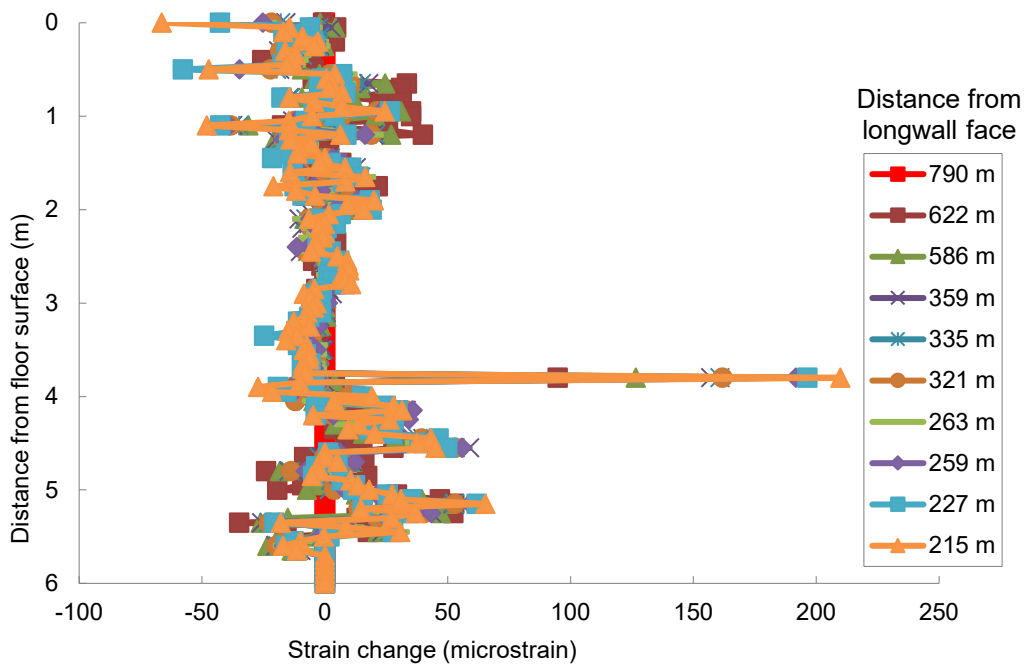


Figure 16: Strain change data from shear strip in Mine B

Due to other operational issues, the monitoring stopped when the longwall face was 280 m inbye from the installation site. The magnitude of the deformation detected from the shear strips was minor. The displacement from the GEL extensometer was also negligible.

## **DISCUSSION**

### **Results at Mine A**

Although the floor instrumentation in Mine A did not show significant floor movement, the field monitoring results from the strain gauged shear strips showed the shear movements along the bedding planes between the floor units. This indicates the bedding separations might be part of the mechanisms of floor failure. Also, the shearing intensity tended to increase as the longwall face became close to the instrumented sites.

The mine experienced floor heave in the tailgate of previously mined panels, LW111 and LW112. This was attributed to the difference in the magnitudes of horizontal stresses exerted in each longwall panel. In LW111 and LW112, floor heave was observed where the depth of cover reached 350 m while LW603 is located at depths of cover ranging from 260 m to 305 m. In addition to this LW603 was the first longwall panel developed and mined in the area (virgin block), therefore horizontal stress concentrations were not adversely impacted by surrounding goafs. Also, the angles between the major horizontal stress and the headings where floor heave took place were approximately 25° in LW111 and LW112 while those in LW603 were typically less than 10°. The depth of cover generally correlates with the magnitude of horizontal stress (Mark and Gadde, 2008), and floor heave on longwall retreat is attributed to the horizontal stress notching effect (Thomas and Wagner, 2006). Overall, it was suggested that the magnitude of horizontal stress was not high enough to cause floor failures in LW603. Since finalising the results, the adjacent longwall block LW604 commenced and experienced intense floor heave of up to 0.5 m in the belt road and up to 1.0 m in the cut-throughs 30 m inbye of the retreating face.

### **Results at Mine B**

Although minor floor heave was noticed near the monitoring location, both the shear strips and GEL extensometer did not capture significant floor movement. This is possibly due to the instruments installed close to the rib. As they were not installed in the middle of the roadway, the floor movement may not have been captured. Multiple sets of instruments at a location will be more effective to provide a full view of floor deformation from a research point of view.

It is worth noting that the high level of water and coal fines in the roadway, adjacent to the monitoring site, could have impacted the readings, particularly the GEL extensometer which is not water proof.

### **Limitations of floor instrumentation**

Several practical issues were identified from this fieldwork using the floor instrumentation. For instance, the instruments in the floor need to be connected to the readout units through cables. The equipment tends to protrude from the floor a few tens of centimetres to connect the cables to the readers unless completely recessed. Thus, the instruments were installed close to the ribs, not at the centre of the roadways, to avoid interfering with underground traffic or equipment. Where cables are exposed, particularly on the floor, they are more susceptible to damage.

Water flowing on the floor was another issue at Mine B. This causes a muddy floor which, in turn, can limit access to the floor instrumentation. Moreover, installing equipment in the floor

immediately after development was not possible in practice due to other operational requirements while the floor deformation shortly after excavation was considered crucial to measure. Future work requires novel technologies that can prevent the floor instrumentation from being interrupted by traffic or mining operations.

Data gathering was another practical issue. Most of the instruments used in this study required portable readout units, and thus, data gathering was only possible during underground trips with limited personnel available. The frequency of data is critical, particularly when the longwall face approaches the instruments, for an accurate and representative insight into ground behaviour. Therefore, a remote reading system would be beneficial in future monitoring sites.

### **SUMMARY AND CONCLUSIONS**

Floor heave monitoring using floor instrumentation was carried out at two underground coal mines. In Mine A, four locations in a longwall panel were selected to investigate the influence of the interburden between the coal seam being mined and the lower coal seam. Four shear strips were installed at each location and a remote reading tell-tale was additionally used for one location. A depth of 2 m into the floor was monitored since the influence of the immediate floor units was considered critical. In both mines, the impact of longwall retreat on floor heave was investigated. In Mine B, one location around the finish line of a longwall panel was chosen as the mine experienced significant floor heave around the finish lines of previous panels. The strain gauged shear strips and GEL floor extensometer were installed at a depth of 6 m into the floor, to capture the deformation of the soft floor unit typically located at around 4 m below the floor surface.

Mine A experienced negligible floor heave around the monitoring locations. Consequently, the data obtained from the instruments did not capture significant movement of the floor. However, minor shear movements were detected between 0.25 m to 1.15 m floor horizon, which may indicate the bedding separations that could be part of floor failure mechanisms. The remote reading tell-tale produced erroneous results possibly due to the impact of the belt structure adjacent to the instrument. The shear strips installed in Mine B showed a minor shear movement 3.8 m below the floor surface while negligible deformation was detected from the GEL extensometer.

Although field measurements using floor instrumentation can be advantageous in understanding the behaviour of the floor, the implementation and routine monitoring of such measurement tools is still challenging. While several practical issues were identified from these field studies, the selection of the monitoring locations was one of the most challenging issues mainly due to underground traffic in an operational mine. Future work is needed to develop new technologies that can prevent the floor instrumentation from being interrupted by traffic or mining operations.

### **ACKNOWLEDGEMENTS**

The authors wish to acknowledge the support of the ACARP project C26064 and the mine sites. The authors would like to recognise the great effort by the industry monitors and all the site personnel who organised the field monitoring and installed the instruments. Gavin Langerak from GEL Instrumentation is appreciated for providing a new floor extensometer, and Adrian Rippon from SCT Operations is appreciated for his involvement in the installation and data analysis of the instruments.

## REFERENCES

- Bigby, D and DeMarco, M, 2001. Development of a remote reading dual-height telltale system for monitoring, in Proceedings 20th International Conference on Ground Control Mining, Morgantown, West Virginia (eds: S S Peng, C Mark and A W Khair) pp 163-172 (West Virginia University).
- Bigby, D, MacAndrew, K and Hurt, K, 2010. Innovations in mine roadway stability monitoring using dual height and remote reading electronic telltales, in Proceedings 10th Underground Coal Operators' Conference, Wollongong, New South Wales (ed: N I Aziz) pp 146-160 (University of Wollongong the Australasian Institute of Mining and Metallurgy).
- Brown, E T and Brady, B H G, 2006. Rock Mechanics for Underground Mining (Springer).
- Buddery, P, Morton, C, Scott, D and Owen, N, 2018. A continuing roof and floor monitoring systems for tailgate roadways, in Proceedings 18th Coal Operators' Conference, Wollongong, New South Wales (eds: N Aziz and B Kininmonth) pp 72-81 (University of Wollongong).
- Corbett, G R and Payne, D A, 1995. Improved intersection design and monitoring in the Sydney Coalfield, in Proceedings 14th Conference on Ground Control in Mining, Morgantown, West Virginia (ed: S S Peng) pp 159-167 (West Virginia University).
- Dowding, C H and Huang, F-c, 1995. Early detection of rock movement with time domain reflectometry, *Journal of Geotechnical Engineering*, 120(8):1413-1427.
- Dowding, C H, Su, M B and O'Connor, K, 1989. Measurement of rock mass deformation with grouted coaxial antenna cables, *Rock Mechanics and Rock Engineering*, 22(1):1-23.
- Dussud, M L, 2002. TDR monitoring of soil deformation: case histories and field techniques, Master's thesis, Northwestern University.
- Galvin, J M, 2016. Ground Engineering - Principles and Practices for Underground Coal Mining (Springer International Publishing).
- Heritage, Y, 2018. Mechanics of rib deformation at Moranbah North mine - a case study, in Proceedings 18th Coal Operators' Conference, Wollongong, New South Wales (eds: N Aziz and B Kininmonth) pp 58-71 (University of Wollongong).
- Kang, Y, Liu, Q, Gong, G and Wang, H, 2014. Application of a combined support system to the weak floor reinforcement in deep underground coal mine, *International Journal of Rock Mechanics and Mining Sciences*, 71:143-150.
- Kukutsch, R, Kajzar, V, Waclawik, P and Nemcik, J, 2016. Use of 3D laser scanner technology to monitor coal pillar deformation, in Proceedings 16th Coal Operators' Conference, Wollongong, New South Wales (eds: N Aziz and B Kininmonth) pp 99-107 (University of Wollongong).
- Kumar, C, 1990. Effects of weak floor interaction on underground room-and-pillar coal mining, PhD thesis, Southern Illinois University at Carbondale.
- Logan, K S, 2008. Analysis of wireless tiltmeters for ground stability monitoring, Master's thesis, Virginia Polytechnic Institute and State University.

## Coal Operators' Conference

- Mark, C and Gadde, M M, 2008. Global trends in coal mine horizontal stress measurements, in Proceedings 27th International Conference on Ground Control in Mining, Morgantown, West Virginia (eds: S S Peng, C Mark, G L Finfinger, S C Tadolini, A W Khair, K A Heasley and Y Luo) pp 319-331 (West Virginia University).
- Mills, K and Puller, J, 2018. Experience of using the ANZI strain cell for three-dimensional, in-situ stress determinations in deep exploration boreholes, in Proceedings 37th International Conference on Ground Control in Mining, Morgantown, West Virginia (eds: B Mishra, T M Klemetti, H Lawson, M M Murphy and K A Perry) pp 44-52 (Society for Mining, Metallurgy Exploration).
- Mills, K W, 2011. Developments in understanding subsidence with improved monitoring, in Proceedings 8th Triennial Conference on Management of Subsidence, Pokolbin, New South Wales pp 25-41 (Mine Subsidence Technological Society).
- Nemcik, J A, 2003. Floor failure mechanisms at underground longwall face, PhD thesis, University of Wollongong.
- Raval, S, Banerjee, B P, Singh, S K and Canbulat, I, 2019. A preliminary investigation of mobile mapping technology for underground mining, in Proceedings International Geoscience and Remote Sensing Symposium, Yokohama, Japan (IEEE Geoscience and Remote Sensing Society).
- Seedsman, R W and Gordon, N, 1992. Weak claystone floors and their implications to pillar design and settlement, in Proceedings 11th International Conference on Ground Control in Mining, Wollongong, New South Wales (eds: S S Peng and N I Aziz) pp 548-555 (University of Wollongong).
- Shen, B, Guo, H, King, A and Wood, M, 2006. An integrated real-time roof monitoring system for underground coal mines, in Proceedings Coal Operators' Conference, Wollongong, New South Wales (eds: N Aziz and W Keilich) pp 64-76 (University of Wollongong and Australasian Institute of Mining and Metallurgy).
- Slaker, B A and Mohamed, K M, 2017. A practical application of photogrammetry to performing rib characterization measurements in an underground coal mine using a DSLR camera, International Journal of Mining Science and Technology, 27(1):83-90.
- Spearing, A J S and Hyett, A, 2014. In situ monitoring of primary roofbolts at underground coal mines in the USA, Journal of the Southern African Institute of Mining and Metallurgy, 114(10):791-800.
- Speck, R C, 1979. A comparative evaluation of geologic factors influencing floor stability in two Illinois coal mines, PhD thesis, University of Missouri-Rolla.
- Sweeney, C, 2015. Importance of monitoring technologies and in situ testing, with relation to numerical analysis for ground control design, in Proceedings 15th Coal Operators' Conference, Wollongong, New South Wales (eds: N Aziz and B Kininmonth) pp 84-93 (University of Wollongong, Australasian Institute of Mining and Metallurgy Mine Managers Association of Australia).
- Tarrant, G, 2005. Skew roof deformation mechanism in longwall gateroads - concepts and consequences, in Proceedings Coal Operators' Conference, Brisbane, Queensland (ed: N Aziz) pp 73-88 (University of Wollongong and Australasian Institute of Mining and Metallurgy).

## Coal Opertors' Conference

- Thomas, R and Wagner, C, 2006. Main gate roof support design and management during longwall retreat in the Australian coal industry, in Proceedings 25th International Conference on Ground Control in Mining, Morgantown (eds: S S Peng, C Mark, G L Finfinger, S C Tadolini, A W Khair, K A Heasley and Y Luo) pp 191-197 (West Virginia University).
- Unal, E, Ozkan, I and Cakmakci, G, 2001. Modeling the behavior of longwall coal mine gate roadways subjected to dynamic loading, *International Journal of Rock Mechanics and Mining Sciences*, 38(2):181-197.
- Vasundhara, 1999. Geomechanical behaviour of soft floor strata in underground coal mines, PhD thesis, University of New South Wales, Sydney.
- Vazaios, I, Vlachopoulos, N and Diederichs, M S, 2017. Integration of Lidar-based structural input and discrete fracture network generation for underground applications, *Geotechnical and Geological Engineering*, 35(5):2227-2251.
- Wang, Y, 1996. Mechanisms and control of mine floor heave, PhD thesis, West Virginia University, Morgantown.
- Whiteley, B, Vasundhara and Sainsbury, B-A, 2005. Systems approach to pillar design, module 2: long term stability of flooded mine workings above claystone floors, ACARP Project C9018 Final Report - Volume 2 (Australian Coal Association Research Program).
- Worotnicki, G, 1993. CSIRO triaxial stress measurement cell, *Rock Testing and Site Characterization*:329-394.
- Wuest, W J, 1992. Controlling coal mine floor heave: an overview (United States Department of the Interior).
- Zhu, S, Jiang, Z, Zhou, K, Peng, G and Yang, C, 2014. The characteristics of deformation and failure of coal seam floor due to mining in Xinmi coal field in China, *Bulletin of Engineering Geology and the Environment*, 73(4):1151-1163.

# THE EVOLUTION OF PRIMARY CABLE SUPPORT AT GRASSTREE MINE

**Edward Steed<sup>1</sup>, Jason Emery<sup>2</sup>**

*ABSTRACT:* An increasing cover depth within a highly variable bedded and laminated roof, coupled with high level longwall retreat performance has required the evolution of cable support for development roadways at Grasstree Mine. This paper briefly addresses the evolution of cable bolting as primary support at Grasstree and captures in detail the theoretical and practical engineering applied to the most recent iteration of cable support, the Jumbo cable.

## INTRODUCTION

Grasstree is an underground coal mine in the central portion of the Bowen Basin, Queensland. Historically, it forms part of the German Creek (GC) / Capcoal complex of mines, as shown in Figure 1. Capcoal has a long rich history of longwall mining and is currently owned and operated by Anglo American. At the time of publication, Grasstree is the deepest longwall mine in Queensland with cover depth reaching 500m in areas.

Central Colliery is located immediately to the north of Grasstree, with Grasstree essentially forming the eastern extension of Southern Colliery (now Grasstree West). Central Colliery was the first longwall mine built in Queensland and ceased operations in 2005, largely due to difficult ground conditions and high levels of gas making the mine uneconomic. In order to better manage high gas levels at Grasstree and extend mine life, many of the panels were formed using three-heading gate roads. Despite being effective for reducing the general body in the longwall return, this mine plan modification required an increased amount of roadway development when compared to a typical chain pillar layout. From LW907 onwards, a two-heading gate road system was successfully implemented by utilising an additional shaft, intake ventilation holes and increasing surface goaf drainage capacity to ensure methane emissions remained within acceptable limits in the longwall returns.

Ultimately, the mine layout at Grasstree necessitated more roadway development for each longwall panel than any of the previous mines in the German Creek complex. The need for additional roadway development coupled with high level longwall retreat performance and changing ground conditions were underlying motivators for innovative solutions to the bottleneck in development. This paper focusses on innovations around primary cable support and focuses on the most recent iteration, the Jumbo cable. These innovations over time have helped enable Grasstree to not only exceed the depths of Central Colliery, but consistently rank as one of the highest producing longwall operations in Australia since 2013.

- 
1. Geotechnical Engineer, Anglo American. Email: [edward.steed@angloamerican.com](mailto:edward.steed@angloamerican.com) Tel: 0478154066
  2. PhD Candidate (Mining), UNSW. Email: [j.emery@unsw.edu.au](mailto:j.emery@unsw.edu.au) Tel: 0447377755



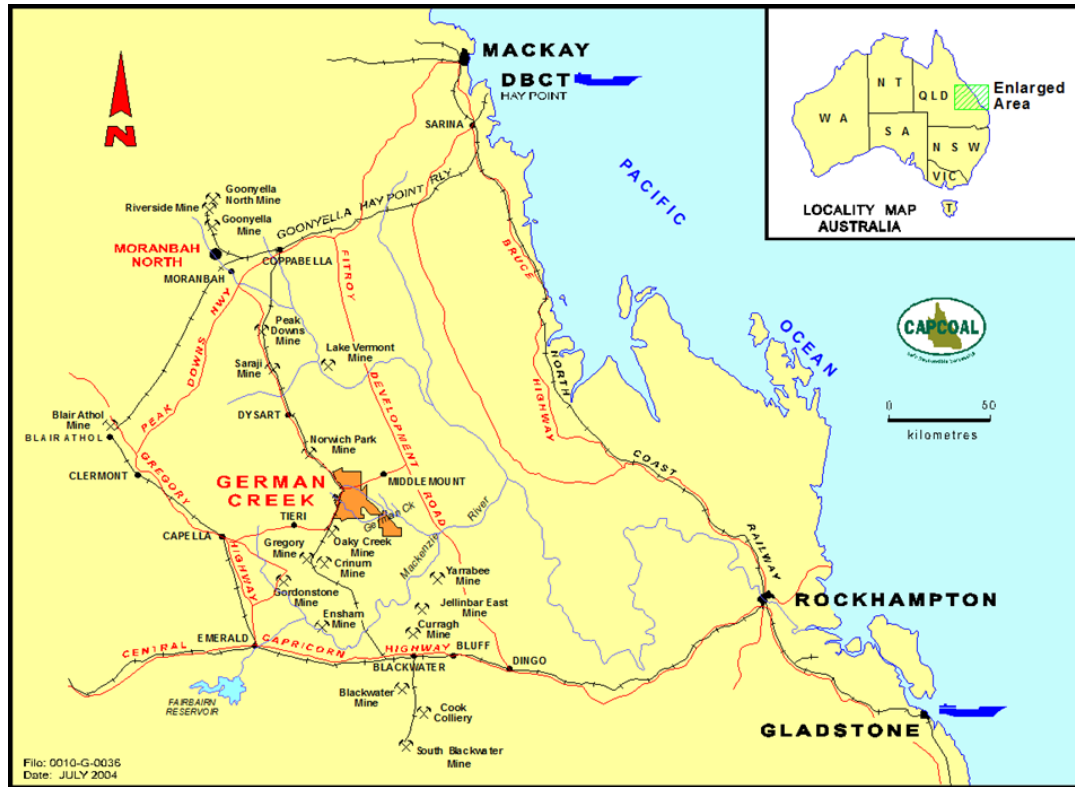


**Figure 1: German Creek mining complex location (Capcoal)**

**GEOLOGICAL AND GEOTECHNICAL SUMMARY**

Grasstree is separated into the 800 series panels on the southern side of the mine and 900 series panels on the northern side by a seven-heading mains section. The longwall panels are 300 – 350m wide and have a 2.6 - 2.8m extraction height. Roadways are developed at 2.8m high and 5.2m wide. The mains arrangement consisting of seven rather than five headings was in order to facilitate more effective removal of gas, adding to the total amount of development required to form each panel. The 900 series panel entries are separated from the mains headings by the Grasstree Dyke, a 10 – 15m very strong dolerite dyke (>100 MPa), as shown in Figure 2. This large intrusion is a key reason the panels were orientated at an adverse direction to the stress field. The GC seam in the 900s is positioned along a broad syncline plunging east-northeast, resulting in a gradual increase in depth of cover from 200m along the western end (Southern Colliery side) of the mine to approximately 500m at the deepest part of the mine. The seam rolls over into a very similar but anticlinal setting in the 800s panels.

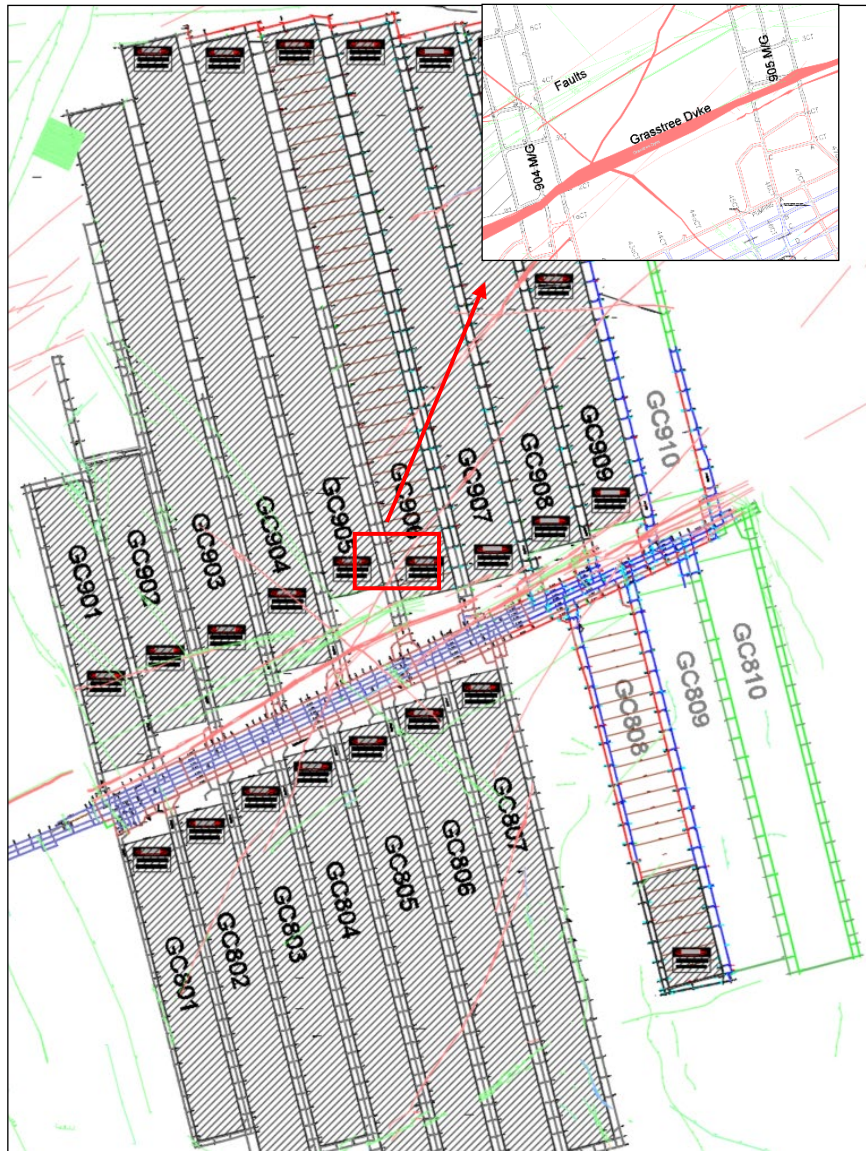


**Figure 2: Grasintree Mine layout and regional geology**

The immediate roof comprises mainly of siltstone and sandstone units, typically thinly to thickly bedded, with anomalous areas of very highly laminated roof. This highly laminated roof is often micaceous and heavily jointed, hence prone to instability despite having relatively high material strength (35 – 55 MPa). This is particularly noticeable at cover depths >300m. The Coal Mine Roof Rating (CMRR) tends to vary from 40 – 50, with an average of 45. However, in areas of highly laminated, jointed micaceous roof, CMRR of 35 is not uncommon. The Geophysical Strata Rating (GSR) typically varies from 55 – 65. The median GSR over the 0 – 3m horizon across the 900 series panels and 808 – 810 panels is shown in Figure 3.

The major principal horizontal stress direction at Grasintree is approximately 030° from North, with variations of +/- 10° across the mine, typically rotating further to the east with depth and locally variable around major discontinuities. The panel orientation at Grasintree results in an approximately 045° angle to the principal horizontal stress on development advance in both the 800 and 900 series panels. A major and minor principal horizontal stress to vertical stress ratio of 2 and 1.2 is typically used for roadway designs.



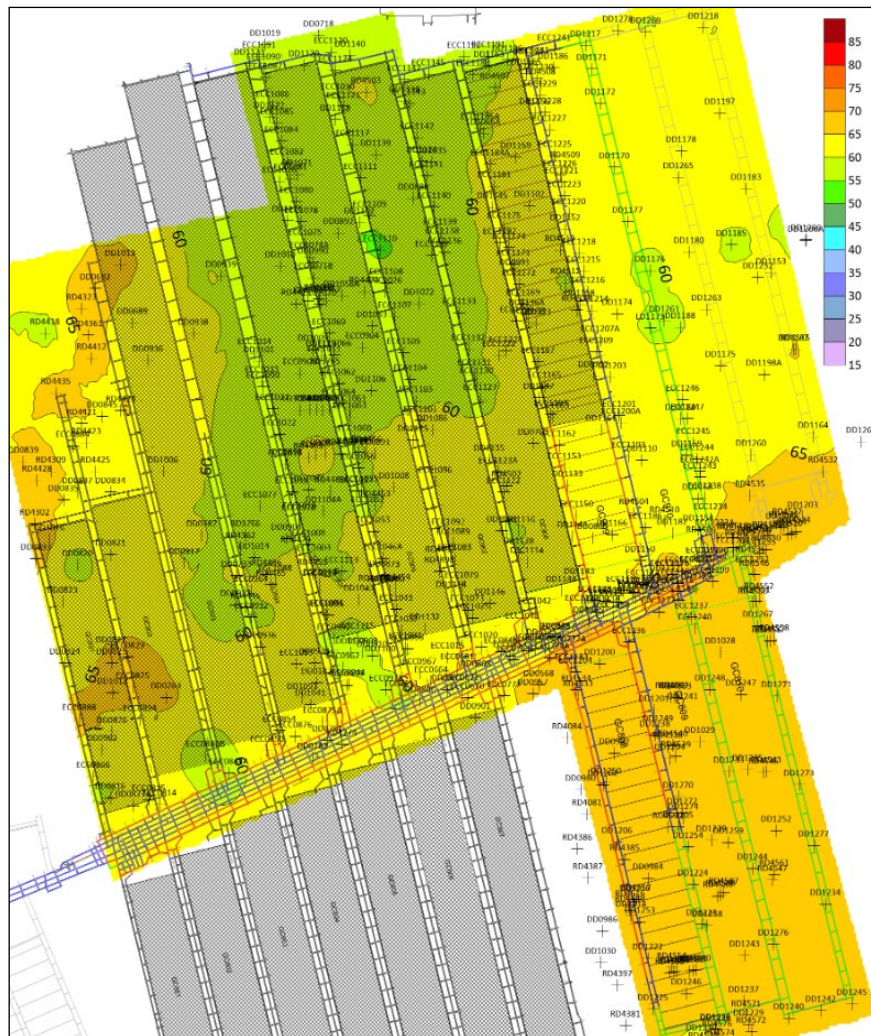


Figure 3: Median GSR (3m roof horizon)

### HISTORICAL CONTEXT

The anticline in the 800s and syncline in the 900s are potential sources of variation in both magnitude and orientation of the principal stresses. Additionally, there are regional faults and folds contorting and segmenting the coal. This structural setting, relatively high cover depth and variable roof conditions has resulted in Grasree experiencing a large range of mining conditions and hence vast change in support strategies throughout its life.

Extracting panels from west to east in a seam that dips in the same direction results increased *in situ* stress for each subsequent panel. In these types of conditions, it is common to reach critical points during roadway development as panel progress in depth and the roof beam transitions from static to buckling behaviour (Thomas, 2007). This transformation is commonly referred to as the overstressing threshold and is usually identified at Grasree by increased rock deformation in the unsupported cut and subsequent ongoing deformation following installation of primary support. Addressing the ground conditions associated with these thresholds was one of the catalysts for modifications to the primary roof support at Grasree.

The step changes in support requirements associated with the overstressing threshold at Grasree typically arose from slow ongoing deterioration behind the continuous miner (CM), rather than uncontrolled strata failure at the faces. This included centreline bagging, guttering, tensile cracking, roof fretting and occasional bolt, mesh or plate failure. Ongoing deterioration

typically required the installation of cable bolts for remedial support. The disruption to the pillar cycle for the remedial works had a severe impact on the pillar cycle time, much greater than that of installing cable support from the CM on advance. During these instances, it became clear to mine personnel that the installation of additional support requirements on advance to address prevailing conditions was more productive than repeatedly reacting to deteriorating conditions. Each step change in support is briefly summarised in this section of the report.

### **Primarily roof bolting only**

Roadway development utilising only 1.8 m roof bolts was successful at Grasstree to 40ct in the East Mains. Level green primary support consisted of 6 x 1.8 m X-grade roof bolts, encapsulated with 1000 mm two speed resin in a four-two pattern at 1.3 m row spacing. A step change in conditions was evident inbye of 40ct, alongside the MG805 panel entry in the 800 series, at cover depth of approximately 330 m. The changes in conditions comprised of heavy guttering, roof slabbing (>300 mm), centreline cracking (>50 mm) and roadway sag (>300 mm).

These conditions would trigger the installation of 4 m Superstrand cables (60 tonne strand capacity) in standard roadways, point anchored with a 1200 mm resin and post tensioned to 20 tonnes. Post groutable cables were utilised for remedial support of intersections. The preferred post groutable cable was a bottom up bulbed Superstrand, i.e. the Bowen Cable. This cable was very difficult to install from the CM and resulted in grouting failure rates in excess of 50%. Cables were only ever installed after the roof had typically already softened significantly (50 – 100 mm). Subsequently, slow ongoing creep type deformation was common.



**Figure 4: Example of guttering and roof sag requiring remedial support in 800 series**

### **Point anchored cable bolts**

From 45ct inbye in the East Mains, cable support was installed from the CM with the same bolting pattern. These cables consisted of either 4 m or 6 m point anchored Superstrand cables, typically at a density of two cables every 2.6 m (every second row). The increase to 6 m cables was implemented due to monitoring data indicating deformations starting to develop above the 3.5 m roof horizon. This support was installed from 45ct to 48ct in the mains, however, delays due to remedial support continued with increased prevalence of plate failure on the 6 m tendons and typically higher levels of overall deformation and ongoing creep. This was deemed unacceptable and the search for a solution continued.

### **Partially encapsulated cable bolts**

The failure of increased cable length to arrest deformations prompted more thought into the cable bolting system. At this stage, the plate capacity was only 45 tonne or 75% of the cable ultimate tensile strength (UTS), presenting a limitation when designing with the suspension methodology (Canbulat, 2010). After much collaboration between technical and operational staff, a decision was made to reduce the primary cable length back to 4 m, however, increase the resin length to generate load transfer along a greater portion of the tendon, adopting a partially encapsulated rather than point anchored system. The shorter cable free length would also be comparatively stiffer, generating greater resistance to roof displacement for the equivalent load. Ideally, the cable bolt encapsulation would overlap the length of the primary roof bolts, ensuring load transfer could be generated in support elements over the full 4 m horizon.

Trials were conducted to ensure this was practically achievable. The goal was to ensure the cable could be inserted into the hole and into the drill motor dolly without having to break the bottom of the resin capsule. At the time, a 1900 mm resin capsule was found to be optimal with a 600 mm medium set resin at the top and a 1300 mm extra, extra slow resin at the bottom giving 2.5 – 3 m of encapsulation. Due to the length of cable required to be spun through the resin, operators were required to relearn how to install cables. This involved adopting a high rotation, slow feed approach where the drill motor was periodically stopped so that the cable could wind its way through the capsule without jamming up or kinking.

It should be noted that the row spacing for bolts was reduced from 1.3m to 1m in conjunction with the implementation of the 4 m partially encapsulated Superstrand cable. The spacing reduction was in line with industry standards for roof of CMRR 40 and depth >300 m. The empirical design methodology Analysis of Longwall Tailgate Support (ALTS) (Colwell et al, 2009), was particularly useful for benchmarking this support density. This innovation was successfully implemented in 2007 and allowed development to advance consistently at rates exceeding 3 m per operating hour with minimal rework. Furthermore, this support strategy was carried across into 806 panel development; performance in this panel far exceeded that of the previous panel.

Intersections remained somewhat problematic and eventually the Bowen cables were replaced with top down groutable MW9 cables from Megabolt. The 4 m partially encapsulated Superstrand cables combined with the top down groutable 6 m and 8 m MW9 cables in the intersections created a robust primary support system allowing the remaining mains and 807 panel to be developed on schedule.

### **High capacity cables**

On completion of 807 panel, the 900 series were opened commencing with 901. For 901 to 903 panels, strong roof conditions (CMRR >50) and relatively shallow cover depth (<250m) prevailed, resulting in primarily roof bolts only for code green support. During development of 904, the overstressing threshold was encountered at approximately 300 m cover depth. Fortunately, the previous lessons allowed the code green primary support to be upgraded to include 4 m partially encapsulated Superstrand cables, stabilising the roof conditions with little impact to the development advance rate. During 904 panel, the cables were changed from smooth wire to indented wire. The indented cable had slightly less capacity but was less prone to unwinding at the base of the encapsulated portion, increasing the stiffness of the free length and overall support system. This improvement was only incremental.

As development progressed into 905 panel, aggressive ground conditions were encountered inbye of the Grasstree dyke. This required 8 x 1.8 m roof bolts per metre and 2 x 4 m Superstrand cables per metre to be installed on advance with ongoing deterioration common.

Remedial support requirements again began to impede development advance. More concerningly, plate/collar failure of the Superstrand cables increased in frequency. In these conditions, primary support often included post groutable 6 m MW9 cables in standard roadways. With the largest roof deformations typically occurring within two bord widths of advance and a daily advance rate of approximately 20 m, the point anchored MW9 cables still allowed significant roof deformation to develop prior to grouting, which was conducted routinely every 24 hours. However, once the cables were grouted, the support system was able to adequately stabilise the roof. The routine installation of MW9 cables on advance impeded development due to the increased hole diameter, increased length, and requirement for post grouting. Coupled with high level longwall retreat rates, this put significant pressure on the life of mine schedule.

This was the catalyst for the development of higher capacity cables as a support element which could match the operational efficiency of the 4 m Superstrand cable. The 100 tonne Goliath cable from Jennmar was deemed most suitable and progressed to trial as it could be readily imported from Japan, where it originated as a common support element for suspension bridges. The underlying premise for the selection of a higher capacity cable was based on increasing system stiffness. In this instance, the increase in stiffness was achieved through increasing cable diameter (A), whilst keeping the elastic modulus of steel (E) constant and maintaining an equivalent section of cable free length (d). The formula for structural stiffness is described by Galvin (2016) and is shown in the following equation.

$$\text{Stiffness, } k, = \frac{L}{\Delta d} = \frac{\sigma A}{\epsilon d} = \frac{EA}{d}$$

Where:

L = Load (N)

d = Distance (m)

A = Cross Sectional Area

E = Elastic Modulus

$\sigma$  = Stress

$\epsilon$  = Strain

A significant body of work was conducted prior to the implementation of the Goliath cable including underground instrumentation, laboratory testing and geotechnical design calculations. This work is largely captured by Medhurst et al. (2016), although at the time of this publication, the Goliath was not yet fully implemented. Following implementation of the Goliath cables, ground conditions were able to be stabilised on advance using 6 x 1.8 m bolts per metre and 2 x 4 m Goliath cables every 2 m at >400 m cover depth. The implementation of the Goliath cable was successful and created significant relief to the development constraints and associated longwall continuity.

#### **IMPLEMENTATION OF HIGH CAPACITY, PARTIALLY ENCAPSULATED CABLE SUPPORT FOR INTERSECTIONS AND WIDENED EXCAVATIONS**

The most recent development in cable support systems at Grasstree is the implementation of the 6 m Jumbo cable. The Jumbo cable was introduced as a high capacity, partially encapsulated, resin anchored cable to replace post groutable MW9 cables in intersections, ultimately eliminating the need to routinely grout during standard development process operations. The use of Jumbo cables has since progressed to other applications including wide drivage (installation roadways) and is the preferred cable support for longwall salvage.

The selection of a 6 m high capacity, partially encapsulated, resin anchored cable was considered separate from the 4 m equivalent, due to the increased free length component of the cable. The free length is increased due to the resin capsule length of a 6 m cable remaining



equal to that of a 4 m cable. As previously mentioned this is due to the mining height requirements and associated installation constraints. The additional cable free length results in bond strength and collar behaviour becoming more critical to the success of the support system. Therefore, the selection criterion for the cable was a compromise of the most advantageous combination of collar capacity, system elongation and bond strength. The Jumbo cable was selected as its bond strength allowed for the cable length to be optimised.

When assessing cable support specifications, the ultimate strand capacity and collar capacity is typically presented separately. On a fully bonded cable system, the difference in capacity is relatively inconsequential as load is transferred to the strata along the entire length of the cable. In partially encapsulated and point anchored support elements, the collar capacity is more critical as it is required to support the load generated in the free length horizon. Prior to full scale implementation, a series of laboratory tests were completed on the Jumbo cable to assess the potential of failure at the collar in accordance with the expected roof movement levels at Grasstree.

Laboratory testing was completed by Megabolt using a horizontal test rig. The first two Jumbo cable samples were 2.6 m in length and consisted of two barrel and wedge sets, one set pre-pressed to 40 tonnes to minimise wedge draw and the other fitted manually after the cable was fed into the test rig. Load and elongation were monitored using a calibrated pressure gauge and linear transducer. The third sample was tested with a plywood backing plate to better simulate softer roof conditions. The test set up is shown in Figure 5.



**Figure 5: Megabolt horizontal test rig**

The data obtained from the laboratory testing is shown in Table 1 and graphed in Figure 6. Testing indicated that cable strands begin to yield at approximately 90% of UTS (82 tonne), with approximately 1.3% cable elongation at the onset of yield. The yield strength and mean collar capacity of the Jumbo cable were both measured at approximately 82 tonnes, which made the available elongation in the cable strand highly dependent on the achieved collar capacity for any given cable, as shown in the results with a range of 1.3 – 2.0% strand elongation across the three samples. The collar capacity is typically less than the strand capacity and will vary due to differential wire loading at the barrel and wedge.

**Table 1: Summary of laboratory collar testing**

Test number	1	2	3
Total free length (mm)	2005	2005	2005
Max load (tonne)	84.0	83.1	80.0
Max cylinder extension (mm)	65.5	56.9	53.0
Wedge draw-in on fitted side (mm)	15.0	15.0	14.5
Cable elongation at max load (mm)	39.8	31.4	25.4
Approximate free length elongation at max load (%)	2.0	1.6	1.3
Plate deformation at max load (mm)	30.5	30.5	30.5
Total system elongation at max load (mm)	85.3	76.9	70.4
Total system elongation at max load (%)	4.3	3.8	3.5

As a support system, displacement is further accommodated through other means, such as bearing plate deformation, wedge draw-in and resin debonding. Measured wedge draw-in and bearing plate deformation were tested in the laboratory and are summarised in Table 1. In practice, bearing plate deformation is highly dependent on immediate roof conditions, i.e. hard stone roof will not deform as much as a coal roof or fractured ground. Debonding was not applicable in these tests but would in practice be expected to add to overall system elongation. This will obviously vary with strata type and cable bond strength.

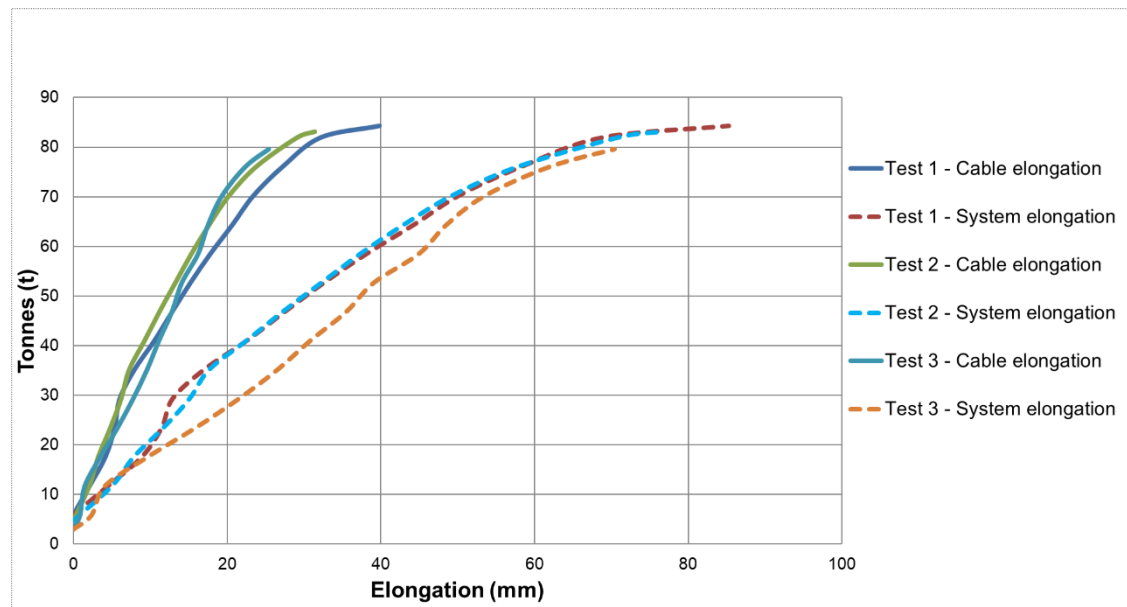


**Figure 6: Plot of laboratory testing**

Following laboratory testing, an underground installation testing and short encapsulation pull testing regime was commenced to determine the pre-tension, encapsulation and bond strength specifications. The data obtained underground was used in combination with the laboratory testing results to more accurately determine the expected range of tolerable cable system elongation. When calculating the system elongation, the data obtained from the laboratory testing of the 2005 mm free length cable was extrapolated to the measured free length underground. The final specifications of the 6 m Jumbo cable installed at Grasstree are shown in Table 2.



**Table 2: Jumbo cable specifications at Grasstree**

Specification	Dimensions	Comments
Cable capacity (nominal / minimum) (tonne)	95 / 92	
Cable yield strength (tonne)	82	
Collar capacity (mean / minimum) (tonne)	82 / 80	
Cable configuration	Spiral wire and un-bulbed	
Cable length (total / in hole) (m)	6.25 / 6.00	
Collar configuration	Barrel and wedge	
Bearing plate size (mm)	300 x 300	Hard forged dome plate backed by square plate
Resin details (mm)	32 x 1650	Two speed resin
Borehole diameter (mm)	35	
Bond strength (tonne / m)	150	Based on short encapsulation pull test data
Encapsulation length (range) (m)	2.3 – 3.0	
Cable elongation (range) (%)	5.0 – 6.0	
System elongation (range / mean) (%)	3.2 – 3.6 / 3.4	
Available free length elongation on a 6m cable (range / mean) (mm)	95 – 130 / 110	Not including resin debonding

## CASE STUDY

### Development intersections

Jumbo cables were first implemented in MG909 development intersections and have since been routinely installed in TG808, MG808 and MG910 gate roads. Since implementation, more than 100 intersections have been supported. Cable support density through the intersections varies between panels and geotechnical domains, but typically comprises 2 x 6 m Jumbo cables at 2 m or 1 m spacing. Secondary support prior to longwall retreat typically comprises fully grouted 8 m MW9 cables at varying densities.

During the initial implementation, load cells were installed in the mouth of each intersection, adjacent to a four anchored tell-tale device or GEL extensometer, as shown in Figure 7. The load cell measurements were plotted against the approximate free length roof movement in Figure 8. This information was used to determine the variance between laboratory and underground conditions. For Figure 8, the laboratory data system elongation curves shown in Figure 6 are normalised to a 3.5 m free length to better correspond with the typical free length and monitoring horizon measured underground at Grasstree.



**Figure 7: Load cell and extensometer monitoring configuration during implementation**

Load cells were monitored on development and longwall retreat. The results indicate that there is a reasonable correlation between the laboratory and underground data. However, no underground data was obtained at high loads due to the load cells being damaged on longwall retreat. The damage occurred at the stem of the load cells as it became pinched between the bagging roof and the bearing plate. Only load cells installed at C26 and C27 gathered usable retreat data. Based on observations, it is considered that additional yielding underground in the

cable system will occur at higher loads due to debonding of the cable from the resin and disproportional movement of the bearing plate compared to the surrounding roof, i.e. the roof tends to bag between cable bolts. This roof bagging will be picked up by monitoring devices but is not necessarily reflective of the movement occurring on the cable system. Further laboratory testing and underground analysis would be useful to better quantify these observations.

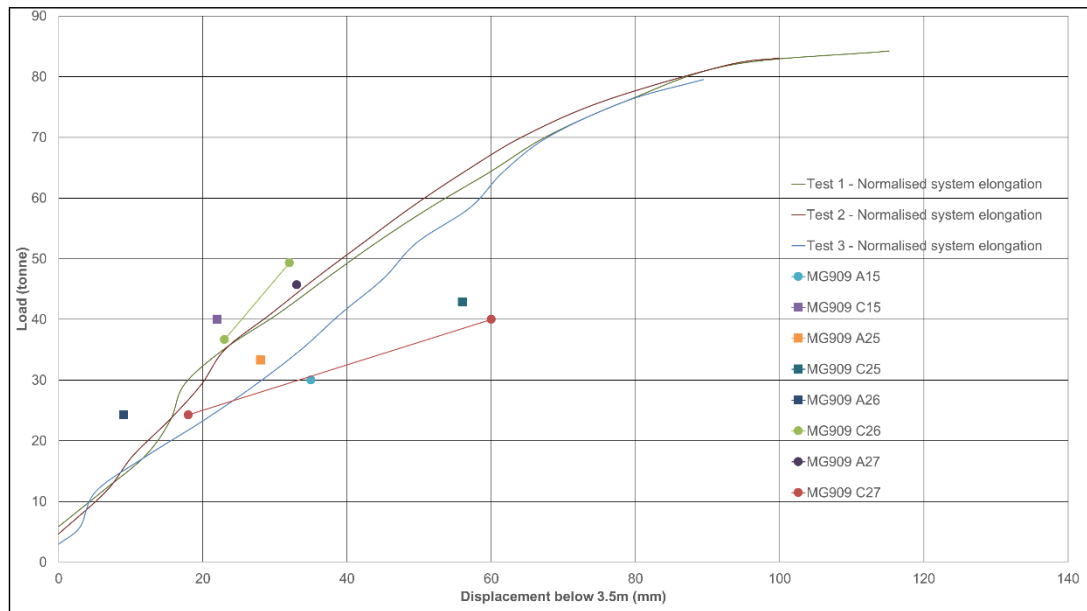


**Figure 8: Underground load cell data / free length deformation data**

Figures 9 and 10 are plots of roof movement by horizon in development intersections and longwall intersections subjected to stress notching conditions. In development, the roof movement in the lower 3.5 m is significantly less than the available free length elongation range for the 6 m Jumbo cables (95 – 130 mm). Stress notched roadways on longwall retreat were also assessed as these tend to generate the greatest amounts of roof movement at Grasstree. To date, there has been one case, at MG909 C25 intersection, where roof movement exceeded the specifications for available system elongation. Despite this, there were no Jumbo cables reported as failing in front of the goaf break-line. It should be noted that secondary support in this intersection comprised an additional 3 x 8 m MW9 cables / 1.5 m.

As part of the implementation, the tensioner pressure settings were reduced by 30%, resulting in a targeted residual pre-tension of approximately 10 tonnes. This was reduced in order to maximise the amount of available elongation in the cable system. No noticeable visual change in roof conditions or changes in monitoring data could be ascertained by this change in pre-tension.

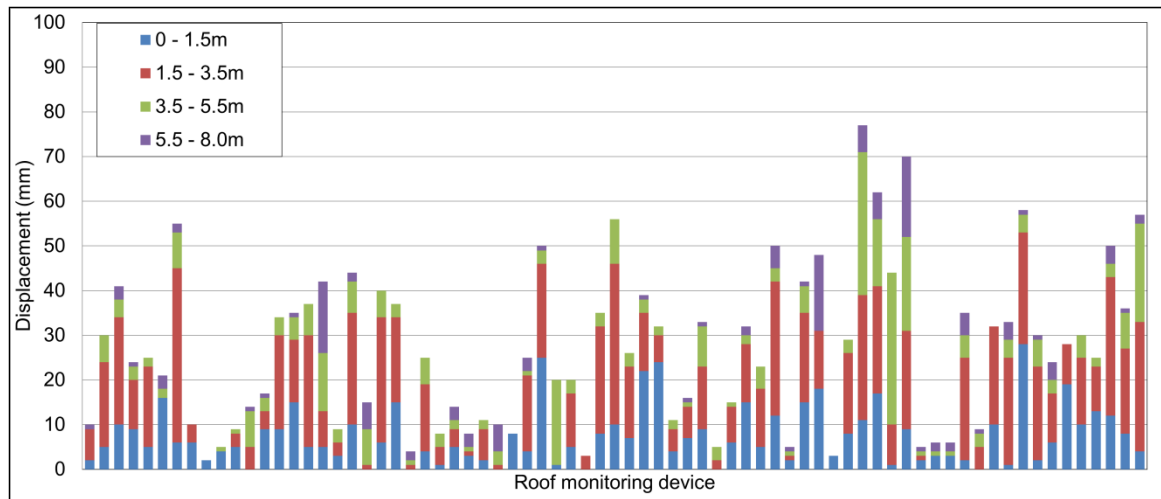


**Figure 9: Roof movement by horizon for development intersection supported with Jumbo cables**

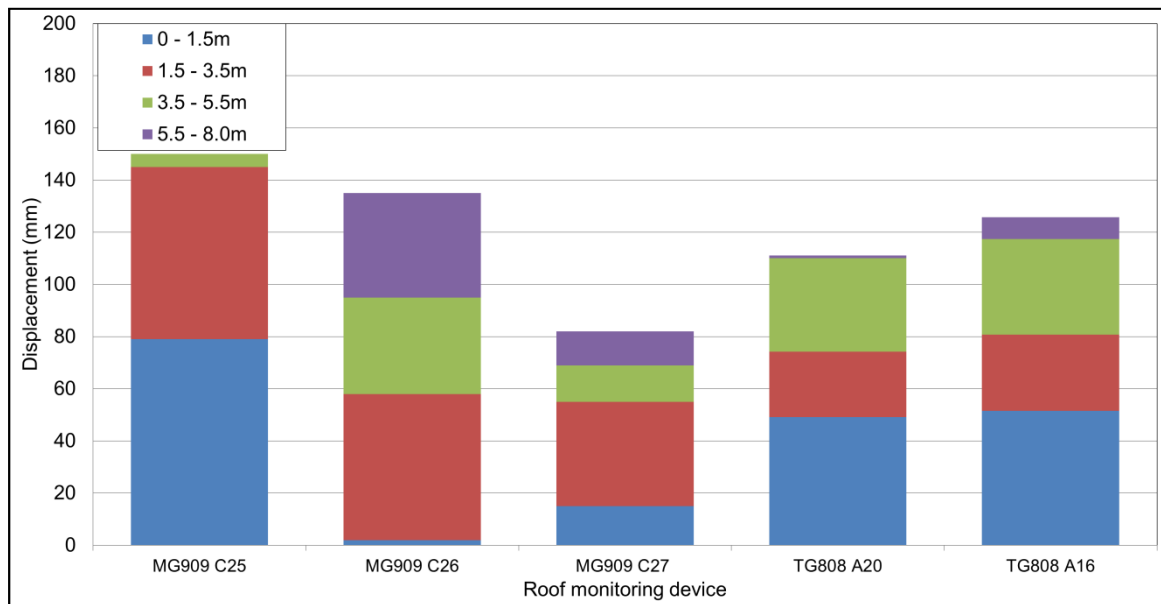


**Figure 10: Roof movement by horizon for stress notched intersections on longwall retreat supported with Jumbo cables**

**Installation roadway**

LW808 installation roadway was developed at depths ranging between 340 m (TG) and 365 m (MG). The CMRR range across the bolted horizon was 44 - 49 and GSR over the 0 – 3 m roof horizon ranged from 60 – 65. The first pass was mined to 5.2 m and widening to 8 m occurred on second pass. Jumbo cables were utilised in both first and second pass excavation, with secondary support comprising of MW9 cables, installed prior to second pass. This is illustrated in Figure 11, with Jumbo cables and MW9 cables indicated by red and yellow plates respectively. The cables indicated by grey represent cables installed on previous sequences. The wider MG and TG stable areas utilised 8 m MW9 cables only.

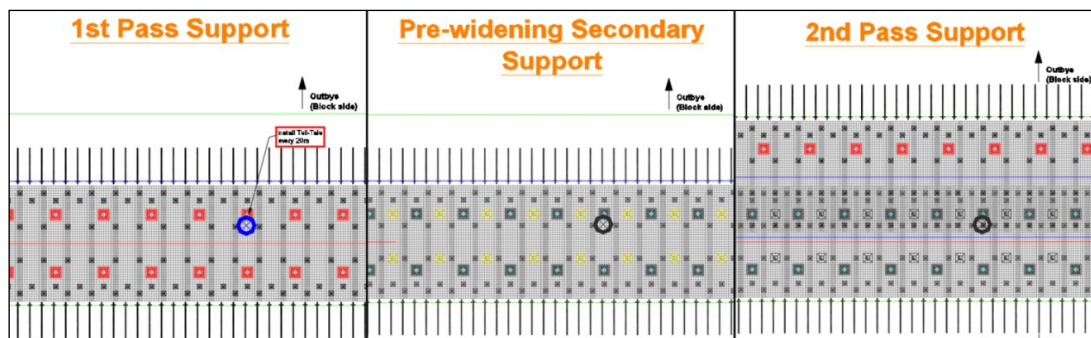


**Figure 11: LW808 installation roadway support plans for standard widening**

First pass development conditions were favourable with only minor guttering, jointing and roof drop-out evident in the roadway and total movement of less than 15 mm. Conditions post widening were less favourable with localised tensile fractures developing between the first and second pass widening, minor roof bagging (100 – 200 mm) and associated centreline cracking in the centre of the first pass roadway and stress side deterioration along large sections of the first pass side of the installation roadway. Note that widening occurred on the stress shadow side. The second pass roof was generally favourable with deterioration largely occurring in the first pass roadway. Examples of the second pass roof and stress biased side deterioration of the first pass roof are shown in Figure 12.



**Figure 12: Second pass roof conditions and stress biased side deterioration of the first pass roof**

Collar loading on the Jumbo cables were monitored during first pass and subsequent widening. MW9 cable collars were not generally monitored as closely for signs of load as they are fully bonded cables and load is not typically transferred fully to the collar. In general, signs of significant collar loading were more common along the installation roadway when compared to gate road intersections. The wedges were regularly noted to be flush or drawn into the barrel, as shown in Figure 13. This was compared to the laboratory testing shown in Figure 14 to give an indicative observational collar loading typically greater than 50 tonnes, with some localised Jumbo cables estimated to be showing loads greater than 70 tonnes.

The cable positioned centrally along the fully widened roadway typically showed the highest levels of collar loading. This was reflective of the roof conditions, as previously described. It was noted that there was minimal bearing plate deformation, likely due to the highly competent immediate roof. By comparison, bearing plate deformation in front of the longwall face on stress notched roadways appears greater due to the broken and bagged nature of the ground.





**Figure 13: Collar loading on Jumbo cables**

Figure 15 summarises the roof movement along the installation roadway following first and second pass excavations. Although the total movement was within the realms of previous Grasree installation roadways, the amount of movement surge and time to reach stable conditions was typically higher than previously experienced. This caused code orange TARP triggers along sections of the roadway and prompted the installation of additional support in the first pass drivage section. The intersection and shearer and gate end stable excavation areas were solely supported with 8 m MW9 cables and showed relatively low levels of movement. Post widening roof movement in the free length section of the cable typically varied from 30 – 60 mm. Comparing this movement with the loads generated from the laboratory conditions suggests loads of approximately 35 – 65 tonnes, which is indicative of the visual observations recorded during inspections.

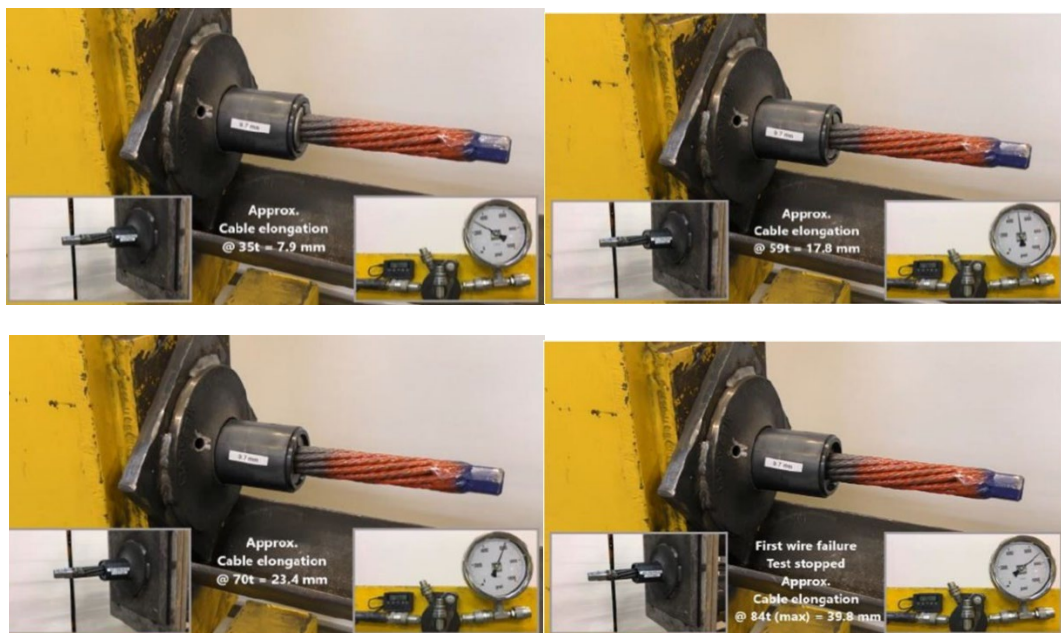


**Figure 14: Example of collar loading during laboratory testing**

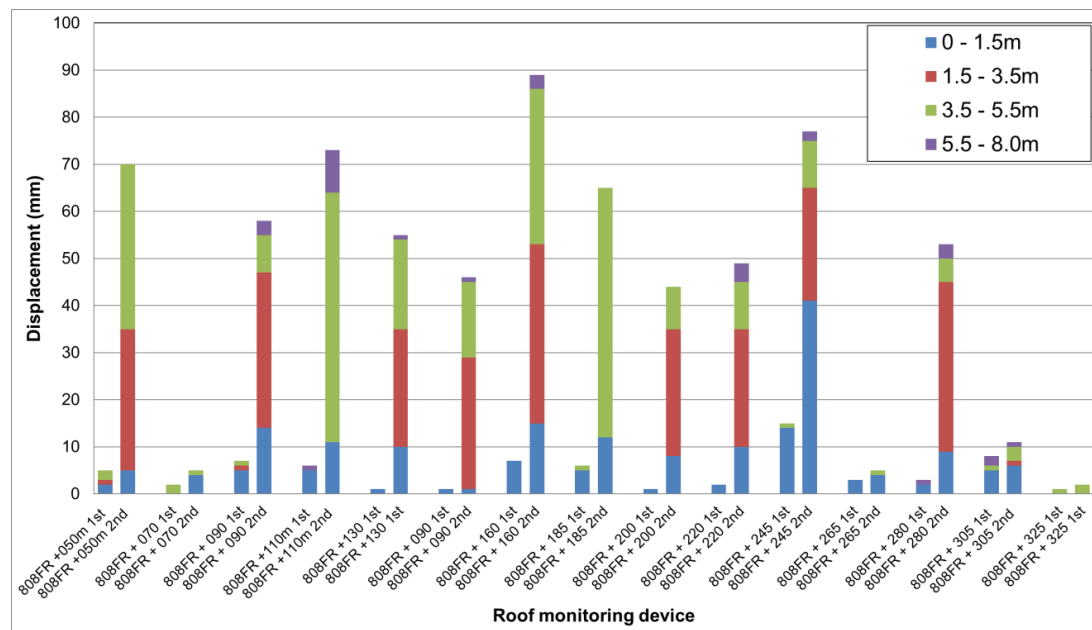


**Figure 15: First and second pass roof movement by horizon along LW808 installation roadway**

The use of Jumbo cables along the LW808 installation roadway was effective in reducing the amount of post groutable support in comparison to previous installation roadways. This highly benefited the second pass widening process, which was completed at a much faster rate than previous installation roadways widened with 8 m MW9 cables. Secondary support still comprised post groutable cables as means of providing some shear resistance and load transfer in the lower 3.5 m section of the roof but it was less than previous 800 series and 900 series installation roadways. It was particularly useful having laboratory tested observational indicators of collar loading, as it allowed for an additional monitoring tool along the installation roadway. Toolbox tools empowered all members of the workforce to conduct this monitoring. This method of monitoring is somewhat lost when cable support predominately comprises full column grouted cables.

The following recommendations relating to the use of Jumbo cables were made following the completion of LW808 installation roadway:

- Ensure that when TARPs are formulated, the triggers take account of the use of an overall softer system as compared to a stiffer system provided by post groutable cables. This will be important when determining widening surge and time to achieve stable conditions triggers.
- Where applicable, incorporate observational indicators of collar loading into the relevant TARPs, i.e. quantifying the amount of wedge draw-in and bearing plate deformation associated with the Jumbo cable.
- Investigate the use of a low protrusion cable option to decrease the risk of collar damage during the widening process. Collar damage on a point anchored or partially encapsulated cable should be considered as more compromising than that of a fully grouted cable bolt.

## CONCLUSIONS AND RECCOMENDATIONS

Grasstree Mine has experienced a large range of mining conditions throughout its operational life. Variation in ground conditions at a mine setting new benchmarks in longwall productivity was the catalyst for the continual development of cable support systems. In development

roadways, the mine has progressed from a primarily bolts only support pattern to a support system combining the use of partially encapsulated and post groutable cables.

Most recently, the mine progressed to a support system utilising partially encapsulated, high capacity cables. This included the addition of the Goliath cable in standard roadways and Jumbo cable for intersections and other widened excavations. This support system has proved capable of providing roof stability in a variety of applications whilst maximising operation efficiency and giving the workforce the confidence to continue safely mining in sometimes very challenging ground conditions. More specifically, it has allowed for quicker cable installation while reducing the need for routine grouting in development operations.

The implementation of the Jumbo cable required a comprehensive understanding of the available elongation in the free length component of the cable, as it had been noted that when using point anchored or partially encapsulated cable support systems, collar failure will potentially occur prior to the full strand capacity being reached. Laboratory testing reflected this and showed that as a support system for Grasstree, the 6 m Jumbo cable can obtain a total of 3.2 – 3.6 % system elongation in the free length component prior to collar failure occurring. The successful implementation of the Jumbo cable on development has also led to operational improvements in other areas of the mine including installation roadways and longwall take offs. A post implementation review of different mining areas supported with Jumbo cables indicated that these cables have accommodated the levels of roof movement experienced at Grasstree.

For Grasstree, the next improvement in cable support systems has been identified as the incorporation of torque tensioning capability to these high capacity, partially encapsulated cables. As with the standard 6 m Jumbo cable, the torque tensioned collar arrangement will need to be tested to determine the available support system elongation. Furthermore, the visual signs of loading on torque tension heads will need to be understood and the potential effect of reduced pre-tension are further assessed. Of critical importance will be to understand how the torque tension arrangement responds to impact. While forming intersections on development or removing shields from a longwall face, cable bolts are often subject to heavy impact from mining machinery. This is an unavoidable reality of longwall mining and it will be unacceptable for a torque tensioned cable bolt to lose tension from machinery impact at the collar. A low protrusion cable option would help to ensure that this risk is minimised.

### **ACKNOWLEDGMENTS**

Anglo American is gratefully acknowledged by the authors for allowing this work to be both conducted and published. All past and present Geotechnical Engineers and development operational personnel at Grasstree Mine are also gratefully acknowledged; this work resulted from collaboration between many persons. Both Jennmar Australia and Megabolt Australia, particularly Peter Craig (Jennmar) and Owen Rink (Megabolt), are gratefully acknowledged for their technical support in product development.

Special thanks must also be given to the late Adam Garde, former General Manager of Grasstree Mine (2012 to 2015). Without Adam's passion, drive and vision for innovations to improve both safety and productivity, this work (and the spin to stall bolting system) may never have succeeded. Operation managers are under constant pressure due to the financial cost of utilising machinery uptime for trials. This was never a problem for Adam; if any new concepts had potential to be both safer and more productive, they were given priority. Adams passing is a great loss to the Australian Coal Industry. Sincere condolences are extended to the Garde family.

## REFERENCES

- Canbulat, I, 2010. Roadway roof support design in critical areas at Anglo American Metallurgical Coal's underground operations. In Proceedings of 10th Underground Coal Operators' Conference (Eds: N Aziz and J Nemcik), pp 50-72, Published by Aus.I.M.M. Illawarra Branch. <http://ro.uow.edu.au/coal/297/>
- Colwell, M, Frith, R Mark, C, 1999. Analysis of Longwall Tailgate Serviceability (ALTS): A Chain Pillar Design Methodology for Australian Conditions. In Proceedings of the Second International Workshop on Coal Pillar Mechanics and Design. NIOSH Information Circular 9448, pp 33-48.
- Galvin, J, 2016. Ground Engineering – Principles and Practices for Underground Coal Mining. (Springer International Publishing, Switzerland).
- Medhurst, T., Emery, J., and Huey, A. 2016. Investigation into roof support behaviour at Grasstree Mine. Coal 2016 - Australasian Coal Operators Conference, AusIMM, pp 176-186.  
<http://ro.uow.edu.au/coal/605/>
- Thomas, R. 2007. Roadway Strata Management in the New South Wales Underground Coal Mining Industry. 26<sup>th</sup> International Conference on Ground Control Mining, Morgantown WV, USA. pp.113-121



# LONGWALL BEHAVIOUR IN MASSIVE STRATA

Ian Gray<sup>1</sup>, Tim Gibbons<sup>2</sup>

*ABSTRACT:* Longwall mining of coal below massive strata now has a 50 year history, and much of it has been problematic. For the first 30 years, there was much experimentation, with some successes, and many failures due to lack of understanding about how such massive strata behaves during caving, and how this differs from the more conventional and successful longwall mining beneath softer strata, which caves readily. This has been compounded over the last 20 years as mines extract wider faces and thicker seams in a single pass, often at quite shallow depths. Today, China is leading the way with thick seam longwalls under massive strata in shallow conditions, though not without problems.

Determination of the required capacity for longwall roof supports in such conditions is still not adequately understood, and overloading of supports remains a common problem in modern mines. The authors' view is that mathematical modelling to determine support requirements can only succeed if the model reflects real observed behaviour in such conditions.

There is an extensive body of technical literature documenting observations of what actually happens. This paper draws on past experience in many different countries to categorise common themes, and then proposes in simple forms the basis for real behaviour. Future modelling should be advanced on this basis. Such models need to incorporate a combination of multiple failure modes, including tensile, bending and shear, which may produce large rock blocks. These may move laterally, vertically, or in rotation depending on the loads which act upon them. Large blocks may impose substantial loading on the face, the powered supports or on the gateroad pillars.

The problems associated with large block formation may be mitigated by preconditioning to break up the massive strata before problems occur, so that manageable blocks are formed. In the United States of America and Australia, the focus has been on hydraulic fracturing. In Europe, China and South Africa, explosives have more often been used.

## INTRODUCTION AND BACKGROUND

Longwall mining originated at depth in fairly weak roof conditions where the stress to strength ratio of the rocks was high. This meant that the rock failed, and readily formed a goaf behind the roof supports. Under these conditions, the major challenge was keeping the gateroads serviceable. The common way to do this was to permit deformation of the roadways by the use of wood lagged arched supports with yielding slip joints. Much of earlier longwall mining was conducted in thinner seams.

Modern longwall mining often occurs in completely different geological environments. In these, we find that the rock is frequently strong in comparison to stress, and therefore does not break readily. Longwall mining is now also frequently conducted at shallow depths where the stresses are lower. The combination of strong rock and low stress means that the rock mechanics focus changes from supporting broken rock, to dealing with unbroken rock, and in particular large

---

<sup>1</sup> Principal Engineer Managing Director, Sigra Pty Ltd. Email: [ian@sigra.com.au](mailto:ian@sigra.com.au) Tel: +61 419 783 535  
<sup>2</sup> Principal Mining Engineer, Sigra Pty Ltd. Email [timg@sigra.com.au](mailto:timg@sigra.com.au) Tel: +61 439 786 330

blocks of rock which may not readily break, but when they do break, can move substantially. The consequences of large rock blocks include:

- unpredictable weightings on the powered supports;
- rock levers developing over the face causing major face break problems;
- large voids at the face as blocks break off and slowly rotate and advance in the direction of the goaf;
- varying face stresses as the blocks apply loadings irregularly;
- rock (coal) bursts associated with the uneven block loadings;
- rock (coal) bursts that are the consequence of seismic events brought about by sudden massive rock failure;
- sudden falls that generate wind-blasts;
- severe vertical loadings on gateroad pillars;
- shear movements on gateroad pillars; and
- uneven subsidence.

The importance of the size of rock blocks is inversely proportional to their distance from the longwall mining roof. For example, if a large cantilever of rock extends out over the longwall and then suddenly fails, its load will be transferred suddenly to the powered roof supports below. If this load is being transferred through already broken rock, then some of the loading will be distributed through this broken material and not directly on to the powered roof supports. How this transference takes place, and what design criteria should be used for powered roof supports, is really not resolved satisfactorily in any published literature.

Strong rock means rock strong in its mass behaviour. This means that it is massive as well as intrinsically strong. It is quite possible to have a strong rock type which is weak in its mass behaviour because of jointing. The real question when dealing with massive rock is "how big will the rock blocks that are formed be?" Rock breakage is primarily determined by jointing and planes of weakness. These still require some stress to break them apart. This can come from gravitational load or from initial stress redistribution. It should be borne in mind that any mining that removes stressed rock will have the consequence that the load (stress x area) it carried will be redistributed somewhere else.

There is an increasing trend to deal with massive rock units through pre-conditioning. This means forming planes of weakness within the rock mass so that goaf failure takes place readily. Pre-conditioning in coal mining may be brought about by hydraulic fracturing in multiple forms, blasting, or a variant thereof - high energy gas fracturing. These developments have progressed both in coal mining and more particularly in hard rock mining, where pre-conditioning is used in both block-caving, sub-level caving, and panel-caving environments. A great deal of the technology of hydraulic fracturing has come from the petroleum industry, where obtaining fluids from low permeability reservoirs became a major focus of interest.

This paper endeavours to explain some measured, and often very odd behaviour, of longwalls in massive strata. These problems affect the face, the powered supports, the gateroads, as well as the installation and recovery rooms. The problem appears to be due to large blocks of rock that move not only vertically, but also laterally. This results in block translation and rotation as the mass migrates in the direction of minimum stress. Such blocks can impose very large loads on the powered roof supports. They can also lead to face spall and pillar failure, including bursts. The cause of the problem is fundamentally the failure of the massive strata to break up. This seems to be worse under shallow conditions, presumably because of the lack of stress to break up the rock blocks.

The problem may be thought of as being at two ends of a spectrum. One has small broken blocks in the roof which behave more like a soil and which will bridge off a short distance above powered roof supports. This leaves the support carrying little load. The other being that of massive blocks which do not fail until a substantial face advance has taken place. These then

fail suddenly and impose huge loads on the mechanical supports. The blocks also slew and may move into the adjacent panel's goaf, severely damaging the tailgate and pillar as they do so.

Longwall mining can be divided into cases of sub-critical and super-critical goaf formations. Where the longwall panel is comparatively deep and narrow, the rock bridges, or arches, across the top of the panel and transfers loads down to the gateroad pillars beneath. In this sub-critical case, the subsidence is minimised. Rock beneath the bridge needs to collapse to form the goaf. If it does not collapse readily then the problem of wind-blast occurrence is of immediate concern. Wind-blasts brought about by roof falls are one of the most dangerous events that can occur in mining. They can induce wind speeds that are a substantial fraction of the speed of sound, with the results that personnel are blown violently around the mine, equipment is dislodged and gas and dust are expelled out of the goaf, with the associated risk of an explosion initiated by friction or electrical damage.

The super-critical goaf is one where the rock within the goaf collapses and transfers most of the load directly through the broken material to the floor. Only where pillars exist is there some disruption to the loading. The formation of the super-critical goaf requires a face width to depth ratio that is large. This ratio has been described as being at least 1.4 but is highly dependent on the rock type.

It is quite possible to have an intermediate situation take place between critical and super-critical goaf formation, where the goaf has collapsed and where substantial lateral stress is re-established in the stratigraphic layers in the upper part of the goaf. The rock bridge dimension is too great to support the goaf, as in a sub-critical situation, but high lateral stresses do exist. This has been noted to occur along longwall panels, as opposed to transversely across them, where the effects of gateroad pillars tend to break up the re-establishment of stress (Gray, Wood and Shelukhina, 2013).

The increasing trend to mine thick seams using longwall techniques leads to more vertical disruption of the strata and a higher probability that lateral stress will not be transferred within the goaf. In cases where the lateral stress is not maintained during longwall mining, the strata can move substantially laterally. This lateral movement is dependent on where the rock may start to move from and the strain it contains prior to mining taking place. For example, if the rock is stressed so that it contains a lateral strain of 500 microstrain across a longwall panel and the panel has a width of 400 m, then the potential movement released by mining at the tailgate is 0.2 m over one panel width. However, this movement is not necessarily limited to a single panel but may be associated with a shear along the roof of the seam that extends to a far greater distance. This is a shear movement between roof and floor that will have to be withstood by the tailgate roadway and its pillar.

Ideally, a longwall mines coal with as little disruption as possible to production and the ground surface. In the case of a shallow mine, there is no sensible choice but to aim for super-critical panel widths. This can be argued on simple economic grounds, as the number of gateroads that would be required for sub-critical mining would mean that it would be pointless having a longwall at all. Wide super-critical panels reduce the disruption to the ground surface associated with gateroad pillars. This disruption may be reduced further if yield pillars are used, as they will crush. The question is whether a yield pillar can be made to protect the tailgate during mining and crush when it becomes part of the goaf?

Because of the inevitable consequences of large-scale rock movements that accompany longwall mining, it is important to design any form of support to behave in a ductile manner. This is achieved by having adequate hydraulic set and yield pressures on the powered roof supports of the longwall face, and most importantly maintaining a reserve displacement capability in the powered roof support hydraulic cylinders once yielding takes place.

Ductile design is no less important for the gateroads. The support system must be able to withstand deformation and survive. This deformation that the gateroads should withstand may include:

- floor heave,
- rib failure of the solid block or or pillars,
- shear of the roof with respect to the floor (taken within the pillar),
- shear within the roof itself,
- compressive failure of the roof,
- tensile failure of the roof,
- flexure of the roof, and inevitably
- slabbing where laminated materials exist.

Any support also needs to be able to deal with jointing or faulting that may be encountered, though support is frequently modified where varying conditions are encountered. It is dangerous to design support for one expected mode of failure when in fact multiple types of loadings may take place.

The use of secondary "standing" roadway support in the form of concrete filled "cans", stone filled wood cribs, or other props is regarded as a last resort because it will severely restrict the serviceability of the roadway, not least for ventilation. The exception is in the use of normal or, self-advancing, powered roof supports at the end of the tailgate and for the extraction of the longwall at the end of a panel in a recovery room.

The art of rock mechanics in longwall mining may be summarised by a simple statement - keep the roof up safely while you are working below it, and get it down as quickly as possible once it is behind the face.

### **EARLY LONGWALLS**

In South Africa, early longwall experiments were undertaken at Durban Navigation in the Klip River Coalfield. Two 1.0-1.2 m seams were mined sequentially under a dolerite sill. The mine experienced sudden unpredictable weightings, erratic surface subsidence, bad falls, methane, and floor heave, along with serious injuries and fatalities (Deats, 1971). From 1976-1980, Coalbrook in the Vaal Basin Coalfield mined the 2.2-2.8 m No.1 seam with roof lithology being competent sandstones and a 40 m thick dolerite sill. The weight of dolerite in cantilever caused breaks in the roof and coal ahead of the face, often associated with flooding (Henderson, 1980). Sigma, also in the Vaal Basin Coalfield, mined the No.3 seam at 115 m depth under a 40 m dolerite sill 50-80 m above the coal. The face experienced excessive weightings, severe coal face spall and flooding (Cloete, 1980). More recently, Matla in the Witbank Coalfield operated shortwalls in the No.2 and No.4 seams. In 2002, the No.4 seam experienced extreme loading of the tailgate pillars. A large dolerite sill block, having detached itself over the maingate, was hanging up some 300 m behind the tailgate over the goaf. Surface pre-split blasting was successfully used to relieve the pressure, resulting in mitigation of facebreak and wind-blast events (Latilla, 2007).

In India in 1990, a state-of-the-art longwall was commissioned at Churcha West in Chhattisgarh to extract a 3.0-3.4 m seam at a depth of 223 m (Deb 2004). It was equipped with a data logger to measure support behaviour. The immediate roof was 80-133 m of sandstone overlain by 112-137 m of dolerite. When the face had advanced 198 m, a weighting destroyed half the 101 Gullick-Jessop 4/680 t chock-shields in 3.6 seconds. Coal and sandstone filled the face to canopy level. Coal between chocks #52-60 was crushed to powder. Similar catastrophic failures involving massive sandstone have occurred at Jhanjri in West Bengal and Godavarikhani ("GDK") 11A in Telangana after 204 m of retreat (Deb 2004).

In Canada, Phalen, in the Sydney Basin, Nova Scotia, began extraction of the 7 East Panel in December 1994. The panel mined the 1.5-3.0 m Phalen coal seam with a 260 m wide face and 3400 m length under the sea 200-700 m below sea level. There were previously flooded workings above the Phalen seam. Over a 30 month period until May 1997, 48 weighting events occurred with five being very serious. The planned extraction period was 18 months. The weightings were caused by the Lower Sandstone Unit (LSU), a massive paleo-sandstone river channel which formed the main roof overlying the weak immediate roof. No weightings occurred when the immediate roof was > 7.5 m thick and LSU < 9.5 m thick. However, when LSU > 9.5 m thickness severe weightings occurred accompanied by violent face spalling (0.5-1.0 m) and loud noise. The first weighting occurred 35 m past the start of the previous and adjacent 6 East goaf. The first serious weighting occurred 30 m past the start of 5 East goaf. The thicker the LSU became, the greater the weighting interval length (MacDonald, 1997).

Australia has also had its share of problems. Ellalong, in the Cessnock Coalfield, commenced operations in 1983 after extensive geotechnical investigations. A 3.0-4.7 m seam at a depth of 320-640 m was overlain by a main roof of thick, strong, massive sandstone, and immediate roof of 6-16 m of conglomerates, sandstones and shales. The first two longwalls experienced severe, rapid weightings and heavy coal face spall (Wold, 1986).

In 1984, South Bulga in the Hunter Valley Coalfield commenced operations as a punch mine from an open cut highwall at 40-160 m depth. The immediate roof was 22-28 m of massive sandstone with UCS of 40-80 MPa and modulus of 13 GPa. The powered roof supports were a combination of 940 t and 1150 t, the highest capacity available at the time. The mine regularly experienced rapid convergence during cyclic loading. By 1998, the mine had become ironbound three times, along with an additional eight rapid convergence events. South Bulga had an extremely low initial stress regime with a horizontal to vertical stress ratio of 0.5 (Sanford, 1998 and 1999).

In the 1990s, wider and more productive longwall faces were introduced in the Newcastle Coalfield, where strata incorporates massive sandstones and conglomerates, some of which formed the immediate roof of the coal seams. The unexpected implications of introducing wider panels included more variable and increased subsidence, severe periodic weightings with associated mid-face falls, as well as wind-blast. In the late-1980s, Teralba in the Newcastle Coalfield experienced surface subsidence four times that previously experienced as a result of increasing face width to 150 m. Similarly, Newstan, near Teralba, experienced seven severe weightings and falls in LW5 on a 225 m face resulting from mining under up to 50 m of conglomerate. A decision to split LW6 into two 90 m faces solved the weighting problem, but induced 80-140 kph wind-blasts (Creech, 2014).

### **LARGE DETACHED BLOCKS**

In 2002, Matla, in the Witbank Coalfield, Mpumalanga, South Africa, operated shortwalls on the No.4 and No.2 seams, and the No.5 seam had been shortwalled in the past. On 13 April 2002, the No.4 seam shortwall suffered a facebreak restricted mainly to the tailgate side due to a thick, near-surface dolerite not breaking. The resultant overloading led to severe pillar damage and subsequent roadway collapse. This was partly due to the premature suspension of longwalling in the overlying No.5 seam, resulting in No.4 seam overloading with severe pillar damage and collapse. The roof collapsed to a height of about 2 m ahead of the face in the tailgate of shortwall panel 8 (Latilla, 2007).

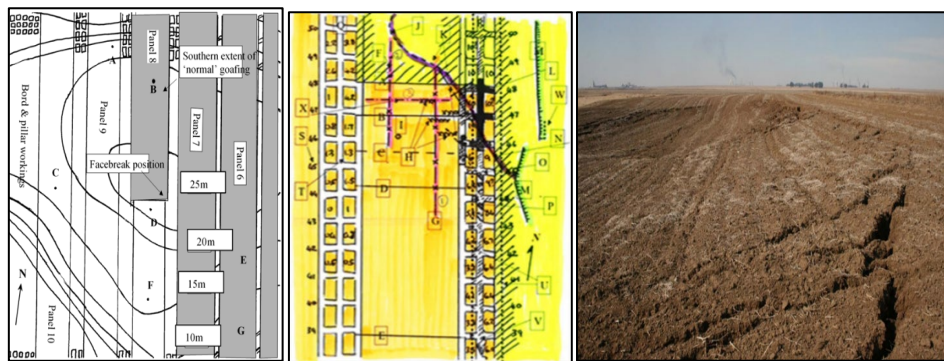
A dolerite sill close to surface had been observed in the past to break in large blocks within the No.5 seam and also overhang as much as 40 m from the goaf edge. The No.5 seam had been longwalled to the west of No.4 seam panel 8. The No.4 seam panel 8 was the first to shortwall under unmined No.5 seam and an intact sill. Higher than usual pillar stress occurred when

tailgate 8 was the maingate for panel 7. Field observations soon after the face break revealed that the dolerite was breaking around 40 m in from the maingate pillar edges but that there was no sign of it breaking along the tailgate side. Extreme loading on the tailgate pillars indicated that the dolerite, having detached itself from the maingate side, was overloading the tailgate pillars. It appeared that the sill was hanging up for about 300 m behind the face on the tailgate side.

Underground, on the tailgate side, it appeared that the goaf of panel 8 was moving towards panel 7 across the two tailgate chain pillars. Cracks on the surface also indicated the same behaviour. It was decided to assist this tendency by blasting a pre-split in the dolerite on surface. Two lines of blast holes were used, the first diagonal to the face to assist the dolerite to break along the surface crack and another parallel to the tailgate to reduce dolerite loading on the tailgate chain pillars. Pre-split blasting used closely-spaced (3 - 4 m) holes.

Line 1 was blasted on 8 May 2002, causing noticeable reduction in load on both the face and tailgate pillars. This reduction in load was evident by the virtual absence of noise from the pillars and roof where previously there was constant noise and pillar spalling. Average powered roof support leg pressures for the tailgate side showed an increase after the pre-split from 19.5 MPa to 26.6 MPa. This appeared contradictory, and a close inspection of pressure readings revealed that the pressures were more uniform after the blast. The maximum and minimum pressures before the blast were 38.3 MPa and 14.9 MPa respectively. Within 30 minutes of the blast, movement was observed on surface with appreciable steps 5-10 cm high forming along cracks. No damage was observed along the shortwall face. An area with cracked roof ahead of this fall remained unchanged. Lines 2 and 3 were blasted on 28 May 2002.

Surface damage from the second blast was severe. The second blast was successful, with goaf falling within 30 minutes. No roof damage was noticed on the tailgate or the face. Shield leg pressures on the maingate side dropped from 32.1 MPa to 28.9 MPa. Blasting relieved the leg pressures and preconditioned the next two panels, with reduction in face break and wind-blast events.



a) Dolerite thickness contours      (b) Presplit lines      (c) 2-3 m surface subsidence

**Figure 17: Matla dolerite presplitting (Latilla 2007) and 2-3 m surface subsidence (Hebblewhite, 2013)**

**GATEROAD ROOF DIVERGENCE (UPLIFT)**

In February 2005, Enlow Fork, in the Northern Appalachian Basin, Pennsylvania experienced a massive sandstone caving event in the LW6-R tailgate. The mine had previously experienced large caving events associated with initial weighting in thick sandstone. However, this event was not related to an initial weighting. Prior to the incident, the tailgate was relatively quiet with no audible fracturing ahead of the face. However, there was significant floor heave which was

normal. Overburden depth was 670 m. The event began with a loud bang, followed by a wind-blast.

Different theories emerged, but a consensus was that a high-strength massive sandstone channel was the primary instigator. Similar conditions were found in the LW7-R gateroad which might affect LW8-R. It was decided to instrument LW8-R tailgate. Convergence stations were installed from cut-throughs 26 to 7. Typical immediate roof was dark, silty shale overlaid by two distinct sandstone strata (lower and upper sandstone). In the vicinity of LW6-R, the roof geology was typified by 6 m thick first sandstone and 9 m thick second sandstone. Top of coal to bottom of sandstone was less than 0.6 m. The interval from the top of the coal to sandstone is important because of its potential to impart wind-blast, and also any bulking of weaker rock below cushions and mitigates wind-blast (Akinkugbe 2007).

During the monitoring programme, an unusual tailgate roof divergence (uplift) was recorded. This roof behaviour contradicts expected norms of roof convergence when the longwall is influenced by periodic weighting. The recorded roof movement data indicated that the roof divergence started well ahead of the longwall face. The most inbye position transducer (cut-through 26) started recording progressive roof divergence when the longwall face was 196 m away. Maximum roof uplift recorded was 22 mm when the longwall face was 91 m from the transducer; thereafter it began to gradually converge. Accelerated convergence only started after a massive caving event with the face within 85 m of cut-through 26. The event resulted in mild wind-blast, with no damage or injury on the face or gateroads. Prior to the event, the roof of the tailgate was observed to be hanging 45 m behind the 15 powered roof supports nearest the tailgate.

After the event, mine roof displacement recorded by transducers at cut-throughs 22-26 were examined. While the transducers at cut-throughs 22-25 recorded minimal to negligible convergence that at cut-through 26 recorded an unusual roof divergence (roof uplift).

After much consideration by the mine personnel, it was agreed that the most likely explanation appeared to be classic beam bending resulting from a roof cantilever effect. It was surmised that the weight of the rock in the hanging sandstone was sufficient to cause a flex in the sandstone resulting in an upward movement of the immediate strata. Although the exact location of the caving event is not known, anecdotal evidence and logic suggest that it most likely happened on the adjacent LW7-R goaf. Face conditions at the tailgate were relatively normal, not exhibiting excessive loading.

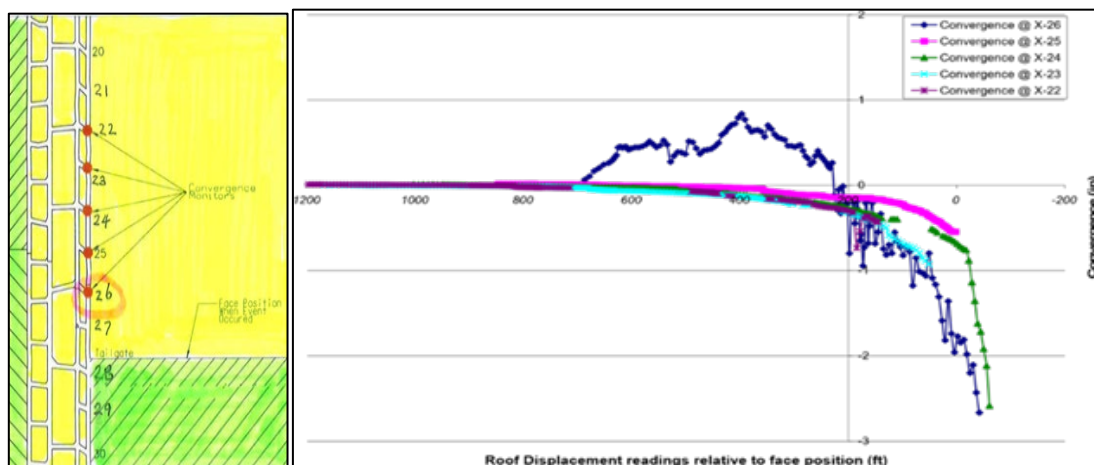


**Figure 18. Enlow Fork roof lithology (Akinkugbe 2007) and roof displacement in LW8-R tailgate cut-throughs 22-26 and 26 (Akinkugbe 2007)**



## FARFIELD HORIZONTAL MOVEMENT

Tower was a longwall mine in the Illawarra Coalfield, New South Wales, now part of the Appin complex. It mined a 2.4 m thick Bulli seam at a depth of 450 m. The surface topography consists of steep-sided river gorges, up to 68 m deep. The surface is mainly natural bushland traversed by a major road which crosses one of the gorges on twin-six-span, box girder bridges with piers up to 55 m in height. Although the road and bridge are outside the conventional concept of angle of draw subsidence influence criteria, and have experienced negligible vertical deformation as a result of mining, there is widespread evidence of regional horizontal deformation of the land surface large distances away from the mining area. Gorge closure and evidence of large headlands moving en masse have been observed. Horizontal movements at Tower up to 350 mm have been recorded.

Of particular concern for the extraction of LW16 and LW17 was the potential subsidence impact on the bridge 600 m away. Overlying strata consists of sandstones, shales, claystones and mudstones. Some of these strata are quite massive and thickly bedded but with dominant vertical jointing persisting through most horizons. Tower has a high ratio of horizontal to vertical pre-mining stress up to 3:1. Most horizontal movement took place towards the gorge and the active goaf, with some movement towards the old goaf. The bridge moved approximately 100 mm en masse towards the longwall panels, fortunately with no impact on serviceability. (Hebblewhite, 2001).

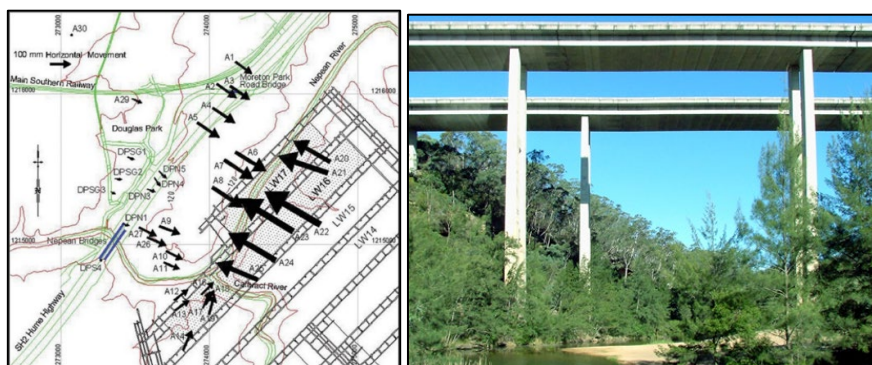


**Figure 19. Tower horizontal movement from LW16 and LW17 and Nepean River bridge (Hebblewhite 2001)**

Narrabri is a mine operating in the Gunnedah Basin, New South Wales. The mine targets a 4 m section of a 4-8 m thick seam 160-180 m deep directly below a 16-20 m thick conglomerate with a history of significant periodic weighting events. The face width is 306 m. Adjacent longwalls are separated by 30 m wide gateroad pillars. As part of an investigation to better understand the weighting events, inclinometers capable of measuring horizontal shear movements through the full section of the overburden strata were installed ahead of mining at two locations 1 km apart, above the centre of two adjacent longwall panels. Horizontal shear movements were observed to develop on shear horizons that correlate closely across the two sites. The horizon on top of the conglomerate mobilised almost immediately after initial deformation of the longwall goaf 425 m ahead of the face. The direction of horizontal movement was consistent with the relief of the major principal horizontal stress. As the face approached each inclinometer, other horizons within the upper overburden began to shear with the upper strata moving further towards the goaf than the immediately lower strata. Within the last 30 m, tilting of the strata associated with the onset of vertical subsidence caused reverse shear offsets (Mills 2015).



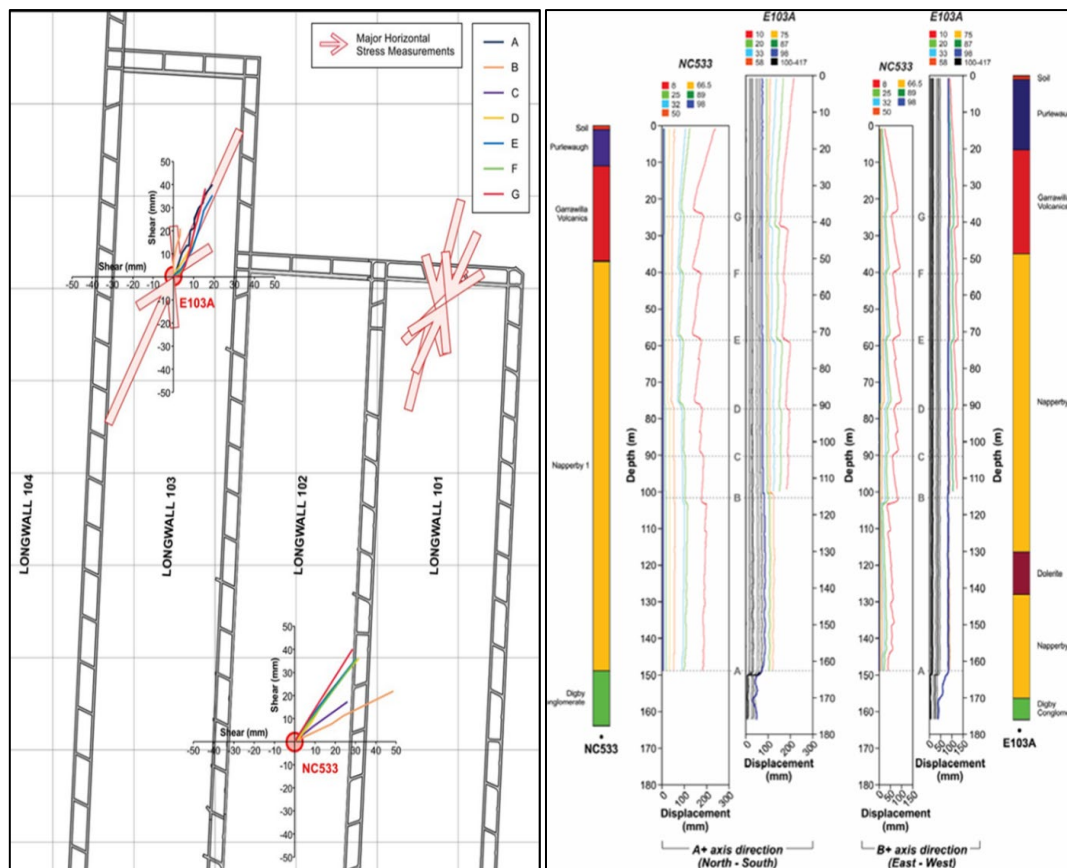
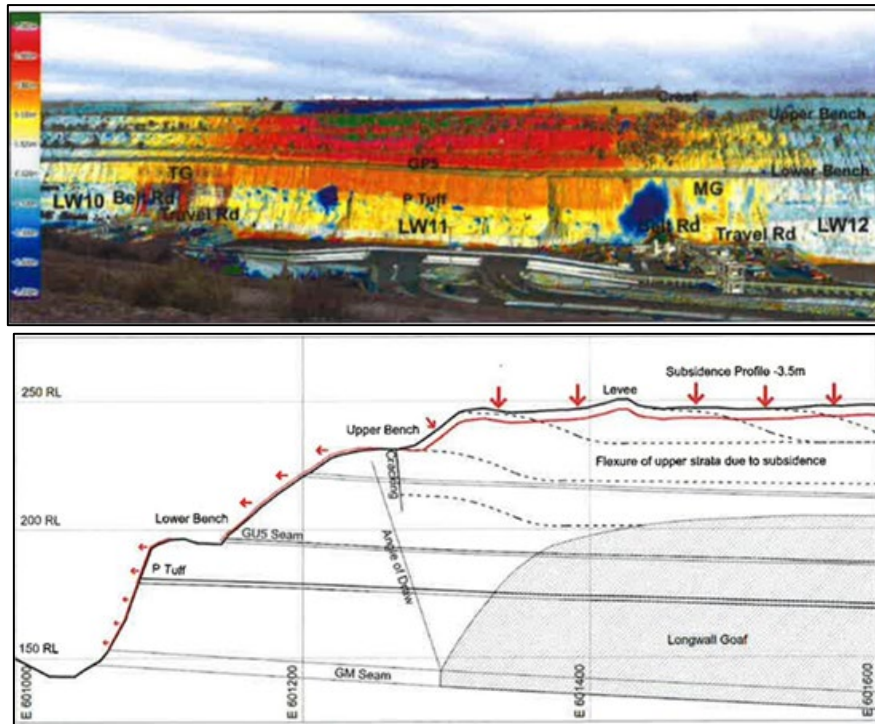


**Figure 20. Narrabri major horizontal stress and horizontal movements (Mills, 2015)**

Broadmeadow, located in the Bowen Basin Coalfield, Queensland, is a punch longwall mine. It has experienced significant highwall movement associated with the effect of longwall subsidence when the longwalls approach their final position close to the open cut highwall. In response to this movement, the mine deploys two types of broad scale highwall monitoring, using both radar and laser scanners. Results from the monitoring found the highwall is displaced to magnitudes unlike those typically measured in open cut mining, and in direct contrast to typical longwall subsidence behaviour.

During the mining of LW11, borehole inclinometer monitoring confirmed that initial horizontal shear movement was towards the centre of the longwall goaf. However, as the longwall approached the final position near the opencut highwall, the ground deformation did not conform to either typical longwall subsidence profiles, or typical highwall movement, with values far exceeding any stability limits in adjacent open cut mines, indicating the onset of slope failure. This outward movement in excess of 1000 mm, shown in green, at the top of the highwall destabilised local areas. Falls are shown in blue as negative horizontal movement. White indicates no movement (Payne, 2019).



(green >1000 mm, red > 800 mm, orange > 400 mm, white zero mm, blue <0 mm)

**Figure 21. Broadmeadow LW11 horizontal and vertical displacement into opencut (Payne, 2019)**

### GATEROAD SHEAR (SKEW ROOF)

A deformation mechanism termed “skew roof” relates the regional influence of differential horizontal strata movement (shear) about longwall extraction to gateroads. Under geological and mining conditions where the skew roof mechanism operates, strata units move progressively further towards the goaf with increasing height into the roof. Skew roof has implications for chain pillar design and indeed all roadways within the vicinity of longwall extraction, including the face itself. At Metropolitan, in the Illawarra Coalfield, New South Wales, horizontal movement was so severe that the immediate roof material was essentially pulverised and flowed out of the roof space between the installed standing supports. This roof behaviour is evident in many Australian coal mines that experience poor roof behaviour, either adjacent to longwall extraction (travel roads), or during approach of the next longwall (tailgates). The propensity to skew is a consequence of strain relief and horizontal strata movement towards the goaf. These movements frequently progressively increase from seam to surface.

The effect is regional in that horizontal movements on the surface can extend in the order of kilometres from longwall mining, and at seam level the influence can extend over many tens of metres and potentially hundreds of metres. The direction of skew is the net influence of the direction from the roadway to the goaf, and the direction of the maximum horizontal stress (Tarrant 2005).

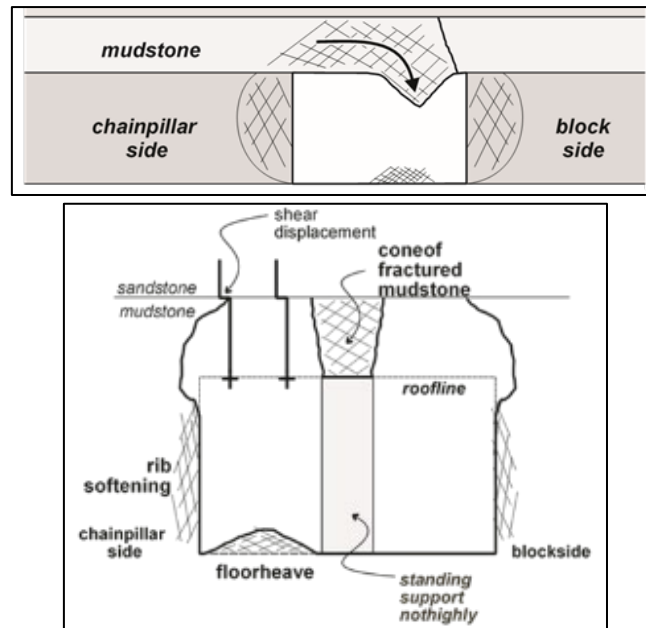


Figure 22. Metropolitan Observed Tailgate Behaviour (Tarrant, 2005)

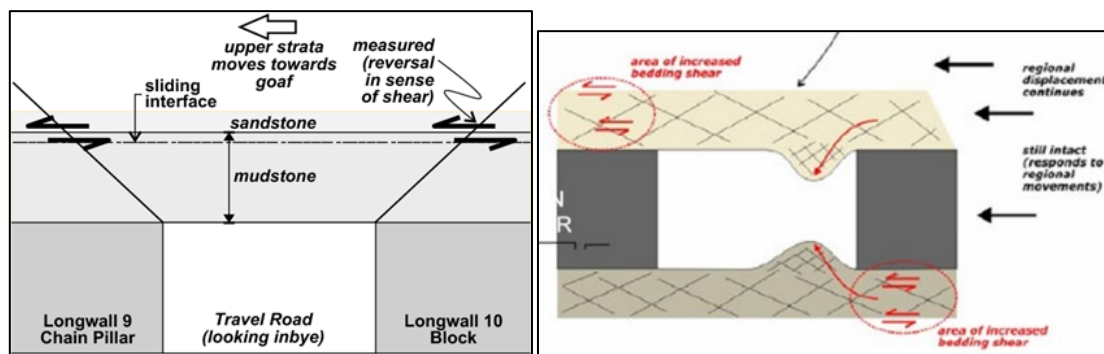


Figure 23. Skew Roof Concept (Tarrant, 2005)

Austar, previously Ellalong, in the Cessnock Coalfield, New South Wales, has a long association with difficult strata conditions due to mining depth, and a highly jointed / cleated coal. Matters of concern include poor longwall face conditions, cyclic loading, heavy tailgate conditions, difficulty in maintaining roadways on development, and in the installation and recovery of longwall faces. The depth of cover is 530 m. The mine experiences significant pressure bumps during development, typically in association with stiffer rock units above and below the seam. The most severe weightings occur when, on cycles between 120-150 m when a Branxton Formation (conglomerate-sandstone-shale) weighting event coincides with a weighting due to the immediate sandstone channel (Moodie 2011).



**Figure 24. Austar gateroad centreline bagging and chain pillar side guttering near bent tendons (Moodie, 2011)**

### WIND-BLASTS

A wind-blast comprises a rapid rise in absolute pressure to a maximum (positive compression phase), usually followed by a similarly rapid fall to below ambient atmospheric pressure (“suck back”). After decreasing to a minimum value, the absolute pressure gradually increases until it becomes equal to the ambient atmospheric pressure. At around the same time, although not necessarily in phase with the overpressure, the wind velocity also rises rapidly to a maximum and then frequently exhibits a sudden reversal into the “suck back” phase. Each event usually lasts for a few seconds. From wind-blast monitoring and the recorded overpressure and wind velocity histories, it has been observed that there is no acoustic precursor to the event in the roadway other than that from “roof talk”. Consequently, people in the working place will receive no warning of the wind-blast before it strikes them (Sharma, 2004).

An analogy often used to describe wind-blast is that of a “leaky piston” where a large intact rock mass initially drops, creating compression below it and a corresponding vacuum above it. When the rock fall ceases, air then “sucks back” into the vacuum above the fall.

Newstan and Moonee mines are located in the Newcastle Coalfield, New South Wales. The wind-blast events at Newstan were localised and confined to where the massive strata was within twice the extraction thickness and bridged the panel. In contrast, at Moonee, incidence of large goaf falls and associated wind-blasts continued for virtually the whole length of the longwall panels other than a few localised faulted zones where regular caving took place. The lower magnitude of the wind-blast parameters at Newstan are due to the fall of the roof element being cushioned by the caved immediate roof, lower volume of air being displaced from the void, and the higher resistance to flow due to partial packing of the goaf by the prior caving of the immediate roof.

**Table 1: Newstan and Moonee wind-blast parameters (Sharma, 2004)**

Parameter	Maximum Value	
	Newstan	Moonee
Peak air velocity	40 m/s	123 m/s
Rate of rise of velocity	50 m/s <sup>2</sup>	138 m/s <sup>2</sup>
Peak over pressure	10 KPa	34.5 KPa
Rate of rise of pressure	25 KPa/s	36.4 KPa/s
Impulse	20 KPa.s	89 KPa.s
Maximum excursion (air flow distance)	67.2 m	184 m





W – wind-blast location, grey – channel > 40 m thick, yellow – septum < 7 m thick

**Figure 25. Newstan wind-blast events and associated massive strata (Creech, 2014)**

### SHALLOW (NEAR SURFACE) LONGWALLS

A large number of shallow coal seams of Shendong Coalfield, Shaanxi, China have been mined in recent years. These have posed serious strata control problems and have been studied (Zhao, 2018). Jinjie coal mine is one of these. Longwall LW31109 mines a 3 m thick seam at a depth of 120 m, with 3.3 MPa vertical stress. Face width is 280 m. There are 162, 1.73 m wide powered roof supports with a maximum working resistance of 12000 KN (1225 t) at 51.6 MPa hydraulic leg pressure. This corresponds to a load per unit width of 6940 kN/m (707 t/m). The setting pressure was 25.2 MPa, but during caving of the main roof the load of some powered roof supports exceeded the maximum support working resistance. Roof collapse and powered roof support failure occurred frequently. The first weighting distance and the periodic weighting distance of main roof have been analysed from November 2013 to June 2014. Immediate roof caving occurred at 63 m. Initial weighting of the main roof occurred when the face had advanced 80 m. The pressure in most of the powered roof supports exceeded 35 MPa with an average pressure of 40 MPa. More than half of the powered roof supports were overloaded during the first weighting.

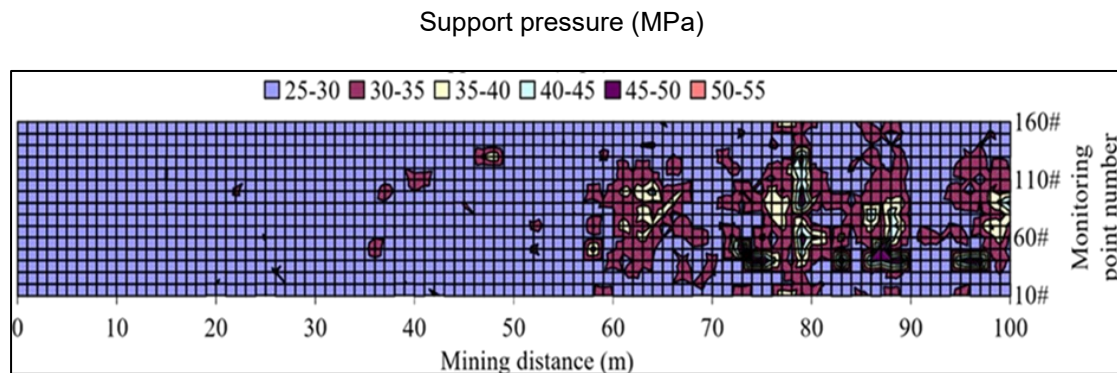


**Figure 26. Hydraulic leg pressure at start of Jinjie longwall LW31109**

In June 2014, when mining advanced from 3045 m to 3160 m, powered roof support pressure distribution was as shown in Figure 27. As can be seen the loadings became problematic with support No 80 reaching a pressure of 52.2 MPa which was above the design capacity of the supports.

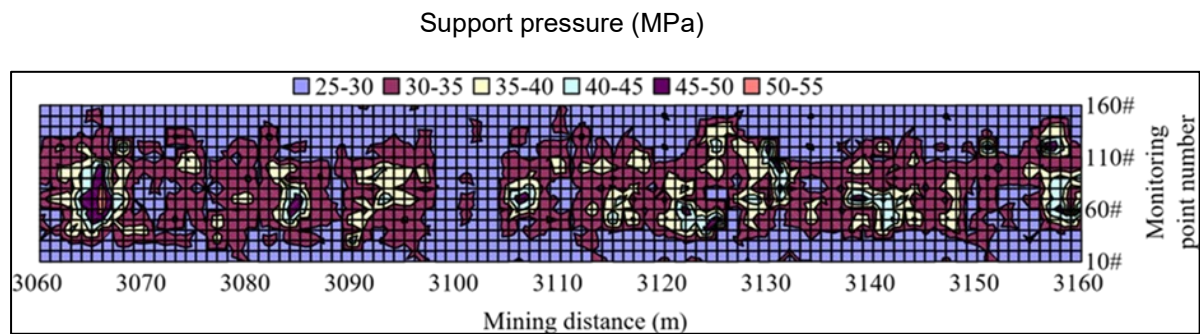


Figure 27. Hydraulic leg pressure from 3060 to 3160 m of Jinjie longwall LW31109

Table 2: Jinjie material properties of the coal strata (Zhao, 2018)

Position	Thickness (m)	Density (Kg/m <sup>3</sup> )	Shear modulus (GPa)	Bulk modulus (GPa)	Cohesion (MPa)	Friction angle (°)
Main roof	6.0	2,550	4.7	6.0	1.2	30
	3.0	2,700	1.6	3.4	1.6	30
	1.5	2,650	1.7	3.5	1.7	32
Intermediate roof	4.5	2,460	2.0	3.2	1.1	18
Coal seam	3.0	1,400	1.5	2.8	0.6	20
Floor	2.0	2,650	1.7	3.5	1.7	32

Shangwan mine is located in the Shendong Coalfield, Inner Mongolia. Longwall LW51104 mines a 6.5m thick seam at a depth of 115m, with face width of 301m and dip angle of 0-5°.

Table 3: Shangwan gross material properties of the coal strata (Wang, 2018a)

Name	Unit weight (KN/m <sup>3</sup> )	Elastic modulus (GPa)	Poisson's ratio	Cohesive strength (MPa)	Tensile strength (MPa)	Friction angle (°)
Sandstone	25.0	36.5	0.22	2.6	1.5	30
Coal	13.1	12.7	0.29	1.2	0.6	27
Siltstone	24.6	37.9	0.20	4.5	3.0	40

There are 11 different lithologies in the Jurassic, Cretaceous and Quaternary rock strata.

Wang, (2018a) reports an observation period during which 20 weightings occurred with intervals of 9.4-32.3 minutes with an average 16.7 minutes. Support resistance varied from 5571-8975 KN (559-901 t) averaging 7107 KN (713 t). The support's rated working resistance was 8638 KN (867 t). During coal mining beneath the thick bedrock and overlying loess layer, the weightings regularly alternated between strong and weak. As part of the periodic weightings, short time intervals corresponded with strong weightings, but normal time intervals had weights which could be either strong or weak.

Lithology	Formation	Depth (m)	Thickness (m)
	Coarse sandstone	81.4	9.0
	Fine sandstone	82.1	0.7
	Sandy clay rock	83.2	1.1
	Siltstone	86.5	3.3
	Coarse sandstone	96.0	9.5
	Sandstone	106.4	10.4
	Sandy mudstone	108.9	2.5
	1 <sup>-2</sup> coal seam	115.4	6.5
	Siltstone	130.4	15.0

Figure 28. Shangwan lithology (Wang 2018a)

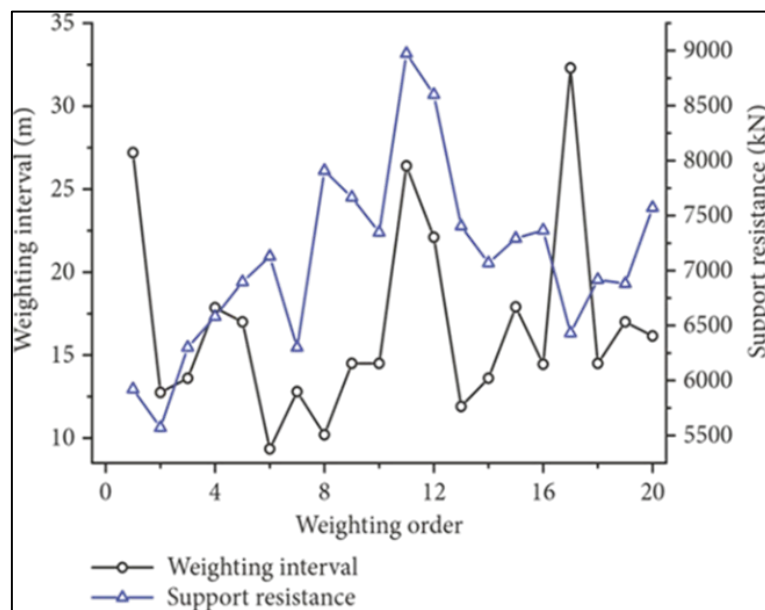


Figure 29. Shangwan weighting order (time sequence) vs weighting interval (m) and support resistance in kN (Wang 2018a)

### SUBSIDENCE IN SHALLOW LONGWALLS

Bulianta, in the Shendong Coalfield of Inner Mongolia, annually produces the most coal for any underground coal mine in the world. It is characterised by multiple, thick coal seams, shallow depth, and thick loess soil layers. Currently, the mine is extracting 30 Mtpa from the 2<sup>-2</sup> seam by longwall methods from under the previously mined bord-and-pillar workings in the 1<sup>-2</sup> seam. LW22307 was mined in the 6.8-7.7 m thick 2<sup>-2</sup> seam at a depth of 100 m with dip ranging from



1-3°, a mining height of 6.8 m, a face width of 300 m, and a panel length of 4954 m. Soil 8 - 23 m thick covers the whole panel. During the mining of LW22307, a detailed study was undertaken because of the severe surface damage at the mine resulting from subsidence and associated cracks.

Subsidence after mining from under a previously mined coal seam is enhanced, which results from the consolidation of the ground, closure of existing cracks, and the stress release in the previously mined area. Ground cracks, as the other product of ground deformation, not only have a great impact on the stability of surface structures, but also threaten the productivity of land and affect the safety of residents in a mining area (Yang, 2019). Figure 30 shows the subsidence along the centre line of the longwall. The zone labelled 0 to 170 m was under a previous goaf while that from 170 to 400 m was under previous pillar workings. The subsidence was reasonably symmetrical between chain pillars. The maximum subsidence was 5.85 m associated with extracting the 6.8 m seam. This subsidence was not an even flexure of the surface but occurred with large surface cracks and block movement as can be seen in Figure 31.

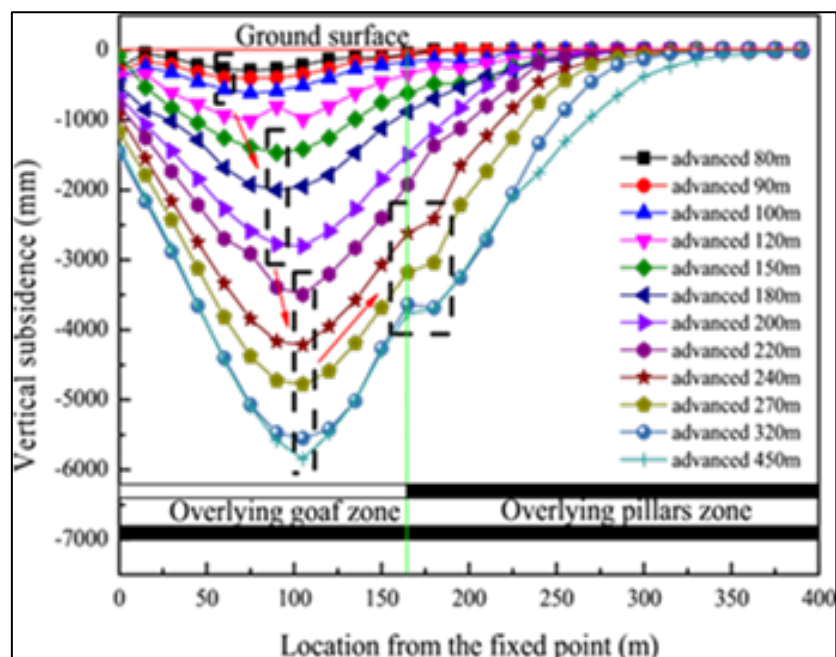


Figure 30. Bulianta LW22307 centre line vertical subsidence in mm. (Yang, 2019)



Figure 31. Bulianta LW22307 surface subsidence and cracking (Yang, 2019)

## **ROCKBURST AND COALBURST (BURSTS)**

Coalbursts involve the sudden, violent ejection of coal or rock into the mine workings. Coalbursts are a particular hazard because they typically occur without warning. Coalbursts are almost always accompanied by a loud noise, like an explosion, and ground vibration. The nature of coalbursts is quite variable. There are a number of forms of coalbursts that include:

- Events that may be partially initiated by gas operating as a component of effective stress in fractures but are principally strain energy events;
- Strain burst type events;
- Events that are associated with the release of seismic energy from the breakage of massive strata in the goaf;
- Events associated with sudden loss of strength on any plane – such as the roof and floor of the seam or of a specific joint.

Despite decades of research, the sources and mechanics of bursts are imperfectly understood, and the means to predict and control them remain elusive. High stress is a universal feature of burst-prone conditions. The overburden depth is responsible for the overall level of stress, but pillar design, multiple seam interactions, and/or mining activity can concentrate stresses in distinct locations. Geological factors also contribute. The presence of strong, massive sandstone near the seam has often been noted where bursts have occurred. In the Utah coalfields of the western United States of America, for example, miners refer to “bump sandwich” geology where the coal seam is slotted between massive sandstone roof and floor (Mark, 2016).

Significant rockburst and coalburst events have been recorded in longwall coal operations in massive strata in the United States of America. These include:

- Sunnyside, Book Cliffs / Wasatch Plateau Coalfield, Utah (Mark, 2016);
- Willow Creek, Book Cliffs / Wasatch Plateau Coalfield, Utah (Richardson 1996, Mark 2016);
- Lynch No.37, Harlan County, Kentucky (Hoelle, 2009);
- Elk Creek, North Fork Valley, Colorado (Mark, 2016).

Most American experience has been associated with deep longwall mining below 500 m of depth. However, this experience has resulted in the development of tailgate yield pillars which have the potential to significantly improve the conditions in shallow, thick seam longwalls in massive strata. The previously described event that destroyed the longwall face at Churcha West in India was undoubtedly a coalburst.



**Figure 32. Elk Creek longwall tailgate coalburst (Mark 2016)**

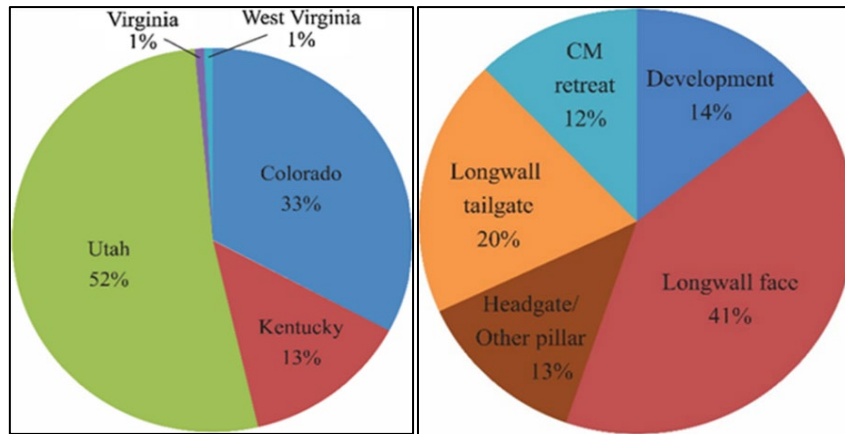


Figure 33. US 1994-2013 coalbursts (140 events) by location (Mark 2016)

### FACE SPALL

Shangwan coal mine is located in the Shendong Coalfield, Inner Mongolia, China. Rib spalling in longwall operations is becoming an increasingly serious safety issue as thicker seams are mined in a single pass. Spalling also contributes to an increase in unsupported roof span at the face and a corresponding increase in roof falls (Zhang, 2016).

Rib spalling has been studied in LW12301 at Shangwan, where the seam was 6.2 m thick at an average depth of 240 m. Here the mining height was 6.0 m, the panel was 249 m wide and 4948 m long. Immediate roof was sandy mudstone 0.63 - 3.87 m thick. The main roof was sandstone 1.3 - 4.2 m thick and the immediate floor was mudstone 0.56 - 2.11 m thick and softened by water. Large areas of face spall exploded into the working area several times during periodic weightings, resulting in fish-scale-like face spall. The maximum depth of spall was 1.7 m.

A study showed that rib instability was generally located below the roof at 0.58 times the mining height. Using a "thin plate" mechanical model, a theoretical study showed that in LW12301, the maximum depth of rib spalling was 0.98 - 1.61 m and the initial rib spalling started 2.53 m below the roof, which is basically consistent with field data.

Coal rib fracturing growth is influenced not only by the vertical stress, but also by the horizontal constraining effect of the intact coal seam beyond the fractured coal at the longwall face. The deformation of the fractured rib coal is inelastic and fractures resulting from compressive stress expand rapidly until rib failure occurs.

Table 4: Shandong mining height and depth of rib spalling on five faces (Zhang, 2016)

Longwall #	Mine	Mining height (m)	Form of rib spalling	Depth of rib spalling (m)
LW12301	Shangwan	3.3	Tension crack	0.83
LW12302	Shangwan	4.5	Tension crack	0.95
LW22307	Bulianta	6.8	Tension crack	1.45
LW52302	Duliuta	6.6	Tension crack	1.35
LW42104	Buertai	3.9	Tension crack	0.45

In general terms, depth of rib spall in the Shendong Coalfield is approximately 25% of the coal face mining height.

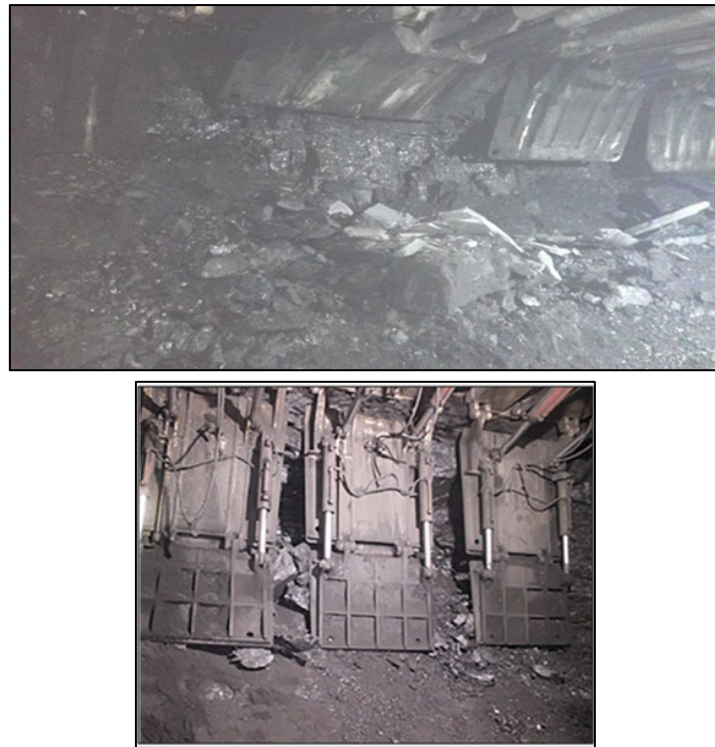


**Figure 34. Shangwan rib spall on a longwall face (Zhang, 2016) and hard coal thick seam longwall face (Wang, 2018b)**

#### **SANDSTONE PALEOCHANNELS**

Su (2001 and 2012) describe problems with mining at 180 m depth under a paleochannel of thick and massive sandstone at Enlow Fork mine in the Northern Appalachian Basin, Pennsylvania. This sandstone channel of 300 m width was known to cause serious longwall face roof control problems in the mine's B-panel area in 1998 and 1999. Some of the problems were large face cavities which caused production delay in the preceding panel. These problems were mitigated by the use of hydraulic fracturing. Early fracture operations improved face conditions but the pancake fractures were of inadequate size to cover the panel. Lu (2014) describes the beneficial effect of good hydraulic fracture design. In this operation fractures were developed of approximately 180 x 120 m horizontal dimension by pumping 16 m<sup>3</sup> of water and lubricant at 5.6 m<sup>3</sup>/min. The purpose of the fracture was to relieve high shear stresses in the roof and was apparently successful.

Broadmeadow, in the Bowen Basin, Queensland, introduced a top coal caving (TCC) longwall face in 2013, but since then has experienced severe convergence events at the start of each panel after 60-70 m of retreat, resulting in equipment damage, and the longwall almost becoming iron-bound.

The longwall is Caterpillar-supplied with 158 x 2 m-wide powered roof supports. The run of the face powered roof supports are two-leg, 1460 t capacity, the gate end special powered roof supports are three-leg supports with a 1580 t capacity, the two powered roof supports covering the front, and rear maingate drives are four-leg with 1800 t capacity. The shearer typically extracts the basal 3.8 m of the seam, with the remainder recovered using the TCC method. Figure 20 shows that periodic weighting has occurred throughout the mine life, due the presence of the moderately strong MP41 and MP42 sandstone units. The MP42 sandstone channel increased in thickness and was located over the start positions of LW7-11, with the



thickest portion over LW10. A thick sandstone unit close to the extraction roof was likely the cause of the convergence events at the start of each longwall panel. (Coutts, 2018).

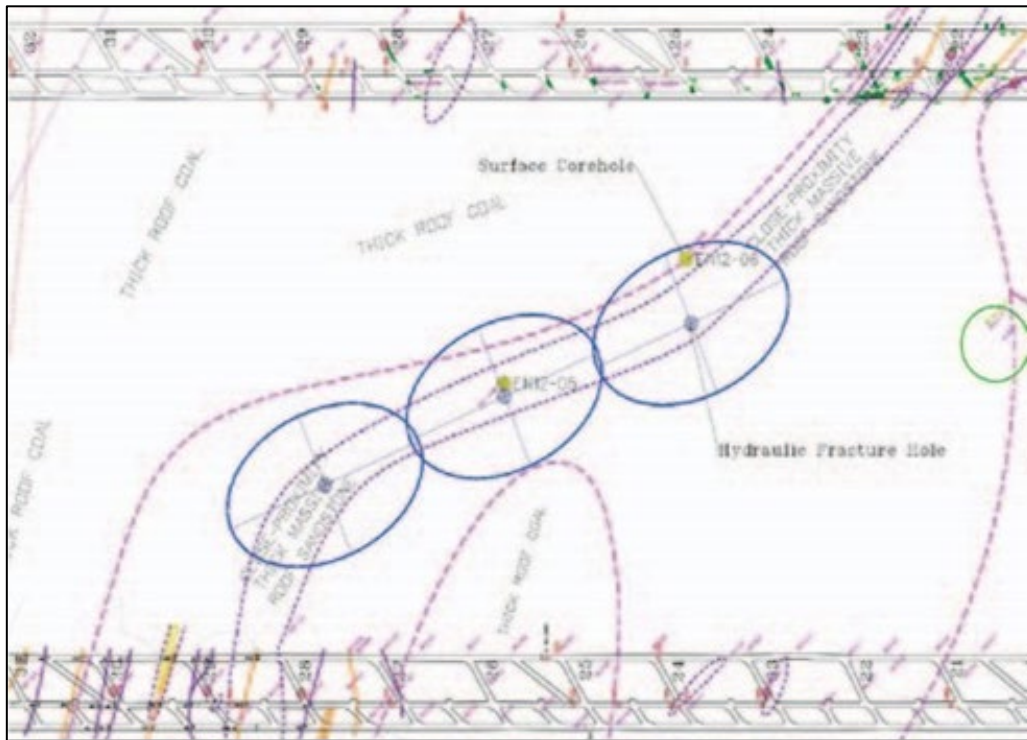


**Figure 35. Enlow Fork sandstone paleochannel traversing longwall panels and hydrofractures (Lu et al, 2014)**

After a severe convergence event on LW10, the powered roof supports were modified to provide 450mm of additional convergence capability. The shearer height was lowered by 150 mm. These changes combined with a planned increase in extraction height to 4.1 m allowed a total of 1300 mm of convergence to be sustained without impacting operability. This was equivalent to 4 days of the worst case convergence experienced in LW10.

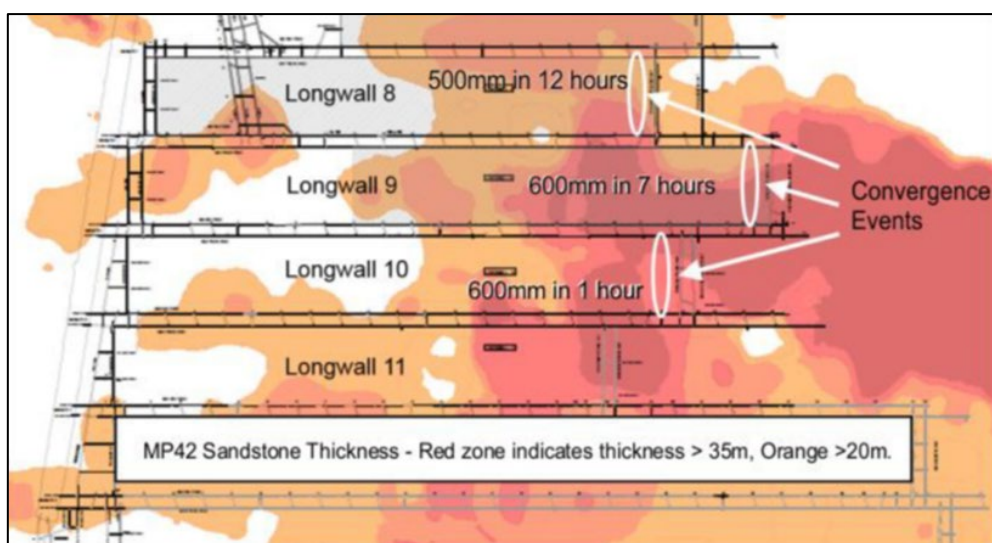


**Figure 36. Broadmeadow MP42 sandstone thickness contours and convergence rates (Coutts 2018)**

## PRECONDITIONING

Preconditioning is a technique used to increase the fracturing of the whole or part of a mineral deposit so that it will cave or fragment more easily. Preconditioning has gradually been introduced into underground coal mining using techniques pioneered in the petroleum industry and underground hard rock mines. The latter have used it to assist block caving, sub-level caving, and panel-caving methods in rock types not traditionally suited to caving (Catalan 2012, Cuello 2018 and Florez-Gonzalez 2019). There are two preconditioning techniques which have met with success in longwall mining: explosives and hydraulic fracturing (often referred to as “hydrofracturing”, “hydrofracking” or simply “fracking”). The Cadia East operation is shown in Figure 37.

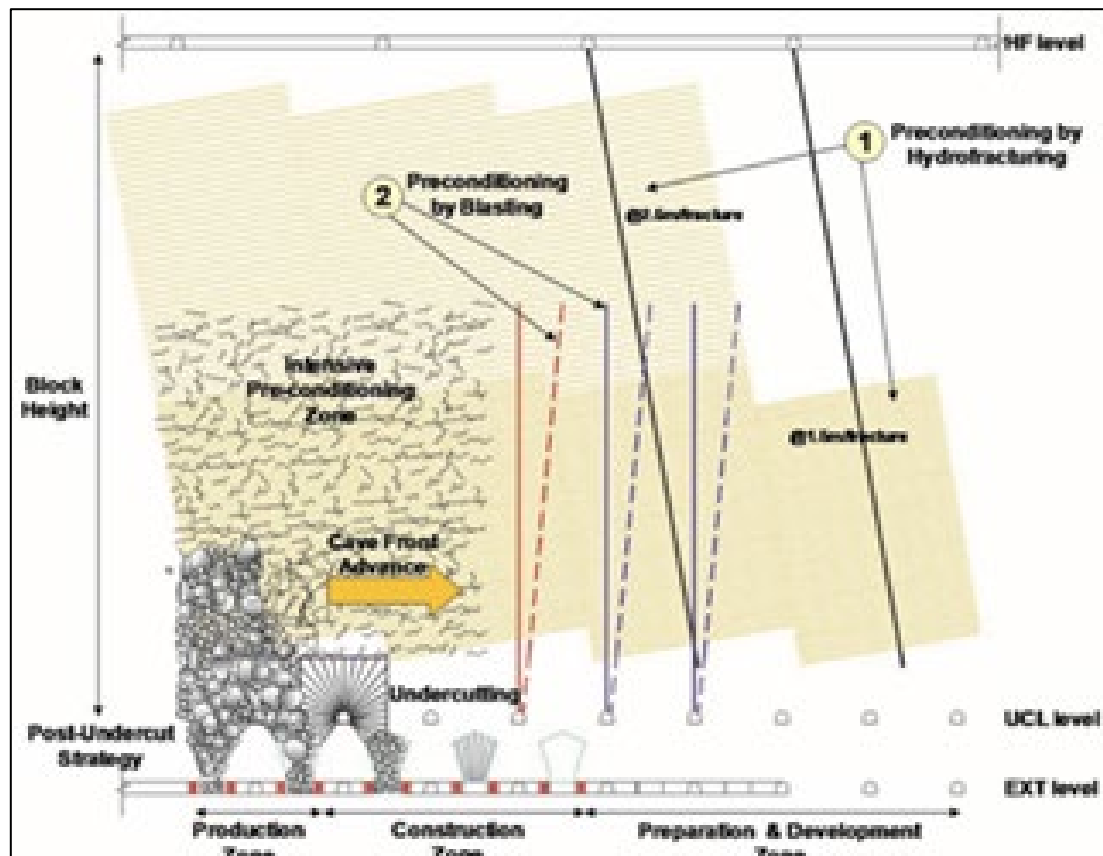


Figure 37. Cadia East intensive block cave preconditioning with explosives and hydrofracturing (Catalan, 2012)

### Explosives

Currently, the major application of explosives preconditioning in underground coal longwall mining is in the Upper Silesian Coal Basin (USCB), shared by the Czech Republic and Poland. Mining in the USCB is at depths of 800-1200 m in massive sandstone and conglomerate strata. The rockburst risk in such conditions is extremely high. De-stress blasting in immediate roof rocks is considered to be the most effective preventative control. All blastholes are drilled upwards at angles of 13-25° from the horizontal. Drilling is carried out in both the maingate and tailgate with holes varying in length from 47-90 m. Hole diameter is generally 95 mm at a spacing of 10 m. Holes are charged with plastic gelatine explosive (heat of explosion 4100 kJ/kg) with sand employed for the stemming (Konicek, 2018).



Because of the lack of a free face, the use of conventional explosives is limited in a confined environment to a fairly small radius of highly fractured material around the borehole. The use of high energy gas fracturing enables the extent of fracturing to be extended significantly. This process involves the use of substances which produce less detonation shock but rather sustain a gas pressure for a prolonged period to extend fractures.

### **Hydraulic Fracturing**

Hydraulic fracturing was first used in Australian longwall coal mining at Moonee in the Newcastle Coalfield to help break up overlying conglomerate to mitigate severe wind-blasts. Holes were drilled into the roof from the longwall face. This technique, although slow and tedious, did succeed (Hayes, 2000). More recent Australian success has been achieved at Narrabri, Gunnedah Coalfield, using vertical surface holes in massive strata to initiate longwall caving (Jeffrey, 2013).

Enlow Fork in the Northern Appalachian Basin, Pennsylvania, a state-of-the-art longwall operation, first attempted hydraulic fracturing in 1998 using oilfield techniques to break up massive sandstone channels in the immediate vicinity of the longwall face, and has used variations of the methodology ever since. Enlow Fork leads the coal world in this application (Su 2001, Akinkugbe 2007, Su 2012 and Lu 2014).

The direction in which hydraulic fractures develop is a function of the stresses and pre-existing planes of weakness within the rock mass. In a uniform rock mass, a hydraulic fracture will develop in a plane that is perpendicular to the minor stress. When structure is taken into consideration, the fractures may develop along these. What happens depends on the minimum energy required to propagate the fracture. Where there are significant planes of weakness (structure) it is unlikely that pre-conditioning by hydrofracture will be required. The focus of hydrofracturing for pre-conditioning is on breaking up massive strata. The stresses that exist within such strata are therefore critical to the success of the operation.

If the minor stress is horizontal and aligned perpendicular to the longwall block, then vertical fractures will form which will be in the wrong direction to promote failure of the goaf. If the minor stress is perpendicular to the future face then multiple vertical holes would need to be drilled and hydrofractured to create face breaks. Alternatively, holes for hydrofracturing need to be drilled in line with the longwall block and stage fractured to create the multiple breaks required.

If the minimum stress is vertical then the fracture will become horizontal. This is the most desirable orientation for a fracture in preconditioning. The fractures formed can be large in area and form a series of separated plates which are more likely to fail in bending. Multiple levels of hydrofracture may be undertaken quite simply in a single vertical hole to break a massive unit into multiple plates. The process for this is to drill and case a hole and then to perforate it at the first level and to hydrofracture this. The hole is then filled with sand to cover the first perforations and then perforated again and hydrofractured. This process may be repeated to achieve the desired degree of fracturing. If the stress field is isotropic and the rock homogeneous then the fractures may form in random directions.

The limitations on hydrofracture are the area of the fracture that can be achieved and the orientation of the fracture. The latter is governed by the stresses and any structures that may exist. The size of fracture is basically limited by the ability of the rock to absorb the hydrofracture fluid versus the flow rate and pressure that can be supplied by the hydrofracture pump. Thus porous, permeable strata require hydrofracture fluids that will seal the hydrofracture surfaces with a filter cake and be more viscous as this will also limit fluid penetration. As with any complex process, there is a trade of which parameters will give the maximum benefit, in this case the largest area hydrofracture. This is the art of the hydrofracture design, which has been the

subject of intense study within the petroleum industry for the purpose of flow stimulation. The difference between petroleum applications and those used for preconditioning are that in the latter there is no need to maintain fluid conductivity within the fracture. This simplifies the fracture process significantly.

### GOAF BEHAVIOUR

We need some model to predict how the goaf will behave behind the longwall. The question is how will the rock break up? This is dependent on the stresses within the goaf and the strength of the material within it. Prior to the goaf forming, the rocks will carry both vertical and horizontal stress. As the coal is removed by the longwall, the vertical stress holding the roof up is removed. There are then several possibilities as to how failure may occur. These include tensile and shear failure.

Tensile failure may occur perpendicular to the free face of the roof of the goaf. It is induced by gravity alone and leads to slabbing. There may also be tensile stress associated with local stress concentrations near the installation road.

At the start of the goaf, there may be a compressively induced shear brought about by the high lateral stress in the roof rock combined with a lack of confinement. Compressive initial failures can be extremely violent when the roof is strong. They can have all the characteristics of a uniaxial specimen failing violently in a universal test machine. In the absence of high compressive strength, shear is a potential failure mechanism brought about by gravitational load acting at each end of the bridged roof. In a low lateral stress environment, the goaf roof rock may simply drop out with steep sides. This form of collapse gets wider and higher as the longwall progresses. The width and height of such a failure may be the piston that drives a wind-blast event.

Once the goaf has formed, there is no compressive stress at the goaf edge near the roof nor further up into the goaf until the rocks begin to form a compressive arch or bridge. Compressive stress related shear failure may take place within this arch. Near the goaf edge the lateral stress has been relieved and the stresses may be stylised to have the form shown in Figure 38.

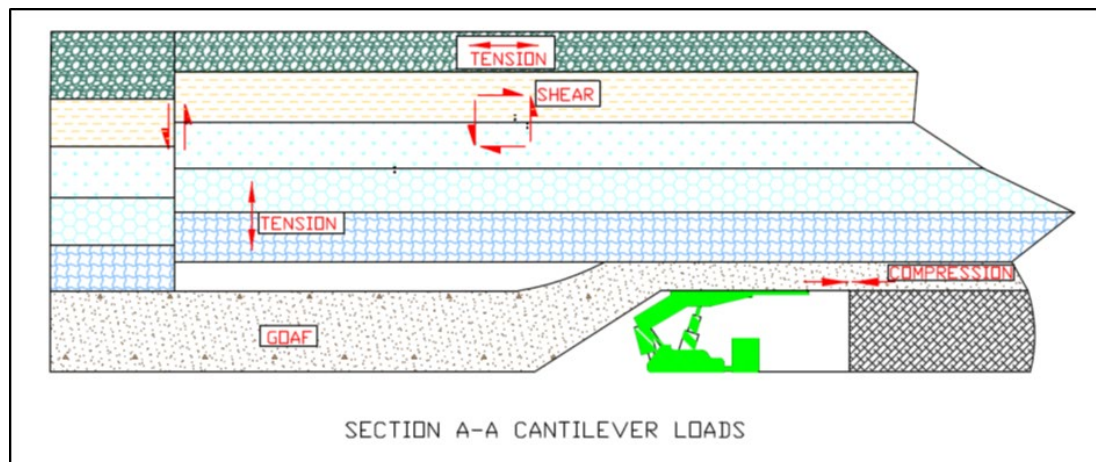


**Figure 38. Stylised view through longwall face and goaf showing stresses**

Figure 38 shows a section through a longwall face and goaf. It shows an immediately collapsed weak roof behind the powered hydraulic support. Whether this has fallen depends on the rock type. The types of stresses in roof above it are shown. Tension may be developed within the hanging mass. This may cause the rock to pull apart. This will normally occur on weak bedding planes.

It is quite possible that these bedding planes may have already been separated by shear developed by the release of lateral strain. If the rock laminations contain varying strain levels, shear may develop between them even while they are ahead of the face, though the lack of confinement after the passage of the face would make this more likely. Alternatively, the rock on the goaf edge may shear from the material above because the rock above it is constrained within an arch or a not properly disrupted goaf. Shear may also occur by the self-weight of a cantilevered section of rock. The shear stress within this is caused by the overhanging mass. This vertical shear has a conjugate shear that will act along the bedding plane. Uniform section elastic beam theory suggests that the shear stress has a parabolic profile with a maximum which is 1.5 times the average shear at the mid height of the beam.

The layers of strata act as plates which may be joined by cohesion and friction but are likely to separate by tensile or shear stress on weak bedding planes. Once separated, they behave as individual units that may be loaded from above. The likely failure mode is then one of tension induced by bending. If the layer of strata is jointed through without infill, it will not have tensile strength. However there are many layers of strata in coal mines which are not jointed. Some of these have very significant tensile strength.

A massive, thick, stratigraphic unit can support its own weight for a substantial distance into the goaf. Simple elastic linear beam theory can be used to describe the distance before it breaks in tension or in shear. The formulae for these are given in Equations 1 and 2 respectively. Equation 1 defines the length of the cantilever subject to a tensile stress failure at its top. Equation 2 defines the maximum cantilever length due to shear stress at the mid-depth of the cantilever. Each case assumes that there is no loading on the end of the cantilever from the goaf.

$$l_b = \sqrt{\sigma_t d / (3\rho g)} \quad (1)$$

$$l_\tau = \frac{2\tau_f}{3\rho g} \quad (2)$$

Where

- $l_b$  is the length of the cantilever unit at failure due to tensile stress
- $l_\tau$  is the length of the cantilever unit at failure due to shear stress
- $d$  is the cantilevering units' thickness
- $\rho$  is the density of the rock
- $\tau_f$  is the shear strength of the rock on a bedding plane
- $\sigma_t$  is the horizontal tensile strength of the rock at the top of the unit.

The question is, what defines the beam or plate thickness? Is it defined by shear along bedding planes caused by pre-existing differential strain between them or is it due to tensile failure across the bedding plane due to gravitational load?

The equations used are based on linear elastic theory though it should be realised that the rock is probably anything but linear in its behaviour (Gray, Zhao and Liu, 2018). In addition to nonlinearity and anisotropy of elastic parameters, the failure behaviour of many of the coal measure rocks are also anisotropic.

In a recent project undertaken by Sigrá, the rock was tested uniaxially, hydrostatically and triaxially for elastic properties. It was also tested for strength uniaxially, in shear triaxially, and also in shear by direct shear on the bedding planes. In addition it was subject to true tensile testing both perpendicular to the bedding planes and in the direction of these. A laminated medium-grained sandstone unit with micaceous bedding planes has the typical properties shown in Table 5.

**Table 5. Rock properties for a medium-grained laminated sandstone with mica on the bedding planes**

Rock property	Units	Value
Uniaxial compressive strength	MPa	62
Mohr Coulomb angle of friction (axial triaxial test)	Degrees	42
Mohr Coulomb cohesion (axial triaxial test)	MPa	13.6
Cohesion (transverse shear)	MPa	2.0
Tensile strength across bedding (axial pull)	MPa	0.5
Tensile strength along bedding (transverse pull)	MPa	5.0
Secant Young's modulus (uniaxial at 10 MPa)	MPa	6517
Ratio of anisotropy (horizontal vs axial) at 10 MPa, (hydrostatic test)		3.6
Non linearity of axial modulus at 10 MPa (hydrostatic test)	MPa/MPa	395
Permanent axial offset at 10 MPa (cyclic axial compression)	$\mu\epsilon$	464
Permanent circumferential offset at 10 MPa (cyclic axial compression)	$\mu\epsilon$	-38

Table 5 shows that the rock is very anisotropic and nonlinear in elastic properties. The cohesion measured from triaxial testing is seven times higher than that measured in direct shear on the bedding plane. The tensile strength measured in the direction of bedding is ten times that measured across the bedding. The rock is also inelastic, showing significant permanent strain at quite moderate axial loading. These factors need to be measured and taken into account when determining rock mechanics behaviour and certainly in the failure mechanism of a goaf. In addition the pre-existing stresses and their associated strains are important. Along with material properties they determine what layer of strata will shear over which, thus determining the thickness of units that are then liable to bending failure.

The actual shape of goaf will be more complex than described by the simple beam model presented above because it has a three dimensional component around the face ends where the effects of pillars will occur.

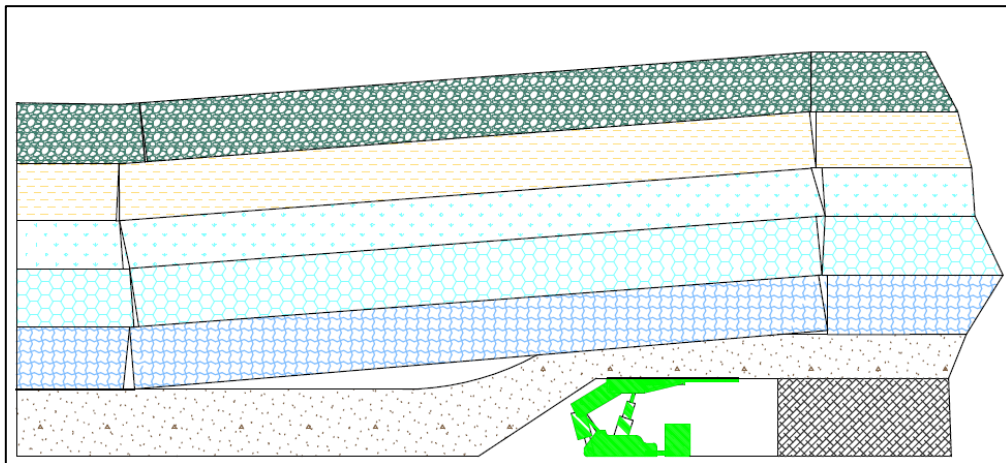
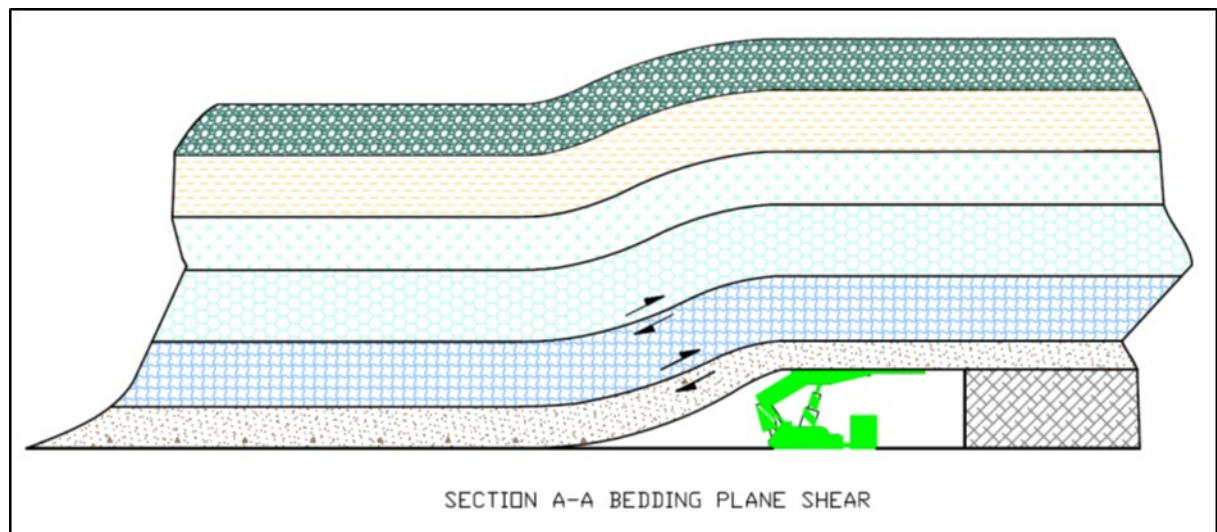
**Figure 39. Block failure behind the face**

Figure 23 shows the type of failure associated with massive strata. In this, the immediate weak roof has fallen but above it is a number of major slabs that have delaminated on weaker planes. These have fallen sequentially from the bottom up. They are shown here breaking just over solid coal in the face. As such, they may by their geometry behave as a lever with a fulcrum just beyond the face, which places enormous vertical load on the coal at the face. This would

cause face spall. The slabs are shown here falling sequentially with connection to similar rock behind in the goaf. Under such circumstances some level of horizontal stress may be maintained along the axis of the longwall (Gray, Wood and Shelukina, 2013) helping to provide a controlled fall as there is friction at the break ahead of the face. If the slabs do not fail evenly and sequentially the slabs can slide backwards into the goaf. This causes open voids above the face, which is associated with rock blocks falling from it on to the armoured face conveyor. Recovering from such an event becomes a major exercise.

If the blocks that form are of sufficient size they can cause major problems for the powered roof supports which have to bear the weight of the block as it breaks from the cantilever, causing a weighting problem.

The tensile failure of massive strata is a mechanism for large seismic energy release, as very little energy is used in creating the failure compared to the shear failure mechanism. This raises the likelihood of rockbursts triggered by seismic events.



**Figure 40. Goaf formation in a weak rock**

By contrast to the massive rock case, Figure 40 shows the even formation of a goaf in weaker rock and higher stresses. Here shearing readily occurs on weak laminations.

The problems at the face are mirrored over the tailgate. Large blocks can move and cause problems such as shear of the tailgate pillars. The formation of large blocks carrying load from the adjacent goaf may load the tailgate pillar unduly. It is Chinese practice to use pre-splitting of a massive roof to prevent this problem (Chen, 2018). This pre-splitting is normally conducted from underground.

## CONCLUSIONS

This paper describes the difficulties associated with longwall coal mining under massive strata that leads to the formation of large blocks. These problems include weighting events, the formation of cavities over the face, face spall, coalbursts, pillar failures, uneven subsidence and wind-blasts. These problems are a horror story for miners.

It is essential before mining commences to determine what the goaf behaviour will be. Will there be problems with massive units or not? This requires detailed measurement of stresses and rock properties well beyond the current practice of simply sending rock samples for uniaxial or triaxial testing to obtain failure properties that do not relate to the failure planes that will form to delineate block boundaries. Armed with this knowledge, it is then possible to start to build a

realistic model that will focus on whether large blocks will form with mining or not, and what their dimension may be. This will be the key to successful powered support design.

Where the formed layer thicknesses and hence block sizes are too great, it is then necessary to consider preconditioning to ensure that the sizes are manageable. Preconditioning can be achieved through the use of hydrofracture or by blasting. The successful use of hydrofracture is dependent upon the stress regime as this will determine the fracture orientation. Where this is unfavourable, a resort can be made to blasting. This has a far more limited range than hydrofracture. It can however be increased by the use of different explosives that primarily generate gas rather than a detonation. In conclusion, mining in massive strata is not easy and should only be undertaken with due consideration.

## REFERENCES

Akinkugbe Y., Su D., Hasenfus G., Morris T.J., and Fisher B. (2007), *The Roof Behavior of a Longwall Tailgate Under Massive Sandstone Strata*, 26<sup>th</sup> International Conference on Ground Control in Mining, 31 July – 2 August 2007, Morgantown, West Virginia, USA.

Catalan A., Dunstan G., Morgan M., Green S., Jorquera S., Thornhill T., Onederra I. and Chitombo G. (2012), *How Can an Intensive Preconditioning Concept be Implemented at Mass Mining Method? - Application to Cadia East Panel Caving Project*, 46<sup>th</sup> U.S. Rock Mechanics/Geomechanics Symposium, 24-27 June 2012, Chicago, Illinois, USA.

Chen C, and Liu C. (2018) *Analysis and Application on Controlling Thick Hard Roof Caving with Deep-Hole Position Presplitting Blasting*, China University of Mining and Technology, Xuzhou, China.

Chen C., Hu Z., Wang J., and Jia J. (2019), *Dynamic Surface Subsidence Characteristics due to Super-Large Working Face in Fragile-Ecological Mining Areas: A Case Study in Shendong Coalfield, China*, School of Environment Science and Spatial Informatics, China University of Mining and Technology, Xuzhou 221116, China, *Advances in Civil Engineering*, Volume 2019, Article ID 8658753, 16 pages <https://doi.org/10.1155/2019/8658753>, published by Hindawi, 22 January 2019.

Cloete C.J. (1980), Contribution to Henderson P.G. (1980), *Experience in Longwall Mining at Coalbrook Collieries, Sigma Colliery, Sasol One (Pty) Ltd, Sasolburg, Orange Free State, South Africa*, South African Institute of Mining and Metallurgy, January 1980.

Coutts R.J., Lynch D.G., Martin M.R., and Mills K.W. (2018), *Management of Initial Convergence at Broadmeadows Mine*, 37<sup>th</sup> International Conference on Ground Control in Mining, Morgantown, West Virginia, USA.

Creech M. (2014), *Moriarty was a Conglomerate – Experiences and Implications of Coal Mining under Massive Strata in the Newcastle Coalfield*, 9<sup>th</sup> International Mining Geology Conference, 18-20 August 2014, Adelaide, South Australia.

Cuello D. and Newcombe G. (2018) *Key Geotechnical Knowledge and Practical Mine Planning Guidelines in Deep, High-Stress, Hard Rock Conditions for Block and Panel Cave Mining*, 4<sup>th</sup> International Symposium on Block and Sublevel Caving, 15-17 October 2018, Vancouver, British Columbia, Canada.

Deats M.J. (1971), *A Follow-Up Report on Longwall Coal Mining at Durban Navigation Collieries (Pty.) Limited*, Journal of the South African Institute of Mining and Metallurgy, April 1971.



Deb D. and Verma A.H. (2004), *Ground Control Problems in Indian Longwall Mines - a Perspective and Future Research Outlook*, Mining Engineering Department, Indian Institute of Technology, Kharagpur, India 721302, Journal of Mines, Metals and Fuels, September 2004.

Flores-Gonzalez G. (2019) *Major Hazards associated with Cave Mining – Are They Manageable?*, 1<sup>st</sup> International Symposium on Mining Geomechanical Risk, 9-11 April 2019, Perth, Western Australia.

Gray I, Wood J., and Shelukhina Y. (2013), *Real Stress Distributions in Sedimentary Strata*, 6<sup>th</sup> International Symposium on In-Situ Rock Stress - RS2013, 20-22 August 2013, Sendai, Japan.

Gray Ian, Zhao Xiaoli, and Lucy Liu (2018), *The Determination of Anisotropic and Nonlinear Properties of Rock through Triaxial and Hydrostatic Testing*. Proceedings of the Asian Rock Mechanics Symposium (ARMS10) 29 October to 3 November, 2018, Singapore.

Hayes P. (2000), *Risk Minimisation in Longwall Operations in Massive Goaf Conditions using Microseismic and Hydraulic Fracturing Techniques*, 2000 Queensland Mining Council Annual Conference, Unpublished.

Hebblewhite B. (2001), *Regional Horizontal Stress Movements associated with Longwall Mining*, 5<sup>th</sup> Triennial Conference of Mine Subsidence, Maitland, New South Wales, Australia.

Hebblewhite B. (2013), *A Review of Current International Thick Seam Mining Practices and Geotechnical Challenges*, Presentation, Bowen Basin Underground Geotechnical Society (BBUGS), 13 September 2013.

Henderson P.G. (1980), *Experience in Longwall Mining at Coalbrook Collieries*, South African Institute of Mining and Metallurgy, January 1980.

Hoelle J. (2009), *Coal Bumps in an Eastern Kentucky USA Longwall Coal Mine 1989 to 1997*, 2009 Coal Operators' Conference, 12-13 February 2009, Wollongong, New South Wales, Australia.

Jeffery R.G., Chen Z., Mills K.W., and Pegg S. (2013), *Monitoring and Measuring Hydraulic Fracturing Growth during Preconditioning of a Rock Roof over a Coal Longwall Panel*, InTech open access article, May 2013.

Konicek P., and Schreiber J. (2018), *Rockburst Prevention via Destress Blasting of Competent Roof Rocks in Hard Coal Longwall Mining*, Czech Academy of Sciences, Institute of Geonics, Ostrava, Czech Republic, Southern African Institute of Mining and Metallurgy, March 2018, ISSN 2225-6253.

Latilla J.W., Van Wijk J.J, Booyesen H., Silver C., and Fourie P. (2007), *Multiple Seam Interactions of Relatively Shallow, High Seam Shortwalls in South Africa*, 26<sup>th</sup> International Conference on Ground Control in Mining, 31 July - 2 August 2007, Morgantown, West Virginia, USA.

Li B., Liang Y., and Zou Q. (2019), *Determination of the Working Resistance based on Movement Type of the First Subordinate Key Stratum in a Fully Mechanized Face with Large Mining Height*, State Key Laboratory of Coal Mine Disaster Dynamics and Control, Chongqing University, Chongqing, China, Journal of Energy, Science and Engineering published 13 February 2019 by the Society of Chemical Industry and John Wiley Sons Ltd.

Lu J., Su D.W.H., Hasenpus G.J, Van Dyke M. and Stull L. (2014), *Mitigation of a Massive Sandstone Channel's Impact on Longwall Face Evaluation and Enhancement of Hydraulic Fracturing Technique*, 33<sup>rd</sup> International Conference on Ground Control in Mining, 29-31 July 2014, Morgantown, West Virginia, USA.

MacDonald R.J (1997), *Significant Weighting Events on the Longwalls in the Phalen Colliery*, 16<sup>th</sup> Conference on Ground Control in Mining, 5-7 August 1997, Morgantown, West Virginia, USA.

Mark C. (2016), *Coal Bursts in the Deep Longwall Mines of the United States*, Int J Coal Sci Technol (2016) 3(1):1–9 DOI 10.1007/s40789-016-0102-9, Published 30 January 2016.

Mills K.W., Puller J., and Salisbury O. (2015), *Measurements of Horizontal Shear Movements Ahead of Longwall Mining and Implications for Overburden Behaviour*, 34<sup>th</sup> International Conference on Ground Control in Mining, 28-30 July 2015, Morgantown, West Virginia, USA.

Moodie A., and Anderson J. (2011), *Geotechnical Considerations for Longwall Top Coal Caving at Austar Coal Mine*, 2011 Underground Coal Operators' Conference, Australasian Institute of Mining and Metallurgy, Illawarra Branch, 10-11 February 2011, Wollongong, New South Wales, Australia.

Payne D., Martin M., Coutts R., and Lynch D (2019), *Highwall Stability Implications from Longwall Mining at Broadmeadow Mine, BHP Coal, Broadmeadow Mine, Moranbah, Queensland*, 19<sup>th</sup> Coal Operator's Conference, University of Wollongong, 18-20 February 2019.

Rice G.S. (1935), *Bumps in Coal Mine of the Cumberland Field, Kentucky and Virginia: Causes and Remedy*, US Bureau of Mines RI 3267.

Richardson A.M., Gilbride L.J., Trackemas J., and Mercier J. (1996), *The Influence of Massive Sandstones in the Main Roof on Longwall Support Loading – Willow Creek Case Study*, 15<sup>th</sup> International Conference on Ground Control in Mining, 13-15 August 1996, Colorado School of Mines, Golden, Colorado, USA.

Sandford J. (1998), *Review of Longwall Mining Experience at South Bulga Colliery*, International Conference on Geomechanics/Ground Control in Mining and Underground Construction, 14-17 July 1998, Wollongong, New South Wales, Australia.

Sandford J., Mahoney S., Conover D.P., and DeMarco M.J. (1999), *Shield Monitoring to Forecast Severe Face Weightings at the South Bulga Colliery*, NSW, Australia, 18<sup>th</sup> Conference on Ground Control in Mining, 3-5 August 1999, Morgantown, West Virginia, USA.

Sharma P. and Fowler J.C.W. (2004), *Wind Blasts in Longwall Panels in Underground Coal Mines*, South African Institute of Mining and Metallurgy, December 2004.

Su D.W.H., Barletta L., McCaffrey J.J., Thomas, E.P. and Toothman, R.C. (2001), *Hydraulic Fracturing of Sandstone and Longwall Roof Control - Implementation and Evaluation, Consol Energy, Pennsylvania*, 20<sup>th</sup> International Conference on Ground Control in Mining, 7-9 August 2001, Morgantown, West Virginia, USA.

Su D.W., Hasenfus G.J., Stull L., Lu, J., Van Dyke, M., Morgan, S., Kelley, P., Teetler, D. (2012), *Mitigation of a Massive Sandstone Channel's Impact on a 1,500-Foot-Wide Longwall Face*, 31<sup>st</sup> International Conference on Ground Control in Mining, 31 July - 2 August 2012, Morgantown, West Virginia, USA.

Tarrant, G. (2005), *Skew Roof Deformation Mechanism in Longwall Gateroads - Concepts and Consequences*, Coal 2005 Conference, 26-28 April 2005, Brisbane, Queensland, Australia.

Wang S., Wu X., Zhao Y. and Hagan P. (2018a), *Mechanical Performances of Pressure Arch in Thick Bedrock during Shallow Coal Mining*, International Joint Research Laboratory of Henan Province for Underground Space Development, Henan Polytechnic University, Published 1 October 2018, Hindawi Geofluids Volume 2018, Article ID 2419659.

Wang J., and Wang Z. (2018b), *Systematic Principles of Surrounding Rock Control in Longwall Mining Within Thick Coal Seams*, College of Resources and Safety Engineering, China

Coal Operators' Conference

University of Mining and Technology, Beijing, China, 37<sup>th</sup> International Conference on Ground Control in Mining, 24-26 July 2018, Morgantown, West Virginia, USA.

Wold M.B. and Pala J. (1986), *The Response of Powered Supports and Pillars to Initial Longwalling under a Strong Main Roof*, The AusIMM Illawarra Branch, Ground Movement and Control related to Coal Mining Symposium, August 1986, Wollongong, New South Wales, Australia.

Yang X., Wen G., Dai L., Sun H., and Li X. (2019), *Ground Subsidence and Surface Cracks Evolution from Shallow-Buried Close-Distance Multi-Seam Mining: A Case Study in Bulianta Coal Mine*, published online 10 January 2019, *Rock Mechanics and Rock Engineering* (2019) 52:2835–2852 <https://doi.org/10.1007/s00603-018-1726-4>.

Zhang H., Fu X., and Shen Y. (2016), *Study on Rib Spalling Mechanism and Spalling Depth in Large Mining Height Fully-Mechanised Face*, Liaoning Technical University, 16<sup>th</sup> Coal Operators' Conference, 10-12 February 2016, Wollongong, New South Wales, Australia.

Zhao J., Liu L., and Zheng Z. (2018), *Law of Strata Pressure Behaviour in Shallow Coal Seam*, China University of Mining Technology, Beijing, IOP Conference Series: Earth and Environmental Science 113 (2018), Published 24 September 2018.

# A ROOF CAVABILITY CLASSIFICATION SYSTEM AND ITS USE FOR ESTIMATION OF MAIN CAVING INTERVAL IN LONGWALL MINING

**Sadjad Mohammadi<sup>1</sup>, Mohammad Ataei<sup>2</sup>, Reza Kakaie<sup>3</sup>,  
Ali Mirzaghobanali<sup>4</sup>, Zahra Faraji Rad<sup>5</sup> and Naj Aziz<sup>6</sup>**

**ABSTRACT:** Proper strata caving in longwall mining guarantees the success of the operation while delayed or poor caving will lead to severe consequences. Therefore, the reliable prediction of strata and its caving potential is essential during the planning stage of a longwall project. This paper reports a novel classification system to evaluate the cavability level of the immediate roof strata in coal mines. A Fuzzy integrated multi-criteria decision-making method was used to incorporate nine inherent parameters that control the caving behaviour. After the determination of parameters' weights and assigning corresponding ratings, the Cavability Index (CI) was defined as the summation of ratings for all the parameters to indicate the potential of caving qualitatively. The proposed classification system was applied to evaluate twelve panels throughout the world. In addition, the applicability of the classification system was investigated through the estimation of the main caving intervals. For this purpose, statistical relationships were developed in which the Cavability Index (CI) and hydraulic radius was independent variables. Model validation indicated that the linear model possesses an acceptable accuracy in the estimation of the main caving intervals for actual cases. These results showed reliable performance of the novel developed classification system from a practical point of view.

## INTRODUCTION

Strata mechanics is one of the important aspects of longwall mining in which the caving process is a fundamental issue. Proper caving guarantees the success of the longwall operation while delayed or poor caving will lead to severe consequences, resulting in reduction of safety and productivity. A thorough understanding of strata mechanics and caving behaviour provides a practical insight into subsidence and ground control design, stability prediction of the face, roadways and gates, determination of the load capacity of shields, and mine layout design. Consequently, the reliable prediction of strata behaviour with respect to its caving potential is essential for the successful planning of longwall projects in a given geo-mining environment.

A number of empirical models (Peng and Chiang, 1984; Ghose and Dutta, 1987; Das, 2000; Singh et al., 2004; Oraee and Rostami, 2008; Yongkui et al., 2014), analytical (Obert and Duvall, 1967; Kuznetsov et al., 1973; Mukherjee, 2003; Manteghi, et al., 2012; Noroozi, et al., 2012; Hao et al., 2015), and numerical models (Kwasniewski, 2008; Sing and Sing, 2009; Sing and Sing, 2010; Shabanimashcool, et al., 2014; Gao, et al., 2014) and physical (Kuznetsov et al., 1973; Wang, et al., 2011; Wu, et al., 2015) have been developed in the literature to predict

- 
1. Ph.D., Shahrood University of Technology, Iran. Email: [sadjadmohammadi@shahroodut.ac.ir](mailto:sadjadmohammadi@shahroodut.ac.ir)
  2. Professor, Shahrood University of Technology, Iran. Email: [ataei@shahroodut.ac.ir](mailto:ataei@shahroodut.ac.ir)
  3. Professor, Shahrood University of Technology, Iran. Email: [r\\_kakaie@shahroodut.ac.ir](mailto:r_kakaie@shahroodut.ac.ir)
  4. Senior lecturer, University of Sothern Queensland, Australia. Email: [ali.mirzaghobanali@usq.edu.au](mailto:ali.mirzaghobanali@usq.edu.au)
  5. Lecturer, University of Sothern Queensland, Australia. Email: [zahra.farajirad@usq.edu.au](mailto:zahra.farajirad@usq.edu.au)
  6. Professor, University of Wollongong, Australia. Email: [naj@uow.edu.au](mailto:naj@uow.edu.au)

roof behaviour and its caveability. The empirical models are the most widely used method in this context, which includes a variety of qualitative and quantitative models. The qualitative models are in the form of a classification system. These models are easy and useful tools that provide qualitative evaluation of the immediate roof with respect to the parameters that influence caving.

These models have provided a significant contribution to predict strata caving behaviour, however, the most obvious shortcoming of these techniques is developing a site-specific model. Additionally, no scientific or systematic approach was applied to evaluate quantitatively the weighting of the impacting parameters. Accordingly, this paper presents a new classification method to qualitatively evaluate the cavability of the immediate roof by incorporating a Fuzzy integrated multi criteria decision making method. Since this model is knowledge-based, these can be applied for a wide range of geo-mining conditions without significant limitation. The proposed model was examined in twelve cases throughout the world. In addition, its practical implementation was studied by developing statistical models to estimate the main caving interval.

### **METHODOLOGY**

In this work, an integrated multi-criteria decision-making method is used to propose a new classification system. The integrated method applied the Analytic Network Process (ANP) technique in combination with the Decision Making Trial and Evaluation Laboratory (DEMATEL) technique by incorporating fuzzy sets theory. ANP is the general form and extension of the AHP method that provides a general framework to deal with complex real problems in which there are independencies within a cluster and among the different clusters (Saaty, 1996). ANP establishes a supermatrix for problem, in which the inner and outer dependencies are merged together to calculate the weight of each parameter. DEMATEL is a robust method used in formulating the sophisticated structures that models the interdependent relationships within a set of criteria under consideration (Gabus and Fontela, 1972; Fontela and Gabus, 1974; 1976). In this paper, the inner-dependence among parameters was evaluated by the Fuzzy DEMATEL. Outer-dependencies as well as weighting of clusters were determined using the Fuzzy ANP procedure through pairwise comparison.

### **DEVELOPING NEW CLASSIFICATION SYSTEM**

Cavability of the immediate roof is an inherent characteristic that the operational factors affect how it is exposed. Therefore, in this study, nine intrinsic parameters were considered in three categories including roof strata characteristics, roof discontinuities properties and local features based on the literature review, experts' opinion and analysis (Figure 1).

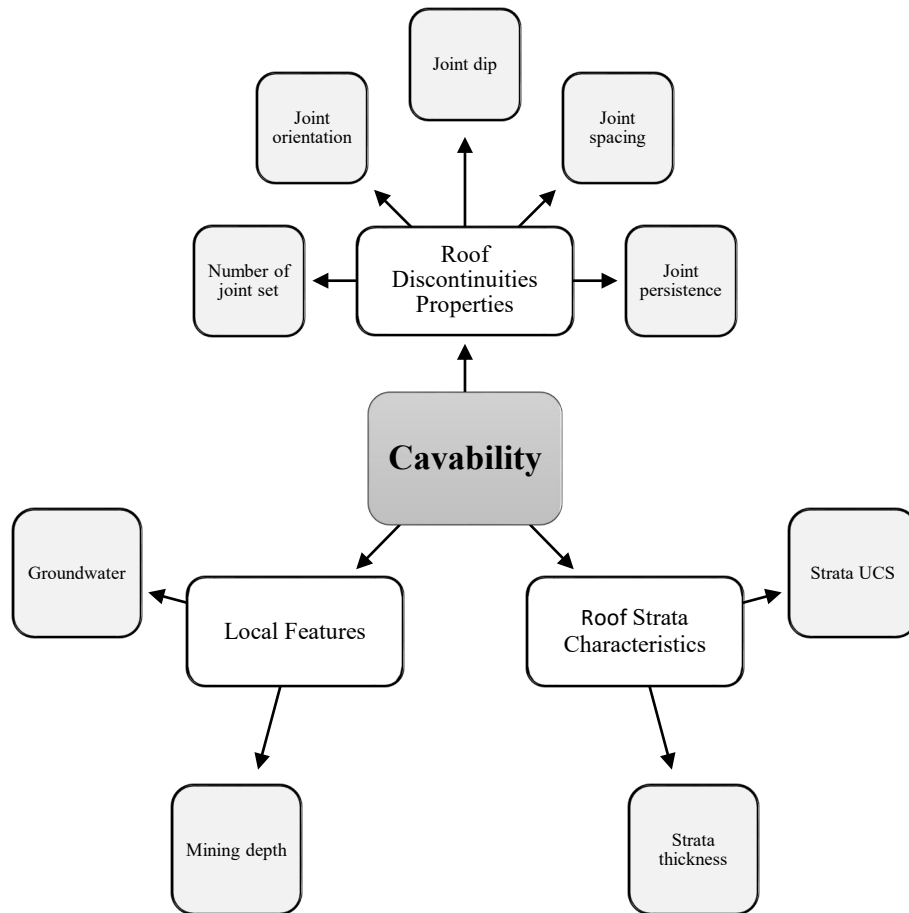
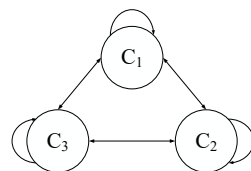


**Figure 1: The significant parameters of caving**

By analyzing the effective parameters on the cavability, the problem network and super-matrix was formed as shown in Figure 2.



$$W = \begin{matrix} & G & C & P \\ \text{Cavability (G)} & \begin{bmatrix} 0 & 0 & 0 \end{bmatrix} \\ \text{Categories (C)} & \begin{bmatrix} W_{21} & W_{22} & 0 \end{bmatrix} \\ \text{Parameters (P)} & \begin{bmatrix} 0 & W_{32} & W_{33} \end{bmatrix} \end{matrix}$$

**a. The cavability network    b. The cavability super-matrix**

**Figure 2: Network and super-matrix of problem**

Initially, questionnaires were distributed among academics and industry experts to gather their opinions and judgments. From the questionnaires returned, data from some seventeen questionnaires was used. In the next step, the inner dependencies matrices ( $W_{22}$  and  $W_{33}$ ) and the outer dependencies matrices ( $W_{21}$  and  $W_{32}$ ) were evaluated using the DEMATEL and the ANP, respectively. Following on an unweighted super-matrix was formed and then a weighted super-matrix was derived by equating the normalized summation of each column to 1. Finally, the weighted supermatrix was raised to limiting powers. Limit supermatrix, in fact, shows the ultimate weight of parameters (Figure 3).



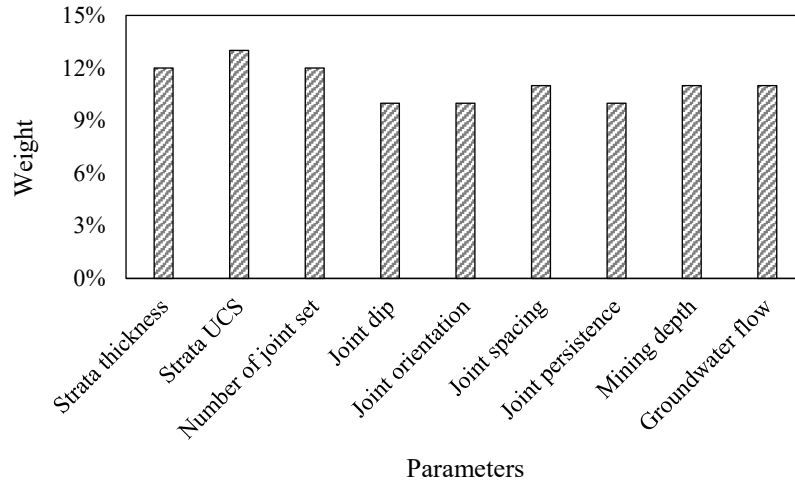


**Figure 3: Parameters weights in the cavability index**

In order to introduce CI, based on the literature and standard guidelines, all parameters were classified into five classes (with the exception of joint persistence which is classified into three classes) with respect to their role in the caving. A corresponding rate of 0 to 4 was assigned to each class. Table 1 shows the proposed rating table of effective parameters in caving. Effects of joint orientation and dip in Table 1 are determined based on Table 2.

**Table 1: System classification parameters**

No.	Parameters	Rating				
		0	1	2	3	4
1	EIRS (Mpa)	> 250	250-100	100-50	50-25	<25
2	Number of joint sets	Massive	1	2	3	Crushed
3	Joint orientation and dip	Very unfavourable	Unfavourable	Fair	Favourable	Very favourable
4	Joint spacing (m)	>1.8	1.8-0.6	0.6-0.2	0.2-0.06	>0.06
5	Joint persistence (m)			0-1	1-3	>3
6	Depth (m)	<100	100-300	300-600	600-1000	>1000
7	Groundwater flow	None	None visible	Light seepage/dripping	Steady seepage/flowing	Heavy seepage/gushing

**Table 2: Expression of joint orientation and dip**

Strike perpendicular to face axis				Strike parallel to face axis		Irrespective of strike
Drive with dip		Drive against dip		Dip 45° - 90°	Dip 20° - 45°	
Dip 45° - 90°	Dip 20° - 45°	Dip 45° - 90°	Dip 20° - 45°			Dip 45° - 90°
Very unfavorable	Unfavorable	Fair	Favorable	Very favorable	Favorable	Fair

It is noted that coal strata are grouped into several composite layers which have different and complex mechanical and caving behaviour. Different strata properties may influence immediate roof properties. Therefore, the Equivalent Immediate Roof Strength (EIRS) was defined as the thickness-weighted average of roof strata uniaxial compressive strength (Mohammadi, et al., 2019):

$$EIRS = \frac{\sum_{i=1}^n t_i \times \sigma_{c_i}}{\sum_{i=1}^n t_i} \quad (1)$$

where  $t_i$  is the thickness of the  $i$ th stratum (m),  $\sigma_{c_i}$  is the UCS of the  $i$ th stratum (MPa), and  $n$  is the number of stratum within the immediate roof.

The cavability index is defined as:

$$CI = \sum_{i=1}^7 w_i \times \frac{P_i}{P_{max}} \tag{2}$$

where  $w_i$  is the weight of  $i$ th parameter,  $P_i$  is the rate of  $i$ th parameter (0 to 4) and  $P_{max}$  is the maximum rate of  $i$ th parameter (i.e. 4 for all parameters with the exception of joint persistence which is 3).

CI represents cavability level of strata within the immediate roof of coal mines. It varies between 5 and 100 and classifies the immediate roof from uncavable to the highly cavable status as is illustrated in Figure 4.

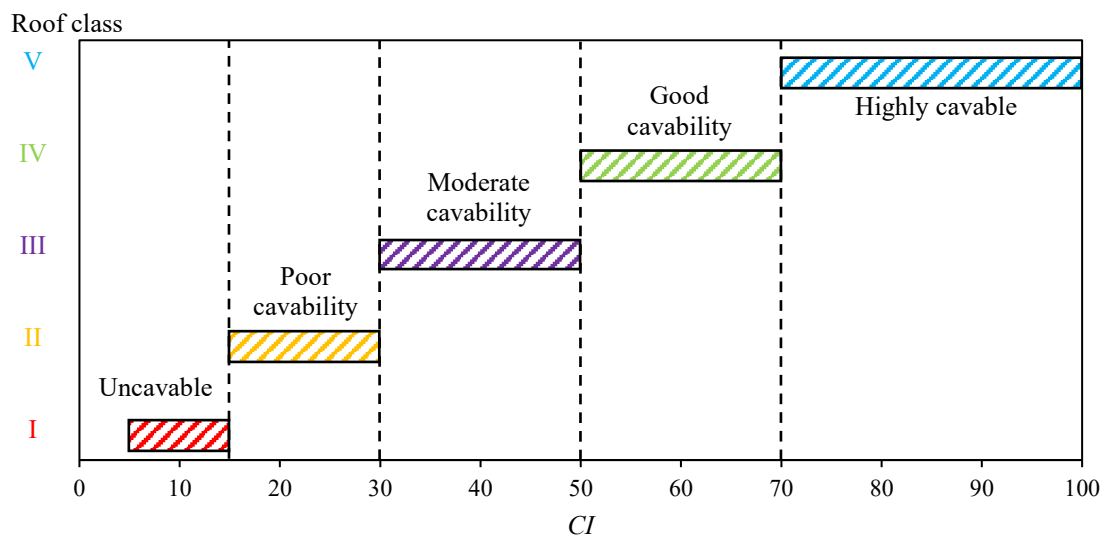


**Figure 4: Classification of cavability level**

**CLASSIFICATION SYSTEM APPLICATION**

Twelve panels from longwall coal mines throughout the world were used to examine the applicability of the proposed classification system. Data for these panels was collected using publications and reports from literature and through underground mine surveys (Table 3).

**Table 3: Relevant data of used longwall panels**

No.	Case	Average cover depth (m)	Extraction height (m)	Panel width (m)	Immediate roof height (m)	EIRS (MPa)	Main caving interval (m)	Reference
1	S. Africa-A	50	1.8	140	6.7	22.89	30	(Sweby, 1997)
2	S. Africa-B	194	2.2	150	4.5	20	15	(Sweby, 1997)
3	S. Africa-C	195	2.4	200	17	42.76	37	(Sweby, 1997)
4	Norway	400	4	250	10	93.75	36	(Shabanimas hcool et al., 2014)
5	Germany	1100	2	300	2.5	112	72	(Gao et al., 2014)
6	USA	670.5	1.7	200	2.5	129	85	(Akinkugbe et al., 2007)
7	India-A	250	3	150	3.7	20.33	78	(Maharana, 2013)
8	India-B	250	3	150	8	31.39	53	(Kumar, 2014)
9	India-C	395.45	2.55	95	11	13.71	26	(Singh and Singh, 2009)
10	India-D	218.29	3	150	12.24	52.92	44	(Singh and Singh, 2009)
11	India-E	325	3	150	3.5	15	65	(Banerjee et al., 2016)
12	Iran	100	2	196	12	52.86	14	Surved by authors

### Cavability evaluation

Cavability levels of the selected panels were evaluated and ranked using a new classification system, as listed in Table 4. The calculated CI value varies from 14.5 to 74.5 which correspond to uncavable and highly cavable, respectively.

**Table 4: Calculated CI and determined immediate roof category for the database**

No.	Case	CI	Cavability level
1	S. Africa-A	59	Good cavability
2	S. Africa-B	67.5	Good cavability
3	S. Africa-C	58.25	Good cavability
4	Norway	46.75	Moderate cavability
5	Germany	43.25	Moderate cavability
6	USA	14.5	Un-caveable
7	India-A	29.5	Poor cavability
8	India-B	45	Moderate cavability
9	India-C	61.67	Good cavability
10	India-D	52.92	Good cavability
11	India-E	46.83	Moderate cavability
12	Iran	74.5	Highly cavable

The variation between the main caving interval and CI introduced in this work is described in Figure 5. It is noted that the main caving interval reduces by increasing the CI value. From Figure 5, it is concluded that the proposed classification system shows a decreasing trend between the cavability level and the main caving interval.

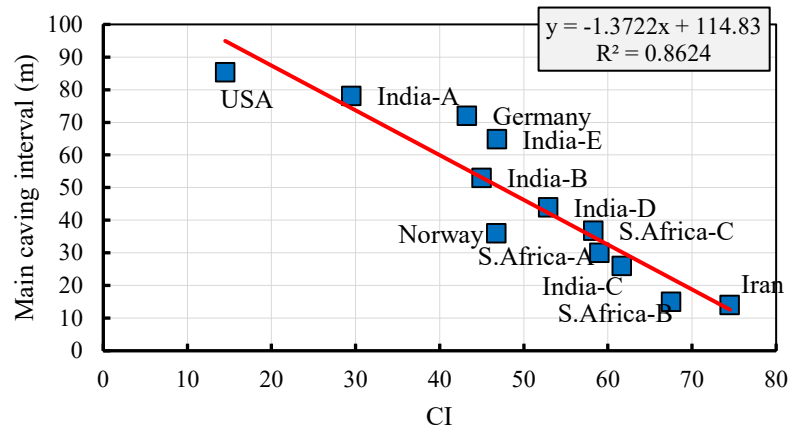


Figure 5: Main caving interval versus CI

### Main caving interval estimation

Statistical models were developed to estimate the main caving interval incorporating the new classification system. CI includes intrinsic parameters, however, to estimate main caving interval, it is required to take operational parameters into account. For this purpose, the Hydraulic Radius (HR) was defined. The Hydraulic Radius is a term used in hydraulics and is a number derived by dividing the area by the perimeter. In this work, it defines dimensions of unsupported space (similar to the undercut in block caving mining) above which strata will be caved:

$$HR = \frac{W \times h}{2(W + h)} \quad (3)$$

where  $W$  is the panel width (face length) and  $h$  is the extraction height.

Ten panels were selected randomly as the training cases to develop predictive models and the remaining were considered as the validation cases to evaluate and compare the performance of the models. Figure 6 shows a 3D scatter plot of the main caving interval versus CI and HR for training data.

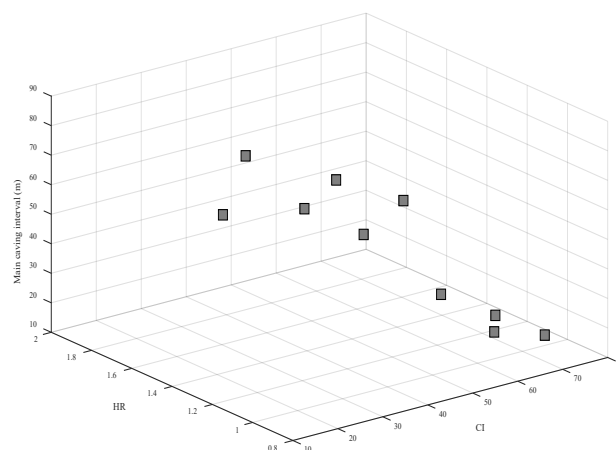
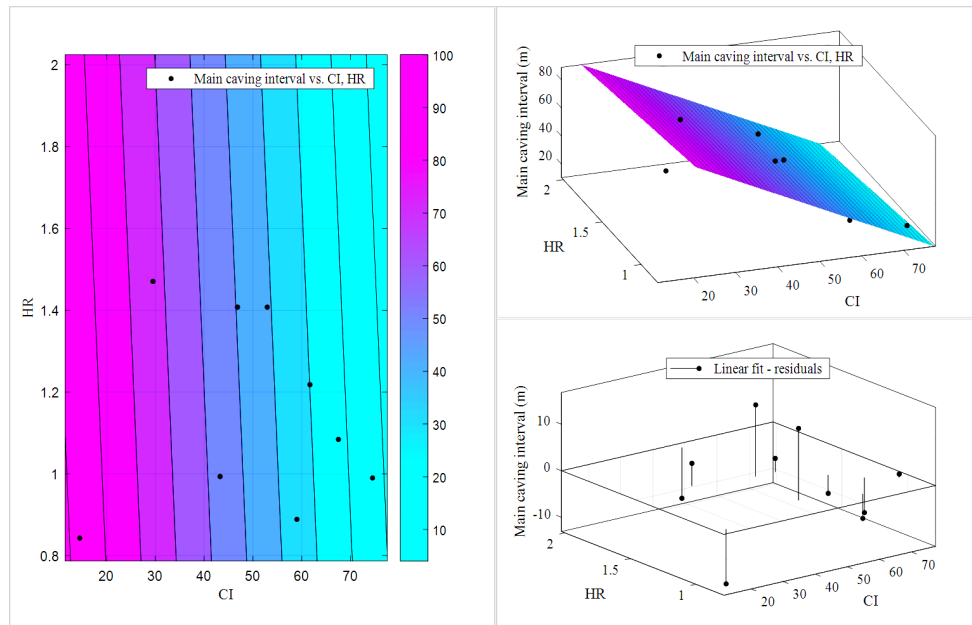


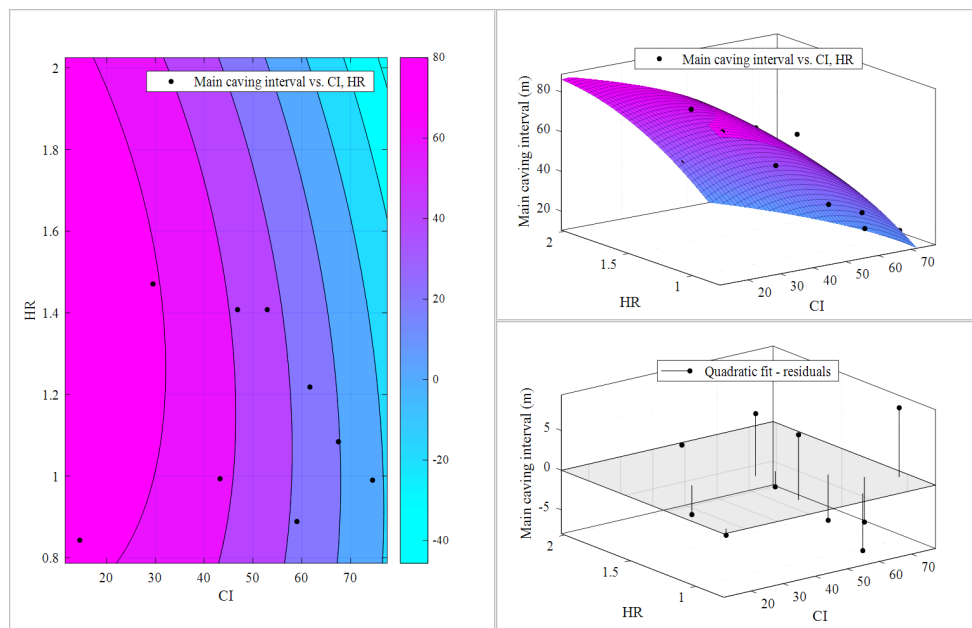
Figure 6: 3D scatter plot of the main caving interval versus CI and HR

In order to develop models, several linear and nonlinear models were fitted to the data. The best model was selected based on the values of the coefficient of determination ( $R^2$ ) and Root

Mean Square Error (RMSE). In this regard, two functions including linear and quadratic polynomial were shown to have the best fits as listed in Table 5. Figure 7 shows the main, residual and counter plots of curved models.



a. Linear model



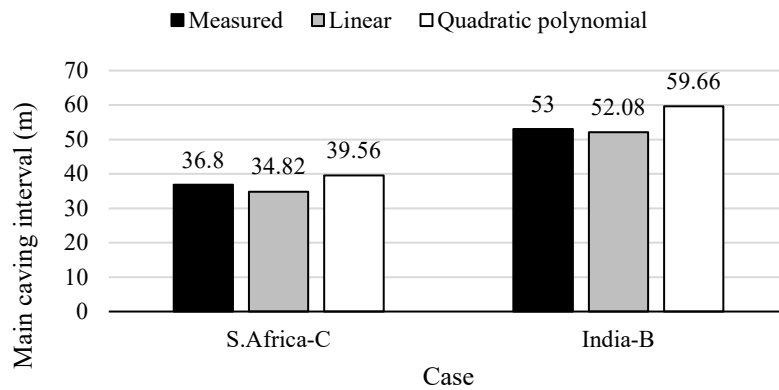
b. Quadratic polynomial model

Figure 7: The main, residual and counter plot of curved models

Table 5: Fitted models and associated RMSE and R<sup>2</sup>

Type	Model	RMSE	R <sup>2</sup>
Linear	$I_s = 119.816 - 1.383 CI - 3.742 HR$	9.35	0.863
Quadratic polynomial	$I_s = 22.4 + 0.408 CI + 111.1 HR - 0.0154 CI^2 - 0.476 CI \times HR - 37.81 HR^2$	9.42	0.944

Performance of the proposed model was evaluated using two cases including S. Africa-C and India-B. A comparison between the measured and estimated main caving interval values is shown in Figure 8.



**Figure 8: Comparison between measured and estimated interval values**

For quantitative comparison, in addition to  $R^2$  and RMSE, two criteria including VAF, and MAPE were used as follow:

$$VAF = 100 \left[ 1 - \frac{\text{var}(y_{meas} - y_{pred})}{\text{var}(y_{meas})} \right] \quad (4)$$

$$MAPE = \frac{1}{N} \sum_{i=1}^N \left| \frac{y_{meas} - y_{pred}}{y_{meas}} \right| \times 100 \quad (5)$$

where  $y_{meas}$  is the measured value,  $y_{pred}$  is the predicted value, and  $var$  is the variance. Smaller RMSE values produce higher coefficients of determination, leading to more accurate fitted curves. In the same direction, higher VAF values and smaller MPAE values are desired for fitted relationships. The calculated values of these indices for the proposed models are presented in Table 6.

**Table 6: Calculated performance criteria for proposed models**

Models	$R^2$	RMSE	VAF	MAPE
Linear	0.9939	1.68	99.79	3.93
Quadratic polynomial	0.9878	4.51	94.74	8.69

According to the visual comparison (Figure 8) and the performance criteria (Table 6), it is inferred that the linear model was capable of estimating main caving intervals with a reasonable accuracy. It performed a higher accuracy when compared to that of the quadratic model.

### CONCLUSIONS

A new classification system was presented to evaluate the cavability nature of the immediate roof by integrating intrinsic parameters. The proposed method was developed by incorporating a hybrid Fuzzy Multi-Criteria decision Making (MCDM) technique. Consequently, the cavability index was introduced as the output of a classification system to classify the immediate roof cavability and to develop a main caving interval predicative model. The following main points were drawn from this study:



(1) It was concluded that the uniaxial compressive strength is the most significant parameter with 13% weight in total. The strata strength represents the reaction of strata to those that happen in the first two stages of caving including initiate and propagation of fracture and subsequently, rock yielding. In addition, UCS is correlated to other strength indices such as tensile, shear and flexural strength which influence caving mechanism. This study was shown that properties of discontinuities in the immediate roof have more than a 50% influence on the cavability. It is stated in the literature that the roof strength of coal mines is influenced by bedding planes and other discontinuities that weaken the rock structure. Furthermore, stratified roof strata are crosscut by sub-vertical joints that are either original or mining-induced. Therefore, the presence of these geological factors reduces the roof integrity.

(2) It was shown that there was a relationship (linear function with  $R^2$  of 0.8624) between CI and the main caving interval. This correlation defines rationally inverse relationship between cavability as a qualitative index and main caving interval as its quantitative index. It is shown that lower cavability is observed when mining is carried out in competent strata, characterized by overall stable immediate roof strata. Under this condition, the main caving interval is higher and thus, higher stress is generated on the shield support. While, an increase in cavability produces lower caving intervals and subsequently, lower stress concentration on the face and support elements.

(3) Applied capability of the new classification system was examined through estimation of the main caving interval incorporating CI and the Hydraulic Radius (HR) of extracted space. The linear function was found to be superior when estimating the main caving interval on the basis of collected data in comparison with the nonlinear function with the coefficient of determination ( $R^2$ ) and Root Mean Squared Error (RMSE) values of 0.9939 and 1.68, respectively.

(4) Results showed that the proposed classification system is a suitable approach to evaluate cavability levels of the immediate roof accurately. In addition, models based on CI and HR are efficient and updatable tools to estimate the main caving interval in longwall mining projects.

Despite meticulous care being taken, there are always some unavoidable limitations. This study can be further extended to classify applied stresses on support systems during the caving process. Also, it can be developed in a manner which predicts dominant caving mechanisms. It should be noted that CI as a general index can be used for sample variability of a geo-mining environment in underground coal mines aimed toward longwall mining. Undoubtedly, the obtained relationships are not applicable to all cases, however, the proposed approach is valid. Since the reliability of the proposed relationships are largely dependent on the size, quality, and consistency of the database, therefore, more cases would always lead to the generation of new relationships with higher reliability.

## REFERENCES

- Akinkugbe, Y, Su, D, Hasenfus, G, Morris, T J and Fisher, B, 2007. The Roof Behaviour of a Longwall Tailgate Under Massive Sandstone Strata. In 26<sup>th</sup> International Conference on Ground Control in Mining, pp 188-195 (West Virginia University)
- Banerjee, G, Kumbhakar, D, Ghosh, N and Yadava, K P, 2016. Assessment of Cavability and categorization of coal measure roof rocks by parting plane approach. Conference on recent advances in rock engineering, pp 301-308 (Bengaluru, India)
- Das, S K, 2000. Observations and classification of roof strata over longwall coal mining panels in India, *International Journal of Rock Mechanics and Mining Sciences*, 37(4): 585-97.
- Fontela, E and Gabus, A, 1974. DEMATEL, innovative methods. Structural analysis of the world problematique. Battelle Geneva Research Institute, Report no. 2.
- Fontela, E and Gabus, A, 1976. The DEMATEL observer. Battelle Institute, Geneva Research Center.
- Gabus, A and Fontela, E., 1972. World problems, an invitation to further thought within the framework of DEMATEL. Battelle Geneva Research Center, Geneva, Switzerland.

- Gao, F, Stead, D and Coggan, J, 2014. Evaluation of coal longwall caving characteristics using an innovative UDEC Trigon approach, *Computers and Geotechnics*, 55, 448-60.
- Ghose, A K and Dutta, D, 1987. A rock mass classification model for caving roofs, *International Journal of Mining and Geological Engineering*, 5(3): 257-71.
- Hao, X, Fan, W, Shan, Z and Liu, P, 2015. An integrated approach for the prediction of underground-induced strata movement over longwall coal mining panels, *Geotechnical and Geological Engineering*, 33(3): 681-92.
- Kumar, C, 2014. of Shield Support in Longwall Mining, thesis, National Institute of Technology, Rourkela, India.
- Kuznetsov, S T, Pekarskii, D G and Korovin, V T, 1973. Determining the normal stresses in a uniform bent cantilever, *Soviet Mining*, 9(5): 478-82.
- Kwasniewski, M, 2008. Numerical analysis of strata behaviour in the vicinity of a longwall panel in a coal seam mined with roof caving, *Continuum and Distinct Element Numerical Modelling in Geo-Engineering*, 1-12.
- Maharana, A K, 2013. Study of Strata and Support of a Longwall Mine, thesis, National Institute of Technology, Rourkela, India.
- Manteghi, H, Shahriar, K and Torabi, R, 2012. Numerical modelling for estimation of first weighting distance in longwall coal mining – A case study. In 12<sup>th</sup> Coal Operators' Conference, pp 60-68 (University of Wollongong the Australasian Institute of Mining and Metallurgy: Wollongong)
- Mohammadi, S, Ataei, M, Kakaie, R, Aziz, N and Rastegarmanesh, A, 2019. Numerical simulation of stress distribution in longwall panels during the first caving interval, in 21<sup>th</sup> Coal Operators' Conference, pp 82-90 (Mining Engineering, University of Wollongong: Wollongong)
- Mukherjee, S N, 2003. Mechanised longwall mining in India e a status review, *Journal of Institution of Engineers (India)*, 81: 5-10.
- Noroozi, A, Oraee, K, Javadi, M, Goshtasbi, K and Khodadady, H, 2012. A model for determining the breaking characteristics of immediate roof in longwall mines. *Yerbilimleri: An Earth Sciences Journal*, 33(2): 193-204.
- Obert, L and Duvall, W I, 1967. *Rock mechanics and the design of structures in roc*, (John Wiley and Sons: New York)
- Oraee, K and Rostami, M, 2008. Qualitative and quantitative analysis of hangingwall caving in longwall mining method using a Fuzzy system. In *21st world mining congress expo*.
- Peng, S S and Chiang, H S, 1984. *Longwall mining* (John Wiley and Sons: New York)
- Saaty, T L, 1996. *The analytical network process-decision making with dependence and feedback* (RWS Publication: Pittsburgh)
- Shabanimashcool, M, Jing, L and Li, C C, 2014. Discontinuous modelling of stratum cave-in in a longwall coal mine in the arctic area, *Geotechnical and Geological Engineering*, 32(5): 1239-52.
- Singh, G S, Singh, U K and Banerjee, G, 2004. Cavability assessment model for longwall working in India, in 3<sup>rd</sup> Asian Rock Mechanics Symposium, pp 295-300 (Organised by ISRM: Kyoto)
- Singh, G S and Singh, U K, 2009. A numerical modeling approach for assessment of progressive caving of strata and performance of hydraulic powered support in longwall workings, *Computers and Geotechnics*, 36(7): 1142-56.
- Singh, G S P and Singh, U K, 2010. Numerical modeling study of the effect of some critical parameters on caving behaviour of strata and support performance in a longwall working, *Rock Mechanics and Rock Engineering*, 43(4): 475-489.
- Sweby, G, 1997. Review the caving mechanisms around high extraction systems and determine the effect of the mechanisms on the safety of the system, Report prepared by CSIR Miningtek for the Safety in Mines Research Advisory Committee (SIMRAC), Final project Report, Project No. COL327. (Johannesburg, South Africa)
- Wang, Z Q, Yang, H, Chang, Y B and Wang, P, 2011. Research on the Height of Caving Zone and Roof Classification of Mining Whole Height at One Times in Thick Coal Seam, *Applied Mechanics and Materials*, 99: 207-212.
- Wu, K, Cheng, G L and Zhou, D W, 2015. Experimental research on dynamic movement in strata overlying coal mines using similar material modeling, *Arabian Journal of Geosciences*, 8(9): 6521-34.

Yongkui, S, Pengrui, L, Ying, W, Jingyu, Z and Meijie, L, 2014. The Prediction of the Caving Degree of Coal Seam Roof Based on the Naive Bayes Classifier, *Electronic Journal of Geotechnical Engineering*, 19(Z2):3775-3784.

# A REVIEW OF OVERBURDEN FRACTURING AND CHANGES IN HYDRAULIC CHARACTERISTICS DUE TO LONGWALL MINING

**Hadi Nourizadeh<sup>1</sup>, Ismet Canbulat<sup>2</sup>, Joung Oh<sup>2</sup>, Chengguo Zhang<sup>2</sup>, Naj Aziz<sup>3</sup>, Ali Mirzaghobanali<sup>4</sup>, Kevin McDougall<sup>4</sup>**

*ABSTRACT:* Longwall mining is a major mining method to extract thick, flat-lying and extensive seams. Due to the nature of this mining method, the overlying strata move continuously downwards into goaf and as a result, surrounding rocks are distressed, deformed and fractured. In the near area above the mined coal seam, both vertical and horizontal fracturing networks are evident, however within the higher zones, bed separation and slippage are the dominant displacements. The enhanced cracks alter hydraulic characteristics (porosity and permeability) of the rock mass, consequently disturbing the groundwater and surface water flow regime. There have been various techniques utilised to study mining-induced fracturing mechanisms and changes in water flow systems. They mainly include empirical, physical, analytical and numerical approaches. Of note is that due to the complexity of the issue and difficulties in the implementation of costly and time-consuming in-situ measurements, currently, numerical simulation is a popular approach. The aim of this review paper is to present the current state of the art in mining-induced goaf overburden fracturing and its interaction with groundwater and surface water.

## INTRODUCTION

When the coal seam face advances forward, the overlying strata above the mining area caves into the voids resulting in deformation of rock masses, opening pre-existing discontinuities and noticeable changes in the hydraulic properties including porosity and associated permeability of the field. Mining-induced fracturing can create a potential path to penetrate aquitards into the goaf, which may result in serious hazards such as water-inrush and fluids. These incidences severely threaten the safety, efficiency, and economy of the mine. Therefore, a good understanding of the initiation, propagation and development of fractures in overlying strata is highly important to implement efficient, safe, and environmentally friendly mining (Wang et al., 2017). Several empirical and in-situ measurement studies have been conducted to simulate the rock deformation and fluid flow in the disturbed rock masses above longwall mining panels. Although these studies are very valuable, there is still difficulty in clearly understanding of rock fracturing and fluid flow mechanisms in the overburden strata, which is mostly because of anisotropic and heterogeneous nature of rock mass properties and the effects of panel geometry. Conversely, the interactive relationships between rock deformation and fluid flow involving highly complex spatial and temporal variations may only be studied accurately through numerical methods. A well numerical model is able to successfully simulate a highly complex problem with true and reliable results. Numerical methods significantly reduce the time and expense of research (Zhang and Sanderson, 2002a). Problems related to the rock mass, which

---

<sup>1</sup> PhD student, School of Civil Engineering and Surveying, USQ, Email: [hadi.nourizadeh@usq.edu.au](mailto:hadi.nourizadeh@usq.edu.au)

<sup>2</sup> School of Minerals and Energy Resources Engineering, UNSW

<sup>3</sup> School of Civil, Mining and environmental Engineering, UOW

<sup>4</sup> School of Civil Engineering and Surveying, USQ

is subjected to loading, can be solved numerically through a continuum and/or discontinuum methods. The models differ in representation ways of the heterogeneity of a fractured medium. Common continuum methods may explicitly estimate enhanced permeability through plastic strains; however, they are not able to directly trace aperture on flow path or predict connectivity of fractures (Poulsen et al., 2018). It is broadly believed that the discontinuum methods such as DEM would be the most reliable method to imitate the response of discontinuous rock mass against loading and excavation.

### **THE HYDRO-MECHANICAL RESPONSE OF OVERBURDEN ROCK MASS TO LONGWALL MINING**

The structure and component of the crustal rocks are generally complex, heterogeneous and anisotropic that make the formulation and determination of the real behaviour rocks more challenging. Fractures are ubiquitous in the earth's crust on all scales from micro-scale to macro-fractures along bedding planes, faults and shear zones. Study of fractures is essential in different engineering fields as they play a substantial role in rock deformation and more importantly, they are major paths for fluid flow in both permeable and impermeable rock masses. Excavation in stratified rocks causes changes in-situ stresses leading to various deformation such as shear fractures, separation and bedding planes, tensile fractures, opening pre-existing joints.

During and after extraction of coal seams by longwall mining, the immediate roof above the panel bends and moves downwards into the void. This movement causes bending and deformation of overlying strata. Additionally, delamination and separation of bedding planes are probable. In a vertical profile of longwall mining, rock mass deformation commences from the mined seam and propagates upwards, however; strata located below the seam may also be affected and deformed. At the first stage of the deformation process, closer layers to the void separate from upper-laying layers, bend and then fracture. The process of overburden deformation (e.g. shearing, delamination and, bending) continuously extends further upwards as mining face advances. Ceasing of ground movement can complete in from a few hours to several years. In general, overburden response to the longwall mining strongly depends on the location and thickness of the overlying strata, as well as mining geometry.

This incident substantially changes the hydraulic properties of the overburden rocks such as void fraction (fissure ratio, porosity, and fracture ratio) and permeability. Figure. 1 shows the various void fractions (fissures, fractures, pores) associated with longwall mining (Wang et al., 2016b).

importantly, the induced voids may connect catchments, aquifers, and goaf together that may cause significant economic and safety issues on mining operations such as rushing huge volumes of water into the mining panel (Islam and Shinjo, 2009).

In general, disturbed overlying strata are divided into three to four distinct zones in each of which fracture and deformation characteristics are similar. Researchers have endeavored to determine the height of these zones being mostly based on-site observations. The heights of these disturbed zones are dependent on geometry and mechanical properties of the overlying strata, as well as coal seams.

The thickness of coal seams and overburden have a direct influence on the height of disturbed zones compared to Poisson ratio, elastic modulus, bulking factor and UCS which have an inverse influence on this height (Rezaei et al., 2015). Additionally, the caving process of overburden can also vary between short and long time scales (Majdi et al., 2012). The overburden cave-in process associated with underground mining significantly alters the regional water flow regime, with impacts to a distance of several kilometers (Tammetta, 2013).

The impacts of underground coal mining on the hydrological behavior of disturbed overburden have been extensively studied by vast in-situ permeability measurements which reveal that the permeability of rock masses significantly increases in particular parts of overburden (Tammetta, 2015, Khanal et al., 2019, Zou et al., 2012). More importantly, the induced voids may connect catchments, aquifers, and goaf together that may cause significant economic and safety issues on mining operations such as rushing huge volumes of water into the mining panel (Islam and Shinjo, 2009).

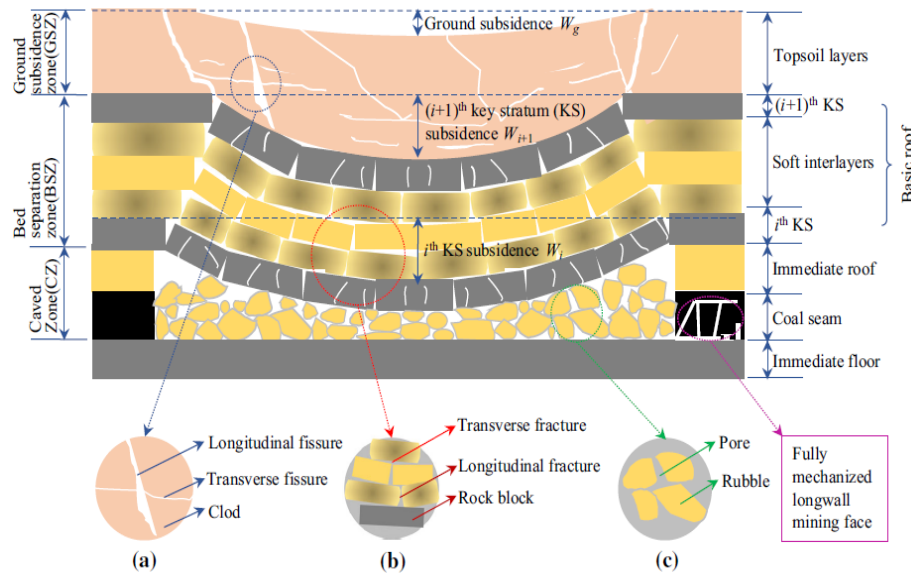


**Figure 1: A schematic overview of overburden strata response to longwall mining and the potential deformations (Wang et al., 2016b)**

In general, disturbed overlying strata are divided into three to four distinct zones in each of which fracture and deformation characteristics are similar. Researchers have endeavored to determine the height of these zones being mostly based on-site observations. The heights of these disturbed zones are dependent on geometry and mechanical properties of the overlying strata, as well as coal seams.

The thickness of coal seams and overburden have a direct influence on the height of disturbed zones compared to Poisson ratio, elastic modulus, bulking factor and UCS which have an inverse influence on this height (Rezaei et al., 2015). Additionally, the caving process of overburden can also vary between short and long time scales (Majdi et al., 2012). The overburden cave-in process associated with underground mining significantly alters the regional water flow regime, with impacts to a distance of several kilometers (Tammetta, 2013). The impacts of underground coal mining on the hydrological behavior of disturbed overburden have been extensively studied by vast in-situ permeability measurements which reveal that the permeability of rock masses significantly increases in particular parts of overburden (Tammetta, 2015, Khanal et al., 2019, Zou et al., 2012).

Impacts can be in the forms of drainage of surface and sub-surface into the goaf and mining area, alteration aquifers, and water quality as well. The evolution mechanism of fractures induced by longwall mining beneath gullies, lakes, catchments, and near aquifers is of great importance as the fractured zones may be developed to these water resources causing severe safety and efficiency problems to the underground mining (Peng, 2006). This issue becomes even more severe, when the coalfield is located in a sensitive ecological environment. The delamination of strata enhances the horizontal permeability of rock media; however, vertical fractures also increase the vertical permeability and it gradually decreases with the increase of

distance from the mining area. According to the previous studies, in the stratified roof near the longwall mining area, hydraulic conductivity (both vertical and horizontal) intends to extend leading to considerable water drainage to the gob. Conversely, the major change in the hydraulic properties of the higher zones is the horizontal conductivity.

**MODELLING OF DEFORMATION OF OVERLYING STRATA AND CHANGES IN HYDRAULIC CONDUCTIVITY ABOVE LONGWALL PANELS**

Several empirical and analytical models have been introduced to simulate mechanical responses of stratified rocks to the in-situ stress alteration due to longwall mining. Furthermore, various numerical modelling techniques have been presented to study the reaction of overburden rocks to longwall mining. Fracturing mechanism of rock mass and subsequently changes in permeability are highly non-linear functions of redistribution of initial stresses due to mining. Various equations have been proposed to calculate the permeability of intact or fractured rocks. However, there is not a general consensus on the formulation of the interaction between rock deformation and permeability changes. Fluids may not flow uniformly within fractured rocks as the hydraulic characteristics (e.g. aperture) of the rock media control its transmissivity. In general, the hydraulic response of rock mass is controlled by the geometric properties of the fracture networks. Rock deformation is considered to have fundamental effects on fluid migration due to alteration of discontinuity geometry including closing and/or opening of fluid conduits, as well as creating new ones. In this section, the current state of the art in the modelling of the longwall-mining induced fracturing and the resulting changes in permeability will be presented.

**Empirical models**

Various empirical formulas have been proposed to describe the height of rock fracturing due to longwall mining mostly based on extensive field studies,(Xu et al., 2017, Majdi et al., 2012). However, these formulas are highly simplified and consider only a few effective factors (e.g. coal seam thickness and mining height), but do not reflect the effects of the other significantly influential geo-mechanical properties of rock masses. For example, the State Bureau of Coal Industry of China proposed some empirical formulas based-on thousands of in-situ measurements for estimation of the maximum height of the fractured zone above longwall mines. In the proposed empirical formulas, the average compressive strength of overburden strata as a lithological characteristic and thickness of mining coal seam have been considered as the basic variables. The maximum height of fractured zones can be calculated from the following equations (Table 1). In the proposed formulas,  $H_i$  is the maximum height of the caved zone and  $\sum M$  is the height of coal seams(Wang et al., 2016a).

**Table 3- The empirical equations for estimating the height of the maximum caved zone**

Lithological conditions	Appropriate equation (m)
Hard overburden	$H_i = \frac{100 \sum M}{1.2 \sum M + 2.0} \pm 8.9$
Mid-hard overburden	$H_i = \frac{100 \sum M}{1.6 \sum M + 3.6} \pm 5.6$
Weak overburden	$H_i = \frac{100 \sum M}{3.1 \sum M + 5.0} \pm 4.0$

In Australia, prediction of the height of caving has been widely studied by many researchers and several empirical models have been established to determine the height of fracturing. The proposed models are generally based on in-situ measurements using extensometer and piezometer tests(Ross and Sutton, 2016). The proposed empirical formulas by Ditton and Merrick (2014) and Tammetta (2013), are the most common approaches used in Australia for



prediction of the height of fracturing induced by longwall mining. The results of these studies are summarized in Table 2. The height of desaturation in Ditton and Merrick's study implies the connective fracturing and complete water drainage in the goaf.

Field measurement-based techniques suffer from an executive restriction mainly because of being costly and time-consuming. However, the combination of gained field-data from this approach with numerical simulation methods would be the best approach to study the response of rock masses to longwall mining. The success of a mechanical model to identify the behavior of rock masses to any change in the ground such as excavation strongly depends on the validity and reliability of the stress-deformation behavior of the rock masses.

**Table 4- Developed models for prediction of the height of fracturing above longwall mining in Australia**

Study	Main Conclusion	Parameters
Ditton and Merrick (2014)	$HoD = 1438 \ln(4.315 \times 10^{-5} \cdot U + 0.9818) + 26$ $U = W \times T^{0.4} \times H^{0.2}$	HoD: Height of Desaturation U: a variable, W: panel width T: mining height, H: cover depth
Tammetta (2013)	Zone 1: up to 20 m above coal seam Zone 2: up to 1 W Zone 3: 1.0 – 1.6 W Zone 4: 1.6 W – 3 W Zone 5: > 3 W	Zone 1: Caved zone Zone 2: Large movement zone Zone 3: Vertical dilation Zone 4: Vertical relaxation Zone 5: No disturbed zone W: Panel width

### Conceptual models

Conceptual models seek to interpret phenomena and behaviour of rock mass in terms of the process involved, with little quantitative description (Zhang and Sanderson, 2002b). Conceptual modelling of the hydro-mechanical behaviour of rocks excessively relies on analytic solutions and interpretation of in-situ measurement data. The results of such models are highly idealized and contain a less quantitative description of the problem. However, these models are a common approach to interpret the response of ground to longwall mining. In such models, the affected rock mass is divided into distinctive zones in which rock behavior and deformation characteristics are equivalent.

Peng (2006) proposed a conceptual model, which divides strata above longwall panel into four zones including caved zone, fractured zone, continuous-deformation zone, and soil zone (Figure. 2) (Peng, 2006). In the caved zone, fractures appear spatially and so immediate roof breaks into different sizes and shapes. Strata in the immediate roof sag downwards and when sagging process reaches the maximum allowable limit, the strata are fractured and broken into different sizes. The phenomenon of overburden collapsing continues until the gap between rock layers is less than the maximum allowable limit. This gap decreases upward as the volume of broken rocks increases compared to the volume of in-situ rocks. Thus, the height of caving zone can be obtained by Eq.1:

$$h_{im} = \frac{H - d}{k - 1} \quad , \quad d \leq d_0 \quad (1)$$

Where;  $h_{im}$  is the height of caving zone,  $d$  is sagging of the un-caved strata,  $d_0$  is maximum allowable limit,  $H$  is mining height, and  $k$  is the bulking factor of the broken rocks and can be defined as the ratio of the volume of the broken rock to the original volume of the same rock.

The height of the caved zone can extend up to 2 to 8 magnitudes of the mining height. In the fractured zone, both vertical fractures and bedding separation can be seen, however, due to the presence of horizontal forces, separated blocks are in contact. The height of the fractured zone is estimated between 28-58 times the mining height. In the continuous deformation zone, rock masses go under a sort of moderate deformation accompanied by bedding separation, however, there is no significant vertical cracking compare to the lower zones. In the soil zone, opening and closing of the cracks are obvious depending on the location of the extracted panel.

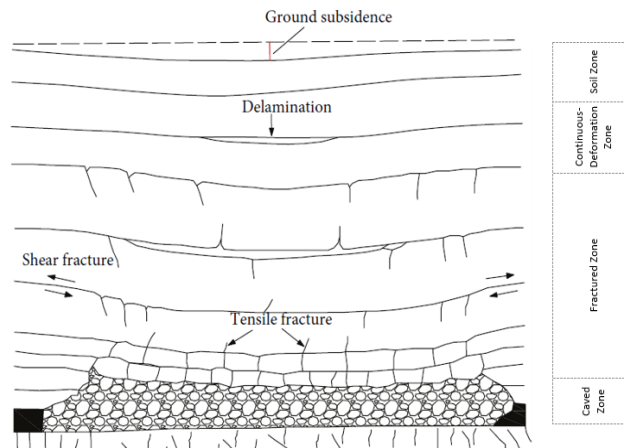


Figure 2: The profile of fractured-roof above longwall mining (Peng, 2006)

Gale (2008) reported that both vertical and horizontal fractures are substantial, however in the fractured and continuous deformation zones, horizontal cracks are the dominant deformation and the density of the vertical fractures decreases with an increase in the distance from the mining panel(Gale, 2008). The height of complete groundwater drainage above longwall panels has been broadly studied using piezometers tests and extensometer tests. The results of these field tests have contributed researchers to propose several conceptual models for hydraulic conductivity ( $K$ ) changes (Tammetta, 2013). Kendorski (2006) proposed a conceptual model with distinctive zones showing the impacts of longwall mining on water flow in the deformed overburden above mined voids(Kendorski, 2006). In another research, Foster and Enever (1992) produced a model that shows the hydrological response of overburden to longwall mining. This model was derived from piezometer data (Figure. 3).

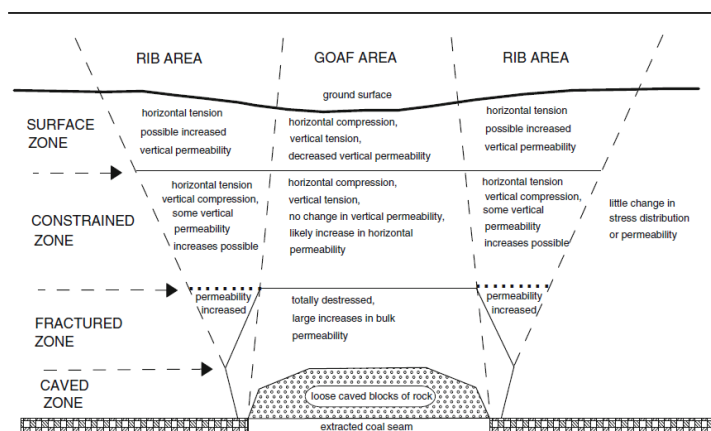


Figure 3: Hydro-mechanical responses of overlying strata to longwall mining

Tammetta (2015) conducted a study to investigate changes in hydraulic conductivity above longwall panels using the direct measurement of pre-mining and post-mining K (Tammetta, 2015). The database consisting of 799 measurements from 18 separate sites worldwide was used to identify K change trends. Finally, a quantitative conceptual model was presented based on the analysis of the obtained database. Figure. 4 shows a generalized cross-section for the ratio of the post-mining K to pre-mining K (R) over a longwall panel. In the disturbed zone, there is a moderate increase in the hydraulic conductivity which indicates that the majority increase in the post-mining K occurs in the horizontal direction mainly along the bedding planes. However, the large increase in the post-mining K in the caved zone demonstrates that vertical components of pre-mining K undertake a significant increase in this zone. Additionally, it is concluded that small differences between pre-mining and post-mining K around chain pillars can be due to the concentration of the vertical stresses in this neighborhood (Tammetta, 2013). Figure. 5 shows pre and post-mining hydraulic conductivity of rock masses above a longwall panel obtained by packer testing at the Dendrobiebum Mine. As can be seen from Figure. 5 pre-mining and post-mining regional K is highly dependent on the lithology and depth of the cover. In general, post-mining K is seen to be 3-10 times of magnitudes higher than the one of pre-mining. However, deeper parts typically experienced a greater increase in K.

Kendorski (2006) proposed a generalized model to conceptually demonstrate the effects of underground mining on the caving process and permeability changes of overburden (Figure. 6). According to this model, overlying strata are divided into five zones in terms of caving mechanisms comprising; caved zone, fractured zone dilated zone, constrained and unaffected zone, and surface disturbance zone. However, in terms of permeability changes the overlying strata consist of three major zones; lower zone, middle zone, and upper zone. The lower zone is highly affected by subsidence and as a consequence vertical permeability increases significantly. This zone comprises of the coved zone and fractured zone. In contrast, the middle zone (including dilated zone) suffers from a considerable increase in horizontal permeability. Finally, the upper zone is not affected by mining and subsidence deformation in termers of permeability changes (Kendorski, 2006).

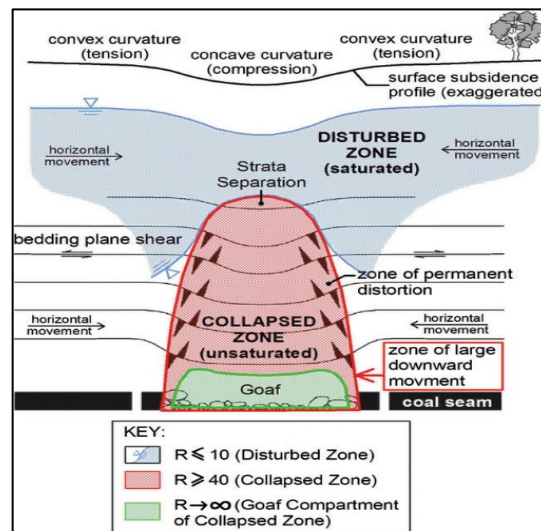
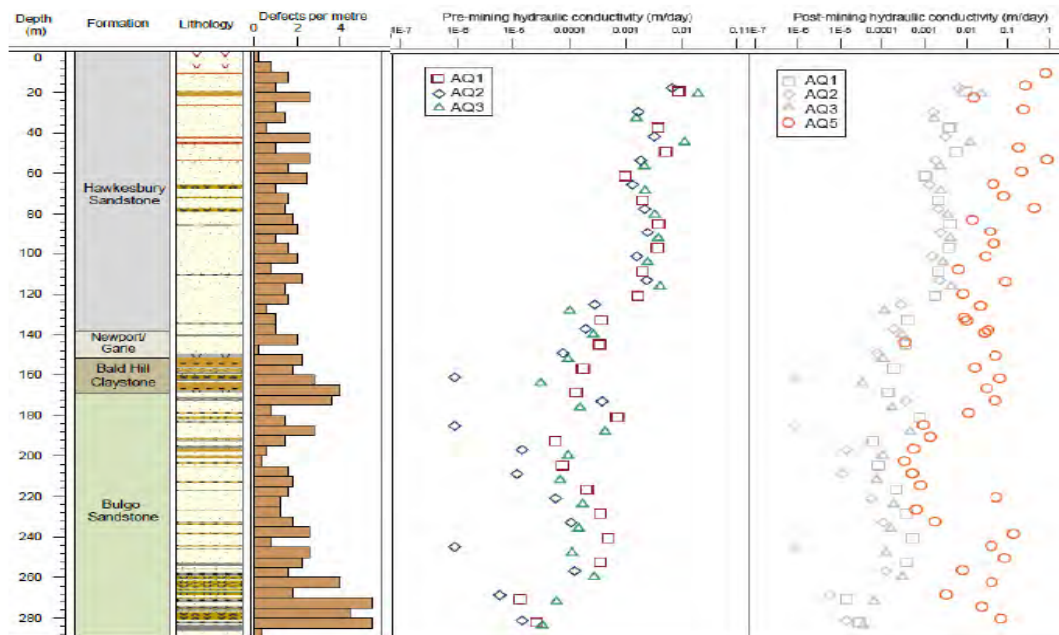


Figure 4: Schematic illustration of the overlying (Tammetta, 2015)



**Figure 5: Pre and Post-mining hydraulic connectivity obtained by packer-test data in Dendribum Coal Mine(Tammetta, 2015)**

### Numerical models

Modern development in the use of computers and particularly in the implementation of numerical modelling has provided powerful and reliable approaches. Due to the complexity of rock behaviour, analytic methods with the inevitable high number of assumptions are not able to reproduce exact solutions. However, successful numerical methods may establish predictive behaviour with acceptable approximations. Numerical methods significantly reduce the time and expense of research particularly in the field of natural processes, though limited experimental investigations are required for calibration of these models. Many powerful computational tools are readily available on the markets with different computer codes for simulation and evaluation of the behaviour of rocks. The fundamental difficulty in studying the rock behaviour, by any means, is that the physical and mechanical properties of rock mass are defined by nature. More importantly, rock media are highly discontinuous, heterogeneous and anisotropic. All these inherent characteristics along with the presence of fracture and fluid create a highly complex environment for mathematically studying through numerical methods. Even more crucial, a perturbation in in-situ stresses due to the man-made excavation will result in creating new fractures and opening pre-existing fractures (Jing et al., 2013, Jing, 2003). The simulation of rock mass behaviour by numerical models can be conducted on the basis of discontinuum methods (DEM, or DFN), continuum methods (FEM, BEM or FDM), and hybrid methods. Several factors affect the selection of the modelling methods (continuum and/or discontinuum) such as the aims of modelling, problem scale, and geometry of discontinuities. Due to the implementation simplicity of continuum modelling, it is very popular and common in the simulation of fluid flow and transport in fractured rocks. There are a number of computer codes using FEM and/or FDM methods in two or three-dimensional such as MODFLOW, FLAC 2D, FLAC 3D, COSFLOW, and etc.

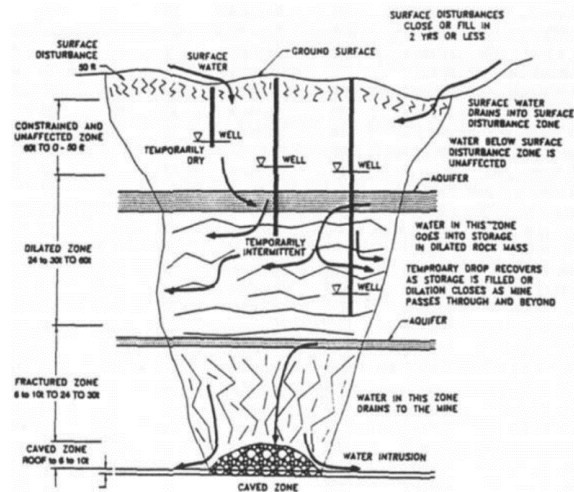


**Figure 6: Hydro-mechanical behavior of overburden rock mass above longwall(Kendorski, 2006)**

Khanal et al. (2019) developed a numerical model using a coupled 3-D mechanical deformation and double multiphase flow finite element code, COSFLOW to investigate the impacts of underground mining on permeability changes of overburden strata (Khanal et al., 2019). The model demonstrates that an increase in the longwall panel width will contribute to enhanced permeability. The results demonstrate that there is a significant increase in the permeability up to 60 m above the coal seam before the mining face reaches the monitoring position. In another study, Khanal et al. (2018) again applied COSFLOW to investigate the progress of connective fractures and water conductivity induced by longwall mining in a coal mine in Australia (Khanal et al., 2018). The results show that there is a significant increase in the post-mining hydraulic conductivity of the immediate roof.

Common continuum-based methods implicitly solve the rock deformation and hydraulic equations; however, they are not able to directly trace fractures and aperture on flow path to predict fractures connectivity. Discontinuities such as faults, joints, bedding planes and cleats which play substantial roles in rock deformation, rock fracturing, and fluid flow regimes, are not explicitly defined in the continuum methods. Therefore, discontinuum-based methods such as DEM and DFN would be only computational simulations to explicitly solve such a complex problem. Presentation of Discrete Element Method (DEM) engendered a significant development in rock mechanics. In DEM methods, a problem domain is usually composed of an assemblage of blocks or particles surrounded with contacts (discontinuities) which must be continuously identified during deformation process by representing suitable constitutive laws. Several computer codes based on DEM have been represented to model the behaviour of rock masses. The most representative codes are UDEC and 3DEC for two-dimensional and three-dimensional problems for blocky systems and PFC 2D and PFC 3D for granular materials represented by Itasca Consulting Group Ltd.

Poulsen et al. (2018) presented a numerical bounded-particle model (BPM) using the PFC in which fracture initiation and propagation, fractures connectivity, and aperture in disturbed overburden above a coal mining panel were calculated in a piecewise manner (Poulsen et al., 2018). Although particle-based models may be able to simulate the response of rock masses to a perturbation due to excavation, the calibration of micro-particle properties to the macro-properties, and the computational time remains as two major challenges using bounded-particle-based methods. Furthermore, several useful coupled hydro-mechanical DEM models using Universal Distinct Element Code (UDEC) have been applied to identify the progressive fracture process and fluid flow within fractured rock masses due to longwall mining.

Shabanimashcool et al. (2014) carried out discrete numerical modelling using the UDEC to investigate the caving mechanism of overlying strata above a longwall panel in the Svea Nord coal mine (Shabanimashcool et al., 2014). The study demonstrates that displacement increases with the coal face advance. The maximum deflection is 2.5 m when the coal face advances 30 m. In addition, the results of the numerical modelling show that the horizontal stresses reach to the maximum magnitudes when the coal face advances to a distance of 35 m and then the immediate roof started to fail in buckling. Gao et al. (2014) presented a 2D numerical model using the UDEC Trigon approach to simulate the caving mechanism of overlying strata in the German Ruhr coalfield (Gao and Stead, 2014). According to the results, compressive shear failure is the dominant mode of failure rather than tensile failure. The model results show that at the first stage when the width of the stope is 12m, only a few fractures are generated. However, as the face advances, fractures are extended wider and deeper. When the face advances 60m the first cave-in occurs. When the face advances more, higher layers also collapse and fall down. A key stratum or primary key stratum plays a substantial role in controlling subsidence of cap overburden. The strength and thickness of the key stratum govern the greatest fracture length among the entire overlying strata. Wang et al. (2017) proposed a theoretical model for calculation of the void ratios of fractures (VRFs) considering the key stratum theory. In addition, a DEM numerical modelling was designed using UDEC and the results show that when the mining face is in the distance of 100 m, fractures mostly come up near abutments and in the centre of the distressed strata. However, when the coal face passes this distance, the fractured zone was concentrated between the two key strata presenting an arch type zone. Wang et al. (2016) adopted the UDEC to investigate the height of fractured zone and the evolution mechanism of fractures in shallow coal seams beneath gully topographies (Wang et al., 2016a). The numerical simulations show that the mining height has a demonstrational effect on the evolution of fractures. When the height of mining is assumed to be 4.0 m and the coal face advances of 90 m (still the coal face is behind the gully), the interconnected bed separations and vertical fractures occur on the strata above the mining-out area.

## **DISCUSSION AND CONCLUSIONS**

In order to have an efficient, safe and economic underground mining a fully quantified and predictive method is required to determine the overburden deformation mechanism. The mining-induced deformation and resultant changes in hydraulic conductivity have been widely studied. Traditional methods such as empirical and conceptual methods, may not convince modern regulations, nor reflect the effects of geological, hydrological and geomechanical conditions (Poulsen et al., 2018). These rule of thumb studies may not provide a reliable investigation for the impacts of longwall mining on the environment. On the other hand, a well numerical model is able to successfully simulate a highly complex problem with true and reliable results. Among the existing numerical methods, many researchers concluded that the continuum methods such as the finite element method and finite difference method may not be appropriate and accurate approaches to numerically simulate the behavior of overlying strata and ground surface movements because of anisotropic and heterogenic properties of the rock mass. Common continuum-based methods implicitly solve the rock deformation and hydraulic equations; however, they are not able to directly trace fractures and aperture on flow path to predict fractures connectivity. More importantly, discontinuities such as faults, joints, bedding planes and cleats, which play substantial rules in rock deformation, rock fracturing and fluid flow regimes are not explicitly defined in the continuum methods. To provide a reliable and precise study, the effects of discontinuities in the problem domain, the geometry of longwall panel layout, the surface topography, the surface, and sub-surface water resources must be considered in the investigation which may only be possible through discontinuum methods. Although several discontinuum-based models have been applied to solve such a complex problem, there is still

a need to develop a robust coupled hydro-mechanic model that can properly represent the fracture development and fluid flow within fractured rock masses in an optimal manner.

### **ACKNOWLEDGMENTS**

I greatly thank Prof. Ismet Canbulat and the other academic staff at the School of Mineral and Energy Resources Engineering, UNSW, who helped me to carry out this research.

### **REFERENCES**

- Ditton, S. Merrick, N. 2014. A New Sub-Surface Fracture Height Prediction Model for Longwall Mines in the NSW Coalfields. Newcastle , NSW.
- Gale, W. 2008. Aquifer inflow prediction above longwall panels. ACARP: SCT.
- Gao, F. Q. Stead, D. 2014. The application of a modified Voronoi logic to brittle fracture modelling at the laboratory and field scale. *International Journal of Rock Mechanics and Mining Sciences*, 68, 1-14.
- Islam, M. R. Shinjo, R. 2009. Mining-induced fault reactivation associated with the main conveyor belt roadway and safety of the Barapukuria Coal Mine in Bangladesh: Constraints from BEM simulations. *International Journal of Coal Geology*, 79, 115-130.
- Jing, L. 2003. A review of techniques, advances and outstanding issues in numerical modelling for rock mechanics and rock engineering. *International Journal of Rock Mechanics and Mining Sciences*, 40, 283-353.
- Jing, L., Min, K.-B., Baghbanan, A. Zhao, Z. 2013. Understanding coupled stress, flow and transport processes in fractured rocks. *Geosystem Engineering*, 16, 2-25.
- Kendorski, F. S. 2006. Effect of full-extraction underground mining on ground and surface waters a 25 year retrospective. 25th International Conference on Ground Control in Mining. Morgantown, West Virginia, USA.
- Khanal, M., Adhikary, D., Poulsen, B. Guo, H. 2019. Mine Site Specific Longwall-Induced Permeability Changes: A Case Study. *Geotechnical and Geological Engineering*, 37, 3271-3282.
- Khanal, M., Guo, H. Adhikary, D. 2018. 3D Numerical Study of Underground Coal Mining Induced Strata Deformation and Subsequent Permeability Change. *Geotechnical and Geological Engineering*, 37, 235-249.
- Majdi, A., Hassani, F. P. Nasiri, M. Y. 2012. Prediction of the height of destressed zone above the mined panel roof in longwall coal mining. *International Journal of Coal Geology*, 98, 62-72.
- Peng, S. S. 2006. Longwall mining, Morgantown, W.Va. : West Virginia University.
- Poulsen, B. A., Adhikary, D. Guo, H. 2018. Simulating mining-induced strata permeability changes. *Engineering Geology*, 237, 208-216.
- Rezaei, M., Hossaini, M. F. Majdi, A. 2015. A time-independent energy model to determine the height of destressed zone above the mined panel in longwall coal mining. *Tunnelling and Underground Space Technology*, 47, 81-92.
- Ross, J. Sutton, G. 2016. Literature Review of Underground Mining Beneath Catchments and Water Bodies.
- Shabanimashcool, M., Jing, L. Li, C. C. 2014. Discontinuous Modelling of Stratum Cave-in in a Longwall Coal Mine in the Arctic Area. *Geotechnical and Geological Engineering*, 32, 1239-1252.
- Tammetta, P. 2013. Estimation of the height of complete groundwater drainage above mined longwall panels. *Ground Water*, 51, 723-34.
- Tammetta, P. 2015. Estimation of the change in hydraulic conductivity above mined longwall panels. *Ground Water*, 53, 122-9.
- Wang, F., Tu, S., Zhang, C., Zhang, Y. Bai, Q. 2016a. Evolution mechanism of water-flowing zones and control technology for longwall mining in shallow coal seams beneath gully topography. *Environmental Earth Sciences*, 75.
- Wang, S., Li, X. Wang, D. 2016b. Void fraction distribution in overburden disturbed by longwall mining of coal. *Environmental Earth Sciences*, 75.
- Wang, S., Li, X. Wang, S. 2017. Separation and fracturing in overlying strata disturbed by longwall mining in a mineral deposit seam. *Engineering Geology*, 226, 257-266.



Coal Opertors' Conference

- Xu, D., Peng, S., Xiang, S. He, Y. 2017. A Novel Caving Model of Overburden Strata Movement Induced by Coal Mining. *Energies*, 10.
- Zhang, X. Sanderson, D. J. 2002a. *Numerical Modelling and Analysis of Fluid Flow and Deformation of Fractured Rock Masses*, Elsevier Science.
- Zhang, X. Sanderson, D. J. 2002b. *Numerical Modelling and Analysis of Fluid Flow and Deformation of Fractured Rock Masses*, Elsevier Science.
- Zou, L., Tarasov, B. G., Dyskin, A. V., Adhikary, D. P., Pasternak, E. Xu, W. 2012. Physical Modelling of Stress-dependent Permeability in Fractured Rocks. *Rock Mechanics and Rock Engineering*, 46, 67-81.

# DESIGN COMBINED SUPPORT UNDER ARBITRARY IMPULSIVE LOADINGS

Faham Tahmasebinia<sup>1</sup>, Ismet Canbulat<sup>1</sup>, Chengguo Zhang<sup>1</sup>  
Serkan Saydam<sup>1</sup>, Onur Vardar<sup>1</sup>

**ABSTRACT:** Rock bolts and cable bolts are usually considered to experience static loads under relatively low-stress conditions. However, in burst-prone conditions, support elements are subjected to dynamic loading. Therefore, it is important to understand cable bolt behaviour under dynamic loading conditions, particularly their energy absorption capacity. Rock bolts and cable bolts as well as steel mesh are widely used as permanent support elements in tunnelling, underground excavations and surface slope stability. This paper aims to determine the amount of the dissipated energy which can be taken into account to design combined yielding supports when subjected to dynamic loading. A ground support approach is suggested for underground excavations undertaking a range of mining-induced coal burst. A bench mark based on the largest expected impact loading is considered to conclude the level of coal burst risk and select an appropriate approach, whether quasi-static or dynamic, for the mine support.

## INTRODUCTION

Current coal burst control techniques can be classified into two groups: preventative controls and mitigating controls. Preventative controls to avoid occurrence of coal bursts are usually implemented at the start of underground mines by optimising the mine design, while mitigating controls are applied as risk mitigation measures to minimise the risks of coal bursts during mining. Coal burst risks still exist even when preventative controls are implemented (Wei, Zhang, Canbulat et al. 2018). Due to the unpredictability of coal burst occurrences, ground support is usually the final and most common line of protection to ensure safety in high risk zones (Cai, 2013). Ground support has a pivotal role in a dynamic environment, which has been well recognised by the mining industry (Cai 2013; Jiang, et al., 2014; Mikula and Brown, 2018). The dynamic capacity of ground support has been the subject of significant research during the last two decades. However, ground support designs (i.e. yielding support) for coal burst is an area where rock engineering is still developing (Potvin, et al., 2010).

A combination of axial and shear is the primary failure mechanism as the bedded strata formations move in various directions (Mirzaghobanali, et al., 2017). Aziz, et al., (2015) described that cable bolts are usually installed perpendicular to the sedimentary rock bedding planes above coal mine openings. Rock movement caused by complex ground stresses usually occur along the bedding planes, resulting in shear stress across the cable bolts. Aziz, et al., (2009) conducted a series of double shear tests to investigate the performance of reinforced bolts in shear under different axial loading conditions. A total of 22 rock bolts with different surface profile configurations were tested, and the effects of various tension loads on the load transfer characteristics of the bolts were also studied. The results showed that the level of the shear load was affected by the ultimate tensile strength of rock bolts as well as the axial loads applied during testing. The shear loads increased with increasing tension loads, and the shear load was affected by the bolt profile configuration.

Rock bolts with energy-absorbing capacities play a critical role in the performance of dynamic ground support, and there are a range of products available including D-Bolts, cone bolts,

---

<sup>1</sup> School of minerals and energy resources engineering, UNSW Australia Sydney, NSW 2052 Australia  
[F.tahmasebinia@unsw.edu.au](mailto:F.tahmasebinia@unsw.edu.au)

Durabar, Roofex, Garford and CRLD (Cai, 2013; Kabwe and Wang 2015; Pytlik, et al., 2016; Wei, Zhang, Canbulat, et al., 2018; Zhou and Zhao, 2011). Of these, the cone bolt, Durabar, Garford solid bolt and Roofex are two-point anchored into the rock; the D-Bolt is multi-point anchored; and the hybrid bolt and inflatable bolt interact frictionally with the rock mass along their entire lengths (Zhou and Zhao, 2011). The dynamic capabilities of ground support are key design parameters when selecting yielding elements for highly stressed, burst-prone or high deformation environments (Plouffe, et al., 2007).

### STATIC AND DYNAMIC MODELLING UNDER APPLIED SHEAR LOADING

The proposed three-dimensional finite element model is developed using the commercial software ABAQUS, due to its ability to deal with complex contact problems. The structural response of the cable bolts using solid elements for all components is examined using the modelling (Tahmasebinia et al 2018). One of the main difficulties in the modelling of steel and concrete members with ABAQUS is the convergence issues which need to be addressed due to the extensive number of contacts required to be implemented between the cable bolt and the concrete boxes. For this purpose, the 8-node linear brick element (C3D8R) with a reduced integration and hourglass control is adopted, which is the element with three transitional degrees of freedom. To validate the finite element models and the developed analytical solution, the obtained results were compared with the reported experimental investigation by Mirzaghobanali, et al., (2017). The reported tests were conducted under static loading, which was used to calibrate the models. Then, the models were extended to dynamic loading (Figure 1).

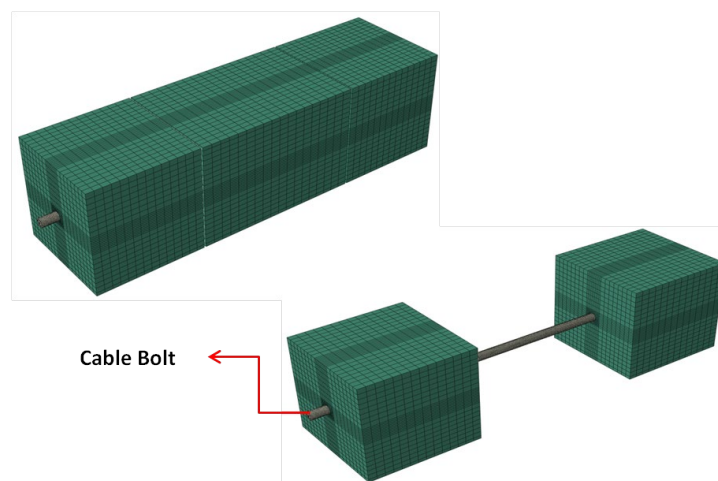


**Figure 1: An example of a 3-D finite element model under static and dynamic loading.**

One of the significant contributions of this study is the development of an analytical solution to assess the behaviour of the cable bolt under quasi-static loading (Tahmasebinia et al 2018). An equation based on the plastic analysis is proposed. The plastic hinge concept stems from the ability of steel to be idealised as elastic-perfectly plastic. Integrating the fully plastic section is equated to taking the moments of the fully plastic stress block forces about the plastic neutral axis. The principle of virtual work is used to calculate the load magnitude at which the plastic mechanism develops and failure occurs. It means that the external work done by the applied load must equal the internal work done by the plastic hinges in the cable section (Figure 2).

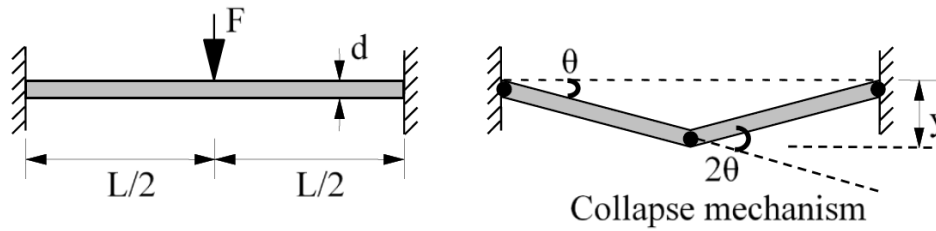


Figure 2: Plastic collapse load of a cable bolt.

The applied shear load versus shear displacement can be calculated by Equation 1

$$F_{\max} = \frac{(k \times N_u \times y_i)^2}{M_u \times L} + \frac{8 \times M_u}{L} \quad (1)$$

where  $F_{\max}$  is the transverse shear force;  $0.1 \leq k \leq 0.5$  the constant-coefficient; and  $y_i$  displacement increments. Also,

$$N_u = \frac{\pi \times d^2}{4} \times f_y \quad (2)$$

$$M_u = \frac{\pi \times d^3}{2} \times f_y \quad (3)$$

where

$N_u$  is design axial tension capacity;

$M_u$  the design bending capacity,

$L$  the cable bolt length,

$d$  the cable bolt diameter; and

$f_y$  the cable yielding stress.

$y_i$  displacement increments can be obtained by Equation.

$$y_i = \left\{ \begin{array}{l} 0 \\ 0.1 \times d \\ 0.2 \times d \\ \dots \\ 1 \times d \\ 1.1 \times d \\ 1.2 \times d \end{array} \right\} \quad (4)$$

Mirzaghobanali, et al. (2017) conducted a series of double shear tests on different cable bolts by developing a new double shear apparatus without contact between concrete blocks to determine the pure shear strength of pre-tensioned fully grouted cable bolts. Figure 3 and 4 illustrate the failure procedure of the cable bolt which is embedded inside the concrete blocks starting from initial deformation until pure shear failure. This can be one of the advantages of using numerical modelling to assess the local behaviour of cable bolts under static loading in the different stages of the failure. After calibrating the numerical models under static loading, the structural behaviour of the simulated models under dynamic loading was also studied. Since preparing the laboratory experiments to simulate the behaviour of cable bolts under dynamic loading is demanding, a validated and novel numerical simulation was developed. To simulate the behaviour of the cable bolts under impact loading, a 110 kg mass at the velocity of 0.2 m/s was dropped on top of the concrete blocks. Figure 5 presents the structural behaviour of the cable bolts under impact loading. As illustrated, the momentum energy from the dropped mass

is initially transferred to the concrete surfaces, and the transmitted energy due to the impulsive loading reaches the cable bolt.

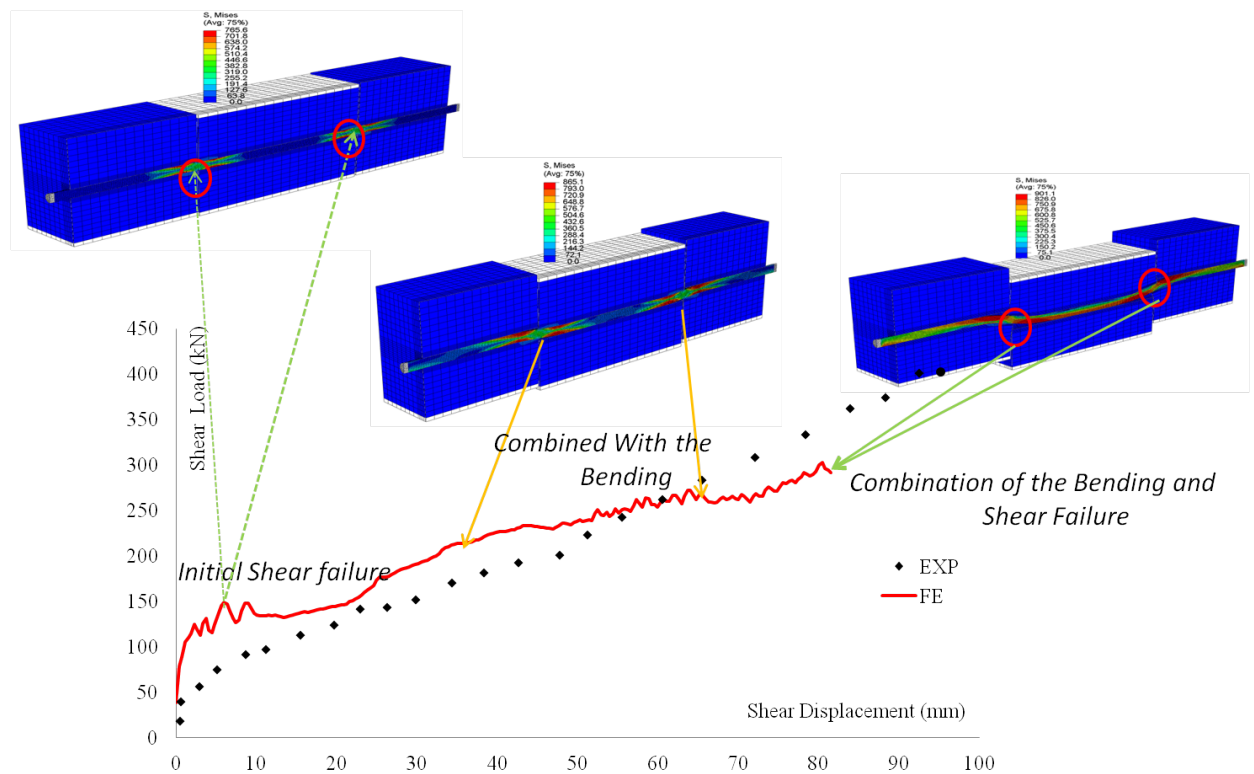


**Figure 3: Shear ductile failure in the cable bolt under static loading, shown in different stages.**

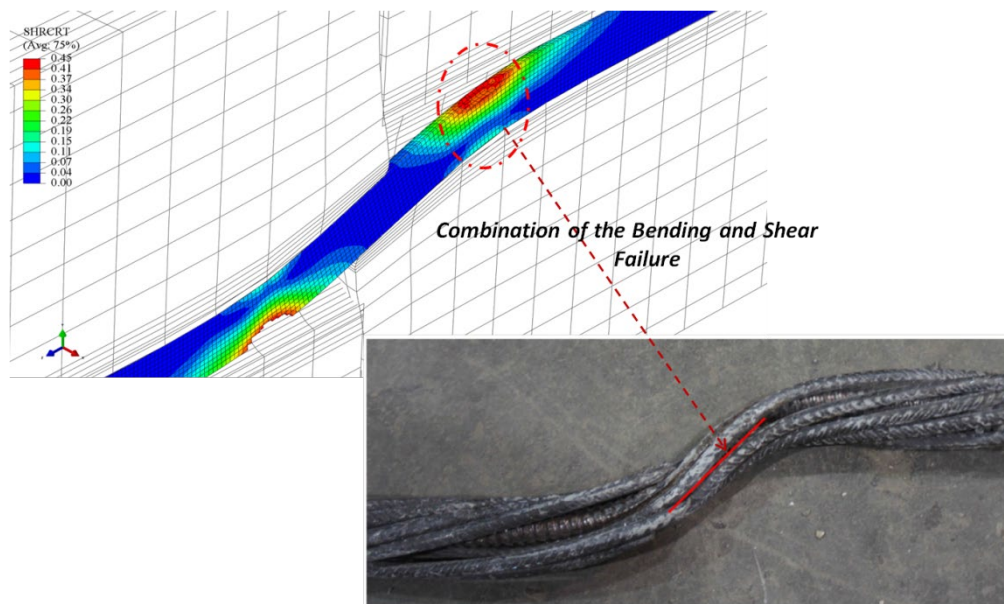


**Figure 4: Combination of the bending and shear failure (Mirzaghorbani, et al., 2017).**

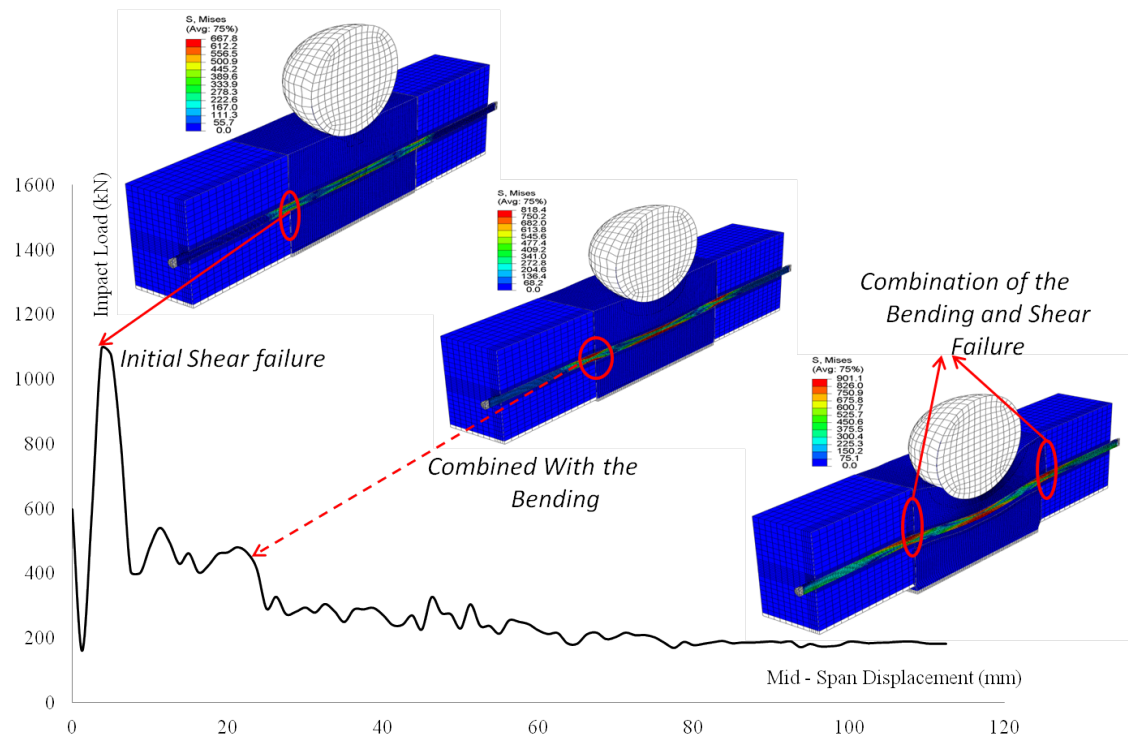


**Figure 5: Shear ductile failure in the cable bolt under impact loading, shown in different failure stages.**

### **SIMULATION OF THE BEHAVIOUR OF THE STEEL MESH UNDER DYNAMIC IMPACT LOADING**

A similar way to simulate the dynamic behaviour of the steel mesh due to the applied dynamic loading was taken into account. The mesh steel reinforcement sizes 20 mm diameter arranged by 100 mm distance centre to centre of the steel bars were tested under free fall of the dropped hammer. The dropped hammer used in the last section was used for this simulation. The 110 kg drop hammer at velocity of 1.5 m/s was dropped on top of the steel reinforcement. Figure 6 illustrates the experimental set up used to simulate the structural behaviour of the steel mesh under impact loading. Steel mesh can play a significant role as part of the yielding support in a coal mine, as it can mitigate the effect of the destructive released kinetic energy due to a possible coal burst. In coal mines, it was observed that both rock bolts and cable bolts might lose the initial bond stiffness at the early stage of the applied dynamic loading due to the failure and separation of the anchored zone in the cable and rock bolts inside embedded coal. The anchorage length in a post-tensioned member and the magnitude of the transverse forces (both tensile and compressive), that act perpendicular to the longitudinal prestressing force, depend on the magnitude of the prestressing force and on the size and position of the anchorage hooks. Both single and multiple anchorages are commonly used in coal mining. Prestressing force anchors transfer large forces to the coal in concentrated areas. Coal is a very brittle material which can cause localised bearing failure or split open the end of members. Thus, the steel mesh can considerably reduce the effect of the induced dynamic loading due to coal burst. In the current simulation, the tensile stress for the steel mesh was  $f_y = 500 \text{ MPa}$  and the ultimate stress for the steel mesh  $f_u = 700 \text{ MPa}$  was taken into account. The post failure of the steel mesh which may rupture the steel bars was also defined. The ductile damage function was determined to simulate the post failure of the steel mesh. Also, the rupturing strain  $\epsilon_{\text{rupture}} = 0.3\%$  was assumed. As the weld properties of the steel mesh can also influence the overall deformation as well as energy absorption of the yielding support, the weld properties were specifically defined in the present steel mesh simulations. The allocated fracture energy which has a considerable role in determining the separation of the welded steel was specified by computing the area of the obtained stress-strain curves from the weld properties.



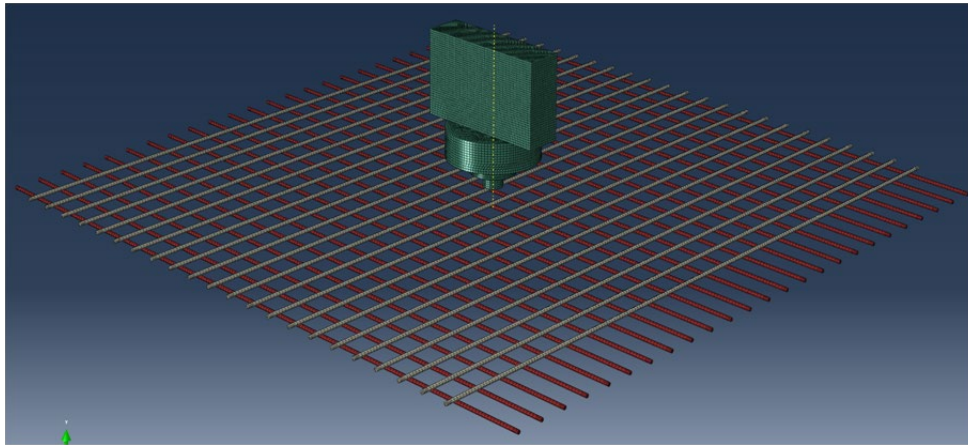


**Figure 6: The test set up for simulating the behaviour of the steel mesh under impact loading**

Figure 7 demonstrates direct brittle failure in the steel mesh under impact loading in different failure stages. As illustrated, at the initial contact between the dropped hammer and steel mesh, the momentum energy was transferred from the common surfaces. The transferred energy due to the dropped test was distributed in different layers of the steel mesh. The transmitted kinetic energy can induce both shear and bending stresses in the steel mesh. As soon as any steel mesh or welding elements reached the yielding and ultimate stresses, permanent deformation of the steel mesh occurred. This permanent deformation might be followed by the rupturing strain which leads to element separation in the simulated model. In general, connections between the steel bars or location of the weld elements are the weakest position in the steel meshes. Thus, the expected failure can occur around the welded connections. This is one of the main reasons why weld properties can play a significant role in generating the overall ductility, the deformability of the steel mesh, and the amount of the energy absorption in both the yielding and combined supports.

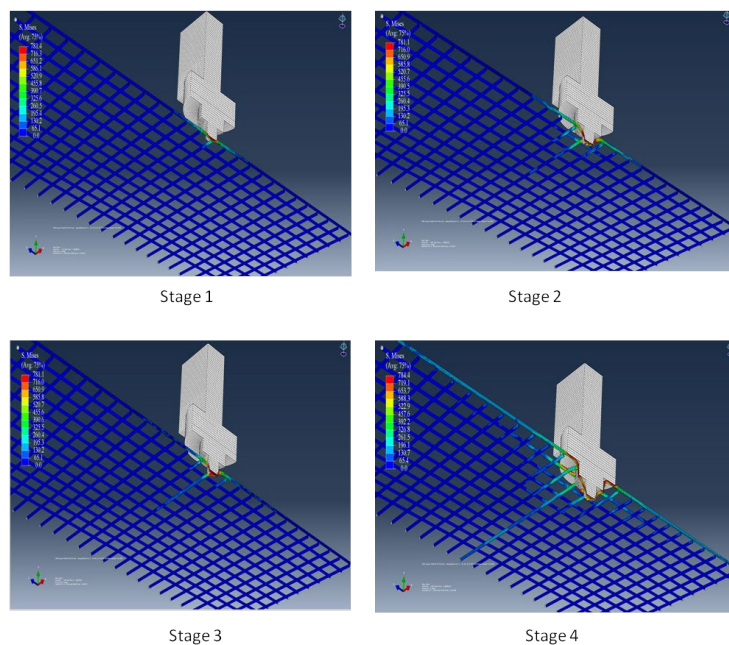
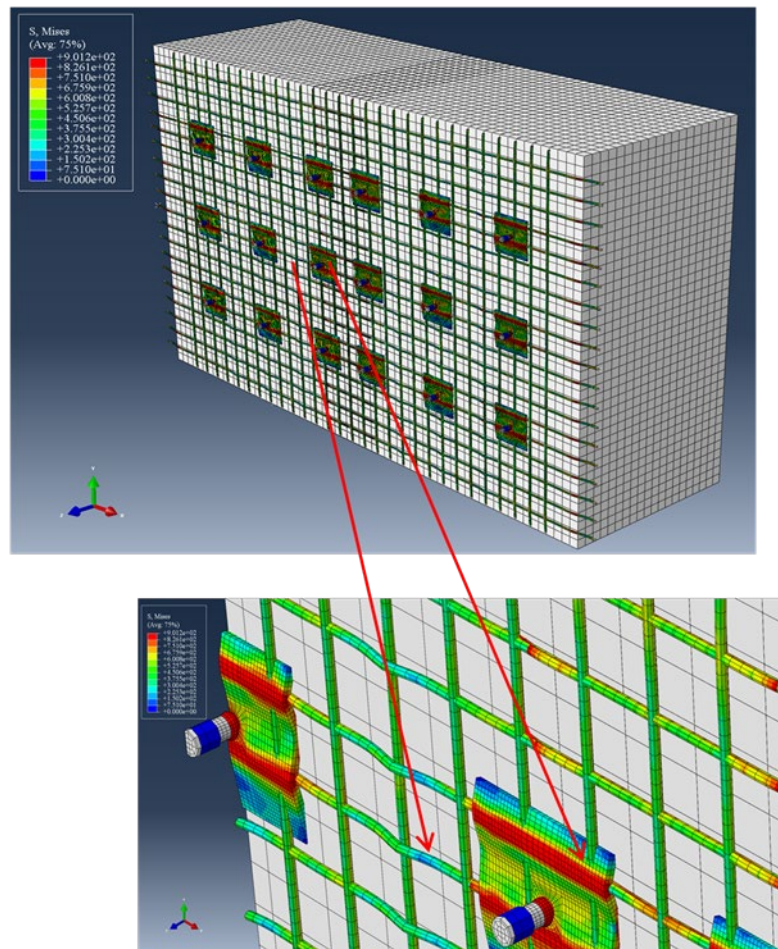


**Figure 7: Direct brittle failures in the steel mesh under impact loading, shown in four stages.**

Figure 8 shows the interaction between the steel plate and welded wire mesh. This figure indicates that steel plates may be subjected to high levels of stress concentrations. Thus, steel

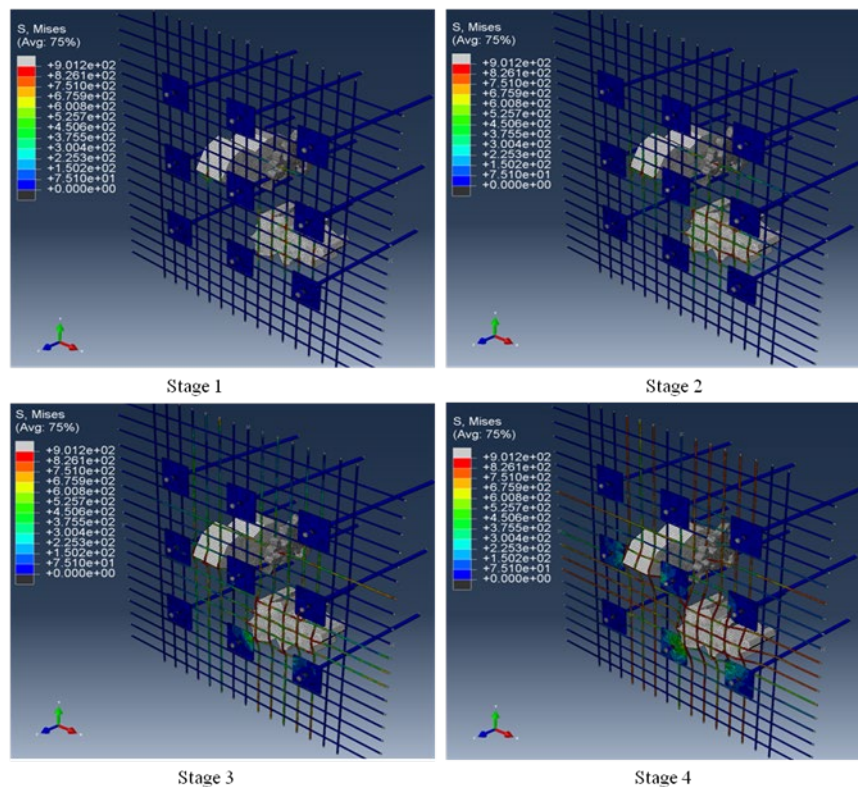


plate buckling capacity in different modes is one of the key factors that may be taken into account when computing overall capacity of a combined support.



**Figure 8: The interaction between the steel plate and weld mesh.**

A similar failure pattern can also be observed in a full scale combined support under loading due to rock ejection. The failure process is illustrated in four stages in Figure 9. The tensile stress caused by the ejected rock mass is transferred on to the steel mesh. Also, while some parts of the steel plates are subjected to the tension, the parts are subjected to the compression due to a combination of the bending and shear reactions around the connections of plates. Similar to the conclusions in the previous section, it is also evident that steel plates can play an important role in controlling the deformability of the steel mesh. Details of the failure stages from the initial steel mesh deformation and buckling of the steel plates are demonstrated in Figure 9. This figure also indicates that the deformed shape of the steel plate can enhance the overall deformability of the welded wire mesh when it is subjected to the impact loading.



**Figure 9: The deformation of the combined support when subjected to the arbitrary fractal rock fall.**

### CONCLUSIONS

This study tested different key elements in combined support under virtual impact loading to complimentary replace testing under real impact loading conditions which is very time consuming and requires access to special impact facilities. The existing impact testing facilities in Western Australia, Canada, Chile and South Africa are expensive and require significant space for the testing facilities. Individual shock absorber equipment must be installed next to the impact frame facilities to create safe and secure testing conditions in the adjacent buildings due to the possible deconstructive effect of the induced impact loading. Special attention should also be devoted to selecting proper measuring equipment to measure induced impact loading as well as the critical displacement in tested samples. For instance, calibrating the load cell located in the head of the impact hammer is a significant task in preparing the impact facilities. Similar complexity can be found when adapting the load cell to the data acquisition system. Filtering and calibrating the data acquisition system due to the effect of the impulsive loading is very cumbersome and requires particular practical experience. The influence of the inertia forces due to the applied impact loading may lead to misjudgment in evaluating the structural performance of the tested sample in the combined support. Thus, developing novel and well validated numerical models to simulate the effect of impact loading on the different key support elements can play a crucial role in designing a combined support in coal mines which might be affected by coal burst.

### ACKNOWLEDGEMENT

This work was supported by an award under the Merit Allocation Scheme on the NCI National Facility at the ANU and part of the computational services used in this work was provided by Intersect Australia Ltd.

## REFERENCES

- ABAQUS USER'S MANUAL, V. E.-. 2008. Providence, RI, USA: Dassault Systèmes Simulia Corp.
- AZIZ, N., CRAIG, P., MIRZAGHORBANALI, A., RASEKH, H., NEMCIK, J. and LI, X. 2015. Behaviour of cable bolts in shear; experimental study and mathematical modelling.
- AZIZ, N., NEMCIK, J., CAO, C. and JALALIFAR, H. 2009. Bolt profile configuration and load transfer capacity optimisation.
- CAI, M. 2013. Principles of rock support in burst-prone ground. *Tunnelling and Underground Space Technology*, 36, 46-56.
- CAI, M. and KAISER, P. 2018a. Rockburst support reference book—volume I: rockburst phenomenon and support characteristics. *Laurentian University*, 284.
- CAI, M. and KAISER, P. 2018b. Rockburst support reference book—volume I: rockburst phenomenon and support characteristics. *Mirarco, Laurentian University, Sudbury*.
- CAI, M., KAISER, P., TASAKA, Y., MAEJIMA, T., MORIOKA, H. and MINAMI, M. 2004. Generalized crack initiation and crack damage stress thresholds of brittle rock masses near underground excavations. *International Journal of Rock Mechanics and Mining Sciences*, 41, 833-847.
- KAISER, P. and TANG, C. 1998. Numerical simulation of damage accumulation and seismic energy release during brittle rock failure—Part II: Rib pillar collapse. *International Journal of Rock Mechanics and Mining Sciences*, 35, 123-134.
- KAISER, P. K. and CAI, M. 2012. Design of rock support system under rockburst condition. *Journal of Rock Mechanics and Geotechnical Engineering*, 4, 215-227.
- KAISER, P. K., MACCREATH, D. and TANNANT, D. 1996. *Canadian rockburst support handbook: prepared for sponsors of the Canadian rockburst research program 1990-1995*, Geomechanics Research Centre.
- MIRZAGHORBANALI, A., RASEKH, H., AZIZ, N., YANG, G., KHALEGHPARAST, S. and NEMCIK, J. 2017. Shear strength properties of cable bolts using a new double shear instrument, experimental study, and numerical simulation. *Tunnelling and Underground Space Technology*, 70, 240-253.
- ORTLEPP, W. and STACEY, T. 1998. Performance of tunnel support under large deformation static and dynamic loading. *Tunnelling and underground space technology*, 13, 15-21.
- ORTLEPP, W., STACEY, T. and KIRSTEN, H. 1999. Containment support for large static and dynamic deformations in mines. *Proc. of Rock Support and Reinforcement Practice in Mining (edited by Villaescusa, Windsor and Thompson)*. Rotterdam, AA Balkema, 359-364.
- ORTLEPP, W. and SWART, A. 2002. Extended use of the Savuka dynamic test facility to improve material and analytical technology in deep-level stope support.
- ORTLEPP, W., VAN ASWEGEN, G. and DURRHEIM, R. The mechanism of a rock outburst in a quartzite tunnel in a deep gold mine. Dynamic rock mass response to mining, Proceedings of the 5th International Symposium on Rockbursts and Seismicity in Mines, South African Institute of Mining and Metallurgy Symposium Series S, 2001a. 53-58.
- ORTLEPP, W., WESSELOO, J. and STACEY, T. A facility for testing of stope support under realistic 'rockburst' conditions. Proceedings of the 5th international symposium on rockbursts and seismicity in mines, dynamic rock mass response to mining. South African Institute Of Mining and Metallurgy, 2001b. 197-204.
- POTVIN, Y., WESSELOO, J. and HEAL, D. 2010. An interpretation of ground support capacity submitted to dynamic loading. *Mining Technology*, 119, 233-245.

Coal Opertors' Conference

STACEY, T. 2001. Review of membrane support mechanisms, loading mechanisms, desired membrane performance, and appropriate test methods. *Journal of the Southern African Institute of Mining and Metallurgy*, 101, 343-351.

STACEY, T. 2012. A philosophical view on the testing of rock support for rockburst conditions. *Journal of the Southern African Institute of Mining and Metallurgy*, 112, 01-08.

STACEY, T. and ORTLEPP, W. Retainment support for dynamic events in mines. Proc. Int. Symp. Rock Support and Reinforcement Practice in Mining, 1999. 329-333.

THOMPSON, A., VILLAESCUSA, E. and WINDSOR, C. 2012. Ground support terminology and classification: an update. *Geotechnical and Geological Engineering*, 30, 553-580.

TIMOSHENKO, S. P. and GERE, J. M. 2009. *Theory of elastic stability*, Courier Corporation.

VOYIADJIS, G. Z. and KATTAN, P. I. 2009. A comparative study of damage variables in continuum damage mechanics. *International Journal of Damage Mechanics*, 18, 315-340.

# Parametric studies of cable bolts using a modified Short Encapsulation Pull-out Test

Danqi Li<sup>1</sup>, Hossein Masoumi<sup>2</sup>

**ABSTRACT:** The laboratory short encapsulation pull out test (LSEPT) has been widely accepted as the most efficient method to characterize the mechanical behaviour of cable bolts under axial loading. In this study, a number of LSEPTs was performed on conventional cable bolts including Plain SuperStrand and TG cable bolts using the improved pull out test design. The effects of several parameters including the uniaxial compressive strength (UCS) of confining medium and grout and the borehole diameter on the mechanical behaviour of both cable bolts were investigated. Analysis of Variance (ANOVA) was employed to quantify the contribution of these parameters on the responses including peak and residual loads and initial stiffness. ANOVA revealed that UCS of confining medium and grout is the key contributing factor to the mechanical behaviour of Plain SuperStrand cable bolt. Also, it was demonstrated that the borehole diameter had a negligible impact on the overall behaviour of TG cable bolt while the peak load of SuperStrand cable bolt was increased due to an increase in the diameter of borehole. Finally, from a comparative analysis, it was confirmed that TG cable bolt exhibits a higher load carrying capacity than Plain SuperStrand cable bolt.

## INTRODUCTION

Cable bolts, as well as rock bolts, have been increasingly used for strata reinforcement in underground coal mines over the past few decades (Aziz et al., 2016; Aziz et al., 2015; Ghadimi et al., 2015; Hyett et al., 1995; Jalalifar and Aziz, 2010; Jalalifar et al., 2006; Li et al., 2017; Li et al., 2016). The types of cable bolts which are currently used in the mining industry can be classified into two main categories, namely conventional and modified (Li et al., 2017). The former is made of several plain steel strands (e.g. plain strand cable bolts) while the latter has different forms of deformed structure such as bulb, nutcage or birdcage.

A number of researchers have investigated the effect of different parameters on the performance of conventional cable bolts in service (Chen and Mitri, 2005; Goris, 1991; Hyett et al., 1995; Reichert, 1991; Stillborg, 1984). The peak load of the load-displacement performance of plain strand cable bolts in pull-out tests was found to increase with encapsulation length (Chen and Mitri, 2005; Goris, 1991; Hassani et al., 1992; Hyett et al., 1992; Stillborg, 1984). Goris (1991), Reichert (1991), and Stillborg (1984) demonstrated that an increase in compressive strength of the grout used to embed the cable bolt lead to an increase in peak shear strength of the plain strand cable bolt at the grout to cable bolt interface. The effect of grout strength on the initial stiffness was inconclusive as on the one hand, Stillborg (1984) reported that the initial stiffness increased with grout compressive strength while Reichert (1991) reported no meaningful correlation between these two parameters. Rajaie (1990), Chen and Mitri (2005) and Mosse-Robinson and Sharrock (2010) concluded that borehole diameter

---

<sup>1</sup> Dr Danqi Li, Monash University. Email: Danqi.li@monash.edu Tel: +61 3 9905 4981

<sup>2</sup> Dr Hossein Masoumi, Monash University. Email: Hossein.Masoumi@monash.edu Tel: +61 3 9905 6468

has a negligible effect on the peak load and initial stiffness of load-displacement behaviour of plain strand cable bolts.

In this study, two types of conventional cable bolts including Plain SuperStrand and TG cable bolts were investigated. The LSEPT facilities and testing procedures can be referred to the study by Li et al. (2018b) as seen in Figure . The advantage of such a testing design is that the rotation of the cable bolt steel strands could be restricted during the pull out of the cable bolt through using the locking key and locking nut (seen in Figure ) that can prevent the relative spinning movement of anchor tube, bearing plate and sample holder tube. Such a device can hence leads to a more realistic reflection of the field testing conditions. The details of ANOVA can be referred to the study by Li et al. (2018a). The effects of a range of parameters including confining medium strength, grout strength and borehole diameter on the performance of both cable bolts were investigated. Finally, an extensive statistical Analysis of Variance (ANOVA) was performed to identify the most influential parameter affecting the performance of the two cable bolts.

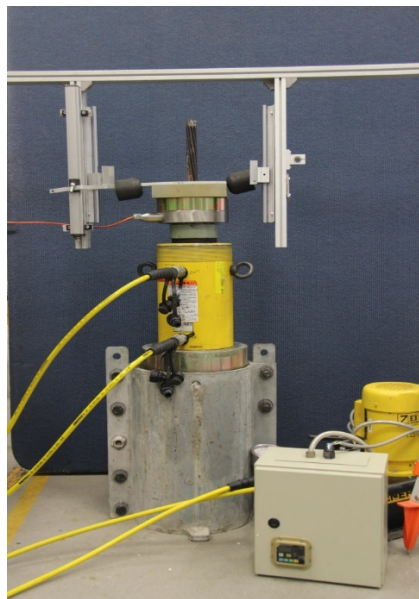


Figure 1: Pull-out test facility

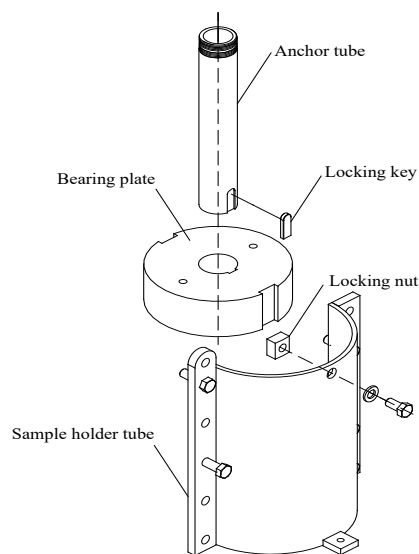


Figure 2: Concept design of anti-rotation devices

## PLAIN SUPERSTRAND CABLE BOLTS

### Experimental design

The confining medium compressive strength and borehole diameter were nominated as the parameters for the investigation of the Plain SuperStrand cable bolt. The experimental program design is shown in Table 1. It should be noted that three replication tests were conducted under each testing condition.

**Table 1: Experimental design for Plain SuperStrand cable bolt**

Testing condition	Compressive strength of confining medium (MPa)	Compressive strength of grout (MPa)	Borehole diameter (mm)	Replications
1	64	71	27	3
2	64	71	37	3
3	11	71	27	3
4	11	71	37	3

### Test results

Both the peak and residual loads increased with compressive strength of the confining medium (see Table 2). It is noted that the increase in confining medium compressive strength from 11 MPa to 64 MPa led to 50% increase in the peak and residual loads of the Plain SuperStrand cable bolt.

**Table 2: Effect of compressive strength of confining medium on the peak and residual loads of Plain SuperStrand cable bolt tested at 27 mm borehole diameter**

Variables	Number of tests	Mean load (kN)	Standard deviation (kN)	Coefficient of variation
Peak load obtained from the test with strong confining medium	3	97	2.5	2.6
Residual load obtained from the test with strong confining		86	11.1	12.9
Peak load obtained from the test with weak confining medium	3	63	9.5	14.9
Residual load obtained from the test with weak confining medium		60	4	6.7

With the 10 mm increase in borehole diameter it was observed that the peak and residual loads increased regardless of the type of confining medium. The combined effect of borehole diameter and compressive strength of confining medium on peak load of Plain SuperStrand cable bolts are illustrated in Figure . In addition, Figure shows that a 10 mm increase in borehole diameter led to an increase in the initial stiffness and residual load. This might in part be due to the significant difference in mechanical properties of resin grout compared to that of the confining medium.



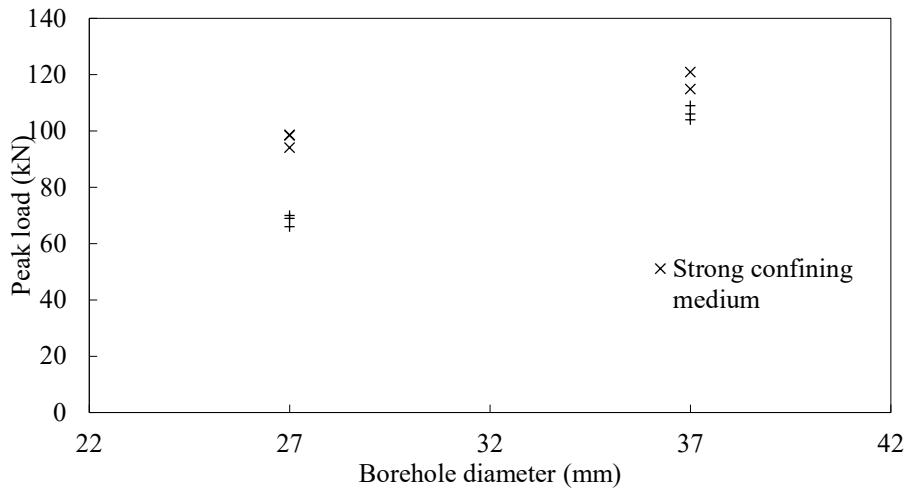


**Figure 3: Effect of borehole diameter on peak load of Plain SuperStrand cable bolts**

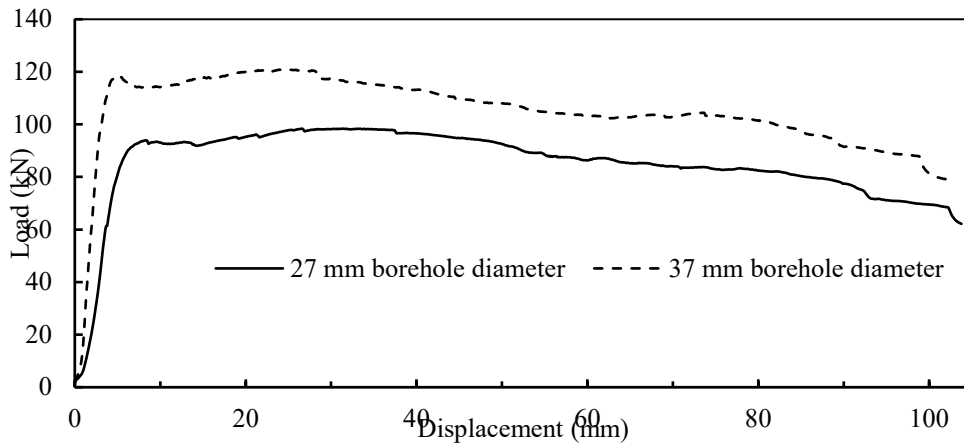


**Figure 4: Examples of load-displacement curves resulted from pull-out test on Plain SuperStrand cable bolts with strong confining medium to assess the effect of borehole diameter on its performance**

**Analysis of variance (ANOVA) for plain SuperStrand cable bolt test results**

The contribution of each parameter (confining medium compressive strength and borehole diameter) to the variation in each response (peak load and initial stiffness) was weighted and the results are shown in Table 3 and Table 4. As a result, the borehole diameter was found to be the most influential factor to peak load of the performance of Plain SuperStrand cable bolt in pull-out tests. This is attributed to the significant difference between the confining medium and resin grout leading to the great variation in the confinement when changing the borehole diameter.

On the contrary, the compressive strength of the confining medium was revealed to be the most influential factor to the initial stiffness of the performance of Plain SuperStrand cable bolt. This is related to the greater stiffness of the confining medium resulted from the higher compressive strength. It is hypothesized that the stiffness of the confining medium has the direct effect on the initial stiffness of the Plain SuperStrand cable bolt.

**Table 3: Summary of ANOVA for peak load of Plain SuperStrand cable bolt**

Source	Sum of square	Degree of freedom	Mean square	F value	Contribution weighting (%)
Confining medium compressive strength	2436.75	1	2436.75	30.62	41%
Borehole diameter	3570.75	1	3570.75	44.87	59%

**Table 4: Summary of ANOVA for initial stiffness of Plain SuperStrand cable bolt**

Source	Sum of square	Degree of freedom	Mean square	F value	Contribution weighting (%)
Confining medium compressive strength	114.083	1	114.083	2.56	97%
Borehole diameter	4.083	1	4.083	0.09	3%

## TG CABLE BOLTS

### Experimental Design

The grout compressive strength and borehole diameter were nominated as the parameters for the investigation of the TG cable bolt. The experimental program design is shown in **Table 5**. It should be noted that three replication tests were conducted under each testing condition.

**Table 5: Experimental design for TG cable bolt**

Testing condition	Compressive strength of confining medium (MPa)	Compressive strength of grout (MPa)	Borehole diameter (mm)	Replications
1	11	80	42	3
2	11	62	42	3
3	11	80	52	3
4	11	62	52	3

### Test results

The means of the peak load and initial stiffness of the performance of TG cable bolts in pull-out tests were summarised in Table 6 with the corresponding CV values. It shows that the 18 MPa increase in the grout compressive strength led to approximately 50 kN increase in the peak load. Such behaviour is associated with the higher shear strength of the stronger grout leading to the higher resistance against the axial displacement of the cable bolt.

**Table 6: Results obtained from pull-out tests on TG cable bolts**

Experiment Condition	Borehole diameter (mm)	Grout compressive strength (MPa)	Mean peak load (KN)	CV (%)	Mean initial stiffness (kN/mm)	CV (%)
1	42	80	293	0.0	78.5	8.6
2	42	62	232	11.2	75.1	2.5
3	52	80	262	6.1	85.0	4.8
4	52	62	216	8.1	74.0	3.4

By contrast, Figure 5 shows that the borehole diameter has negligible effect on the full load-displacement performance of TG cable bolt despite of some minor deviations during the large displacement. Such an effect might be attributed to the mechanical properties of the confining medium and grout.

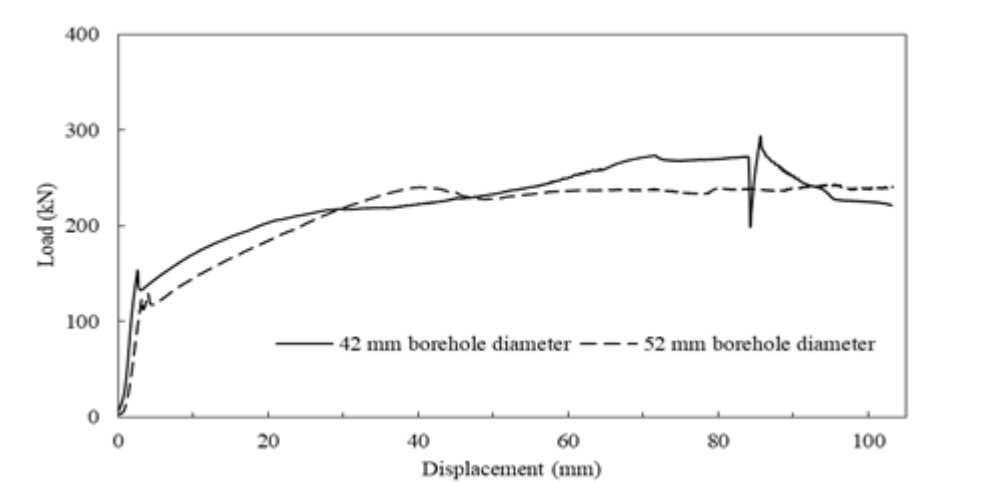


**Figure 5: Example of full load-displacement performance of TG cable bolt with grout compressive strength of 80 MPa**

#### Analysis of variance (ANOVA) for TG cable bolt test results

The contribution of each parameter (grout compressive strength and borehole diameter) to the variation in each response (peak load and initial stiffness) was weighted and the results are shown in Tables 7 and 8. As a result, the grout compressive strength was found to be the most influential factor to peak load and initial stiffness of the performance of TG cable bolt in pull-out tests. On the contrary, the overall performance of TG cable bolt was insensitive to the borehole diameter in which 10 mm change had negligible effect on either the peak load or the initial stiffness. Such a finding might be attributed to the mechanical properties of the confining medium and grout.

**Table 7: Summary of ANOVA for peak load of TG cable bolt**

Source	Sum of square	Degree of freedom	Mean square	F value	Weighting contribution (%)
Borehole diameter	1633.3	1	1633.3	5.24	15
Grout UCS	8748	1	8748	28.06	83
Residual	161.3	1	161.3	0.52	2

**Table 8: Summary of ANOVA for initial stiffness of TG cable bolt**

Source	Sum of square	Degree of freedom	Mean square	F value	Weighting contribution (%)
Borehole diameter	21.87	1	21.87	1.22	10
Grout UCS	156.963	1	156.963	8.75	71
Residual	42.563	1	42.563	2.37	19

### CONCLUSIONS

Extensive parametric studies on the performance of Plain SuperStrand and TG cable bolts were conducted followed by in-depth analysis of the experimental result using ANOVA technique. It was found that the confining medium strength is the most influential parameter to the initial stiffness of Plain SuperStrand by contrast to borehole diameter as the most influential variable to the peak load. For TG cable bolts, grout strength has a more significant effect on the peak load and initial stiffness of the cable bolt than borehole diameter.

### REFERENCES

- Aziz, N., Craig, P., Mirzaghobanali, A., Nemcik, J., 2016. Factors Influencing the Quality of Encapsulation in Rock Bolting. *Rock Mechanics and Rock Engineering*, 49,(8), 3189-3203. 10.1007/s00603-016-0973-5
- Aziz, N., Mirzaghobanali, A., Nemcik, J., Heemann, K., Mayer, S., 2015. Shear strength properties of plain and spirally profiled cable bolts. *Canadian Geotechnical Journal*, 52,(10), 1490-1495. 10.1139/cgj-2014-0504
- Chen, J.Y., Mitri, H.S., 2005. Shear bond characteristics in grouted cable bolts, 24th International Conference on Ground Control in Mining, Lakeview Scanticon Resort Conference Center, Morgantown, WV, USA.
- Ghadimi, M., Shahriar, K., Jalalifar, H., 2015. A new analytical solution for the displacement of fully grouted rock bolt in rock joints and experimental and numerical verifications. *Tunnelling and Underground Space Technology*, 50, 143-151. <http://dx.doi.org/10.1016/j.tust.2015.07.014>
- Goris, J.M., 1991. Laboratory evaluation of cable bolt supports. Department of the Interior, Bureau of Mines.
- Hassani, F.P., Mitri, H.S., Khan, U.H., Rajaie, H., 1992. Experimental and numerical studies of the cable bolt support systems, in: MaCreath, K.a. (Ed.), *Rock Support in Mining and Underground Construction*. Balkema, Rotterdam, pp. 411-417.
- Hyett, A.J., Bawden, W.F., Coulson, A.L., 1992. Physical and mechanical properties of normal Portland cement pertaining to fully grouted cable bolts, in: Kaiser, P.K., McCreath, D.R. (Eds.), *Rock Support in Mining and Underground Construction*. International Symposium Rock Support, Rotterdam, Netherland, pp. 341-348.
- Hyett, A.J., Bawden, W.F., Macsporrnan, G.R., Moosavi, M., 1995. A constitutive law for bond failure of fully grouted cable bolts using a modified hoek cell. *International Journal for Numerical and Analytical Methods in Geomechanics*, 32,(1), 11-36.
- Jalalifar, H., Aziz, N., 2010. Analytical behaviour of bolt–joint intersection under lateral loading conditions. *Rock mechanics and rock engineering*, 43,(1), 89-94.

Jalalifar, H., Aziz, N., Hadi, M., 2006. The effect of surface profile, rock strength and pretension load on bending behaviour of fully grouted bolts. *Geotechnical Geological Engineering*, 24,(5), 1203-1227. 10.1007/s10706-005-1340-6

Li, D., Masoumi, H., Saydam, S., Hagan, P.C., 2017. A constitutive model for load-displacement performance of modified cable bolts. *Tunnelling and Underground Space Technology*, 68, 95-105.

Li, D., Masoumi, H., Saydam, S., Hagan, P.C., 2018a. Mechanical Characterisation of Modified Cable Bolts Under Axial Loading: An Extensive Parametric Study. *Rock Mechanics and Rock Engineering*, 51,(9), 2895-2910.

Li, D., Masoumi, H., Saydam, S., Hagan, P.C., Asadzadeh, M., 2018b. Parametric study of full grouted cable bolts subjected to axial loading. *Canadian Geotechnical Journal*, 10.1139/cgj-2018-0470.

Li, X., Aziz, N., Mirzaghobanali, A., Nemcik, J., 2016. Behavior of Fiber Glass Bolts, Rock Bolts and Cable Bolts in Shear. *Rock Mechanics and Rock Engineering*, 49,(7), 2723-2735. 10.1007/s00603-015-0907-7

Mosse-Robinson, S., Sharrock, G., 2010. Laboratory experiments to quantify the pull-out strength of single strand cable bolts for large boreholes, in: Hagan, P., Saydam, S. (Eds.), *Second Australian Ground Control in Mining Conference*. AusIMM, Sydney, Australia. pp 31-42

Rajaie, H., 1990. Experimental and numerical investigations of cable bolt support systems, Department of Mining and Metallurgical Engineering. McGill University, Montreal, Canada. pp 102-108

Reichert, R.D., 1991. A laboratory and field investigation of the major factors influencing bond capacity of grouted cable bolts, Department of Mining Engineering. Queen's University, Otario, Canada. pp 212-220

Stillborg, B., 1984. Experimental investigation of steel cables for rock reinforcement in hard rock, Divison of Rock Mechanics. Lulea University of Technology, Lulea, Sweden. pp 231-238

# STATIC AND DYNAMIC TESTING OF TENDONS

**Saman Khaleghparast<sup>1</sup>, Sina Anzanpour<sup>1</sup>, Naj Aziz<sup>1</sup>, Alex Remennikov<sup>1</sup>, Ali Mirzaghobanali<sup>1,2</sup>**

*ABSTRACT:* Underground support system using tendons has been one of the significant achievements in Civil and Mining engineering endeavours in facing challenges of ground control. However, shear failure of rock bolts is still one of the least monitored phenomenon in underground excavations with respect to seismic events. The understanding of the performance of rock bolts under dynamic loading condition requires a great deal of research. A series of tests were undertaken utilising a drop hammer mass of 600 Kg from a maximum height of 3.7 m over concrete blocks in the double shear box with chemical resin encapsulated a rock bolt to investigate the performance of rock bolts under dynamic shear load. Load cells, displacement laser and high speed camera were used to monitor the test. Results from the data analyses are presented in the form of displacement, hammer mass drop velocity, acceleration and force variation with time for all components involved in each test. The time factor was found to contribute 30 % of the shear load in static testing in comparison with dynamic; In particular, the force-displacement curve and energy absorption for the reinforcement system are presented to examine the performance of rock bolts and conclusion drawn.

## INTRODUCTION

Characterisation of the strength of rock bolts and cable bolts for underground mining is generally based on tensile and shear strength. These two properties are determined by static testing, however and in recent years, many tests have been reported on dynamically (Player, 2004, Plouffe, et al., 2008), The current thinking of ground reinforcement in underground mining has moved away from emphasising solely on ground support. The increased rate of mining development, production and mine operator safety is continuing to gain equal importance with ground support and its resilience in adverse mining environment. The prospect of ground seismicity and rock bursts requires special attention on support infrastructure installation effectiveness, both in metal and coal mining. The Beaconsfield gold mine collapse, in Tasmania, triggered by seismic activity and pressure bursts at Austar coal mine, due to high levels of stress contribution caused by the presence of disturbed structural geology in the region with fault zones and shear zones as reported by Galvin and Hebblewhite (2016) are stark reminder of the challenges that mines are faced with in adverse conditions. This necessitates the need for credible research on ground support under these adverse conditions under both static and dynamic conditions. The need for effective research on ground support credibility is of equal importance to the collapse of the ground due to gas outbursts, which are more common in coal mines worldwide and are well documented (<http://miningst.com/category/coal-mine-outburst/>). It is obvious that dynamic testing of tendons appears to focus on axial tensile testing and no reporting has been made on dynamic testing in shear. Tendon shear strength characteristics are important when shear deformation occurs across joints and shear zones, which are the weakest zones in ground structure that normally yields readily to rock burst or

---

<sup>1</sup> University of Wollongong, Wollongong, Australia, [naj@uow.edu.au](mailto:naj@uow.edu.au), Tel: +61 242213449

<sup>2</sup> University of Southern Queensland, Toowoomba, Australia

any other seismic activity. This paper describes the method of dynamic shear testing of tendons using double shear apparatus and compares the findings with static method.

## METHODOLOGY

The methodology used in this study will utilise testing of tendons by double shear tests.

### Double Shear Box

Aziz, et al., (2019) described four different types of the double shear boxes for undertaking research on tendon technology. They are;

- MK-I DSB; 600mm long consisting of a 300mm long prism block, sandwiched between two 150 mm side cubes. This rig is used mostly for testing small diameter rebar up to 24 mm in diameter as well as FG dowels.
- MK-II DSB; 1050mm consisting of a 450mm 300mm<sup>2</sup> central rectangular block sandwiched between 300mm<sup>3</sup> blocks
- MK- III DSB Friction free rig; a modified MK-II rig with lateral truss system consisting of four open channels braces attached to two 30 mm thick plates to maintain confinement for friction free shearing of the tendon, by maintain a constant gap between the joint planes of the concrete blocks
- MK- IV DSB (Naj's box); a 300mm diameter circular shear box of 450mm long central cylinder sandwiched between two 300 mm<sup>3</sup> blocks.

Two sizes of the double shear box were used in this study, MK-I and MK-III double shear boxes. These selected rigs were based on the comparative studies undertaken under both static and dynamic conditions as reported in this paper. Figure shows both types of double shear boxes used for static testing of various tendons. MK-I DS box was used for solid rock bolting study while MK-III was used for testing of cable bolts of varying shear failure strength. MK-III DSB was developed for testing of tendons for friction free sheared joint faces; with the near total applied shearing load being spent on cable bolt shearing.

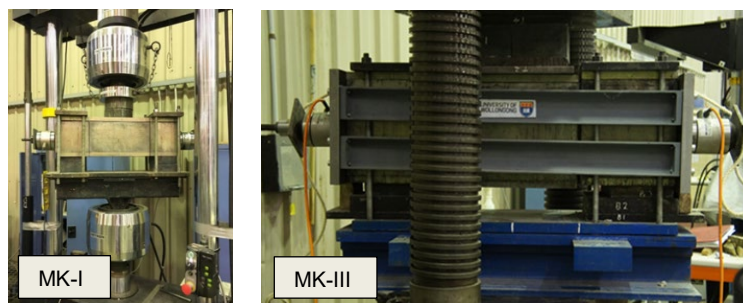


**Figure 1: MK-I and MK-III Double Shear Boxes**

### The High Capacity Impact Machine

The drop hammer test method simulates a high energy impact load condition similar in amplitude and velocity to a rock burst event. Therefore, in this study, the drop hammer was employed to examine the impact and shear performance of conventional rock bolts and cable bolts. Figure shows schematic and general view of the drop hammer load impact rig. The core of the test rig is the free-fall hammer having 592 Kg weight that can be dropped from a maximum height of 3.7m, or equivalent to the drop velocity up to 7.5 m/s. A 1200 kN dynamic load cell (Type Interface Model 1200) is attached to the hammer that can measure the force applied to the medium at the time of the impact. The drop hammer test method simulates a high energy impact load condition similar in amplitude and velocity to a rock burst event.



As the hammer falls, a laser gate triggers the load cell which allows data to be recorded by a data acquisition system. The data collected is transferred to a computer where the result can be analysed. High speed camera Fastec trouble-shooter was utilised to capture the high-energy impact between the drop hammer and the MK-I shear box with high accuracy. This allows an accurate analysis of the displacement of the central block during the shearing load over the period of time. Shearing displacement of the central block was also monitored through utilising a laser placing underneath the central block.

The MK-I set up box was seated on a U shape beam. The beam was placed between two based plates, which were anchored to the ground. The outer frames of the shear box were then clamped tightly with the base platform to avoid rotation of the blocks during drop loading impact. A laser was located beneath the U shape beam on the floor to capture the displacement of the central block during the experiment. To ensure the load from the drop hammer distributed evenly over the central block also prevent damaging to the box, a 30 mm thick plate was used on the top of the central block covered with a 3 mm thick plastic rubber. The potential height for each specimen was calculated based on the absorbed energy in static test calculated from the area under the Load-displacement curve.

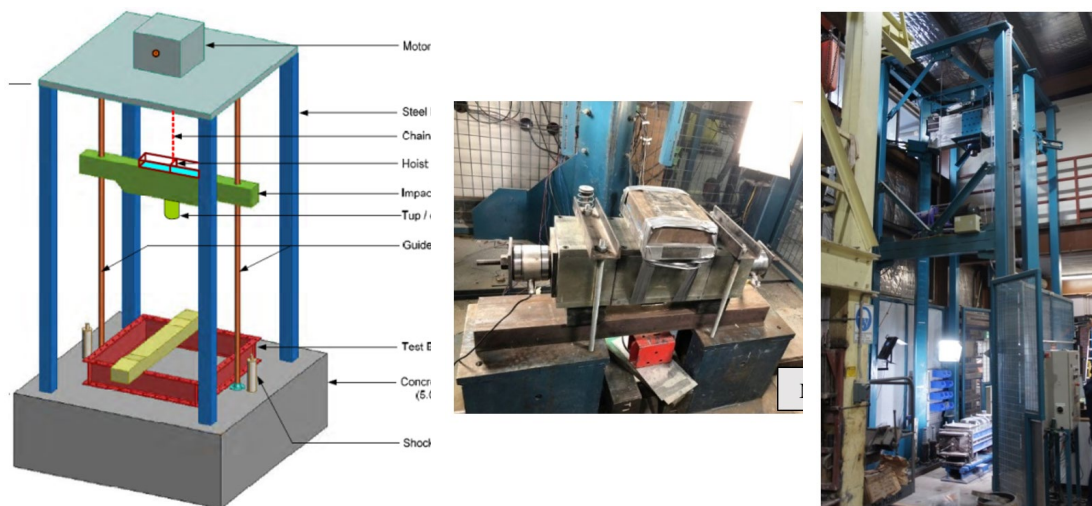


**Figure 2: Drop hammer test and MK-I set up**

### **Concrete block preparation**

For both box sizes the preparation of concrete blocks were cast in marine plywood moulds, although the steel frames of each box type could also be used satisfactorily. Two types of conduits were used to create holes for tendon insertion axially in each box and grouted. Three sizes of holes were created for shear testing, a 24mm, 42mm and 46mm holes. For 24mm hole in MK-I shear box, a 24mm plastic conduit covered with 3 mm electrical wire wrapped around it placed in the small moulds to created holes up to 24 mm in diameter for the desired bolt installation and encapsulation and also for larger borehole a 35mm solid steel rod with 6mm diameter PVC wrapped around it was used to create 46mm borehole. For larger MK-III diameter hole creation a 30mm solid steel pipe with 8 mm diameter PVC wrapped around it was used to created 42mm diameter hole.

Once mixed, the cement mortar, consisting of sand, cement, aggregate and water, was poured into each section of moulds. The mould was thoroughly covered with neutral grease for ease of concrete and steel pipe release. Once poured concrete was thoroughly vibrated using a hand vibrator and trawled to level and smoothen. Figure shows general views of both MKI and MKIII double shear boxes.

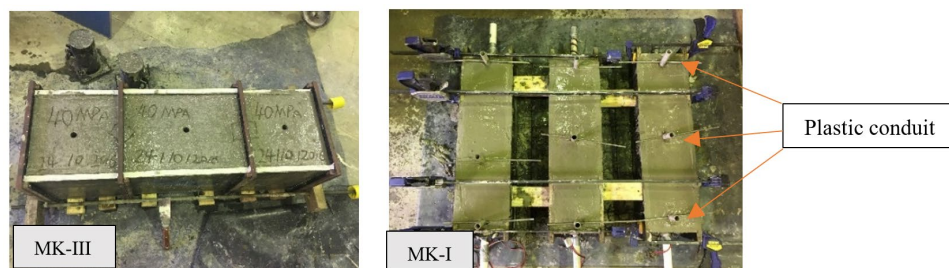


**Figure 3: Casting the concrete blocks**

Three small plastic conduits were inserted perpendicularly to reach the middle laterally placed conduit in the blocks as shown in Figure . Once the concrete was semi hardened, the conduit was removed from the centre of the blocks and the coaxial wire or tube was pulled out, leaving the hole wall with the image of the printed groove surface. The concrete was left for 24 hours to set and then removed and placed in a water bath for 30 days to cure. The concrete strength for this study was confirmed from UCS tests on 200 mm and 100mm diameter concrete cylinders prepared during concrete pour. Two types of rock bolt were examined for this study. 18mm DSI smooth rock bolt and 18mm Jennmar ribbed profile rock bolt. The double shear test also extended to include 15 mm diameter 7 wire cable bolts. A 1400mm long rock bolt with 300 mm thread on both ends was fixed into the concrete blocks using Minova Stratabinder HS cementitious grout with water: cement ratio of 0.4 for the encapsulation. Prior to grouting, pretension load was applied through tightening simultaneously the nuts on the both ends with wrench. Load was monitored using 150 kN load cells attached to data-taker. Once the pretension load reached, the sample left for 5 min allowing for relaxation and stabilization of the pretension load and then filled with grout. The specimen was left for seven days to cure. The specimen was then mounted in a steel frame shear box fabricated for this purpose. The testing apparatus consisted of a series of 20 mm thick steel plates secured by 34, 300mm screws. A base platform that fitted into the bottom ram of the Instron Universal Testing Machine, capacity 50 kN, was used to hold the MKI shear box. Two steel blocks with a thickness of 55 mm were placed beneath the two-outer entity of the concrete blocks to allow for central block to travel vertically as 110mm when shearing load is applied. The outer entity of the shear box was then clamped tightly with the base platform to avoid rotation of the blocks during shear loading. The applied displacement load on central block was set to the rate of 1mm/min and was controlled during the test process. Moreover, the vertical movement of the central block was limited into 100mm for each test. The compression machine embedded recording system was utilized to record the shear load, shear displacement and the axial load by data-taker hooked up to the load cells. The shearing load, displacement and axial load was monitored during loading throughout the test and it was possible to be visually seen on the computer screen.

#### **MK-III test sample preparation**

Individual concrete blocks were first mounted on the carrier base plate. The outer blocks were laid on solid steel plates while the central block was supported with adjustable height and removal metal base. The minimum block stand height was in the order of clearance height of 100 mm. A short 50 mm diameter PVC tubes were inserted between the central hole ends to bridge the gap across concrete joints and allow the flow of the grout in the hole. This is further reinforced with glued circular compressible foam ring packers, to ensure no leakage occurring in gaps between concrete blocks during cable grouting. Meanwhile, a lateral truss system was mounted axially across the assembled blocks to maintain and hold concrete blocks in a set place and prevent the adjacent concrete joint faces coming in contact with each other during pretensioning and shearing stage. The trust system consisted of two lateral 9 mm thick opened channel steel braces, which were mounted on each side of the shear box and screwed on two 30

mm thick side plates to prevent subjecting normal load on concrete blocks during shearing. Once the cable is inserted in the concrete frame and pre-tensioned to the required axial load, the cable as fitted with load cells at both ends and plates, followed by insertion of tightening barrel and wedges. The cable was then pre-tensioned using Blue-Healer tensioner to the recommended tension load. The pre-tension load on cable bolt was monitored by load cells connected on a data taker and computer. When the pre-tension load reached the required load, it was maintained loaded for several minutes and the hydraulic jack was then removed after the load to let the cable grouting to harden and ready shear testing at a predetermined grout aging period. This was the followed by grouting using Minova Stratabinder HS grout of the cement/ ratio of 0.4. The grout was then injected on to the install cable bolt hole poured through vertical connecting holes cast on the blocks and left to harden/set. The double shear assembled box was then covered with the top steel plates, clamped and tightened to a minimum of 40 kN for effective confinement. To avoid rotation and toppling of the side block during shear loading, eight steel bars were inserted into the base platform plate and to hold them firm on the base platform as shown in Figure 4. A total of five rock bolts and a cable bolt were tested prior to proceeding to the drop hammer test. The results are shown in Table .



Figure 4: MK-III Double Shear assembly

Table 1: Results of static and dynamic tests carried out on rock bolts and cable bolts

Test No.	Test Properties							Test Results		Test Analysis			
	Tendon Type	Tendon Ø (mm)	Pretension (kN)	Borehole Ø (mm)	Drop Height (m)	Concrete Strength (MPa)	Internal Confinement	Static Load (kN)	Dynamic Load (kN)	70% Static Load (kN)	Effective friction (%)	Absorbed Energy (kJ)	
											Static	Dynamic	
1	Ribbed Bolt	18	3	24	2	40	Yes	324.2	230	227	70	11.26	7.88
2	Smooth Bolt	18	5	24	1.5	40	Yes	332	227	232.5	68	10.57	7.12
3	Ribbed Bolt	18	3	24	2	40	Yes	324.2	236	227	72	11.26	7.62
4	Ribbed Bolt	18	5	24	2	40	Yes	342.8	200	240	58	13.07	8.55
5	Ribbed Bolt	18	3	46	2	20	NO	270	160	189	59	13.51	8.0
6	Plain Cable	15	5	42	2	40	NO	314	225	220	72	8.83	14.7

### RESULTS AND ANALYSIS

Table 1 lists the number of tests carried out in this programme of study. The table provides details of two different rock bolts and one cable bolt and their characteristics. Rock bolts and

cable bolts were tested in different strength concrete blocks of 20, 40 and 60 MPa, encapsulated with Stratabinder grout. The peak static and dynamic double shear loads, as well as energy absorbed by the DST system are shown in Table 1. The absorbed energy of the system was calculated, based on the static test at the loading rate of 1 mm/min, by estimating the area underneath the load-displacement graph using trapezoidal rule, shown as shaded section in Figure. . The drop test is a more reliable simulation of the in situ rock burst since the seismicity and the rock burst occurs suddenly at a short duration, similar to the situation of free weight drop. The input energy can be adjusted by the drop height. Weight drop height was considered to be constant at 2m to reduce the variable in the test.

A single impact load (tup) was applied to each specimen. When the first tup impacted the specimen, the specimen started to close-in laterally for 1-2 ms and then began to bounce back. The specimen started to accelerate vertically downwards when the rock bolt resistance exceeded the impact force with the middle block acceleration stopping within 10ms. Plastic deformation occurred when the dynamic load exceeded the elastic limit of the rock bolt. As a result of the impact load the load displacement with time graph, shown in Figure. can be divided into three stages. The initial stage (point1) is when the tup contacted with the plastic rubber and compressed the rubber until the specimen started bearing the load. In this stage the velocity of the tup decreased whilst the velocity of the specimen increased. This change is known as inertia effect and can be seen from the graph at the peak point (point 1). The second stage (point 2) occurs when both the tup and the specimen move downwards together, which is clearly shown in the displacement graph. In this stage the rock bolt played an important role in resisting any changes, due to a dramatic stress changes. The last stage (point 3) occurred when the rock bolt ruptured because of the dynamic force induced by the tup was greater than the bolt resistance force.

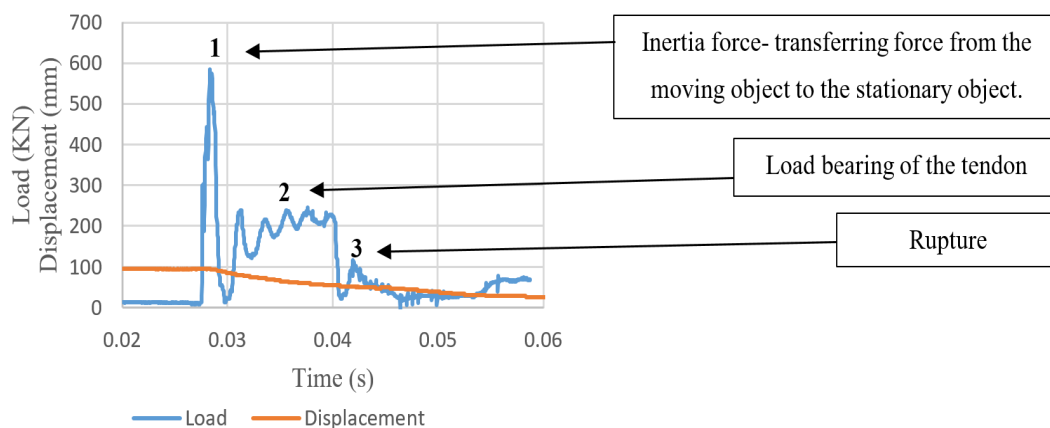


**Figure. 5: Load and displacement graph vs time in dynamic test of rock bolt**

### Internal confinement

Figure 6 illustrates effect of internal confinement on the performance of rock bolts in static and dynamic tests. The internal confinement of the concrete block contributes to increased concrete strength and stiffness, which minimises early concrete deformation around the tendon close to sheared joint faces, thus reducing concrete deformation depth at the hinge points by as much as 40%. As can be seen in 6, the slope of the graph with internal confinement is much steeper than no confinement graph, which means that the rock bolt is under greater shear stress than being in tension. Also the internal confinement prevents or minimises crack propagation axially along the sample, which indicates that the concrete will not fail early and the rockbolt eventually will fail in true shear rather than tension. Insufficient concert confinement would cause radial as well as axial cracking of the concrete blocks in the shearing zone, which would ultimately cause



the shear displacement to rise and this excessive deformation contributes to tendon failure in more tension rather than in shear (Figure.7).

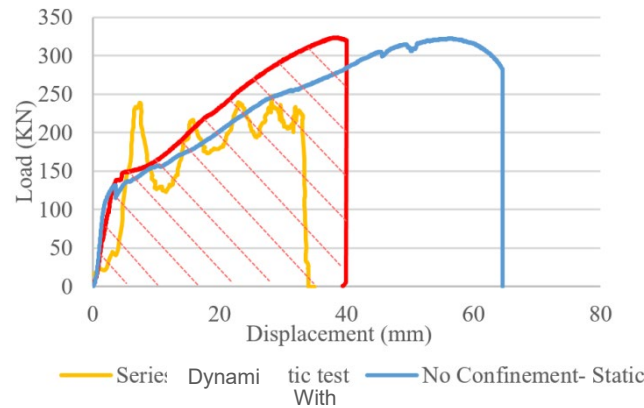


Figure 6: Test 2 Load- Displacement results and absorbed energy



Figure 7: Test 3- Sheared surface of 16 mm rock bolt in a confined concrete  
The effect of friction

The first generation of double shear box (MKI) is not frictionless, meaning that the friction is actively effective during the experimentation of tendon strength subjected to shearing. Therefore, the peak shear load is not the actual maximum shear load spent on tendon shearing rather it is attributed to the combination of shear load as well as the amount of load required to overcome the concrete joints face friction. A mathematical equation, based on Mohr- Coulomb and Fourier series system, was developed to calculate the friction force between the sheared joint faces of the host medium (Aziz, et al. 2015).

$$\tau_p = \left( \frac{a_0}{2} + \sum_{n=1}^3 a_n \cos\left( \frac{2n\pi T}{2\pi} \cos^{-1} \left[ \frac{-4a_2 + \sqrt{16a_2^2 - 48a_1a_3 + 144a_3^2}}{24a_3} \right] \right) \right) \tan(\phi) + c$$

Where  $\tau_p$  is the shear stress,  $C$  is cohesion,  $\phi$  is the angle of friction,  $a_n$  is Fourier Coefficient,  $n$  is the number of Fourier Coefficient, which varies between 0 and 3 and  $T$  is the shearing force travel, which is the characteristics of the shearing machine. Aziz, et al., (2015) found that 30% of the total shear force was spent on overcoming the friction between the shear joints. Aziz, et al. (2016) verified the effect of the equation with experimental test results. According to the outcome of the current research experiment, the dynamic shear load of rock bolt is equivalent to its static double shear load when the effect of friction is removed. The assumption is that

when the specimen is subjected to dynamic double shear load the effect of friction becomes negligible because the friction is a time dependent factor and the impact load occurs in a fraction of a second, therefore the time effect can simply be considered ineffective. As a matter of fact, this study verified the validity of the Mohr- Coulomb and Fourier series above stated equation.

Also, the 30 % effective friction can also be verified by the absorbed energy of the system calculated from the load-displacement graph. It can be claimed that the absorbed energy, calculated from the drop test, is close to pure shear capacity of the rock bolt. The static absorbed energy for test 3, Test 4 and Test 5 of 10.57 kJ, 11.26 kJ, and 13.07 kJ respectively, while the dynamic absorbed energy, as calculated from the Load-displacement graph of 7.12 kJ, 7.61 kJ, and 8.55 kJ of almost 70% of that from the static test (Figure. 8).

It is worth noting that dynamic testing of tendons can also be used for the study of ground reinforcements in areas prone to seismic activates and rock bursts, which is the current focus of research interest in coal mines of Australia and USA.

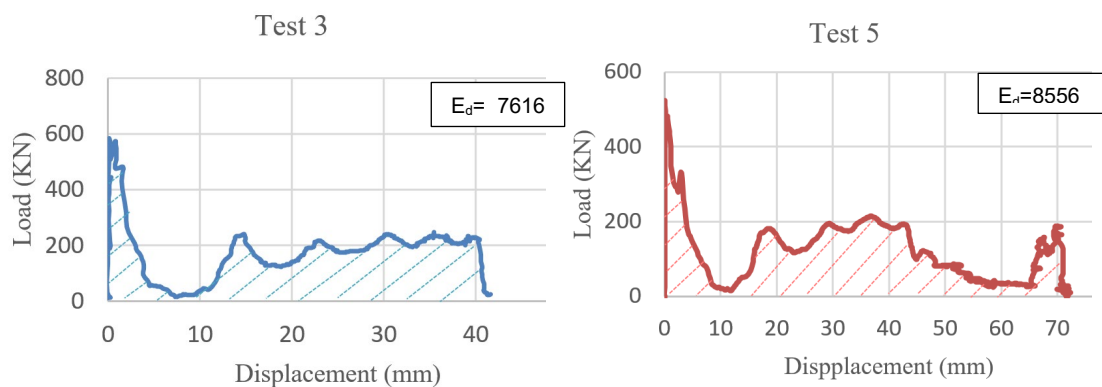


Figure 8: Load – Displacement in Dynamic test

## CONCLUSIONS

- The internal confinement for the current experimental research has proven to be effective methods, as it improves the strength of the host medium, which eventually leads to the tendon failure in more shears rather than in tension regardless of the effect of friction.
- The dynamic impact test results have verified the credibility of the Mohr- Coulomb and Fourier series equation in correctly estimating the proportion of the applied shear load spent on overcoming joint faces friction and to simulate the shear strength of bolted concrete blocks.

## REFERENCES

- Villaescusa E, Thompson, A and Player J R, 2005. Dynamic testing of ground support systems, Phase I, MERIWA project No M3492, 109 p,
- Plouffe m, Anderson T, Judge K (2008). Rock bolts testing under dynamic conditions at Cenmet- MMSL, in proc 6<sup>th</sup> international Symposium on ground support in mining and civil construction, TR Stacey and D F Malan(eds) 30<sup>th</sup> March -3<sup>rd</sup> April 2008,Cape town, South Africa< the south African Institute of Min and Met ], Johannesburg, pp 581 -395.
- Player, J P , Villaescousa, E and Thompson, A G., (2004), Dynamic testing of rock reinforcement using the momentum transfer concept, Ground support in mining and underground construction, Proceedings of the fifth international Symposium on ground support 28-30 September, Perth, pp 327-339 (Ed: Ernesto Villaescusa and Yves Potvin. ]

## Coal Operators' Conference

- Aziz, N., Craig, P., Mirzaghobanali, A., Rasekh, H., Nemcik, J. and Li, X., (2015b). Behaviour of cable bolts in shear; experimental study and mathematical modelling. Coal Operators' Conference, Wollongong, University of Wollongong, pp. 146-159. <http://ro.uow.edu.au/coal/559/>
- Stillborg, B., (1984). Experimental investigation of steel cables for rock reinforcement in hard rock. PhD Thesis, Lulea University, Sweden.
- British Standard BS7861-1, (2009). Strata reinforcement support systems components used in coal mines – Part 2: Specification for flexible systems for roof reinforcement, 48p.
- Aziz, N., Mirza, A., Nemick, J., Li, X., Rasekh, H. and Wang, G., (2016a) . Load Transfer Characteristics of plain and spiral cable bolts tested in new non rotating pull testing apparatus, Coal Operators' Conference, Wollongong, University of Wollongong, pp. 32-39. <http://ro.uow.edu.au/coal/591/>
- Aziz, N., Mirza, A., Nemcik, J., Rasekh, H. and Li, X., (2016b). A Follow up to Study the Behaviour of Cable Bolts in Shear: Experimental Study and Mathematical Modelling, Coal Operators' Conference, Wollongong, University of Wollongong, pp. 24-31. <http://ro.uow.edu.au/coal/590/>



# PERFORMANCE OF BOLTING SYSTEMS IN TENSION AND THE INTEGRITY OF THE PROTECTIVE SLEEVE COATING IN SHEAR

**Naj Aziz<sup>1</sup>, Antoine Schneiderwind<sup>2</sup>, Sina Anzanpour<sup>1</sup>, Saman Khaleghparast<sup>1</sup>, Duncan Best<sup>1</sup>, Travis Marshall<sup>1</sup>**

*ABSTRACT:* a series of laboratory tests were carried out on sleeved bolt and domed washer plates and nuts to determine;

- the tensile strength properties of 24 mm (200 mm core) diameter rock bolts (M24 Bolt),
- pull through testing of the bolting system consisting of bolt, domed washer plate and nut integrity,
- Integrity of the rock bolt fitted with protective plastic sleeve subjected to shearing.

All these tests were carried out on rock bolts and dome washer plates supplied by Dextra / Pretec. Pull testing was carried out in accordance with British Standard (BS 7861.1:2007). It was found that the average strength of tested bolts was 32.5 t, elongation 14.5 %. The maximum dome plate deformation load was in the order of 275 kN. No visible deterioration of the protective plastic sleeves was observed when bolts were sheared for vertical shear displacement of up to 25 mm.

## INTRODUCTION

The application of tendon technology in mine openings and tunnelling has become a corner stone of ground reinforcement and stability. The technology application revolutionised the way that underground openings been constructed and led to the birth and success of the New Austrian Tunnelling Method (NATM). One benefit of the use of bolting technology has been the excavation space saving as ground reinforcement NATM with bolting/mesh and shotcrete. Less ground is excavated for bolting support for the establishment of a competent opening and has had significant economic, space and efficiency benefit in comparison other methods of steel arched concrete and masonry construction tunnelling.

Steel rock bolts or cable bolts tend to deteriorate in time with respect to corrosion when tendons are left exposed to water and moisture over prolonged period of time. Accordingly, the effectiveness and endurance of the used steel tendon system depend on the quality of encapsulation, the ground stress variations and seismicity. The use of plastic sleeves has become a focus of interest in recent years for providing protection to bolts from corrosion for long-term ground stabilisation particularly around tunnels and long term underground mining structures. Ground movement and deformation can cause elongation, bending or shearing of tendon systems, which may lead to deterioration and formation of cracks in the bolt encapsulation coating as well as the plastic sleeves, allow humidity and ground water to come

---

<sup>1</sup>School of Civil, Mining and Environmental Engineering. University of Wollongong, NSW, Australia.

E-mail: [naj@uow.edu.au](mailto:naj@uow.edu.au), Tel:+61 242213449

<sup>2</sup> Dextra Building Products (Guangdong) Co., Ltd. China, E-mail: [aschneiderwind@dextragroup.com](mailto:aschneiderwind@dextragroup.com) Tel: +86 20 2265 9457

in contact with steel rock bolts thus affecting the system long term functioning . Accordingly, this paper deals with the laboratory study of the sleeved rock bolts system supplied by Dextra / Pretec to determine:

- Tensile strength properties of 24 mm (200 mm core) diameter rock bolts (M24 Bolt),
- Integrity of the rock bolts fitted protective plastic sleeves subjected to shearing. The 3 mm thick sleeves used was 30mm diameter and was not conical in shape as was used in cable bolt coating sleeve reported by Aziz, et al., (2017)

### EXPERIMENTAL PROCEEDURE

Table 1 shows the list tests carried out in accordance with the program of testing between Dextra Building Products Ltd, China / Pretec Pty Ltd and the University of Wollongong.

**Table 1: List of test types**

Component	Test Type	Parameters	No of tests	Test method
Bolt (1m)	Tensile	Yield Strength (YS), Ultimate Tensile Strength (UTS), Elongations at Yield Point (YP) at max. force	3	BS 7861.1:2007, Annex A
Bolt system	Pull through test	Dome washer plate deformation, pull through force and nut/ thread integrity	1	BS 7861.1:2007, Annex D
Rock bolt sleeve shear	Double shear test	Determination of the integrity of the rock bolt coated sleeve in shear	One test per vertical displacement of 15, 25 and 25 mm	UOW method of double shearing

#### Tensile failure testing of rock bolts

The tensile strength test involved subjecting the bolt to tension until failure, to determine the Ultimate Tensile Strength (UTS), elongation at both the yield point and at failure. Three 1.0 m bolts, supplied by Dextra were tested for ultimate failure. All three 1.0 m long bolts had the threaded ends cut out, leaving the middle 600 mm central section to be tested for tensile failure. About 350 mm lengths of the ribbed bolt sections were installed between the two large grip jaws of the 50 t Instron Universal Testing Machine (IUTM) and individually tested to failure. Figure 1 shows a general view of the tested sample and Figure 2 shows the load displacement graphs of all three tested bolts. The recorded yield load, peak failure load and displacement were listed in Table 2. Typically, all bolts failed in tension at the near mid-section, characterised with early necking of the bolt along the strained length. The tensile failure surfaces of snapped bolt sections were characteristically of cone and cup shapes formation as shown in Figure 3.

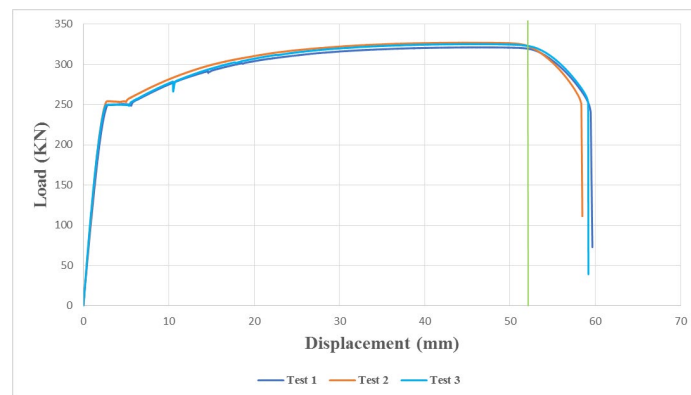
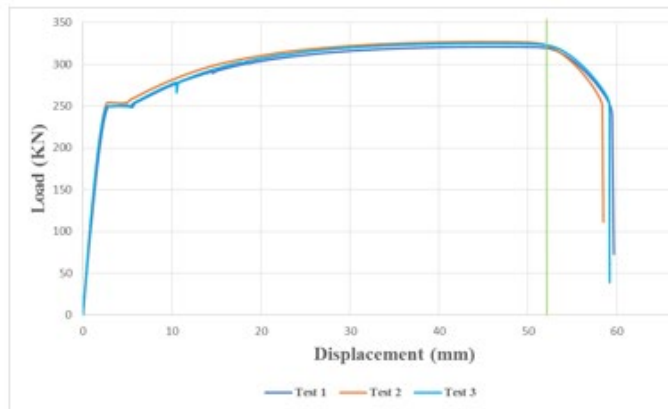


**Figure 1: 50 t Instron Universal testing machine**

**Figure 2: Load - displacement profiles of three bolts tested at a loading rate of 1 mm/min.**

**Plate deformation tests**

One dome plate fitted to sleeved bolt was tested for a plate deformation study. A loading frame was used for the pull testing. Figure 4 shows the assembled dome plate at the end of the sleeve bolt mounted on the test loading frame. Tests were carried out in accordance with the British standard (BS 7861-1:2007 /Appendix D). Additional photographs of the testing are shown in Figure 5 with the dome plate hole being enlarged from 55 mm to 63 mm through pulling, which enabled the bolt spherical grout injection head to pass through the enlarged hole.

Figure 6 shows the results of the dome plate deformation pull testing. The graph shows various stages of dome plate deformation and the bolt spherical grout injection head pulling through the loading frame hole. The following loads were obtained during the processing of pull testing;

1. The maximum peak load, achieved prior to the commencement of the plate deformation process was 274.73 kN with system elongation / deformation of 24 mm,
2. The second peak load depicting the start of the sudden incremental slipping of the bolt's spherical grout injection head through the gradually enlarged hole of the flattened dome-plate,
3. The third peak load in which the second sudden incremental drop of the spherical grout injection head begin to pass through the dome plate hole and gradually enlarging the dome plate hole ( Figure 5).

- Final spherical head passing fully through the enlarged dome head hole of diameter of 63 mm with a pulling force of 53 kN. This stage occurred after stage 3 pull out was stopped as shown in Figure 5.

**Table 2: test details of three M24 bolts tested to failure. In (A) the individual ultimate tensile failure load and elongation, yield load and their respective elongations/displacements are shown. In (B) the average values of UTS, yield point, displacements and percentage elongation are given.**

<b>(A) Bolt sections tensile strength test results – DEXTRA Bolts</b>							
Test No.	Date	Tested bolt length (mm)	UTS (kN)	Max elongation (mm)	% elongation	YP (kN)	TP Disp. (mm)
Test 1	09/05/2019	362	321.41	51.79	14.3	250	2.9
Test 2	09/05/2019	350	327.23	51.76	14.7	253	2.7
Test 3	10/05/2019	354	325.55	52.10	14.6	247	2.7

<b>(B) Results Summary</b>	
Average UTS (kN)	324.73
Average of max elongation (mm)	51.8
Average elongation (%)	14.5
Average yield point (kN)	250
Average elongation at YP	2.76



**Figure 3: Pull tested rock bolts to failure, the failure points were at /near the middle of each test sample. Note the cone and cup failures of snapped bolt at the necking zones.**

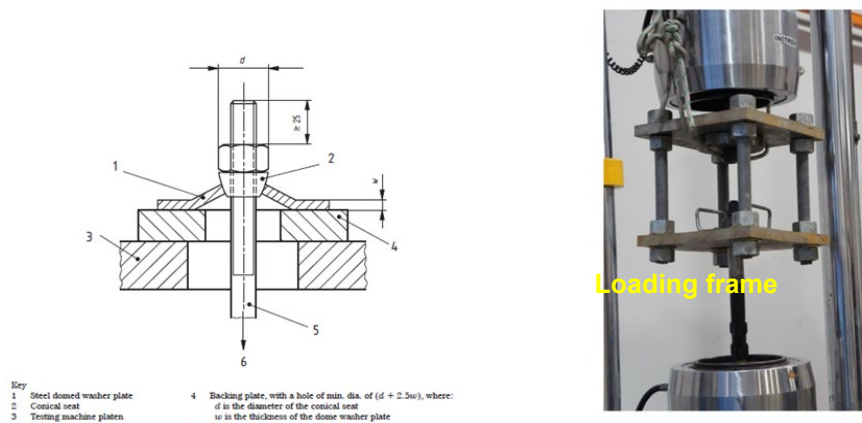


**Figure 4: Test arrangement for tensile deformation testing of dome plate mounted**



**Figure 5: Dome washer plate and enlarged plate hole with the bolt spherical grout injection dome being pulled through the plate**

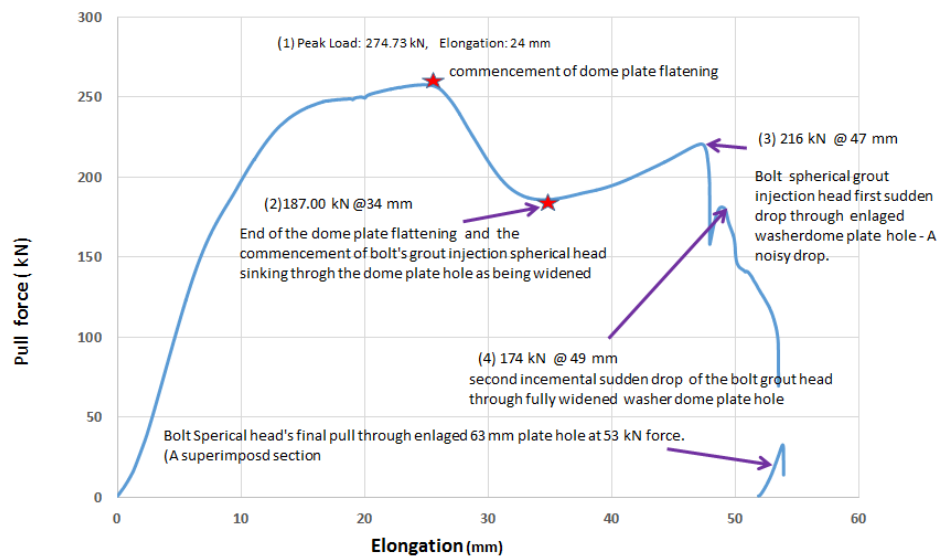


**Figure 6: Pull testing of the bolt system during the various stages of pulling the bolt out of the dome washer plate**

### Double shear strength of sleeved bolts

The shear testing rig used was DS MK1 type rig consisting of two 150 mm side cubes and a central 300 mm rectangular central block. The rig size was adequate because of the type of test undertaken, as a limited shear displacement was needed in this study. The 300 mm long middle section of the double shear apparatus was vertically shear loaded at the rate of 1 mm/min for a specified vertical displacement. The rate of loading and displacement was monitored and simultaneously displayed visually on a PC monitor. Also monitored was the build-up of the axial loads during the shearing process. The process of preparing the sleeved bolt for double shear testing involved, grouting the sleeve on the bolt, preparation of the concrete blocks and encapsulation of the bolts in the concrete.

*Grouting of the sleeve on each bolt:* Prior to double shear testing the plastic protective sleeve was secured over the bolt by internal grouting. The 2 mm thick sleeve is around 33 mm in diameter with bulges, which makes the overall diameter in the order of 41mm. Figure 7 shows the methodology of the internal grouting of the sleeve on each bolt. Once held vertically the grout was poured through the hole in the spherical head of the bolt down the column annulus space between the bolt and sleeve. The grouted sleeve was left to harden for 24 hours prior to assembling the system in the double shear rig.



*Concrete blocks preparation:* The strength of the concrete used in the double shear testing of the sleeved bolts was 20 MPa, in order to simulate shearing in relatively soft rock formation. The sleeved bolt was to be encapsulated in 45 mm diameter hole cast in the double shear box. Concrete blocks were cast in marine plywood moulds of the same dimension as the actual steel double shear box confinements. A 30 mm diameter steel conduit rod wrapped with 8 mm diameter PVC plastic tube was used to create 45 mm hole along the concrete blocks central axis. The constituents of the concrete solid ingredient mix proportion consisted of cement /sand/gravel with the ratio of 1:1.5:3 through the pre-cut holes in the centres of the blocks. Gravel of average of 5 mm was sieved to control its size. Figure 8 shows three vertical holes cast in concrete blocks to permit charging grout through and encapsulation of the sleeve bolts in the concrete block. A 20 mm diameter PVC pipes were used to create three holes along the axial length, with one hole being made per block. Three double shear samples were cast at the same time. Once the concrete was poured into assembled moulds and let to semi harden for a period of six hours, the conduits were removed from the set concrete blocks, then followed by the removal of 8 mm PVC tubes. Figure 9 shows a typical view of the PVC tube wrapped steel conduit for creating a 45 mm hole in the concrete blocks. After 24 hours of the initial casting the concrete blocks were removed from the moulds and placed in a water bath for a period of 28 days to cure. The rock bolts were then installed in the cured blocks and each pretensioned to 50 KN force and grouted. Figure 10 shows the fully assembled DS MK-I rig being tested for shear.



Figure 7: Sleeve grouting on to bolts



Figure 8: Vertical holes connecting with the sleeved encapsulation hold for sleeved bolt encapsulation

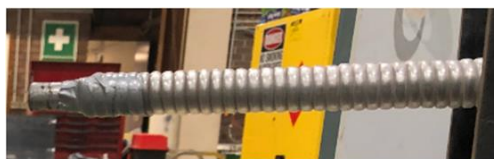


Figure 9: Rifling of central hole for bolt encapsulation

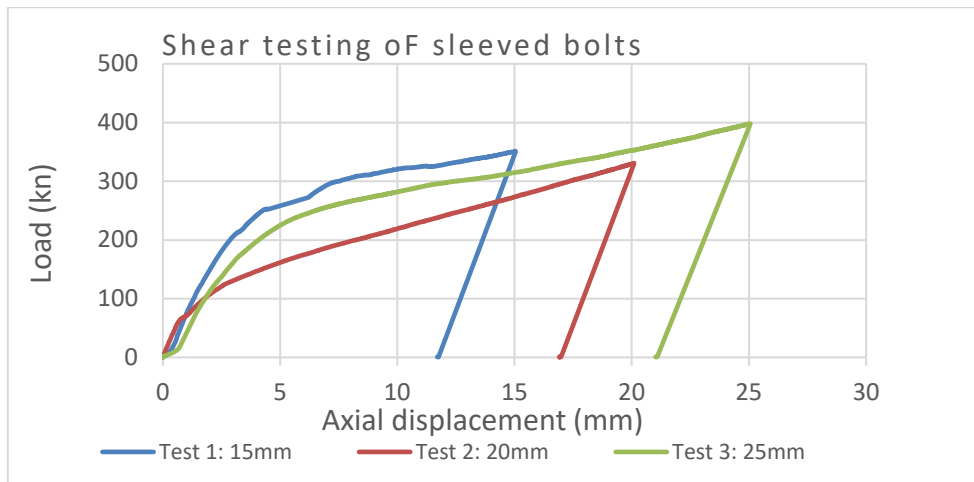


Figure 10: Fully assembled DS MK-I rig with a pretensioned body

### TEST RESULTS AND DISCUSSION

Three assembled bolts were tested for vertical shear displacements of 15, 20 and 25 mm. The rate of shearing load was maintained constant at 1 mm/min. Figure 11 shows the profiles of the

shearing for three vertical shear displacement combined into one shear load – displacement graphs. Table 3 shows the details of the three tests with maximum loads.



**Figure 11: Profiles of the shearing for three vertical shear displacement combined into one shear load – displacement graphs**

Figure 12 shows the photos of the tested blocks and exposed grouted bolt post testing. Figure 13 shows the views of the three post-test sleeves. No sleeve was torn in any of the three shear-tested bolts, however.

**Table 3: Details of the three tests with maximum loads**

<b>Test Name:</b>	Shear Test	
<b>Test Date:</b>	3/07/2019	
<b>Test properties:</b>		
sample size	MK1 (300*1050*300)	
sample strength	20 MPa	
borehole dia	45 mm	
grout type:	Crosbe (W/C 0.32%)	
Loading Machine	Instron	
Loading rate	1 mm/min	
<b>Test results:</b>	<b>Max vert displ (mm)</b>	<b>Max load (kN)</b>
test 1	15	351
test 2	20	331
test 3	25	398

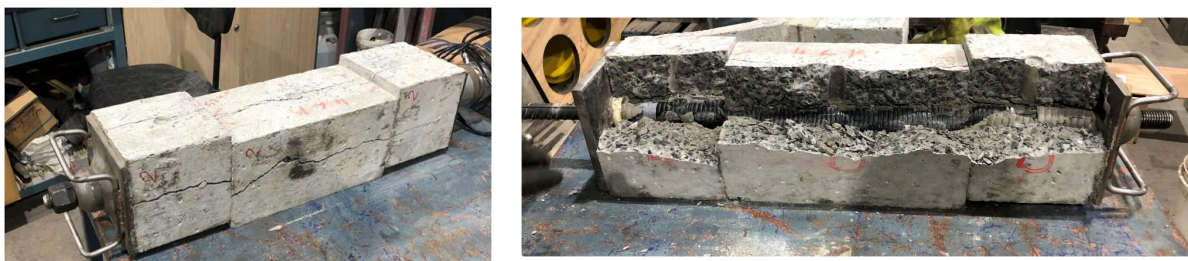


**Figure 12: photos of double shear tested block and exposed grouted bolt post testing**



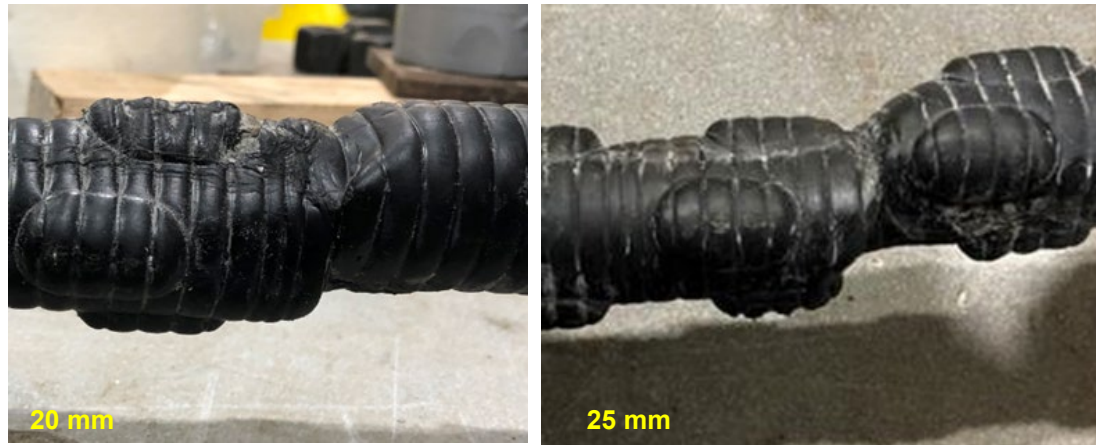


**Figure 13: Typical deformation of the bolt sleeve at shear displacement of 20mm and 25 mm**

### CONCLUSIONS

The following conclusions are drawn from the study:

- 1) *Bolt strength*: The average UCS of the three tested bolts was 324.73 kN, the average maximum elongation was 51.8 mm and average yield point was 250 kN
- 2) *Bolt plate and system deformation*: The maximum peak load achieved prior to the commencement of plate deformation process was 274.73 kN, at system elongation/deformation of 24 mm. The spherical head passed fully through the enlarged dome head hole of diameter of 63 mm with a pulling force of 53 kN.
- 3) *Double shear strength of the sleeved bolts*: No visible deterioration of the plastic sleeves was observed when bolts were sheared for vertical shear displacement of 15, 20 and 25 mm respectively.

### REFERENCE

Naj Aziz, Ali Mirzaghobanali and Matthew Holden, 2017. The extent of shearing and the integrity of protective sleeve coating of cable bolts, Coal Operators Conference, PP 239-245.

British Standards BS 7861-1, 2007. Strata reinforcement support system components used in coal mines. Part 1, specifications for rock bolting.

# THE EFFECT OF ELEVATED TEMPERATURE ON RESIN-ANCHORED ROCK BOLTS

Kent McTyer<sup>1</sup>

**ABSTRACT:** Resin-anchored roof bolts are used for primary roof support in all Australian underground coal mines. This popularity is due to a combination of technical performance, installation efficiency and cost. Further, many years of research exists pertaining to the load transfer of resin-anchored bolts. However, the composition of the load transfer medium – the resin anchor – means the resin-anchored bolt system is susceptible to possible degradation if high temperatures are applied. Thankfully, while high temperatures of more than 100°C are uncommon in coal mines, there is a rare event that can cause high sustained temperatures – a coal mine fire.

Modern firefighting methods are often successful in extinguishing mine-wide fires. Once extinguished, re-entering the mine and re-establishing coal production becomes a focus. However, introducing workers underground requires careful evaluation of the condition of the existing heat-affected resin-anchored roof bolts. It was the shortage of research into heat effects on resin-anchored roof bolts led to this study. The key aims were to quantify the degree of heat conducted along the roof bolt, the effect of elevated temperature on roof bolt load transfer, and identify any effects on the exposed steel elements that comprise the lower anchor of the roof bolt. Test information produced by this study allows mines to both better evaluate ground stability risk, and identify remedial ground support requirements during mine re-entry.

## INTRODUCTION

Resin-anchored rebar bolts are the minimum-level of ground support used in the roof of every Australian underground coal mine. These primary support elements are used due to a combination of cost, efficiency of installation, and technical performance. However, like all things, the resin-anchored roof bolt has a working range that is subject to environmental conditions. While much research has been performed on the load transfer of roof bolts when subject to parameters such as axial and shear load at routine temperatures, less focus has been placed on the effect of extreme environmental factors such as high temperature. This is not surprising given that all coal mines in Australia operate within a relatively narrow ground temperature range from approximately 10 to 30°C. Thankfully rare however, is an event that can lead to extremely high temperatures within a mine – this being an underground fire.

Underground coal mine fires can be one of two general types; localised - such as a fire on a conveyor belt (Figure 1a) or extensive - such as those that may initiate in a longwall goaf and progress to other parts of the mine. Either way, the presence of an underground fire results in very high temperatures adjacent to the flame front. Accurate coal mine fire temperatures are unknown, but physical tests in a decommissioned vehicle transport tunnel have measured gas temperatures of between 1280 and 1370°C at the roof level (Ingason et al 2011, and

Bechtel/Parsons Brinckerhoff (1995). In addition, coal fire tests at a purpose-built mine fire model gallery by the Central Mining Research Institute in Dhanbad India (Figure 1b) recorded maximum temperatures of 1100°C (Singh and Ray 2005). Even allowing for the temperature dissipating effect of convection, fires have the potential to dramatically increase the temperature

---

1. *Geotechnical Engineer, DSI Underground. Email: [kent.mctyer@dsiunderground.com.au](mailto:kent.mctyer@dsiunderground.com.au) Tel: +61 400 262 818*

of the protruding tail of steel roof bolts. How this high temperature affects the integrity of resin-anchored bolts - including their ability to continue providing ground support – is untested. This was a key concern of mine management when considering re-entering areas of the mine affected by fire.



**Figure 1: (a) rescue team fighting a conveyor belt fire (Conti 2001), and (b) Dhanbad fire test gallery (Singh and Ray 2005).**

Limited research exists into the effect of elevated temperatures on resin-anchored roof bolts. Further, none exists that replicate the mechanisms involved during a mine fire. The mechanism involved is relatively simple. Heat from a fire is transferred to the protruding tail of the roof bolt via convection. Then, via conduction, the heat travels along the bolt some distance. In so doing, the heat will also raise the temperature of the cured resin in the annulus between the bolt and the rock of the surrounding drill hole. Currently unknown is both how far the conducted heat travels along the bolt, and how this conducted heat affects the resin bond between bolt and rock.

A further question relates to the effect of the elevated temperatures on the properties of the protruding steel elements. The lower anchor of a bolt is comprised of the bar, nut, dome ball and bearing plate. These bolt elements are composed of steel of different grade, and formed using different temperatures and methods. The high temperatures will logically alter the properties of these steel elements. How the altered lower bolt anchor responds to the forces applied during ongoing ground support duty is also currently untested.

This study aimed to quantify several key impacts on roof bolts used for ground support in Australian coal mines. These are:

- The conduction of heat along a commonly used steel roof bolt.
- The effect of heat conduction on the load-transfer capacity of the bolt-resin-rock bond.
- The effect of heat on the performance of the steel lower-anchor elements of a roof bolt.

The objective was to identify the potential effect of mine fires on the performance of resin-anchored roof bolts. With this information mine site engineers will have both greater understanding of the state of installed support, and be able to assess and design remedial support for areas affected by elevated temperatures. Without access to a mine fire-affected area, this study was performed in a laboratory-based setting. Thus, results presented are representative of relatively controlled conditions – something to be considered when evaluating the effects from a real mine fire.

## TEST PROCEDURES

Tests were performed using the following consumables:

- 1.8 m-long HSAC840 grade steel, 21.8 mm core diameter steel bolts (840 MPa). These are hot-rolled bars (approximately 1200°C) with cold-rolled threads. Bolts were fitted with 36AF nuts (350 MPa), dome ball, and 150 mm diameter x 5 mm thick star plate (400 MPa).
- Resin capsules used were 1200 mm-long 24 mm diameter two-speed polyester resin (with limestone filler).
- 1800 mm-long, 101.7 mm outer diameter, 93.7 mm inner diameter steel cylinders filled with approximately 80 MPa cementitious grout.

Drilling and installation of resin-anchored bolts was conducted using the DSI coal mine equivalent Sandvik D0100 drill rig. 28 mm-width round-button PCD drill bits were used to drill the holes before resin-bolt installation. The drilled hole simulates underground drilling conditions in a homogenous strata-type. Instrumentation during bolt installation recorded bolt travel (displacement) and revolutions per minute (rpm). These measurements ensured consistent installation practice occurred for the tested bolts.

Once installed, resin-bolts were stored for more than two-weeks at ambient temperature to allow full curing of the resin to occur. Protruding bolt tails were then placed in a gas-fired Martin Furnace with an operating temperature of approximately 950°C (Figure 2). Duration of heat application was approximately 28 hours to ensure heat conduction equilibrium would occur along the bolt length. Bolts were placed tail-first into the furnace to simulate the heat application during a mine fire. Thermocouples were placed on two bolts encased in grout. Steel, grout and resin was removed in slots to allow fitment of adjustable ring thermocouples (Figure 3). The purpose of the thermocouples was to measure the conduction of heat along the steel bar. A further three bolts encased in grout cylinders were placed in the furnace without thermocouples for later load transfer testing. These heat-affected bolts were compared to three bolts installed into grout cylinders but not exposed to the furnace. Lastly, bolts not installed into grout cylinders were placed in the furnace for later tensile testing of the lower anchor components.

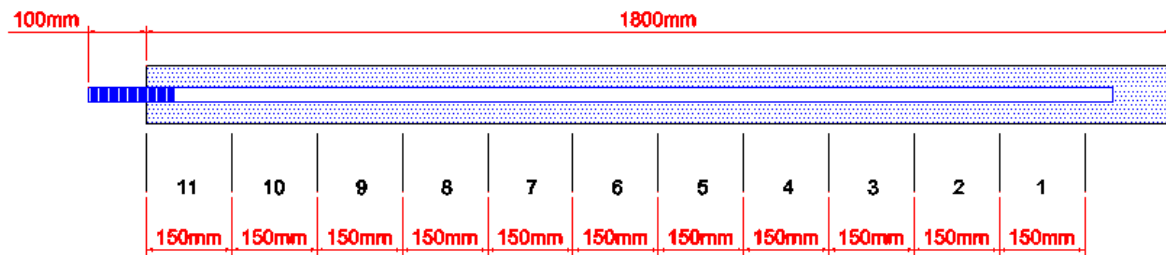


Figure 2: DSI Martin Furnace with test pieces (left) and max. furnace temperature (right)



**Figure 3: Thermocouples were fitted to a 1.8 m-long bolt installed in a grout-filled steel cylinder. Note the resin was removed to allow fitment of the thermocouple to the bolt steel.**

Bolts installed in grout-filled cylinders were then sectioned for load transfer testing by the push-test method. Sample length was 150mm (Figure 4). Push-testing was chosen as it provides a full load-transfer profile along the entire bolt.



**Figure 4: Push test sample arrangement**

Heated bolts that were not installed into grout cylinders were tested under axial loading to evaluate any change in performance of the lower anchor components. The tensile test arrangement included the roof bolt lower anchor components of nut, dome ball, and bearing-plate (Figure 5). The heat-affected bolts were compared with non-heat affected bolts. Free length between cross-heads was 600mm for all tensile tests. Both push tests and tensile tests were performed on a Universal Test Machine (UTM) located in the DSI test laboratory.

## RESULTS AND DISCUSSION

A total of eight bolts were installed on the drill rig. Installation averages are shown in Table 1.

**Table 1: Average bolt installation parameters**

Number of Bolts	Bolt Insertion Rate	Mix Time at Top of Hole	Rotation Hold Time
8	135 mm/second	5 seconds	40 seconds





**Figure 5: Tensile test arrangement of complete lower-anchor assembly comprising bolt, nut, dome and bearing-plate**

The manually-controlled bolt installation measures show they were both consistent and simulate manufacturer's recommended underground installation practice. Consistency was important to reduce variability when conducting the load transfer testing – especially drill hole profile. Feed rate during drilling was set to 48 mm/second which created a uniform rifled profile (Figure 6).



**Figure 6: Example of the drill hole profile produced using a consistent drill feed rate**

After installation and curing the bolt tails were placed in the furnace (Figure 7). Exposure time was 28 hours. During testing the section of the bolt protruding into the furnace was glowing yellow-orange which equates to approximately 950°C (Figure 7).

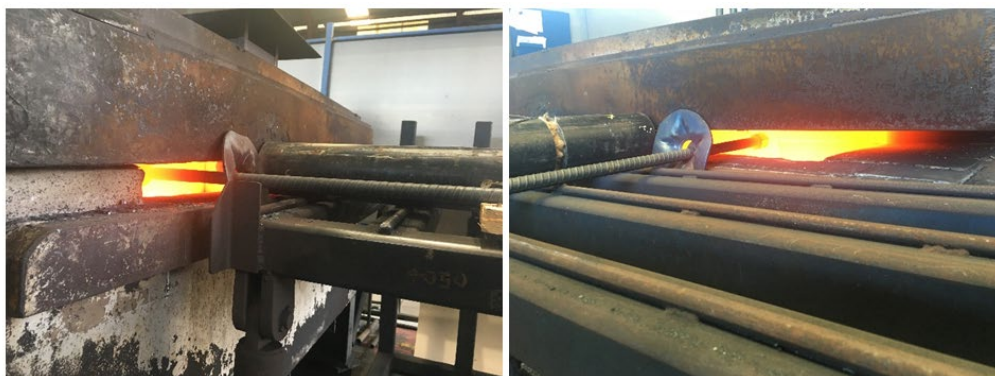


**Figure 7: Bolt colour appeared yellow-orange or approximately 950°C**

#### **Heat conduction along the bolt**

The datalogger had four channels. Thus, two separate heat conduction tests were performed. The first fitted thermocouples at 100, 300, 500 and 700 mm from the furnace, while the second

fitted thermocouples at 900, 1100, 1300 and 1600 mm from the furnace. There was a slight variation in the recorded time of maximum temperature between the two test days due to variation in ambient temperature. During test day 1 the maximum temperature was recorded at 02:30, and during test day 2 at 01:00. The plot of the temperature over time (**Figure 8**) indicates that maximum temperature for the given test arrangement was achieved – allowing for convective heat loss to atmosphere.

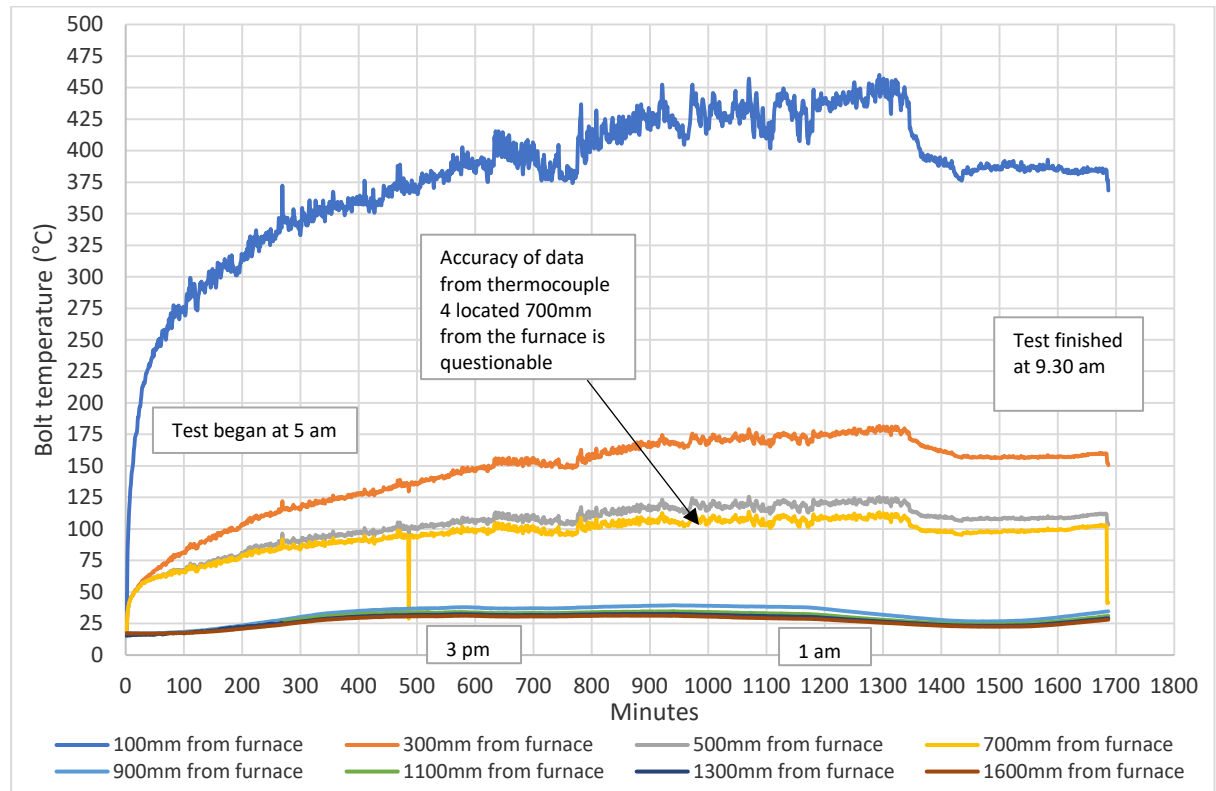


**Figure 8: Plot of thermocouple temperature over the 28-hour test period**

Not surprisingly, the highest temperature was recorded at the thermocouple closest to the furnace (Table 2). From this point an exponential decay in temperature was measured (Figure 9). Unfortunately, the thermocouple located 700 mm from the furnace appears to have read erroneously high. A smoother temperature decay curve was expected.

**Table 2: Median and maximum temperature measured along the grout-encased bolt**

Distance from furnace (mm)	0	100	300	500	700	900	1100	1300	1600
<b>Median temperature (°C)</b>	925	387.0	156.7	108.4	98.6	35.0	31.5	29.6	28.4
<b>Maximum temperature (°C)</b>	950	460.1	181.8	125.7	113.8	39.5	34.9	32.7	31.3



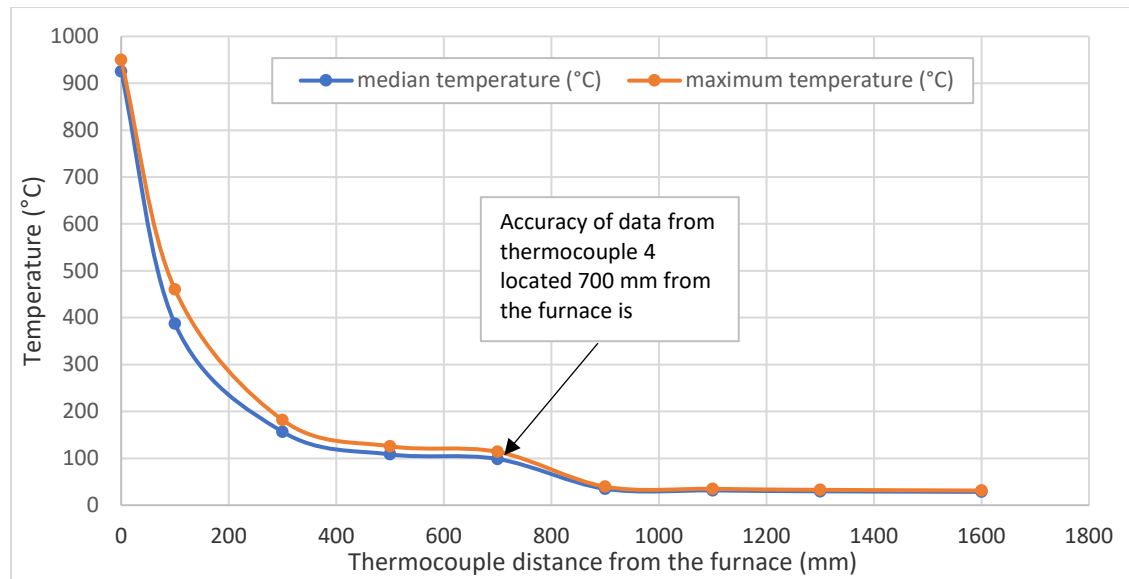


**Figure 9: Median and maximum temperature measured along the grout-encased bolt**

It is noted that the ambient temperature during testing ranged from approximately 17°C to 25°C. However, the maximum temperatures were recorded when the furnace-adjacent factory door was shut at night. This suggests the test temperature measured was more strongly affected by convection conditions than the ambient temperature. Thus, it is proposed that in a mine environment, where convection is negated, higher temperatures would be conducted further along the bolt for similar bolt tail temperatures.

**Heat effects on rock-resin-bolt load transfer**

Six bolts installed into grout-filled cylinders were sectioned for bolt push-out load testing. Three bolts were exposed to the furnace and three were not. Bolts were cut into 150mm-long test pieces (eleven per bolt) to give a total of 66 samples. After sectioning evidence of soft, uncatalysed resin was observed in the upper 300-400 mm of the heat affected bolts and upper 400 mm of one of the non-heat affected bolts (Figure 10). This phenomenon has been previously documented when using small catalyst percent resin capsules common to the Australian market (Campbell and Mould 2003, Campbell et al 2004, Compton and Oylar 2005, McTyer 2015). Uncatalysed resin was attributed to the geometric relationship between drill hole diameter, bolt diameter and catalyst to mastic cross-section within the capsule.





**Figure 10: 150 mm-long samples prepared for push-testing (top), uncatylsed resin (bottom left), and heat-affected sample (bottom right)**

Push testing was conducted using a consistent loading rate. The peak push-out load was achieved between 2-4 mm of bolt displacement. Average push test load results are plotted in Figure 11 and assembled in Table 3. The resin bolt load transfer tests displayed inherent variability, typically higher for the heated bolts, as noted by the standard deviation. Uncatylsed resin affected both the upper 300-400 mm of the heated bolts, and the upper 400 mm of one of the non-heated bolts. This resulted in a substantial reduction in load transfer. The general load transfer trend from the non-heated bolts was a reduction in load from the bottom to the top of the bolt. The trend was less visible in the heated bolts where uncatylsed resin affected the upper portion of the bolt, and elevated temperature affected the bottom.

**Table 3: Individual push test results, averages and standard deviations**

Sample Horizon	Heated 1 (kN)	Heated 2 (kN)	Heated 3 (kN)	Average (kN)	Standard Deviation
0 to 150 mm	6.1	16.8	16.8	13.2	6.2
150 to 300 mm	40	34.5	51.8	42.1	8.8
300 to 450 mm	44.4	42.6	59.7	48.9	9.4
450 to 600 mm	18.4	30.1	31.4	26.6	7.2
600 to 750 mm	19.8	41.3	29.8	30.3	10.8
750 to 900 mm	44.6	65.5	33.6	47.9	16.2
900 to 1050 mm	25.6	29	26.9	27.2	1.7
1050 to 1200 mm	23.4	33.8	24.6	27.3	5.7
1200 to 1350 mm	17.9	27.7	7.1 <sup>1</sup>	17.6	10.3
1350 to 1500 mm	1.4 <sup>1</sup>	32.4	6.1 <sup>1</sup>	13.3	16.7
1500 to 1650 mm	0.3 <sup>1</sup>	3.6 <sup>1</sup>	3.9 <sup>1</sup>	2.6	2.0
Sample Horizon	Non-Heated 1 (kN)	Non-Heated 2(kN)	Non-Heated 3 (kN)	Average (kN)	Standard Deviation
0 to 150 mm	91.8	62.6	Failed to record	77.2	20.6
150 to 300 mm	69.3	65	71.1	68.5	3.1
300 to 450 mm	79.3	71.3	79.6	76.7	4.7
450 to 600 mm	44.6	44.1	38.4	42.4	3.4
600 to 750 mm	Failed to record	36.6	47	41.8	7.4
750 to 900 mm	37.5	26.4	32.7	32.2	5.6
900 to 1050 mm	62.5	36.8	30.3	43.2	17.0
1050 to 1200 mm	43.2	38.3	30.3	37.3	6.5
1200 to 1350 mm	74.6	5.7 <sup>1</sup>	27.6	36.0	35.2
1350 to 1500 mm	54.3	41.7	28.2	41.4	13.1
1500 to 1650 mm	24.3	1.8 <sup>1</sup>	29.6	18.6	14.8

<sup>1</sup> strongly affected by uncatylsed resin

The heated bolts returned lower loads for all horizons (except 750-900 mm) than the non-heated bolts. These lower load transfer results – especially above 900 mm – are not considered a function of the 10 to 15°C elevated temperature above ambient. Rather, it is judged an anomaly of the current tests, but uncertainty remains. The higher heated bolt result at 750-900

mm is also considered uncharacteristic, with the 65.5 kN result due to bolt connection with the grout. In comparison, the lower overall loads for heated bolts make sense near the furnace where heat altered the resin and surrounding grout (Figure 10). Resin and grout were visibly discoloured in the lower three 150 mm-long samples. The lower 750 mm of the bolts saw the greatest adverse effect of heat when compared with the non-heated bolts. Load transfer was reduced by 83% from 0-150 mm, 39% from 150-300 mm, 36% from 300-450 mm, 37% from 450-600 mm, and 28% from 600-750 mm. It is noted that from 750-1200 mm the load transfer was approximately 30% higher for the non-heated bolts. Thus, it is judged that the adverse effect of heat was only seen to approximately 600 mm from the furnace. This location corresponds to a median bolt temperature of approximately 100°C as measured by the thermocouples, and suggests that temperatures below 100°C did not result in the deterioration of the resin. Thus, load transfer performance was maintained.

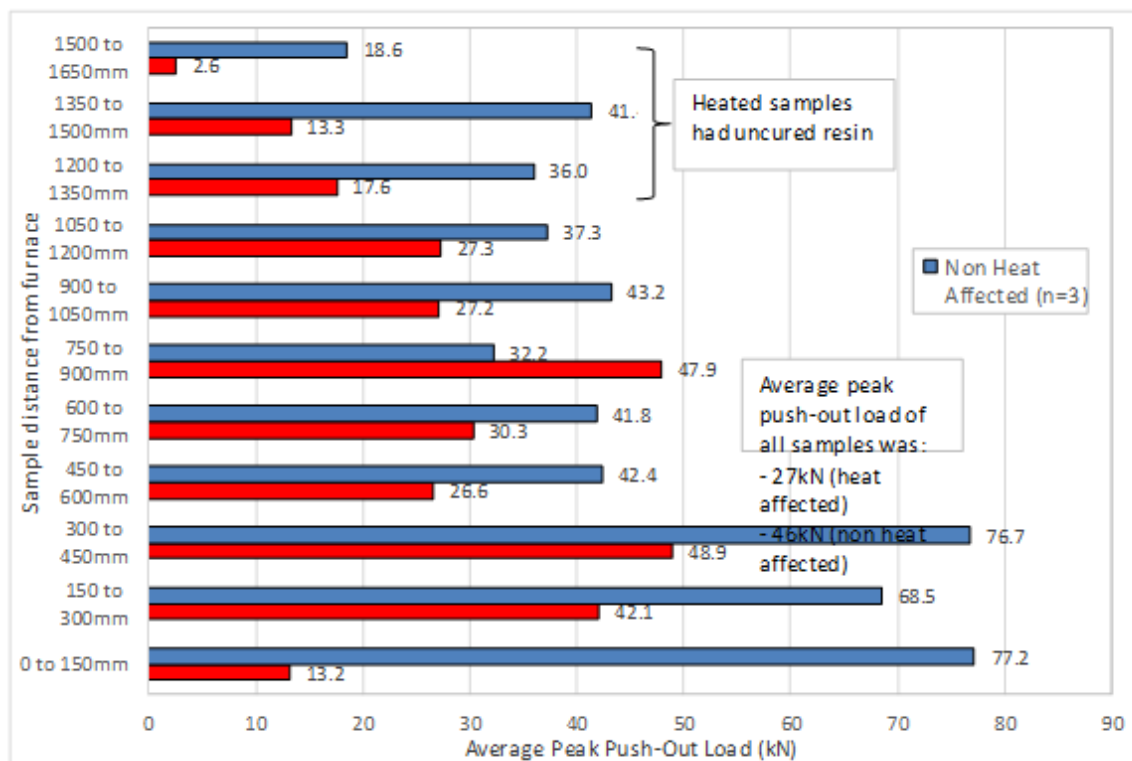


Figure 11: Average peak push test load by sample distance from the furnace

Overall, the effect of heat was to reduce the load transfer capacity of the lower 600 mm of the bolt. As the upper half of the bolt was deemed unaffected, the bolt will still function as designed from this upper anchorage – so long as the steel elements of the lower anchor are also unaffected.

#### Heat effects on tensile performance of the bolt lower anchor

Two tensile test methods were used. Firstly, a test of the complete lower-anchor assembly (including the bearing plate) over a steel plate with 70 mm diameter hole. This test aimed to compare the heated and non-heated plate performance. Secondly, a thread tensile test over a 30 mm diameter hole. This second test on the same bolts aimed to compare the effect of heat on the bar. Tests were performed on two heated bolts and two non-heated bolts (Figure 12).

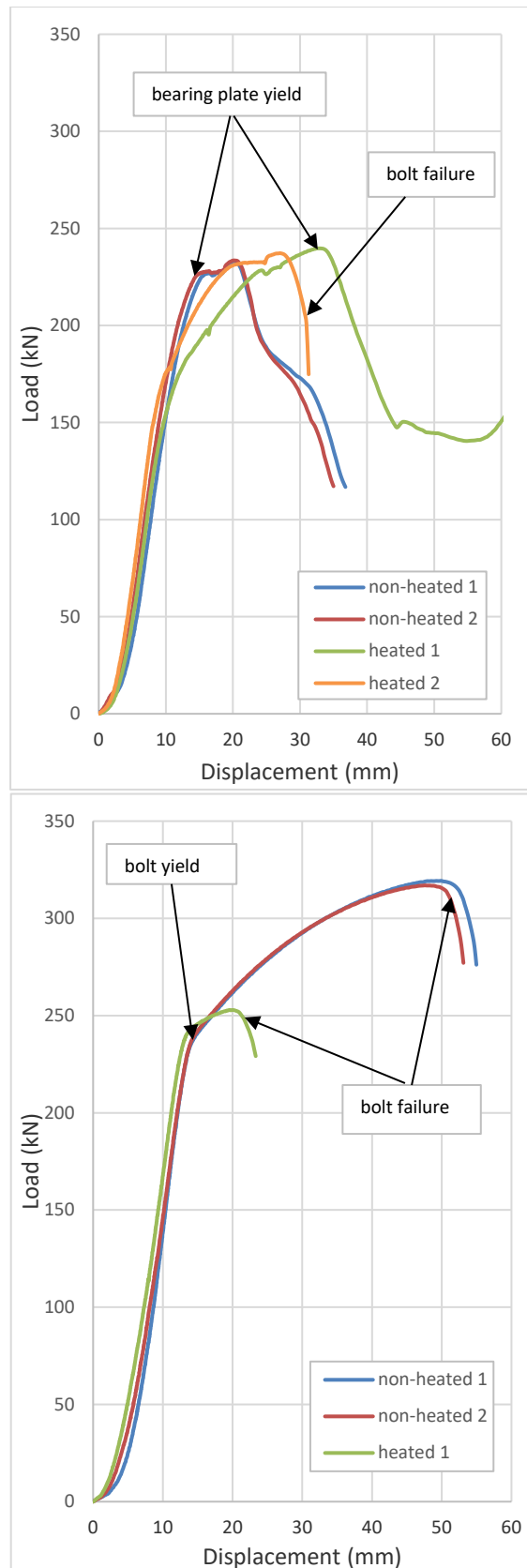


Figure 12: Complete lower-anchor assembly tensile tests (left), and thread tensile tests (right)

The two non-heated bolts passed the complete lower-anchor assembly test by folding over the plates without bolt failure. One heated bolt also successfully passed this test. However, the other heated bolt broke through the threaded section at a load of 237 kN without significant bearing plate deformation. The effect of heat was to reduce the stiffness of the plates. It is also noted that the stiffness results from heating were substantially more variable than the non-heated plates.

The thread tensile test was used to break the bar of the bolts that passed the complete assembly test. The non-heated bolts averaged 318 kN, with both failing through the threaded section of the bolt. In comparison, the heated bolt returned 253 kN – a load reduction of 20% - with failure occurring through the non-threaded section (Figure 13). The thread tensile test found both a substantial 30 mm reduction in bolt elongation after initial bolt yield, and lower peak strength. This, suggests the lower bolt has been embrittled and weakened by exposure to heat.

### SUMMARY

This project aimed to understand the effects of high temperatures on the performance of resin-anchored roof bolts. The project simulated routine underground bolt installations and then subjected the bolts to temperatures approximating mine fire conditions by placing the end of the bolts into a gas-powered furnace at 950°C for 28 hours. Heat conduction along the bolts was measured using thermocouples. The bolts installed into grout-filled cylinders were then sectioned for load transfer testing using the push-test method. Two bolts not installed in grout, but exposed to the furnace, were tensile tested to understand the effect on the bolts lower anchor region.



**Figure 13: Bolts failed during tensile tests – non-heated at top and heated at bottom**

The results fit with established theory. Heat conduction displayed an exponential decay away from the heat source. Measured temperatures dropped to less than 100°C at approximately 600-700 mm from the furnace. This location and temperature corresponds with a change in load transfer performance. Load transfer was reduced by 83% in the 150 mm sample closest to the fire. From 150-600 mm from the furnace the load transfer was reduced by approximately

one-third. However, from 600 mm to the top of the bolt it was judged there was no difference between the heated bolts and the non-heated bolts. Tensile tests of the complete lower-anchor assembly found the bearing plates did not lose peak load capacity, but did lose stiffness. Tensile tests of the bolt bar and thread found the heated bolts both lost approximately 20% in peak load capacity and a substantial reduction in bolt elongation after yield and prior to failure.

Overall, the test methods provided a means to evaluate the effect of elevated temperatures on the dominant primary roof bolt used in Australian underground coal mines. The heat conduction reached an equilibrium point during the tests, and the adverse effects on load transfer were not seen at more than 600 mm from the furnace. However, the heat was found to embrittle the bolt tail reducing elongation and tensile strength. Thus, the application of heat modified a full resin encapsulated bolt to a partially encapsulated bolt with a weaker and more brittle lower anchor region.

### **ACKNOWLEDGEMENTS**

The author would like to thank the following for their inputs and support of the project. DSI Underground Australia, specifically Derek Hird and David Evans, who provided the resources and time to complete this work. Michelle Mathwin, Luke O'Grady, Josh Dimmock and Gary Wilson for doing all the dirty work to make the project happen. Finally, Arthur Dybowicz for his support in scoping the project. Without these people the project would not have been possible.

### **REFERENCES**

- Bechtel/Parsons Brinckerhoff, 1995. Memorial Tunnel Fire Ventilation Test Program – Test Report. Prepared for the Massachusetts Highway Department and Federal Highway Administration.
- Campbell, R., Mould, R., 2003. Investigation into the extent and mechanism of gloving and unmixing resin in fully encapsulated roof bolts. In Proceedings of 22nd International Conference on Ground Control in Mining, Morgantown, WV. pp 256-262.
- Campbell, R. Mould, R. MacGregor, S., 2004. Investigations into the Extent and Mechanisms of Gloving and Unmixed Resin in Fully Encapsulated Roof Bolts. In Proceedings of the Coal Operators Conference 2004, Wollongong.
- Compton, C., Oyler D., 2005. Investigation of fully grouted roof bolts installed under *in situ* conditions. In Proceedings of the 24th International Conference on Ground Control in Mining, Morgantown, WV, pp 302-312.
- Conti R.S., 2001. Responders to Underground Mine Fires. Proceedings in the Thirty-Second Annual Conference of the Institute on Mining Health, Safety and Research, Salt Lake City, UT.
- Ingason H., Lönnemark A., Li Y.Z., 2011. Runehammar Tunnel Fire Tests. SP Report 2011:55, SP Technical Research Institute of Sweden, Borås, Sweden.
- McTyer, K, 2015. Optimisation of roof bolt length based on improved resin performance. Final report to ACARP, Project C21023.
- Singh R.P. and Ray S.K., 2005. Effects of Open Fire on Ventilation in Coal Mines. In Proceedings of the Eighth International Mine Ventilation Congress, Brisbane, QLD.



# DEVELOPMENT OF SUPPORT SYSTEMS FOR LONGWALL MINING IN THE BOWEN BASIN, CENTRAL QUEENSLAND

**George Klenowski<sup>1</sup> and Phil McNamara<sup>2</sup>**

*ABSTRACT:* The first longwall mine in Queensland was Central Colliery, located at the German Creek Mines. Production commenced in 1985 and shortly afterwards it broke the world record for longwall coal production. At that time longwall mining was generally not considered viable in Queensland due to technical problems associated with weak coal and excessive gas and water. Engineering solutions were developed and included properly designed chain pillars, in-seam methane drainage and efficient, dewatering pumping systems (Klenowski 2000; Klenowski and Winter, 2017).

Following success at Central Colliery longwall mining commenced at the Oaky No.1 Underground Mine and Southern Colliery. This was followed by Gordonstone, North Goonyella and the Moranbah North Mines. Longwall mining is now accepted as the most efficient extraction method in Queensland coal mining with rapidly increasing annual production rates to 10 million tonnes from one longwall at the Grasree Mine.

## INTRODUCTION

Longwall mining commenced in Queensland in 1985 at the Central Colliery. At that time support systems in underground coal mines mainly comprised point anchored roof bolts, W-straps and timber beams, props, pig-sties and sprags. A number of innovative solutions which were developed at Central Colliery, Southern Colliery, Oaky North, North Goonyella, Moranbah North and Grasree Mines, have become standard practice in Australian mines. The Bowen Basin continues at the leading edge of the industry in Australia.

Fully encapsulated rock bolts with two speed, integral resins were designed to ensure adequate pre-load. Bolting patterns were varied according to the geotechnical conditions, as defined by hazards plans and sections. Mesh mats and butterfly plates were introduced for fretting roof and massive strata. Cable bolts and pre-stressed Megabolts with extended anchorages replaced timber props as secondary support. Drill bit improvements included a modified tri-flush blade bit for puggy roof conditions and the PCD bit for longer holes.

Cutable dowels were designed to support longwall ribs. Fibreglass dowels were initially used but were subsequently replaced with plastic dowels to reduce washing plant contamination. Shotcrete is now being applied for primary rib support.

Passive support systems which included fibrecribs and tin cans, were introduced to withstand abutment load and unstable roof conditions. Fibrecribs installed in longwall panels are extracted by the longwall shearer.

Dual pass continuous miners were initially used for heading drivage in conjunction with hand held drills to install roof and rib supports. Roof and rib bolters were progressively mounted onto

---

<sup>1</sup> Manager, Australian Mining Engineering Consultants. Email : [amec1@bigpond.net.au](mailto:amec1@bigpond.net.au) Tel +61 417 187 149

<sup>2</sup> Mining Engineer. Email : [philmcnamara@outlook.com.au](mailto:philmcnamara@outlook.com.au) Tel +61 428 409 584



continuous miners leading to the current standard configuration of a full face continuous miner equipped with four roof bolters, two rib bolters and temporary hydraulic roof support.

Computer modelling has been used to design efficient powered supports. Four leg chocks were originally installed but now two leg shields are used. Support capacity has increased from 800 tonnes to well over 1100 tonnes. High pressure hydraulic circuits now operate at 420 bars and set pressure is 90% of yield pressure, which prevents face spall. The hydraulic fluid reservoir is stored on the panttechnicon. Face sprags mounted on the fronts of shields are used on some faces. Improved horizon control systems for longwall shearers are being developed. On board inertial navigation systems provide accurate positioning and shearer tracking is recorded and replicated.

Support techniques for roof cavities and longwall recovery have improved. Polyurethane injection is used to control roof falls on longwall faces. Take-off measures now include Huesker minegrid and fully supported and backfilled, pre-driven, recovery roadways.

Ventilation shafts are constructed and lined remotely. Pre-sink excavations are either excavated conventionally or supported using the secant piling method. Shafts are completed by raise boring or blind boring using drilling mud. Lining is completed using robotic shotcrete machines or with steel casing. Nitrogen inertisation is required for raise boring.

Future advances in heading development will include increased automation of continuous miners with continuous coal discharge and robotic roof and rib bolters. Longwall operation is trending towards remote control with TV cameras and automated guidance.

### **HISTORICAL OVERVIEW**

Prior to 1985 much underground support for headings comprised point anchored roof bolts, W-straps and timber beams, props, pig sties and sprags. Better systems were needed to improve production and safety. Heading development needs to proceed in advance of longwall retreat for optimum production.

New, technologically improved support systems were developed at Central Colliery, Southern Colliery, Oaky North, North Goonyella, Moranbah North and Grasstree Mines. These innovations have now become standard practice in Australian underground coal mining. The Bowen Basin continues as the leading edge of the industry in Australia.

#### **Rock Bolts, Mesh Mats and Butterfly Plates**

Rock Bolts with resin anchorage and W-straps have been routinely used for roof support in coal mines. At the commencement of Central Colliery roof bolts were installed using hand held drills but roof bolting rigs are now mounted on continuous miners. Because wing bits became blocked in pughy mudstone bands a modified tri-flush blade bit was designed (Figure 1). The central tungsten carbide insert protects the central waterway and there are two grooved waterways on the outer sides of the bit.

Point anchored rock bolts were initially used at Central Colliery with 300 mm long, fast set resin cartridges. Because fully encapsulated bolts are far more effective, particularly under abutment load, trials were completed to obtain full encapsulation and proper tensioning. Celtite Pty Ltd developed an integral, dual speed, resin cartridge which consisted of an upper fast set section separated from the lower slow set portion by a partition seal. These cartridges are now routinely used.

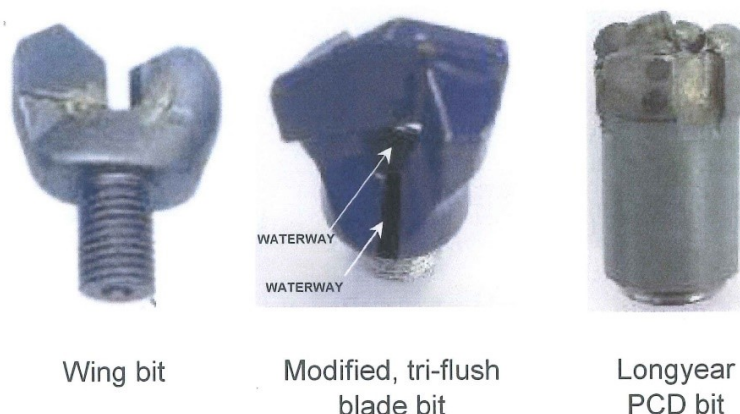


**Figure 1: Roof support drill bits**

Bolt spacing varies depending on the roof conditions and the effects of stress. Bolts are normally installed in rows ranging from 1.5 m to 1.0 m apart, with four to six bolts per row. Bolt lengths are generally 1.8 m to 2.4 m with longer bolts being installed where headings are wider. Where roof rider seams occur, bolt lengths and densities need to be varied according to the strength of the partings.

The immediate roof at Central Colliery is laminite. With increasing *in situ* stress and abutment load, fretting of the immediate roof occurred with loose rock fragments being detached. The Aquila Steel Company Limited recommended trialling mesh mats for improved safety. The trial was successful and installation of mesh mats became routine throughout the industry as primary roof support with patterned rock bolts.

At the initial longwall panels of Southern Colliery the immediate roof consists of massive sandstone. Because of the competent strata, butterfly plates were used instead of W-straps to speed up development. Butterfly plates and rock bolts are a simple support system for competent roof strata which do not readily delaminate.

### **Cable Bolts and Megabolts**

Cable bolts were introduced at Central Colliery mainly to replace timber props and pig-stie supports in intersections, areas of deteriorating roof and for longwall installation roads, which are wider. The initial cable bolts at Central Colliery were actually cable dowels which were not pre-stressed. Sonic extensometers were used to determinate height of strata delamination. Cable bolts were generally 6 m or 8 m long. Cementitious grout was used. Drilling of cable bolt holes using wing bits was inefficient. Polycrystalline Diamond (PCD) bits (Figure 1) were introduced at Central Colliery, resulting in much more rapid installation.

Megabolts were developed by W. Hutchins and J. Hetherington in 1996 and were then commercially produced by Megabolt Australia Pty Ltd. The advantages of Megabolts include a high pre-load, increased bolted horizon and the ability to be installed as primary support using an initial, point anchored, resin cartridge and tensioning for immediate resistance, followed by later cementitious grouting for full encapsulation (Figure 2).

Following a major roof fall at the Oaky North Underground Mine in June 1998 Megabolts were first used as primary roof support in a longwall mine. Two rows of 8 m long Megabolts at 2 m spacing, together with mesh mats and pattern rock bolts were installed.

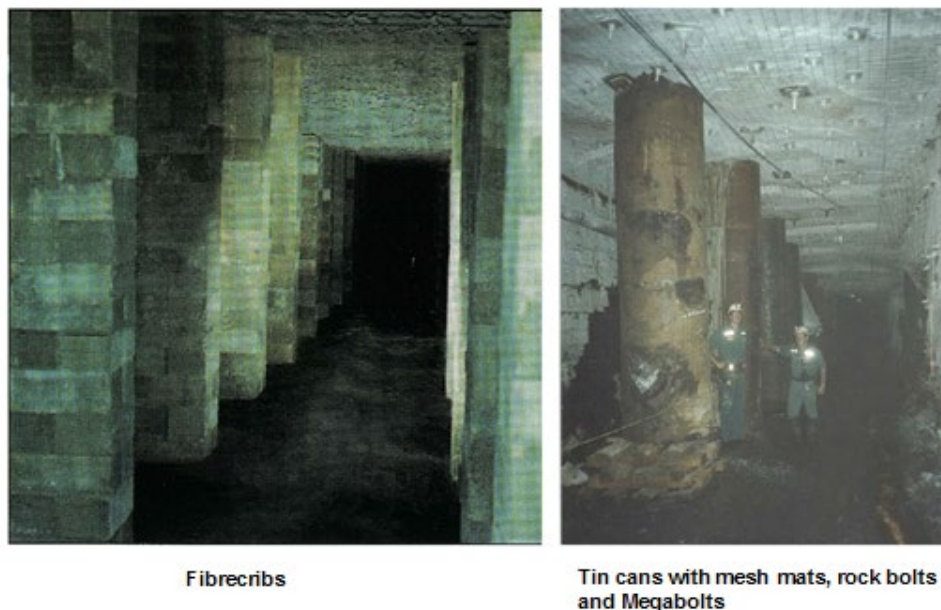


**Figure 2: Passive support systems**

### **Rib dowels**

At the commencement of longwall mining of 301 panel, the first panel at Central Colliery, timber sprags were used to prevent maingate rib spall adjacent to the conveyor. Celtite Pty Ltd was engaged to develop a dowel which was cuttable by the longwall shearer. A fully encapsulated, 1.2 m long, fibreglass dowel with a plywood plate was successfully trialled. Because the fibreglass dowels caused wash plant contamination Du Pont (Australia) Ltd was commissioned to produce a plastic dowel which replaced the fibreglass dowel.

### **Passive Support**

Resistant passive support is required in headings subjected to increasing abutment load, which can result in roof and rib failure. Pig-sties and heavy timber props were originally manually installed.

Fibrecribs are steel-fibre, reinforced concrete cribbing which when installed are a positive, passive, support system (Figure 2). The main advantage of fibrecribs is that they are cuttable and can be removed by the longwall shearer. They are transported as pallet sized bundles.

Fibrecribs were first used at Central Colliery in downdip, stub headings, excavated in longwall panels to collect tailgate water. Fibrecribs were installed to prevent these sumps from collapsing under front abutment load. The longwall then successfully mined through these supported excavations.

Tin cans were developed by Burell Mining International and consist of steel lining filled with cementitious composite (Figure 2). They have been extensively used for tailgate support at mines such as Crinum. The tailgate needs to remain open for ventilation under abutment load, until the longwall passes.

### **Longwall Equipment**

Longwall equipment comprises powered supports, Armoured Face Conveyor (AFC), stage loader, shearer (Figure 3) and pantechinon. During initial longwall mining in Queensland, powered supports were four leg chocks but now two leg shields are used. Initial chocks each had 800 tonnes capacity and generally functioned well even under periodic weighting. Regular

checking of longwall hydraulics was necessary to ensure that an adequate set pressure of at least 80% of yield pressure was achieved.

Computer modelling was completed to analyse powered supports. The SUBSOL, three-dimensional boundary element program and the LUSAS, finite element program were used. Analyses included lemniscate linkage, legs configuration, canopy and pontoon base areas and canopy tip to face distance. Design faults were rectified prior to fabrication.

Initially at Central Colliery the chocks hydraulic fluid (Solcenic emulsion and water) reservoir was located outbye in the main headings. Because of accessibility and monitoring problems the reservoir tank was attached to the longwall pantechnicon. This reduced the total fluid volume in use, improved fluid filtration, reduced contamination and decreased fluid return line pressures.

A longwall shearer is shown in Figure 3. A 1.0 m wide web has been generally cut. Coal drums and stone drums were developed to be able to cut basaltic dyke rock with strengths to 200 MPa.



**Figure 3: Longwall face equipment**

### **Pillar stability**

Pillars in main headings need to be designed as rigid pillars whereas chain pillars in longwall gate roads are designed as yield pillars to minimise coal sterilisation. At the German Creek Mines, the rigid pillars in coal with an average laboratory uniaxial strength of 9.6 MPa were designed with a minimum safety factor of 1.5, using Bieniawski's tributary load method (Bieniawski, 1982).

The Minlay displacement discontinuity program (Wardle and Klenowski, 1988) was used to design yield chain pillars for increasing depths of cover. This approach allowed for a chain pillar safety factor of 1.5 after single panel extraction and 1.0 after second panel extraction. Recommended solid chain pillar widths for increasing depth of cover are included in Table 1. These chain pillar widths have now been generally adopted throughout the Bowen Basin.

**Table 1: Recommended solid chain pillar widths**

Pillar width (m)	Depth range (m)	
	Laminite Roof	Sandstone Roof
15	70 – 100	70 – 120
20	100 – 160	120 – 180
25	160 – 210	180 – 230
30	210 – 270	230 – 280
35	270 – 320	280 – 330
40	320 – 380	330 – 390
45	380 – 400+	390 – 400+

### CURRENT MINING PRACTICE

Heading development rates and longwall production have increased significantly in recent times. This has been achieved through technological improvements, more efficient work practices and effective methane drainage.

#### Heading Development

Full face continuous miners with retractable cutting heads are now being used for heading drivage (Figure 4). Cutting width varies from 4.2 m to 5.2 m. Four roof and two rib bolters are mounted on the continuous miner (Figure 4). The continuous miners typically operate a hydraulically powered temporary roof support to provide additional protection for operators. Primary roof support generally comprises mesh mats, pattern rock bolts and where necessary, Megabolts or similar longer restraints.



**Figure 4: Current continuous miner**

Cutttable rib dowels are routinely used in longwall ribs and steel dowels are usually installed elsewhere. Where adverse geological structures such as mid-seam shear zones and excessive coal cleats consistently affect rib stability, shotcrete is now being applied as primary support. Different types of shotcrete are being trialled.

#### Longwall Equipment

Powered supports are now invariably two leg shields each with a capacity well over 1000 tonnes. Face sprags are sometimes installed to support spalling faces and immediate roof (Figure 3). Efficient longwall retreat now occurs electro-hydraulically in sequence.

It is important for the powered supports to have a set pressure of at least 80% of yield pressure, but preferably 90%. A high set pressure reduces roof delamination and face spall. Set



pressures need to be constantly measured and yield valves accuracy should be routinely checked. High pressure hydraulic circuits now operate at 420 bars.

Longwall top coal caving has been developed for very thick seams where good quality roof coal is left because longwall equipment is currently unable to operate beyond a 5 m mining height. The lower section is cut by a conventional shearer. The shield has a longer rear canopy extending past the base into the goaf (Figure 5). The extended canopy has a sliding door to capture goafed roof coal. This mining method was successfully introduced into Australia at Austar Mine and is currently being trialled elsewhere.



**Figure 5: Top coal caving shield**

Efficient longwall ploughs which can cut 3 to 4 million tonnes are now being used for thin coal seams with unstable roof conditions. The plough web thickness can be varied to suit the roof geotechnical condition. Manufacturers are aiming to achieve an annual production rate of 6 million tonnes.

During mining longwall faces tend to be dusty even with efficient water sprays. Pre-drained coal generates more dust. Air stream helmets have been introduced for safer breathing on longwall faces and foams are being developed to mix with dust suppression water.

At the end of each longwall panel equipment recovery is a technically difficult operation due to adjacent goafed roof. Initial take-off roof support comprised up to 10 rows of roof bolts and W-straps at 1.0 m spacing installed between the canopies tips and the longwall face during final longwall retreat.

A fully supported, pre-driven, recovery road way was trialled at Central Colliery. During entry the weak coal fender between the longwall and recovery road failed, resulting in excessive load on the chocks. Continuous yield occurred and the chocks almost became iron bound. Subsequent recovery roads are now pre-driven, supported and backfilled with filler prior to holing in.

Conventional longwall recovery is currently achieved using Huesker minegrid which is progressively installed during final longwall retreat (Figure 6). This system was initially pioneered at the Oaky North Underground Mine and now has widespread usage.

Systems for polyurethane injection were introduced to assist in the control of cavities formed from roof falls on longwall faces. Expanding cuttable void fillers were also used to reduce the risk to operators in these recovery procedures.

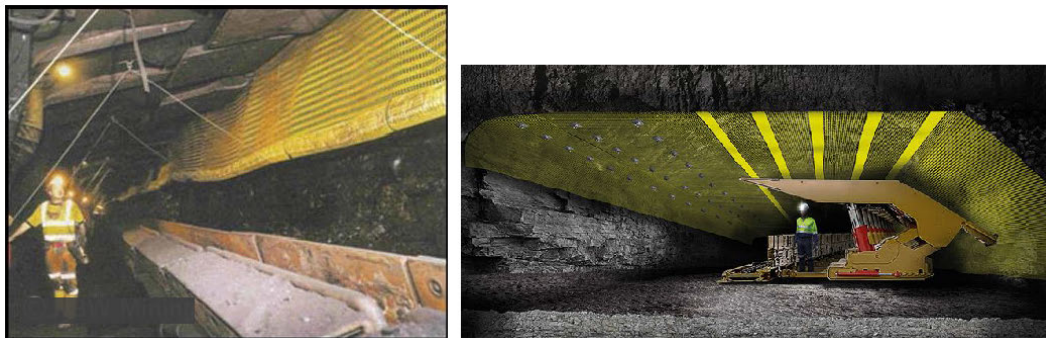


**Figure 6: Huesker minegrid take-off support**

During mining of NLW2 panel at the Oaky North Underground Mine in 1999 the longwall became badly bogged on a soft mudstone floor. During major roof failure a vast sinkhole formed on the surface 90 m above the longwall. Topsoil and tree roots gravitated down to the longwall face. Because of the extremely difficult situation it was decided to retrieve the longwall by excavating a slot from the surface using two draglines (Figure 7). The excavation was completed with one dragline located on the ground surface and another operating at a depth of 45 m. Safe blasting procedure was achieved by using programmable, electric detonators which restricted the maximum peak particle velocity to 45 mm/sec. The longwall was successfully retrieved in 12 weeks at a cost of \$13 million. At that time a new longwall was worth about \$55 million.



**Figure 7: Longwall retrieval using two draglines**

### **Ventilation shafts**

Downcast and upcast ventilation shafts are required in longwall mines. Shafts were originally excavated by drilling and blasting with initial mesh and rock bolt support, followed by a final lining of concrete or shotcrete.

Ventilation shafts are now mechanically excavated and lined. The two construction methods used are raise boring and blind boring. Prior to raise boring a pilot hole is drilled and a pre-sink excavation is completed down to fresh rock by both conventional excavation and concrete lining, or by drilling and installing a circular, secant pile concrete wall. During raise boring nitrogen inertisation is used at the cutter head, for safety. Following excavation weak zones



and coal seams are fibrecrusted. A robotic shotcrete machine is now used (Figure 8). Fibrecrete thickness generally varies from 50 mm to 150 mm. Where structural strength is required thickness is increased to 300 mm. Robotic rock bolters are currently being investigated.

Blind bored shafts are drilled at the required diameters to include lining. Drilling mud is used to maintain stability. Steel casing is used to line down to fresh rock. Commonly the full shaft length is steel lined. It is possible to shotcrete weak zones and coal seams below the surface steel liner but there are problems associated with dewatering and ventilation.



**Figure 8: Robotic shotcrete machine in a ventilation shaft**

### **FUTURE ROBOTICS**

Longwall mining is progressing towards full automation. Research emphasis is now on robotics.

#### **Heading development**

In the future continuous miners could be automated to remotely do full face drivage, discharge coal onto a continuous haulage system and install rock bolts and rib dowels. Bolts and dowels could be stored in carousels. Break offs for cut throughs would initially need to be manually controlled. With advancements in shotcrete application coal ribs could be simultaneously supported as mining proceeds.

#### **Automated longwall production**

Longwall shearers can now operate remotely using on board inertial navigation systems. As a coal seam rolls the re-training of the shearer tracking is required. For automation video cameras need to transmit back to the control room and shear tracking needs to be electronically monitored. Laser guidance will assist in maintaining horizon control. Recently the longwall at Grosvenor Mine was remotely operated for 24 hours. Longwall automation is achievable with advanced electro-hydraulic controls and periodic, manual retraining of the shearer as the coal seam dip changes.

### **DISCUSSIONS AND CONCLUSIONS**

A number of innovative support systems and design criteria were implemented at Central Colliery, Southern Colliery, Oaky North, North Goonyella, Moranbah North and Grasstree Underground Mines and these have become standard practice in Queensland longwall mines.

In rock bolting integral, dual speed, resin cartridges have been developed for proper pre-load and full encapsulation. A modified, tri-flush, spade bit was fabricated to drill through pughy mudstone without blockages. Mesh mats were introduced to replace W straps in fretting roof

## Coal Operators' Conference

conditions and butterfly plates replaced W straps in massive sandstone roof. Rock bolt spacing and lengths were determined for differing geotechnical conditions, with adequate factors of safety. Plans and sections of geotechnical hazards were developed for safety and to predict conditions in advance of mining.

Cable bolts were introduced at Central Colliery to replace timber props and pig sties. Cementitious grout was used. Following roof failure at the Oaky North Mine Megabolts were installed as primary support in weak strata.

Cutable rib dowels were developed to replace timber sprags. Fibreglass dowels were initially used but were replaced with plastic dowels to prevent blockage problems at the wash plant.

Resistant passive support which has been implemented for headings subjected to increasing abutment load and for unstable roof conditions includes fibercribs and tin cans. Fibercribs which are cuttable, were successfully used to support sump headings in panels during longwall retreat with front abutment loading. Tin cans have successively supported tailgate roadways under abutment stress.

Powered longwall supports have been analysed by computer modelling to determine required capacity and to complete design checks. High set pressure alleviates stability problems. Two leg shields are now invariably used with support capacity of well over 1000 tonnes and all hydraulic circuits are electronically monitored.

Extensive modelling and *in situ* stress measurements have been completed to design stable rigid pillars and safe, yielding chain pillars which minimise coal sterilisation. Monitoring under abutment load has confirmed the accuracy of design parameters.

Current full face continuous miners now have four mounted roof and rib bolters and are equipped with hydraulic temporary roof support. Primary heading support generally comprises mesh mats, pattern rock bolts, Megabolts and rib dowels. Shotcrete is now being applied as primary rib support.

Powered supports are invariably two leg shields each with a capacity well over 1000 tonnes and recommended set pressure of 90% of yield pressure, which needs to be routinely checked. High set pressure reduces face spall.

Longwall top coal caving has been developed for very thick seams and has been successfully implemented in Australian longwall mines. Additional coal is extracted using this method.

Longwall shearers generally mine bi-directionally and stone drums have been designed to cut igneous dyke rock with strengths to 200 MPa. Drums can be changed to cut a 1.0 m web or a 0.5 m web where roof conditions are unstable and the prop free front needs to be reduced. Shearer tracking can now be recorded and remotely repeated.

Longwall retrieval is difficult due to adjacent, flushing goaf and significant abutment load. Huesker minegrid is now commonly used for controlled support during longwall take-off. An alternative is to enter a fully supported, recovery roadway which has been backfilled with filler.

Ventilation shafts are mechanically excavated by raise boring or bling boring. Secant piling is sometimes used for pre-sink excavations. During raise boring nitrogen inertisation is required and shotcrete lining is applied to coal seams and weak zones using robots. Steel lining is generally installed in blind bore shafts.

Future heading development could become fully automated. Self-controlled continuous miners could have robotic roof and rib bolting drilling rigs equipped with appropriate support installers. Video monitoring would reveal the geotechnical conditions and be used to control mining advance.

Longwall shearers can now operate remotely and have recorded tracking for repeated cutting. With current technological advances continuous, remotely controlled longwall operation will be possible. Longwall shearers will use video cameras and inertial navigation systems providing accurate three dimensional positioning data.

#### **REFERENCES**

- Bieniawski, Z T, 1982. Improved design of room-and-pillar coal mines for U.S. conditions. Proc. First Int. Conf. on Stability in Underground Mining, pp. 19-48, A.I.M.E., New York.
- Klenowski, G, 2000. The influence of subsidence cracking on longwall extraction beneath water courses, aquifers, open cut voids and spoils piles, ACARP Report Project Number C5016.
- Klenowski, G and Winter, S, 2017. Inflows into longwall mines from inundated overlying workings, 13th AusIMM Underground Operators' Conference 2017.
- Wardle, L J and Klenowski, G, 1988. Rational longwall layout design based on numerical stress analysis. The AusIMM Illawarra Branch, 21st Century Higher Production coal mining systems – their implications, Wollongong, NSW, 1988.

# APPLICATION OF CONTINUOUS MECHANICAL CUTTING TO COAL OVERBURDEN REMOVAL

Isaac Dzakpata<sup>1</sup>, Dihon Tadic<sup>2</sup>, Joji Quidim<sup>3</sup>

**ABSTRACT:** Conventional overburden removal in coal mining is typically achieved using drill and blast. However, drill and blast is a cyclical (or batch) process that has inherent inefficiencies and offers limited opportunities for enabling automation technologies. Existing mechanical rock cutting systems such as surface miners, continuous miners, roadheaders, impact hammers and tunnel boring style machines are commonly applied in underground excavation environments and also in some mining operations. Most of these technologies are based on pick-based machines, mechanical indentation and hammer impact. A review of industry literature and OEM data indicates that beyond rock strengths of about 40MPa UCS, the cutting cost for pick-based systems escalates exponentially due to high pick consumption rates and low machine productivity. However, with the emergence of undercutting with oscillating discs (developed by Joy Global as DynaCut™), potential exists for economic mechanical excavation spanning the broad range of typical coal overburden materials - even those well beyond 40 MPa UCS.

This paper presents key findings from investigating the application of continuous cutting systems for surface coal mine overburden removal. Komatsu's DynaCut rock cutting machine was used for cutting trials at a sandstone quarry, to quantify performance in representative rock domains typical of overburden material found in Australian coal operations: (a) low-strength (<30 MPa UCS); (b) medium-strength (~30-50 MPa UCS); and (c) higher-strength (+50/60 MPa UCS). In total, approximately 500 m<sup>3</sup> of in-situ rock (overburden) was cut along a 40m bench section, with a 3m high x 5m wide working face.

The quarry cutting trial successfully demonstrated the performance of the DynaCut technology in representative overburden material domains. A general trend of increasing *specific energy of cutting* (SE) with increasing material strength was reported. The SE ranged from about 1.0 MJ/m<sup>3</sup> to 6.9 MJ/m<sup>3</sup>, averaging between about 3.5 MJ/m<sup>3</sup> and 3.8 MJ/m<sup>3</sup> across the three rock domains. The instantaneous cutting rate (ICR) ranged from about 35 m<sup>3</sup>/hr to 120 m<sup>3</sup>/hr. This field experiment has shown the potential for a DynaCut system (using undercutting technology) to provide a competitive solution for mechanical overburden cutting, particularly for materials beyond 40MPa UCS, where traditional cutting systems become rapidly ineffective and inefficient. Early field results indicate that an up-scaled DynaCut system could average around \$2.00/BCM for a mine with a broad material spread up to >100 MPa UCS.

## INTRODUCTION

Coal overburden removal is a critical bottleneck in the production of surface coal. Conventionally, surface coal overburden removal, handling and disposal in surface coal mining operations is typically achieved by means of drilling, blasting and haulage (Oggeri et al., 2019; Scott et al., 2010; Hustrulid et al., 2013). Figure 1(a) shows the typical overburden removal methods in Australia (Scott et al., 2010; Westcott, 2004) and Figure 1(b) shows a typical cost

---

<sup>1</sup> Work Area Leader, Mining3,

Email: [ldzakpata@mining3.com](mailto:ldzakpata@mining3.com) Tel: +61 7 3346 5618

<sup>2</sup> Principal Research Engineer,

Email: [dtadic@mining3.com](mailto:dtadic@mining3.com) Tel: +61 7 3346 5602

<sup>3</sup> Technical Specialist, Mining3,

Email: [jquidim@mining3.com](mailto:jquidim@mining3.com) Tel: +61 7 3365 5677

breakdown of strip coal mining (Thompson, 2005) . This illustrates that overburden removal is the single most expensive unit activity in surface coal mining (approximately one-third of total costs), with more than 60% of the material moved by truck and shovel. It also shows that approximately 95% of the mining methods would require some level of drilling and blasting to enhance the productivity of the primary loading equipment (draglines and shovels).

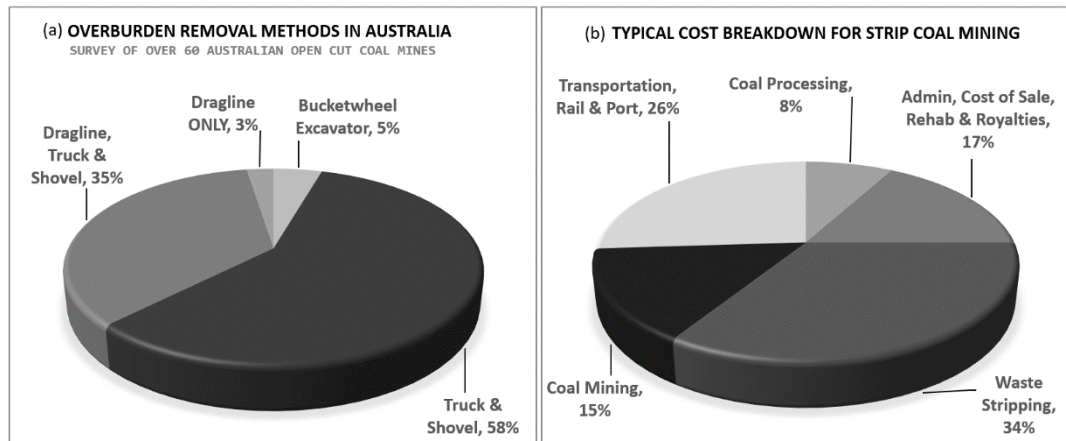


**Figure 41: (a) Typical overburden removal methods (b) cost profile of surface coal mining**

Mechanical rock cutting has been the subject of research interest over many decades for hard rocks (Kovalyshen, 2015; Pickering and Ebner, 2002; Erarslan and Ghamgosar, 2016; Karekal, 2013) and soft-medium rocks (Tiryaki and Dikmen, 2006; Abu Bakar et al., 2014; Cheng et al., 2018; Snowdon et al., 1982). Some of the identified benefits include the reduced need for explosives, consistency of fragmentation (with potential to sort ore from waste), opportunity for precision mining, improved stability of pit walls and amenability of mining to high levels of automation (Darling, 2011; Hood et al., 2005). The fundamental study and advances of the Oscillating Disc Cutting (ODC) technology have been discussed extensively by Hood et al. (2005); Hood and Alehossein (2000); Erarslan and Ghamgosar (2016); Karekal (2013); Grashof et al. (2019), with the cutting performance being a function of rock mass properties (including abrasivity and fracturing), and machine operating parameters including cutting force, amplitude of oscillation and frequency of oscillation.

Mechanical rock cutting systems typically include pick-based and indenter-based machines (e.g. surface miners, continuous miners, tunnel boring style machines). A baseline assessment was performed by Mining3 researchers, considering cost and productivity competitiveness of mechanical cutting with current mining systems. This was part of a study to understand the potential to replace drill-blast-load with mechanical cutting, at a reasonably large scale – i.e. using the nominal capacity of a large mining shovel (~40 Mtpa) as an indicative target for a cutting system. The assessment indicated that mechanical cutting machines for high-capacity overburden removal were more productive and cost-effective in lower-strength overburden materials (<40 MPa UCS), however, traditional machines rapidly become ineffective and inefficient as the material strength increases above 40-50 MPa UCS.

The chart in Figure 2 indicates that the costs for cutting of materials below ~30 MPa UCS typically ranges between \$1.00-\$2.00/BCM. The results also showed that the Dynacut undercutting disc technology may be competitive with drill-blast-load (averaging around \$2.00/BCM) and, critically, that this technology would be far more capable in higher strength (>40 MPa UCS) materials than traditional pick-based cutting systems.

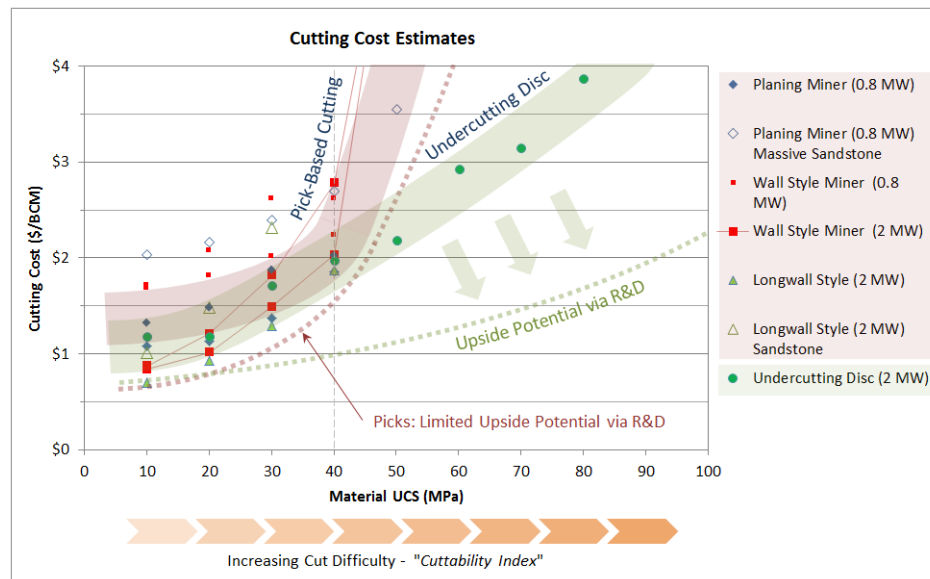


**Figure 2: Estimated cutting cost trends of current and emerging rock cutting technologies**

In fact, the Dynacut technology has proven effective even in materials far stronger than 100 MPa UCS, and would therefore handle essentially any coal overburden material likely to be encountered. Key findings of this initial work aligned well with those presented in the cost and productivity survey of 71 surface coal operations in Australia by Scott et al. (2010).

This paper presents the initial results of field trials aimed at investigating the cutting performance of Komastu's Dynacut rock cutting technology in multiple overburden domains. The cutting test was conducted in representative rock domains typical of overburden material found in Australian coal operations; (a) low-strength (<30 MPa UCS); (b) medium-strength (~30-50 MPa UCS); and (c) higher-strength (+50/60 MPa UCS).

### TEST EQUIPMENT AND SUPPORT EQUIPMENT

#### Main test equipment

The DynaCut test machine is a modified roadheader carrier with a customised boom, designed for basic testing in a controlled experimental environment. The extendable boom and cutting head carries a single cutting disc, with reach that allows for cutting a face approximately 5m wide x 4.5m high without moving the carrier. The test machine has basic material handling capability, incorporating two backhoe attachments to clear material from the floor at the face between cuts as required (not used in this field testing). To minimise potential rotational movement of the carrier during cutting, the test machine was attached to a steel rail bolted to the floor alongside the machine. The boom can cut in any direction and can be operated in manual or semi-autonomous modes (with pre-defined cutting profiles and sequence). Figure 3 shows front and side views of the test machine.

The cutting process involves the disc attacking the surface in an undercutting mode (using the oscillating motion of the cutting head), excavating a relatively thin slice of the face as the boom slews. The cut path is typically the width of the cutting disc and about 40-140 mm deep (depending on the rock type and disc design). Optimum cutting performance is generally achieved when the cut depth is adjusted to deliver the maximum Instantaneous Cutting Rate (ICR); a product of the cutting velocity, cutting width and depth of cut.





**Figure 3: Main test equipment- modified roadheader with DynaCut cutting systems**

Several cutting discs were used for this quarry trial, including new purpose-built designs that were more aggressive than previous discs made for hard rock material. The cutting discs ranged from 650 mm to 700 mm in diameter, with each incorporating a ring of inserts bits around the perimeter, at the primary rock engagement edge. Various insert designs and cutter profiles were tested; however, the specific details of these cutters are excluded from this paper in compliance with non-disclosure agreements.

Ancillary and services equipment for the trial included those to supply power, air and water to the DynaCut test machine, and equipment for rock sample extraction and materials handling. In order to maximise the cutting machine utilisation during the limited trial duration, a 13-tonne excavator was utilised to remove cut material from the base of the advancing face. This was much quicker than using the on-board backhoe arms, which do not reflect the type of system that would be incorporated in a production system.

### **TEST METHODOLOGY**

The trial was designed to evaluate performance of the DynaCut test machine across several key domains and therefore some preliminary assessment was required to confirm that suitable zones would be available and accessible. The field cutting trial was therefore carried out at a quarry located on Seventeen Mile Road in Helidon and operated by Rock Trade Industries. The quarry extracts Helidon Sandstone, which it produces in several forms including rough-cut blocks, cut slabs, boulders, sand and gravel. The general deposit is relatively massive with a reported range of material strength from <10 MPa to >100 MPa (UCS). Investigations of suitable trial locations at the site were conducted, identifying areas aligning with the three target domains (<30 MPa, 30-50 MPa, > 50/60 MPa UCS). Whilst the quarry did not have accessible material representing the full range of rock strengths in Australia's coal overburden (e.g. including 100+ MPa UCS), the available material at the quarry (up to about 80 MPa) still allowed the project to achieve its core objectives. Initial core samples were extracted from the areas identified as target test sites and sent for UCS laboratory testing. Upon material domain/strength confirmation, final test blocks were selected that provided vertical cutting faces approximately 5 m wide x 3 m high, with block lengths of approximately 12 m. This would suit the boom reach of the DynaCut test machine and provide a sufficient block for cutting about 150 m<sup>3</sup> in each domain, time permitting, during the trial period.

### **Coring and Sample Extraction**

Core samples were periodically taken from upper and lower portions of the cut face during the cutting trial, from which multiple specimens were prepared for UCS testing. The Core samples

were 54 mm in diameter, with UCS testing specimens typically prepared to 150 mm in length. The UCS results in Table 1 support the observation of lower-strength material (<40 MPa UCS) in the earlier bench faces (1-4) and higher-strength material (up to 85 MPa UCS) in the latter bench faces (5-9). Although there was minimal material substantially below 30 MPa UCS, the weakest sample measured was 11 MPa UCS and there was significant material around 30 MPa UCS to provide data for the low-strength domain.

**Table 1: Summary UCS test results from sampling faces (87 specimens tested)**

Bench position:	Face 1		Face 2		Face 3		Face 4		Face 5		Face 6		Face 7		Face 8		Face 9	
	2.5m		5.5m		9.0m		17.5m		20.5m		23.5m		31.5m		34.5m		39.0m	
	16 Aug		17 Aug		21 Aug		29 Aug		30 Aug		30 Aug		7 Sep		13 Sep		21 Sep	
UCS Mpa	ID#	UCS (MPa)	ID#	UCS (MPa)	ID#	UCS (MPa)	ID#	UCS (MPa)	ID#	UCS (MPa)	ID#	UCS (MPa)	ID#	UCS (MPa)	ID#	UCS (MPa)	ID#	UCS (MPa)
90	1.1.1	36.8	2.1.1	38.7	3.1	54.8	4.2.2	40.5	5.1.1	60.7	6.2	61.6	7.4.1	19.1	8.2	52.8	9.2	64.3
80	1.1.2	44.1	2.2.1	38.4	3.2.1	41.7	4.4	55.7	5.1.2	58.5	6.3	64.9	7.4.2	69.8	8.5	62.6	9.3	61.5
70	1.3.1	36.9	2.2.2	48.5	3.2.2	40.5	4.6.1	55.0	5.2.2	53.5	6.4	51.3	7.5	51.8	8.6.1	63.3	9.4	66.7
60	1.3.2	28.5	2.4	41.0	3.3.1	37.5	4.7.2	43.5	5.4.1	28.8	6.5	51.0	7.6.1	68.1	8.6.2	72.7	9.5.1	69.3
50	1.6	34.1	2.6.1	34.3	3.3.2	41.7	4.8	28.3	5.4.2	43.7	6.6.1	62.0	7.6.2	29.3	8.7	59.4	9.5.2	52.8
40	1.8.1	40.6	2.6.2	34.6	3.4.1	46.2			5.7.1	60.1	6.6.2	59.6	7.7.1	68.5	8.8.1	64.7	9.6	71.7
30	1.8.2	48.4	2.7	29.2	3.4.2	45.0			5.7.2	61.9	6.7.1	62.8	7.7.2	70.5	8.8.2	46.7	9.7.1	60.9
20			2.8	11.0	3.6	46.8			5.9.1	63.8	6.7.2	63.5	7.8.1	64.6	8.9.1	62.5	9.7.2	71.8
10			2.9.1	34.0					5.9.2	60.2	6.8	59.1	7.8.2	67.4	8.9.2	66.0	9.8	59.4
			2.9.2	33.2					5.10	60.3	6.9.1	61.3	7.9.1	69.6	8.11.1	81.5	9.9.1	65.9
			2.10.1	30.3							6.9.2	56.7	7.9.2	70.6	8.11.2	77.6	9.9.2	57.3
			2.10.2	25.1							6.10.1	59.5	7.10.1	68.0	8.12	84.5		
			2.11.1	26.8							6.10.2	56.2	7.10.2	70.4	8.14	74.8		
			2.11.2	31.0							6.11	60.9	7.11	67.3				
											6.12	62.5	7.12	14.2				

**EXPERIMENTAL PROGRAM**

The experimental program focused on assessing the performance of the DynaCut technology in several rock domains with the intent of investigating cutting rates, cutter wear performance and energy efficiency, to enable extrapolation of productivity for a larger-scale machine or system. The trial enabled the characterisation of cuttings (chip) properties and material handling requirements and other operational considerations such as noise, dust and vibration during cutting. There were two key operational variables for the cutting experiments; *Cutter Type/Design* and *Depth of Cut* (DOC). In all, four different cutters of various bit designs and body geometries were tested (650 mm and 700 mm in diameter). The DOC ranged from 30 mm to 160 mm, typically adjusted in 10 mm increments. The strategy was to initially test various cut depths to identify a typical depth that produced the highest Instantaneous Cutting Rate (ICR), and to use this optimum depth for most of the experiments to build a substantial data set. Figure 4 shows a grid-frame image of the cutting location ordered along the faces where the core samples were extracted.

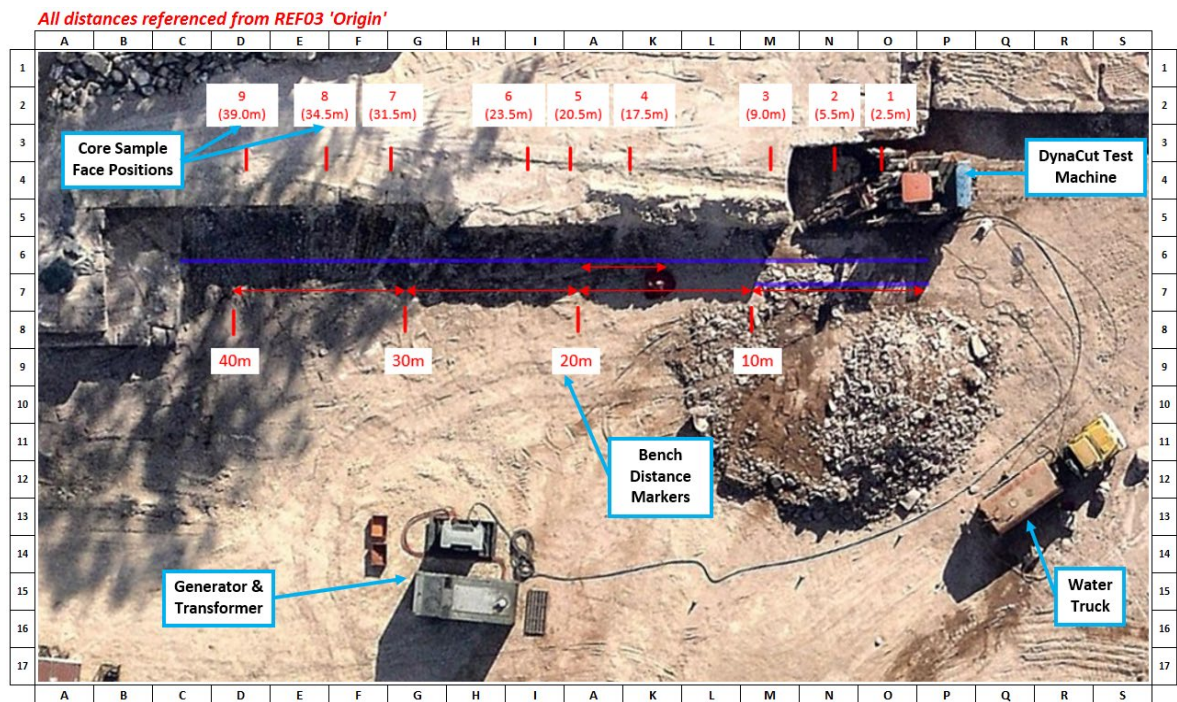


**Figure 4: Grid-frame aerial view of the cutting location and ordered faces**

### SUMMARY OF FIELD OBSERVATIONS

Overall, the performance of the purpose-built cutters indicated very low cutter wear rates. For example a single cutter was used for over 200 m<sup>3</sup> of rock (mostly 30-60 MPa UCS) with very little signs of wear. The machine readily adjusted to respect cutter force limit set points, contributing to the excellent cutter longevity. In all material domains, there was significant variation in ICR and SE. This was attributable to rock mass properties, which significantly affect the cuttability of material; in particular, accessible discontinuities, which enhance fracture propagation and chipping or block generation during cutting. To minimise the effect of these rock mass properties, and consequently build more comparable data sets for each domain, the test blocks were chosen to avoid structural variation where possible - at least as far as preliminary observation allowed.

Noise levels during cutting were not typical of general mining equipment, e.g. not similar to a large shovel or excavator. Dust generated was relatively very little compared to typical cutting machines and far less than the pick-based quarry rock saws operating nearby, even with the DynaCut dust suppression sprays off during some tests. No abnormal vibration was apparent, compared to typical mining equipment such as drills, shovels or excavators. Cuttings were typically plate-like, varying in size up to about the disc diameter. Occasional blocks dislodged from the face in zones with structural discontinuities. These occurred mostly in the upper section of the face due to the intersection of the discontinuities, the cut face and the upper bench surface. Material swell was determined by comparing loose cuttings pile volume to the excavated bench volume after 215 m<sup>3</sup> of cutting. The estimated swell was approximately 1.33 (33% volume increase).

### DISCUSSION OF RESULTS

In all, over 1500 individual slew cuts were performed during the trial, through approximately 40 m of bench section that transitioned between sandstone of varying properties, resulting in approximately 500 m<sup>3</sup> of in-situ material volume cut.

### Depth of cut

Approximately 50 slew cuts were initially performed at the start of the trial to investigate the depth of cut (DOC) which would produce the best cutting performance i.e. the highest ICR. This identified an optimum depth of ~120 mm. Similar, although fewer, tests were completed upon each cutter change to ensure this depth was still in the optimum range. Table 2 presents the summary results of this cutting data, comparing results from cut depths of ~140 mm, ~120 mm and ~90 mm with cutter #218. The minimum, maximum and average ICR peaked with the 120mm cut depth; the minimum, maximum and average SE all bottomed with the 120 mm cut depth also. In this case, reducing the cut depth from 120 mm to 90 mm saw a reduction in average ICR from ~84 m<sup>3</sup>/hr to 54 m<sup>3</sup>/hr, with a corresponding increase in average SE from ~ 3.4 MJ/m<sup>3</sup> to 5.2 MJ/m<sup>3</sup>. These results highlight the importance of identifying the optimum cutting depth for a particular material, and potentially periodically re-testing to ensure optimum cutting rates are maintained.

### Rock strength and cutting performance

A summary of the data for the different domains appears support a general trend of increasing average SE with increasing material strength (low-strength: 3.47 MJ/m<sup>3</sup>, medium-strength: 3.57 MJ/m<sup>3</sup>, high-strength: 3.83 MJ/m<sup>3</sup>). A wide range of SE and variability of average SE within each domain indicate that this trend may not be significant, or is being confounded by other controlling parameters such as rock mass structural properties. Table 2 provides a summary of different cutters in the three main testing domains. The results in Table 2 suggests that different cutters may be best suited to particular rock properties (intact properties including but not limited to rock strength; but also rock mass properties such as jointing, fractures and other discontinuities). This further suggests that a particular cutter simply performs better with decreasing rock strength or increasing general "rock mass cuttability". Regardless of the suitability of a specific cutter to a particularly range of material properties, this results shown in Table 2 general supports the trend of decreasing ICR with increasing SE and rock strength.

**Table 2: Summary of different cutters in the three main testing domains**

Material Strength	Face Zone	Valid cuts	Cut Depth (mm)	ICR (m <sup>3</sup> /hr)			Specific Energy (MJ/m <sup>3</sup> )			Cutter ID
				Min.	Max.	Avg.	Min.	Max.	Avg.	
Low	2	39	121-126	66.9	109.5	78.2	1.00	4.45	3.57	#167; 650mm
Med	1	11	102 - 122	63.7	80.9	73.0	3.30	4.89	4.03	#166; 650mm
	2	13	121 - 127	54.1	106.6	65.8	1.23	5.75	4.67	#166; 650mm
	3	26	102 - 122	59.0	95.0	72.8	3.25	5.27	4.19	#166; 650mm
	4	23	121 - 124	78.5	118.5	101.7	1.02	3.46	2.02	#166; 650mm
		73	102 - 127	54.1	118.5	80.69	1.0	5.7	3.57	
High	5	24	121 - 124	79.4	111.7	94.0	1.75	3.30	2.78	#167; 650mm
	6	25	91 - 141	34.7	103.1	63.7	2.74	6.48	4.51	#218; 700mm
	7	24	102 - 122	69.0	110.7	87.5	1.47	4.20	3.03	#218; 700mm
	8	38	121 - 124	63.7	111.8	83.3	2.29	4.79	3.53	#218; 700mm
	9	27	81 - 122	42.1	67.4	56.0	4.24	6.88	5.27	#218; 700mm
		138	81 - 141	34.7	111.8	77.01	1.47	6.88	3.83	

Results of the cutting performance for the various rock strength domains were as follows:

- Performance in low-strength material (Domain 1):* 39 valid data sets from the three bench horizons. The results showed a significant variation in SE from about 1 – 4.5 MJ/m<sup>3</sup>. This variation is likely due to the structural features of the rock mass that appear to have been responsible for the SE increasing from horizon 1 (top of bench) to 3 (lower in bench), with the cutting in horizon 1 effectively assisted by these structural features compared to the more confined and massive nature of the lower material around horizon 3.



- b) *Medium-strength material (Domain 2)*: 73 valid data sets (from 73 valid cuts) at the selected horizons with cutters #166 and #167. These cutters were identical in design; however, #166 had very minor prior use (several m<sup>3</sup> of sandstone in a laboratory rock bunker test), whilst #167 was in as-new condition. The ICR with this cutter design averaged about 81 m<sup>3</sup>/hr, with SE averaging about 3.6 MJ/m<sup>3</sup>. As with the results from the low-strength material, there was also significant variation in both the ICR and SE.
- c) *Performance in higher-strength material (Domain 3)*: 138 valid data sets (from 138 valid cuts) at the selected horizons using a variety of cutters and cut depths. The average ICR varied with cutter type and cut depth from about 56 m<sup>3</sup>/ hr to 94 m<sup>3</sup>/ hr, with the average SE of cutting varying from about 2.8 MJ/ m<sup>3</sup> to 5.3 MJ/ m<sup>3</sup>. As with the results from the low-strength and medium-strength materials, there was also significant variation in both the ICR and SE for each specific cutter and cut depth.

### Cutter type and cutter designs

Four different cutter rings (three different designs: #166/167, #218, #220) were tested during the trial, resulting in approximately 500 m<sup>3</sup> of excavated bench volume. All cutters except #218 were pre-tested before the field trials. Table 3 provides a summary of performance data of the three cutter designs with the lower half of the table filtered for only 120mm depth of cut. The results show that that cutter #167 performed relatively better (higher ICR and lower SE) than cutter #218 and #220, with cutter #220 being the least effective in these materials. The results also show a similar trend for the filtered results, given the spread is reduced across the three cutter types. This brief analysis highlights the significance of rock mass properties in cutting performance.

**Table 3: summary result of investigating the optimum Depth of Cut (DOC)**

Face Zone	Valid cuts	Cut Depth (mm)	ICR (m <sup>3</sup> /hr)			Specific Energy (MJ/m <sup>3</sup> )			Cutter ID
			Min	Max	Avg.	Min	Max	Avg.	
5	24	~120	79.4	111.7	94.02	1.75	3.30	2.78	#167; 650mm
6-9	99	~90 - 140	34.7	111.8	76.58	1.47	6.48	3.84	#218; 700mm
9	15	~80 - 120	42.1	65.1	52.62	4.24	6.88	5.48	#220; 700mm
5	24	~120	79.4	111.7	94.02	1.75	3.30	2.78	#167; 650mm
6-9	69	~120	62.3	111.8	83.88	1.47	4.84	3.41	#218; 700mm
9	2	~120	59.7	63.8	61.76	4.44	4.67	4.56	#220; 700mm

### Limitation of field trials

Two key limitations are highlighted throughout the analysis of field trials results: (a) the limited data sets for each cutter were inadequate for thorough statistical evaluation and comparisons of cutters and cutting parameters over broad domain areas; (b) simply classifying rock domains using measures of uniaxial compressive strength (UCS) is insufficient for the cuttability of a rock mass when applying this type of cutting technology.

### KEY FINDINGS

Data collected from the quarry trial was compared to the initial baseline performance results (productivity and cost performance estimates for the DynaCut rock cutting system), to determine the existence of any aberrations and whether these deviations (if any) were reasonable both in relation to cutting rate and cost performance. This section presents these key findings from the field trail observations and analysis of the results.

### Cutting rate (productivity)

Concerning the low-strength material (<30 MPa), the quarry trial results showed a slightly lower performance (higher actual SE) for material averaging about 29 MPa UCS compared to the baseline estimates. For the medium-strength material (30-50 MPa), the quarry trial result appears to support the baseline cutting rate estimates, indicating similar performance (similar actual SE) for material averaging about 43 MPa UCS. Finally, for the high-strength material (>55 MPa), the quarry trial cutting rate appeared to be slightly higher compared to the baseline performance estimate, indicating better performance (lower actual SE) than anticipated for the ~63 MPa UCS material. Figure 5 shows the revised cutting rate and cost trends estimates for pick-based and undercutting disc systems, for various larger-scale machines (between 0.8 MW and 2 MW power).

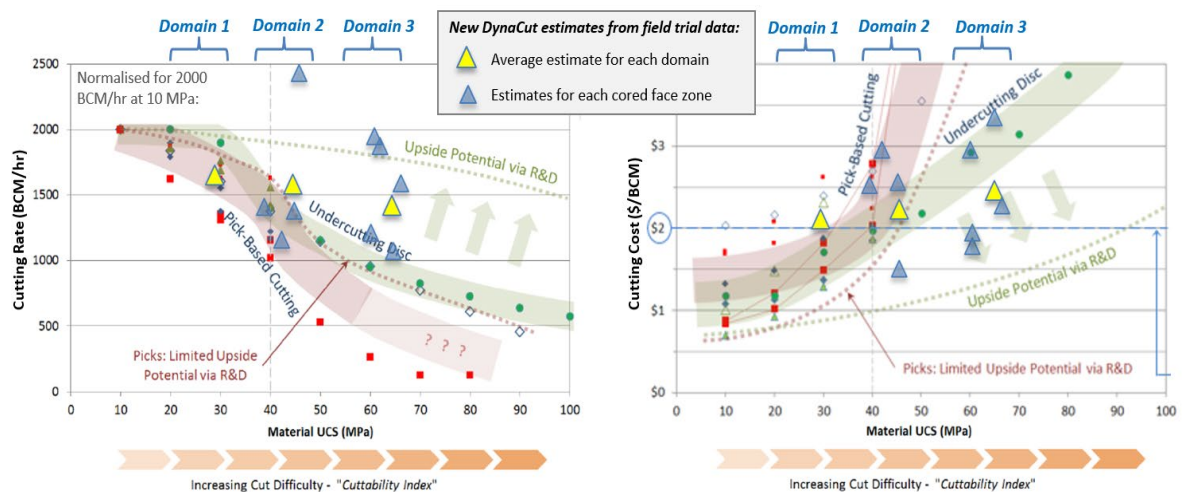


**Figure 5: Revised estimates of cutting rate (left) and cutting cost (right) for pick-based and undercutting disc technologies – based on new test results**  
(Updated to include cost estimates based on quarry trial data points)

### Cost (estimate) performance

In generating the cutting cost chart in Figure 6, the DynaCut cost estimates (the green Undercutting Disc band) for an up-scaled 2 MW cutting system were derived using an extrapolation of minimal data from preliminary cutting tests in small test-bunker constructed with sandstone rock boulders in a concrete matrix. The average UCS of test samples extracted from these boulders was ~80 MPa.

Based on the results obtained from the trials, for Domain 1 material (<30 MPa) earlier cutting cost estimates appear to be slightly low, with the quarry trial data indicating slightly higher costs (higher actual SE only partially offset by better cutter wear performance) for material averaging about 29 MPa UCS. for Domain 2 material (30-50 MPa), earlier cutting cost estimates appear to be well supported, with the quarry trial data indicating similar costs (slightly higher actual SE, offset by better cutter wear performance) for material averaging about 43 MPa UCS. for Domain 3 material (>55 MPa), earlier cutting cost estimates appear to be slightly high, with the quarry trial data indicating lower costs than anticipated (due to lower actual SE and better cutter wear performance) for material averaging about 63 MPa UCS.

### Energy performance (Specific Energy)

Based on the data analysed in this field trial, the average SE (one average value for each face zone per domain) ranged from about 2.0 to 5.3 MJ/m<sup>3</sup> with the lowest SE for individual cuts



being  $\sim 1.0 \text{ MJ/m}^3$  (low-strength domain, face 2; medium-strength domain, face 4) and the highest SE for individual cuts being  $\sim 6.9 \text{ MJ/m}^3$  (high-strength domain, face 9). In the previous limited tests in sandstone blocks, the average SE was  $5.0 \text{ MJ/m}^3$ , with a range from  $2.2$  to  $8.4 \text{ MJ/m}^3$ . This correlates relatively well with the findings from the current quarry trial. Figure 6 shows a reproduced chart from a prior phase report (ACARP C24011 final report). This chart now includes a summary of the SE data from the recent quarry cutting tests, as well as a data point from previous preliminary sandstone tests in a constructed test bunker. The green and blue data points on the chart represent two SE models for pick-based rock cutting performance estimation.

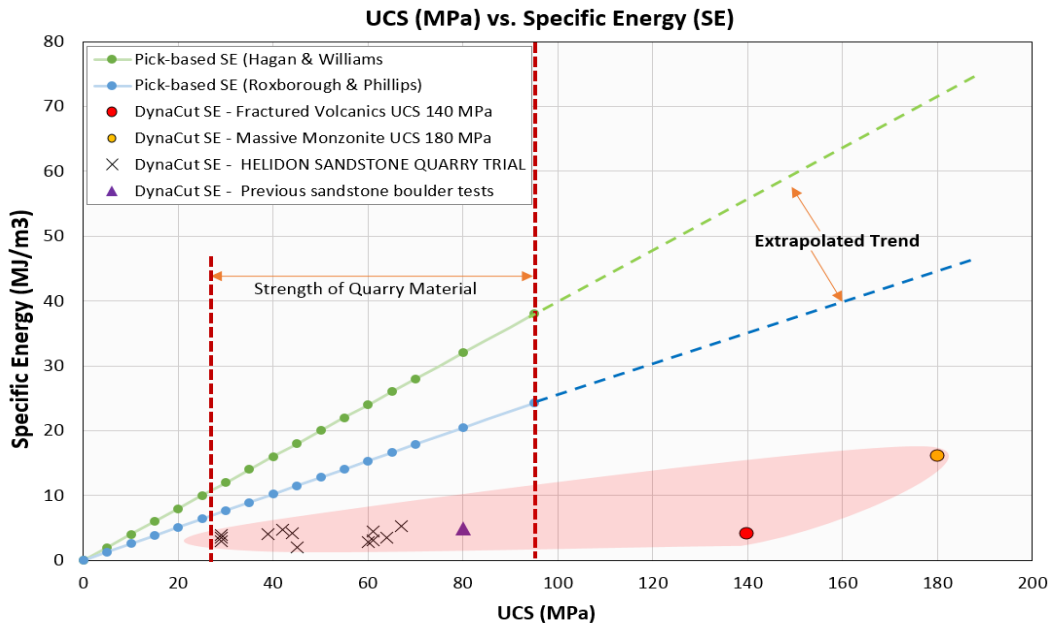


**Figure 6: Comparison of SE data of trials to cutting performance estimates by Roxborough and Phillips (1975) and Langham-Williams and Hagan (2014)**

The red and yellow data points represent DynaCut cutting tests by Komatsu on massive Monzonite (yellow data point) and fractured Volcanics (red data point). The new DynaCut quarry cutting data is shown as black crosses; it includes one data point (average SE value) for each face zone across the three material domains. The broken portions of the trend lines for pick-based SE are projected based on a linear extrapolation from the region below 100Mpa (UCS).

As shown in Figure 7, the new results obtained from the current field trials highlights the relatively low SE of the DynaCut technology, and supports the hypothesis that for material in the 20-80 MPa UCS range, the SE is consistently and significantly lower than that for traditional pick-based cutting systems.

**CONCLUSIONS AND RECOMMENDATIONS FOR FURTHER RESEARCH**

The quarry cutting trial successfully demonstrated the performance of the DynaCut technology in representative overburden material domains. There was a general trend of increasing *specific energy of cutting* (SE) with increasing material strength. The SE ranged from about  $1.0 \text{ MJ/m}^3$  to  $6.9 \text{ MJ/m}^3$ , averaging between about  $3.5 \text{ MJ/m}^3$  and  $3.8 \text{ MJ/m}^3$  across the three rock domains. The Instantaneous Cutting Rate (ICR) ranged from about  $35 \text{ m}^3/\text{hr}$  to  $120 \text{ m}^3/\text{hr}$ . The ICR and SE varied significantly within each rock domain, due mainly to rock mass

properties controlling the cuttability; in particular, discontinuities that assisted fracture propagation and facilitated chip or block generation during cutting.

Cutting rate and cost estimates from the previous project phase were generally well supported by the new data. Refined estimates, based on the new data, indicate slightly flatter cost and rate curves than anticipated, with higher performance (higher cut rate and lower cost than expected) in the higher-strength material. Indicative average cutting costs for material across the three domains tested are around \$2.00 to \$2.50 per BCM for an up-scaled machine. Since the technology is still relatively new in comparison to conventional cutting systems, there is undoubtedly still upside in performance to be realised through continued RD and engineering aimed at improvement of overall system performance and operating costs.

The investigation of these key performance factors and parameters forms the basis of future research work, which aims to identify further design and operational improvements, validate these through additional testing, and use the results to inform (and de-risk) the design of an up-scaled test machine. Future research would also investigate and test key DynaCut parameters outside of the limits of the current test machine, and in particular rock types or rock mass conditions to ascertain if cutting performance may be enhanced by operating the cutter at an oscillation amplitude beyond the capability of the current machine

### **ACKNOWLEDGMENTS**

Key Individuals, teams and management personnel of the following organisations (named in the full report) are gratefully acknowledged for their assistance with this project:

- Komatsu Mining Corp: Research Partner and execution of the cutting trial:
- ACARP: Research sponsor and team of Industry Monitors
- University of Queensland: Preparation of rock testing specimens
- Rock Trade Industries: Team at Helidon Quarry – for hosting field trial
- Aggreko: discounted rental of power equipment for the trial

This ongoing research initiative is a joint collaboration between Mining3 and Komatsu Mining Corp, with funding support from ACARP. This project directly addresses the ACARP Research Priority “Investigate continuous cutting technology for overburden and coal removal e.g. no drill and blast (high volume surface longwalls, surface miners, etc.)”.

### **REFERENCES**

- Abu Bakar MZ, Gertsch LS and Rostami J. (2014). Evaluation of Fragments from Disc Cutting of Dry and Saturated Sandstone. *Rock Mechanics and Rock Engineering* 47: 1891-1903.
- Cheng Z, Sheng M, Li G, et al. (2018). Imaging the formation process of cuttings: Characteristics of cuttings and mechanical specific energy in single PDC cutter tests. *Journal of Petroleum Science and Engineering* 171: 854-862.
- Darling P. (2011) Chapter 7.1 Mechanical Rock Breakin. *SME Mining Engineering Handbook (3rd Edition)*. Society for Mining, Metallurgy, and Exploration (SME), 417.
- Erarslan N and Ghamgosar M. (2016). An Innovative and Effective Approach to Hard Rock Cutting. *ISRM International Symposium - EUROCK 2016*. Ürgüp, Turkey: International Society for Rock Mechanics and Rock Engineering, 913-916.
- Grashof B, Alvarez Grima M, Schott DL, et al. (2019). Oscillating disc technology for rock excavation. *Proceedings of the 8th International Conference on Discrete Element Methods*. pp 1-11.

- Hood M and Alehossein H. (2000) A development in rock cutting technology. *International Journal of Rock Mechanics and Mining Sciences* 37: 297-305.
- Hood M, Guan Z, Tiryaki N, et al. (2005). The benefits of oscillating disc cutting. *Australian Mining Technology Conference: 'New Technologies to Produce More with Less'*; 27 - 28 September 2005, Fremantle, W.A. Carlton, Vic.: AusIMM, 267-275.
- Hustrulid WA, Kuchta M and Martin RK. (2013). *Open Pit Mine Planning and Design*, Two Volume Set CD-ROM Pack: V1: Fundamentals, V2: CSMine Software Package, CD-ROM: CS Mine Software: CRC Press.
- Karekal S. (2013). Oscillating Disc Cutting Technique for Hard Rock Excavation. *Proceeding of 47th U.S. Rock Mechanics/Geomechanics Symposium*. San Francisco, California: American Rock Mechanics Association, 8 : 2395-2402.
- Kovalyshen Y. (2015). Analytical model of oscillatory disc cutting. *International Journal of Rock Mechanics and Mining Sciences* 77: 378-383.
- Langham-Williams J and Hagan P. (2014). An assessment of the correlation between the strength and cuttability of rock. *Proceedings of 14th Coal Operators' Conference*. Wollongong: University of Wollongong, pp 186-192. [<https://ro.uow.edu.au/coal/512/>]
- Oggeri C, Fenoglio TM, Godio A, et al. (2019). Overburden management in open pits: options and limits in large limestone quarries. 29: 217-228.
- Pickering R and Ebner B. (2002). Hard rock cutting and the development of a continuous mining machine for narrow platinum reefs. *Journal-South African Institute of Mining and Metallurgy* 102: 19-24.
- Roxborough FF and Phillips HR. (1975). Rock excavation by disc cutter. *International Journal of Rock Mechanics and Mining Sciences Geomechanics Abstracts*. Elsevier, 361-366.
- Scott B, Ranjith PG, Choi SK, et al. (2010). A review on existing opencast coal mining methods within Australia. *Journal of Mining Science* 46: 280-297.
- Snowdon RA, Ryley MD and Temporal J. (1982). A study of disc cutting in selected British rocks. *International Journal of Rock Mechanics and Mining Sciences Geomechanics Abstracts* 19: 107-121.
- Thompson R. (2005). *Surface strip coal mining handbook*. Surface strip coal mining handbook. Johannesburg: South African Colliery Managers Association (SACMA).
- Tiryaki B and Dikmen AC. (2006). Effects of Rock Properties on Specific Cutting Energy in Linear Cutting of Sandstones by Picks. *Rock Mechanics and Rock Engineering* 39: 89-120.
- Westcott P. (2004). Dragline vs truck/shovel. *Australian Journal of Mining* 17: 47-52.

# ROLLING DYNAMIC COMPACTION FOR HAUL ROAD CONSTRUCTION AND MAINTENANCE – AN UPDATE

**Derek Avalue<sup>1</sup>, Brendan Scott and James Miedecke<sup>2</sup>**

*ABSTRACT:* The construction and management of haul roads remains a critical element in the efficient operation of all mines. Significant effort has been applied to design practices, extending the use of design charts and computer programs. Attention has been paid to the pavement materials and material properties, based on decades of geotechnical data and experience. Opportunities still exist for improvements to be realised in compaction protocols, particularly in the use of rolling dynamic compaction (RDC). RDC involves the delivery of a dynamic compactive effort using non-circular towed compactors, which are designed to deliver a combination of potential energy of a falling weight and kinetic energy mobilised due to the relatively high towing speed. The objectives include the proof-rolling and preparation of subgrade areas, exposing soft spots and weak zones and often establishing a sufficiently competent raft layer, as well as deep lift compaction offering cost-efficient construction of ramps and haul road pavements with programming benefits. The ability to compact deeper lifts allows fill particles to be larger without inhibiting the compaction process, which increases the sustainability of the process through reducing the constraints on the fill materials by allowing a larger maximum particle size. Case studies are cited where RDC has been trialled on several mine sites and many mines have benefited from the use of the technology. The continued attention to improving haul road construction will result in less road maintenance, less vehicle damage and improved truck tyre life, and RDC offers a method of contributing to these improvements. The compaction energy of RDC offers more leniency in moisture conditioning where adequate compaction densities can be achieved with much lower water addition than conventional laboratory optimum moisture content. When applied to coarse surface layer materials RDC will generate sufficient fines to provide a high-friction tyre-friendly low-maintenance finish on haul road surfaces.

## INTRODUCTION

Impact rollers have been utilised on mine sites for well over 30 years. They fall under the general category of “rolling dynamic compaction”, or RDC, and comprise a non-circular towed module that impacts the ground at regular intervals delivering a dynamic compactive force. The benefits of the use of RDC in mining applications have been explored in the past (Avalue 2006, Scott Jaksa 2012, Thompson et al 2019), and include rock rubbilisation to minimise tyre wear and deep lift compaction. This paper summarises past experience and presents additional case study information to support the on-going development of confidence in the RDC technique for use in haul road construction, acknowledging the benefits offered in quality, programming, risk mitigation and cost.

---

<sup>1</sup> Senior Engineer, Broons Group. Email: [derek@broons.com.au](mailto:derek@broons.com.au) Tel: +61 430 445 486

<sup>2</sup> Roads and Drainage Specialist, Proof Engineers. Email: [james@proofengineers.com.au](mailto:james@proofengineers.com.au) Tel: +61 418 130 253

## WHAT IS RDC?

RDC (impact rolling) comprises the densification of the ground using a non-circular compactor module, generally between 5 t and 12 t in mass, with three, four or five sides, towed at speeds of 10 to 12 km/h. The energy delivered by this means of compaction far exceeds that produced by conventional cylindrical drum rollers. It also far exceeds the comparative energy transmitted to a Proctor compaction mould in the laboratory used for the preparation of a moisture-density relationship curve.

This paper focuses on the 4-sided or “square” impact roller, as shown in Figure 1. Other shapes, such as 3 and 5-sided modules, operate in a slightly different manner and are not discussed further in this paper.



**Figure 1: The 4-sided or “square” impact roller, with tow tractor**

The opportunities offered by RDC are numerous, and include the following (Scott et al 2012a, Thompson et al 2019):

- Fast and efficient proof-rolling of subgrade areas to develop a denser, more uniform thicker subgrade for haul road construction;
- Identifying soft spots or weak zones that may need to be remediated in advance of the placement of fill;
- Allowance for the placement of thicker fill lifts, significantly increasing the production rate of well compacted fill;
- Thicker fill lifts permit the use of larger maximum particle sizes, reducing the constraints on the fill materials and improving the sustainability of the process;
- Delivery of a denser and more uniform road pavement end product, resulting in reduced road maintenance, reduced vehicle wear and tear, and increased tyre life; and
- The reduced requirements for the addition of water as the higher energy delivered by RDC makes it less dependent on maintaining conditions close to the Optimum Moisture Content (OMC) derived in the laboratory.

These points are explored further in the following sections.

## THE COMPACTIVE ENERGY AND PRODUCTIVITY OF RDC

“Compaction is critical to the success of a road building project” (Thompson et al 2019); this statement applies equally to all types of roads, but particularly so in the capital-intensive mining sector. The condition of mine haul roads depends on numerous factors, not the least of which are the pavement materials and their means of compaction.

Research into the compactive energy of impact rollers has progressed significantly in recent years (Scott et al 2012a and 2012b, Scott et al 2019a and 2019b). The 8 t 4-sided impact roller

has been shown to deliver approximately 24 to 30 kJ of energy per impact at typical operating speeds of 10 to 12 km/h (Scott et al 2019b), with depth effects theoretically predicted to vary from at least 0.75 m in cohesive soils to about 2 m in granular materials – in practice, greater depth effects have frequently been measured. These factors lend themselves to the application of impact rollers to deep lift compaction, thus allowing the maximum particle size limitation to be relaxed, e.g. permitting up to 375 mm diameter particles for loose layer thicknesses of 750 mm.

The relatively high energy delivered by the impact roller means that specified relative density levels can be achieved with moisture contents significantly below OMC. In haul road design, it is commonly accepted that vehicle maintenance requirements and tyre life are directly related to haul road conditions. Adding water (or drying back when borrow materials are over-moist) may be essential if material moisture contents are not close to OMC when utilising conventional drum rollers. However, being less sensitive to the actual field moisture regime, while still achieving specification, makes RDC attractive in terms of cost, water consumption and programme.

The production of compacted fill can be computed simply as follows:

$$P_{\text{compact}} = \frac{W_r \nu h}{n_{\text{passes}}} \quad (1)$$

where

$P_{\text{compact}}$	Production rate (compacted cubic metres per hour) ( $\text{m}^3/\text{h}$ )
$W_r$	Width of roller or rolled path (m)
$\nu$	Speed (km/h)
$h$	Compacted layer thickness (mm)
$n_{\text{passes}}$	Number of passes required to achieve compaction specification

For the 8 t 4-sided impact roller, travelling on a wheelpath  $W_r$  of 2.3 m at a speed  $\nu$  of 11.5 km/h, working on a loose layer thickness of 1,200 mm, compacting it to a compacted thickness  $h$  of 900 mm, with  $n_{\text{passes}} = 6$  passes (assumed for indicative purposes), will deliver about 4,000  $\text{m}^3$  of compacted material per hour, covering around 4,400  $\text{m}^2$  of surface area per hour, and involving the placement of approximately 5,300  $\text{m}^3$  of loose fill per hour. For runs with overlapping module prints, i.e. an effective rolling width  $W_r$  of 1.2m, the production rate of compacted fill is about 2,100  $\text{m}^3$  of compacted fill per hour.

### APPLICATION EXAMPLES

The use of RDC for deep lift compaction on mine haul roads generally requires attention to the optimal lift thickness, both in relation to the rate of placement of the loose fill to maintain the productive value of the impact rollers utilised, as well as in relation to particle size limits and moisture requirements. It is frequently beneficial to undertake detailed verification trials to ascertain the most cost-effective and time-efficient parameters, and many methods are available for such trials (Scott et al 2016, Whiteley and Caffi 2013).

Trial sections can be set out in a suitable location, utilising the materials intended for use in construction, and instrumented and tested to obtain all relevant data to assist in the assessment of the technique. Scott and Jaksa 2012 outline the execution of a trial programme for thick layer compaction at a mine site. Obtaining the optimal arrangement of layer thickness and number of impact roller passes to deliver the requisite quality of compacted material forms the basis of any trial, and in the particular case study sighted, layers of 850 to 1,000 mm thickness were verified for between 10 and 30 impact roller passes, respectively, with the resultant benefit in the use of a larger maximum particle size.



**CASE STUDY: COMPACTION TRIAL FOR HAUL ROAD CONSTRUCTION**

In addition to the trial described in Scott and Jaksa (2012) for thick lift compaction of deep fill, another impact rolling trial was specifically undertaken for the construction of haul roads at a different mine site. The objective of the trial was to find an efficient relationship between the number of passes, placed layer (fill) thickness, moisture content and corresponding density that could be achieved with a 4-sided 8 tonne (Broons BH-1300) impact roller.

Target specifications of at least 95% SMDD (Standard Maximum Dry Density) were required. Compacted layer thicknesses up to 1,500 mm thick were proposed for haul road sub-base and subgrade layers. The fill used to construct the test pad was dumped mining (shot rock) material, which was spread with a dozer and compacted with an impact roller. The fill material, its moisture content and placement were representative of the construction methods proposed for the project. Fill layers up to 1,500 mm were chosen for the compaction trial as shown in Figure 2. Different sections of the test pad were compacted using 10, 20, 30 and 40 passes of the impact roller, respectively.

A key advantage of the test pad configuration shown in Figure 2 was that all of the post-compaction testing could be undertaken at the same time, this was largely due to readily available space, equipment and shot-rock material on site, as well as a desire to make the post-compaction testing as efficient as possible. After impact rolling was completed, targeted testing using the following methods was undertaken to determine the effectiveness of the impact roller: dynamic cone penetrometer (DCP) testing, surface settlement measurements and field density testing at the base of test pits (benched excavations). Soil classification tests (particle size distribution and Atterberg limits) were undertaken on selected samples excavated from the test pits to quantify the properties of the fill material but are not included in the paper due to space constraints.

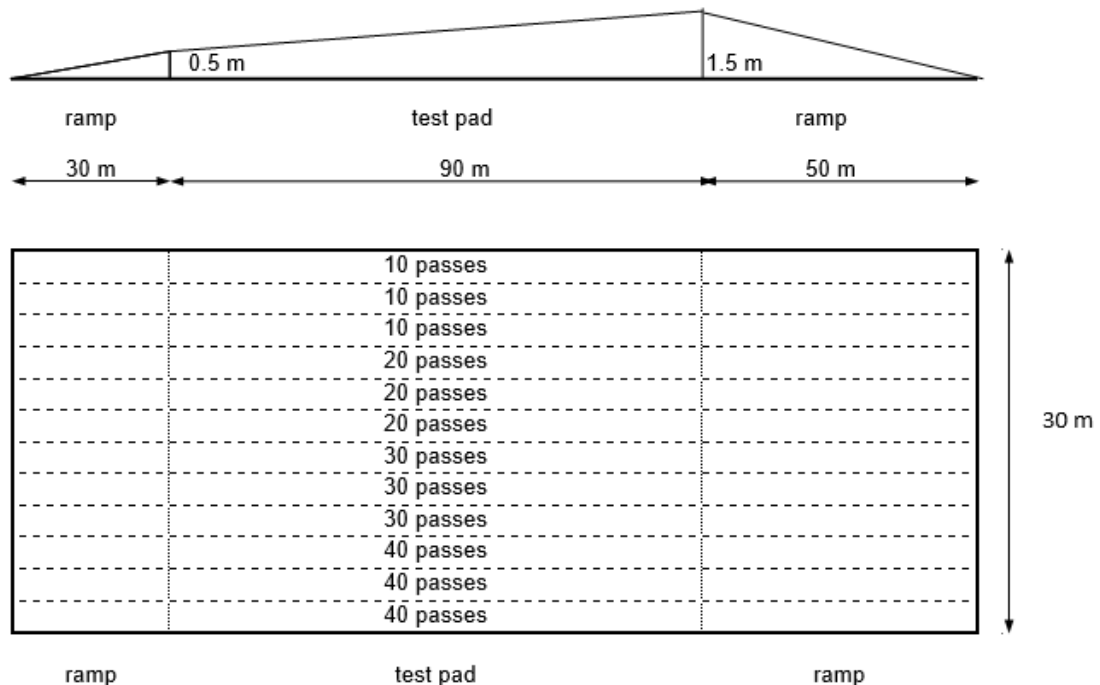


**Figure 2: Test pad for impact rolling trial**

Dynamic Cone Penetration tests were undertaken in accordance with AS 1289.6.3.2-1997. Figure 3 shows the average number of blows per 100 mm penetration versus test depth for 10, 20 and 30 passes, respectively. Due to damage to the equipment on oversized particles in hard ground, no DCP test results could be obtained in the 40-pass lane. It is evident in Figure 3 that there is noticeable improvement (higher blow counts) with increasing passes from 10 to 20 passes; however, there was minimal difference between the 20 and 30 pass results. Due to the presence of gravel, cobble and boulder-sized particles, DCP testing was often somewhat problematic.

Sixteen test pits were excavated in the centre lanes of the 10, 20, 30 and 40 pass sections of the test pad (4 no. in each section). The centre lane within each compactive effort zone was chosen for testing to be sure of accurately quantifying the applied compactive effort, as it is known that the impact roller has a lateral zone of influence extending beyond the wheelpath width, as described in Scott and Jaksa (2014). Test pits excavated to different depths enabled field density results to be obtained from varying depths. The test pits were excavated using a 32 tonne excavator with an 1,800 mm wide smooth bucket to minimise disturbance. Visually, the test pit excavations looked reasonably consistent across the test pad, although at some locations there was an obvious increase in larger particle sizes, including some instances of large boulders up to 1,700 mm in length. Generally, the sides of the test pits were stable and there was evidence of breakdown of the shot rock material and rearrangement of smaller particles around larger sizes due to impact rolling.

Of the 16 field density test results undertaken in accordance with AS1289.5.8.1-2007, all 16 test results recorded dry density ratios of at least 95% (with respect to the Standard Proctor compaction test used as a baseline for the specification), with 12 results recording dry density ratios of at least 98% SMDD as shown in Figure 4. There was no noticeable trend of increasing passes resulting in increased dry density; the test results obtained appeared to be more of a function of material variability. There was a general trend that dry density ratio reduced with depth below the ground surface; however, the test results indicated that the impact roller could successfully compact the shot-rock material in layers up to 1,500 mm thick.

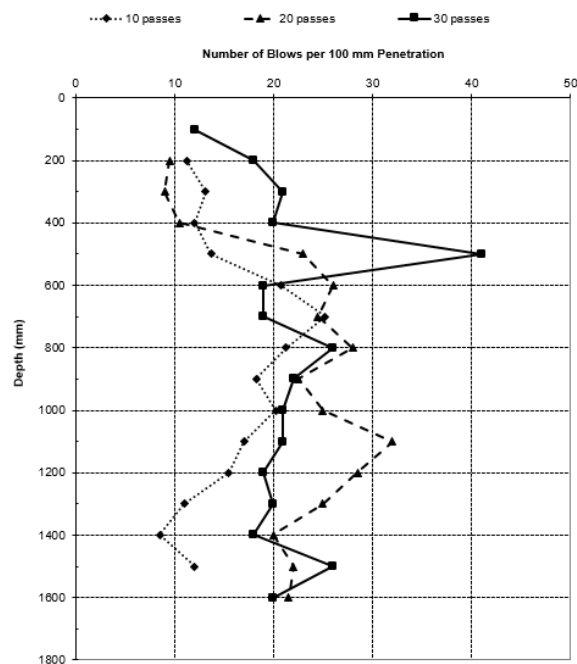
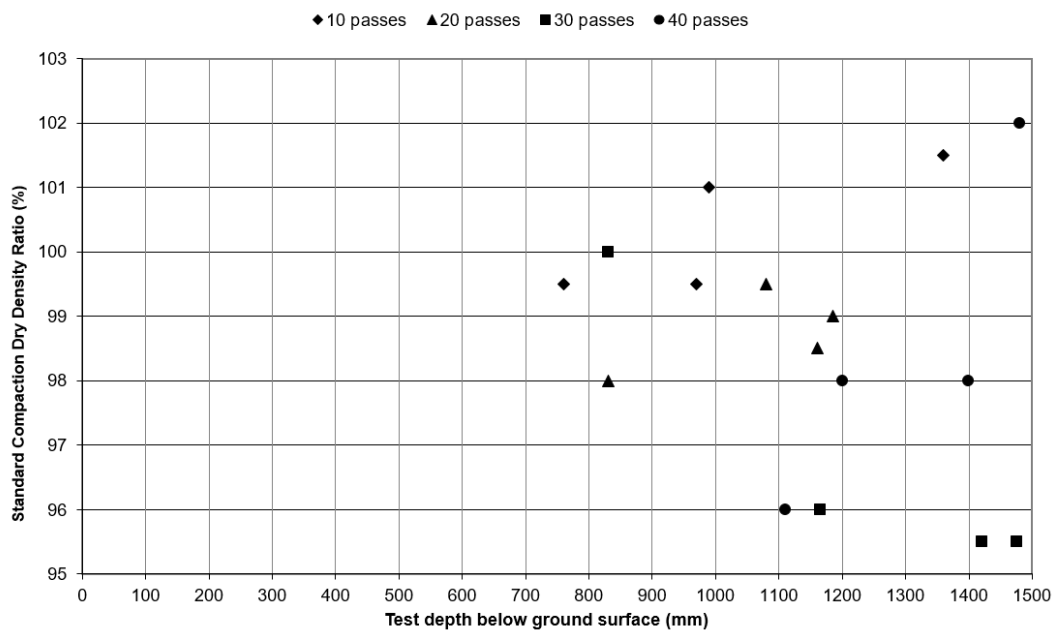


Figure 3: Dynamic cone penetration test results with increasing compactive effort

According to the 16 laboratory tests undertaken, the optimum moisture content of the fill material varied between 9 and 12.5% corresponding to a maximum dry density that varied between 1.85 and 2.07 t/m<sup>3</sup>. The field moisture content varied between 4.4 and 9.6%, with field dry densities varying between 1.83 and 2.05 t/m<sup>3</sup>.

The results of the compaction trial indicated quantifiable improvement between 10 and 20 passes of the impact roller, but minimal benefit in adopting more than 20 passes, providing that the material was suitably moisture conditioned and did not contain significant oversized material. An advantage of using the impact roller for the compaction of deep fill layers is that less screening of oversized particles is required when compared to deep fills that are placed and compacted using conventional circular drum rollers. Based on visual observations of excavated test pits, the quantity of oversized material was significant and removing large boulders from the shot-rock material was recommended such that the maximum particle size within the fill was restricted to nominally half to two thirds of the placed layer thickness.



**Figure 4: Dry density ratio versus test depth for varying passes**

A key outcome of the compaction trial was to determine the optimum number of passes for the layer thickness, taking into consideration the equipment used to dump and spread the material and moisture conditioning. The results of the compaction trial enabled an appropriate method specification to be developed; a layer thickness up to 1500 mm could be successfully compacted with at least 20 passes of the impact roller to achieve the target project specification of 95% SMDD. Whilst there was a preference to place as deeper layer as possible, thinner layers with fewer passes may be better suited to complement the processes and equipment available on site.

### VERIFICATION

The verification regime is an important aspect of deep lift compaction, as it may not be feasible (or desirable) to excavate an array of test pits to enable physical field density measurements through the full depth of the compacted layer on working haul road construction. A better approach has proven to be the intensive testing of trial pads using several testing techniques, with a resultant method specification and, if necessary, a non-intrusive verification technique. An example of this is provided by Whitely and Caffi 2013, where geophysics was employed

alongside density, dynamic cone and electrical friction-cone penetrometer testing during intensive impact roller trials.

As an example of currently available non-intrusive geophysical techniques that deliver engineering properties of the materials, Heymann 2007 describes the use of Continuous Surface Wave (CSW) testing to obtain the stiffness profile in the top few meters from the surface. The other surface wave techniques, Spectral Analysis of Surface Waves (SASW) and Multichannel Analysis of Surface Waves (MASW) also provide information on the shear wave velocities of subsurface layers. They can all be utilised before, during and after impact rolling to qualify the overall improvement and depth of improvement, as well as to quantify the amount of improvement. The shear wave velocity is related to the Shear Modulus, and hence to the Young's Modulus, of the materials. The choice of testing methods will depend on the nature and scope of the project, the technical requirements and the specifications.

### **APPLICATION EXPERIENCES - RECONSTRUCTION OF COAL MINE ROADS**

The constraints of reconstructing mine haul roads during active operations are substantial, with consistent water and construction material supply being the most influential. Other challenges include operational changes due to mine planning demands and traffic control. Speed of construction is essential to help minimise these challenges and to be able to maximise progress. Construction progress is determined by compaction and moisture conditioning capacities and the size specification of the available fill material. Adequate compaction is determined from experience and/or laboratory analysis, a certain water addition and the number of passes required by the available compaction equipment.

Conventional layered construction with traditional vibrating or static equipment is limited by shallow layer thicknesses and the need for near optimum moisture content (OMC) to achieve the desired compaction level.

In the mining environment fill quality and water supply can be influenced by:

- Drill and blast quality.
- Unpredicted variability of rock quality, especially in sedimentary sequences.
- Random oversized material supplies due to production demands (budgeted BCM/hour) preventing the loading operator from adequately selecting for size, where BCM, or Bank Cubic Metres, is the volume in situ prior to excavation/blasting, placement and compaction.
- Unnotified changes in material quality/specification.
- Hot weather (dusty) and equipment availability (e.g. water carts).

Time is of the essence in haul road reconstruction; longer than necessary construction adversely impacts production schedules which brings along with it challenges such as:

- Management pressure on production units to perform to budget.
- Reducing cooperation from production units due to the above.
- Weather delays, lightning, dust and rain.

Impact rollers (RDC) help address the variabilities delivered by the mining environment and have proven to be essential to maintain construction progress and quality. Fill quality will in the most part be highly variable due to the issues mentioned above. RDC units, when operated correctly are highly productive (over 2,000 BCM/hour, as discussed above). Thicker layers during construction allow for significant variability in particle size. The high energy delivered by RDC assists in breaking many of the oversized particles and to minimise voids in the fill.

Moisture conditioning in a highly productive and often restricted work site with conventional compaction equipment is difficult to maintain and will result in production delays. RDC with its

high energy delivery readily achieves compaction with lower moisture contents; where there is a shortage of water, it may simply be necessary to add more RDC passes to achieve the desired density.

When working in a dynamic mining environment traditional quality control testing with people on the ground is undesirable and disruptive. Proof rolling by large loaded trucks or RDC and observation of the minimal layer deflection is ample confirmation of compaction quality.

### **CONSTRUCTION QUALITY AND THE ROLE OF COMPACTION AIDS**

The construction quality of mine haul roads is reliant on several important factors after the alignment design phase, including:

- Drainage.
- Material selection, using the strongest and best available materials.
- Construction equipment, selecting the most appropriate equipment, from spreading bulldozers to compaction equipment that suit the material and water constraints of the site.
- Construction methodology that reduces voids in the compacted fill, maintains adequate moisture during construction, maximises production and compaction, and reduces lamination/separation in the constructed layers.
- Maintenance strategies that maintain drainage and road surface geometry.

A factor that can influence construction productivity and quality is the effectiveness of moisture conditioning. Achieving more even distribution of moisture and closing the gap to OMC during construction has two main benefits, the first being using lower energy to achieve the design compaction, (i.e. fewer passes with the RDC unit), the second being increased laydown rates (BCM/hour) resulting in quicker construction.

There are several techniques to achieve this, some being mechanical processes and another effective method is the use of polymer surfactants and dispersants. Surfactants are surface-active agents added to the compaction water at very low dosage rates (as low as 0.05%) that break the surface tension between the water and the soil allowing faster and more even dispersion of the water through the bulk material. This will result in direct water savings, easier to achieve compaction and lower void ratios. Dispersants polymers can be added into the compaction water to separate the fine soil particles from each other during compaction to reach the required compaction level using less compaction effort and water. The dispersing effect of the polymer at low dosage rates (approx. 0.3 litres per m<sup>3</sup> material) has a lubricating effect on the soil particles, offers good clay swelling reduction and can reduce the OMC of the material.

### **CONCLUSIONS**

Impact rollers offer mine owners, mine earthworks contractors and truck operators and managers, an extremely effective technique to deliver subgrade proof-rolling and deep-lift compaction for haul roads. Attributes and potential benefits include efficiency of road construction and programming advantages, reduced constraints on materials and improved sustainability of the process, reduced road and vehicle maintenance, and increased tyre life, and improved risk management.

The 4-sided impact roller has been, or is being, used on at least 25 coal mines in Queensland, at least 16 coal mines in New South Wales, and, amongst others, mines in Victoria, South Australia, New Zealand and in several other countries, over the last 40 years or so. RDC is a technology that has a proven record in delivering quality mine haul roads.

### **REFERENCES**

- AS 1289.5.8.1, 2007. Soil compaction and density tests - Determination of field density and field moisture content of a soil using a nuclear surface moisture-density gauge – direct transmission mode. Standards Australia, Sydney, Australia.
- AS 1289.6.3.2, 1997. Soil strength and consolidation tests - Determination of the penetration resistance of a soil – 9 kg dynamic cone penetrometer test. Standards Australia, Sydney, Australia.
- Avalle D L, 2006. Reducing haul road maintenance costs and improving tyre wear through the use of impact rollers, paper presented to *Mining for Tyres*, Perth, December.
- Heymann, G, 2007. Ground stiffness by the continuous surface wave test, *Journal of the South African Institution of Civil Engineers*, Vol 49, No 1, pp. 25-31
- Scott, B T and Jaksa, M B, 2012a. Mining applications and case studies of rolling dynamic compaction, in *Proceedings 11<sup>th</sup> Australia – New Zealand Geomechanics Conference*, pp 961-966 (The Australasian Geomechanics Society: Melbourne).
- Scott, B, Jaksa, M and Kuo, Y K, 2012b. Use of Proctor compaction testing for deep fill construction using impact rollers, in *Proceedings Int. Conf. on Ground Improvement and Ground Control*, pp. 1107-1112 (University of Wollongong: Australia).
- Scott, B T and Jaksa, M B, 2014. Evaluating rolling dynamic compaction of fill using CPT, in *3<sup>rd</sup> Int. Symp. on Cone Penetration Testing*, pp. 941-948 (Las Vegas, Nevada, USA).
- Scott, B, Jaksa, M and Mitchell, P, 2019a. Ground response to rolling dynamic compaction, *Geotechnique Letters*, **9(2)**:99-105.
- Scott, B, Jaksa, M and Mitchell, P, 2019b. Depth of influence of rolling dynamic compaction, *Ground Improvement*, Available from: [doi.org/10.1680/jgrim.18.00117](https://doi.org/10.1680/jgrim.18.00117) [Accessed: 23 August 2019].
- Scott, B T, Jaksa, M B and Syamsuddin, E, 2016. Verification of an impact rolling compaction trial using various in situ testing methods, in *Proceedings of Geotechnical and Geophysical Site Characterisation 5*, pp. 735-740 (Australian Geomechanics Society: Australia, Eds. Acosta-Martinez and Kelly).
- Thompson, R J, Peroni, R and Visser, A T, 2019. *Mining Haul Roads: Theory and Practice* (CRC Press, Taylor Francis Group: London).
- Whiteley, R J and Caffi, P, 2013. Evaluating the effectiveness of rolling impact compaction at a brownfield site with high and low frequency seismic surface waves and geotechnical testing, *Journal of Near Surface Geophysics*, doi: 10.3997/1873-0604.2013053.



# **DRILL RIG CHARACTERISTICS AND DRILLING TECHNIQUES REQUIRED FOR MAXIMUM BOREHOLE DEPTH WITH DIRECTIONAL DRILLING**

**Frank Hungerford<sup>1</sup>**

*ABSTRACT:* Directional drilling has been the established form of in-seam drilling for gas drainage, exploration and water management for the past three decades. Although there has been a desire to achieve longer boreholes to depths similar to that achieved with surface drilling, seam conditions, equipment capacity and drilling methods have limited in-seam drilling depths. Development into a new area of Metropolitan Colliery required boreholes to depths of 2000 m to provide the required gas drainage. This offered an opportunity to use a combination of slide and rotary drilling similar to that used with Surface to Inseam (SIS) drilling to achieve the required depths. This paper presents the results of the drilling, describes the drilling techniques used and defines the equipment specifications required for undertaking a range of in-seam directional drilling projects.

## **INTRODUCTION**

Directional drilling in coal mining has been developed to a stage where standard practices allow boreholes to 1400 m to be drilled regularly in slide drilling mode with the occasional borehole being drilled to beyond 1700 m. The record depth for in-seam boreholes was 1761 m in 2002 in Australia (Valley Longwall, 2002). To extend the depth to 2000 m, a combination of directional slide and rotary drilling was planned to be applied from the start. Slide drilling mode involves feeding the Down Hole Motor (DHM) into a borehole with “flip-flopping” orientations to provide directional control while with rotary drilling mode; the drill string is rotated over extended lengths while the desired trajectory and alignment are maintained.

Metropolitan Colliery is developing in the Bulli seam into a new area which has high gas content; carbon dioxide being the dominant seam gas. Limited access did not allow the standard gas drainage drilling program to be employed to drain the gas prior to mining. With the proposed gate-roads 2000 m long, the colliery approached VLI to attempt drilling long, in-seam boreholes to 2000 m and beyond to provide drainage coverage since drilling shorter holes would necessitate a staged and disrupted development to allow a progressive cycle of drilling and gas drainage. Directional drilling practices incorporating both slide and rotary drilling were developed (Hungerford and Green, 2016) with comprehensive data recording was employed to allow analysis of drilling performance.

This paper presents the results of the successful completion of that drilling and defines the key elements of equipment specifications required for the directional drilling of longer boreholes.

---

<sup>1</sup> *Global Technical Services Manager, Drilling Division, VLI E-mail: [FHungerford@Vli.com.au](mailto:FHungerford@Vli.com.au)  
Tel: +61 249 642 300*

## DEPTH LIMITATIONS

As in-seam directional drilling was being developed in Australia in the late 1980's, the standard NQ sized configuration used a 73 mm diameter DHM fitted with a 1° bend to drill an 89 mm diameter borehole. Directional control was achieved by repeated "flip-flopping" of the alignment of the DHM bend; usually at 6m intervals. The feed pressure provided by the drill rig started surging beyond 60 m so the feed rate was progressively reduced to prevent stalling of the DHM as borehole depths increased (Hungerford, *et al*, 1988). Eventually surging and the resultant stalling caused the termination of drilling with 1005m being the longest borehole achieved.

Larger diameter drilling using a higher torque capacity DHM was proposed to reduce the effects of in-hole friction. A 2-7/8" Accu-drill DHM was offered to the industry in 1992 through Asahi (Walsh and Hungerford, 1993.). This unit had a non-magnetic, high-torque, low-speed 4-5 lobe motor section (Hungerford, 1995) which, when fitted with a 1.25° bend and combined with a 96.1 mm diameter Poly Crystalline Diamond (PCD) drill bit, greatly reduced surging with drilling rates and depths improved. In 1993 and 1994, the first two boreholes drilled with this configuration achieved lengths of 1233 m and 1535 m (Walsh and Hungerford, 1993). This configuration was established as a standard for in-seam directional drilling in Australia and eventually the world. The deflection provided vertical control through a variety of seam conditions while also allowing adequate lateral deviation to achieve curved borehole layouts.

With the higher thrust loading involved, the capacity of in-hole equipment was going to be tested. Analysis of drilling data collected from long-holes (with torque/drag models established) showed the NQ drill rod strength was adequate for the depths being achieved (Gray, 1991), but the suggestion was that borehole depths would eventually be limited due to helical buckling with the current drilling techniques (Gray, 1992). Tests of rod strength had proven that the preferred drill rod joint classed as CHD76 being adopted by the industry was the superior rod in strength and ease of handling in jointing (Gray and Daniel, 2000). Table 1 gives a comparison of torque capacities and the torque of the larger CHD90 rods. Withdrawal friction and rotational torque were also thought to be possible limiting factors from these analyses.

**Table 1: Drill Rod Specifications**

Rod	Diameter (m)	Weight - 3m (kg)	Max Torque Rating (Nm)
NQ	69.9	23.4	750
CHD76	69.9	24.5	2430
CHD90	88.9	36.3	3150

The maximum borehole depths being achieved varied without apparent changes in drilling practices or conditions but comprehension recording of drilling data allowed trends to be established (Hungerford, *et al*, 2012):

- The thrust required in all boreholes started increasing more rapidly as significant depths were reached (Figure 1).
- The maximum thrust capacity of the drill rig was not usually reached before drilling was terminated due to stalling of the DHM.
- Altering the orientation of the DHM at 3m intervals as shown in Borehole MG40-30-1 (Figure 1) greatly reduced the depth achieved.
- Boreholes with substantial lateral curves early achieved equivalent or greater borehole depths.

It was established that as the axial loading through the rods increased, the rods were being flexed through the regular left/right curves created by the “flop/flop” directional drilling and forced into the outside walls of curves in the boreholes. With axial loading greatest in the rods closest to the collar of the borehole, the nature of the curves early in the borehole had greatest effect on the borehole friction. And as this friction is overcome to start moving the rods in the borehole, the rods surge forward driving the bit into the face to create a torque loading spike which tends to stall the DHM. Even with high enough thrust capacity, the rig can't feed the DHM into the face at a consistent rate that avoids stalling.

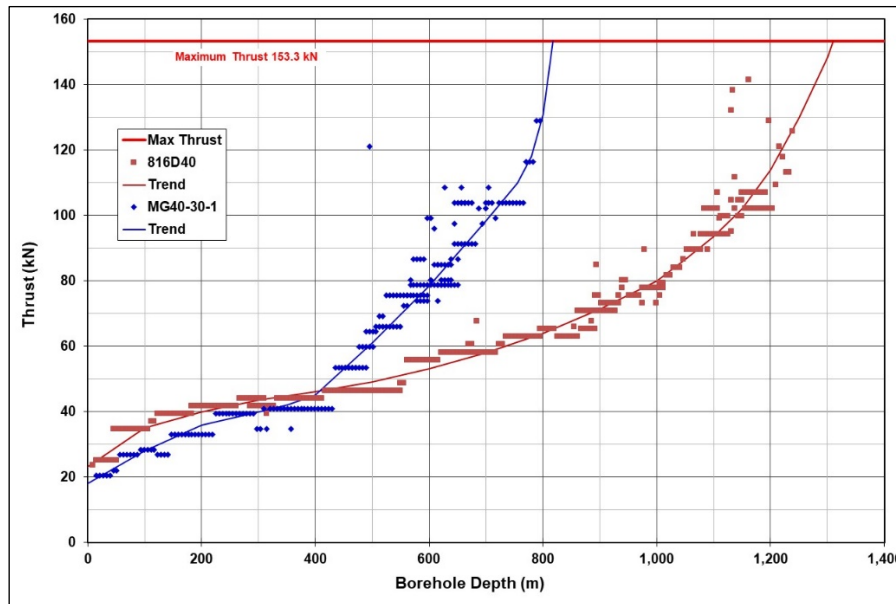


**Figure 1: Thrust loading in directional drill boreholes with 6m and 3m orientation changes**

### Surveying

The survey systems were thought to be a limiting factor with some signal problems being experienced previously when drilling boreholes beyond 1500m. Subsequent development of the Drilling Guidance System (DGS) (McCabe and Hellyer, 2013) had apparently improved signal strength and transmission but this had yet to be proved over the greater depths.

### Rig capacity

The initial drill supplied for the project was a modular VLI Series 1000. This drill rig had a thrust capacity of 104.6 kN (compared to 140 kN of the track mounted Series 1000) and a torque capacity of 2430 Nm. The lesser thrust capacity was thought to be a possible limitation in achieving 2000 m when compared to the 220 kN capacity of the Fletcher LHD used previously for the record drilling to 1761 m.

### Drilling practice

Since it was known that borehole depths were going to be limited to only 1500m with conventional slide drilling, a version of rotary/slide drilling was proposed. The method of drilling termed “Production Drilling” is commonly used by SIS drilling and previously in some shorter underground drilling operations (Eade, 2002).

Before drilling commenced, the drillers were instructed on the drilling practices required for the project. Most drillers had used rotary/slide for short sections of drilling on previous projects so were comfortable with adopting the practice. The initial drilling parameters included:

- Slide drilling to establish position and dip within the seam and on alignment/azimuth.
- Slide drilling to maintain lateral borehole curve to maintain horizontal positioning of the borehole (follow the flight path).
- Slide drilling to target the seam roof for seam profile definition.
- Slide drilling to establish each subsequent branch.
- 200 litres/min water flow to operate the DHM.
- Rotary drilling whenever possible when comfortably on line.
- Rotary drilling at 30 – 60 rpm to limit damage and wear to the DHM.
- Record usual drilling parameters of thrust and hold-back hydraulic pressures and water idle and drilling pressures.
  - Record main hydraulic pump pressure when rotary drilling.
  - Survey at 6 m intervals and also record each 3 m intermediate survey.
  - Avoid short interval orientation changes when slide drilling.

The project was undertaken operating with two man shifts (a driller and one off-sider) of eight hour duration at the site. This allowed the drilling of each borehole to continue without regular significant delays.

### **Drilling configuration**

The DPI equivalent of the non-magnetic 4/5 Accu-Dril DHM was used with a 1.125° bent housing fitted with a 1 mm thick wear pad. A standard Asahi 96.1 mm diameter PCD bit was used which combined for an off-set at the bit (B) in Figure 2 (Hungerford and Green, 2016) of 6.7 mm. This was equivalent to being fitted with a bent housing of 1.22°. When initially rotating the DHM, the heel of the bend would be flexed 2.9 mm to fit within the 96.1 mm diameter until either the hole diameter was increased by the rotation or a straighter section of borehole is created.

After the first hole, the bit size was increased to 99 mm by moving the outer cutters outward. This reduced the offset at the bit (B) to 5.3 mm and thus reduced the effective bend to 1.12°. In rotating the DHM, the heel of the bend fitted within the 99 mm diameter and avoided any forced flexing of the DHM.

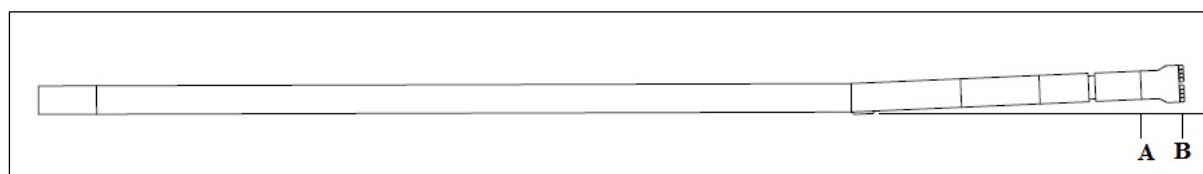


**Figure 2: Deflection of DHM (A) and bit (B) with wear pad**

### **Drilling Conditions**

Ultimately, drilling conditions have an influence on the borehole depths achieved. Good intact coal conditions allow for easy directional drilling with DHMs with minimal problems of in-hole collapse and bogging. If any unstable conditions are experienced, ongoing drilling beyond that point would always be suspect with loss of expensive equipment being the main concern. Drilling to extreme depths beyond the 600-700 m over-coring capacity eliminates over-coring recovery as insurance and plans need to be in place to eventually recover the equipment when intersected by mining. The Bulli seam has an average thickness of 3.0 m with no geological structures expected in the area of the proposed drilling.

## Drilling results

The details of the eleven boreholes were completed from two drill sites are shown in Table 2 in the sequence of drilling. All boreholes were drilled with a combination of slide and rotary drilling with each borehole having different applications of rotary drilling, off-set entry angle and eventual lateral deviation. That delivered a different depth in each borehole from which slide drilling could no longer continue and drilling was continued with rotary drilling only. The table indicates the depth to which slide drilling was possible, the lateral deviation and the reason for terminating each borehole. The first borehole (EX03) which was used as an exploration borehole to define the seam profile involved more roof intersections and subsequent branching and more metres drilled. Most boreholes were completed with average drilling rates above 100 m/shift.

**Table 2: Borehole Data**

Borehole	Depth (m)	Total Drilling (m)	Slide to (m)	Lat Dev (m)	Shifts	Drilling Rate (m/shift)	Terminated
EX03	1779	2775	1746	116 L	33	84.1	No signal
EX02	1875	2124	1851	58 L	16	132.7	Floor
DH01	1971	2205	1803	31 L	17	129.7	Floor
DH04	2001	2196	1821	129 L	17	129.2	Roof
DH05	2007	2568	1653	78 R	28	91.7	To design
DH08	2151	2568	1743	40 L	20	128.4	No rods
DH09	2103	2451	1761	83 L	21	116.7	No rods
DH10	2007	2610	1761	121 L	26	100.4	To design
DH11	2016	2451	1920	166 L	21	116.7	No rods
DH06	2007	2154	1923	145 R	21	102.6	To design
DH07	2013	2184	1884	0 L/R	18	121.3	To design

Figure 3 has the eleven boreholes plotted on the mine plan showing the proposed gate-road development. Drilling conditions were found to be stable with no structures or boggy conditions experienced.

With little geological and RL information in the area of the proposed drilling, the initial borehole (EX03) served as an exploration hole with regular roof intersections to define the seam profile. This borehole was terminated at 1716 m, which had established a new world record for underground drilling.

Each subsequent borehole increased that record until DH08 established the world record at 2151 m (Table 2). Being the first borehole from the 9 c/t site, regular roof intersections were completed for seam profile definition (Figure 4). The borehole was drilled with a combination of slide and rotary out to 1743 m (Table 2, Figure 5); at which point 45% had been slide mode with 55% rotary. The remainder of the borehole was drilled in rotary mode.

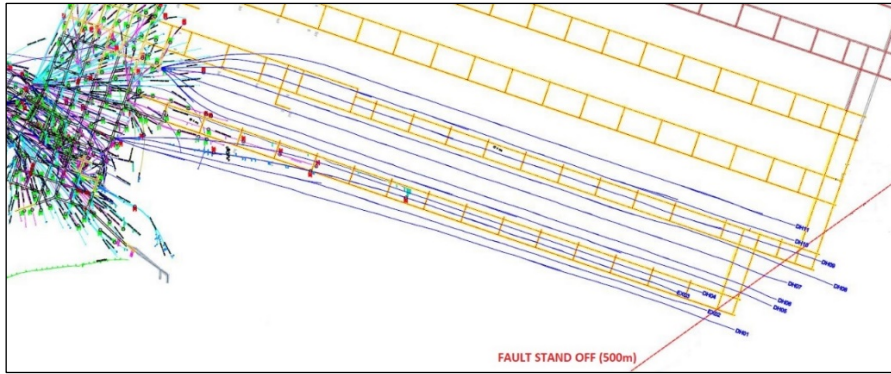


Figure 3: Plan of longhole coverage of proposed gate-roads

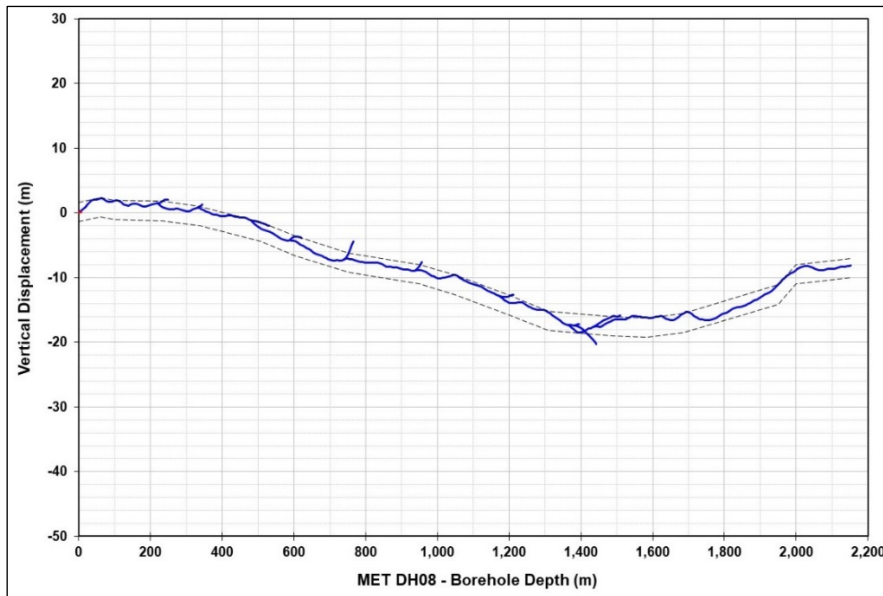


Figure 4: Seam and borehole DH08 profile

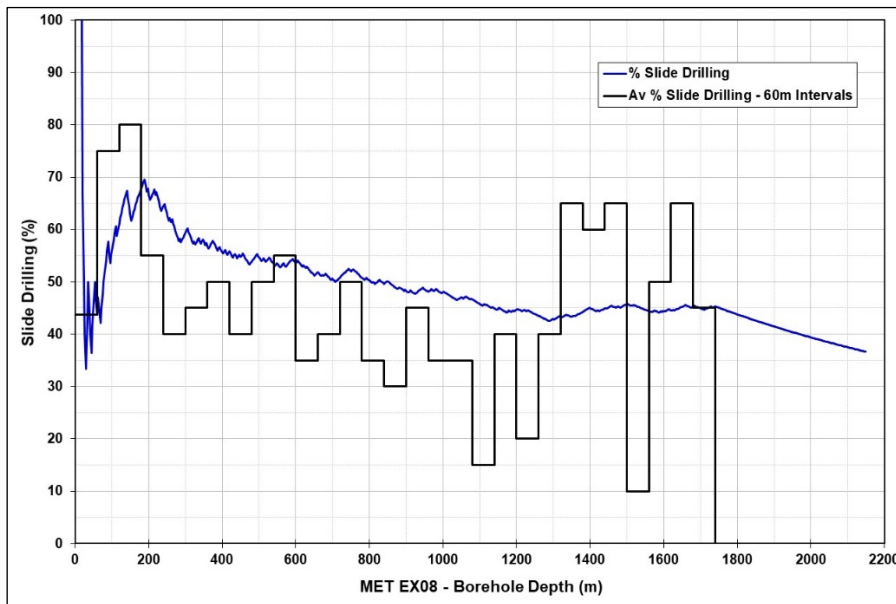


Figure 5: Drilling mode – slide and rotary drilling



Because of limited access, the boreholes could not be designed as straight holes along their target azimuth with a zero lateral deviation. They were designed with off-set angles and lateral curves to provide the required drainage coverage and not set up specifically to create depth records. The lateral deviations are plotted for the boreholes from the two sites (Figures 6 and 7).

The plot of thrust on the drill string for slide drilling (Figure 8) displays the usual trend of increased drilling rate increase with depth, indicating the increased friction effect of curves earlier in the borehole (Hungerford, *et al*, 2012). This trend extrapolated to 140 kN thrust indicated the greater capacity track mounted Series 1000 rig would possibly have managed slide mode drilling to 1850 m in this borehole if surging didn't stop drilling beforehand.

In rotary drilling mode, in-hole friction is greatly reduced (Figure 8) and only starts to increase gradually from the 1400 m depth.

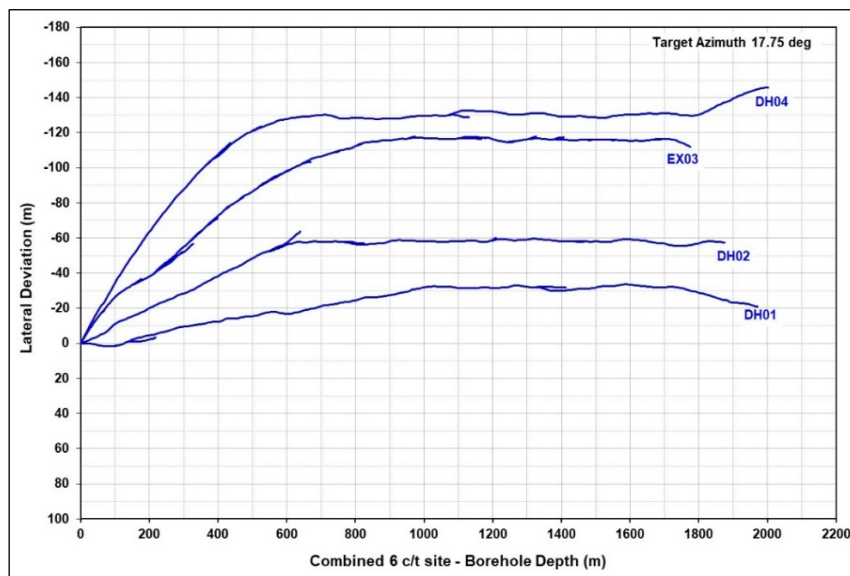


Figure 6: Lateral deviation of boreholes from 6c/t site

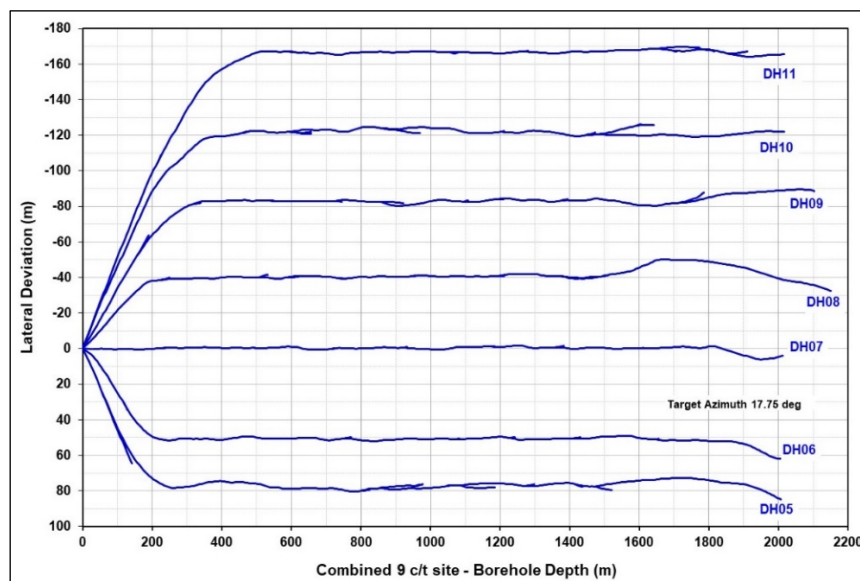
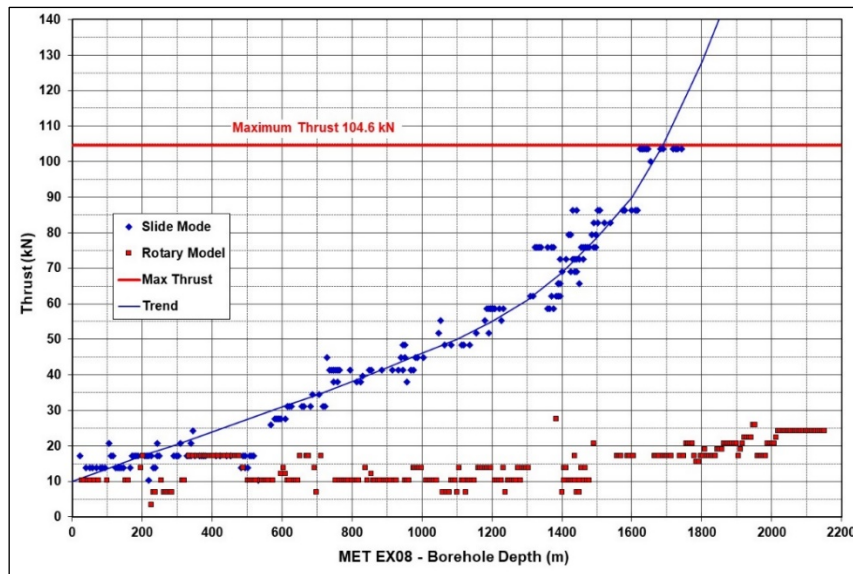


Figure 7: Lateral deviation of boreholes from 9c/t site



**Figure 8: Thrust loading in slide and rotary drilling modes**

As the trend data from more boreholes are added to the thrust graph (Figure 9), it becomes apparent that the rapid increases in thrust later in each borehole are relatively consistent. The depth at which the rapid increases begin seems to correspond with thrust in the 50-60 kN range with the rate at which that thrust is achieved determining the final depth achieved. The friction due to curves early in each borehole influences the rate of increase in thrust loading and at a thrust loading of 50 kN, the rods are starting to be flexed and driven laterally into the outer sides of each alternate curve in the borehole.

Slide drilling was terminated in all boreholes drilled with the modular rig due to the maximum thrust capacity of 104.6 kN being reached. Slide drilling in the last three boreholes using the higher capacity 140 kN track rig was terminated due to surging feed well under the maximum thrust capacity.

Borehole DH11 was the most successful with depth drilled before slide drilling could not continue. This borehole had the greatest initial off-set angle to the target azimuth and the largest lateral deviation of 166 m to the left. The percentage of slide drilling did not differ appreciably from other boreholes but it was noted that all drilling from 60m to 600m was either slide drilling to the right or rotary drilling.

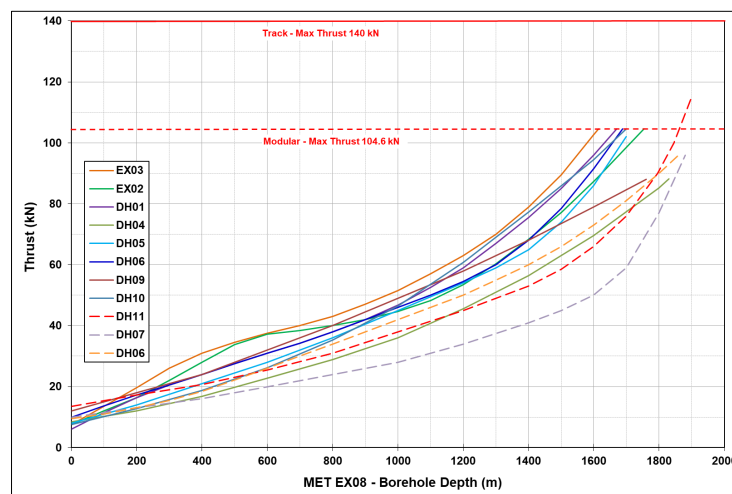


**Figure 9: Thrust loading trends**

The reduction in friction provided by rotating the drill rods also provided consistent feed at the bit compared to the surging feed experienced in slide mode. With consistent loading on the bit, drilling rates are more consistent over depth (Figure 10) compared to the rapid reduction in the slide drilling rate to avoid stalling the DHM. The rapid decline of drilling rate corresponded with the rapid increase in thrust loading.

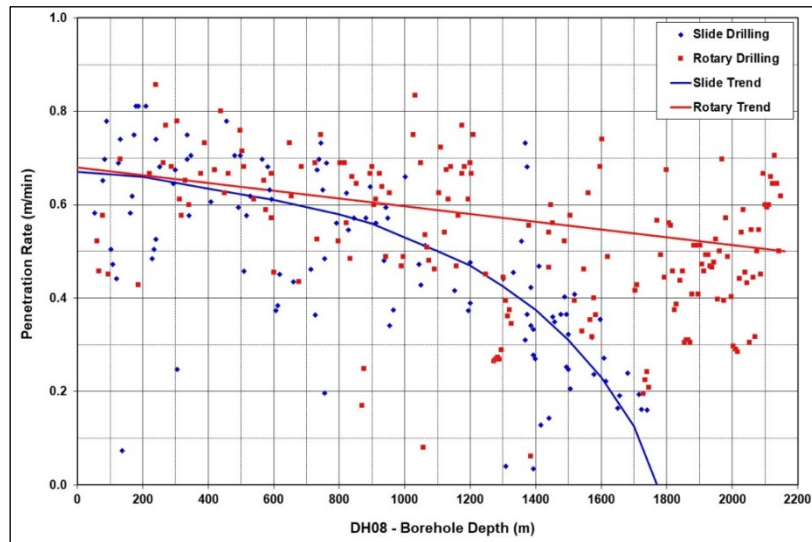


**Figure 10: Drilling rate – slide and rotary drilling**

Although the thrust loading was approximately 25% capacity while rotary drilling, the rotational torque loading (Figure 11) was at approximately 70% capacity at depths of 2000 m. The increase in torque loading was relatively linear with increase in depth so apparently not influenced by the extent and magnitude of deviations in the boreholes. At the limit of directional (slide) drilling (1800m), only 62% of the torque capacity was employed. An extrapolation of the trend has the maximum torque capacity reached at 2800 m.

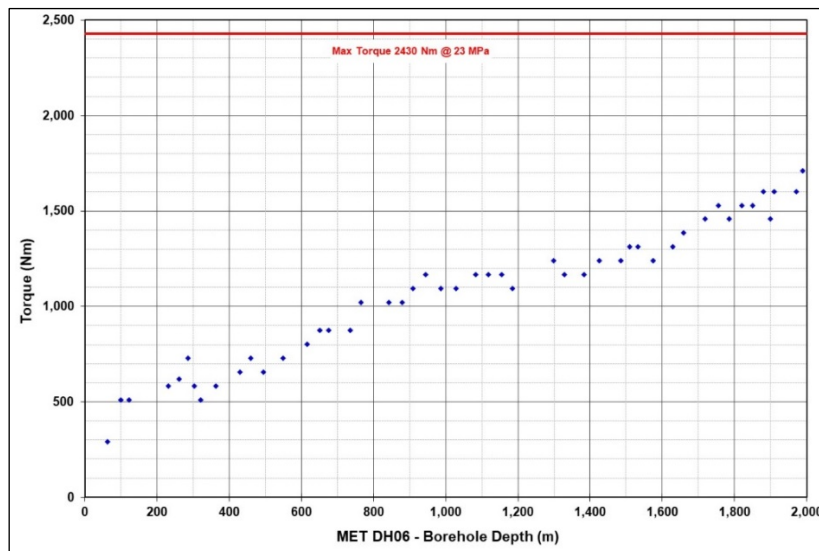


**Figure 11: Torque loading when rotary drilling**

The drilling used 200 litres/min water flow to assess the progressive increase of pressure with depth and identify any potential problems of water pressure capacity. From Figure 12, the idle

pressure increased from 1.5 MPa (at the start) at a rate of 0.15 MPa/100 m. The drilling pressure decreased gradually over the depth of the borehole as drilling rates decreased.

Although the idle pressure was more than 2 MPa below the maximum available pump pressure at depths beyond 2000 m, some problems were encountered when starting the DHM. Water pump capacity would likely be the limiting factor of rotary depth capacity of the drilling system.

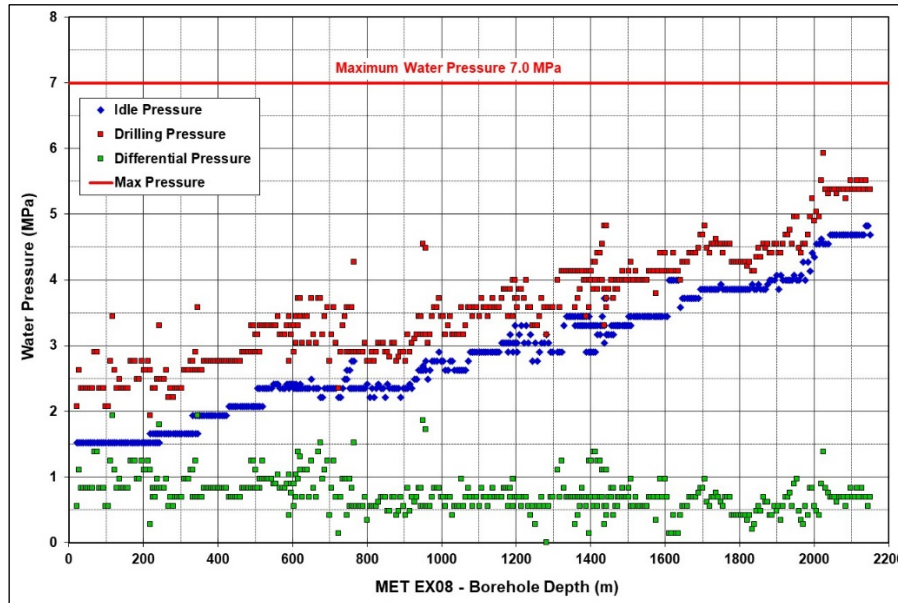


**Figure 12: Drilling water pressure**

The vertical and lateral deviations over each 3 m interval were plotted for both slide and rotary drilling (Figure 13). The rotary drilling did not create straight sections of borehole but the deviations were reduced as seen by the tighter grouping in Figure 13.

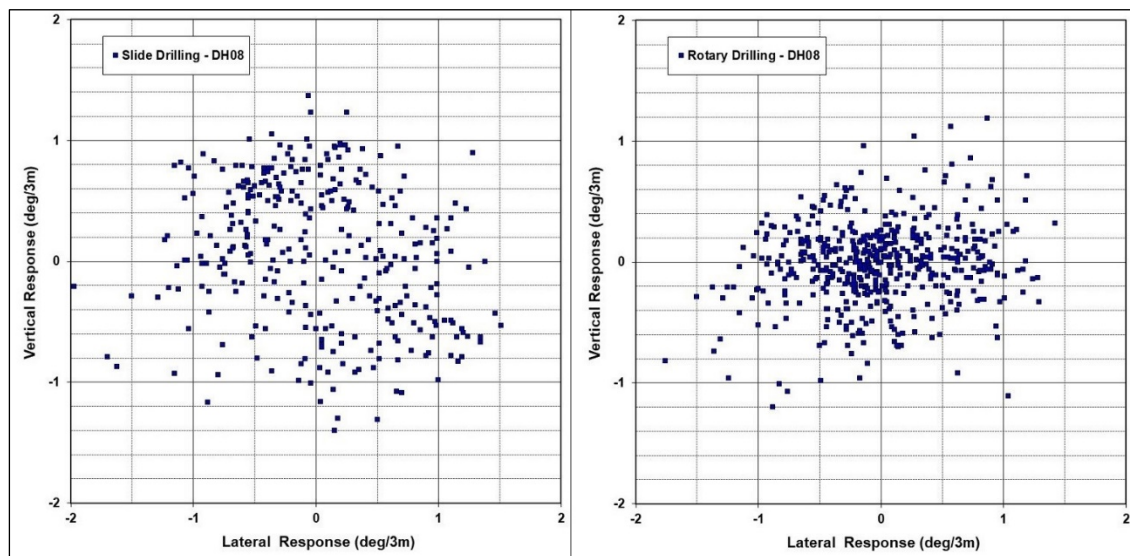


**Figure 13: Deviation of slide and rotary drilling per 3 m intervals**

Although the drillers were limited to rotational speeds below 60 rpm in the pre-drilling instructions, the drillers experimented with traditional rotary drilling variations of increased rotational speed (to 180 rpm) and reduced drilling rate to curve the borehole downwards. Conversely, they reduced rotational speed and increased drilling rate to curve the borehole

upwards. This was used successfully to extend all boreholes past the no slide depth. The most effective was in borehole DH08 with an additional 408 m being drilled with rotary drilling to the final depth of 2151 m (Table 1) after slide drilling was no longer possible.

The drillers noticed that they had some lateral control with the vertical control parameters. They believed climbing parameters deflected the borehole to the right and dropping parameters deflected the borehole to the left.

## CONCLUSIONS

Conventional directional drilling only with N sized rods and 73 mm DHM will always be limited to depths of approximately 1500 m due to the effects of in-hole friction.

Significant increase in bit diameter and matching DHM deflection with the current system may change the friction dynamics enough to extend the directional drilling depth capabilities to and beyond 2000m.

The combination of slide and rotary drilling with a DHM can extend the directional drilling capacity to approximately 1900 m but increasing the thrust capacity of drill rigs will not overcome the surging which ultimately limits the maximum depth of all directional drilling. Extending drilling past the depth to which directional drilling is possible can only be classed as rotary drilling – slide drilling for directional control is no longer possible.

DHMs must always be provided with enough deflection to provide directional control both vertically and laterally. Reducing the deflection to provide just enough vertical control may not provide enough lateral deviation to follow flights plans with significant lateral off-set. The increased clearance provided by the bit size and DHM deflection for steering also results in significantly more deflection when rotary drilling than is experienced by low clearance core drilling. As such, rotatory drilling with a DHM will always produce some deflections in the borehole contributing to increased friction and eventual surging.

DHMs with higher torque capacity can be used to reduce the susceptibility to stalling.

The VLI Series 1000 drill rig was essentially designed as a 1000 m capacity directional drilling rig for the Chinese underground drilling market. But the drilling parameters defined by this project have shown:

- With the 104.6 kN thrust capacity of the modular Series 1000 drill rig, directional drilling can reach depths of 1700-1800m before the maximum thrust capacity is reached.
- With the 140 kN thrust capacity of the track mounted Series 1000 drill rig, drilling depths can be extended until surging causes the termination of directional drilling. The maximum thrust capacity of the drill rig has not been utilised.
- The hydraulics of the rotation system is set at a maximum of 23 MPa (of the 29 MPa available) to provide a maximum torque of 2430 Nm. This torque is listed as the maximum working torque of the CHD76 rods (Table 1) and the maximum recommended pre-torque to which the rod joints should be tightened. Rotary drilling utilised only 1500 Nm (62% of maximum) at the 1800m depth to which directional drilling was regularly achieved.
- The higher rotation torque in reverse could be provided to separate tight rod joints.

In defining the capacity of a directional drill rig, the three key characteristics that must be considered are:

- Thrust capacity to provide the maximum thrust required for the size of directional drilling,
- Rotational torque capacity to match the maximum operating torque capacity of the rods being used, and
- Water pump flow and pressure capacities to suit the DHM being used.

The specifications of the Series 1000 drill rigs have been shown to be sufficient (with some margin) to manage longhole directional drilling projects. Any increase in capacity of drill rig for N sized directional drilling is unwarranted and will not extend the depths beyond what is achievable.

#### REFERENCES

- Eade P, 2002. Case study – Outburst and gas management, Proceedings Underground Coal Operator's Conference (ed: N Aziz), University of Wollongong, p 105. February, 2002.pp 105 -113. <http://ro.uow.edu.au/coal/199/>
- Gray I, 1991. Limits of directional drilling for coal exploration, Australian Coal Association Underground Coal Mining Exploration Techniques, Brisbane 8-9 November, 1991.
- Gray, I, 1992. Development of in-seam drilling for the production of methane, Symposium on Coalbed Methane Research and Development in Australia, Coalseam Gas Research Institute, James Cook University of North Queensland. Townsville, 19-21 November 1992.
- Gray I and Daniel B, 2000. Testing of and research into drill rod joints for longhole drilling, Final Report ACARP Project 4039, June, 2000.
- Hungerford F, 1995. Status of Underground Drilling Technology, Keynote Address, in Proceedings of the International Symposium cum Workshop on Management Control of High Gas Emission and Outbursts in Underground coal mines, Wollongong 20-24 March 1995 pp. 397-404.
- Hungerford F and Green W, 2016. In-seam boreholes to and beyond 2000 m with a combination of slide and rotary drilling, in Proceedings of the 2016 Coal Operators' Conference (ed: N Aziz), University of Wollongong, 10-12 February, pp 224-235.
- Hungerford F, Kelly M, Saghafi A, Williams R, 1988. Long-Hole Drilling for Gas Emission Control at Appin Colliery NSW, Australia, Fourth International Mine Ventilation Congress, Brisbane, Queensland, July 1988.
- Hungerford F, Ren T, Aziz N, 2012. Directional Control in Longhole Drilling, 2012 Coal Operators' Conference. University of Wollongong, Feb 2012.pp.268-276. <http://ro.uow.edu.au/coal/415/>
- MacCabe M and Hellyer A, 2013. Reduction of outbursts through directional drilling, MEMMES 60th Anniversary Convention, 2013.
- Valley Longwall P/L, 2002. Unpublished drilling records, borehole S7TG-B1, Newlands Colliery. February, 2002.
- Walsh R and Hungerford F, 1993. Exploring longwall domains using directional longhole drilling. Longwall in Australia continuous improvement or crisis, ACIRL Underground Mining Seminar, Sydney, Australia. 19-20 November, 1993



# A DISCUSSION ON CAUSATION MECHANISMS FOR OVERBURDEN BUMPS AS DISTINCT FROM COAL BURSTS

Russell Frith<sup>1</sup>, Guy Reed<sup>2</sup>, Martin Mackinnon<sup>3</sup>

**ABSTRACT:** The entire subject area of micro-seismic events due to stored strain energy, as distinct from gas-driven coal outbursts, can be readily sub-divided into firstly events with their energy source from within the coal seam (termed “bursts”) and secondly, event with their energy source outside of the coal seam in either the overburden and/or floor strata. The reason for sub-dividing micro-seismic events in this manner is that if the causation mechanisms and associated geotechnical conditions are materially different, then effective pre-mining predictions and subsequent operational controls may also differ. Attempting to explain a multitude of micro-seismic event types without consideration of varying source mechanisms will inevitably lead to inadequate causal explanations and effective controls.

The paper outlines several different causal mechanisms for bumps emanating from both the overburden and/or floor of a coal seam by reference to both theoretical treatments and known associated case histories. These include massive pillar collapses (including the Coalbrook disaster in 1960), large-scale shear slip along fault planes/other geological discontinuities, the compressive failure of thick and strong strata units and finally, multi-seam stress effects.

The objective of the paper is to provide an initial “*cause and effect*” list of geological and geotechnical circumstances that can and indeed have resulted in large magnitude micro-seismic events during underground coal mining activities, being able to predict the likely propensity for such significant events prior to mining being the first requirement in an effective prevention or consequence mitigation process.

## INTRODUCTION

In relation to the specific phenomenon of development coal bursts, as distinct from overburden and/or floor bumps, Frith and Reed (2019) outlined a first-principles causation mechanism and specific geological circumstances related to the 2014 Austar tragedy and more general features of the reported development coal-burst prone, Sunnyside Mine in Utah, USA. A clear distinction was made between generic “bursts” whereby the energy source is within the coal seam, as distinct from “bumps” whereby the energy source is within the overburden or floor of the seam (this being the definition of the term “bump” herein), and “outbursts” which are gas-pressure driven. These three fundamental event types were represented as a Venn diagram (Figure 1), the potential for hybrid events with more than one energy source involved being recognised, but in no way proven in the field.

---

<sup>1</sup> Principal Geotechnical Engineer, Mine Advice Pty Ltd. Email: [russell.frith@mineadvice.com](mailto:russell.frith@mineadvice.com) Tel: +61 409056514

<sup>2</sup> Principal Geotechnical Engineer, Mine Advice Pty Ltd. Email: [guy.reed@mineadvice.com](mailto:guy.reed@mineadvice.com) Tel: +61 407496283

<sup>3</sup> Senior Geotechnical Engineer, Mine Advice Pty Ltd. Email: [martin.mackinnon@mineadvice.com](mailto:martin.mackinnon@mineadvice.com) Tel: +61 417431172

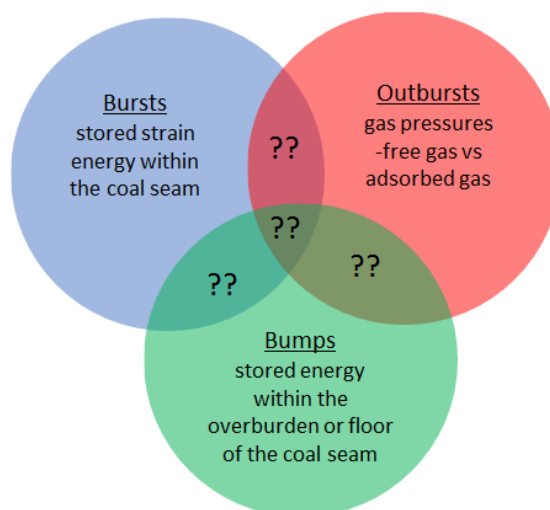


**FIGURE 1: Suggested Classification of High Energy Release Events in Underground Coal Mining (Frith and Reed 2019)**

Frith and Reed 2019 made the statement that “a general review of the literature relating to coal bursts quickly reveals an obvious lack of consistent terminology across bursts, bumps and gas outbursts...”, the point being that without clear definitions of event type and in particular, associated causation mechanism, there might be a tendency to categorise individual events incorrectly, this potentially leading to increased confusion rather than clarity. This was to a large degree demonstrated in the recent ACARP-sponsored coal burst workshop in Australia whereby international experts from several countries were invited to share their knowledge, the vast majority of which related to overburden bumps or gas outbursts, rather than development coal bursts of the type that occurred at Aустar. This is not to diminish these contributions, simply to indicate that there clearly remains general confusion as to what constitutes a “burst” as distinct from a “bump” in terms of causation.

It is hypothesised that part of the confusion may be a disjoint between the observation of an event manifestation, as compared to the source of and release mechanism of the driving energy. How an event may be experienced by persons in the mine or the resultant altered conditions of the mine workings following an event (e.g. violent coal rib failure, rapid floor heave, significant closure of an excavation etc.) may be similar for a range of different energy-release event types. As such, attempting to define and understand energy sources and release mechanisms using the resultant impact on the mine workings may be less than reliable, hence the confusion along the lines just described.

This paper seeks to provide an improved level of clarity by considering potential energy sources and release mechanisms from overburden and/or floor bumps rather than their direct impact on the mine workings, this being based on both a theoretical problem treatment and the use of selected case histories.

### **GENERIC BUMP MECHANISMS AND ENERGY RELEASE MECHANISMS**

When discussing mining-induced seismicity and “rockbursts” Brady and Brown 2005 consider that two distinct source mechanisms may be involved, one related to shear-slip along pre-existing geological discontinuities, the other due to crushing of the rock mass, noting also that the study of such events may be best facilitated by accounting for energy changes within the system. These basic principles are at the core of the discussion herein relating to “bumps” in underground coal mining.

The bump causation mechanisms outlined herein are based on the following generic principles:

- (i) Two of the three distinct failure mechanisms of a linear arch.
- (ii) Stress-driven shear slip along large-scale pre-existing planes of weakness.

Examples of these general behavioural mechanisms using coal mining field experience will be provided, prior to which it is necessary to briefly summarise the governing principles of a linear arch or Voussoir beam, as well as stress-driven shear slip along a pre-existing plane of weakness. It is also useful to have a frame of reference for energy release magnitudes when considering bump causation mechanisms at a fundamental level.

### Governing Principles

The Linear or Voussoir Arch is outlined in detail in Brady and Brown 2005. The general beam configuration and the associated internal compression arch, as originally put forward by Evans 1941, is shown in Figure 2, the critical characteristic being that such a beam can fail in one of three distinct modes – (a) vertical abutment shear, (b) horizontal compression at or close to the crown of the beam or (c) uncontrolled buckling. On the basis that buckling is generally not associated with a rapid significant energy release, the discussion herein will focus on vertical abutment shear and compressive failure of intact material as two potential coal mine bump causation mechanisms.

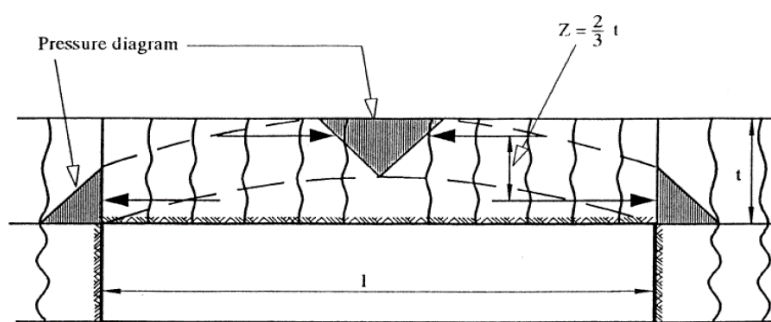


**FIGURE 2: Linear Arch Concept (Evans 1941)**

Stress-driven shear slip along pre-existing major geological discontinuities such as faults, is well established in the seismology literature, the application herein relating to mining seismicity on a smaller-scale than that involved in regional earthquakes for example. The basis for stress-driven shear-slip along a plane of weakness involves two distinct aspects – (i) resolving the acting ground stresses into shear (parallel), and normal (perpendicular) components relative to the plane, and (ii) assessing whether the resultants will result in shear slip along the plane using a Mohr-Coulomb representation. Figure 3 is taken from National Research Council 2013 and illustrates the basic problem as just described, including the potential influence of pore pressure,  $p$ , if relevant.

Both the linear arch and stress-driven shear slip along a plane of weakness are simple to understand and analyse, the applicability of both to coal mine bump propagation being considered in more detail later in the paper.

If one accepts the hypothesis that a bump is a direct consequence of energy release from either the roof or floor strata, it is useful to start with the general equation for a changing mechanical or potential energy state of any system (kinetic energy being ignored in this instance), namely:

$$\text{Initial Total Stored Energy (TSE}_i\text{)} + \text{work done} = \text{Final Total Stored Energy (TSE}_f\text{)} \quad (1)$$

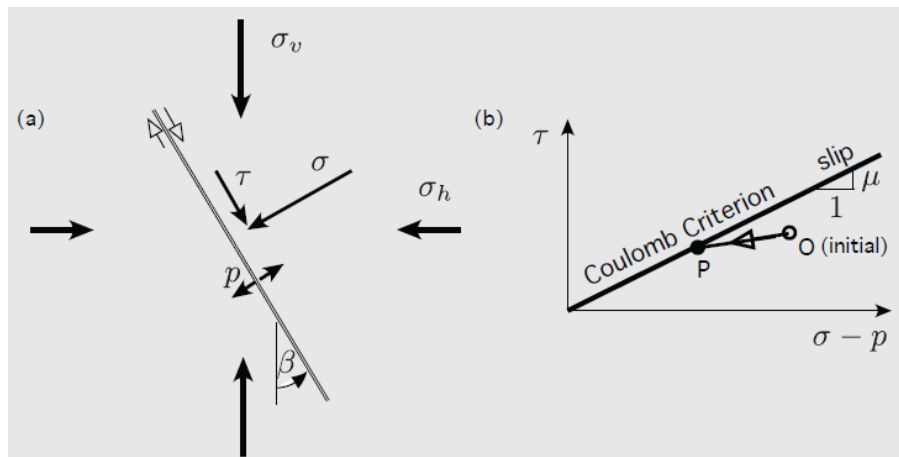


**FIGURE 3: Shear and normal stress components along a plane of weakness and a Mohr-Coulomb shear strength representation (National Research Council 2013)**

In other words, the energy released should  $TSE_f$  end up being less than  $TSE_i$  can be considered as “negative work”, the general equation for work being given by:

$$\text{work} = \text{force} \times \text{distance} \quad (\text{or in this case } \underline{\text{stress} \times \text{area} \times \text{strata displacement}}) \quad (2)$$

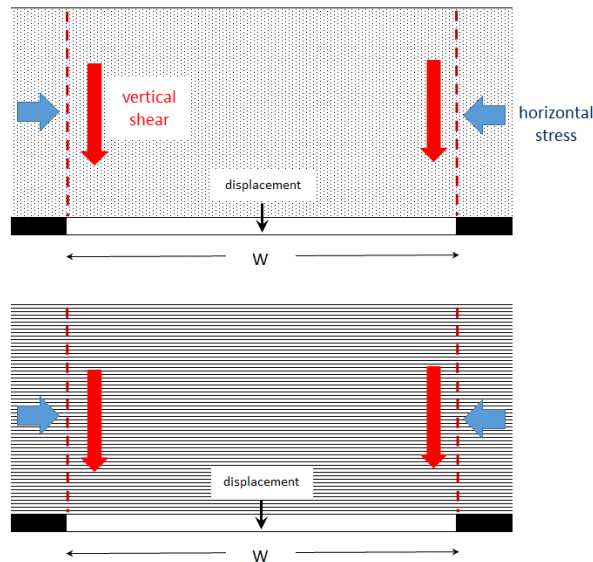
Equation 2 identifies three distinct components of work or energy release that should be relevant to the bump problem, namely (i) ground stress magnitudes, (ii) the area from which ground stresses are released, and (iii) the magnitude of strata displacement before equilibrium is re-established. The greater the magnitude of ground stress that is dissipated or relieved over a larger area and the further that the strata moves before an equilibrium condition is re-established, the greater the work done, hence the greater the energy release. In seismology, this defines a seismic event's *magnitude*.

Table 1 is taken from a larger table contained within USGS 2014 and outlines the links between event magnitude (Richter Magnitude), equivalent energy released (in Joules) and interestingly for context, a description in practical “explosion” terms. In terms of the manner by which a bump event is experienced in the mine workings (termed *intensity*), either audibly, via strata damage levels or via physical shaking of the excavation, the dissipation of energy with increasing distance from the epicentre of either a seismic or in this case, a micro-seismic event is of direct relevance. How seismic events are experienced at any given location (i.e. their intensity) is a highly complex subject and was initially addressed via an empirical scale known as the “*Modified Mercalli Intensity Scale*” which is similar to Mohs Scale of Hardness in that it contains 10 distinct categories with no numerical relativity relationship between the categories.

Analysing seismic event intensity numerically involves a whole range of technical considerations that are well beyond the scope of this paper and are in fact, uniquely the realm of the professional seismologist. However, for the purpose of this paper it is sufficient to state that seismic event intensity generally decreases as a direct function of increasing distance from the event epicentre, the energy decay commonly being quoted as being exponential (i.e. proportional to  $1/r$  where  $r$  is the distance from the epicentre). Therefore, distance from the mine workings to the epicentre of a bump event is the fourth variable to be aware of.

**TABLE 1: Seismic Event General Descriptions (extract from USGS 2014)**

Approximate Richter Magnitude	Equivalent TNT for Seismic Energy Yield	Joule Equivalent	Example
0.0	15 g	63 kJ	
0.2	30 g	130 kJ	Large hand grenade
1.5	2.7 kg	11 MJ	Small construction blast
2.1	21 kg	89 MJ	West fertilizer plant explosion

**FIGURE 4: Thought-Experiment Representations: Massive and Laminated Overburdens Including Vertical Joints and Horizontal Stress (Frith and Reed 2018)**

### Vertical Abutment Shear

Frith and Reed 2018 described an overburden stability model for coal mining that is fundamentally consistent with that of vertical abutment shear within the linear arch model, in that it recognises that one mode of large-scale overburden instability is linked to the horizontal stress acting across vertical joints being overcome by vertical shear, as illustrated in Figure 4.

A “blocky” overburden collapse mode can be demonstrated by reference to overburden extensometry data from longwall extraction. Willey *et al* 1993 report surface extensometry data from the extraction of LW4 at Cook Colliery in QLD, the measured outcomes being contained in Figure 5. The data indicates that with the longwall face less than 40 m past the borehole extensometer location, an almost instantaneous large-scale vertical “slip” event occurred, for all of the anchors that were still operating at that time, in the depth range from at least 50 m to 218 m.

Figure 5 shows similar surface extensometry data for a longwall face at shallower depth (90 m) with the overburden containing more than 50 m of dolerite material immediately above the coal seam. Again, there is clear evidence of large-scale blocky overburden collapse within credible measurement data, as might logically be expected.

In terms of whether this type of overburden collapse mode might have the ability to cause a high energy release and so drive an overburden bump, is demonstrated by reference to two documented coal pillar collapses, the first being that at Coalbrook in 1960, the second being a highwall mining pillar collapse at Ulan Mine in New South Wales.

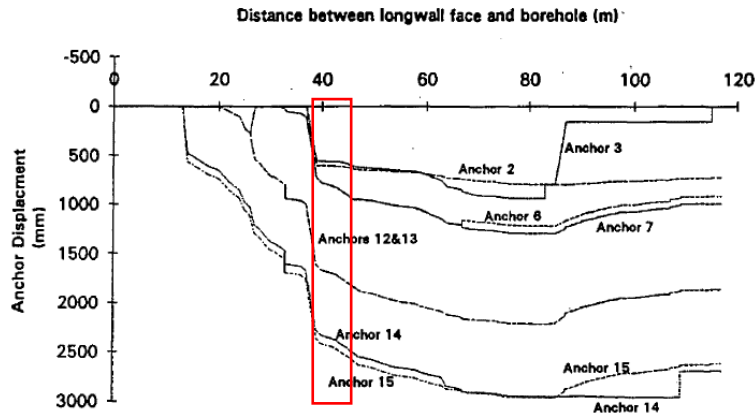


FIGURE 5: Crossline Subsidence Profile, Castor Seam Longwall 4 (Willey et al 1993)

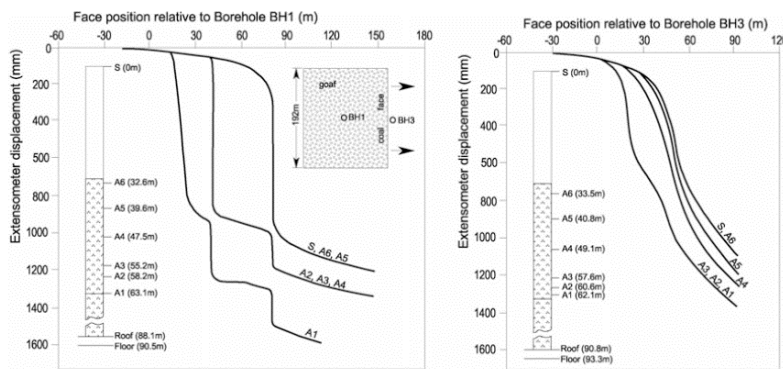


FIGURE 6: Graphs Showing Progressive Step-Failure of a Dolerite Sill as Recorded using Surface to Seam Borehole Extensometers (reproduced from Galvin 2016)

Van Der Merwe 2006 describes the circumstances and experience of the Coalbrook disaster, in particular the major event in early 1960 following the local “*experiment*” collapse in late 1959. The following quotations are taken from that paper:

*At about 16:00, the miner in charge of a section which was then working just West of Section 10, was alarmed by loud shot-like noises coming from the direction of Section 10 and pillar spalling.*

*At 16:20, the miner in charge of a gang working just South of Section 10 also became aware of problems in Section 10 by a strong wind blast from that direction and sounds like heavy thunder.*

*Sometime after 19:00, the men replacing the ventilation stoppings South of Section 10 became aware of increasing thunder-like noises from Section 10 and increasing methane emissions. They withdrew but before they could reach a safe place, were “overtaken by a hurricane of dust laden air accompanied by crashing like thunder”.*

*The following seismic events were recorded that can be connected to the collapses:*

*28 December at 19:16, Richter Magnitude 0.5*

*21 January at 16:45, Richter Magnitude 0.3*

*21 January at 19:26, Richter Magnitude 1.0*

*The events on 28 December and at 16:45 on 21 January exhibited single amplitude peaks while the one at 19:26 on 21 January lasted for 5 minutes, with three distinguishable amplitude peaks during that period. Comparison of the times at which the seismic events were recorded to the times at which wind blasts and other observations indicating collapse underground were made, leads to the conclusion that the seismic events were caused by the collapse and were not minor earthquakes leading to the collapse.*



The mine collapse at Coalbrook was demonstrably accompanied by a significant amount of seismic activity that was both audible in the mine workings and measurable via seismic networks. This raises the obvious questions as to (a) the source of the energy released during the collapse and (b) the associated release mechanism.

Frith and Reed 2018 examined the key question of whether, in a pillar collapse, it is the pillars or the overburden that fails first, the conclusion being that it is almost certain that the coal pillars go post-peak strength well before the overburden become critically unstable *en masse*. Therefore, it logically follows that the Coalbrook seismic events almost certainly emanated from the overburden eventually becoming critically unstable and collapsing, rather than coal pillar failures. In this context, it is judged that the energy source and associated release mechanism was more likely comparable with that illustrated in Figure 4, namely one of vertical abutment shear when the stabilising influence of horizontal stress was eventually overcome by the super-incumbent weight of an unstable overburden mass and so rapidly released.

The highwall mining collapse at the Ulan Mine is documented in CSIRO 2001 with the following statement being of relevance to this paper:

*On 18th of March, 2000, a highwall panel failure occurred in HW3 Trench encompassing up to an estimated 119 entries. The failure occurred quickly at 6 a.m. There were no injuries nor was any equipment damaged. The failure was recorded as a seismic event by the Australian Geological Survey Organisation who calculated a local magnitude of ML = 3.8 for the event. This is approximately equivalent to a 1000 tonne "mine blast".*

Whilst not from the same mine, Figure 5 shows a HWM pillar failure from distance, the propagation of vertical abutment shear through substantial portions of the overburden below near-surface weathered material being self-evident.

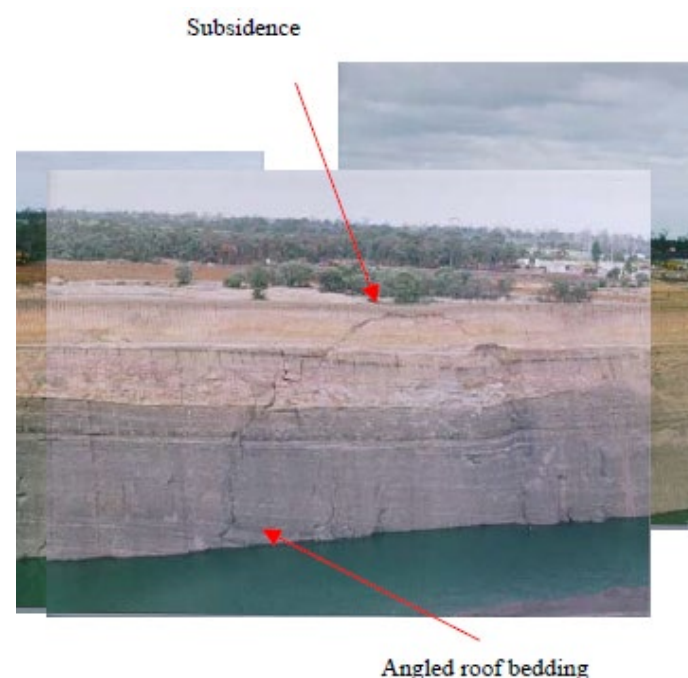


**FIGURE 5: Photograph of overburden above a HWM pillar failure, Yarrabee Mine (CSIRO 2001)**

A 3.8 Richter Magnitude event is broadly equivalent to an energy release (or work done) in the order of 30 GJ. Using Equation 2, this can be achieved via a combination of (a) a 2 MPa horizontal stress reduction, (b) a vertical shear displacement of 0.5 m and (c) a shear area

30,000 m<sup>2</sup>, which is the equivalent of a perimeter of 300 m (i.e. 100 m + 100 m + 100 m) and a sheared interval of 100 m thickness, which is judged to be credible for a HWM layout. In other words, it is easily conceivable than even in a low horizontal stress environment at shallow cover depth in proximity to an open cut highwall, a substantial energy release event can occur in conjunction with a coal pillar collapse.

The preceding discussion has attempted to demonstrate that even relatively small-scale pillar collapses have the potential to develop substantial micro-seismic energy events via the release of horizontal stress from the overburden due to a vertical abutment shear mechanism.

### Compressive Failure of Intact Material

Frith and Creech 1997 reported the results of micro-seismic monitoring from West Wallsend Colliery in NSW, specifically related to the narrowing of a longwall face beneath a known thick, massive, near-seam conglomerate unit with the inferred potential to cause significant periodic weighting effect and associated face instability if allowed to “weight” and cave in an unrestricted manner.

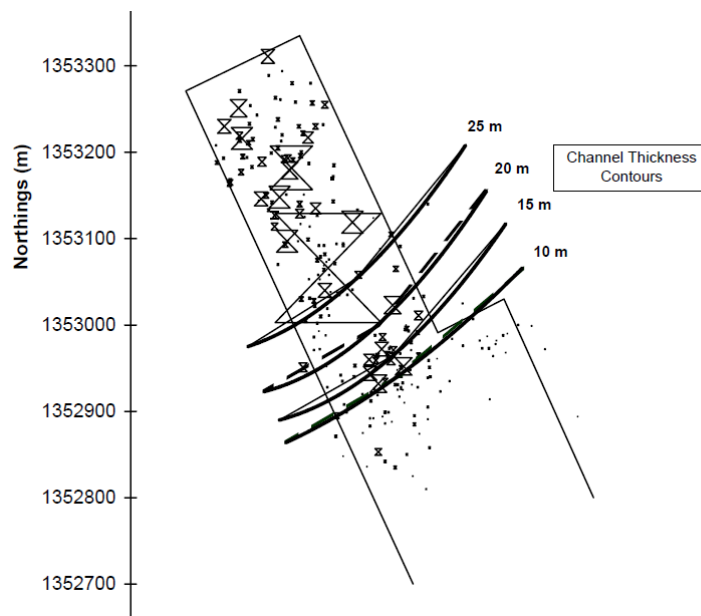


**FIGURE 6: Location and Magnitude of Events in Relation to Panel and Channel Geometry, LW12 West Wallsend Colliery (Frith and Creech 1997)**

Figure 6 contains the plan location and associated magnitude of measured micro-seismic events associated with initially narrowing of the longwall face from 240 m wide to 150 m and subsequently the thickening up of the massive conglomerate channel from 10 m to in the order of 25 m outbye. As described in the research report, not only did the event magnitudes dramatically increase (the largest single event had a calculated Richter Magnitude in the order of 2), the associated source mechanism was found to be compressive rather than shear (as was almost entirely the case for measured events at the full face width of 240 m), with the location of large compressive events at 150 m panel width being generally behind rather than ahead of the longwall face.

This monitoring data fully demonstrates that with the necessary thick, massive and strong overburden conditions and an extraction width that results in spanning of strata via the development of a substantial compressive linear arch across the extraction width, large

magnitude micro-seismic events can be generated during active mining, this being consistent with the horizontal compression failure mode of a linear arch.

**Stress-Driven Shear Slip Along Pre-Existing Planes of Weakness**

For the purpose of illustration, reference will be made to the significance of mid-angled discontinuities in uncontrolled roadway roof instability, the associated theoretical basis then being increased in scale to that of major faults and broader ground stress considerations.

The critical geotechnical characteristic of a mid-angled discontinuity in relation to overburden bumps, is exactly the same as its ability to cause large-scale roadway roof falls with little or no obvious pre-cursor warning signs (as discussed in detail in Frith 2016), the reason being that under certain conditions, such a plane of weakness becomes naturally unstable under the action of horizontal stress, so that uncontrolled stress-driven shear-slip occurs along the plane, thereby dissipating horizontal stress and so rapidly leading to a major roadway roof collapse unless adequately supported. The problem of shear-slip along a mid-angled plane of weakness under the action of horizontal stress (the vertical stress having been removed due to the formation of the mine roadway below), is illustrated in Figure 7, with the necessary condition for shear-slip being that the Friction Angle ( $\Phi$ ) along what is an assumed cohesionless plane of weakness, must be less than  $90-\theta$  where  $\theta$  is the inclination of the fault plane to the horizontal.

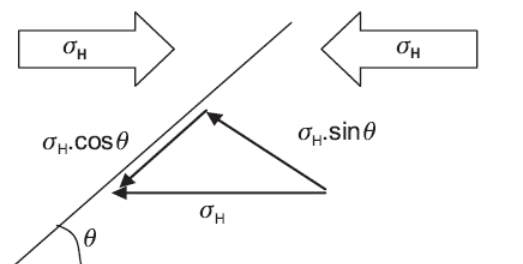


**FIGURE 7: Arrangement of Horizontal Stress Across a Mine Roadway, an Inclined Discontinuity and Resolving Horizontal Stress Along the Discontinuity (Frith 2016)**

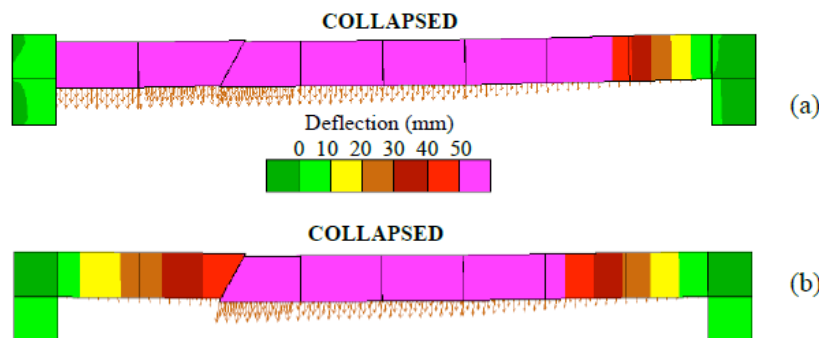


**FIGURE 8: Deflection Contours for Single Steeply Dipping Joint (dip 60°): (a)  $\sigma_h = 0$  MPa; (b)  $\sigma_h = 4$  MPa (Oliveira and Pells 2014)**

For a mid-angled fault plane with an inclination of  $60^\circ$  to the horizontal, the plane will inevitably be unstable under the action of horizontal stress for an Angle of Friction of  $< 30^\circ$ , this being one of the reasons why mid-angled faults can result in highly unstable roadway roof conditions, Friction Angles  $< 30^\circ$  being readily achievable along fault planes having undergone significant displacement. This critical mechanistic aspect of mid-angled discontinuities under the action of horizontal stress, is fully confirmed in Oliveira and Pells 2014 whereby they analyse tunnel roof

stability containing a cohesionless plane of weakness inclined at  $60^\circ$  to the horizontal, with an assumed Friction Angle of  $30^\circ$ , the stability outcome being shown in Figure 8, the “strong” and “weak” sides of the discontinuity being obvious. This suggested fault-slip overburden bump mechanism is fully consistent with that shown in Figure 9 from the Yima Mine in China.

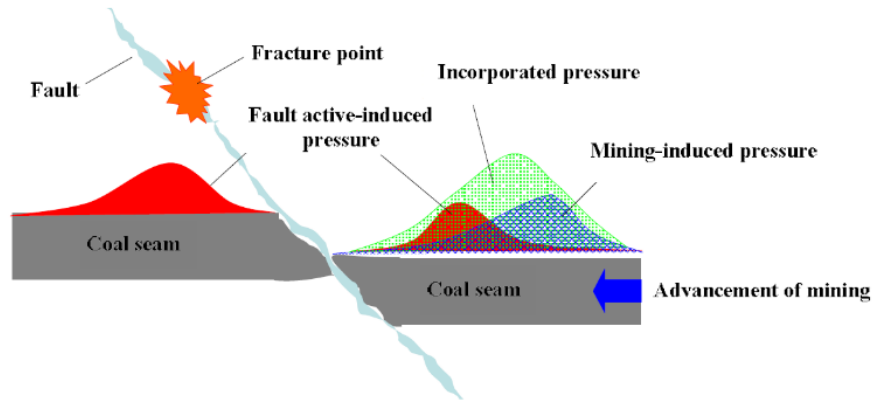


FIGURE 9: Tectonic Structure in Yima Coal Mine, China (CSIRO 2016)

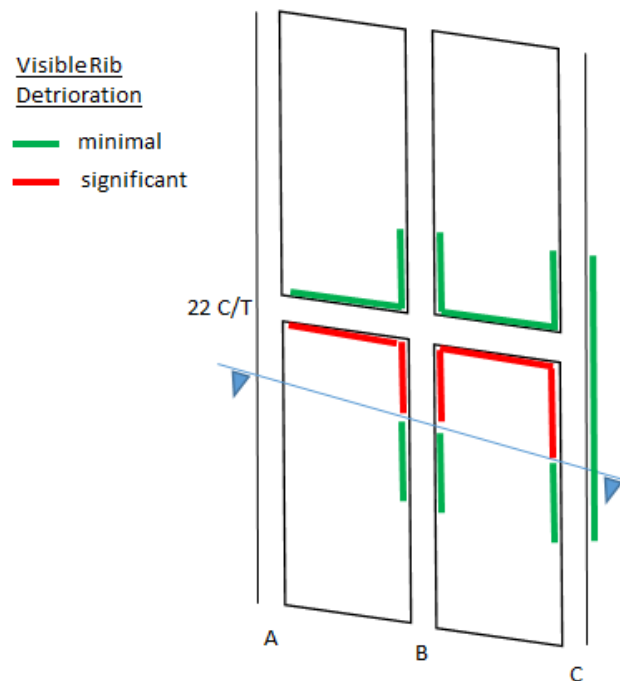
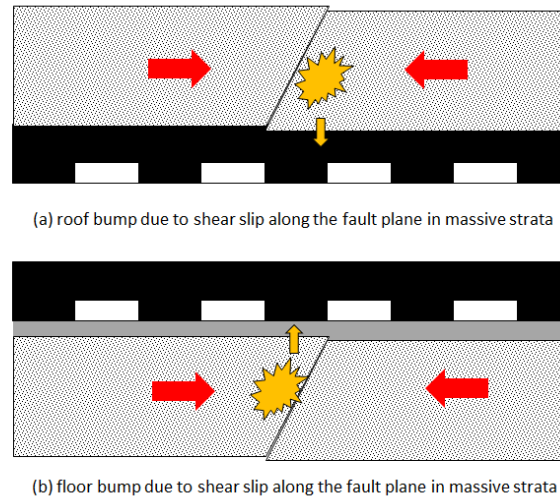


FIGURE 10: Observed Roadway Rib Conditions in Proximity to a Development Bump-Prone Mid-Angled Fault Plane



**FIGURE 11: Schematic Illustration of Overburden and Floor Bumps Due to Horizontal Stress-Driven Shear Slip Along a Mid-Angled Fault Plane**

Figure 10 shows the result of rib condition mapping on the under-hade side of a mid-angled fault plane under the action of a very high level of major horizontal stress that proved to be bump-prone (but not burst-prone) during roadway development. The substantial rib damage on the under-hade “weak” side as compared to the over-hade strong side, is self-evident, the logical conclusion being that both the bumps and deteriorated ribs were directly due to horizontal stress-driven shear slip on the under-hade side of the overlying mid-angled fault.

The combination of a mid-angled fault plane with a significant magnitude of horizontal stress acting perpendicular to the strike of the fault, may also give rise to the phenomenon of floor bumps, as the strong side of a mid-angled fault plane in the roof above the coal seam, is actually the weak side in the floor, as illustrated in Figure 11.

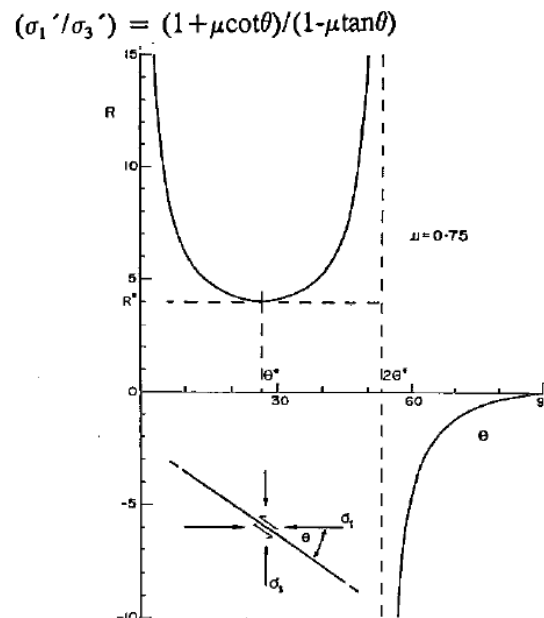


**FIGURE 12: Stress Ratio (R) Required for Frictional Re-Activation (Hatherly et al 1993)**

The same type of stress-driven shear slip analysis can also be undertaken on vertical fault systems by considering the alignment of the major horizontal stress with the strike of the fault



plane and the friction acting along the plane, this being illustrated in Figure 12. The basic mechanism of horizontal-stress driven shear slip along a major fault plane is actually fundamental to the development coal burst model for Austar and Sunnyside mines outlined in Frith and Reed 2019, the reported experience from Sunnyside Mine being one of many substantial overburden bumps (as distinct from coal bursts) during active mining that resulted in noticeable offsetting of surface railway lines, this being interpreted as evidence of horizontal shear movement along pre-existing fault planes.

It is evident based on a theoretical treatment supported by mining experiences, that the major horizontal stress can, under certain circumstances, drive significant shear-slip events along major fault planes during active mining, resulting in substantial energy releases that manifest as reported overburden or floor bump events.

### Multi-Seam Events

Mark 2017 describes two pillar burst events at the Manalapan 17 Mine in Kentucky, which are worth considering in the context of how multi-seam mining appears to be far more pillar-burst prone than virgin conditions. Cover depths involved were in the order of 510 m with the overlying seam being worked at the time of the pillar bursts being in the order of 50 m above the pre-existing lower seam workings. As an example of many such layout plans that have been viewed, Figure 13 contains the layout plan for the two separate incidents at the Manalapan 17 Mine.

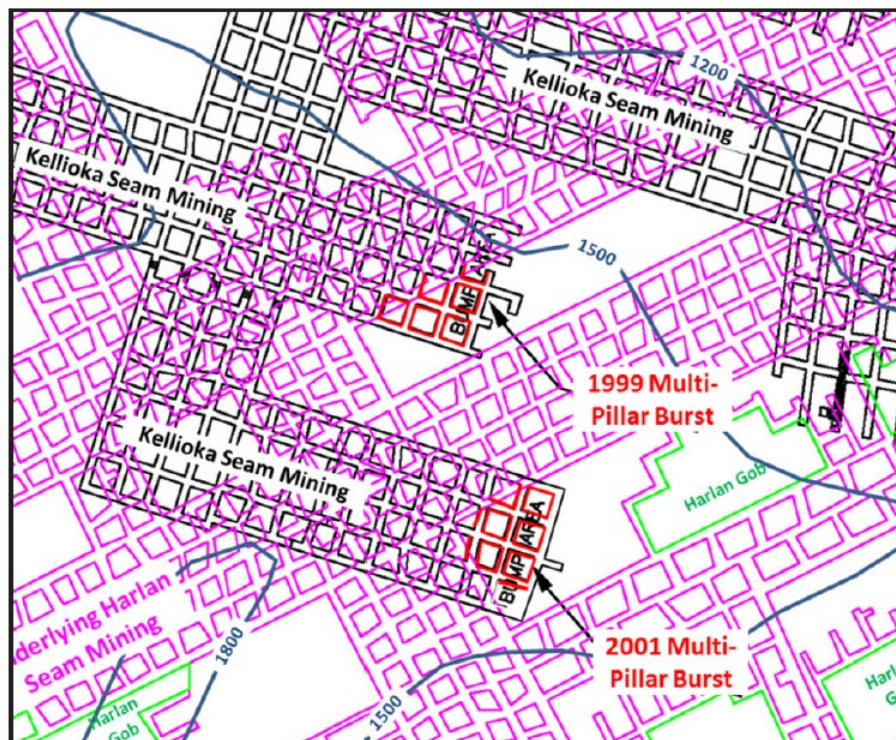


**FIGURE 13: Locations of Burst Events in the Manalapan No. 17 Mine (Black) Relative to Underlying Harlan Seam Workings (magenta and green) – Mark 2017**

For the purpose of this paper, only two observations need to be made, namely that:

- (i) the areas of defined “burst” coal are above solid remnant pillars in the underlying seam, rather than areas of either standing production pillars or extraction. Therefore, given the technical discussion herein as to the various source mechanisms of overburden and/or floor bumps and with no major geological structures being identified in the direct vicinity,



it is seemingly self-evident that the reported pillar bursts cannot be a direct consequence of any form of overburden bump event.

- (ii) the cover depth involved is not extreme, as compared to coal mining in Germany for example at well in excess of 1000 m, which is understood is pre-dominantly coal-burst prone due to multi-seam mining effects rather than high cover depth in isolation.

The required mechanics for a large-scale pillar burst is beyond the scope of this paper, a detailed discussion being planned for publication in the near future, the critical role of low overburden stiffness and elevated pre-mining vertical stresses due to pre-existing mine workings, whether due to multi-seam effects or from within the same seam being considered in first-principles level detail.

### **SUMMARY**

The paper has described several potential source-mechanisms for overburden bumps based on fundamental structural models and selected case-histories, all but one being directly linked to stress-driven shear-slip along pre-existing planes of weakness, this being entirely consistent with one of the well-stablished large-scale earthquake causation models. It has further demonstrated the hypothesis presented in **Frith and Reed 2019** that overburden bumps are mechanistically distinct from development coal-bursts, as per that which occurred at Aустar in 2014, due to the location of the primary energy source (coal seam or overburden/floor) and the associated mechanism(s) of energy release.

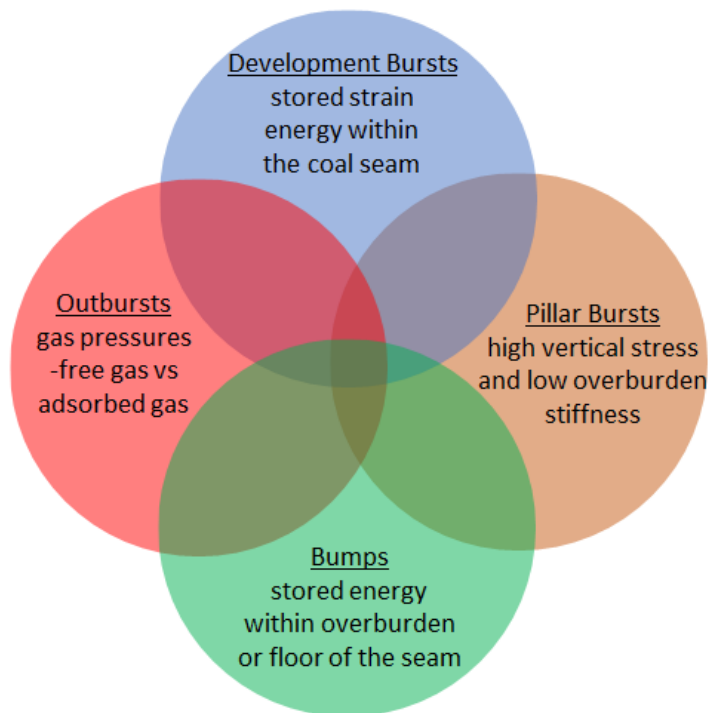


**FIGURE 14: Suggested Classification of High Energy Release Events in Underground Coal Mining for 4 Fundamental Event Types**

The paper has also briefly considered published case-histories for coal-pillar bursts, concluding that they cannot be directly explained by either the development coal burst or overburden bump causation models, hence there must be a further event-type to be identified and analysed, this to be the subject of a future technical paper. However, this does require that the Venn diagram representation of Figure 1 be updated to include four fundamentally different event types, as

shown in Figure 14, the need to understand event-types in isolation from each other being even more critical than with only three in Figure 1.

## REFERENCES

- Brady, B., and Brown E. (2005). *Rock Mechanics for Underground Mining*. Third Edition, Kluwer.
- CSIRO (2001). *Optimal Design and Monitoring of Layout Stability in Highwall Mining – Chapter 6*. Final Report, ACARP Project C8033.
- CSIRO (2016). *Review of Chinese Coal Burst Experience and Analysis of Micro-seismic Data from Australian Mines*. CSIRO Report No. EP167887.
- Evans, W.H. (1941). The Strength of Undermined Strata. *Trans. Inst. Min. Metall.* 50, pp. 475 - 532.
- Frith, R. Creech, M. (1997). *Face Width Optimisation in Both Longwall and Shortwall Caving Environments*. Final Report, ACARP Project C5015.
- Frith, R. (2016). *Structural Engineering Principles in Coal Mine Ground Control – the Common Link Between Empirical Models, Numerical Models and Practical Solutions*. Chapter 3, *Advances in Coal Mine Ground Control*, Elsevier.
- Frith, R., Reed, G. (2018). *Coal Pillar Design When Considered a Reinforcement Problem Rather Than a Suspension Problem*. Proceedings COAL 2018, University of Wollongong.
- Frith, R., Reed, G. (2019). *A Causation Mechanism for Coal Bursts During Roadway Development Based on the Major Horizontal Stress in Coal, Very Specific Structural Geology Causing a Localised Loss of Effective Coal Confinement and Newtons' Second Law*. Proceedings COAL 2019, University of Wollongong.
- Galvin, J. (2016). *Ground Engineering: Principles and Practices for Underground Coal Mining*. Switzerland: Springer International Publishing, pp. 684.
- Hatherly, P. Shepherd, J. Evans, B. Fisher, N. (1993). *Integration of Methods for the Prediction of Faulting*. Final Report, NERDDC Project 1588.
- Mark, C. (2017). *Coal Bursts that Occur During Development: A Rock Mechanics Enigma*. Proceedings of the 36th International Conference on Ground Control in Mining, Morgantown, West Virginia.
- National Research Council (2013). *Induced Seismicity Potential in Energy Technologies*. The National Academies Press, Washington DC, USA.
- Oliveira, D, Pells, P. (2014). *Revisiting The Applicability Of Voussoir Beam Theory For Tunnel Design In Sydney*. *Australian Geomechanics*, Vol. 49, No. 3, September.
- USGS (2014). *FAQ – Measuring Earthquakes*. Download from [www.earthquake.usgs.gov](http://www.earthquake.usgs.gov).
- Van Der Merwe, J. N. (2006). *Beyond Coalbrook: Critical Review of Coal Strata Control Developments in South Africa*. In: *Proceedings of the 25th International Conference on Ground Control in Mining*. Morgantown, WV: West Virginia University, pp. 335–346.
- Wiley, P. Hornby, P. Ditton, S. Puckett, G. McNally, G. (1993). *Improved Methods of Subsidence Engineering*. Final report, NERDDP Project No 1311.

# **DYNAMIC EVENTS AT LONGWALL FACE, CSM MINE, CZECH REPUBLIC**

**Petr Waclawik<sup>1</sup>, Jan Nemcik<sup>2</sup>, Radovan Kukutsch<sup>3</sup>, Libin  
Gong<sup>4</sup> and Gaetano Venticinque<sup>5</sup>**

**ABSTRACT:** Presented here are the details of the seismic events that occurred at longwall 11 located at the CSM mine in the Ostrava coal region, Czech Republic. This longwall was excavated in a very complex area located within the shaft protective pillar and adjacent to the 50 m wide and steeply inclined fault zone at a depth of 850 m. In addition, 10 longwalls were extracted below each other over many years in several sloping seams located on the other side of the large sloping fault zone resulting in complex stress fields and large subsidence. The immediate roof above longwall 11 was a very strong sandstone and sandy siltstone with a uniaxial compression strength of 80 – 160 MPa. When the longwall started, continuous seismic monitoring of the longwall area indicated 470 small seismic events with energy smaller than  $<10^2$  J. The first high energy event of  $3.3 \cdot 10^5$  J occurred when the longwall advanced 85m past the starting line. Some 30 minutes later a rockburst occurred registering energy of  $2.2 \cdot 10^6$  J, causing significant rockburst damage at the tailgate located near the large tectonic zone. The roadway steel arches were significantly deformed and the maximum floor heave reached up to 1.5 m. To investigate the complex strata behavior in that area, a large FLAC3D model  $0.27 \text{ km}^3$  in volume was constructed and 10 longwalls were extracted in several sloping seams adjacent to the large fault zone. The model under construction is now ready to study the complex strata behaviour and the associated stress fields together with the dynamic strata behaviour to match the modelled seismic events with those measured underground.

## **INTRODUCTION**

The success of mining operations is heavily dependent upon controlling the fractured ground especially in coal mine areas where complex sedimentary strata exist. In nature, the mechanisms of rock failure can be typically a dynamic phenomenon that up to now has not been fully understood. The numerical models of rapidly developing failures can be predicted numerically including the rock or coal bursts. They are more appropriate in depicting the reality as the exact mechanisms of strata failure in stressed rock cannot be fully observed. These predictions can be highly beneficial during the mine planning stages where identification of possible dynamic occurrences could minimise potential hazards.

A collaborative research project between the Institute of Geonics, the Academy of Science of Czech Republic and the University of Wollongong was set up to research strata failure zones around excavations. The aim of this project was to numerically simulate various types of strata behaviour and rock failure in both hard rock and coal mines. Previous research of the coal bursts done at the University of Wollongong indicated suitability of both the FLAC2D and

- 
- 1 . *The Czech Academy of Sciences, Institute of Geonics, petr.waclawik@ugn.cas.cz, Tel: +420 596 979 701*
  2. *Dr.Honorary Senior Fellow, University of Wollongong. Email: jnemcik@uow.edu.au Tel: +61 2 4221 44920*
  3. *Dr./Researcher, The Czech Academy of Sciences, Institute of Geonics, kukutsch@ugn.cas.cz, Tel: +420 596 979 242*
  - 4 . *Dr./ Researcher, The Czech Academy of Sciences, Institute of Geonics, libin.gong@ugn.cas.cz, Tel: +420 596 979 701*
  5. *Dr / Research Engineer, SCT Operations Pty Ltd, Australia, [GVenticinque@sct.gs](mailto:GVenticinque@sct.gs), Tel. +61 2 4222 2710*

FLAC3D software to simulate various types of strata failure including the dynamic events in underground environments.

### GEOLOGICAL AND MINING CONDITIONS

The assessed area in this case study is quite complex from a geomechanical point of view. There are several faults of regional importance which divide the rock mass amongst separate mining blocks (see Fig. 1). There is the wide tectonic zone of the Albrechtice Fault with a total throw of up to 420 m located in the western area. The dip of this fault ranges from 60° to 70° towards the west. In the central area Fault "A" is present with a throw of up to 100 m and a dip of 60° towards the north. Fault "X" in the northern part of the area has a throw of up to 350 m with a dip of 60° towards the south. The significant regional tectonic fault zone "Eastern Thrust" (Grygar & Waclawik, 2011; Waclawik, Ptacek & Grygar, 2013) is located in the southern part of the studied area. The Eastern Thrust has a very small dip ranging from 10° to 35° with strike in the northeast-southwest direction and dip towards the northwest. Vertical displacement fluctuates around 5 m, but the range of horizontal displacements is usually much greater and can vary from tens to hundreds of metres.

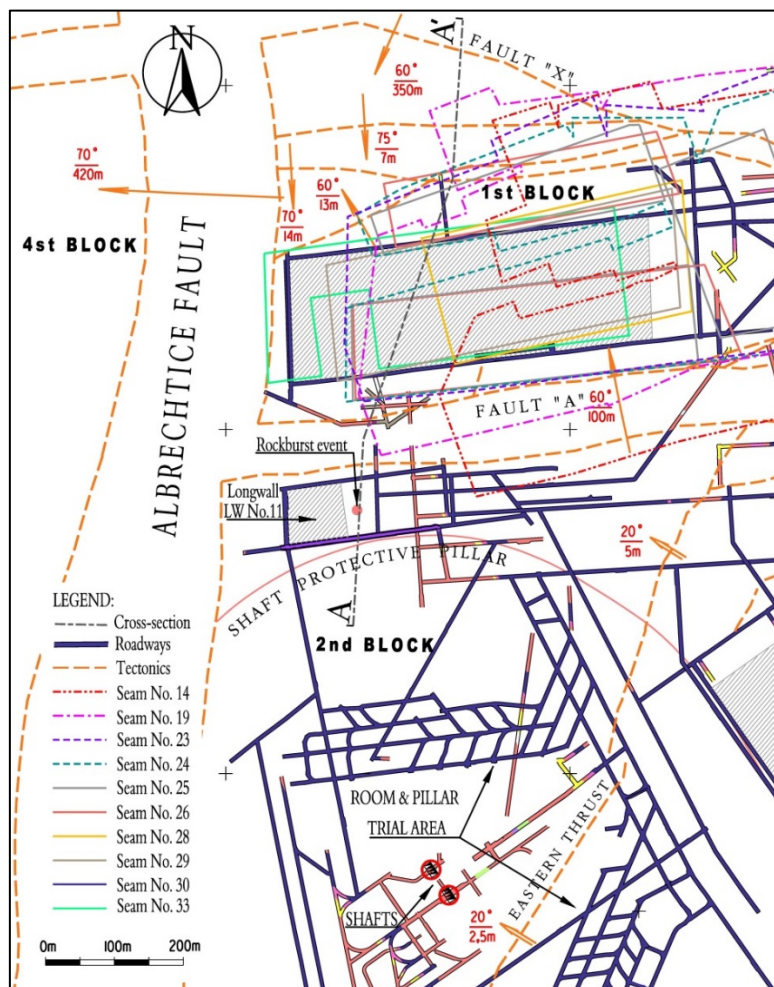


**Figure 1: Tectonic situation and location of longwall panel No. 11**

Concerned longwall panel No. 11 is located near the shaft protective pillar in the footwall of the wide tectonic zone Fault "A". This latest panel was mined in the coal seam No. 30+31 at a depth of approximately 830 – 880 m below the surface. Above the coal seam there is a 400 m thick

complex carboniferous rock mass with an overlying tertiary sedimentary rock strata which is 450 m thick with approximately 20 m thick quaternary soil overburden. The strata dip oriented in the northeast direction ranges from 8° to 17°. The roof rocks are represented by the rhythmical alternations of sandstone, siltstone and mudstone layers typically for lithological development of Sucha member (Dopita et al., 1997). The immediate roof of targeted seam No. 30 is formed by a very strong sandstone and sandy siltstone with a uniaxial compression strength of 80 – 160 MPa (average 115 MPa).

The longwall panel No. 11 was extracted by a fully mechanised longwall face (drum shearer SL 300, mechanical support FAZOS 15/33). The thickness of the coal seam ranged from 4 m to 5 m within the area of the longwall panel. The longwall panel was very small with a length of 100 m and a 75 m wide face. Geo-mining details of the longwall are summarized in Table 1.

**Table 1: Geomining details of the longwall panel No. 11**

Parameters	Description
Location of panel	2nd mining block
Seam thickness	4.2 – 5.0 m
Depth of cover	830 – 880 m
Average dip of seam	12°
Panel size	7600 m <sup>2</sup>
Working height	3.3 m
Average daily advance	5 m per day
Mining technology	Fully mechanised longwall with caving
Immediate roof	Sandstone, Sandy Siltstone,
Immediate floor	Coal, Siltstone

Ten coal seams (No.14 to No.33) were progressively extracted north of the longwall 11 panel in the 1<sup>st</sup> mining block. These coal seams were gradually mined from 1977 (seam No.14) to 2011 (seam No.33). The longwall panel No.11 was extracted over three months in 2018. The mutual positions of the extracted longwall panels are shown in Figures 1 and 2.

According to the effective local methodology (OKD, 2006), the rockburst risk in the area of the 2<sup>nd</sup> mining block (area of longwall panel No.11) was classified as “without risk”. Nevertheless, continuous seismic monitoring was used to analyse the geomechanical activity of the rock mass during mining. Currently, there are two seismic networks that monitor seismicity caused by mining activities and evaluate these events for the purposes of rockburst prevention. This monitoring provides detailed information obtained at individual mining operations from the local network of seismic stations in mines, and information from a wider area within the currently mined Karviná portion of the Czech section of the Upper Silesian coal basin via the regional seismic network. The current local mine network has 30 mining stations and the regional seismic network has 10 surface and mine stations. This combined seismic network system provides very reliable data for registration and evaluation of seismological activity during longwall advance.

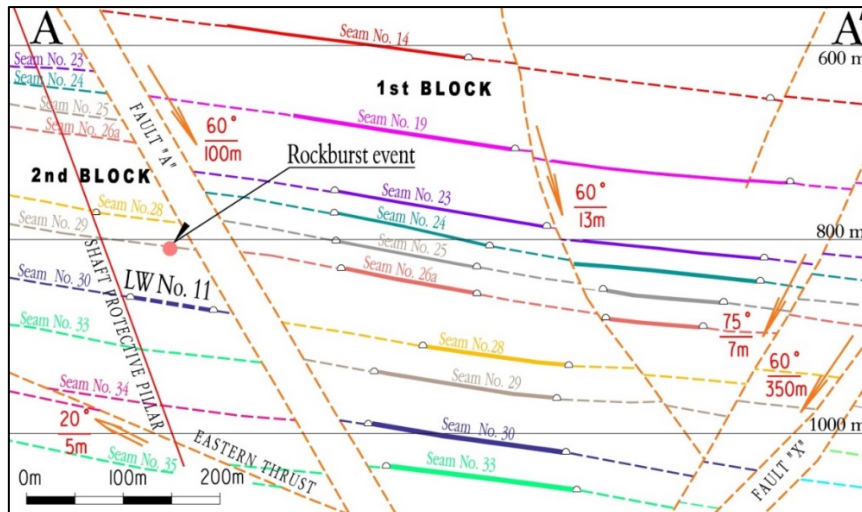


Figure 2: Strata cross-section across the studied area

SEISMIC ACTIVITY DURING MINING

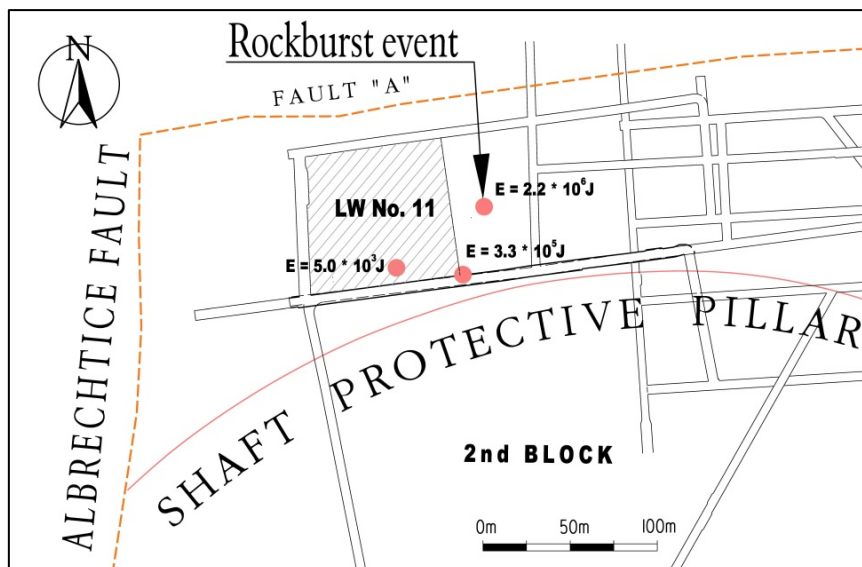


Figure 3: Locality of significant seismic events - longwall 11 area

During the first month of longwall No.11 mining (20.3. 2018 – 13.4. 2018) predominantly low-energy seismic events with energy smaller than  $<10^2$  J were registered nearby. The daily advance of the longwall panel was approximately 5 m per day. During that time a total number of 470 small seismic events were recorded. Only 130 seismic events with energy higher than  $10^1$ J ( $10^1$  to  $10^2$  J) were registered. However, during this time, the weekly energy sum variation increased every day (see the graph in Fig. 4). The graph of weekly energy sum variation helps to identify the anomalies. The seismic events ( $5 \cdot 10^3$  J and  $3.3 \cdot 10^5$  J), the second with considerable energy, were registered on 13.4. 2018 (see Figure 3). Finally, the rockburst occurred only 30 minutes after previous stronger seismic events was registered. At this stage, the longwall face was 85 m from the installation gate. This seismic event registered energy of  $2.2 \cdot 10^6$  J. Significant rockburst damage was recorded at the tailgate located near the tectonic zone Fault "A" where roadway steel arches were significantly deformed with maximum floor heave reaching up to 1.5 m (see Fig. 5), while no slippage was recorded. In the maingate, the maximum floor heave was 1.0 m with minimum deformation of steel arches and slippage of around 0.15 m. Floor heave of around 0.5 m was also recorded at the longwall coal face. After



repairs mining continued for almost a month after the rockburst but with implemented active and passive rockburst preventative measures. The daily advance of the longwall face was regulated to a maximum of 2 m per day. During this phase of mining only low-energy seismic events with energies smaller than  $<10^2$  J were measured in the surrounding area.

The focal mechanism of registered rockburst has the characteristic combination of an initial multiple phase primary failure and a low significant shear failure followed by a significant expansion phase accompanied by a shear failure. Vertically inclined shear planes may correspond to the directions of significant tectonic zones in the area (Fault "A" and Albrechtice Fault).

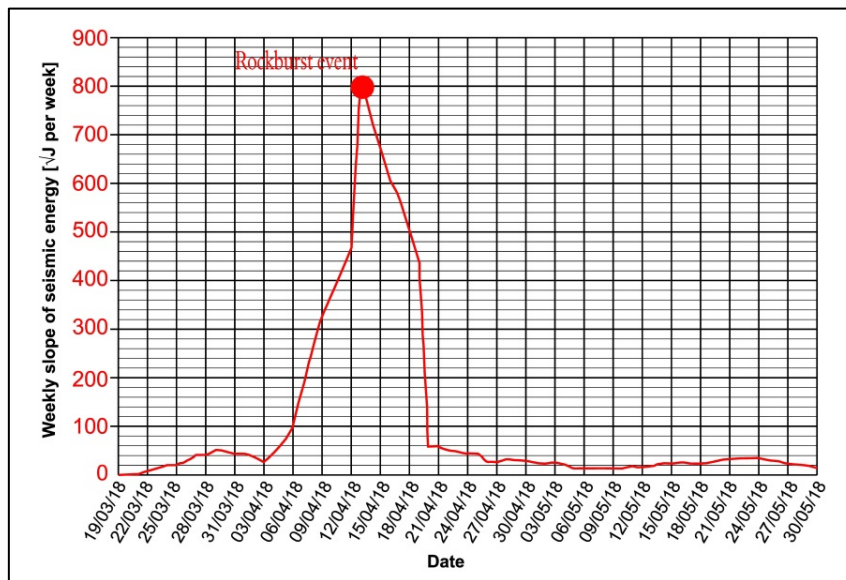


Figure 4: Summary of weekly energy sum variations in area of longwall panel No.11

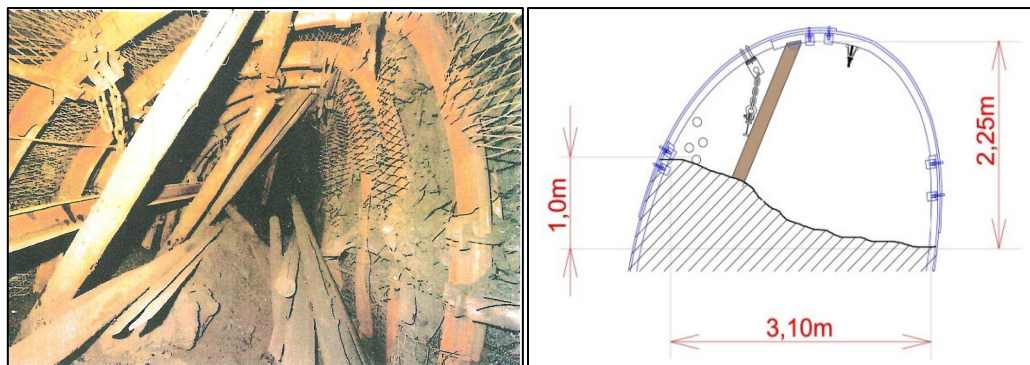


Figure 5: Impact of rockburst at the tailgate

### NUMERICAL MODEL

Part of this project is to study the complex strata behaviour and changing stress fields in the multi-seam operation in a CSM coal mine. A large FLAC3D model (Itasca, 2012) 0.27 km<sup>3</sup> in volume was constructed encompassing several sloping coal seams to model numerous longwall excavations. A steeply inclined 50 m thick fault "A" zone intercepted all seams. The model was constructed to investigate the probable stress fields and strata movements due to past mining. This is needed for future dynamic modelling to see whether the seismic events that occurred at longwall 11 can be numerically simulated. Due to the complexity of the inclined

multi-seam extraction geometry adjacent to the steeply dipping fault zone, the model had to be very large to reveal the complex stress fields and large subsidence that occurred due to 10 previously excavated goafs. Considerable time and effort was spent to construct the working model shown in Fig 6. This was mainly due to writing lengthy subroutines using the FISH software to automate the input of the geometry, in-situ stress, progressive mining of the inclined seams involving excavations of the individual zones in the steeply dipping seams as the mining progressed shear by shear while monitoring the roof to floor contacts to control the goafs, among other things. Most of the progressive excavations and cavity contacts were done using the internal FISH software commands to speed up the execution time of the models.

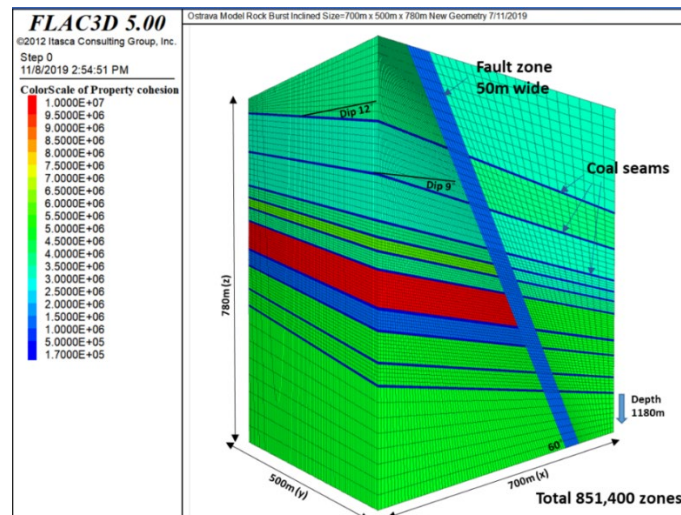


Figure 6: Geometry of the inclined multi-seam mining at CSM Mine, Czech Republic

The initial in-situ pre-mining stress was calculated and inserted into each zone using FISH software subroutines noting that the magnitude of lateral stress was calculated according to the Young's modulus. This is apparent in Figure 7 (a) where a lower Young's modulus in coal attracts lower lateral stress. Ten old multi-seam goafs were progressively extracted, zone by zone, starting from the upper goaf while time-stepping. All goafs were gradually excavated as was the case underground. The direction of all old longwalls advance was down with a dip of 12°.

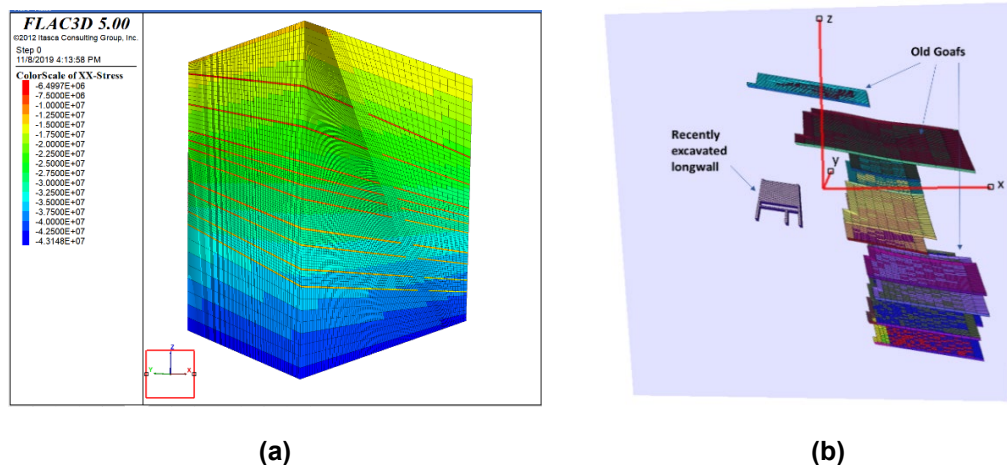


Figure 7: (a) Lateral stress in x-direction before mining, (b) 10 sequentially excavated old longwall goafs inside the model including the recent longwall

The modelled rock and coal seam properties were derived from the laboratory rock core tests and are presented in Table 2. The thickness and rock mass characteristics are given in Tables 2 and 3.

**Table 2: Rock properties used in the model**

Strata	E	v	K	G	d	c	t	$\phi$
Siltstone	23	0.14	10.67	6.67	2500	3.74	2.9	38
Sandstone	35	0.15	10.67	6.67	2500	4.52	3.5	38
Mudstone	18	0.18	10.67	6.67	2500	3.0	1.0	35
Fault Zone	18	0.18	10.67	6.67	2500	3.0	1.0	35
Coal	2.6	0.25	1.60	0.53	1400	0.17	0.1	33

E= Young modulus in GPa, v= Poisson ratio, K= Bulk modulus in GPa, G=Shear modulus in GPa, d=density of rock mass in kg/m<sup>3</sup>, c=cohesion in MPa, t=tension in MPa,  $\phi$ = Angle of internal friction in degree.

**Table 3: Layers characteristic in the model**

LEFT SIDE OF MODEL				RIGHT SIDE OF MODEL			
Layer Nr.	Seam Nr.	Rock type	Thickness of excavation [cm]	Layer Nr.	Seam Nr.	Rock type	Thickness of excavation [cm]
L1LF	-	sandstone		L1R	-	sandstone	
L2LF	35	coal	0	L2R	33a	coal	300
L3LF	-	sandstone		L3R	-	sandstone	
L4LF	34	coal	0	L4R	30+31	coal	370
L5LF	-	sandstone		L5R	-	sandstone	
L6LF	33	coal	0	L6R	29	coal	520
L7LF	-	sandstone		L7R	-	siltstone	
L8LF	31	coal	120*	L8R	28b	coal	
L9LF	30	coal	210	L9R	28	coal	180
L10LF	-	sandstone		L10R	-	sandstone	
L11LF	29	coal	0	L11R	26	coal	180
L12LF	-	siltstone		L12R	-	siltstone	
L13LF	28	coal	0	L13R	25	coal	220
L14LF	-	sandstone		L14R	-	mudstone	
L15LF	26	coal	0	L15R	24	coal	310
L16LF	-	siltstone		L16R	-	mudstone	
L17LF	25	coal	0	L17R	23	coal	140
L18LF	-	mudstone		L18R	-	mudstone	
L19LF	24	coal	0	L19R	19	coal	260
L20LF	-	mudstone		L20R	-	siltstone	
L21LF	19	coal	0	L21R	14	coal	290
L22LF	-	siltstone		L22R	-	mudstone	

\* mined together – total thickness 3.3 m

The applied stresses were extrapolated from the overcore stress measurements (Waclawik et al. 2016a) and (Kumar et al. 2019) undertaken in the modified room and pillar trial (see Fig. 1) and are shown in Table 4.

**Table 4: The overcore stress measurement values**

Stress	MPa	Bearing [°]	Dip [°]
$\sigma_1$	19.2	9 <sup>0</sup>	-67 <sup>0</sup>
$\sigma_2$	3.9	205 <sup>0</sup>	-23 <sup>0</sup>
$\sigma_3$	0.3	113 <sup>0</sup>	-6 <sup>0</sup>

At this stage no results from the numerical model are reported here due to various uncertainties that exist in the complex strata environment in the CSM mine. It is expected that the large fault "A" zone behaviour together with the 10 previously excavated goaf areas will have a profound influence on stress changes, overall strata movement and rock/seam behaviour adjacent to longwall 11. The unknown fault zone properties would probably produce a gradual fault slippage occurrence over the years of mining. An accelerated fault slip may have been experienced due to longwall 11 extraction. Such slip can produce a significant moving shear stress zone where the longwall 11 was situated. This was already indicated in the preliminary numerical model investigations. Numerical trials have already begun using varying fault zone properties to study fault slip movements and their effects on surrounding strata.

### SUMMARY AND CONCLUSIONS

The studied area located at a considerable depth within the CSM mine is quite complex with several major faults of regional importance which divide the rock mass amongst separate mining blocks. These fault zones can significantly influence mining geometry and strata control and must be taken into consideration for mine planning purposes. The seismic events commonly occur in this mine and require careful planning of mining activities. The strata properties, mining geometry, fault zone details, stress state, previous rockbursts, interpretation of seismic monitoring and historical experience need to be known to implement safe mining.

The seismic monitoring used in the mine is very comprehensive and ideal to assist with rockburst predictions. This study has clearly demonstrated that the seismic energy events that occurred during the longwall 11 extraction showed a strong relationship between the seismic frequency, seismic energy levels and the rockburst.

The available numerical model is probably the only tool that can predict the 3-dimensional stress state in the area where the complex geological environment exists. This is a significant step forward in understanding strata behaviour in a complex stress environment. The dynamic option of the model can be very useful to simulate the past rock burst occurrences leading to future predictions of such events.

### ACKNOWLEDGMENTS

This article is written in connection with the Project International mobility of researchers of IGN (Reg. No. CZ.02.2.69/0.0/0.0/16\_027/0008478), Institute of Geonics of the CAS, Czech Republic, which is supported by the European Structural and Investment Funds, Operational Programme Research, Development and Education, Programming 2014-2020 and the Czech Republic project for the long-term conceptual development of research organisations (RVO: 68145535).

## REFERENCES

- Dopita M, Aust J, Brieda J, Cerný I, Dvorák P, Fialová V, et al. Geologie české části hornoslezské pánve. Geology of Czech part of the Upper Silesian Coal Basin (in Czech). Ministry of the Environment of the Czech Republic; 1997. p.278.
- Grygar, R and Waclawik, P, 2011. Structural-tectonic conditions of Karvina Subbasin with regard to its position in the apical zone of Variscan accretion wedge, *Acta Montanistica Slovaca*, Vol. 16, No. 2, pp 159-175.
- Itasca. FLAC3D (Fast Lagrangian Analysis of Continua in 3 Dimensions), Version 5.0, Itasca Consulting Group Inc., Minneapolis, Minnesota, 55401, USA, 2012.
- Kumar, A, Waclawik P, Singh R, Ram S, and Korbek, J, 2019. Performance of a coal pillar at deeper cover: Field and simulation studies, *International Journal of Rock Mechanics and Mining Sciences*, vol. 76, pp. 88-97.
- OKD, DPB, Inc. Rockburst prevention rules (in Czech). OKD, DPB, a.s., Paskov; 2006.
- Waclawik, P, Ptacek, J and Grygar, R, 2013. Structural and stress analysis of mining practice in the Upper Silesian Coal Basin, *Acta geodynamica et geomaterialia*, Vol. 10, Issue 2, pp. 255-265.
- Waclawik, P., Stas, L., Nemcik, J., Konicek, P., Kalab, T.: 2016a. Determination of stress state in rock mass using strain gauge probes CCBO. *Procedia Engineering*, Vol. 149, pp. 544-552
- Waclawik, P., Konicek, P., Kukutsch, R. & Nemcik, J. 2016b. Stress-state monitoring of coal pillars during room and pillar extraction. *Journal of Sustainable Mining*, Vol. 15, pp.49-56.

# THE INFLUENCE OF INTRA-SEAM COAL CHARACTER VARIATION ON OUTBURST RISK POTENTIAL.

Patrick Booth<sup>1</sup>, Jan Nemcik<sup>1</sup>, Ting Ren<sup>1</sup>

**ABSTRACT:** Effective quantification and management of risk associated with sudden gas release during mining (outburst) is reliant on coal and gas properties measurement bases being representative of the local geological and operational conditions. Contemporary gas emission calculation techniques often inappropriately generalise, or neglect, known site-specific extraction geometry, geological conditions, or heterogeneity and anisotropy within the working seam.

Over 5000 coal core gas sample results, obtained from two Southern Sydney Basin Bulli Seam underground coal mines, plus coal samples collected from multiple locations at one studied mine, have been analysed in various geospatial and mining process-based context. Analysis has focused on the alignment of spatiotemporal relationships between; in-situ coal and gas reservoir character, stress regimes influenced by stratigraphic features and geological structure, and gas emission response to mining extraction processes.

Sampling and experimental processes have been developed to facilitate the alignment of experimentally determined coal and gas characteristic properties and their response to applied stress, with datasets typically collected as part of mine gas and outburst risk management practice. Results demonstrate the high degree of intra-seam variability and anisotropy possible in Bulli Seam coal within relatively small lateral and vertical extents.

Generalised relationships between increased applied confining stress and reduced gas permeability were found to be consistent with the literature. However, in specific cores featuring bright horizontal bands, bedding plies, or other visible cleat fractures, the permeability response to increased stress load was found to vary up to two orders of magnitude greater than those cores without such features. Furthermore, gas emission data from the assembled coal gas core results database, combined with density-based CT analysis and other characterisation of spatially referenced coal samples, confirmed laterally extensive uniform floor-to-roof intra-seam coal character and gas emission response patterns. These patterns, consistent with geochronological deposition sequence, may be used to reduce the apparent variability in observed gas emission behaviour.

Results demonstrate the criticality of retaining both spatial and intra-seam context in the measurement of gas sorption capacity, content and emission behaviour. Measurement should therefore be undertaken at a resolution appropriate to the local in-situ conditions and degree of intra-seam vertical heterogeneity. This additional context may facilitate ongoing spatiotemporal alignment of observed gas emission response and hence improvement to outburst risk management processes as higher resolution information becomes available with mining advance.

## INTRODUCTION

---

<sup>1</sup> University of Wollongong, School of Civil, Mining and Environmental Engineering (CME)  
Corresponding Author: Patrick Booth – University of Wollongong. Email: [pbooth@uow.edu.au](mailto:pbooth@uow.edu.au)



Emission predictions are essential for the quantification and management of risk associated with sudden gas release during mining (outbursts), and accumulation of noxious or combustible gases within the mining environment. Unexplained variation in gas and coal character rightly requires conservative mining practices to manage such risks (Balusu, et al, 2010). In many cases, risks are identified later in the mining cycle where remedial action is typically more expensive and is more likely to incur production delay or loss.

The improved resolution and definition in the prediction of site-specific transient gas emission character, in terms of source location, quantity, composition, flow path and timing is acknowledged by several authors as critical for maintaining current production rates. (Karacan, et al, 2011; Packham, et al, 2011; Wang, et al, 2011). Extensive gas and coal datasets of various forms are typically collected as part of best-practice in mine gas and outburst risk management. However, these datasets may range in spatial resolution, timeliness and quality, resulting in commensurate ranges in calculation outputs for gas emission volumes and rates used in the assessment of risk.

The Southern Sydney coalfields have not been immune to gas explosions and outbursts with fatal consequences. Multiple fatalities occurred in gas explosions at Old Bulli Colliery, Mt Kembla Colliery and Appin Colliery resulting in the loss of over 200 lives. Documented gas outbursts have also occurred at almost all mines operating in the Bulli Seam within the region, resulting in the loss of 12 lives (Harvey, 2001). The Collieries that are the subject of this research, have recorded over 150 and 250 outburst events respectively, with each mine also experiencing outbursts on the longwall face (Walsh, 1997; Hyslop, 2017).

Following the last fatal Bulli seam outburst at West Cliff Colliery in 1994, a directive was issued to all Bulli seam coal mine operators, under the powers of the Coal Mines Regulation Act 1982 Section 63, prescribing Threshold Limit Values (TLV) to manage outburst risk and prevent future coal and gas outbursts (NSW DMR, 1995). Original TLVs ranging from 6 to 9 m<sup>3</sup>/t represent the maximum allowable gas content, relative to seam gas composition, considered safe for mine operations via normal mining, outburst mining procedures, or remote mining only. Pre-drainage of coal seam gas, to reduce initial gas content below 6 m<sup>3</sup>/t, has been clearly demonstrated to reduce the likelihood of such hazardous occurrences. Furthermore, in jurisdictions where TLV legislation has been enacted and enforced, pre-drainage of coal seam gas to below the TLV has eliminated fatalities due to outburst.

Delay to development advance for reduction of gas content and outburst risk may be tolerable in the overall economics of specific mines. However, more frequent delays to development and subsequent longwall production, given increasing depths of mine workings and higher seam gas contents with lower in-situ permeability is unlikely to be sustainable (Mitchell, 2014).

### **RELEVANT GAS AND COAL FUNDAMENTALS**

Coal seam gas generation and transportation behaviour is dependent on fundamental physical and chemical characteristics, and changes in both magnitude and form of energy sources available within the specific mining environment being considered (Booth, et al, 2016). Physical and chemical properties of gas molecules and their constituent atoms have a profound effect on gas behaviour during adsorption, desorption, diffusion, and bulk flow. Molecular-scale modelling has provided detailed simulation of the physical adsorption processes between typical species of coal seam gas and coal (Mosher et al, 2013).

Although many models for adsorption and desorption principles are described in the literature, the most common are the Langmuir single layer model, the BET multi-layer model, and the Dubinin pore-filling model presented schematically in Figure . In either model, the critical parameters are the *accessible* surface area available for the sorption process to occur, which is a function of the coal adsorbent structure, and the physical properties of the fluid adsorbate.

Rates of gas adsorption and desorption may be estimated experimentally as part of isotherm determination, however the controlled (i.e. crushed) particle sizing typically used in such experiments may not be representative of in-situ conditions, and this additional context may prove critical in true assessment of outburst risk.

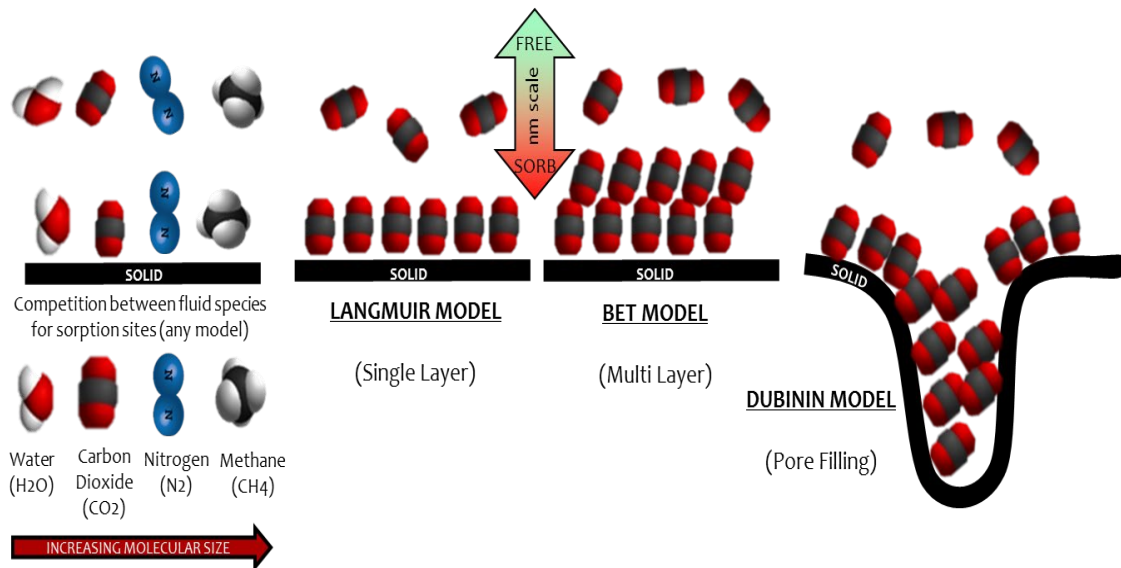


**Figure 1: Common models for fluid to solid sorption process at Nanometre (nm) scale**

Saghafi (2009) suggested the gas concentration (content) rate of change ( $\partial c$ ) with respect to time ( $\partial t$ ) can be expressed as shown in Equation (1), where  $\vec{\nabla}$  is the divergence operator,  $\vec{\psi}$  is the viscous gas flow, and  $s$  is the rate of gas desorption or adsorption dependent on the diffusivity of the coal.

$$\frac{\partial c}{\partial t} = \vec{\nabla} \cdot \vec{\psi} + s \quad (1)$$

The diffusive length becomes the key determining factor in practical estimation or calculation of both the amount and rate of diffusive gas flow, as it becomes more probable that molecules will be subject to much larger external energy forces (e.g. pressure gradients) in shorter timeframes. Gas diffusivity applied in coal represents the ease of gas migration from micropores and into macropores and cleat or fracture systems. Depending on the gas type and pore geometry, diffusive flows are typically dominated by the surface diffusion where the gas species is strongly adsorptive such as with CO<sub>2</sub> (Saghafi, 2007).

When considered with respect to time ( $t$ ), diffusive flow volume from coal  $Q$ , as a proportion of total volume  $Q_m$ , has been reported by researchers to be simply represented by Equation (2), where  $a$  is one-half of the average cleat spacing (Gunther, 1965; Airey, 1968; Saghafi, 2007). Moreover, by rearranging Equation (2) to allow comparison and fitting of experimental data, a single parameter  $\tau$ , representing a time constant as shown in Equation (3) may be used to replace a measured value of the diffusion coefficient  $D$ . Therefore, as the length ( $a$ ) becomes increasingly smaller, while maintaining all other parameters constant, the rate of diffusive gas flow increases.

$$\frac{Q}{Q_m} = \frac{6}{\sqrt{\pi}} \sqrt{\frac{Dt}{a^2}} \quad (2)$$

$$\tau = \frac{a^2}{D} \tag{3}$$

The relative effect of the key variables of diffusive length (a) and diffusion coefficient (D) on the proportional amount of initial gas available at the boundary with respect to time is illustrated in Figure . For example, with a diffusion co-efficient of 1 x 10-8 m2/s, a reduction in sample diffusive length from 5mm to 1mm would result in four-fold increase in the amount of gas diffused within 10 seconds. However, for a diffusion co-efficient of 1 x 10-10 m2/s, only 10% of gas is diffused from the 1mm sample within 10 seconds initially, and less than 5% of gas is diffused for samples of 5mm diffusive length or greater over a period of up to 120 seconds.

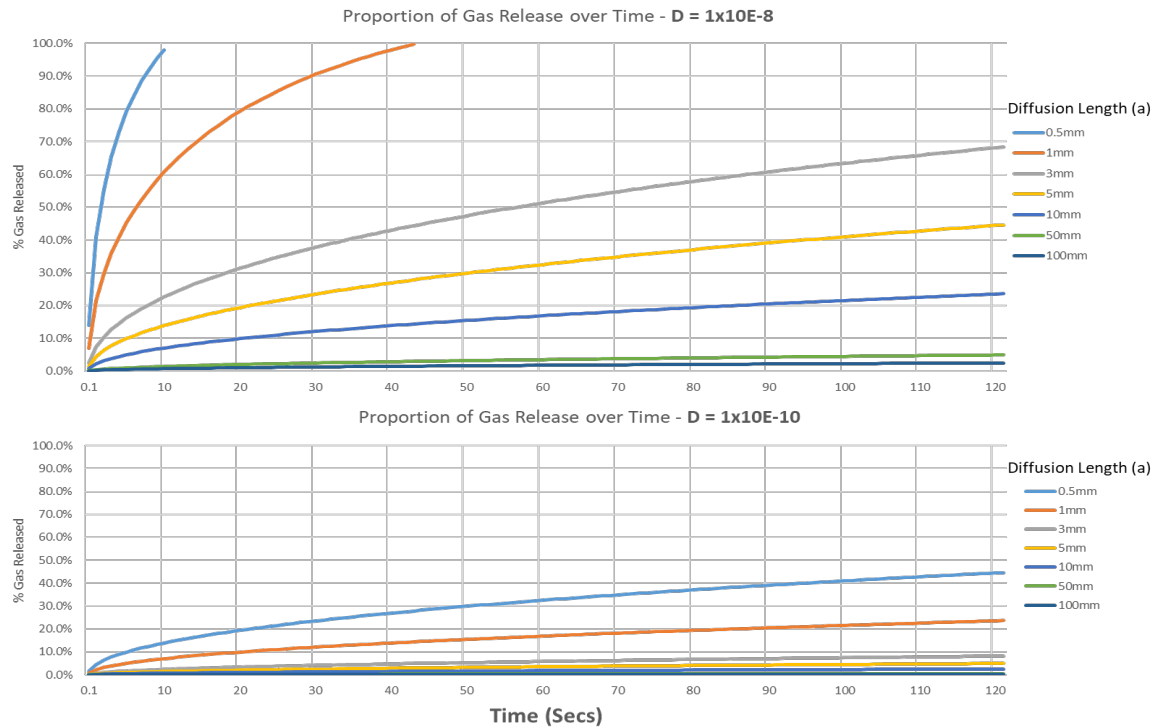


**Figure 2: Comparison of gas diffusion rates over time with diffusion co-efficient and length**

Darcy’s Law describes bulk *free gas flow* under the influence of a pressure differential. It may be applied to either single-phase gas or two-phase gas-liquid flow. The timing ( $\delta t$ ) of pressure differential ( $\delta p$ ) is significant in the application to transient gas emission behaviour from coal, as the combination of time and magnitude of pressure differential will largely determine the gas emission flow rate. The level of gas emission risk exposure throughout the mining interaction processes is thus directly proportional to flow rate, and the larger the pressure differential in the shorter timeframe would generally increase the level of potential risk.

Conservation of mass and energy dictates that the gas reservoir response to a change in boundary conditions will be to re-establish equilibrium by transitioning from higher to lower energy states. Transition timing is dependent upon both initial quantity of gas *available for free flow* to points of lower energy, and the magnitude of the differential. The flow quantity over time may be described by an exponential decay function of the form shown in Equation (4), where  $Q(t)$  is flow at time  $t$ ,  $Q_0$  is the initial flow, and Tau ( $\tau$ ) is a constant reflecting the rate of flow decay. Various parameters, which are discussed in detail following, affect the time constant Tau.

The exponential decay function may also be applied in terms of pressure equalisation over time, between two volumes at different commencing pressures.

$$Q(t) = Q_0(e^{-\frac{t}{\tau}}) \quad (4)$$

For application of the exponential decay function to the mining environment, assumptions related to the boundary conditions include;

- a) Mining interactions are being undertaken from locations initially containing **air**, at or near atmospheric pressure.
- b) Initial gas reservoir conditions (pre-mining interaction) are typically at a much higher pressure than atmospheric pressure, which is typically in the order of 100 kPa.
- c) A pressure differential between two points in space still requires a pathway for any amount of free gas to flow. The number and effective resistance of each pathway to flow may change dynamically as a complex function of changing stress conditions.
- d) Additional gas sourced from coal matrix desorption and diffusion processes may contribute to Darcian flow throughout the period of equilibrium transition.
- e) In-situ initial gas reservoir pressures may, or may not, equal the pressure indicated by a traditional calculation of hydrostatic pressure using depth of cover as a basis.

For calculation of gas emissions and assessment of potential risk, the combination of gas available to be desorbed and diffused within short timeframes, plus already existing free gas must be considered. Gas emission may be limited by either diffusion processes, or the pressure gradient, but in either case the geometry and properties of the coal are critical as demonstrated in Figure .

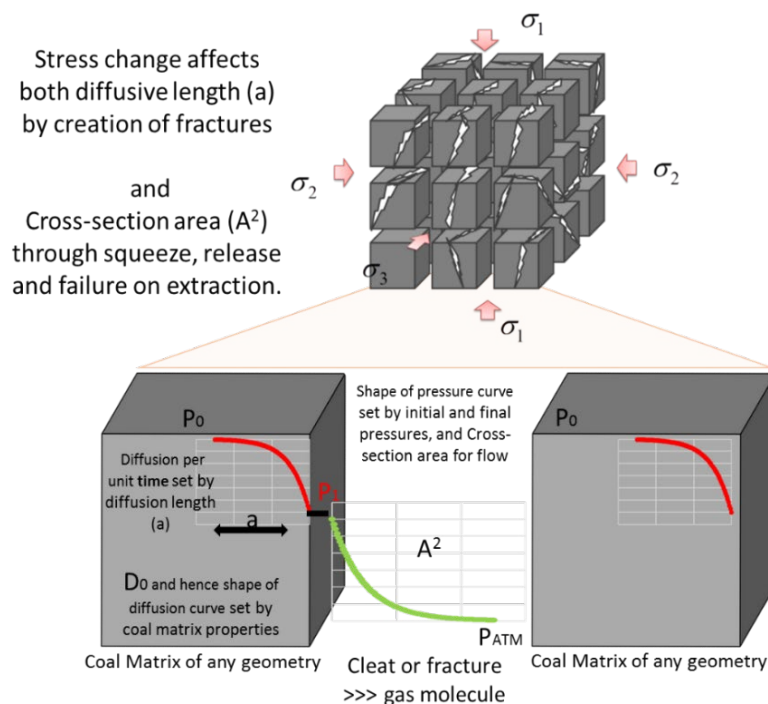


**Figure 3: Generalised effect of stress change on critical gas emission geometric parameters**

Coal is a heterogeneously complex and combustible sedimentary rock made of plant debris and plant derivatives. Originally deposited firstly as peat, and secondarily as mud, coal undergoes physical and chemical processes resulting from compaction and heat over time. At

a fundamental level, coal properties are a combination of three primary parameters, each of which is determined by factors involving the source matter and geological history. The three primary parameters are; organic including the maceral constituents, inorganic including the minerals, ash or other inorganics associated with the structure of maceral components, and the rank reflecting the temperature and pressure to which the source matter has been subjected over time (O'Keefe, et al, 2013).

Maceral types typically used to describe coal are vitrinite, liptinite and inertinite. Within humic coals there is a range from bright (vitrinite-rich) to dull (liptinite- and inertinite-rich) materials (O'Keefe, et al, 2013). Macerals present in coal may be identified through coal petrographic analysis, using reflected light microscopy (Black, 2011). Coal rank is generally reported as increasing by a function of temperature, depth of burial, geothermal gradient, and the length of time the organic material remains in each environment. However, O'Keefe, et al (2013) suggested the maximum temperature to which the source matter has been exposed, and the time for which it was held at that temperature, as the most critical factor in determining coal rank.

Coal rank is typically measured using the vitrinite reflectance technique detailed in Australian Standard AS 2856.3-2000 (SAI Global, 2013). Higher rank coals are typically harder and stronger, containing a bright black vitreous lustre, also characterised by reduced moisture levels, increased carbon content and calorific values.

Prior research within the study region has identified and quantified several coal properties which influence both absolute gas sorption capacity and rate of sorption and desorption (Saghafi, et al, 2007; Black, 2011; Zhang, 2012). Critical coal properties, such as those obtained by proximate analysis, including; carbon content, ash, volatile matter and moisture, have been found to consistently influence coal sorption capacity in a similar way. Conversely, some coal sorption isotherm tests, reportedly undertaken on coal from the same location, yielded results varying by more than 20% on a cubic metre per tonne (m<sup>3</sup>/t) basis. Such variability in results suggest other factors may also influence sorption capacity.

To examine the relative influence of potential alternate parameters in this study; the drilling, coring and laboratory history of core samples used for isotherm testing during Zhang's study were obtained. As isotherm tests were completed on crushed coal core after original gas content analysis, the original core descriptions and results from those analyses were considered in spatiotemporal context. Results reported by Saghafi, et al (2007), Black (2011) and Zhang (2012), while holding coal source and gas type constant, are consistent with previous studies of coal sorption capacity influenced by the parameters summarised in Table .

Isotherm tests are typically carried out using crushed coal samples to reduce sorption equilibrium time to practical experimental timeframes. However, using crushed samples may not be a reliable indicator of accessibility of gas to coal surfaces for sorption and desorption processes in real time, considering the rapid rate of change of stress conditions induced by mining processes.

The coal structure hence plays a significant role in the adsorption and desorption character, but this does not necessarily mean that coal of certain properties, and whose sorption capacity is described by a particular isotherm, actually contains that amount of gas for a given coal volume. Measurement of gas content must therefore be undertaken to determine the degree of saturation of the coal. Limitations in the direct measurement of key gas content inputs for emission calculation remain the subject of debate between researchers (Diamond, et al, 1981; Williams, et al, 1992; Black, 2011), but are addressed concisely in Saghafi (2016). In the latest revision of AS3980-2016, "Determination of gas content of coal and carbonaceous material - Direct desorption method" (SAI Global, 2016), notable modifications include; a changed Q3

**Table 1: Summary changes in coal sorption capacity with various influencing factors.**

Controlling Parameter	Parameter change	Reported capacity trend	Reported sensitivity	Comments
Temperature	Increase	Decrease	25-50% per 10°C $\Delta$ Temp	Aligns to kinetic theory
Moisture	Increase	Decrease	10-20% per 5% $\Delta$ Moisture	Competes for sorption sites
Ash content	Increase	Decrease	10-20% per 5% $\Delta$ Ash	Blocks access to sorption sites
Particle size	Decrease	Increase	10-20% per 2 x $\Delta$ Particle Size	Faster access to more surfaces, but faster desorption rates too.
Micropore proportion	Increase	Increase	10-20% per 10% $\Delta$ $\mu$ Pores	More surface area is available, subject to accessibility to the area
Confining Stress*	Increase	Decrease	10-50% per $\Delta$ MPa	Reduces access pathways for fluids to sorption sites

\* Not applicable if the gas is generated prior to stress being applied

method to extend measurement until an equilibrium is reached, addition of a Q3' method "if required", inclusion of a measurement uncertainty requirement and upgraded reporting requirements (Bull, 2017).

Detail and examples of the required calculations for lost gas determination, temperature correction, measurement uncertainty, and calibration are presented within the Standard. However, it is now critical to establish and standardise site field procedures for core recovery and treatment of samples, to ensure that gas content and composition measurement uncertainties are minimised, and repeatability is maximised. Many authors have compared the slow and fast desorption gas content testing techniques (Williams, et al, 1992; Black 2011). Fundamentally however, it must be recognised that fast desorption testing technique to acquire Q3 deliberately alters the core sample, by crushing to <200  $\mu$ m coal particle size, in the interests of timely gas content measurement.

The direct effects of the crushing process are a reduction of the diffusive length for which desorbing gas needs to pass through the coal matrix, and the complete removal of any in-situ fracture network and stress orientation which may contribute to directionally sensitive gas migration, be that diffusion or pressure driven.

Recording of initial gas desorption rates, core condition and appearance properties, whilst the sample is intact and before the crushing process, therefore becomes even more critical to identification of potentially hazardous or abnormal conditions for which the gas content measurement process is designed. These include Initial Desorption Rate of an intact sample in the first 30 minutes (IDR30), and other desorption rate based derivative measurement concepts.

### SAMPLING AND EXPERIMENTAL METHODS

For validation of the use of spatially interpolated input data for modelling of gas emission response, a series of bulk coal samples were obtained from several locations at one mine and subjected to various characterisation experiments. Experimental methods were designed to maintain three-dimensional spatial integrity and traceability of samples and sub-samples back to source. Statistically significant factors determined experimentally may then be compared on a spatially representative basis at various resolutions. Where available, experimental results



may also be compared with other characterisations previously undertaken at study sites. Critically, these include any of the available gas content testing datasets.

Collection of fresh bulk coal samples was limited in some situations due to production and maintenance activities, however complete roof to floor samples were obtained and subjected to the characterisation experiments outlined in Figure including;

- High resolution external imaging for general appearance and geometry
- CT analysis for quantification of relative density, joint and cleat geometry
- Coring in various alignments parallel and perpendicular to bedding joints
- Proximate, porosity and pore size distribution analysis
- Permeability in various gas pressure, gas composition and tri-axial stress context
- Sorption and desorption response to mixed gases and controlled pressures
- Petrographic analysis and Uniaxial Compressive Strength (UCS) testing

Permeability, sorption and desorption experiments have involved the augmentation of a high pressure triaxial apparatus originally constructed for measuring a range of material behavioural characteristics under the influence of variable stress and fluid pressures. The apparatus has been fitted with a real time supervisory, control and data acquisition system which has allowed a range of novel experimental techniques to be trialled. Most significantly, this includes the observation of gas desorption processes from coal samples under the influence of variable pressure reduction quantity and time. It is expected that simultaneous control of gas pressure and triaxial confinement may more adequately represent and simulate practical gas drainage and mining extraction processes, albeit at laboratory scale.

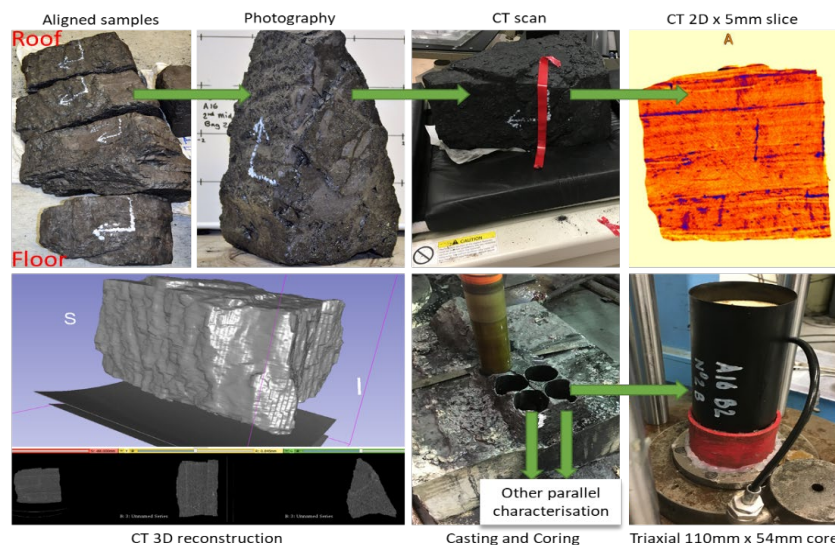


**Figure 4: Outline of experimental characterisation process. (After Booth, et al, 2019)**

## **GAS CONTENT DATABASE ALIGNMENT**

The most critical piece of spatio-temporal data alignment in this research was incorporation of laboratory coal core gas analysis results with the influencing factors derived from accurate 3D geometry. Furthermore, analysis of coal core properties and descriptions allowed additional intra and inter-seam context to be applied and aligned with drilling trajectories, underground field observations, and samples obtained for laboratory experimental processes. The detailed process for calculation of the relevant spatial properties used to inform modelling of gas emissions is described in detail in Booth, et al (2016) and includes;

- Establishment of a subsurface strata Digital Elevation Model (DEM) using best available vertical level and geological structure data specific to the mining location.
- Derivation of slope, aspect, curvature, and catchment parameters based on the DEM
- Alignment of other known gas and strata material properties with the DEM
- Alignment of key properties to mining geometry and cycle timing
- Identification of trigger points for reset of input conditions and increased calculation resolution where appropriate.

Through alignment and restructuring of gas laboratory data tables relationships between gas types, gas content component analysis and coal properties can be exposed. Gas type and value pairs may be related to standard gas properties, avoiding the need to repeat calculations of standard factors and facilitating easy analysis by gas type. Similarly, for gas content component analysis, transforming  $Q_1$ ,  $Q_2$ ,  $Q_3$  and  $Q_T$  data into gas content component and value pairs, facilitates comparison of the influence of core spatial, temporal, and coal structural properties. Examples of analysis of the influence of core appearance, coal density and desorption rate on gas content component and composition measurements are shown in the results.

Relative pre-drainage gas reservoir conditions were established by reference to the closest previously obtained virgin gas content core data. Spatial database alignment allows parameters from original laboratory analysis to be compared critically, including a description of the core analysed. Details of the methods to create seam floor referenced DEMs for the calculation of high-resolution depth-of-cover and in-situ stress values are provided in Booth, et al (2016).

Intra-seam vertical location with respect to seam floor is not currently recorded for gas content coal core. However, informed estimates may be made based on XY location, ash, density, and core description records, specifically noting the core appearance recorded on reference samples. Comparison of density and core appearance data from both gas content laboratory analysis and CT experiments are critical to alignment of estimates and results.

The assembled gas content database has been used to perform critical analysis of core results by many different parameters, however three specific relationships are explored in detail within this paper.

- The relationship between gas content results and sample density due to potential influence of intra-seam coal property change on gas emission behaviour,
- The relationship between core gas content analysis component ( $Q_1$ ,  $Q_2$ , and  $Q_3$ ) and total gas content for a range of core appearance properties.
- The relationship between core appearance, gas composition and desorption rate.

### **Core sample coal density**

The density probability distribution of the total sample set by core appearance and sample area is presented in Figure . There is a distinct trend to lower density values for cores with a bright appearance. Furthermore, and as expected, the trend is independent of the sample area due

to the potential for core samples to be drilled and taken from anywhere within a vertical horizon defined by the seam thickness.

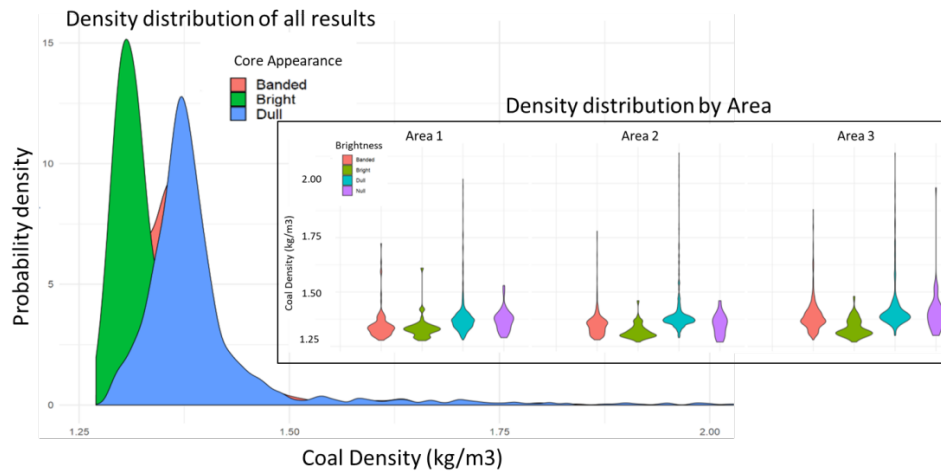


**Figure 5: Core sample density distribution by core appearance and sample area**

Analysis of the density of each sample also allows comparison of gas content results on an uncorrected for apparent relative density (ARD) basis. The apparent relative density changes between distinct coal bedding planes may also be obtained from X-Ray CT based measurement as discussed in following sections. Although both the dip and the azimuth may be recorded by core drilling guidance and survey systems, the dip value is commonly not recorded as part of core sample location or database records.

#### **Gas content component (Q<sub>1</sub>, Q<sub>2</sub>, and Q<sub>3</sub>) vs Q<sub>T</sub> and core appearance**

Unlike most assessments of gas content components within total gas content measurements where values of Q<sub>1</sub>, Q<sub>2</sub>, and Q<sub>3</sub> analysed in terms of m<sup>3</sup>/t, for this study the data has been configured to allow analysis of component contribution to total gas content expressed as a percentage. This facilitates exposure of additional core properties, such as core brightness or appearance, and allows these to be considered simultaneously as illustrated in Figure .

As expected, there is a distinct overall trend to lower Q<sub>3</sub>, and higher Q<sub>1</sub> and Q<sub>2</sub> contribution as total gas content Q<sub>T</sub> increases. This result supports the fundamental gas transport mechanisms described in Chapter 2, however the rate of decrease of Q<sub>3</sub> contribution from bright samples at lower values of total gas contents highlights a potential for higher rates of gas release, particularly where the desorbed gas is CO<sub>2</sub>. The number of bright samples whose Q<sub>1</sub> and Q<sub>2</sub> contributions are higher at lower total Q<sub>T</sub> values is also noted. The denser appearance of the dull samples' facet of Figure purely reflects the greater number of dull samples (2543) of the overall total samples (4388).

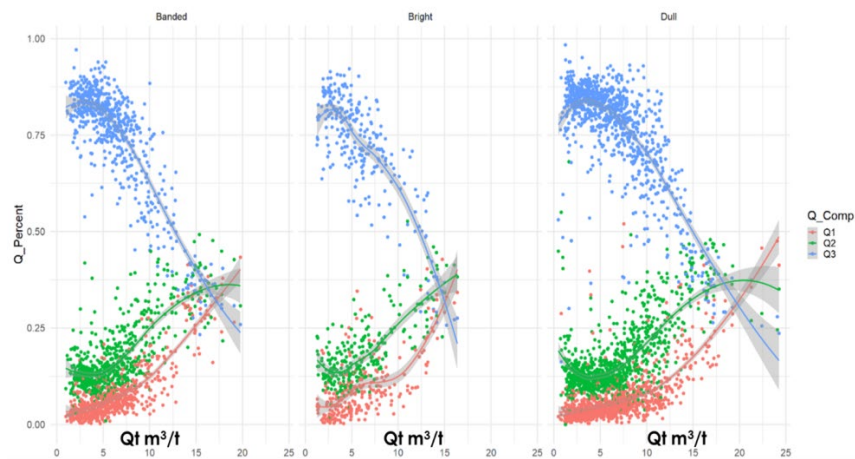


**Figure 6: Gas content component contribution to total gas content by core appearance.**

**Core appearance and gas composition influence on desorption rate**

The effect of core appearance and gas composition on measured gas desorption rates was assessed as illustrated in Figure . As defined by South32 Cordeaux Gas Laboratory practices, desorption is calculated as the square root of millilitres per minute of gas evolved per kg of core material (Bull, 2017). Higher CO<sub>2</sub> core samples are typically observed to have higher desorption rates than mixed gas or High CH<sub>4</sub> samples across all core appearance types. However, the rate of increase of High CO<sub>2</sub> desorption at total gas contents of above 10m<sup>3</sup>/t is much greater in the bright samples than other core appearance types.

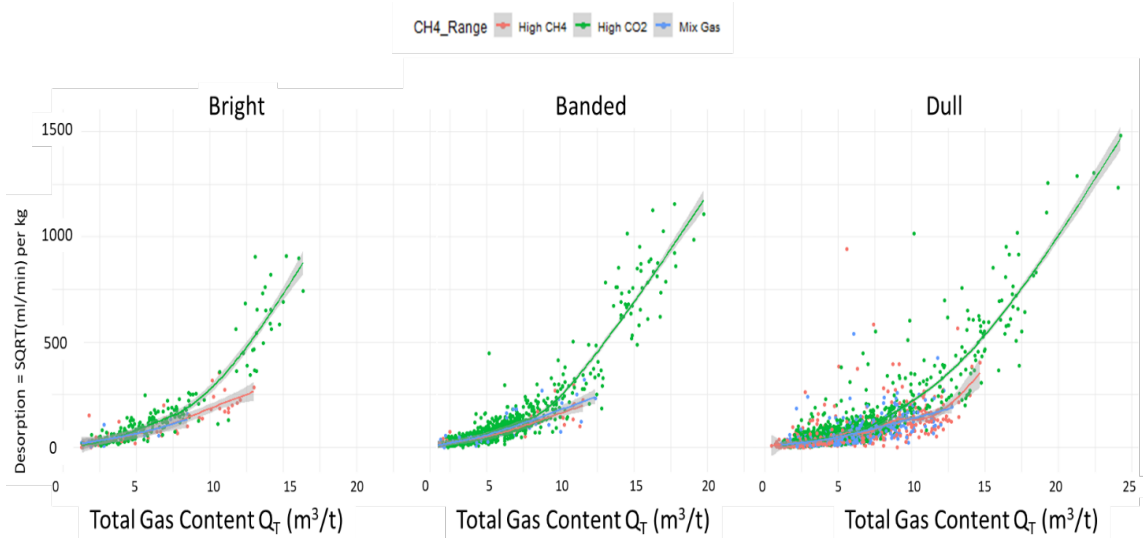


**Figure 7: Analysis of desorption rate by core appearance and gas composition**

Furthermore, for High CO<sub>2</sub> samples, bright core appearance samples are observed to consistently display higher desorption rates than banded and dull samples. This observation is consistent with the bright samples having a more developed internal microfracture network and is discussed in further detail in light of the experimental results.

## EXPERIMENTAL OBSERVATIONS AND RESULTS

### Sample Density

Similar to measurement of coal core density in all laboratory gas content tests referenced, the “as received” density of all 110mm x 54mm diameter right cylinder coal cores subsamples retained for this study was measured using a precision microbalance.

**Table 2: Coal sample density measurements by horizon (kg/m<sup>3</sup>) as received**

Horizon	Samples	Min	Average	Max	Variance
Roof	3	1371.5	1383.3	1389.2	70.2
Mid-Roof	1	1392.9	1392.9	1392.9	0.0
Mid	2	1392.4	1397.9	1403.5	30.4
Mid-Floor	1	1412.8	1412.8	1412.8	0.0
Floor	5	1367.9	1382.6	1405.7	188.0
<b>Total</b>	<b>12</b>	<b>1367.9</b>	<b>1388.7</b>	<b>1412.8</b>	<b>187.9</b>

While density measurements may appear relatively consistent, the horizon, orientation and sample sizing of the coal core all mask significant variations that occur in the horizontal plane consistent with bedding. Such variations can be observed with the naked eye on the surface of cores and block samples, however computerised tomography (CT) techniques may also be used to highlight internal structure and density changes as illustrated in Figure . As demonstrated in later sections, density may also be used as an indicator of coal property changes consistent with geochronological sequence, provided the vertical distance from floor of seam is known.

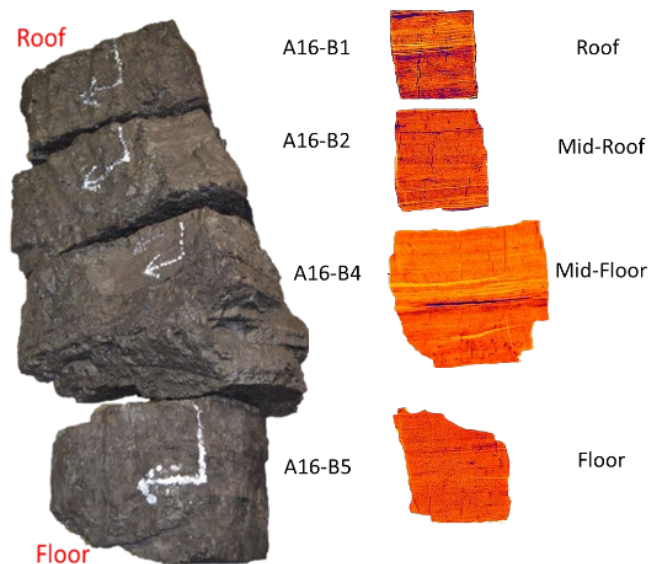


**Figure 8: Example intra-seam coal sample sequence with corresponding density CT images.**

In the above Figure , reverse contrast has been used in post-processing of raw CT DICOM images. Darker blue areas relate to lower density and light yellow to higher density. In most cases the bright horizontal banding, visible to the naked eye on the raw block sample, was able to be directly correlated to the CT density value. Furthermore, in most cases, the coal directly



above the lower density bright horizontal band was consistently much higher density than surrounding coal material. Cases of vertical orientation of lower density appear to correspond to either face or butt cleat, depending on the original orientation of the sample in-situ. Consistent patterns in roof to floor intra-seam sequence were observed when aligning samples from various Bulli seam locations as illustrated in Figure .

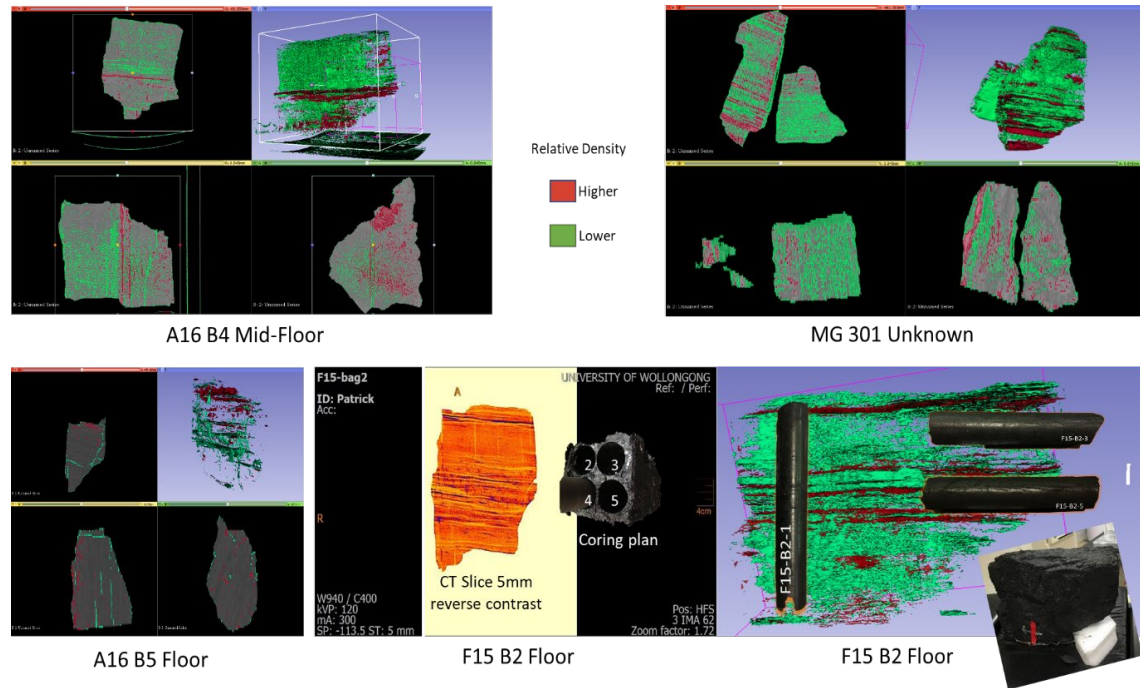


**Figure 9: Relative density measurement and core alignment using 3D CT imaging**

By tuning CT window and level values using Slicer3D image post-processing software, alternating density banding in the horizontal plane could be used to estimate the relative intra-seam location of the sample, even when the original sample horizon was unknown. This is illustrated in where the sample orientation and intra-seam vertical alignment of the MG 301 sample was unknown. The pattern of horizontal banding was consistent with the F15 B2 and A16 B5 Floor samples, and the lower section of the A16 B4 Mid-Floor sample.

Due to the 5mm slice resolution of CT images in this study, it is unlikely that any consistent relationships between cleat height, thickness, and vitrain boundaries can currently be discriminated. Further measurement and analysis of cleat patterns above and below identified stone ply may allow further insight of this behaviour, if it exists. Furthermore, it is possible that micro-CT analysis will allow discrimination of inter vitrain-durian consistency, particularly within observed brittle bright bands.

### Proximate analysis

Similar to density results, proximate analysis results shown in appear relatively consistent, with the exception of two results showing much higher ash and consequently lower carbon content. Depending on the horizon, orientation and sample sizing of the coal sample analysed, results may mask variations that occur in the vertical dimension consistent with bedding. In general, there appears to be a trend to higher ash and lower carbon content with intra-seam depth from roof to floor. All Bulli seam density and proximate analysis results appear consistent with those obtained from publicly available AGL Bootleg program and other surface exploration boreholes drilled in the north of the study area in the 1980's.



Where intra-seam referenced proximate analysis has been performed, also illustrated in Booth et al (2018), results show similar intra-seam trends from roof to floor except where a 25-50mm thick shale band has been included in analysis. In the Bulli Seam, this typically reflects a much denser and stronger stone ply band commonly observed throughout the mines studied. Furthermore, this may explain the high ash results from this study shown from two locations in red in Table . Proximate analysis results in this table are reported on an Ash-dried, Fixed Carbon and Moisture air-dried and Volatile Matter dry-ash-free basis.

**Table 3: Proximate analysis results - Bulli Seam by intra-seam location**

Horizon / Sample	Ash (Ad%)	Fixed Carbon (Fcad%)	Moisture (Mad%)	Volatile Matter (Vdaf%)
<b>Roof</b>	<b>10.71</b>	<b>70.22</b>	<b>0.96</b>	<b>20.76</b>
A16-B1-1N	7.61	73.67	0.77	19.65
C16-B1-1N	7.90	72.76	0.76	20.66
MG27-B2-1A	16.63	64.23	1.36	21.96
<b>Mid-Roof</b>	<b>9.03</b>	<b>71.72</b>	<b>0.85</b>	<b>20.51</b>
A16-B2-1B2	10.13	70.21	0.87	21.22
A16-B2-2C	8.21	72.11	0.84	20.78
A16-B2-3B2	8.72	73.19	0.97	19.04
A16-B2-6B	9.59	70.86	0.82	20.98
A16-B3-2B	7.84	70.96	0.88	22.52
A16-B3-6A	8.76	72.69	0.91	19.62
F15-B3-1N	9.98	72.03	0.70	19.44
<b>Mid</b>	<b>10.01</b>	<b>65.64</b>	<b>1.01</b>	<b>26.33</b>
MG27-B1-1A	10.01	65.64	1.01	26.33
<b>Mid-Floor</b>	<b>7.67</b>	<b>72.29</b>	<b>0.87</b>	<b>21.09</b>
A16-B4-3A	8.71	73.30	0.83	19.21
A16-B4-6B	6.62	71.28	0.91	22.97
<b>Floor</b>	<b>13.56</b>	<b>67.19</b>	<b>0.98</b>	<b>21.43</b>
300B8-B1-1A	25.75	58.34	1.15	20.52
A16-B6-2B	10.74	70.58	1.09	20.07
F15-B1A-1NA	13.53	68.57	0.67	20.18
F15-B2-1C	11.56	68.00	0.95	22.38
F15-B2-4B	6.26	70.50	1.03	24.03
<b>Unknown</b>	<b>5.43</b>	<b>75.25</b>	<b>0.87</b>	<b>21.96</b>
MG301-2-1B	5.43	75.25	0.87	21.96
<b>Total</b>	<b>10.21</b>	<b>70.22</b>	<b>0.91</b>	<b>21.24</b>

### Coal petrography

Coal petrographic analysis was undertaken during this study to determine if any consistent patterns in coal type or coal rank could be used to explain observed gas emission character and permeability testing results. Distinct bright bands typically associated with higher coal rank were observed in samples obtained from several locations. Coal type refers only to the source matter and depositional origin of the coal. (O'Keefe, et al, 2013) Coal types reflect the nature of the plant debris from which the source matter was derived, including the combination of plant and non-plant components. Coal type also reflects the depositional environment at the time of peat accumulation prior to burial.

Five samples as shown in Figure were crushed, encapsulated in contrast resin, polished, and then subjected to petrographic analysis including photomicrography by SGS Pty Ltd. In accordance with Australian Standards, reflected white light under oil immersion (refractive index of 1.518) at 500x magnification was used. Each example photomicrograph in the lower section of Figure is approximately 265 microns in width by 200 microns in height.

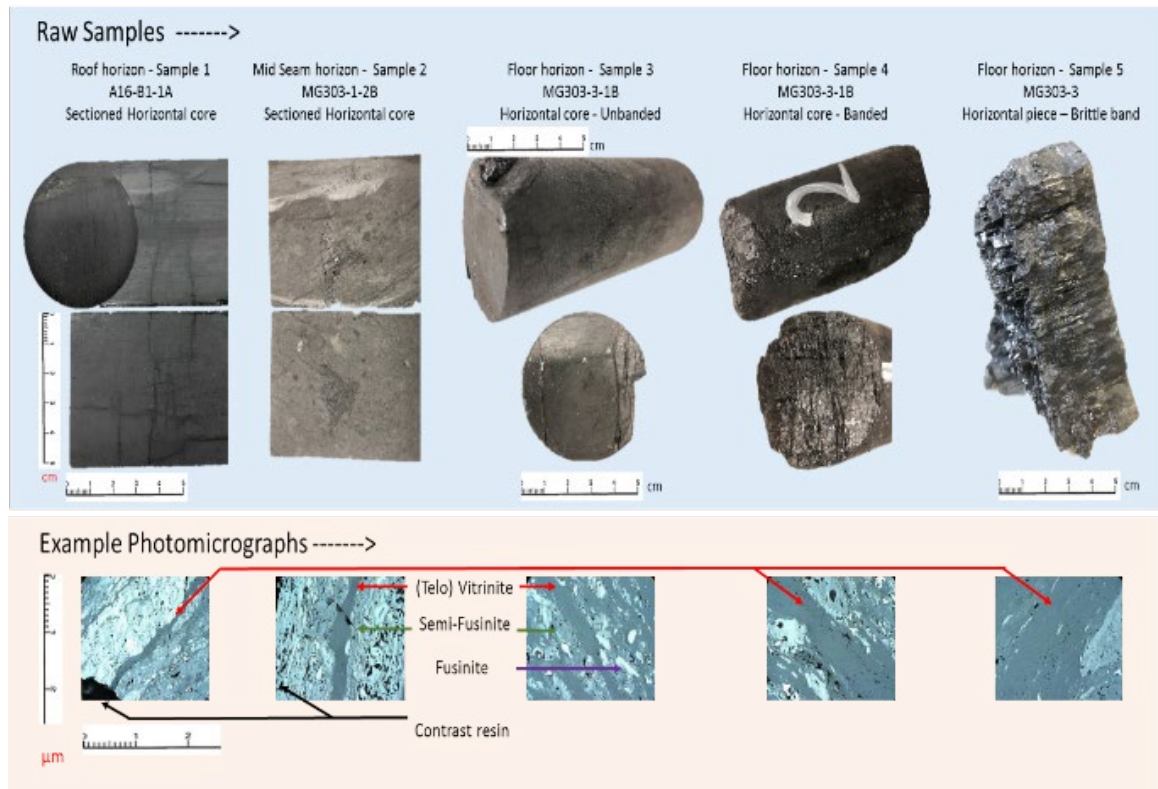


**Figure 10: Coal Type and Rank samples with example photomicrographs**

Due to the crushing process, images at micrometre scale are completely random in orientation and may contain artefacts of the resin encapsulation and polishing process. Results summarised in Figure show an overall increasing proportion of the Telovitrinite maceral subgroup type from roof to floor. Furthermore, the distinct bright and brittle band (Sample 5) had the highest vitrinite proportion (54%).

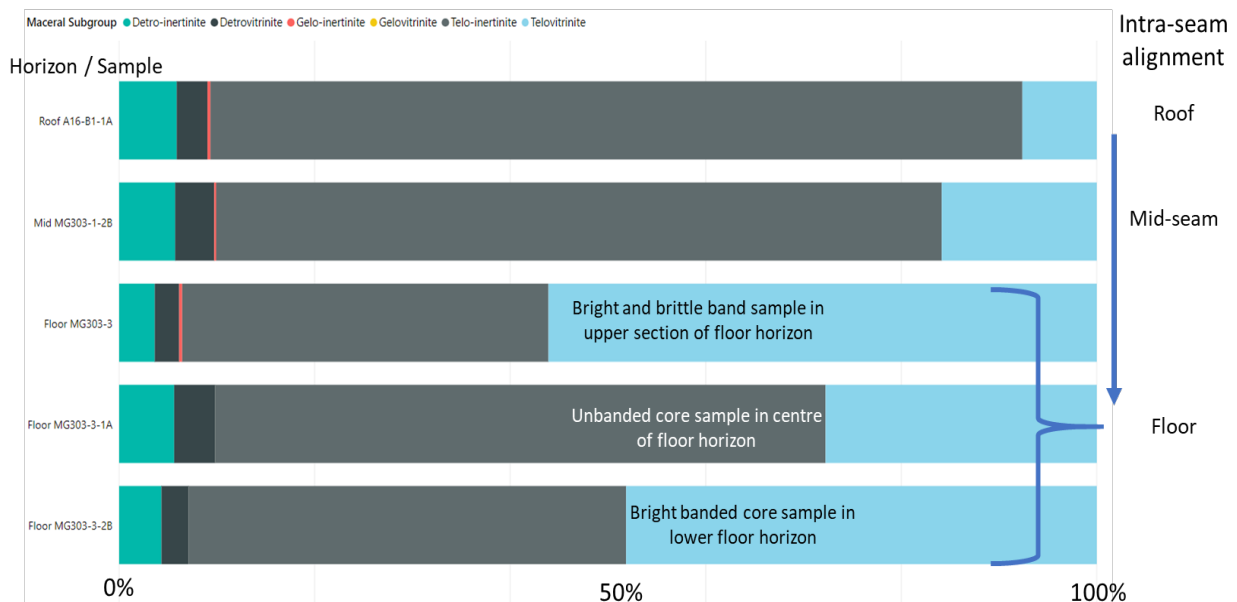


**Figure 11: Intra-seam maceral subgroup proportion by horizon and sample**

Throughout the coalification process, source organic matter undergoes both physical and chemical change. The degree to which the source matter alters, or morphs, as it matures, is

referred to as the “rank” of the coal. Critically, in the case of study sample locations, the heat from localised magmatic intrusion and/or hydrothermal fluids is recognised to have a potential to completely alter certain intra-seam bands over an otherwise consistent regional apparent rank. Results summarised in Table show an overall trend of slightly increasing rank from roof to floor samples, however the bright and brittle sample (MG303-3) again had the highest maximum and mean reflectance of all samples tested.

**Table 4: Intra-seam sample rank measurement by horizon using vitrinite reflectance.**

Horizon	Floor			Mid	Roof
	MG303-3	MG303-3-1A	MG303-3-2B	MG303-1-2B	A16-B1-1A
Calculated Mean Random Reflectance (%)	1.35	1.33	1.32	1.32	1.29
Maximum Value (%)	1.51	1.49	1.50	1.48	1.44
Mean Maximum Reflectance (%)	1.43	1.41	1.40	1.40	1.37
Minimum Value (%)	1.28	1.33	1.31	1.32	1.25
Number of Measurements	50.00	50.00	50.00	50.00	50.00
Standard Deviation	0.04	0.03	0.04	0.04	0.05

### Coal strength

Mechanical properties of coal and adjacent strata play a critical role in determining in-situ permeability, gas reservoir response to fluid withdrawal and mining processes, and eventual gas emission. Ultimately of interest, for both permeability and gas emission calculation, is the stress state at which a coal will fail (fracture) and the nature and geometry of such failure. In practice, sedimentary rock and coal mechanical properties are non-linear, anisotropic, and subject to the character and magnitude of any fluid that may be contained within the porous spaces of the material.

Each of the key mechanical properties of Young’s modulus and Poisson’s ratio have a 3-dimensional response to the same number of dimensions of applied stress. Gray (2017) concluded that stress measurement and modelling are hence reliant on a thorough understanding of material parameters in the context in which measurements are taken or model results are to be applied. Unconfined compressive strength (UCS), measuring the ability of coal to withstand uniaxial loading (stress) without failure is another such mechanical property where the context of measurement is critical. In contrast to other sedimentary rock types adjacent to the Bulli seam, coal has less than one-half or even one-quarter of the strength of typical mudstones and sandstones found in the study area.

Five coal cores of 54mm diameter were prepared from samples obtained from the Bulli Seam within the study area as shown in Figure . Four of the cores were drilled from samples taken at different intra-seam horizons at the same location, and the final core drilled vertically in a hard-to-drain area.

Right cylindrical cores with smooth ends were fitted to the UOW 100kN Instron testing apparatus and compressed at a load rate of 0.2mm/min. UCS test results presented in Table have been corrected for length to diameter (L/D) ratio in accordance with NSW RMS rock testing standards. Furthermore, the scale effects of sample size have been considered by further reduction of laboratory UCS results by a factor of 0.58 in accordance with previous testing of Bulli Seam coal by Tarrant (2006). Recent literature addressing scale effects and strength anisotropy also supports such a reduction in laboratory UCS results.

**Table 5: Intra-seam sample UCS test results**

Horizon - Sample - Orientation	Peak Raw Load (MPa)	Maximum compression %	Corrected L/D Max Load (MPa)	Corrected UCS (MPa)
Mid-Roof - A16-B2-6A - Horizontal	10.58	1.37%	9.53	5.72
Mid - A16-B3-4A - Horizontal	14.17	1.27%	12.75	7.65
Mid-Floor - A16-B4-6A - Horizontal	5.72	3.83%	5.15	3.09
Mid-Floor - MG303-2-1B - Vertical	12.20	1.90%	10.98	6.59
Floor - A16-B6-3A - Horizontal	12.36	2.29%	11.12	6.67

A significantly lower UCS result of 3.09 MPa was recorded for Mid-Floor horizon sample A16-B4-6A. This sample had a noticeable 3-5mm thick horizontal bright band with a crystalline appearance through the centre of the core. Unlike all other cores, which were relatively solid and dull in appearance, this core did not exhibit a sudden failure and reduction in strength as illustrated in Figure . Further discussion of this observed behaviour in the context of permeability is contained in the following section.

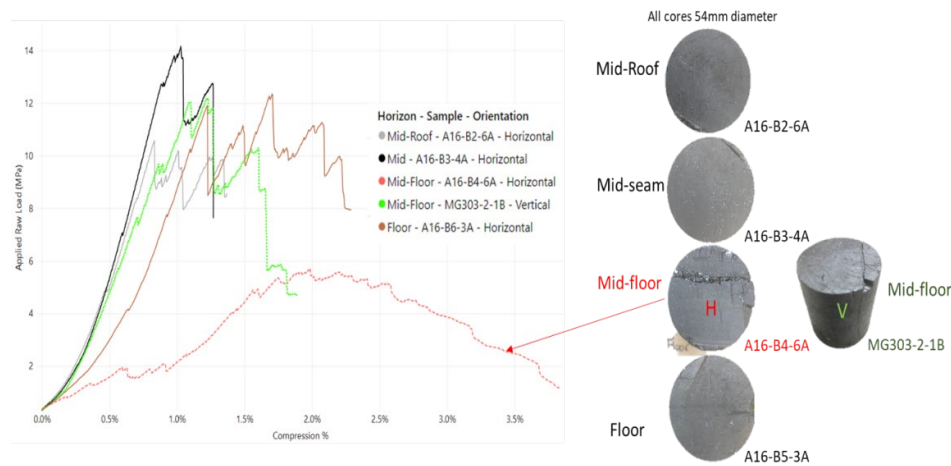


**Figure 12: Intra-seam UCS samples and load-strain curves**

**Sample Permeability and relationship to stress conditions.**

Coal samples from three separate locations, and four vertical horizons within the Bulli seam were tested for permeability under a range of confining stress and gas pressure conditions. The UOW high pressure triaxial apparatus was used for all permeability testing of eight separate 110mm x 54mm diameter cores in total. For the calculation of the permeability in all of the coal samples tested in these experiments, Equation (5) was used, where  $k$  is the permeability (mD),  $Q_a$  is the volumetric rate of flow ( $\text{cm}^3/\text{s}$ ) at atmospheric reference pressure,  $P_a$  (Pa),  $\mu$  is the fluid viscosity (cp),  $L$  is core sample length (cm),  $A$  is the cross-sectional area of the core specimen ( $\text{cm}^2$ ),  $P_{in}$  is inlet gas pressure (Pa), and  $P_{out}$  is outlet gas pressure (Pa). Generally, permeability tests were executed with gas outlet pressure at (or near) atmospheric pressure.

$$k = \frac{2Q_a P_a \mu L}{A(P_{in}^2 - P_{out}^2)} \tag{5}$$

Permeability anisotropy in coal is well established in prior literature, and hence orientation and geometry of coal core with respect to bedding planes has been recorded for each sample tested in this study. When placed in the triaxial rig, cores drilled in a horizontal alignment parallel to bedding planes have the applied confining stress ( $\sigma_1 = \sigma_2$ ) equivalent to a vertical stress orientation. In this case, the minimum stress ( $\sigma_3$ ) variation is axial in orientation and, due to the

fixed configuration of the apparatus axial loading, is directly proportional to the Poisson's ratio of the coal. In this configuration, the apparatus measures the effective horizontal gas permeability subject to changes in vertical load (i.e. typically the depth of cover). Cores drilled in a vertical alignment and normal to bedding planes have the applied confining stress ( $\sigma_1 = \sigma_2$ ) equivalent to a horizontal stress orientation. In this case, the minimum stress ( $\sigma_3$ ) variation remains axial in orientation proportional to the Poisson's ratio of the coal. In this configuration, the apparatus measures the effective vertical gas permeability subject to changes in horizontal load (i.e. typically the principal horizontal in-situ stress). All gas permeability test results are subject to the specific test conditions applied to the apparatus at time of testing including; confining stress state, applied gas pressure and source (gas bottle regulated, or inlet void free gas), gas type and elapsed time between first admission of gas and flow measurement.

While permeability is clearly a function of fluid gas pressures and viscosity, the effect of varying stress magnitude and orientation on permeability is less obvious. The net effective stress magnitude and orientation (as a function of both confining stress and fluid pressure) must be considered carefully in any experimental or field result. The clear relationship between confining stress, applied gas pressure, and gas permeability for three separate samples is demonstrated in Figure , where log10 permeability (mD) is plotted against the linear increase in confining stress (kPa). The relative applied gas pressure for each confining stress stage is shown in colour, red being values approaching 80% of the confining stress, to green being approximately 20% of the confining stress. It is acknowledged that simultaneous desorption-based deformation may contribute to the observed permeability illustrated in Figure , however limitations of experimental equipment and unreliability of optical distance measuring transducers made accurate measurement of these competing simultaneous processes complex to achieve in practice.

While initial values of permeability are relatively low, the trend of rapid reduction in permeability, by an order of magnitude per 2-3 MPa increase in confining stress, is also of critical importance when comparing laboratory test results to likely field stress conditions. Summary permeability test results for core samples are demonstrated in Table , and clearly demonstrate the role of observed bright bands aligned to bedding in improved observed permeability. Furthermore, the role of successive horizontal bands within relatively short vertical distance is suggested to allow improved permeability despite increases in applied confining stress. This result of consistent with failure modes exhibited in UCS tests.

**Table 6: Summary permeability test results**

Core Sample ID	Horizon	Orientation	Features	Initial Permeability (mD)	Additional Stress to reduce one order of magnitude permeability (MPa)	Comments
A16-B2-2B	Mid-Roof	Horizontal	1 x 3mm bright band	0.0049	2.5	Band aligned to bedding
A16-B6-2A	Floor	Horizontal	Solid - no obvious band	0.0015	2	No obvious cleat
F15-B5-1	Roof	Horizontal	Solid - no obvious band	0.0009	3	Minor cleat/fracture
F15-B2-1B	Floor	Vertical	2 x 3mm bright bands	0.0005	2	Bands aligned to bedding
F15-B2-5A	Floor	Horizontal	5 x 2-3mm bright bands	0.0136	10	Bands aligned to bedding
MG303-1-1A	Mid seam	Horizontal	1 x 2mm bright band	0.0019	2	Band aligned to bedding Core failed CO2 saturation
MG303-2-1A	Mid-Floor	Vertical	1 x 5mm band + 1 cleat	0.0213	2	Band aligned to bedding Cleat orthogonal to bedding
MG303-3-2A	Floor	Horizontal	3 x 3-5mm bands	0.0053	2.66	Bands aligned to bedding & fully developed along core



Due to an apparent higher initial and stress resistant permeability result obtained from Sample F15-B2-5A latter samples were deliberately cored to attempt to establish any clear relationship between bright band frequency, geometry, and measured permeability. Other distinct features in latter samples included a shale/stone ply approximately 50mm thick observed at 0.8m above the floor, and noticeable bright and brittle plies ranging between 10 and 25mm in thickness at 1.0m above the floor.

The initial measured permeability of samples at constant confining pressure of 2MPa and gas pressure of 1MPa, and the rate of permeability decline with increase in applied stress, was found to be improved in cores displaying bright banding as illustrated in Figure . The role of successive horizontal bands within relatively short vertical distance is hence suggested to allow improved permeability despite increases in applied confining stress. The (vertical) permeability of the F15-B2-1B sample is believed to be more typical of the vertical permeability likely to be experienced in the Bulli seam due to the spacing of master cleating being observed in the range between 200-700mm. Importantly the observed increase in vertical permeability along cleat fractures quickly reduced with application of additional (horizontal) stress.

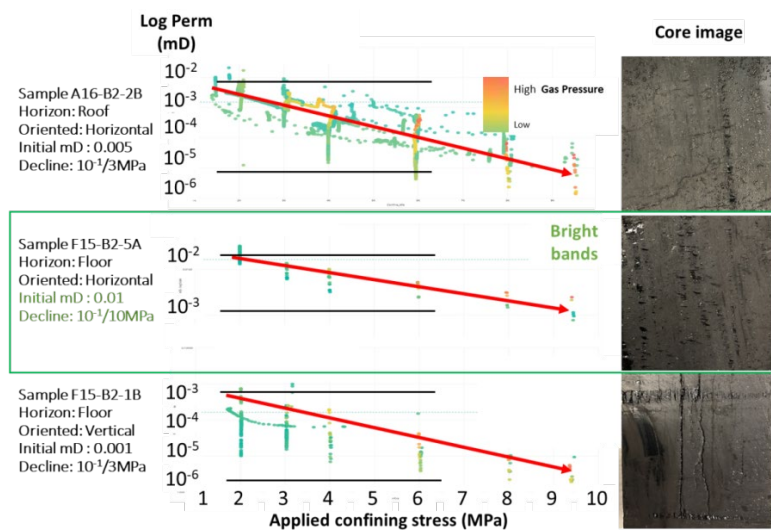


**Figure 13: Observed stress-permeability relationship in selected cores tested.**

### Conclusions and further research

Estimation of in-situ permeability in coal seams is a complex multi-dimensional function of coal and gas reservoir properties and geometry, but necessary for calculation of gas emission and outburst risk. Evidence within this study suggests that by careful observation of intra-seam coal property variation, and separate calculation of potential lateral and vertical stress conditions earlier in the mining cycle, much of the previously unforeseen gas emission behaviors' due to dynamic permeability change may be explained fundamentally. The determination of permeability, as a result of highly dynamic stress changing mining processes, relative to cleat and bedding plane geometry, in similar time resolution, is very challenging.

Dual acting diffusive and Darcian gas flow processes, combined with the relative geometry of coal matrix to coal cleat, are critical inputs to the calculation of gas emission and outburst risk. Consistency in geometry and coal character on an intra-seam floor to roof basis, and relative permeability, were tested experimentally in this study. Results from the static permeability experiments conducted demonstrate the degree of variability possible in intra seam vertical and horizontal permeability of the Bulli Seam, even within relatively small lateral constraints. Horizontal permeability of samples tested ranged from 0.001 to 0.01mD, and as such would



generally be described as an impermeable coal. Visible features of each of the samples tested may explain the relative range in results. Vertical permeability of samples cored in that orientation ranged widely from 0.0005 to 0.02mD. The relatively high permeability observed from one sample, is believed to be significantly influenced by the presence of a cleat fracture oriented parallel to the core.

A general log form relationship between increased applied confining stress and reduced gas permeability was found to be consistent with the literature. Effective permeability was also found to increase with increasing gas pressure consistent with Biot's co-efficient. However, both the initial measured permeability at constant confining pressure of 2MPa and gas pressure of 1MPa, and the rate of permeability decline with increase in applied stress, was found to be improved in cores displaying bright banding. The role of successive bright horizontal bands within relatively short vertical distance is hence suggested to allow improved permeability despite increases in applied confining stress.

Gas content core database analysis suggests that bright core appearance samples' consistently display higher desorption rates than banded and dull samples. This observation would appear consistent with the bright samples having a more developed internal microfracture network, the experimental results for bright banded core permeability response to increased applied stress, and core UCS test results. One potential explanation, consistent with all of these observations, is that, due to the altered but narrow distribution of mechanical properties within observed bright coal bands, multiple smaller incremental failures occur on application of increased stress. This may present as both an increase in gas permeability and a reduction of coal particle size, due to the increase in the number and random orientation of microstructural failures, and the number of pathways available for gas flow as stress is applied and then released with mining extraction. While this study has not provided any quantitative justification to draw such a conclusion, this explanation would appear consistent with the results observed.

The variation in results from coal sorption isotherm tests undertaken on coal from the same location, but at different vertical horizons, combined with the observed gas emission behaviour of core samples recorded with bright appearance, therefore illustrate the criticality of intra-seam context in the assessment of coal sorption capacity and gas emission behaviour. Considering such appearance and character is generally aligned horizontally with bedding geochronological deposition sequence, the need for intra-seam vertical reference, at a resolution appropriate to the local in-situ conditions and degree of vertical heterogeneity, may be justified.

Given the sensitivity of any gas emission calculation or assessment of outburst risk to several of the coal properties and geometries illustrated, results suggest a level of intra-seam character and context should be incorporated into assessment of outburst risk. This is particularly relevant in the case of either bedding or plies within the seam having significant change in properties, or where plies are known to have a wide distribution range of permeability values. Where geological structure is known to exist and has potential to cause rapid stress magnitude or orientation change, consideration of loss of confinement in orientations other than for standard linear advance should be undertaken. This is due to the potential for high permeability plies to connect laterally and extensively to coal which has failed and significantly reduced in grain size proximate to the structure plane. Critically, this potential exists independent of the relative geometry of structure to the excavation. High permeability pathways may provide opportunity for rapid pressure loss, triggering rapid desorption of gas from the failed coal with limited diffusive restriction. Structure fault planes may also provide vertical conductivity to otherwise relatively disconnected high permeability horizontal plies, further amplifying potential outburst risk.

The data compiled and analysed in this study may be used to critically assess and optimise outburst risk management and gas drainage designs moving forward, but also demonstrate it is essential for all measurement data to retain the context of location and orientation relative to a common co-ordinate system, including in respect of vertical alignment, throughout the process to facilitate ongoing spatiotemporal alignment of results.

### ACKNOWLEDGMENTS

This research has been conducted with the support of the Australian Government Research Training Program Scholarship. The authors gratefully acknowledge the financial support of MeCee Solutions Pty Ltd towards this research. The technical assistance and provision of coal samples and data from the respective anonymous study sites is appreciated. The authors acknowledge use of the X-Ray Computer Tomography scanning facilities housed at the Centre for Geomechanics and Railway Engineering of the University of Wollongong (UoW). The support of fellow researchers at UOW and China University of Mining Technology in the provision of coal sample analysis is also acknowledged.

### REFERENCES

- Airey, E M, 1968. Gas emission from broken coal. An experimental and theoretical investigation, *International Journal of Rock Mechanics and Mining Sciences and Geomechanics Abstracts*, 5(6):475-494.
- Balusu, SY, Ting, XR, Shi, S and Moreby, R, 2010, Strategic Review of Gas Management Options for Reduced GHG Emissions, C17057, ACARP.
- Black, DJ 2011, 'Factors affecting the drainage of gas from coal and methods to improve drainage effectiveness.', Doctor of Philosophy thesis, University of Wollongong.
- Booth, P, Nemcik, J and Ren, T 2016, 'A Critical Review and New Approach for Determination of Transient Gas Emission Behaviour In Underground Coal Mines', paper presented to 16th Coal Operators' Conference, University of Wollongong, 10-12 February 2016, <http://ro.uow.edu.au/coal/623/>.
- Booth, P, Brown, H, Nemcik, J and Ren, T, 2017. Spatial context in the calculation of gas emissions for underground coal mines, *International Journal of Mining Science and Technology*, 27(5):787-794.
- Booth, P, Brown, H, Nemcik, J and Ren, T, 2018, Determination of Gas Emission in the Mining Life Cycle, in *Proceedings of the 18th Coal Operators' Conference*, N. Aziz and B. Kininmonth, Editors. Mining Engineering, University of Wollongong, p. 273-283.
- Booth, P, Brown, H, Nemcik, J and Ren, T, 2019. The development of a new gas emission prediction model for underground coal mining, paper presented to the 11th International Mine Ventilation Congress. Xi'an. People's Republic of China, 2018.
- Diamond, W P and Schatzel, S J, 1998. Measuring the gas content of coal: A review, *International Journal of Coal Geology*, 35(1-4):311-331.
- Gray, I, 2017. Coal Measure Rock Properties. Presentation to coal and gas outburst seminar June 2017, Illawarra Master Builders Club, Wollongong.
- Harvey, C, 2001. Analysis and management of outbursts: with particular reference to the Bulli coal seam, Doctor of Philosophy (unpublished), University of Wollongong.
- Hyslop, A, 2017. Metropolitan LW Outburst. Presentation to the Coal and Gas Outburst Seminar, June 2017 Illawarra Master Builders Club, Wollongong

## Coal Operators' Conference

- Karacan, CÖ, Ruiz, FA, Cotè, M and Phipps, S 2011, 'Coal mine methane: A review of capture and utilization practices with benefits to mining safety and to greenhouse gas reduction', *International Journal of Coal Geology*, vol. 86, no. 2–3, pp. 121-56.
- Mitchell, G W, 2014. Longwall Mining, in *Australian Coal Mining Practice* (ed: E Baafi), pp 340-375
- Mosher, K, He, J, Liu, Y, Rupp, E and Wilcox, J 2013, 'Molecular simulation of methane adsorption in micro- and mesoporous carbons with applications to coal and gas shale systems', *International Journal of Coal Geology*, vol. 109–110, no. 0, pp. 36-44.
- O'Keefe, J M K, Bechtel, A, Christanis, K, Dai, S, DiMichele, W A, Eble, C F, Esterle, J S, Mastalerz, M, Raymond, A L, Valentim, B V, Wagner, N J, Ward, C R and Hower, J C, 2013. On the fundamental difference between coal rank and coal type, *International Journal of Coal Geology*, 118:58-87.
- Packham, R, Cinar, Y and Moreby, R 2011, 'Simulation of an enhanced gas recovery field trial for coal mine gas management', *International Journal of Coal Geology*, vol. 85, no. 3–4, pp. 247-56.
- Saghafi, A 2016, 'Determination of the Gas Content of Coal', in N Aziz and B Kininmonth (eds), 16th Coal Operators' Conference, University of Wollongong, pp. 347-56.
- Saghafi, A, 2017. Discussion on determination of gas content of coal and uncertainties of measurement, *International Journal of Mining Science and Technology*, 27(5):741-748.
- Saghafi, A, Faiz, M and Roberts, D, 2007. CO<sub>2</sub> storage and gas diffusivity properties of coals from Sydney Basin, Australia, *International Journal of Coal Geology*, 70(1-3):240-254.
- Saghafi and Roberts, 2008. CSIRO Report IR1033 Measurement of CO<sub>2</sub> and CH<sub>4</sub> reservoir properties of coals from Westcliff Mine.
- Standards Australia, 2016. AS 3980-2016 Determination of gas content of coal and carbonaceous material—Direct desorption method.
- Tarrant, G 2006, PhD Thesis. 'New concepts in tailgate strata behaviour and implications for support design'. Unpublished. University of New South Wales.
- Williams, RJ, Yurakov, E and Ashelford, DJ 2001, Gas Emission Modelling of Gate Road Development, Research Online.
- Zhang L, 2012. A Study of coal sorption characteristics and gas drainage in the Bulli Seam, Ph.D Thesis, University of Wollongong, Wollongong.

# DYNAMIC ANALYSIS OF FAULT SLIPS AND THEIR INFLUENCE ON COAL MINE RIB STABILITY

Jan Nemcik<sup>1</sup>, Gaetano Venticinque<sup>2</sup> and Libin Gong<sup>3</sup>

**ABSTRACT:** Historical data indicate that in deep coal mines the presence of faults in close proximity to excavations affect the frequency of coal bursts. A number of researchers have attempted to correlate the fault geometries to the frequency and severity of coal bursts but dynamic numerical modelling has not been used to show how faults can affect coal ejection from the rib side. The dynamic numerical analysis presented here show how different orientations of fault slips may affect coal bursts. To prove the concept, 89 cases of slipping fault geometries were modelled using the FLAC<sup>3D</sup> software and their effect on rib stability investigated. The results indicate that there is a simple and logical correlation between the fault location, its slip velocity and the ejection of the yielded coal rib side. The seismic compressive wave generates rock/coal mass velocities that directly impact the rib side. If the coal rib is relatively disturbed and loose, these velocities can cause its ejection into the excavation. The slip direction typically impacts one side of the mine roadway only. A 1 m thick loose coal block attached to the 3 m high rib side in mine roadway was ejected at speeds ranging from 2.5 to 5 m/s depending on the fault location, its orientation and the maximum fault slip velocity modelled at 4 m/s.

## INTRODUCTION

Many researchers participated in investigating the origins and causes of rock/coal bursts with various success including Bräuner (1994), Brown, S. (1998), Brune (1993), Chengguo (2017), Dou (2016), Hebblewhite (2017), Mark (2014), Moodie (2011), Muller (1991), among many others. The lengthy principles and mechanisms of fault and seismic behaviour in these investigations are not included here, instead this description is focused directly on the principles behind the investigations and the modelled results as reported in the ACARP C26054 project (Nemcik et al. 2019).

The seismic waves in rock generate a 'back and forward' sinusoidal motion of the individual rock particles at relatively low speeds, usually several m/s. The maximum velocity of this particle movement is also known as the peak particle velocity (PPV) caused by the seismic waves (Saharan, 2004). This movement transfers the energy momentum along the rock mass at very fast speeds of up to several km/s. PPV is widely used as a threshold for damage to the rock mass (Brinkmann, 1987) and can determine the magnitude of damage caused by seismic events. This mechanism is similar to the Newton's cradle motion. When rock/coal motion approaches the unconfined rib side, it may rip apart the already weakened coal rib and 'knock' the failed/loose coal out into the excavation. This is depicted in the top layer in Figure 1(e) where the detached last ball (mass) is knocked out and carry the accumulated energy with it. No wave reflection occurs. On the other hand, if the edge mass (shown in the bottom layer) is firm/attached, the seismic wave is reflected and no rib mass is damaged or ejected Figure 1 (e) and (f). Another view of the same burst mechanism is schematically depicted in Figure 2 where

---

<sup>1</sup> Honorary Senior Fellow, University of Wollongong. Email: jnemcik@uow.edu.au Tel: +61 2 4221 4492

<sup>2</sup> Senior Geotechnical Engineer, SCT Operations Pty Ltd, Email: gventicinque@sct.gs

<sup>3</sup> Researcher, The Czech Academy of Sciences, Institute of Geonics, libin.gong@ugn.cas.cz, Tel: +420 596 979 701

the mass momentum travels through the laterally compressed seam knocking the loose rib mass into the excavation. Typically, the yielded coal located close to the roadway is broken and relatively loose with lower confining stress and therefore it can be easily knocked out of the rib.

There are many types of stored potential energy that can contribute to the coal burst. Examples of these include: slip of highly loaded fault plane, geologically weakened coal-rock interfaces, high additional loads due to nearby mining, among others. For the rock burst to occur, a dynamic event such as a fault slip is needed to generate the seismic waves and supply enough energy to dislodge the already stressed or non-existent bonds between the coal seam and the roof/floor rock interfaces.

Two sources of the seismic energy can be in play simultaneously consisting of the propagating seismic disturbance from the fault slip together with the release of stored energy in the compressed coal seam. The example of generated seismic waves is depicted in Figure 3. However, the fault slips may generate sufficient amount of seismic energy to produce a coal burst on its own.

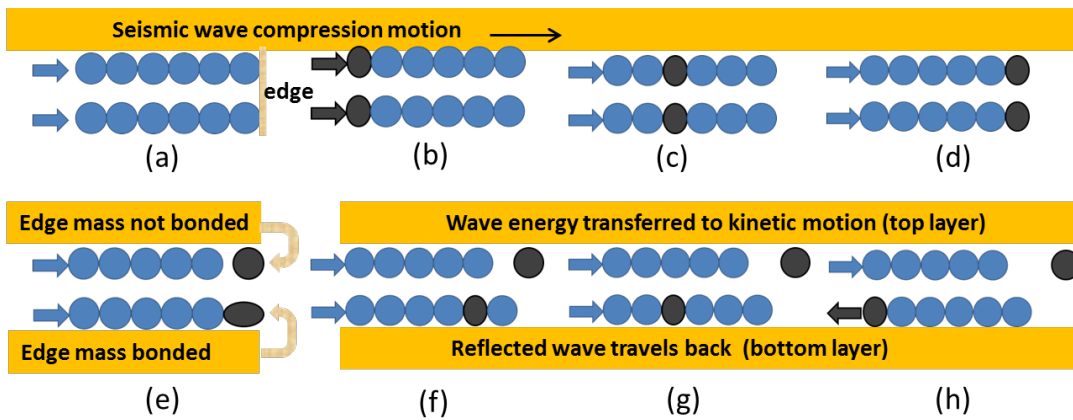


**Figure 1: Schematic of seismic compression wave in rock, (a) and (b) Seismic wave hits and compresses the rock mass, (c) and (d) Compression in rock mass is travelling at sonic speed, (e) in the top layer, the disconnected rock mass flies out into the empty space - no reflection occurs. In the bottom layer the connected mass stretches and rebunds back impacting the mass on the left side – reflection occurs, (f), (g) and (h) in the bottom layer the reflected seismic wave propagaes back to the left at the sonic speed.**

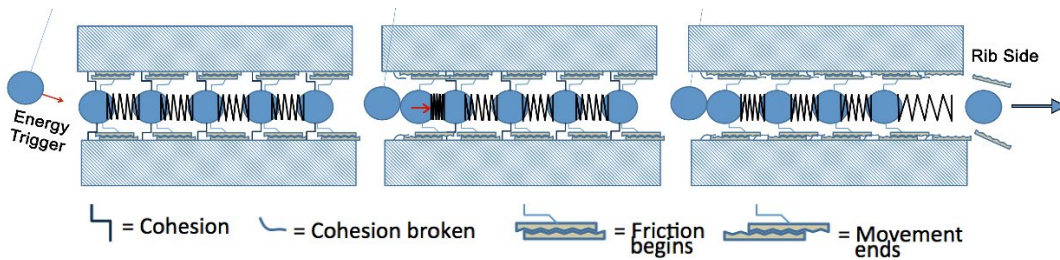


**Figure 2: Modified Newtons Cradle as an analogy of the rock burst where the yielded coal is ejected from the rib**

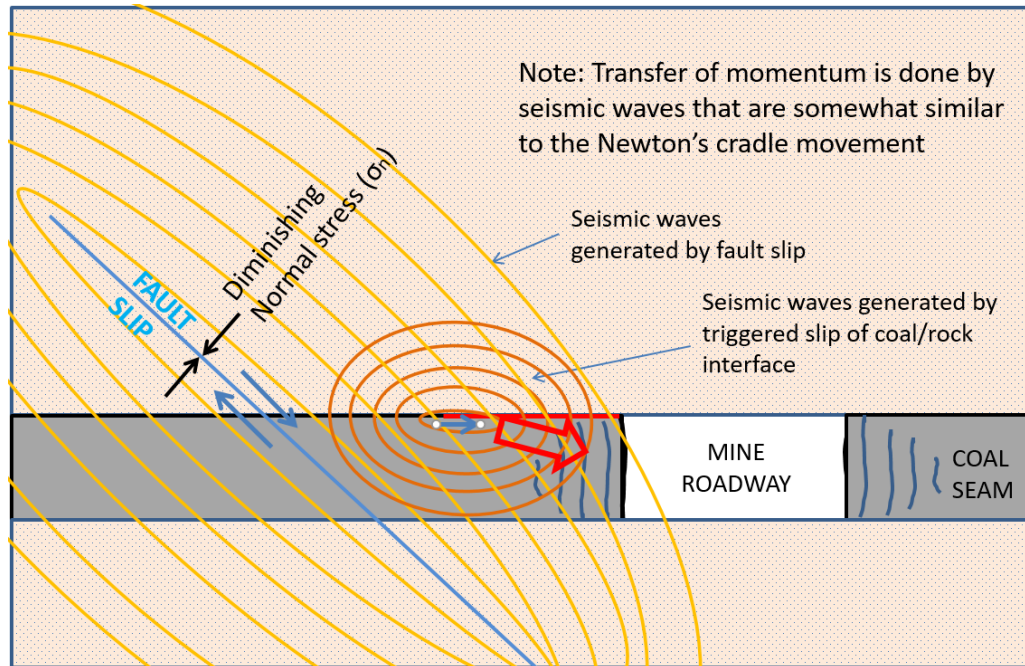


**Figure 3: Fault slip mechanism, generation of seismic waves and their impact on coal**

The exact mechanism of the fault slip is still not very well known. Many researchers carried out back analysis of seismic events trying to estimate fault properties and their influence on PPV in the near field. Their research indicates that various fault surface properties appear to influence the seismic parameters (Sainoki and Mitri, 2016). From the far-field S-wave pulses in a deep underground mine McGarr (1991) estimated fault slip velocity rates ranging from 1 to 5 m/s.

The purpose of this dynamic numerical model presented here is to investigate the overall rib behaviour when the nearby fault slip occurs. For that the fault slip value equal to 4 m/s was chosen. To evaluate the influence of this particular fault slip on coal rib stability, an average seismic energy impacting the rib side was calculated for 1 m length of roadway. This was derived from the kinetic momentum of an ejected coal block that was loosely attached to the coal rib at the studied locations. These calculations and geometries aimed at producing basic results to prove that this method could be used to flag dangers of coal burst occurrence for certain fault orientations that may exist near excavations. Many models with various fault orientations produced data shown in Table 1. To avoid any complications that may occur with yielded zones, elastic models were set up to carry out the sensitivity studies investigating the influence of fault orientation, distance from the excavation, direction of probable fault slip and side/location within the excavation that may experience the coal burst. Once the location of the fault zone is known, the mine excavation side where rib ejection may occur can be estimated. This makes this research very valuable for safety in coal mines as workers may be able to keep from the harm's way while mining through certain zones of fault influence.

**Table 1: Model Strata Properties**

Mechanical properties	Sandstone	Coal
Density	2500 kg/m <sup>3</sup>	1400 kg/m <sup>3</sup>
Bulk modulus	10.67 GPa	3.33 GPa
Shear modulus	6.4 GPa	1.11 GPa



DYNAMIC MODEL SETUP IN FLAC<sup>3D</sup>

The constructed model was 80 m wide (perpendicular to the mined roadway), 80 m high and 40 m thick as shown in Figure 4. To examine the first 44 fault geometries with the fault plane aligned with the mine roadway, the 5 m wide mine roadway was excavated through the model centre in a 3 m thick coal seam. A continuous 2.9 m high and 1 m thick coal block was attached to the rib side in the mine roadway to measure kinetic momentum of seismic waves delivered to the rib side. For the remaining 45 fault models a shorter mine roadway was excavated to the centre of the model and a 1 m thick, 2.9 m high and 2 m long coal block was attached to the rib side adjacent to the roadway face. Elastic properties of the strata were chosen to enable measurements of the maximum possible kinetic energy transfer through the rock and coal seam without complications of the yielded zones. Typical sandstone rock and coal properties were assigned to the roof, floor and the coal seam as specified in Table 1.

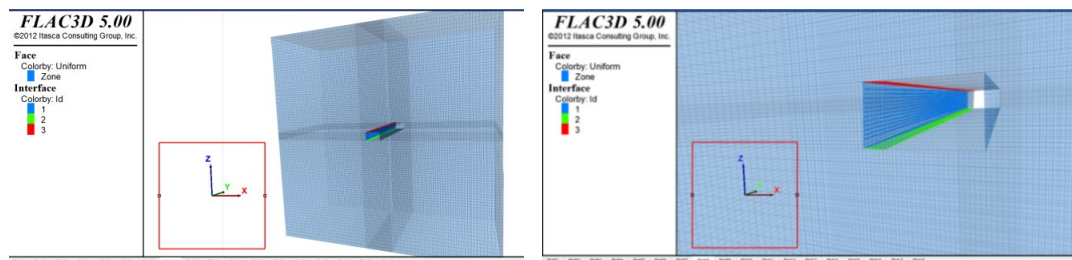


**Figure 4: Model geometry showing excavated mine roadway**

Each model was run until static equilibrium was achieved. A simple one way dynamic fault slip was artificially modelled by assigning variable slip velocities along each fault using the decay equation:

$$y(t) = A^{-\lambda ct} \cos(2\pi ct + \varphi) \quad (1)$$

Where  $A$  is wave amplitude (18.4 m/s – not the actual fault slip velocity produced)  
 $\lambda$  is constant (10)  
 $\varphi$  is phase (90°)  
 $c$  is constant (7) and  
 $t$  is time (between 0 to 0.07s)

The chosen equation constants produced the maximum fault slip velocity of 4 m/s that occurred at time  $t = 0.013$  seconds after the slip began and subsequently decayed to zero at approximately 0.07 seconds, producing total slip displacement of 119 mm. The graph of fault slip vs time (from Eq1) is shown in Figure 4(a). These values were estimated from previous dynamic numerical models by studying mining induced fault slips in metalliferous mines (Sainoki, 2014). The first rib dynamic impact was produced by the rapidly increasing velocities within the short time of 0.013 seconds as the kinetic momentum carrying waves spread through the strata at sonic speeds. Subsequent decay velocities during the fault slip did not seem to significantly influence the mine roadway stability.

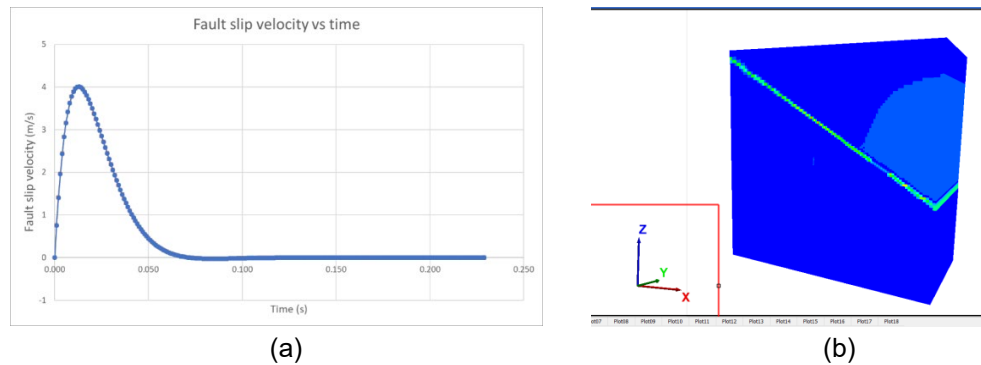


**Figure 5: (a) Fault slip velocity versus time using Eq (1), (b) geometry of one of the slipping faults**

### MODELLED FAULT SLIP FAILURE AT VARIOUS FAULT ORIENTATIONS AND THEIR INFLUENCE ON ROADWAY RIB STABILITY

Horizontal faults parallel to the seam were modelled 2 m, 5 m, 10 m, 15 m, 20 m and 30 m below the seam floor. This was repeated in the roof with the same distances above the seam roof. These faults were subsequently rotated from  $0^\circ$  to dips of  $15^\circ$ ,  $30^\circ$ ,  $45^\circ$ , and  $60^\circ$  through the fault rotation point which was located below the roadway centre and above in the roof at the same distances from the seam roof and the floor. Additional 45 runs of the vertical fault at various distances and bearings ahead of the roadway face were also trialled.

The fault slips were arranged so that the impact from the slip was oriented towards the rib side where the attached coal block was placed. As the fault slipped, it produced seismic waves carrying the kinetic energy (momentum) that travelled towards the rib. To measure the rib side impact energies, a continuous 1 m wide coal block was attached to the rib side in the first 44 modelled faults. This block was used to simulate the yielded and only slightly confined coal mass typically found in the fractured coal rib. This block was important to measure the rib momentum more precisely as the rock mass in FLAC model is continuous and the model zones cannot normally part from the rib. A section of coal was excavated, interfaces were assigned to its surface, and the block placed in the roadway touching the rib. The model was first brought to a static equilibrium and then the fault slip was initiated. The seismic waves impacted the block, ejecting it from the rib side. This mechanism provided the controlled way to measure the impact velocities generated by the seismic waves at the coal rib. The fault slip induced seismic waves quickly spread through the surrounding strata impacting the roadway rib. Note that the slip direction typically impacts only one side of the roadway. This is shown in Figure 6(a) where the grid velocities initiated by the seismic wave are spreading away from the slip boundary in the direction of the final block ejection. Note that the fault slip directions can be determined from the ground stress.

After the seismic waves dissipated through the surrounding strata, the seismic momentum, locked inside the block, propelled the block at velocities above 4 m/s shown in Figure 6(b). For non-elastic conditions smaller dynamic impacts may occur. Further work is needed to incorporate fully yielded models, faults affected by stress relief due to excavation, and use fault slip data measurements if available.

For the vertical faults numbered 45 to 89, the mine roadway was excavated half way into the model centre and faults inserted in front of the roadway face. A coal block 1 m thick, 2.9 m high and 2 m long was attached to the roadway rib side adjacent to the roadway face. An example of this block ejection velocity of 4 m/s after the fault slip is shown in Figure 7.

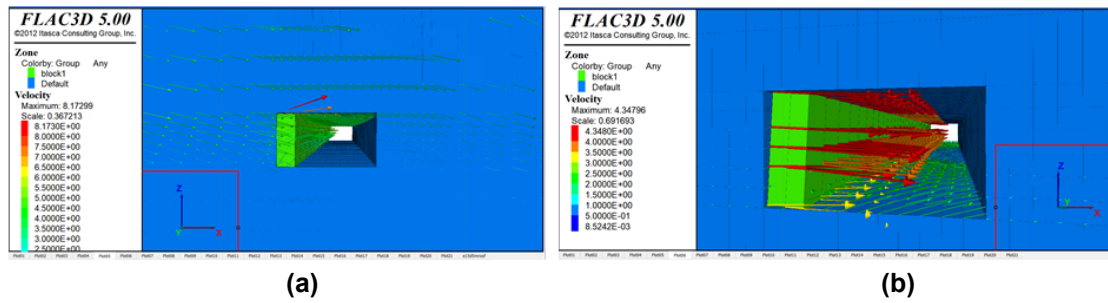


**Figure 6: (a) Development of velocities induced by slipping fault (15° dip) 5 m above the roadway at time of 0.012 seconds after fault slip began, (b) View inside the mine roadway showing the coal block ejection at an average velocity above 4 m/s at time of 0.07 seconds.**

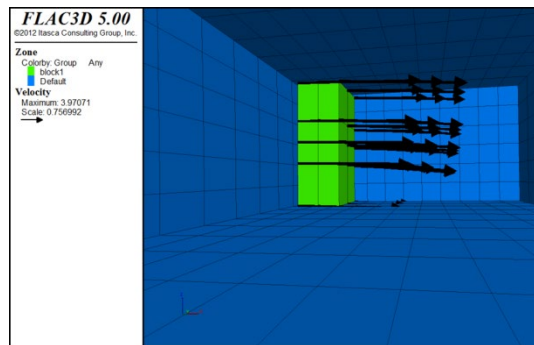


**Figure 7: View inside of the excavated mine roadway showing the coal block and its ejection away from the rib side**

### CALCULATIONS OF SEISMIC IMPACT AT THE RIB SIDE

The simplified method chosen to enable calculations of the dynamic impact produced by seismic momentum reaching the mine roadway rib is defined by the kinetic momentum delivered to the rib per m of roadway perpendicular to the rib (first impact only)  $P = mv$ , where  $P$  is the kinetic momentum (kgm/s),  $m$  is ejected mass (kg) and  $v$  is the mass velocity (m/s).

The kinetic energy delivered to the rib per m of roadway perpendicular to the rib (at first impact only) is:  $E = \frac{1}{2}mv^2$  where  $E$  is the kinetic energy (Nm),  $m$  is ejected mass (kg) and  $v$  is the mass velocity (m/s).

The first 44 models examined influence of faults with their plane aligned parallel to the roadway mining direction at various distances above and below the seam and dips varying from horizontal to 60° degrees. The vertical faults numbered from 45 to 89 were at various distances ahead of the roadway face and various orientations from 60° to -60°, 0° being parallel to the roadway face. The calculations of coal block ejection velocities, kinetic momentum and kinetic energy were performed for each fault slip at various locations and orientations and are summarised in Table 2.

**Table 2: Modelled fault geometry, block ejection velocities and rib impact energy due to fault slip**

Fault No	Strike (°)	Dip (°)	Fault Distance from seam (m)	Block Ejection average velocity (m/s)	Block Momentum (mv)	Energy impacting the rib (kNm)
1	Parallel to seam	0°	20m Roof	4.1	17.1	35.8
2	Parallel to seam	0°	15m Roof	4.3	17.5	37.5
3	Parallel to seam	0°	10m Roof	4.4	17.9	39.3
4	Parallel to seam	0°	5m Roof	4.3	17.5	37.5
5	Parallel to seam	0°	2m Roof	3.5	14.2	24.9
6	Parallel to seam	0°	2m Floor	3.9	15.8	30.9
7	Parallel to seam	0°	5m Floor	4.5	18.3	41.1
8	Parallel to mining	0°	10m Floor	4.6	18.7	43.0
9	Parallel to mining	0°	15m Floor	4.6	18.7	43.0
10	Parallel to mining	0°	20m Floor	4.5	18.3	41.1
11	Parallel to mining	15°	20m Roof	4.1	16.6	34.1
12	Parallel to mining	15°	15m Roof	4.3	17.5	37.5
13	Parallel to mining	15°	10m Roof	4.3	17.5	37.5
14	Parallel to mining	15°	5m Roof	4.4	17.9	39.3
15	Parallel to mining	15°	2m Roof	4.3	17.5	37.5
16	Parallel to mining	15°	2m Floor	4.3	17.5	37.5
17	Parallel to mining	15°	5m Floor	4.6	18.7	43.0
18	Parallel to mining	15°	10m Floor	4.4	17.9	39.3
19	Parallel to mining	15°	15m Floor	4.7	19.1	44.8
20	Parallel to mining	15°	20m Floor	4.2	17.1	35.8
21	Parallel to mining	30°	20m Roof	4.0	16.2	32.5
22	Parallel to mining	30°	15m Roof	4.5	18.3	41.1
23	Parallel to mining	30°	10m Roof	4.4	17.9	39.3
24	Parallel to mining	30°	5m Roof	4.2	17.1	35.8
25	Parallel to mining	30°	2m Roof	4.2	17.1	35.8
26	Parallel to mining	30°	2m Floor	4.2	17.1	35.8
27	Parallel to mining	30°	5m Floor	4.2	17.1	35.8
28	Parallel to mining	30°	10m Floor	4.3	17.5	37.5
29	Parallel to mining	30°	15m Floor	4.3	17.5	37.5
30	Parallel to mining	30°	20m Floor	4.2	17.1	35.8
31	Parallel to mining	45°	15m Roof	4.2	17.1	35.8
32	Parallel to mining	45°	10m Roof	4.4	17.9	39.3
33	Parallel to mining	45°	5m Roof	4.4	17.9	39.3
34	Parallel to mining	45°	2m Roof	4.4	17.9	39.3
35	Parallel to mining	45°	2m Floor	4.2	17.1	35.8
36	Parallel to mining	45°	5m Floor	4.2	17.1	35.8
37	Parallel to mining	45°	10m Floor	4.2	17.1	35.8
38	Parallel to mining	45°	15m Floor	4.2	17.1	35.8
39	Parallel to mining	60°	10m Roof	3.7	15.0	27.8
40	Parallel to mining	60°	5m Roof	3.6	14.6	26.3
41	Parallel to mining	60°	2m Roof	3.6	14.6	26.3
42	Parallel to mining	60°	2m Floor	3.0	12.2	18.3
43	Parallel to mining	60°	5m Floor	3.0	12.2	18.3
44	Parallel to mining	60°	10m Floor	2.8	11.4	15.9
45	0°	90°	3 m	4.9	19.9	48.7
46	0°	90°	6 m	4.9	19.9	48.7
47	0°	90°	9 m	4.9	19.9	48.7
48	0°	90°	12 m	5.0	20.3	50.8
49	0°	90°	15 m	5.0	20.3	50.8

Fault No	Strike (°)	Dip (°)	Fault Distance from seam (m)	Block Ejection average velocity (m/s)	Block Momentum (mv)	Energy impacting the rib (kNm)
50	15°	90°	3 m	4.9	19.9	48.7
51	15°	90°	6 m	4.9	19.9	48.7
52	15°	90°	9 m	4.9	19.9	48.7
53	15°	90°	12 m	5.0	20.3	50.8
54	15°	90°	15 m	4.8	19.5	46.8
55	30°	90°	3 m	4.5	18.3	41.1
56	30°	90°	6 m	4.5	18.3	41.1
57	30°	90°	9 m	4.6	18.7	43.0
58	30°	90°	12 m	4.6	18.7	43.0
59	30°	90°	15 m	4.4	17.9	39.3
60	45°	90°	3 m	3.8	15.4	29.3
61	45°	90°	6 m	3.8	15.4	29.3
62	45°	90°	9 m	3.8	15.4	29.3
63	45°	90°	12 m	3.8	15.4	29.3
64	45°	90°	15 m	3.8	15.4	29.3
65	60°	90°	3 m	2.7	11.0	14.8
66	60°	90°	6 m	2.7	11.0	14.8
67	60°	90°	9 m	2.8	11.4	15.9
68	60°	90°	12 m	2.8	11.4	15.9
69	60°	90°	15 m	2.8	11.4	15.9
70	-15°	90°	3 m	4.5	18.3	41.1
71	-15°	90°	6 m	4.6	18.7	43.0
72	-15°	90°	9 m	4.7	19.1	44.8
73	-15°	90°	12 m	4.6	18.7	43.0
74	-15°	90°	15 m	4.2	17.1	35.8
75	-30°	90°	3 m	4.2	17.1	35.8
76	-30°	90°	6 m	4.15	16.8	35.0
77	-30°	90°	9 m	4	16.2	32.5
78	-30°	90°	12 m	3.9	15.8	30.9
79	-30°	90°	15 m	3.8	15.4	29.3
80	-45°	90°	3 m	3.2	13.0	20.8
81	-45°	90°	6 m	3.2	13.0	20.8
82	-45°	90°	9 m	3.2	13.0	20.8
83	-45°	90°	12 m	3.2	13.0	20.8
84	-45°	90°	15 m	3.2	13.0	20.8
85	-60°	90°	3 m	2.5	10.2	12.7
86	-60°	90°	6 m	2.5	10.2	12.7
87	-60°	90°	9 m	2.5	10.2	12.7
88	-60°	90°	12 m	2.5	10.2	12.7
89	-60°	90°	15 m	2.5	10.2	12.7

The results summarised in Table 2 indicate that the faults with the same slip characteristics at close proximity to the excavation appear to produce similar block ejection velocities. These velocities seem to be similar to the maximum fault slip velocity. This is not surprising. When tracing the velocities surrounding the slipping fault, the 'particle' velocities that spread through either the rock or softer coal have similar maximum velocities and directions to the slipping fault if located nearby. This simplifies the understanding of basic seismic wave front propagation close to the faults.

It may be confusing to think of seismic waves as the 'extremely fast moving compressive or shear fronts'. It seems more logical to interpret the coal/rock matrix movement thinking about the 'peak particle velocities' (PPV) as vectors in rock that tend to disturb the unconfined

rock/coal integrity at the boundaries. The seismic wave conservation of kinetic momentum can also be better understood by imagining either large or small particle collisions in the wave front inside the rock matrix as shown earlier in Figure 1.

A minor refraction of seismic waves at the rock/coal seam interface (due to a slower speed of seismic waves in softer coal) produced velocity concentrations within the seam. Extra 45 dynamic runs were done modelling coal as rock to avoid the refraction of seismic waves. These tests indicated that there was a small decrease of 'rib coal block' ejection velocities in the 'rock seam' when compared to the 'coal seam'. This work indicates that the change in seismic velocity within soft coal seam has a magnifying effect on the rib impact magnitudes with increasing velocities ranging from being negligible to 20 %.

Observations of the coal block ejection indicated that the block side located closer to the slipping fault experienced dynamic impact sooner than the other block side. This caused block rotation and uneven ejection of these blocks. Furthermore, fault inclination produced inclined impact velocities to the rib, affecting block ejection trajectories further, causing the block to bounce up and down. This is illustrated in the examples shown in Figures 8 to 10. Note: To avoid the influence of friction along the roof and the floor, friction and cohesion properties along each interface were reduced to a bare minimum not to affect coal block velocities with time.

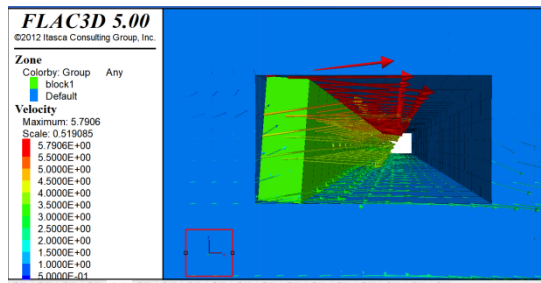


Figure 8: Block displacement and rotation after 0.07 seconds induced by horizontal fault slip 10 m above mine roadway

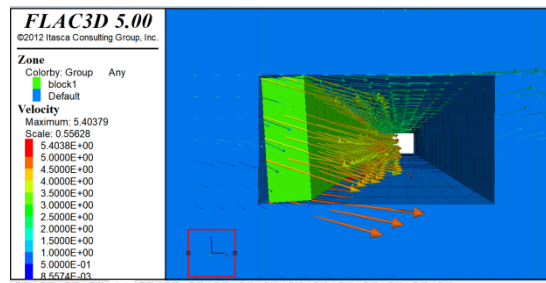


Figure 9: Block displacement and rotation after 0.07 seconds induced by horizontal fault slip 10m below mine roadway

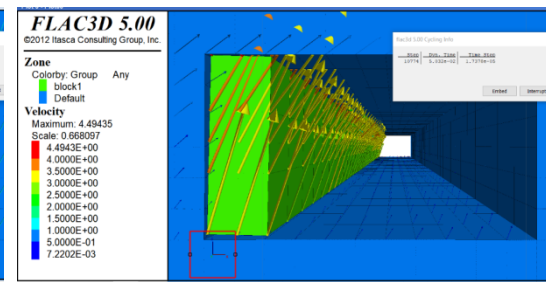
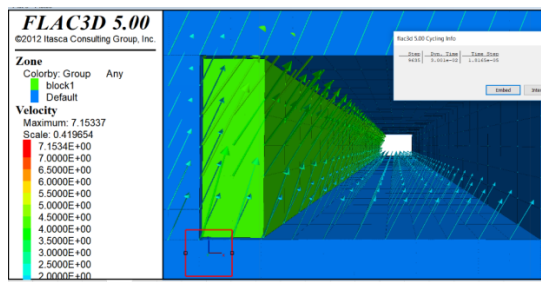


Figure 10: Block displacement induced by inclined (60° dip) fault slip 10m below mine roadway after (a) 0.024 seconds, (b) 0.05 seconds

### SUMMARY

To study the fault induced seismic waves and its influence on coal bursts in 3-dimensions, 89 dynamic models of various fault-slip locations and directions were modelled using the FLAC<sup>3D</sup>. The fault slip failure shows that this mechanism can generate sufficient amount of seismic energy to produce a coal burst on its own. Fault slip can typically occur as the progressive nearby excavations gradually relieve stress normal to the fault plane. The initial rib impact appears to be approximately proportional to the maximum velocity of fault slip. These fault slips release fast seismic waves that generate rock mass sinusoidal movement parallel to the fault



that can exceed several m/s. This study modelled many fault slips in various locations and orientations adjacent to the mine roadway showing fast ejections of the detached blocks into the roadway.

The results indicate the occurrence of coal burst to typically originate from one side of the roadway where the seismic waves directly impact the rib side. The models also show the tendency of seismic waves to concentrate inside the coal seam producing faster coal rib ejections. Once the location of the fault zone and the probable direction of fault slip is estimated, the side of the roadway where rib ejection is probable, can be predicted. This makes this research very valuable for safety in coal mines as workers may be able to keep from the harm's way by minimising their presence at the side where a potential rib impact may occur, while mining through certain zones of fault influence. It is suggested that more detailed dynamic numerical studies of the underground coal burst cases related to the presence of faults be undertaken.

## REFERENCES

- Bräuner, 1994, Rock bursts in coal mines and their prevention. Rotterdam:A.A. Balkema, ISBN: 978-1351418034
- Brinkmann, 1987. Separating shock wave and gas expansion breakage mechanism  
2nd International Symposium on Rock Fragmentation by Blasting (1987), pp. 6-15
- Brown, S., 1998. Friction heating of faults, Stable sliding versus stick slip. Journal of Geophysical research Solid Earth, Vol. 103 (B4).pp 7413-7420.
- Brune, J. N. Brown, S. and Johnson P.A., 1993. Rupture mechanism and interface separation in foam rubber models of earthquakes: a possible solution to the heat flow paradox and the paradox of large overthrusts. Science Direct,Tectonophysics, Vol. 218. Issues 1-3, pp 59-67.
- Chengguo, Z., Canbulat, I., Tahmasebina, F. and Hebblewhite, B. 2017. Assessment of energy release mechanisms contributing to coal burst. International Journal of Mining Science and Technology, Vol. 27 (1), pp. 43-47.
- Dou L., Mu Z., Li Z. Cao A. and Gong S., 2016. Research of rock burst monitoring, forecasting and prevention in coal mining in China. In proceedings of the 9th International Symposium on Green mining, Wollongong, Australia, University of Wollongong – Mining Engineering, pp. 382-391.
- Hebblewhite, B. and Galvin, J., 2017. A review of the geomechanic s aspects of a double fatality coal burst at Austar Colliery in NWS, Australia in April 2014. International Journal of Mining Science and Technology, (Section A: Mining Industry), Vol. 100, pp. 22-30.
- Itasca FLAC<sup>3D</sup> Manual, 2015. Fast Lagrangian Analysis Continua – version 7.0 User Manual. Minneapolis, Minnesota, USA: Itasca Consulting Group.
- Mark, C., (2014). Coal bursts in deep longwall mines of the United States. In: Proceedings of the 3rd Australasian Ground Control in Mining Conference (AusRock) Vol. (3), pp 33-40.
- McGarr, A., 1991. Observations constraining near-source ground motion estimated from locally recorded seismograms. J. Geophys. Res., 96 (B10) (1991), pp. 16495-16508
- Moodie, A. and Anderson, J., 2011. Geotechnical considerations of longwall top coal caving at Austar Coal Mine. In Proceedings of 30th Int. Conference on Ground Control in Mining, Morgantown, WV, USA, pp. 238-247.

Coal Opertors' Conference

- Muller W., 1991. Numerical simulation of rock bursts. International Journal of Mining Science and Technology, Elsevier Science Publishers, Vol. 12 (1), pp. 27-42.
- Nemcik J., Venticinque G. and Karekal S. (2019) Modelling of Dynamic Fracture Mechanisms for Improved Strata Control Design and Coal Burst Assessment, ACARP report C26054.
- Saharan, M. (2004). Dynamic modelling of rock fracturing by destress blasting, Mining & Materials Engineering, McGill University, Montreal, QC, Canada (2004)
- Sainoki, A. (2014). Dynamic modelling of mining-induced faultslip, PhD Thesis Department of Mining & Materials Engineering McGill University, Montreal, Canada
- Sainoki, Atsushi; Mitri, Hani S. (2016). Back analysis of fault-slip in burst prone environment. Journal of Applied Geophysics. Volume 134, 159-171.
- Venticinque, G. & Nemcik, J., 2017. Presentation at the 9th International Symposium on Green mining, Wollongong, Australia Green Mining Conference, Innovation Campus, University of Wollongong. Presentation only.

# NUMERICAL MODEL OF DYNAMIC ROCK FRACTURE PROCESS DURING COAL BURST

Gaetano Venticinque<sup>1</sup> and Jan Nemcik<sup>1</sup>

**ABSTRACT:** Coal bursts present one of the most severe hazards challenging the safe operations in underground coal work environments. In Australia, these events are becoming increasingly frequent as coal measures are mined progressively deeper. This study is supported by the Australian Coal Association Research Program (ACARP) which aims to better understand the phenomena of coal burst. In this paper the dynamic fracture process of coal bursts was successfully simulated in the coal roadway. This was achieved using dynamic analysis utilising DRFM<sup>2D</sup> routine by Venticinque and Nemcik (2017) in FLAC<sup>2D</sup> (Itasca, 2015) which complemented previous study observations by Venticinque and Nemcik (2018). This is significant because until now the evolving dynamic rock fracture process during coal burst remained unknown. Additionally, coal/rock burst events were shown from simulation as being largely driven by the propagation of shear fractures from within the rib. This was demonstrated to produce effect forcing the dynamic conversion and release of potential energy stored as compressive strain in the rib into kinetic movement of the entire rib section. This entire process was shown to occur very fast taking approximately 0.2 seconds for a coal burst to fully establish, with ejection of several meters of rib at a velocity of 1.6 m/s produced in the model of an underground coal roadway having 550 m depth of cover.

## INTRODUCTION TO MODELLING COAL BURST

Coal bursts are very difficult to predict as they are inherently not frequent, isolated and occur without warning. To minimise the occurrence of coal burst it is necessary to first understand how the mechanism of coal burst arises. Frequent miss-use of conventional elastic-plastic, strain softening and hence otherwise static based models are attributed towards significantly limiting both theoretical derivation and computational ability in analysing fast dynamically occurring events such as coal bursts. This highlights the serious shortcoming of trying to model dynamic material response behaviour of strata around excavations; hence such models should not be used. The importance of built in dynamics is therefore recognised in dynamic analysis for incorporating inertial effects, enabling real time simulation of dynamic ground movement. Likewise, when using these models, correct approach is necessary to isolate and observe what mechanisms are taking place.

A 2-Dimensional Dynamic Rock Fracture Model (DRFM<sup>2D</sup>) has been undergoing development at the University of Wollongong for more than 5 years. The theoretical basis of this model has been successfully implemented across numerous problems with outputs producing model fractures as observed in laboratory tests Venticinque and Nemcik (2017). Subsequently the DRFM<sup>2D</sup> subroutine in FLAC (Itasca, 2015) is capable of producing the associative dynamic effects from fractures in real time and in doing so is well suited towards capturing the conversion of kinetic motion response naturally produced in the rib during coal burst.

---

<sup>1</sup> University of Wollongong: Email: gv667@uowmail.edu.au Tel: +61 414 799 325;  
jnemcik@uow.edu.au Tel: +61 2 4221 449

## MODELLING PROCEDURE

Using FLAC<sup>2D</sup> (Itasca, 2015), an excavation of a standard underground coal mining roadway 5m width by 3m height was modelled within in a 3m thick coal seam bound by competent sandstone roof and floor strata at a depth of 550m, illustrated in Figure 1 and having rock mass strata properties listed in Table 1.

**Table 1 – Rock mass strata properties.**

<b>Sedimentary Floor and Roof Rock</b>		
<i>Mechanical Properties</i>		
Density	2500	kg/m <sup>3</sup>
Bulk Modulus	6.67	GPa
Shear Modulus	4.0	GPa
UCS	40.1	MPa
Internal Friction $\phi$	37	°
<b>Working Coal Seam</b>		
<i>Mechanical Properties</i>		
Density	1400	kg/m <sup>3</sup>
Bulk Modulus	3.33	GPa
Shear Modulus	1.11	GPa
UCS	0.8	MPa
Internal Friction $\phi$	35	°

### Configuration of Strata in FLAC Model

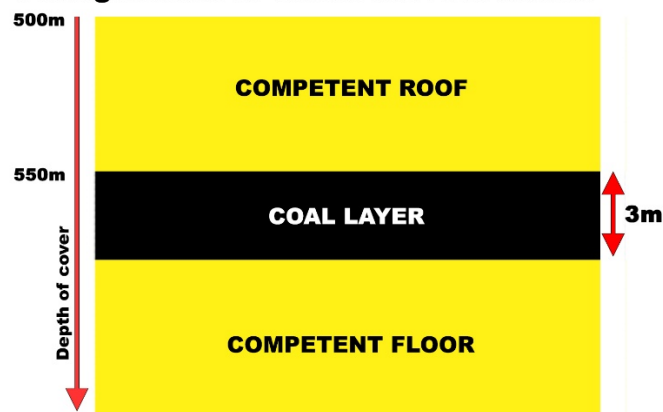


**Figure 1: Model of strata**

Initially, the model was brought to static equilibrium prior to dynamic solution being initiated as per described in Itasca (2015). In order to simulate the dynamic coal burst event, bond failure was artificially induced within a single interface element located at the roofline between the coal and sandstone strata 4m from the rib side. With reference to the vertical stress profile of the rib the artificially failed zone coincided with the maximum vertical and horizontal stress location at the coal/rock interface as well as the inflection point of the stress gradient profile before steeply

declining towards the rib side shown in Figure 2. From Venticinqué and Nemcik (2018), this was identified as being the most appropriate region for coal burst to be initiated from.

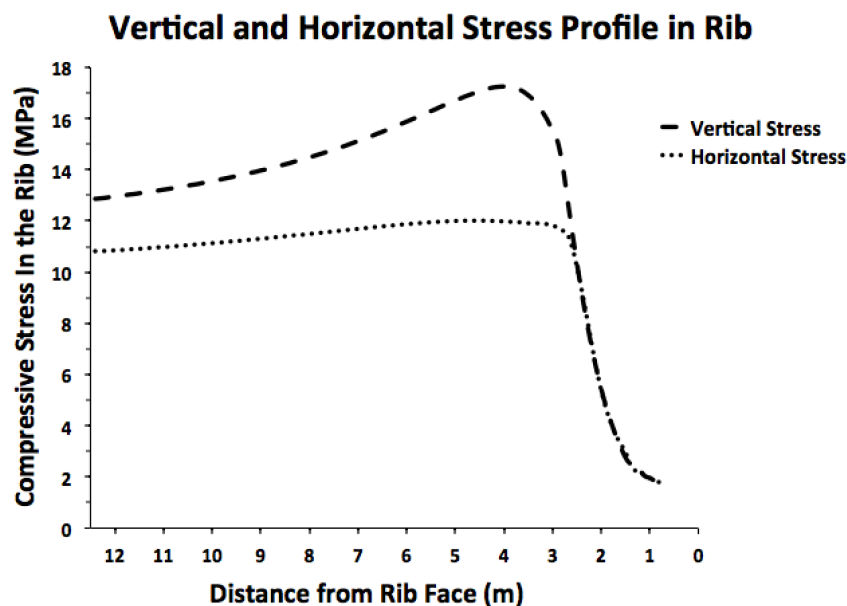


**Figure 2: Stress profile along coal roof line adjacent to rib face prior to coal burst occurring.**

Following artificial initiation of coal burst from behind the rib, the DRFM<sup>2D</sup> subroutine was executed enabling the real time dynamic propagation of fractures to naturally evolve concurrent with the dynamic response effects evolving within the rib. During simulations, dynamic fracture propagation and velocity mass response of the rib was monitored with respect time.

## RESULTS

Monitoring the dynamic fracture propagation and velocity mass response over time, model outputs revealed the development of coal burst phenomena to occur over several distinct stages. These are presented in Figure 3.

Through interpretation of simulation results in Figure 3, the evolution of a coal burst event is identified to occur several distinct stages. In sequential order these are:

- a. Generation of initial compression wave produced from a shear fracture initiating behind the rib and propagating in the direction towards the free surface of the rib-side.
- b. Arrivals of the compression wave at the rib face promoting tensile dislocation with possible block spall ejection.
- c. Displacement of near-face rib mass from the free surface, producing a cascading effect of shear failure towards the higher stressed rib mass behind. It is understood that the displacement of rib
- d. mass from the initial rib surfaces results in a sudden drop of confinement being supplied to the higher stressed rib mass behind. This effect drives unstable shear fracturing attributing further subsequent dynamic release of stored energy to occur from behind.
- e. Entire rib movement dynamically driven by the release of potential stored energy through fracturing. This movement eventually causes previously fractured surfaces in shear to open in tension becoming dislocated from the rib mass behind, with ejection of a large rib mass.

### Stages of Coal Burst Development

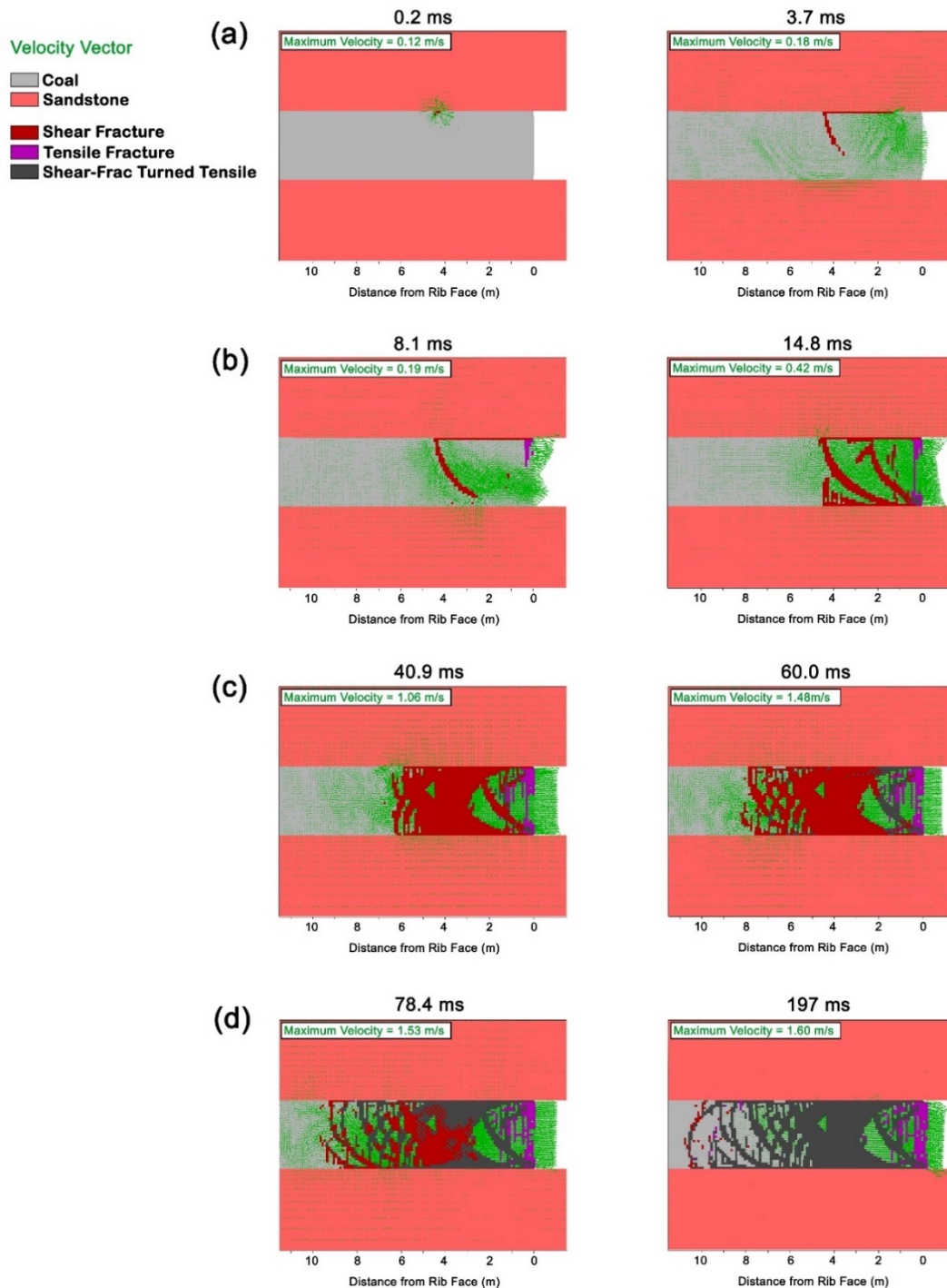


**Figure 3: Development of coal burst phenomena over time.**

From simulation, the phenomena of coal burst can be recognised to initiate from shear failure localised behind the rib which continues being driven by shear fracture afterwards. This is where the initiated fracture continued propagation along the coal/rock interface towards the rib, while another shear fracture continued through the coal, downwards curving towards the rib side as shown in Figure 4.



### Shear Fracture Advancement Towards Rib Surface

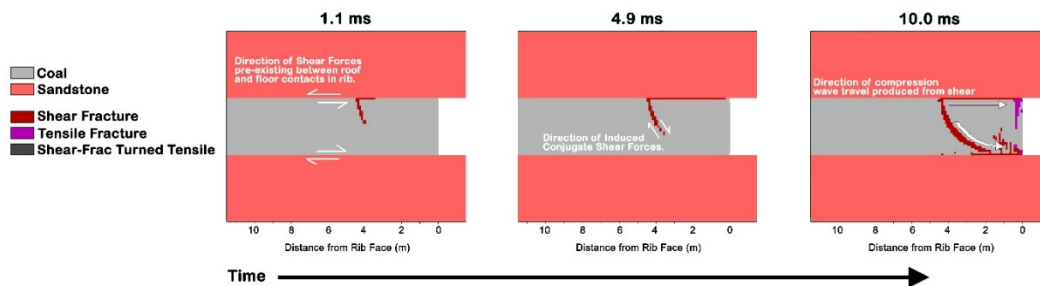


Figure 4: Shear failure mechanism driving coal burst production

The dynamic effect produced these from these shear fractures forces the dynamic conversion and release of a significant amount of potential energy stored as compressive strain into kinetic movement of the entire rib section. This is demonstrated by the migration of high vertical stresses deeper into the pillar and increase of rib-mass ejection velocity in Figure 5.

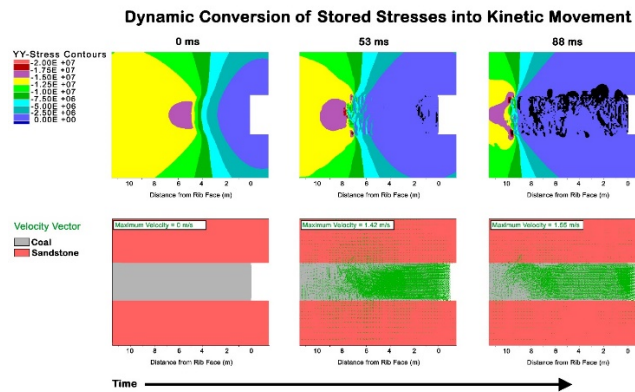


Figure 5: Evolution of compressive stored stresses into kinetic movement with time.

As the velocity of the rib mass accrues momentum, unloading from displacement of the rib removes confinement from the seam, causing failure to be driven deeper into the seam producing further subsequent dynamic release. The final fracture pattern supplied in Figure 6 can be noted to produce similar triangular wedged velocity and hence displacement profile to that initially observed in previous simplified simulations by Venticinque and Nemcik (2018). Subsequently the final ejection velocity of 1.6 m/s of the entire coal mass rib reinforces the observed mechanism involving release of potential energy stored as compressional stresses and strains into kinetic movement of the relieved unconfined/loosened coal rock mass.

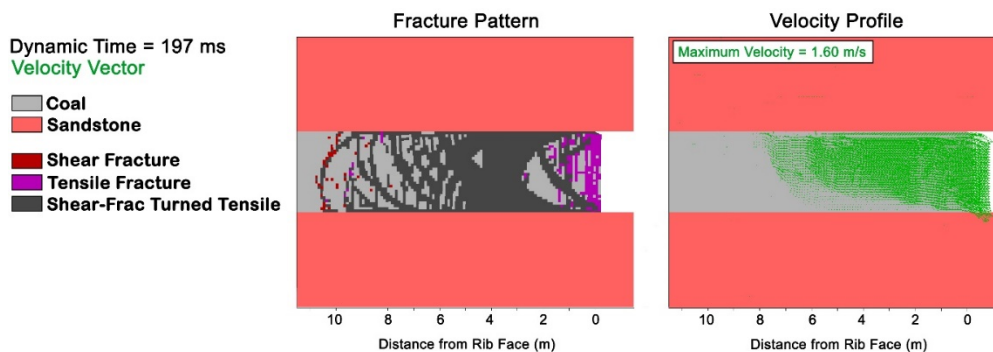


Figure 6: Final fracture pattern and velocity profile produced by DRFM<sup>2D</sup>

Finally, the simulated duration of process producing coal burst phenomena in the model is remarked as matching average measured time period durations of approximately 0.2 seconds obtained from monitoring roadways in coal burst prone collieries by Li, *et al.*, (2018). This adding further degree of relevance and confidence in the simulated dynamic coal burst phenomena produced from the model.

### CONCLUSIONS

Numerical models using dynamic analysis with DRFM<sup>2D</sup> in FLAC successfully simulated the real time dynamic evolution of coal burst phenomena in detail about the coal roadway. This is significant because until now coal bursts have not been able to be numerically reproduced or able to be studied at this level of detail which has restricted many of their features from being studied. For the first time the stages occurring during a developing coal burst event were sequentially identified and explained.

The ability to generate dynamic fractures in real time during the model proved to be valuable in helping realise important characteristics of underlying complex dynamic processes involved during coal burst. This where the propagation of shear fractures within the rib is evidenced from outputs as having a significant role in driving the coal burst phenomena. In conclusion, the aim of the study and ACARP objectives based on an improved understanding on coal burst is considered to have been achieved.

### ACKNOWLEDGEMENTS

This paper outlines the dynamic fracture process of coal bursts that is part of the broader funded ACARP project (C 26054). The collaboration and in-kind support from participating companies including SCT Operations, Glencore, South32 and Minova is greatly appreciated.

### REFERENCES

- Itasca FLAC<sup>2D</sup> Manual, 2015. Fast Lagrangian Analysis Continua – Version 7.0 User Manual. Minneapolis, Minnesota, USA: Itasca Consulting Group.
- Brown, S., 1998. Friction heating of faults, Stable sliding versus stick slip. *Journal of Geophysical research Solid Earth*, Vol. 103 (B4).pp 7413-7420.
- Brune, J. N. Brown, S. and Johnson P.A., 1993. Rupture mechanism and interface separation in foam rubber models of earthquakes: a possible solution to the heat flow paradox and the paradox of large overthrusts. *Science Direct, Tectonophysics*, Vol. 218. Issues 1-3, pp 59-67.
- Li, Zhen-lei He, Xueqiu and Dou, Linming Song, Dazhao., 2018. Comparison of rockburst occurrence during the extraction of thick coal seams using top-coal caving versus slicing mining methods, *Canadian Geotechnical Journal*. 55. 10.1139/cgj-2016-0631.
- Matheson, D., Brown and S. Bodin, P., 1998. Laboratory observations of fault-normal vibrations during stick slip *Journal of Geophysical Research Atmospheres* 1032(B12):29931-29944, DOI:
- Venticinque, G. and Nemcik, J., 2018. Numerical model of coal burst mechanism, *in proceedings* of the 18th Coal Operators' Conference, Mining Engineering, University of Wollongong, 214-220.
- Venticinque, G. and Nemcik, J., 2017. Modelling dynamic fracture propagation in rock, *Procedia Engineering*, 191 1185-1193. Ostrava, Czech Republic ISRM European Rock Mechanics Symposium, EUROCK 2017.

# IMPACT OF CORE SAMPLE RECOVERY TIME ON ACCURACY OF GAS CONTENT MEASUREMENT

**Dennis Black<sup>1</sup>**

*ABSTRACT:* Gas content measurement has a significant impact on mine safety and operational efficiency at many Australian underground coal mines. There is an expectation that reported gas content results are accurate and correctly represent the gas content of the coal seam in the area where the coal samples were collected. The practice of some coal sample testing service providers to add 'correction' factors to the measured gas content of coal samples increases the reported gas content to account for assumed loss of gas content due to extended recovery time. The methodology used by one gas testing service provider to establish a gas content correction factor to apply to coal samples with extended recovery time has been investigated and discussed.

A new approach to testing the impact of extended core sample recovery time on the accuracy of gas content measurement has been developed and is presented. Initial results from testing at three Australian underground coal mines indicates that, for core sample recovery times extending to 180 minutes, there is no discernible loss of gas content that would warrant the addition of a 'correction factor'.

## INTRODUCTION

Gas content measurement of coal seams in advance of mining is a significant tool in the assessment and management of outburst risk within the Australian underground coal industry. All Australian underground coal mines refer to a defined gas content threshold in the permit to mine process which determines whether mining is permitted to take place. It is therefore of great importance for the safety and productivity of mine operations that the measurement of gas content is accurate and correctly reports the seam gas conditions in the area from which the coal sample was collected.

Standards Australia have developed and published guidelines for measuring the gas content of coal samples which includes the fast desorption method typically used to measure the gas content of core samples collected from Australian underground coal mines (AS3980, 2016). The fast desorption method is widely used among gas content testing laboratories and it is generally accepted that measurement accuracy is within  $\pm 10\%$ . While AS3980 recommends reporting gas content in either an as-received (AR) and/or dry-ash-free (DAF) basis, some laboratory service providers do apply in-house determined correction factors for variables, such as relative density (RD) of the coal sample and core sample recovery time, that increases the value of the reported gas content.

Coal samples used for gas content testing are typically sourced using one of the following three methods: (a) drilling from surface, (b) drilling from underground, or (c) collection of fresh coal samples from the working face area. This paper focuses on the gas content testing of coal samples sourced from underground-to-inseam (UIS) drilling.

---

<sup>1</sup> Principal Consultant, CoalGAS. Email: [db@coalgas.com.au](mailto:db@coalgas.com.au) Tel: +61 401 999 542

If the time to recover a core sample from a UIS borehole exceeds a nominal threshold time period of say 40 minutes – is there an increasing loss of gas from the coal sample that warrants the addition of a 'correction factor'? Current practice assumes gas loss does occur and the measured gas content is less than the in situ content of the seam which supports the addition of correction factors. This study investigates the potential impact that core sample recovery time has on the accuracy of gas content measurement.

### GAS CONTENT TESTING IN AUSTRALIAN UNDERGROUND MINES

The method used to determine the gas content of coal samples collected from Australian underground coal mines is described in Australian Standard AS3980:2016 – Determination of gas content of coal and carbonaceous material – direct desorption method.

The total measured gas content of a coal sample (QM) is comprised of three main components: - lost gas during coal sample collection (Q1), desorbed gas content (Q2), and residual gas content (Q3), as illustrated in Figure 1. Further explanation of the three gas content components is provided below.

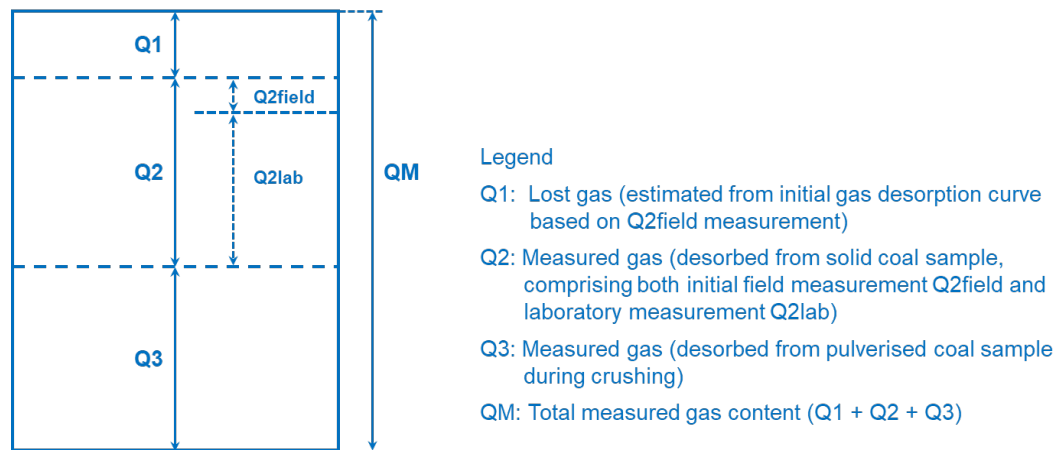


**Figure 1: Gas released from coal at different stages of gas content testing (after AS3980:2016)**

#### Lost Gas Content (Q1)

During the time taken to drill a core sample, recover the sample from the borehole, transfer the sample from the core barrel and seal it into a desorption canister, gas will be lost from the coal sample. The volume of gas lost from the sample cannot be measured and it is accepted practice to estimate the lost gas content (Q1). For gas content testing of underground bore cores, gas is assumed to start escaping from the core when the surrounding fluid pressure is equal to or less than the gas pressure in coal (at time  $t_0$ ), which is assumed to start from midway through the coring cycle (AS3980, 2016).

As soon as practical after recovering the core sample from the UIS borehole and sealing the core sample into a gas canister, the canister is connected to a gas desorption measurement apparatus at the drilling site, the valve opened, and volume of gas desorbed is measured incrementally over a period of typically 20 minutes. The gas volume desorbed from the core sample during this initial field measurement period is referred to as Q2field. Figure 2 provides an example of the initial Q2field desorbed gas volume measurements recorded during the initial 20 minute period, 34.5 to 54.5 minutes, after sealing the core sample into the gas canister ( $t_1$ ), 34.5 minutes ( $t_e$ ) after the assumed start of gas loss from the core sample ( $t_0$ ).

Plotting the cumulative readings of the initial desorption volume against the square root of elapsed time, selecting the linear portion of the curve, and extrapolating that line to the Y-intercept at  $t_0$  is taken as the volume of lost gas (AS3980, 2016). The lost gas content  $Q_1$  is determined by dividing the volume of lost gas (in millilitres) by the 'as-received' mass (in grams) of the sample in the canister.

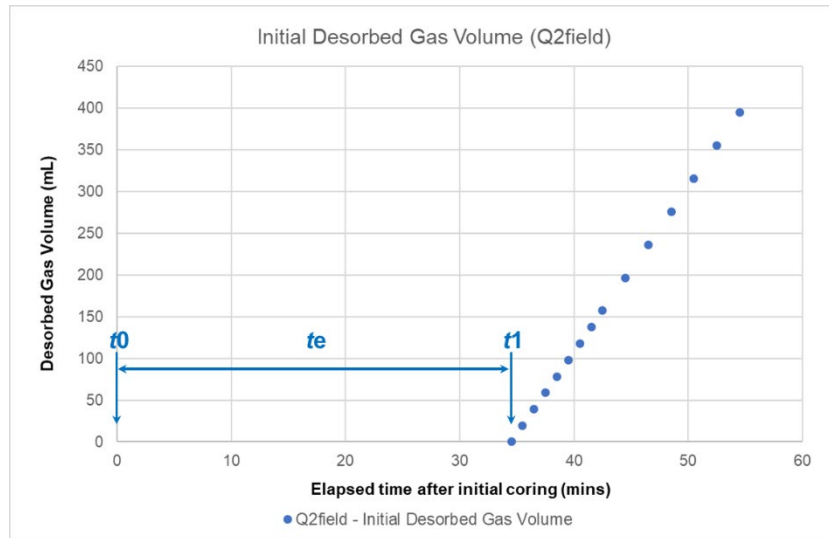


**Figure 2: Q2field initial desorbed gas volume measurements 34.5 to 54.4 minutes after  $t_0$**

Figure 3 provides an example using the Q2field desorbed gas volume measurements presented in Figure 2 to estimate the gas loss from the core sample while being recovered from the borehole, 1541.8 mL at the Y-intercept corresponding to  $t_0$ . Dividing the estimated lost gas volume (mL) by the known sample mass (g) gives the lost gas content  $Q_1$  ( $m^3/t$ ).

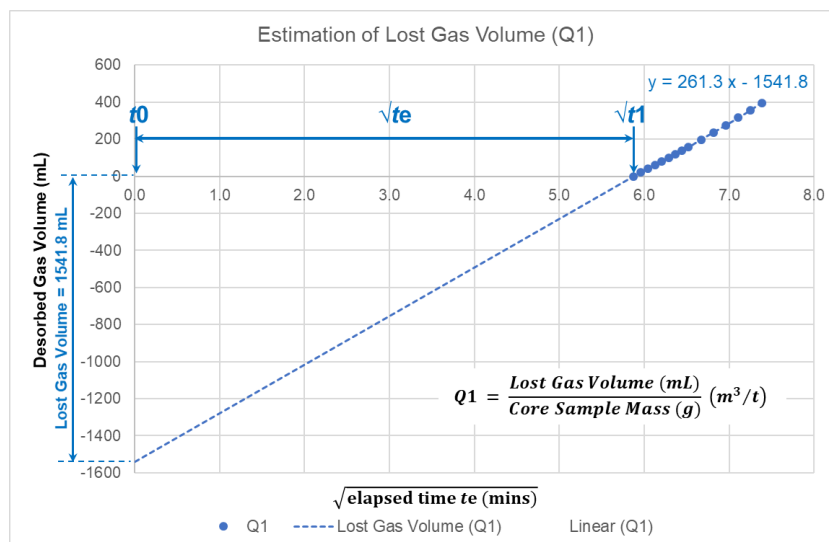


**Figure 3: Using initial Q2field gas desorption data to estimate the lost gas content  $Q_1$  ( $m^3/t$ )**

The volume of gas lost prior to sealing a coal sample into a desorption canister generally depends on sample retrieval time, physical character of the sample, the type of drilling fluid, and water saturation/relative amount of free gas (Diamond *et al.*, 2001). Virtually all methods

for estimating lost gas benefit from minimizing the lost-gas time over which measured desorption data must be extrapolated.

The assumption of linearity of desorbed gas volume relative to square root of time is only valid for short values of core sample recovery time and the error of Q1 estimation increases with increasing recovery time (AS3980, 2016). It is therefore recommended that core samples are retrieved as quickly as possible, and initial desorption measurements completed without delay. AS3980 also warns that significant errors will occur in the determination of lost gas if the initial gas desorption is not measured within about 40 minutes of zero time ( $t_0$ ).

Kissell *et al.* (1973) and McCulloch *et al.* (1975) demonstrated that the physical character of the retrieved coal sample can influence the desorption rate and hence the volume of lost gas that must be estimated. Blocky coals which remain intact during coring and subsequent retrieval emit their adsorbed gas at a relatively slow rate in comparison to friable coals which tend to break apart into smaller fragments releasing their adsorbed gas at a faster rate due to the shorter diffusion distances.

### **Desorbed Gas Content (Q2)**

The desorbed gas content of a coal sample (Q2) is a measure of the gas desorbed at near atmospheric pressure from the non-pulverized coal sample; expressed as the volume of gas per unit mass of sample (AS3980, 2016).

The total quantity of gas evolved from the coal core sample contained within the gas desorption canister is measured volumetrically by the water displacement method in the field (Q2<sub>field</sub>) and subsequently in the laboratory (Q2<sub>lab</sub>) using apparatus similar to that illustrated in Figure 4 (AS3980, 2016).

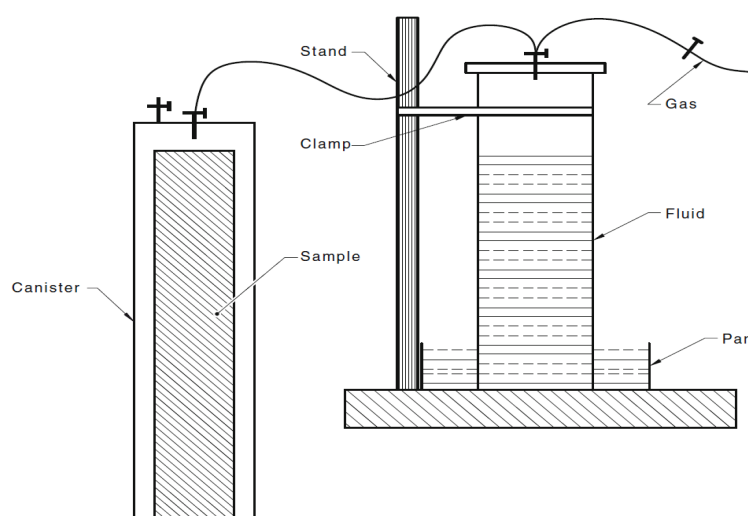


**Figure 4: Volumetric desorbed gas measurement apparatus (AS3980:2016)**

### **Residual Gas Content (Q3)**

Coal will naturally retain gas at atmospheric pressure and to measure the volume of gas retained within the coal sample, known as residual gas content (Q3), representative sub-samples of the coal core are crushed to a fine powder. The crusher shall have the capability to release the gas either during or after crushing and the volume of gas released during crushing is recorded and divided by the sub-sample mass to determine Q3 ( $m^3/t$ ).



AS3980 (2016) states the crusher shall be capable of pulverizing the sample to 95% of material passing through a 212  $\mu\text{m}$  mesh. Each sub-sample is to be crushed separately and for no longer than the time taken to ensure that at least 95% of the material passes 212  $\mu\text{m}$  mesh. This will vary from seconds to minutes depending on the quantity and quality of the sample and the mill configuration.

Figure 5 shows a photo of four ring mill crushers used to crush coal sub-samples of approximately 200-gram mass for measurement of Q3. This figure also shows an example of the result of crushing one coal sub-sample for seven (7) minutes which indicates over-crushing and wafer-like agglomeration of fine coal particles.



**Figure 5: Ring mill crushers for Q3 residual gas content measurement and pulverised coal**

### **Factors that Affect the Precision and Accuracy of Gas content Testing**

AS3980 (2016) lists and explains the factors considered to potentially affect the accuracy of gas content measurements that include:

1. System leakage resulting in loss of gas during transport and testing;
2. Origin and integrity of the coal sample;
3. Solubility of carbon dioxide in water;
4. Partial pressure effects on the equilibrium end point for desorption;
5. Desorption rate (effect on lost gas calculation);
6. Temperature (effect on magnitude of measured desorbed gas);
7. Barometric pressure (effect on magnitude of measured desorbed gas);
8. Borehole back pressure (effect on assumed start time of gas desorption during sample recovery);
9. Sample moisture content; and
10. Accuracy of the desorbed gas measuring apparatus

### **GAS CONTENT ERROR DUE TO EXTENDED CORE RECOVERY TIME**

AS3980 (2016) states that significant errors will occur in the determination of lost gas if the initial gas desorption is not measured within about 40 minutes of zero time ( $t_0$ ). Whilst it is ideal to recover core samples in the shortest time possible, there are many circumstances and examples in operating underground mines where the time to recover core samples from UIS boreholes cannot be achieved within the recommended 40 minute timeframe. In such cases, some coal mine operations and their gas content testing provider will either deem the sample to be 'invalid' or add an additional gas content 'error' factor to the measured gas content and

report a higher gas content to account for the uncertainty and assumed gas loss during the extended core sample recovery time.

An assessment of the methodology used by one gas content testing service provider to determine the error in gas content measurement resulting from extended core sample recovery time has been undertaken and summarised below. Once established, an additional gas content 'correction' is added to measured gas content of core samples with recovery time exceeding the nominated threshold values that is typically 40 minutes, to account for the corresponding 'error'.

The methodology is based on recovering coal core samples from UIS boreholes within the threshold time period and then conducting Q2field gas desorption measurements at the drill site for an extended period, recording the desorbed gas volume at short time increments, approximately 2 minute intervals, extending to approximately 200 minutes following initial coring ( $t_0$ ). Figure 6 provides an example of the extended Q2field desorbed gas volume measurements from one UIS core sample, recorded at 2-minute intervals for a period of 202 minutes following initial coring.

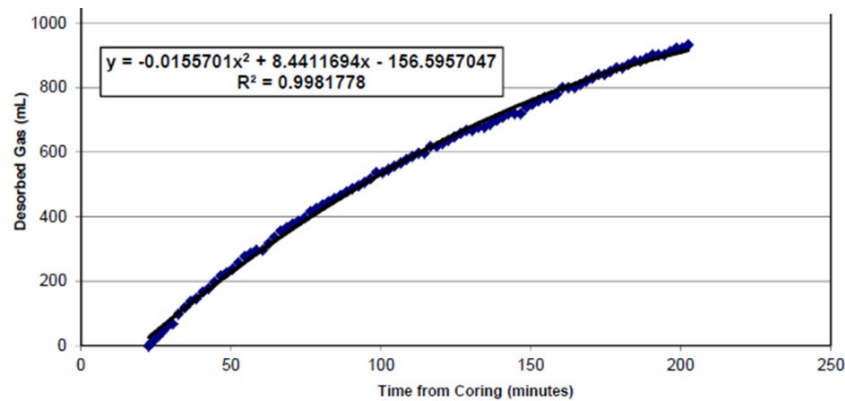


**Figure 6: Extended Q2field desorbed gas volume and corresponding regression line**

Using the data collected during the extended Q2field gas desorption, extended core sample recovery time ( $t_e$ ) is simulated and Q1 is estimated based on  $t_1$  at increasing time periods. Figure 7 shows nine 20 minute Q2field gas desorption intervals that have been selected to represent extended core sample recovery time, i.e. indicating  $t_1$  commencing 20, 40, 60, 80, 100, 120, 140, 160 and 180 minutes following initial coring ( $t_0$ ).

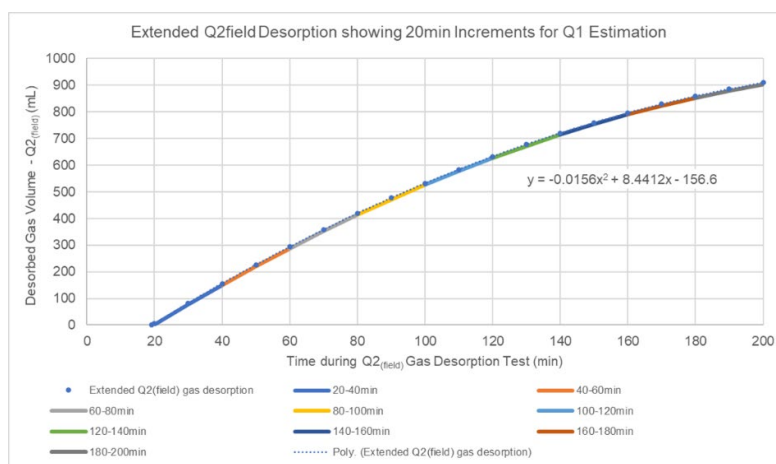


**Figure 7: Assumed desorbed gas volume at increasing sample recovery time**

The recorded desorbed gas volume for the 20 minute period following each selected extended core samples recovery time ( $t_1$ ) is plotted relative to square root of time to determine the corresponding lost gas content estimate for each extended core sample recovery time. Figure 8 shows the Q1 estimation curves, desorbed gas volume relative to square root of time, for the nine 20 minute time intervals using the desorbed gas volume data recorded during the extended Q2field gas desorption period. From the data presented in this example, it is shown that Q1 increases, reaching a maximum at approximately 120-130 minutes after which Q1 decreases.

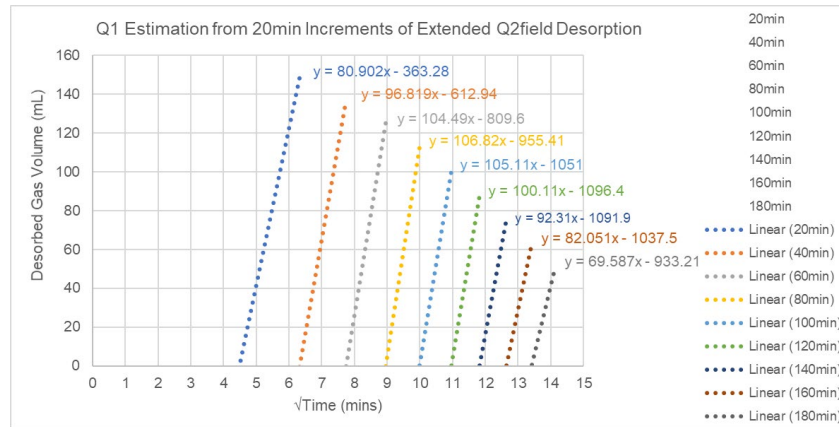


**Figure 8: Desorbed gas volume at increasing core sample recovery time ( $t_1$ ) based on extended Q2field desorbed gas volume measurement**

The results reported by the gas testing service provider for testing on this core sample are summarised in Table 1A and 1B. The results indicate the total measured gas content (QM) was 6.41 m<sup>3</sup>/s, residual gas content (Q3) was 4.18 m<sup>3</sup>/t and the desorbed gas content recorded in the laboratory (Q2lab) was 1.26 m<sup>3</sup>/t. This methodology assumes that Q2lab and Q3 remain constant and extending core sample recovery time only affects Q2field, which in turn affects Q1.

**Table 1A: Reported gas content at simulated core retrieval times**

Simulated Core Retrieval Time (minutes)	Lost Gas (m3/t)	Lab Q2 (m3/t)	Field Q2 (m3/t)	Q3 (m3/t)	Measured Gas Content Qm (m3/t)
20	0.25	1.26	0.63	4.18	6.32
30	0.34	1.26	0.58	4.18	6.36
40	0.42	1.26	0.53	4.18	6.39
50	0.49	1.26	0.48	4.18	6.41
60	0.55	1.26	0.44	4.18	6.43
70	0.60	1.26	0.39	4.18	6.44
80	0.65	1.26	0.35	4.18	6.44
90	0.69	1.26	0.31	4.18	6.44
100	0.72	1.26	0.27	4.18	6.43
110	0.74	1.26	0.24	4.18	6.42
120	0.75	1.26	0.21	4.18	6.39
130	0.75	1.26	0.17	4.18	6.37
140	0.75	1.26	0.15	4.18	6.33
150	0.73	1.26	0.12	4.18	6.29
160	0.71	1.26	0.09	4.18	6.24
170	0.68	1.26	0.07	4.18	6.19
180	0.64	1.26	0.05	4.18	6.13
190	0.61	1.26	0.03	4.18	6.09

**Table 1B: Reported gas content error at simulated core retrieval times**

Simulated Core Retrieval Time (minutes)	Calculated Qm (m3/t)	Original Qm (m3/t)	% Error
20	6.32	6.41	1.41
30	6.36	6.41	0.84
40	6.39	6.41	0.37
50	6.41	6.41	0.01
60	6.43	6.41	-0.26
70	6.44	6.41	-0.42
80	6.44	6.41	-0.48
90	6.44	6.41	-0.44
100	6.43	6.41	-0.31
110	6.42	6.41	-0.07
120	6.39	6.41	0.27
130	6.37	6.41	0.71
140	6.33	6.41	1.24
150	6.29	6.41	1.88
160	6.24	6.41	2.62
170	6.19	6.41	3.45
180	6.13	6.41	4.39
190	6.09	6.41	5.05

Table 1B summarises the %Error associated with extended recovery time which is the difference between the Original QM and the Calculated QM values. The reported methodology does not provide any detail as to how and when the original QM value is determined. Given there is no reference to duplicate core samples being used in this testing methodology, one would assume that at the conclusion of the extended Q2field desorption period, the core canister would be sealed and transported to the laboratory where Q2lab and Q3 would be determined. Q1 would be based on the Q2field gas desorption during the initial 20 minute period after sealing the core into the gas canister. The results presented in Table 1A and 1B do not support this assumption.

The %Error in gas content measurement reported against increasing core retrieval time is presented in Figure 9. The results indicate that relative to the reference 'Original QM' value, gas content values calculated for recovery times less than 50 minutes and greater than 110 minutes will be understated and the gas content values calculated for core retrieval times between 50 and 110 minutes will be overstated.

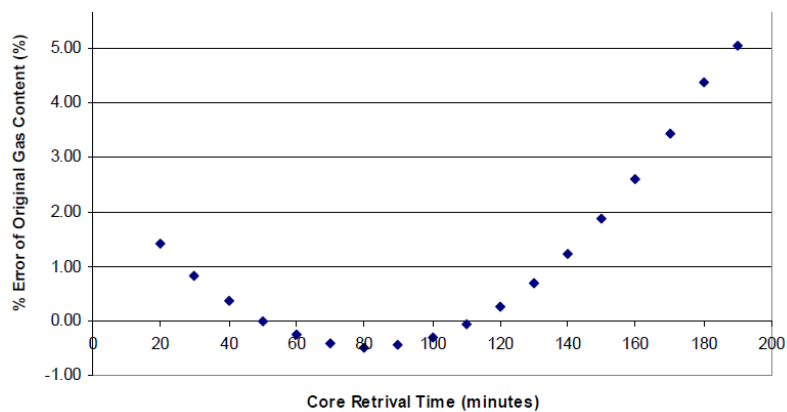


**Figure 9: Reported gas content error from extended Q2field comparative analysis**

The gas testing service provider then presents the results obtained from similar testing on multiple core samples which are used to determine the gas content correction factor recommended for the mine site. Figure 10 shows the correction factor recommended to be added to the measured gas content for core samples with extended recovery time, which is the average of the results obtained from extended Q2field gas desorption testing on multiple core samples plus three (3) standard deviations.

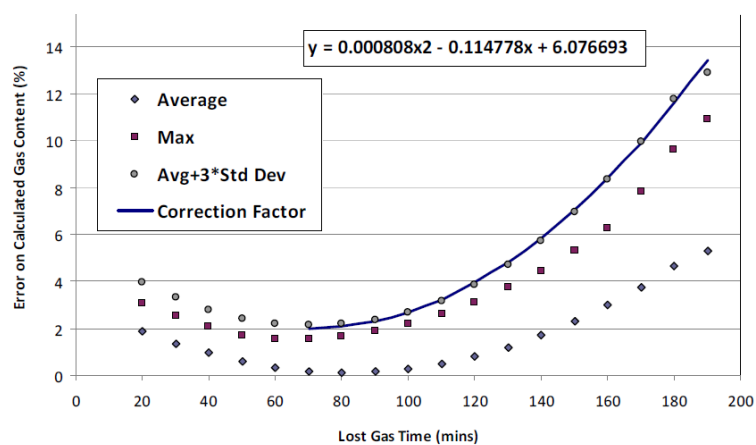


**Figure 10: Reported gas content error from extended Q2field comparative analysis**

Given the many operational scenarios in an underground coal mine that would warrant the collection of core samples for gas content testing that take greater than 40 minutes to recover from the borehole, it is important that the impact of extended core sample recovery time on the accuracy of gas content measurement is fully understood and appropriately dealt with in gas content measurement and reporting.

### NEW APPROACH TO ASSESS IMPACT OF CORE RECOVERY TIME ON GAS CONTENT MEASUREMENT ACCURACY

While some may consider the methodology reported above to be appropriate for estimating 'error' in gas content measurement due to extended core sample recovery time, this section describes an alternate approach. This new approach involves the collection of five core samples from the same location in the coal seam and testing each core, in accordance with the AS3980 guideline, to measure and report the gas content.

As illustrated in Figure 11, a 3.0 metre core barrel is used to collect a representative section of core from the target coal seam using UIS drilling. A core sample collection and testing procedure has been developed to maintain consistency in testing procedure at each mine site. UIS drillers collecting the core samples are to complete a roof touch to confirm hole position in the seam approximately 20 metres prior to reaching the target coring depth. The drillers are instructed to maintain the borehole parallel to the coal seam through coring to collect the 3.0 metre length of core from the same coal ply.

At each test location, the objective is to recover the core from the borehole in less than 40 minutes. Upon recovering the core barrel from the UIS borehole, a 600 mm length of core is removed from the core barrel and sealed into a prepared gas canister and Q2field desorption testing is completed for the recommended 20 minute period. The measured gas content of the first core sample recovered from the UIS borehole provides a baseline gas content for the test location and the measured gas content of the remaining core samples are compared against the baseline to assess the potential impact of simulated extended core sample recovery time.

The remaining 2.4 metre of core remains contained within the core barrel, placed in a 3.0 metre length of 6" pipe filled with water, to simulate extended core sample recovery time. For the purpose of this investigation, five 600mm sections of core sample are removed from the core barrel at time intervals of 60, 90, 120 and 180 minutes following initial coring ( $t_0$ ). As each section of core is removed from the core barrel following the simulated period of extended recovery time, it is sealed into a prepared gas canister and Q2field desorption testing completed prior to transporting to the nominated gas testing service provider to complete the gas content testing in accordance with AS3980.

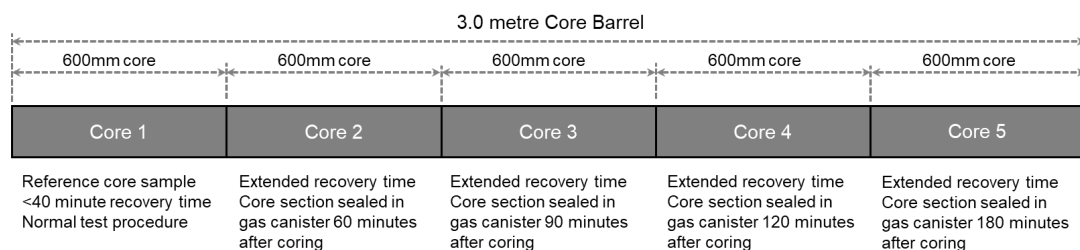


**Figure 11: UIS core sample in a 3.0m core barrel for extended Q1 gas content testing**

Figure 12 illustrates the testing sequence and timeframes to complete the core sample collection and gas content testing at each nominated test location. The objective of this testing program is to collect gas content data from test locations covering a broad range of Australian coal seam conditions and to analyse the results to determine if increasing the recovery time of

coal core samples from UIS boreholes has a material impact on the accuracy of gas content measurement. This study will also consider whether the addition of a 'correction factor' to the measured gas content of core samples with extended Q1 time to account for 'error' due to gas loss is warranted.

ACARP PROJECT C28007 - CORE SAMPLE TESTING PROGRAM TO INVESTIGATE THE IMPACT OF CORE RECOVERY TIME ON GAS CONTENT ACCURACY.																																								
TEST SAMPLE	3 METRE CORE BARREL	TESTING SEQUENCE AND ESTIMATED TIMING																																						
		1 hour					2 hour					3 hour					4 hour					5th hour																		
		10	20	30	40	50	60	70	80	90	100	110	120	130	140	150	160	170	180	190	200	210	220	230	240	250	260	270												
CORE A (<40 mins)	Core Canister No.1	Prep for coring (3m core barrel)	Rods back into hole	Core	Recovery Core from UIS Borehole					Q2field Readings																														
									10	20	30	20 min																												
CORE B (60 mins)	Core Canister No.2	Wait - leave remaining core in the 3m barrel. After 60 mins from end of core run, remove ~500-600mm of core from barrel, seal into canister and complete Q1 testing.							Q2field Readings																															
									10	20	30	40	50	60	20 min																									
CORE C (90 mins)	Core Canister No.3	Wait - leave remaining core in the 3m barrel. After 90 mins from end of core run, remove ~500-600mm of core from barrel, seal into canister and complete Q1 testing.									Q2field Readings																													
											10	20	30	40	50	60	70	80	90	20 min																				
CORE D (120 mins)	Core Canister No.4	Wait - leave remaining core in the 3m barrel. After 120 mins from end of core run, remove ~500-600mm of core from barrel, seal into canister and complete Q1 testing.												Q2field Readings																										
														10	20	30	40	50	60	70	80	90	100	110	120	20 min														
CORE E (180 mins)	Core Canister No.5	Wait - leave remaining core in the 3m barrel. After 180 mins from end of core run, remove remaining core from barrel, seal into canister and complete Q1 testing.																		Q2field Readings																				
																				10	20	30	40	50	60	70	80	90	100	110	120	130	140	150	160	170	180	20 min		

Figure 12: Sequence and timing of core sample collection and gas content testing

Results of testing conducted in three, methane rich, Australian coal seams, has shown minimal difference in the measured gas content of core samples with extended recovery time compared against the initial baseline QM measurement for each test location. In all but one coal sample tested to date, the variability in measured gas content values of the five cores from each test location is within 10% of the baseline reference and is below the 10% target maximum variability considered acceptable by the Australian Standard (Danell *et al.*, 2003 and Saghafi and Williams, 1998).

**Summary of Results from comparative extended Q1 gas content testing**

Figures 13, 14 and 15 show the summary results obtained from comparative testing at three mines, each in different coal seams, to assess the impact of delayed core sample recovery (extended Q1) on the accuracy of gas content measurement. Each of the five graphs includes ±10% error bands based on the first core sample recovered that was tested without delay as recommended by AS3980 (2016). In addition to the measured Q1, Q2 and Q3 gas content components, each graph also shows the gas content value reported by the testing laboratory for each core sample. Figure 13 shows results from Mine A operating in Seam 1. At this mine, an increasing gas content error correction factor is applied to the measured gas content of samples with recovery times between 40 and 120 minutes. Any core samples taking longer than 120 minutes to recover from UIS boreholes are deemed invalid and discarded. It is interesting to note that in the case of Mine A, with an outburst threshold gas content value of 7.0 m³/t, the measured gas content of the core sample with 99 minute recovery time was 6.93 m³/t and with the addition of the correction for extended sample recovery time, the reported gas content was increased to 8.76 m³/t.

Figure 14 shows results from Mine B operating in Seam 2. The results obtained from testing at Mine 2 do not indicate a loss of gas content from samples with longer recovery time. While both



graphs indicate the addition of gas content correction factor for samples with recovery time exceeding 70 minutes, the reported gas content from the 33 minute (benchmark) and 68 minute sample at location 1 (left graph) are greater than the measured gas content which is the result of an RD correction factor applied by the gas testing service provider.

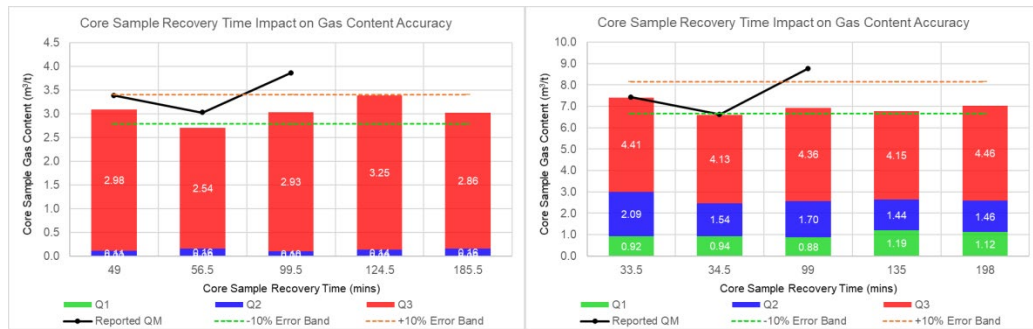


Figure 13: Extended Q1 Gas Content Results – Mine A, Seam 1

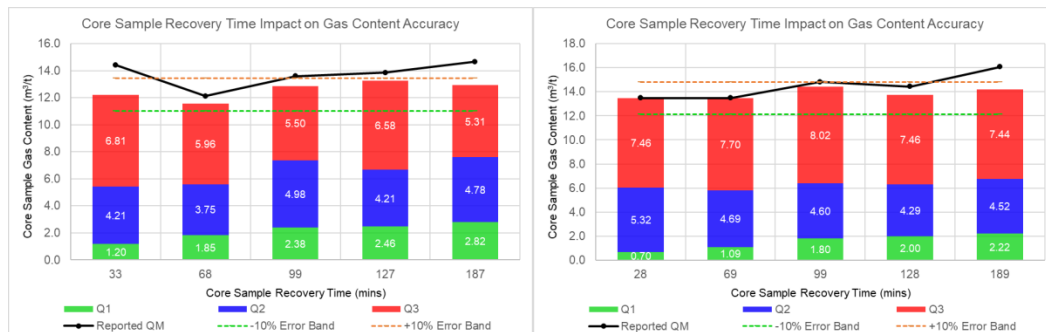


Figure 14: Extended Q1 Gas Content Results – Mine B, Seam 2

Figure 15 shows results from Mine C operating in Seam 3. While only three of the planned five core samples were recovered from this test location, the results are consistent with those obtained from Mine A and Mine B. Overall the results do not indicate gas content error, outside of the bounds of accepted test repeatability, from core samples that take longer than the preferred 40 minute time period to recover from the UIS boreholes.

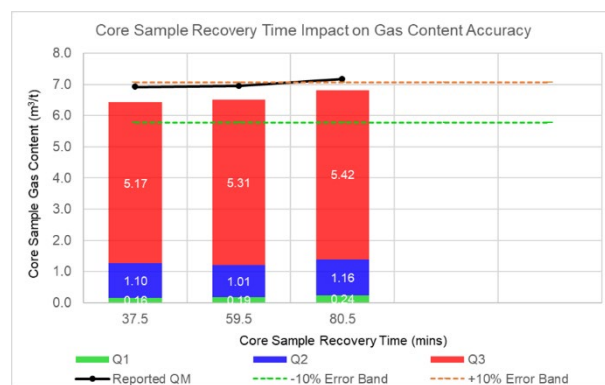


Figure 15: Extended Q1 Gas Content Results – Mine C, Seam 3

### Trending of Gas Content Component Values

Figures 16, 17 and 18 show results of the measured gas content component values, Q1, Q2 and Q3, obtained from the extended core sample recovery time testing at each of the three test mines.

Contrary to the simulated Q1 values obtained during the extended Q2field desorption testing discussed in the section above, the results obtained from Mine A, B and C all show a consistent increase in Q1 value relative to increasing sample recovery time.

The results of testing at location 1 at Mine A with  $QM \approx 3.0 \text{ m}^3/\text{t}$ , shown in the left graph of Figure 16, has no recorded Q1 gas content, very low Q2 gas content and minor variability in Q3 gas content. The measured variability in Q3 gas content from samples collected at the same test location in a low gas content area, highlights the variability in repeatability of gas content measurement among laboratory services providers, which is acknowledged within the Australian Standard.

In addition to increasing Q1 in response to extended sample recovery time, the results from each test location also indicate decreasing Q2 and relatively constant Q3 gas content component values. These results are consistent with accepted gas desorption theory, with a greater percentage of the total gas contained within the core sample being desorbed and lost from the coal sample with increasing time period between initial coring and sealing inside the gas canister. The non-desorbing, residual gas content Q3 component, is not expected to change significantly over the 180 minute extended desorption period as this time period is less than the standard Q2lab desorption time period.

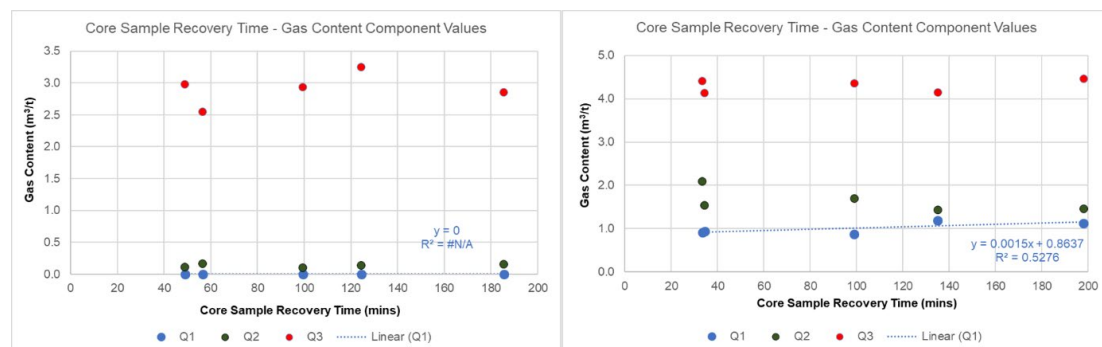


Figure 16: Extended Q1 Gas Content Component Values – Mine A, Seam 1

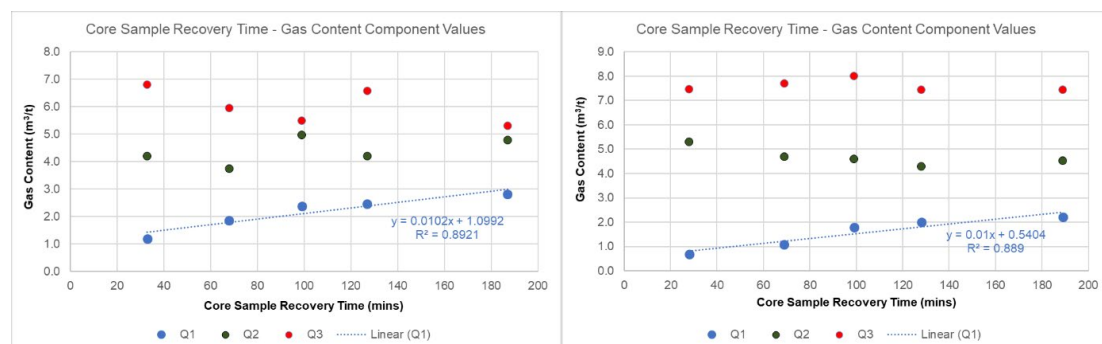


Figure 17: Extended Q1 Gas Content Component Values – Mine B, Seam 2

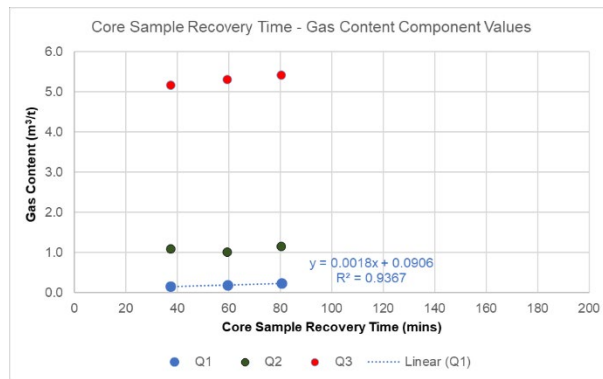


Figure 18: Extended Q1 Gas Content Component Values – Mine C, Seam 3

### CONCLUSIONS AND RECOMMENDATIONS

Given the significant impact that gas content measurement has on mine safety and operational efficiency among Australian underground coal mines there is an expectation that reported gas content results are accurate and correctly represent the gas content of the coal seam in the area from which the coal sample was collected. There is a practice among some coal sample testing service providers to add 'correction' factors to the measured gas content of coal samples. These 'correction factors' increase the reported gas content to account for assumed loss of gas content due to extended recovery time and even for variability in relative density of the coal sample.

The methodology used by one gas testing service provider to establish a gas content correction factor to apply to coal samples with extended recovery time has been investigated and discussed. A new approach to testing the impact of extended core sample recovery time on the accuracy of gas content measurement has been presented. The initial results obtained from testing at three Australian underground coal mines indicates that for core sample recovery times extending to 180 minutes, there is no discernible loss of gas content that would warrant the addition of a 'correction factor'. Figure 19 shows the percentage variance in the measured gas content of core samples at increasing recovery times relative to the initial benchmark gas content recorded at each test location.

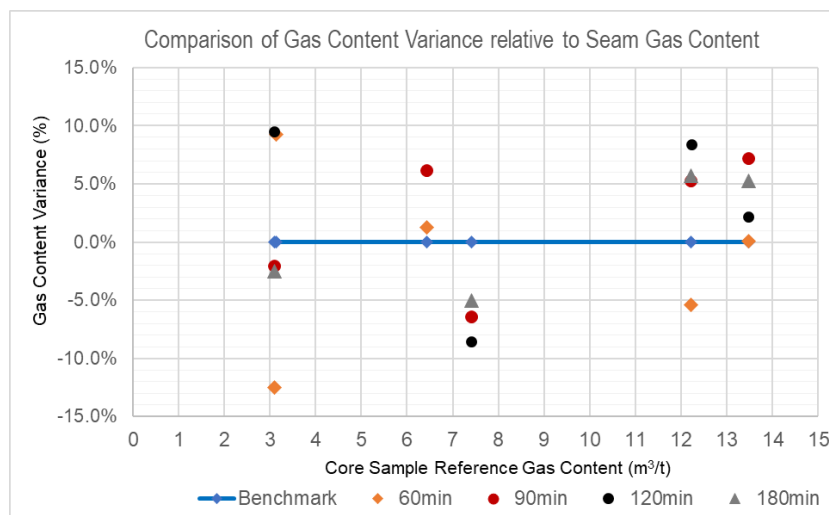


Figure 19: Variance in Gas Content during Extended Q1 Testing Relative to Benchmark

Further testing is planned to increase the size of the reference dataset covering a broad range of Australian coal seam conditions to establish if the results found from this initial investigation apply to all Australian coal seams. Australian underground coal mines interested in participating in this study are invited to contribute.

### **ACKNOWLEDGMENTS**

The author acknowledges and thanks ACARP for its continued support and the Australian underground coal mines that have supported and contributed to this research project.

The author also acknowledges the University of Wollongong for its continued support of gas and outburst related research.

### **REFERENCES**

- AS3980, 2016. Determination of gas content of coal and carbonaceous material – direct desorption method, Standards Association of Australia, p 41.
- Dannell, R E, Saghafi, A, Williams, R J and Wood, J, 2003. Reproducibility of gas content measurements using the fast desorption technique, Australian Coal Association Research Program, Project Report C8024, p 61.
- Diamond, W P, Schatzel, S J, Garcia, F and Ulery, J P, 2001. The modified direct method: A solution for obtaining accurate coal desorption measurements, in *Proceedings of the 2001 International Coalbed Methane Symposium*, University of Alabama, Tuscaloosa, 14-18 May, pp 331-342.
- Ellicott, C W, 1983. Coal seam gas content and composition: Investigation of methods of measurement, Department of Mineral Resources New South Wales, p 89.
- Kissell, F N, McCulloch, C M and Elder, C H, 1973. The direct method of determining methane content of coalbeds for ventilation design, U.S. Bureau of Mines, Report of Investigations 7767, p17.
- McCulloch, C M, Levine, J R, Kissell, F N and Deul, M, 1975. Measuring the methane content of bituminous coalbeds, U.S. Bureau of Mines, Report of Investigations 8043, p22.
- Saghafi, A and Williams, D J, 1998. Factors influencing the accuracy of measurement of gas content of coal: inter-comparison of quick crush technique, Australian Coal Association Research Program, Project Report C6023, p 69.

# AN IMPROVED TECHNIQUE FOR MONITORING EXPLOSIBILITY OF GASES

David Cliff<sup>1</sup>

**ABSTRACT:** Monitoring the potential for explosion in an underground coal mine traditionally centres on using the Coward Triangle, the Hughes Raybould Diagram, the USM explosibility diagram or the Ellicott diagram. None of these allow for analytical trending over time, it is difficult to determine rates of change of gas atmospheres using these techniques and thus predict if and when an atmosphere may become explosive. The Ellicott X Y diagram was an attempt to overcome this, This diagram suffers from the lack of bounds and the absence of an easy way to link the values to the limits of reality eg, fresh air, completely inert or completely fuel rich. In addition it requires separate plotting of the two parameters X and Y against time. Mines rescue guidelines and re-entry guidelines outline zones for safe entry and zones for no entry. Plotting these zones accurately on the X Y diagram is problematic, as there are four zones of interest – air rich, fuel rich, explosive and inert. Each of the three non-explosive zones would have different X and Y values to set as alarm points, making simple graphics impossible. This paper outlines a novel technique that allows for the plotting of the percent flammability independent of which zone the gases are in and indicating the zone separately. This enables easy time based trending to occur. This should enable wider acceptance and better understanding of explosion risk

Monitoring the potential for explosion in an underground coal mine traditionally centres around using the Coward Triangle, the Hughes Raybould Diagram, the USM explosibility diagram or the Ellicott diagram. None of these allow for analytical trending over time, it is difficult to determine rates of change of gas atmospheres using these techniques and thus predict if and when an atmosphere may become explosive. The Ellicott X Y diagram was an attempt to overcome this, This diagram suffers from the lack of bounds and the absence of an easy way to link the values to the limits of reality eg, fresh air, completely inert or completely fuel rich. In addition it requires separate plotting of the two parameters X and Y against time. Mines rescue guidelines and re-entry guidelines outline zones for safe entry and zones for no entry. Plotting these zones accurately on the X Y diagram is problematic, as there are four zones of interest – air rich, fuel rich, explosive and inert. Each of the three non-explosive zones would have different X and Y values to set as alarm points, making simple graphics impossible. This paper outlines a novel technique that allows for the plotting of the percent flammability independent of which zone the gases are in and indicating the zone separately. This enables easy time based trending to occur. This should enable wider acceptance and better understanding of explosion risk

## BACKGROUND

Traditionally explosibility assessments in mining regulations have been cast in terms of the Lower Explosive Limit (LEL) of methane – 5% in air. Various explosion risk zones, and trigger points for the safe use of equipment and access by people have been gazetted in terms of this value. Modern mining regularly has to cope with situations where the atmosphere is well above the LEL and indeed may be well above the Upper Explosive Limit (UEL). Situations arise

---

<sup>1</sup> Professor, University of Queensland, Email: [d.cliff@mishc.uq.edu.au](mailto:d.cliff@mishc.uq.edu.au); Tel: +61 7 3346 4086

such as equipment (eg, borehole cameras) are being deployed into longwall goafs where the atmosphere is essentially pure methane. Currently if the equipment is not certified intrinsically safe by an Australian testing laboratory, the regulations prohibit its use. Highwall mining with inertisation may get into situations where the methane concentration exceeds the LEL but there is no oxygen present. In both cases there is no risk of explosion as there is no oxygen present. There is a need however in those situations to track any deviation in the atmosphere particularly if it trends toward an explosive atmosphere.

Currently representation of explosibility is best done graphically, with the Coward triangle and Ellicott diagram most commonly used in Australia however elsewhere the USBM Flammability Diagram is used. A full description of the various techniques can be found in many texts including Cliff, Brady and Watkinson, 2018.

The Coward Triangle plots the percentage of oxygen against the total percentage of flammable gases in the sample of interest (Figure 1). The three critical limits are all calculated for the particular sample from which the four zones; explosive, fuel lean, fuel rich and non-explosive are all determined and delineated on the diagram (Figure 2). The total flammable gas and oxygen concentrations in the sample of interest allow a datum point to be plotted on the triangle, indicating the explosibility status for that sample.

The expected behaviour of the gas mixture's explosibility status under various scenarios can be predicted as illustrated below (Figure 3). Adding fresh air makes the point head toward the top left corner (20.95% oxygen). Adding inert gases makes the point head toward the bottom left corner (no oxygen and no flammable gas). Adding more combustible gases makes the point head toward the bottom right corner of the triangle (100% flammable gas). The triangle limits are fresh air (20.95% Oxygen), inert gas and 100% flammable gas.

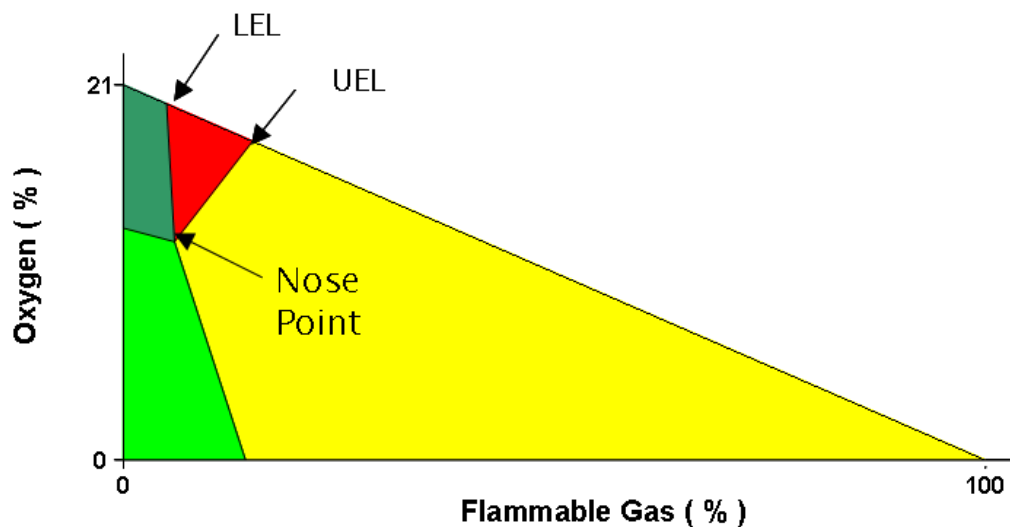


Figure 1: Coward Triangle (Cliff et al, 2018)



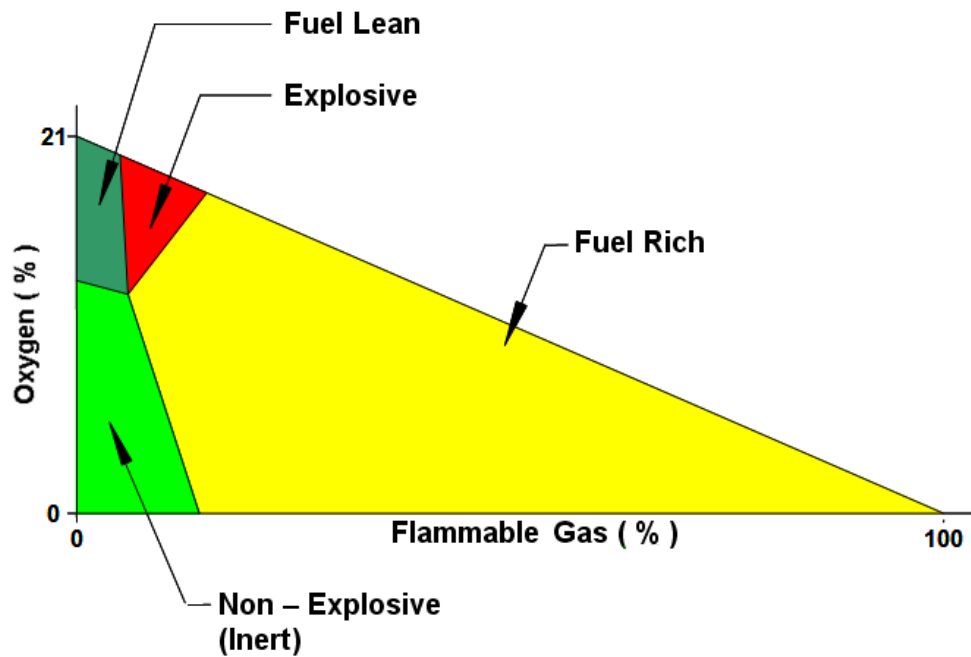


Figure 2: Zones on the Coward Triangle (Cliff et al 2018)

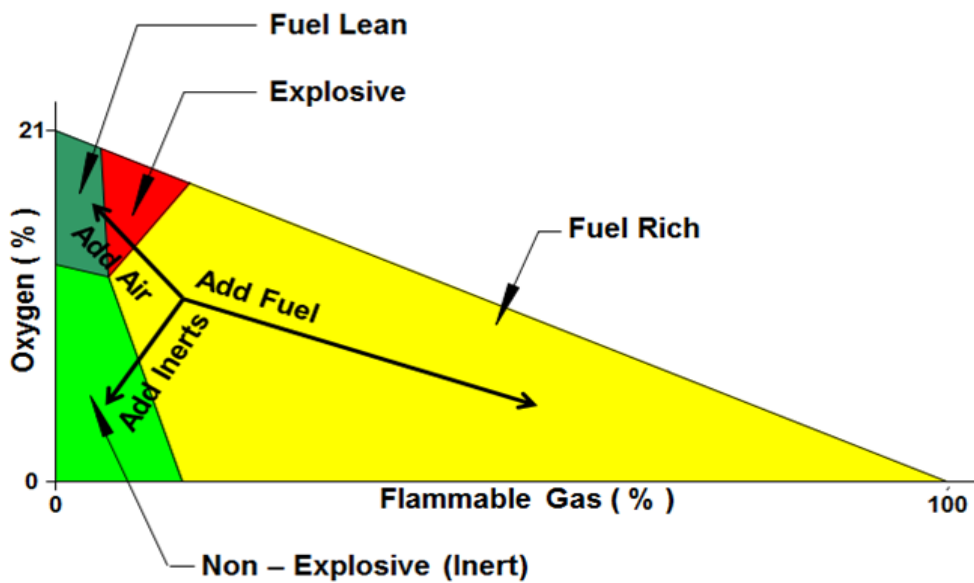


Figure 3: Trends on the Coward Triangle (Cliff et al 2018)

The work done by Coward was just for methane however Hughes and Raybould (1961) utilised Le Chatelier's additive principle (1891) to determine the upper and lower explosive limits for a sample with a mixture of flammable gases weighted by the concentration of the individual concentrations of the flammable gases.

The Ellicott diagram is a modification of the Coward Triangle. The triangle is transformed into a rectangle, with the centre point being the nose point (the point of minimum explosibility) and the axes radiating from there being the delineating barriers of each of the four different explosibility classifications (Figure 4);

- The + Y axis delineates the fuel lean zone from the explosive zone,
- The + X axis delineates the explosive zone from the fuel rich zone,

- The - Y axis delineates the inert zone from the fuel rich zone and
- The -X axis delineates fuel lean zone from the inert zone.

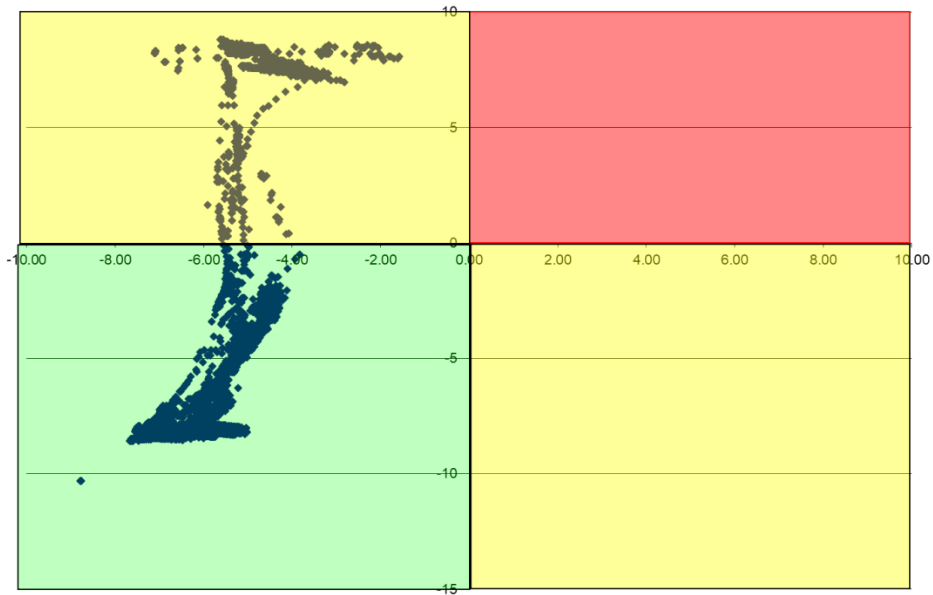


Figure 4: Ellicott diagram

As the Ellicott diagram is a distortion of the Cowards triangle with fixed sized zones, caution must be taken when assessing the explosibility status of a sample in relation to how close it is to other zones. There are only certain areas where it is possible for a plot to occur. Figure 5 shows the valid region for methane, hydrogen and carbon monoxide mixes with air on the one Ellicott diagram.

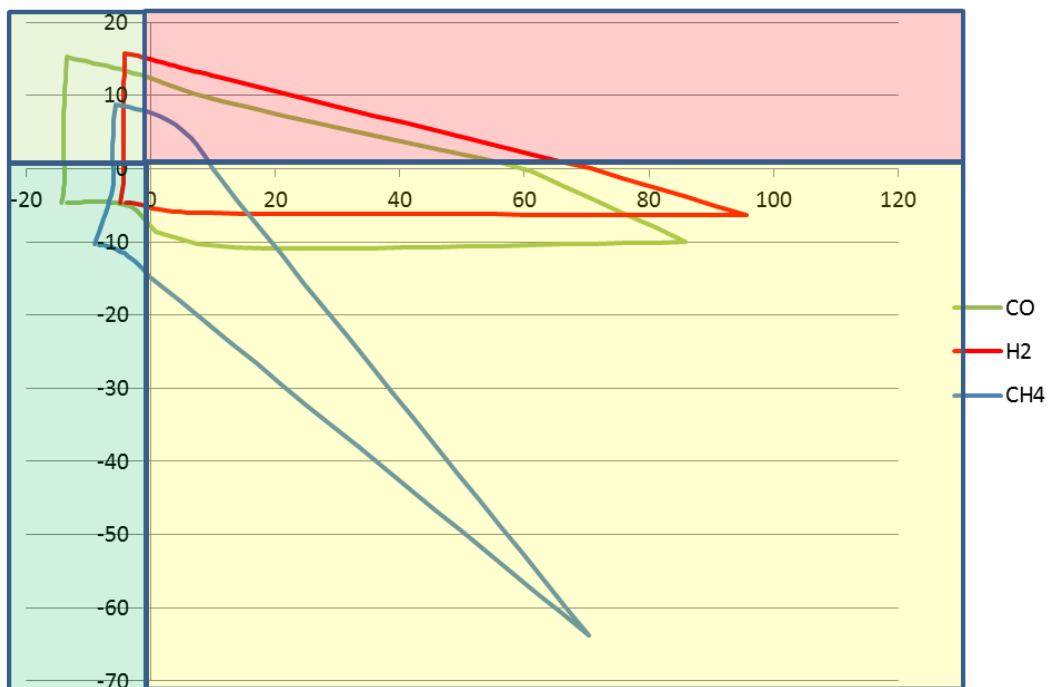


Figure 5: Limits of the Ellicott diagram

Many common modern depictions of the Coward and Ellicott diagram include zones that align with Trigger Action Response Plans (TARPs) and assist in the management of the flammability risk. Mines Rescue guidelines also utilise these zones in determining whether or not rescue teams can deploy. Figure 6 indicates such zones

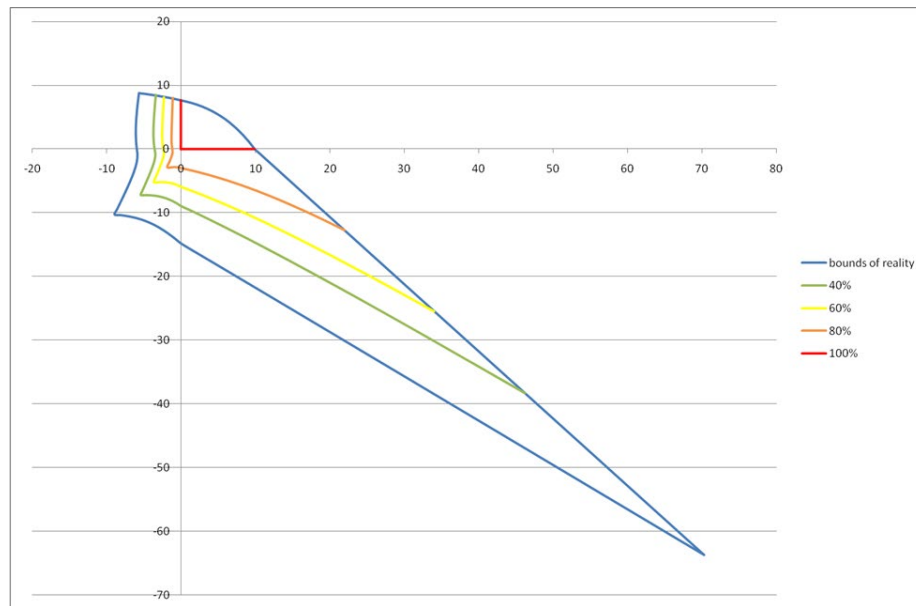


Figure 6: Explosibility safety margins for methane air mixes

Although trending is possible on a Coward triangle or an Ellicott diagram there is no means of incorporating a time scale. On an Ellicott diagram for a gas to be explosive it must have a positive X and Y value. By extracting the values for Ellicott X and Y from the software generating the plots, it is possible to plot both against time and make a prediction of not only if the location is going to become explosive but when as seen in Figures 7.

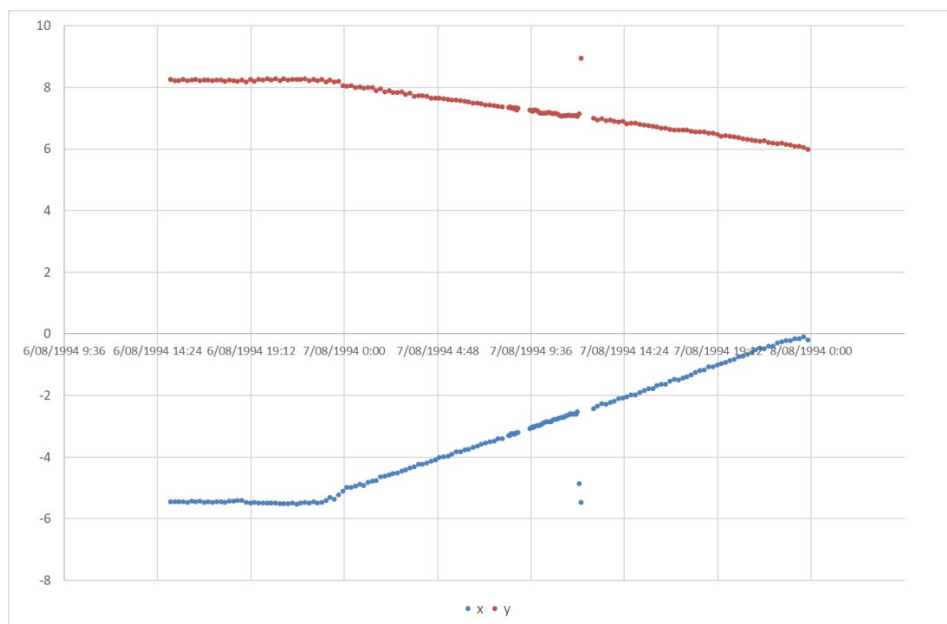
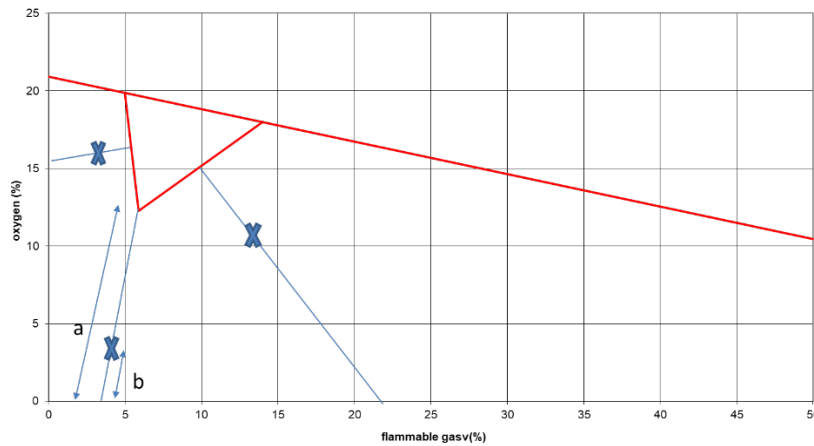


Figure 7: Ellicott X and Y diagram

The limitation of this technique is not knowing the proximity of the data to boundaries of the diagram and establishing the relationship to the TARPs.

**THE NEW EXPLOSIBILITY DIAGRAM.**

To overcome these issues a diagram was developed that overtly displayed the percentage of the explosive limit for the data point as a function of time. Colour coded data points were used to explain in which zone of the Coward triangle the data was based. The percentage explosibility was simply estimated from the percentage along the shortest line linking the closest boundary to the nearest explosive limit line passing through the data point (b/a as % in diagram below). An example is shown graphically below. In general this line is perpendicular to the explosive limit line. In the areas where this is not possible (as in Figure 8) then the line linking either the LEL, UEL or nose point to the boundary was used.



**Figure 8: Calculating the percent flammability**

Using the traditional colours from the Coward triangle this can now be plotted against time. The diagram below (Figure 9) illustrates this for a highwall mining operation using inertisation to manage the flammability risk. The yellow indicates that it starts out in the fuel lean zone from fresh air and transits to the inert zone (green). The traditional Coward triangle and Ellicott X Y plots are shown for comparison (Figures 10 and 11).

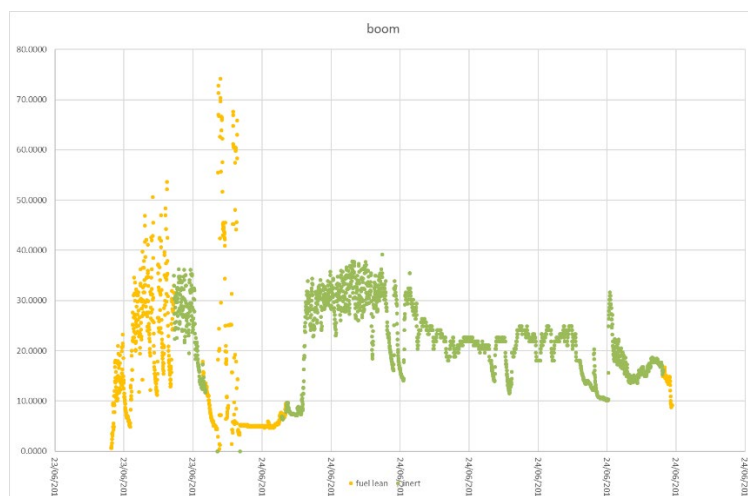


**Figure 9: Explosibility time diagram for a highwall mining operation**

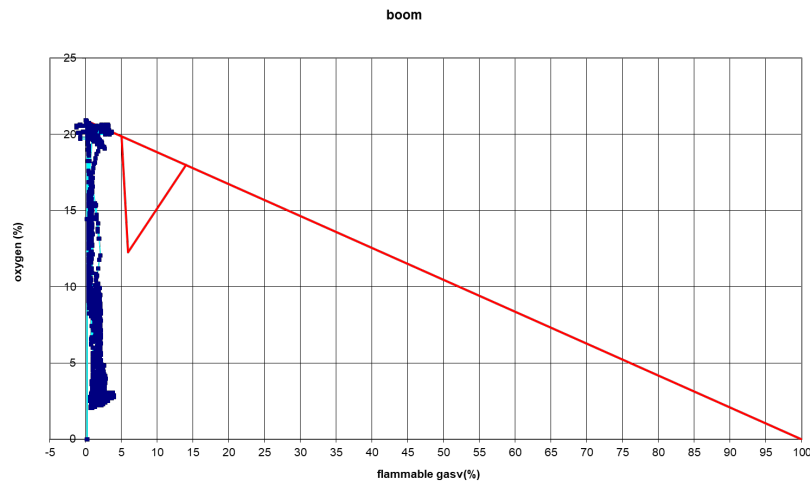


**Figure 10: Same data depicted on the traditional Coward Triangle**

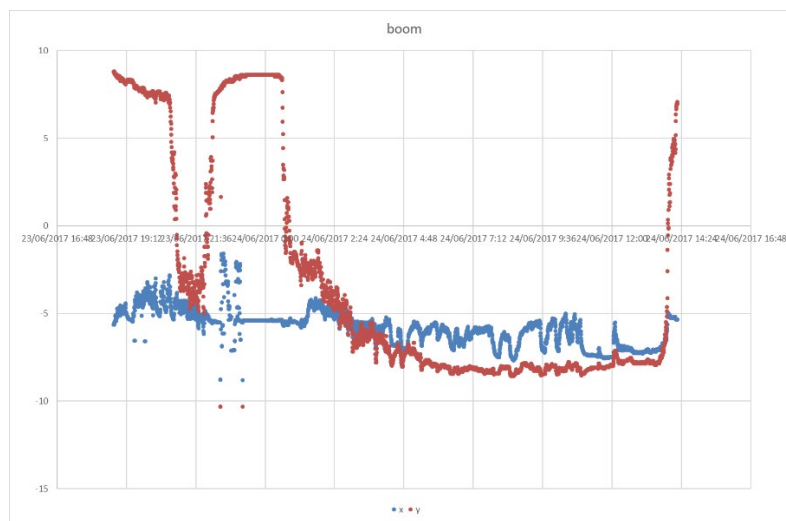


**Figure 11: Highwall mining data on Ellicott X Y diagram**

Another example would be the explosions at Moura No.2 mine in 1994. The traditional Ellicott X Y is depicted below as well as the new explosibility diagram (Figures 12 to 13\5). In the cases of the Coward triangle and the Ellicott diagram, had an observer been watching them develop over time then it would have been clear that the atmosphere would become explosive. It would have been more difficult to gauge the rate of movement. The Ellicott XY diagram allows easy prediction of when the explosive atmosphere would occur (both X and Y need to be positive), however it is not possible to easily estimate what percentage of the LEL was occurring and thus what TARP would be triggered. The new diagram clearly demonstrates both the rate of progress and also what percentage of the LEL is occurring as the atmosphere progresses from essentially fresh air toward the LEL (yellow dots). The new diagram also clearly demonstrates that, initially at the monitoring point, there was a fuel rich atmosphere (the brown dots) which mixed with air over time and actually formed an explosive atmosphere (the red dots) after the first explosion and slowly dissipated through air inflow before the second explosion occurred. The known monitoring location, was sampling from a different location to the 512 panel seal.

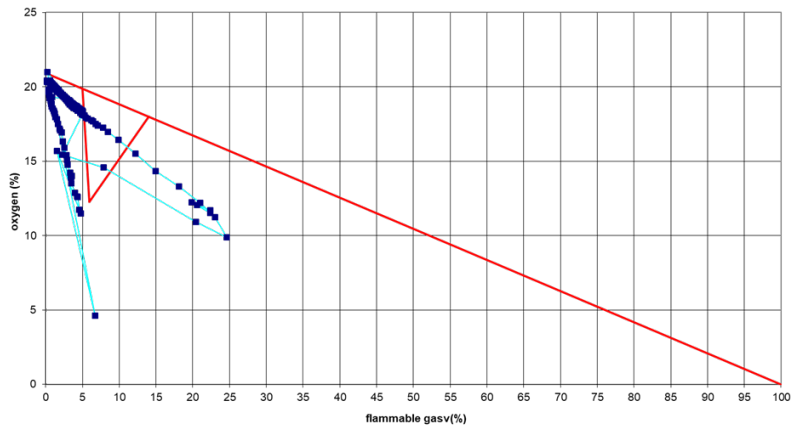


Figure 12. 512 seal data on Coward Triangle

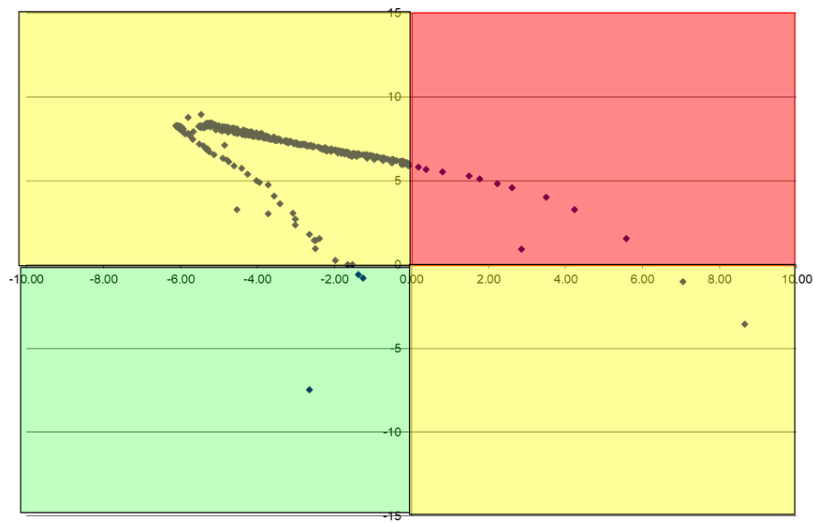


Figure 13. 512 seal data on Ellicott diagram

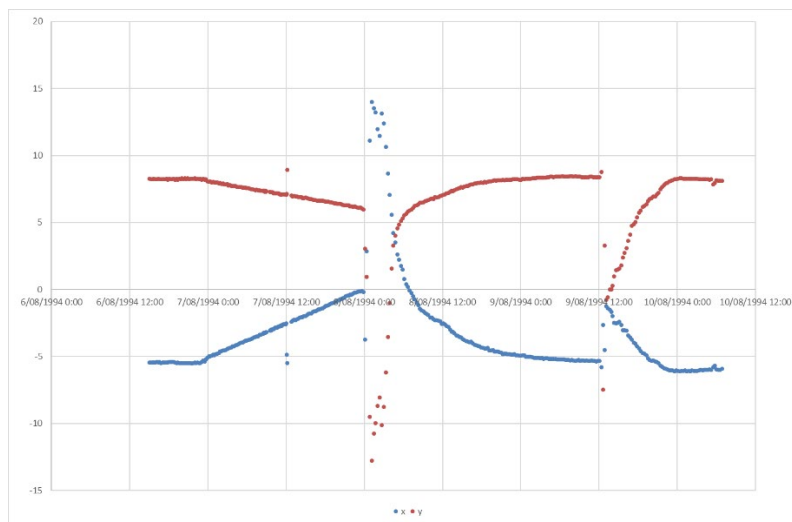


Figure 14: Ellicott XY plot of 512 data



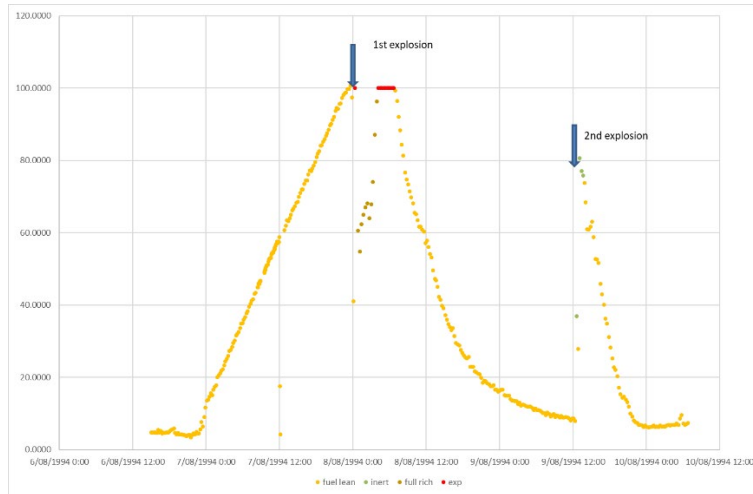


Figure 15: 512 data on new explosibility diagram

### CONCLUSIONS

Traditional explosibility diagrams have limitations when used to trend the potential for explosion over time. A new diagram has been developed in an effort to overcome those issues. It is able to plot the percentage of the explosibility (LEL or UEL) from any of the zones as a function of time, giving better perception of the explosibility risk. This diagram should find application in emergency situations as well as when working with atmospheres that are fuel rich.

### REFERENCES

- Cliff D, Brady D, and Watkinson M, 2018. *Spontaneous Combustion in Australian Coal Mines*, Edited by Forrester L and Watkinson M, (SIMTARS, Redbank, Queensland, Australia).
- Hughes A J, and Raybould W E, 1961. The rapid determination of the explosibility of mine fire gases, *Mining Engineer*, 120(1), pp37-53.
- Le Chatelier H, 1891. Estimation of firedamp by flammability limits, *Annals of Mines*, 19. As cited in Muzyczuk J, 1987. General Criteria of applying the Le Chatelier's rule for the determination of explosibility limits of complex gas mixtures, *International Symposium of Rescue Services in the Service of Mine Workers*, Szczyrk, Poland.

# GAS MONITORING WHAT WE KNOW SO FAR

Martin Watkinson<sup>1</sup>, Martin Tsai<sup>2</sup>, Larry Ryan<sup>3</sup>

**ABSTRACT:** Remote gas monitoring started in the early 1960's when carbon monoxide detectors were used in Germany to monitor spontaneous combustion activity. These systems were modified and used in the United Kingdom in the late 1960's to proactively monitor the underground atmosphere; the tube bundle systems we know today. Real time methane detectors and carbon monoxide detectors were used in British Coal in the mid 1980's. Large mines in Australia can have up to 60 tube bundle monitoring points and up to 200 individual gas sensors underground. This paper discusses the development of these systems as well as potential issues relating to data handling and interpretation.

## Introduction

### Tube bundle systems

Infra-red carbon monoxide analysers were first used in Germany for the detection of and control of spontaneous combustion. The tube based system brought the sample back to the underground Mairhak analyser was adopted in Scotland in the UK. In the late 1960's this technology was quickly adopted by the National Coal Board for the detection of spontaneous combustion with the analysers on the surface - the typical tube bundle system we still have today some 50 years later.(Chamberlain et al 1971). The reason for this adaptation was the commercial availability of bundle of tubes which were being developed for hydraulic control systems.

A handbook describing tube bundle systems was released by The National Coal Board in 1972. This handbook was revised with an emphasis to make it suitable for a wider audience and published in 1977 as *The Tube Bundle Technique for the Continuous Monitoring of Mine Air* (National Coal Board 1977).

The foreword of the handbook stated that it was notes on the use and installation of tube bundles for the continuous monitoring of mine air based on the accumulated experience of eight years' research by Scientific Control and some 80 pit installations. Figure shows a schematic for the surface layout of a tube bundle system. The handbook made many recommendations for the successful application of the system: these include:-

Use low density polyethylene and colours for tube identification, cap the tubing before using to keep dirt out, do not cut the tube with the suction on or dust will enter the system and use compression type joints.

Details of the installation of the tubes recorded on scale a plan including the route of each tube, the location of junction boxes and the sampling point. A sketch diagram was also prepared of the same information. Install one in tube in the intake and one in the return from each active district and undue lengths of tube on the surface are to be avoided.

---

<sup>1</sup> Executive Mining Engineer, Simtars. Email: [martin.watkinson@simtars.com.au](mailto:martin.watkinson@simtars.com.au) Tel +61 7 3810 6686

<sup>2</sup> Senior Computer System Engineer, Simtars. Email [martin.tsai@simtars.com.au](mailto:martin.tsai@simtars.com.au) Tel +61 7 3810 6310

<sup>3</sup> Computer System Engineer, Simtars. Email [larry.ryan@simtars.com.au](mailto:larry.ryan@simtars.com.au) Tel +61 7 3180 6354

Slinging of tube point to point was to be avoided as water condensation and blockages may occur at low points, single tube were to be supported at 2-4 m intervals three or more tubes at 2 m intervals.

Water traps were used at the bottom of the shaft, in the analyser room and in roadway low points. Flame traps were also included as an added protection for tubes above 9.4 mm outside diameter.

Leak testing by was undertaken by introducing a known gas at the inbye end of the tube or vacuum testing for 24 hours with negligible loss being the pass criteria. The volume flow entering each sampling point was measured by flow meters recorded by deputies on their statutory reports. Spare drums of tube were held centrally for emergency response.

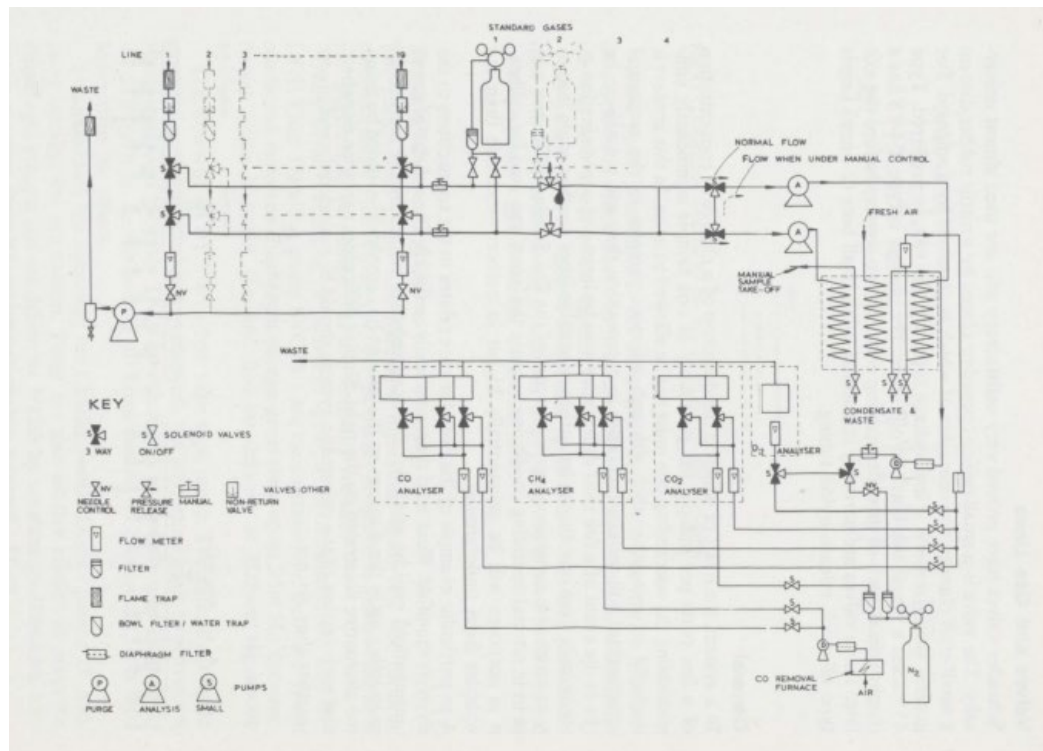


**Figure 1: Schematic of an early tube bundle system (from National Coal Board 1997)**

The hand book made the following recommendations for the surface installation:

The installation must be readily accessible by road, the pumps housed separately due to vibration and noise and have suitable ant-vibration mounts to protect the pump and motor bearings. The installation should include a high capacity scavenge (purge) pumps and a sample pump where the absolute inlet pressure of the sample pump must be greater than that of the scavenge/purge pump to avoid reversal of the flow when the line is sampled. The excess gas should be discharged to the outside atmosphere. The pump design should ensure there is no contamination with oil or vapour from the pump. Other subtleties in the design included the avoidance of dead volumes in the tubing, the same train of dust traps and humidity conditioner for the calibration gases as the sample gas, automatic water trap at the humidifier and the temperature in the room should be kept stable.

The instruments used were infra-red (IR) and multi range:

Carbon monoxide (CO) 0-100 parts per million (ppm) and 0-1000 ppm using subdivided cells.  
Methane (CH<sub>4</sub>) 0-5%, 0-20% and 0-100% using subdivided cells.

Carbon dioxide (CO<sub>2</sub>) 0-5% and 0-15% using subdivided cells.  
Oxygen (O<sub>2</sub>) 0-25% paramagnetic analyser, flow sensitive.

### **Real time systems**

Real time sensors were first introduced in the 1980's, these were mainly carbon monoxide and methane and were used in the Selby Coal Field in the UK.

Underground real-time systems were prescribed legislation in Queensland in the coal mine regulations introduced in 2001 (now dated 2017). Similar requirements for real time systems were also introduced into NSW regulations.

Underground methane detectors were also used to trip power automatically. Most detectors were electrochemical, pellistor type detectors were developed for CH<sub>4</sub> along with IR sensors being available for CH<sub>4</sub> and later for CO<sub>2</sub>. Initial installations were at the outbye/return end of longwall panels and at key locations on conveyor roads such as at the interface between mines in the Selby Coal Field

## **CURRENT STATUS**

### **Tube bundle**

There are four suppliers of tube bundle systems in Australia and two of them have developed software for the control of the system. Systems are now built to comply with the specifications required by AS/NZS 60079-10.1 2009 Explosive atmosphere classification of areas-Explosive gas atmospheres (IEC 60079-10.1, Ed.1.0 (2008) MOD). This is required because the sample pump supplies the gas to the analyser at positive pressure and if there was a leak a hazardous gas accumulation could occur in the analyser room. The National Coal Board (1977) discussed the possible use of negative pressure to supply the sample to the analyser, it is not known whether this was tried or not. If this process was proven all of the tubes in the analyser room would be under negative pressure and the requirements to comply with AS/NZS 60079-10.1 2009 could be reviewed.

There have been several design changes made over the years to make the building of the system cheaper. For example in 1997 one of the authors purchased a system from one of the suppliers and it came with five identical pumps, four were purge pumps and one the sample pump. Each purge pump had five tubes assigned to it. The system also came with needle valves to regulate the flow in all tubes to be the same i.e. balance the flows to match the longest tube. The system also came with four analysers 0-100 ppm and 0-1000 ppm CO, 0-10% and 0-100% CO<sub>2</sub>, 0-10% and 0-100% CH<sub>4</sub> and 0-25% O<sub>2</sub>. Calibration was done with a zero gas and a gas around 90% of full scale on both ranges. The CO was also zeroed using fresh air as the ultra-high purity nitrogen for zeroing contained around 0.7 ppm of CO. Both scales were calibrated and adjustments to the potentiometer were done manually. The same supplier had to be convinced to install an automatic water trap at de-humidifier and the introduction of calibration gases at the same point as the gas samples as suggested by the National Coal Board (1977).

Current systems from the same supplier now come with one analyser with a shared optical path for the IR gases and are single range; 0-1000 ppm for CO and 0-100% for CH<sub>4</sub> the supplier recommends the use of 0-50% for CO<sub>2</sub> for improved accuracy on CH<sub>4</sub>. The instrument is calibrated at zero and 100% with electronic adjustments being made.

All of the suppliers provide two purge pumps for a twenty point system, this makes the piping arrangement simpler. Current instructions from the supplier are to put all the tubes of the same length on the same purge pump, this is not a practical solution at a mine site as there will be

variability in tube lengths and then changes as the mine develops. Regulating needle valves are not supplied unless requested.

The authors are aware of one mine that had a problem with the sample pump stalling when switching to certain tubes at the mine, the apparent resolution to this was to install check valves in line. These check valves later became an operational liability due to blockages. Note the National Coal Board (1997) recommendation of "*absolute inlet pressure of the sample pump must be greater than that of the scavenge/purge pump.*"

It is quite normal to site a seal panel, connectors and self-draining water trap, adjacent to a seal. Operationally is this the best place to locate it? The sample will come out of the seal at high humidity and higher temperature than the mine roadway. Condensation will occur and if the gradient is favourable the water will drain back to the water trap. If the gradient is not favourable the water will run in the opposite direction, if the tubes are in the return there is a likelihood that little condensation will occur until the tube enters intake (colder) roadways. This could possibly be the best place to locate the 'seal panel.'

Marshalling panel design also needs to be considered as some suppliers have low points where water can accumulate; these low points are underneath the installed water traps. One supplier insists on supplying a 10 point marshalling panel even if the bundle run is a seven core.

Tubes supplied in bundles can either be colour coded with identifying markings or all black with identifying markings. The authors have had personal feedback that the all black tubes were very well marked. Other suppliers provided coloured tubes but at least one insists on supplying bundles of tubes with different shades of yellow, blue and red which can be difficult to distinguish in underground installation conditions.

Other installation tips are to use catenary wire for the installation of tubes and attach the tube to the catenary wire every 2-3 m avoiding slack and undulations where water can accumulate. Another trick is to ensure that the analyser room is not too cold as condensation will occur in the tubing and not at the de-humidifier as planned.

All maintenance of the installations are covered by the AS2290 Part 3 2018 which now requires the testing of gas alarms and hardware alarms on a monthly basis.

The accuracy of tube bundle analysers are not specified in AS2290 Part 3 2018; the standard states that they shall be in accordance with the respective manufacturers specifications.

### **Real time systems**

Real time gas monitoring systems are now an integral part of mine environmental gas monitoring. With return airways monitored for methane, carbon monoxide, carbon dioxide and oxygen. Elsewhere in the mine there are discreet methane monitors with an electrical power tripping function, carbon monoxide monitors along conveyor belts. Other real-time monitors are available for ventilation velocity, pressure and temperature with diesel particulate matter monitors now being introduced to the industry.

Large mine can have over 200 monitors installed which creates an appreciable workload on the electrical department to install and maintain the system. This does not include the monitors on mobile plant or the hand held monitors carried by statutory officials and key coal mine workers.

Each monitor has to be calibrated on a monthly basis in line with AS 2290 Part 3 2018 along with a response time test and a telemetry test. The standard requires the maintenance records to be kept for four months. There is a separate 6 monthly calibration requirement the records of which need to be kept for two years.

There are a number of issues that have been identified with real-time systems and tests to identify if they are occurring and remedy the situation have been include as part of the requirements of AS2290 part 3 (2018). These include the checking that all displays reflect the

same value, the response time for the detector to react to the applied gas and that the telemetry system is physically capable of sending a full range value to the surface control room. The standard also provides advice on the maximum pressure that the gas sensor is exposed to (50 Pa). Specifically:

- The requirement to check that the local display and the remote display, in the control room, show the same readings when the calibration is being done.
- Establishment of the  $T_{90}$  for the sensor the acceptable criteria is less than 30 seconds for CH<sub>4</sub> and less than 60 seconds for all other detectors.
- The telemetry test is only applicable if the gas detector raises a remote alarm or tripping function. This would mean all underground sensors are required to be tested this way. There is no specified time for a pass but this must be specified in the mines safety system.
- Dynamic range test is required to ensure that the full range of the sensor values can be communicated across the telemetry system. I.e. if the detector is exposed to 5% CH<sub>4</sub> the full value will be communicated to the surface control room.

The accuracy of methane detectors is prescribed as follows in Figure 2.

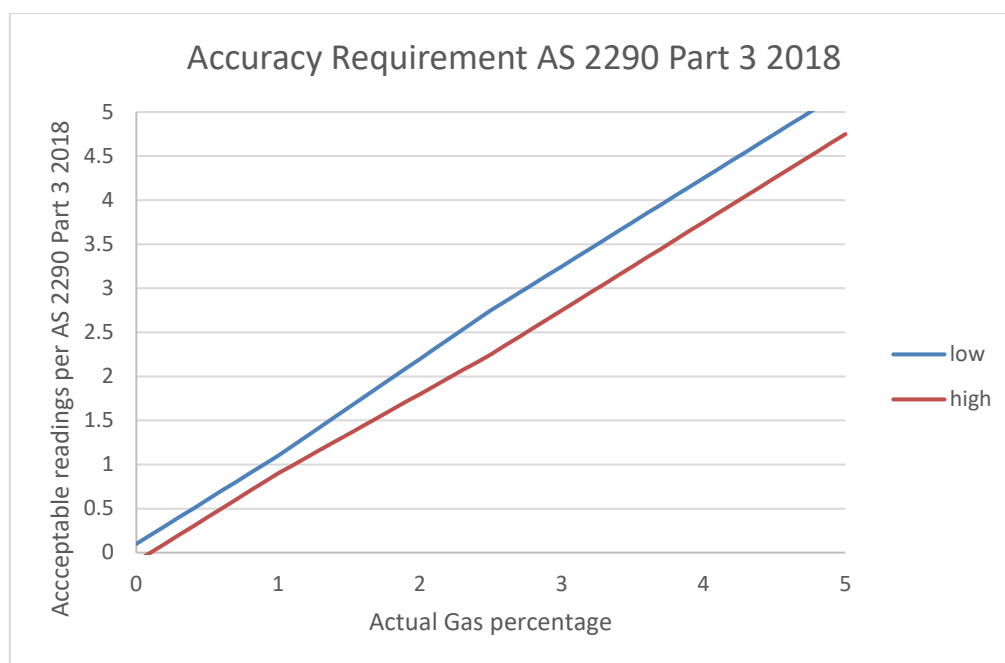


**Figure 2: Accuracy requirements for methane detectors to 5% AS 2290 part 3 2018**

It can be seen that a detector that is exposed to a methane percentage of 2.5% could read between 2.25% and 2.75% and still pass the requirements of AS 2290 Part 3 2018.

The standard also provides information on the effect on  $T_{90}$  times when sensors are blocked and provides an example of when a calibration cup is pressurised with a 2.5% challenge gas the detector will read 2.75%. If the detector is then calibrated to read 2.5% at this pressure. When the detector is exposed to a real gas concentration of 2.5% it will report an actual concentration of 2.2%.

---

<sup>1</sup>  $T_{90}$  is the time taken for a detector to read 90% of the value applied gas concentration.



With over 200 sensors to maintain this becomes a full time job for a dedicated team of electrical staff when production priorities call there is a danger that the routine maintenance of the gas monitoring system will be neglected.

### **DATA HANDLING AND INTERPRETATION**

AS 2290 Part 3 2018 requires the maintenance records for calibrations to be kept for four months. There is a separate 6 monthly calibration requirement the records of which need to be kept for 2 years.

The NSW Work Health and Safety (Mines and Petroleum Sites) Regulation 2014 S58 Records of air monitoring require the keeping of the gas records for seven years. Given that hand-held instruments and mobile plant are in fact an integral part of the gas monitoring system it is possible that there could be a need to keep these results also.

In Queensland the ventilation reports are required to be kept as part of the mine record but the requirement for keeping the real time gas data is not clearly defined under the Queensland regulation 2017. However, recognised standard 09 the monitoring of sealed areas (2009) requires the records for each seal to be kept for the life of the mine, this is the tube bundle data.

The Queensland regulations 2017 s 222 Gas monitoring system also requires "*the keeping the information on which the values and trends mentioned in paragraph (d) were based at the mine in a way that enables the information to be easily accessed and inspected*".

### **Gas Monitoring Data Improvements**

#### **Data storage**

It has been observed that "excess gas data" has occurred in data storage/databases for some real-time systems. This condition caused the gas data file to become "bloated" with repeated data, hence the file size is much larger but contains no extra gas information.

Excessive data storage rate leads to following issues:

1. The gas monitoring system is sluggish in trends and display and the control room operator (CRO) is not able to pursue further investigation into the gas record.
2. Alarm generation and acknowledgement could be delayed or take a long time to complete.
3. The computer equipment struggles to store or display the data.
4. The history gas data file becomes excessive in size, becomes unusable and fills all the available disk space.
5. Extremely difficult to share the data file with internal and external experts.

20 megabyte (MB) is the practical limit for email, many accounts have smaller limits, so the file has to be shared by online file transfer services. A standard tube bundle file can be between 20 and 150 MB and a real-time system can generate files from several hundred MB to a few gigabytes (GB) in size.

In a recent test at Simtars, the uploading of a 6 GB file took approximately 4 hours (50 MB/s download, 20 MB/s upload). As most mine sites are in remote areas, the internet connect will probably be slower than the tested connection and therefore it would take even longer to share the gas data once that data file size exceeds few hundred MB.

The size of the gas data is a severe limitation to the rapid response required after a serious incident onsite. The size of the gas data can be excessive due to the following reasons –

1. Gas data storage rate is too high.
2. All the gas data is stored into a single repository.
3. The time range of data is too large.

Some of these issues can be resolved by sending a copy of the gas data to a secure website for sharing to various parties, as required. The advantage of this approach is the data is always available for download and only the user account access needs to be shared in the case of an emergency. In addition, if the data were stored in smaller time periods, the downloads would be a more manageable size.

Finally, the trending of the gas data must be managed in the real-time system. Due to the rapid sampling rate, a typical real-time system has records stored every 3-20 seconds per location. A single location can produce 201,600 records in a week period. The excessive data size can be even worse if the user chooses to trend data with longer time range then compare multi location data in the same graph.

Some systems display the average gas data between set intervals and this can mask out the important information. It is important to display correct gas value acquired. Transient gas changes occur for a reason and thus provide an opportunity to better understand the operation of the mine ventilation/gas monitoring system. For example, a rapid drop in the barometric pressure will cause the goafs to breathe out while a spike on a real-time sensor will show when it was calibrated.

Therefore, the gas monitoring system should apply two different approaches –

1. Represent all values in trend when reasonable dataset size is chosen.
2. Present using a correct data managed approach such as set value filtering or rate of change should be applied if a large quantity of information is selected.

Such data management will allow the user to filter certain percentage of the background data to reduce the data size. In the same time, the system will keep all the sharp rise peaks and present all the data values that exceed a pre-defined threshold.

Such an approach will enable the user to carry out a quick analysis on the overall data for a set period and apply further data analysis at a detail level without compromise.

### **Data process**

Although tube bundle and real-time systems operate using different principles and hardware, both systems are monitoring the same gas parameters in the same environment and should be used to compensate each other. However the modern tube bundle and real-time systems still operate as single individual system. The end user must go through different methods to merge data in to a single repository before further analysis can be done. This is not a simple process and is usually avoided by the mine site.

In addition, standard single longwall block can take a few months to 1+ years to complete. The background history data can help the user understand the overall gas condition for the life of the longwall block. Unfortunately, it is common for the standard modem gas monitoring practices to keep a small amount live history data and archive all the rest. Such an approach is done to allow faster system response time. The problem is the end user left with multiple history data files that require further merging processing or a large history data repository where the user requires sufficient computer skills to navigate and obtain the useful information.

In order to overcome above and retain the same response user experience, a separate centralised database can be used to address this problem. Such a share repository should allow collected data through different hardware such as real-time, tube bundle or even a gas chromatograph. This approach offers greater flexibility in term of cross reference between gas data and will not increase workload on the operation of the monitoring system. A graphical interface application with simple interface should be use allow user analysis data without in-depth computer skillset.

### Quality of gas data

The quality of the raw gas data is vitally important as this will be one of the limiting factors in the accuracy of all the gas ratios/explosability calculations. Typically, the gas ratios/explosability calculations are an important consideration as to the course of action required when the mine has a heating etc. As the old saying goes Garbage In = Garbage Out.

The quality of the gas data can be affected by:

1. Gas monitoring method used (Tube Bundle, real-time, Gas Chromatograph, hand held.)
2. The analyser/sensor uncertainty (the quality/range of the sensor)
3. Maintenance level (frequency of calibration, how well it is calibrated)
4. Skill of the operator (bag sample collection, analysis, etc.)
5. When the sample was collected (goaf sample collected when the barometer was falling)
6. Speed of sample analysis (if the sample is not analysed quickly, some gas components are lost (hydrogen,))

More attention needs to be given to the uncertainty of gas analysers/detectors and the gas ranges that these uncertainties apply to. If the gas analysers/detectors uncertainty is not transparently stated in its manual then how do you know accuracy of the gas readings?

Choosing an analyser with tighter gas uncertainties should be part of the analyser selection process, for example for a carbon monoxide (CO) analyser with 1% uncertainty full scale -

For Example – An analyser with a 100 ppm range may have an uncertainty of  $\pm 1$  ppm, hence if the actual gas value is 5 ppm then the analyser reports 4 – 6 ppm while still being within specifications. The table below provides a couple of examples of the range of values within the 1% uncertainty full scale specification.

Range	1% Uncertainty Full Scale	Tolerance Range for 5 ppm Actual Value
0 – 100 ppm	$\pm 1$ ppm	4 – 6 ppm
0 – 50 ppm	$\pm 0.5$ ppm	4.5 - 5.5 ppm

The smaller the gas range and the lower the uncertainty, the greater the accuracy of the resulting gas measurement. For spontaneous combustion events, early detection is vital and hence smaller ranges in the 0 – 50 ppm with a low uncertainty should provide a better representation of the gaseous environment underground.

The challenge testing of gas analysers/sensors between scheduled calibrations can be useful in detecting drift and other maintenance issues.

Another opportunity exists where the final gas data at a particular location may need to be verified prior to storage.

For example - where the data departs from the trend etc. or two different gas monitoring devices return different results.

In these cases, the gas values and measure techniques need to be double checked to ensure that the discrepancy is resolved and correction action is taken to ensure the integrity of the gas monitoring in the future. If it wasn't for the same gas values returning different results, the issue with the gas monitoring system would not have been identified.

The final gas data at a particular location may need to be verified prior to uploading for various data types i.e. where the data departs from the trend etc. or two different monitors/devices generate different results.

## **Data exchange**

During incidents, the sharing of gas monitoring and other data is a priority so people can work in parallel to analyse/resolve the current situation. Naturally, the various parties will all have their preferred analytical software i.e. Segas Professional, SMARTMATE, Citect and Spreadsheets.

As there are many different types of gas monitoring systems and they each have their own data format, in an emergency situation, the gas monitoring data will need to be periodically (typically at the end of each shift) converted from the native data type into a common format for each of the various parties to analyse.

The fast data conversion and it's uploading to the various parties is an important aspect of the emergency response. It would be a step forward, if there was a standardised gas sample format that each of the various gas monitoring systems could export their data into. A standardised gas sample format would reduce data handling errors, scaling errors, conversion errors and speed up the generation of reports for third parties.

The emergency management system software used by the mine to store the events, actions, tasks and data relating to the incident would be improved by having a regularly updated summary of the important gas information. The running summary would allow the mine worker coming onto shift to quickly see an overview of incident and its current status. The information and directions handed over at the end of shift, if misunderstood, can quickly lead to undesired events, hence an easily assessable running summary could reduce potential misunderstandings and well as keep everyone up to date on the incident.

## **CONCLUSIONS**

This review has not included the data from hand held instruments and gas chromatographs or the correlation of GC data to tube bundle data. Gas monitoring is at the forefront of ensuring that gas hazards are under control and it is safe to be underground. There were two serious spontaneous combustion incidents in 2018, one in NSW and one in Queensland and both states saw an increasing trend in the reporting of high potential incidents relating to gas concentrations in particular methane in longwall panels. The prescribed limit for CH<sub>4</sub> in Queensland is in the process of being reduced to 2% from 2.5%.

It is therefore critical that underground coal mines have reliable and accurate gas monitoring systems with data that is readily accessible for trending and interpretation. The paper has discussed some of the issues faced in the installation and maintenance of the system and the data handling and interpretation therefore the authors recommend that:-

1. Suppliers should of tube bundle systems review their designs to see how they compare with the requirements of the National Coal Board publication The Tube Bundle Technique for the Continuous Monitoring of Mine Air
2. Suppliers of tube bundle systems should review their designs for practical application underground i.e. different colours in bundles and marshalling panels that do not have low points in them are two examples.
3. Mine sites should take note of the information contained in the National coal board publication The Tube Bundle Technique for the Continuous Monitoring of Mine Air when ordering tube bundle systems.
4. Mine site electricians should be trained in the correct calibration process for real time monitors and consideration be taken for a dedicated team of maintenance electricians to report directly to the mine ventilation officer.
5. Mine sites should review their data storage protocols and increase data storage intervals when gas values exceed a pre-described amount.

6. Mine sites need to establish a protocol whereby internal and external experts have access to the gas data to provide support during incidents and emergencies
7. Graphing packages should show the peak values for the selected time range and graphing protocols need to be amended to reflect this requirement.
8. A common files interchange system needs to be developed to allow the sharing of mine gas data and enable the development of situation reports in mine emergency response systems.

#### REFERENCES

- Chamberlain, EAC, Donaghue, WR, Hall, DA Scott, C 1971, 'The continuous monitoring of mine gases: the development and use of a "tube bundle" technique', presented at a *General Meeting of the North England Branch of the Institution of Mining Engineers*, Newcastle upon Tyne, 5 August 1971 (Published in *The Mining Engineer*, vol. 133, March 1974, pp. 239-251).
- Coal Mine Safety and Health Regulation 2017* (Queensland, Australia).
- Lyne, B 1996, *Approved Standard for the Use of Gas Monitoring Systems QMD 96 7398*, Queensland DME, Queensland, Australia
- National Coal Board, 1977. *The Tube Bundle Technique for the Continuous Monitoring of Mine Air*, National Coal Board, London.
- Recognised standard 09. *The monitoring of sealed areas (2009)* (Queensland Australia).
- Standards Australia 1009. *Explosive atmosphere classification of areas-Explosive gas atmospheres* (IEC 60079-10.1,Ed.1.0(2008) MOD). ASNZS 60079-10.1 2009 SAI Global Limited.
- Standards Australia 2018. *Electrical equipment for coal mines - Maintenance and overhaul, Part 3: Maintenance of gas detecting and monitoring equipment*, AS 2290.3-2018, SAI Global Limited.
- Windridge, F. W., Parkin, R.J., Neilson, P.J., Roxborough, F.F. Ellicott, C.W. 1996. *Report on an Accident at Moura No. 2 Underground Mine on Saturday, 7 August, 1994: Wardens Inquiry*, Queensland Government, and Brisbane, Australia.
- Work Health and Safety (Mines and Petroleum Sites) Regulation 2014 (2014-799)* NSW Australia.

# **OXYGEN DEFICIENCY IN GRAHAM'S RATIO, EVALUATION**

**Snezana Bajic<sup>1</sup>, Sean Muller<sup>2</sup>, Mladen Gido<sup>3</sup>**

*ABSTRACT:* There are a number of indicators used to determine the level of coal oxidation in underground coal mines. The common indicator Graham's ratio is the amount of carbon monoxide produced in proportion to the amount of oxygen consumed by the coal. The more carbon monoxide produced relative to the oxygen consumed (oxygen deficiency), the greater the intensity of the coal's reaction. Graham's ratio is often used as a trigger for Trigger Action Response Plans (TARPs) for the management of spontaneous combustion. This emphasises the importance of accurate measurement of oxygen deficiency and ability to successfully determine the status of underground atmosphere. Samples with a similar composition to air may return a negative or minuscule measured oxygen deficiency unsuitable for Graham's ratio. The same problem is identified in samples diluted with seam gas or when there are inaccuracies in other measured components when nitrogen is calculated by difference.

If the oxygen deficiency is inadequate and insufficient, the Graham's ratio result can be overestimated and trigger a TARP level. If the minimum oxygen deficiency is set to inadequate level, in order to avoid alarm "fatigue", there is a concern that valid data may be excluded from interpretation. The optimal value which indicates the beginning of spontaneous combustion event is site specific. This paper will present the case studies where the oxygen deficiency minimum limit has been adjusted to suit the mine site actual real data and analysis technique.

## **INTRODUCTION**

Australian legislation is processed based legislation where mines are encouraged to manage and monitor their own risks. The mining companies achieve this through internally developed systems and processes, which effectively reduce the risks to acceptable levels. Spontaneous combustion is regarded as principal hazard in Queensland mines. Mines Principal Hazard Management Plan (PHMP) must identify the risks associated with principal hazards. To enable this identification TARPs are established, which outline trigger points at which action must be taken to prevent any incident from escalating (Cliff, Watkinson and Brady, 2018). Graham's ratio is often used as a trigger for TARPs for the management of spontaneous combustion. This emphasises the importance of accurate measurement of oxygen deficiency and ability to successfully determine the status of underground atmosphere. If the oxygen deficiency is inadequate and insufficient, the Graham's ratio result can be overestimated and trigger a TARP level. If the number of these false alarms is large, it can affect Control Room Operator (CRO) fatigue and introduce another risk of missing important non-false alarms.

As mentioned in Muller, et al., (2017), raw carbon monoxide concentrations are not always indicative of the intensity of a heating due to dilutions or accumulation of gases. By comparing carbon monoxide generated to oxygen deficiency a more relative measurement can be made (Graham's ratio). This measurement is independent of air flow and various forms of the equation account for dilution effects (Cliff, Hester and Bofinger, 1999). In order to incorporate

---

<sup>1</sup> Technical services Manager, Simtars, [snezana.bajic@simars.com.au](mailto:snezana.bajic@simars.com.au); ph +61 475 808 493

<sup>2</sup> A/Senior Analytical Chemist, Simtars, [sean.muller@simars.com.au](mailto:sean.muller@simars.com.au); ph +61 447 202 238

<sup>3</sup> Control Systems Engineer, Simtars, [mladen.gido@simars.com.au](mailto:mladen.gido@simars.com.au); ph +61 477 718 027

the initial gas readings, and to incorporate nitrogen by difference to include effects of dilution, the following equation is applicable:

In order to incorporate the initial gas readings, and to incorporate nitrogen by difference to include effects of dilution, the following equation 1 is applicable:

$$\text{Graham's Ratio} = \frac{100 \times (\text{carbon monoxide}_{\text{final}})}{(0.265 \times \text{nitrogen}_{\text{final}}) - \text{oxygen}_{\text{final}}} \quad (1)$$

Note that the constant 0.265 is simply the theoretical ratio of oxygen to nitrogen in air. In order to incorporate the initial gas readings, and to incorporate nitrogen by difference to include effects of dilution, the following equation 1 is applicable:

$$\text{Graham's Ratio} = \frac{100 \times (\text{carbon monoxide}_{\text{final}})}{(0.265 \times \text{nitrogen}_{\text{final}}) - \text{oxygen}_{\text{final}}} \quad (1)$$

is commonly used to calculate GR on real time sensors underground. The assumptions in this instance are that the ratio between oxygen and nitrogen in the inlet stream is the same as in fresh air, and that inlet contains no carbon monoxide. This is not applicable for inlet stream that is depleted in oxygen, enriched in carbon monoxide or enriched in nitrogen.

It is very important for a mine to establish a database for its deposit individual conditions. Using a measured fresh air value and taking dilution into account is represented by equation 2;

$$\text{Graham's Ratio} = \frac{100 \times \left( \text{carbon monoxide}_{\text{final}} * \frac{\text{nitrogen}_{\text{final}}}{\text{nitrogen}_{\text{initial}}} \right) - \text{carbon monoxide}_{\text{initial}}}{\left( \text{oxygen}_{\text{initial}} \times \frac{\text{nitrogen}_{\text{final}}}{\text{nitrogen}_{\text{initial}}} \right) - \text{oxygen}_{\text{final}}} \quad (2)$$

Equation 2 is a common equation used to calculate Graham's ratio for tube bundle monitoring points in underground coal mines. The measured fresh air point is typically from a point on the surface at the tube bundle building, or from an intake roadway underground. More detailed explanations are presented in Muller, et al., (2017).

As oxygen cannot be generated underground, it is logical that final oxygen can never exceed initial oxygen. Analysing equipment has a typical tolerance of +/- 0.2 % and small error is expected, which occasionally could present higher final oxygen readings than initial oxygen readings. Negative oxygen readings will produce negative Graham's ratio, which is impossible result.

Muller, et al., (2017) states that current practice in mines is to apply the minimal oxygen deficiency requirement of 0.3 %, which eliminates the majority of non-reliable data points. Brady (2007) stated that Graham's ratio can be unreliable for oxygen deficiencies below 0.3 %. Strand and MacKenzie-Wood (1985) state that the calculation is subject to analytical limits and that oxygen deficiency of less than 0.2 % would introduce gross errors. As the technology advanced since 1985, it is now possible to investigate, with greater confidence, the threshold value for this equation.

Investigation performed in Muller, et al., (2017) indicated that an oxygen deficiency of less than 0.3 % may still be reliable in some situations and generate critical data for underground air monitoring.

## METHODOLOGY

As per conditions set in Muller, et al., (2017), the minimum oxygen deficiency value selected was 0.05 %, as this value appears to be the lowest and most conservative value. Data in the form of tube bundle logs were obtained from gas monitoring software. These logs were obtained from two underground coal mines in Australia, all of which had previously experienced and



flagged invalid Graham's ratio triggers in their alarm logs and had their filter threshold points were set to 0.05 %. The locations containing low oxygen deficiencies (around 0.5 % or less) were chosen for the study. Each relevant data log was extracted to a Comma Separated Values file (CSV) containing the following information:

- Date and time of measurement and monitoring point number (location)
- Methane, Carbon Monoxide, Oxygen and Carbon Dioxide concentrations (%)
- Carbon Monoxide Make (Litres per minute)
- Graham's ratio - calculated.

As per Muller, et al., (2017), in addition to these gas components, the Graham's ratio calculated from the gas monitoring software, as per industry standards, was extracted with each set of gas readings. The CO value correlating with each data measurement was also extracted. These extracted data logs were processed in order to calculate a theoretical oxygen deficiency and theoretical Graham's ratio values based on fresh air as the initial readings for real time data, and fresh air point for tube bundle data. For several tube bundle locations the measured initial air values were used rather than the theoretical initial values. This allowed the Graham's ratio calculation to be replicated as accurately as possible, reproducing the actual values calculated by the mine site monitoring system before extraction. Locations processed in this regard were compared to locations processed using theoretical air values, as a means to validate extrapolation of the theoretical data.

The calculated Graham's ratio value for each measurement was categorised based on the following thresholds:

- Normal data was defined as any data with corresponding theoretical Graham's ratio calculated at 0.2 or below. This range is often used as normal conditions for spontaneous combustion management TARPs in Queensland mines (Mines Rescue Gas Detection and Emergency Preparedness, 2014).
- Investigate data is defined in this testing as any data with theoretical GR's calculated at 0.2 to 0.4. This range is often used as an 'investigate' trigger for spontaneous combustion management TARPs in Queensland mines (Mines Rescue Gas Detection and Emergency Preparedness 2014).
- An invalid trigger is defined as any data with theoretical Graham's ratio calculated at over 0.4 without a corresponding significant increase in carbon monoxide or CO make.
- A valid trigger is defined as any data where the theoretical Graham's ratio is calculated at over 0.4 with a corresponding significant increase in raw carbon monoxide or CO make associated with the data. By definition any Graham's ratios over 0.4 which are not valid triggers are considered invalid triggers.

Filtering of tube bundle and real time data sets were based on minimum oxygen deficiency set points. Overall data retention, retention of normal data, investigate data points removed, invalid data points eliminated and valid data points eliminated were evaluated for each filtered data set.

## **RESULTS AND DISCUSION**

Two mines presented data for a three month period. The locations investigated in this paper were selected based on feedback from each mine. The locations showed the need to adjust applied filters in order to reduce control room operator alarm fatigue.

In the real time data set presented in Figure , the mine experienced large quantity of RG alarms, as the filter applied in that location was  $O_{2i} - O_{2f} \geq 0.3$  % filter, ( $O_{2i}$  is oxygen initial and  $O_{2f}$  is oxygen final). Around 20<sup>th</sup> January, (note dates have been adjusted for confidentiality

purposes), the GR values exceeded 1 and triggered TARPs at the mine. Figure presents the same data set pre and post time when oxygen deficiency filter 0.05 % was applied. This filter, although conservative, removed the majority of invalid high triggers.

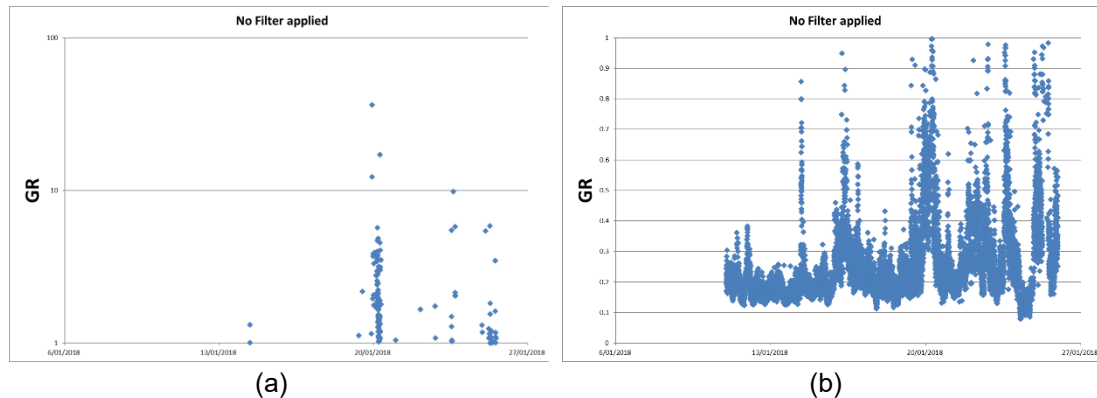


Figure 1: Case study, mine 1, Graham's ratio (no oxygen deficiency filter (a) logarithmic scale, (b) values between 0-1 GR)

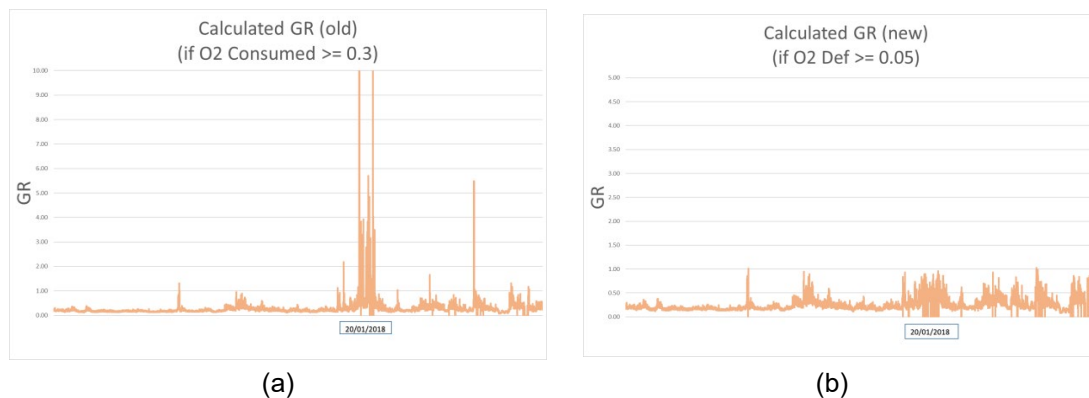


Figure 2: Case study, mine 1, Graham's ratio ((a)  $O_{2i} - O_{2f} \geq 0.3$  % filter, (b) oxygen deficiency filter 0.05 %)

In Figure , various filters were applied to investigate the most appropriate filter for this situation. Although the normal data retention was 100 %, 0.05 % filter did not achieve the reduction of invalid triggers. With the application of 0.2 %, 0.25 % and 0.3 % filters in oxygen deficiency, all suspect invalid data points were removed, while the retention of normal data points was 99.9 % for 0.2 % filter and 74.6 % for 0.3 % filter. The 0.2 % filter achieved a 42.89 % reduction in suspected invalidated triggers, while retaining 68.7 % of data points.

Similar to the mine 1 results, the tube bundle data set from mine 2 indicated that no filter application, if  $O_{2i} - O_{2f} \geq 0.3$  %, would result in false trigger alarms as in Figure a. With the application of 0.05 % filter on oxygen deficiency, these false alarms would be removed as in Figure b (around 23/08/2017).

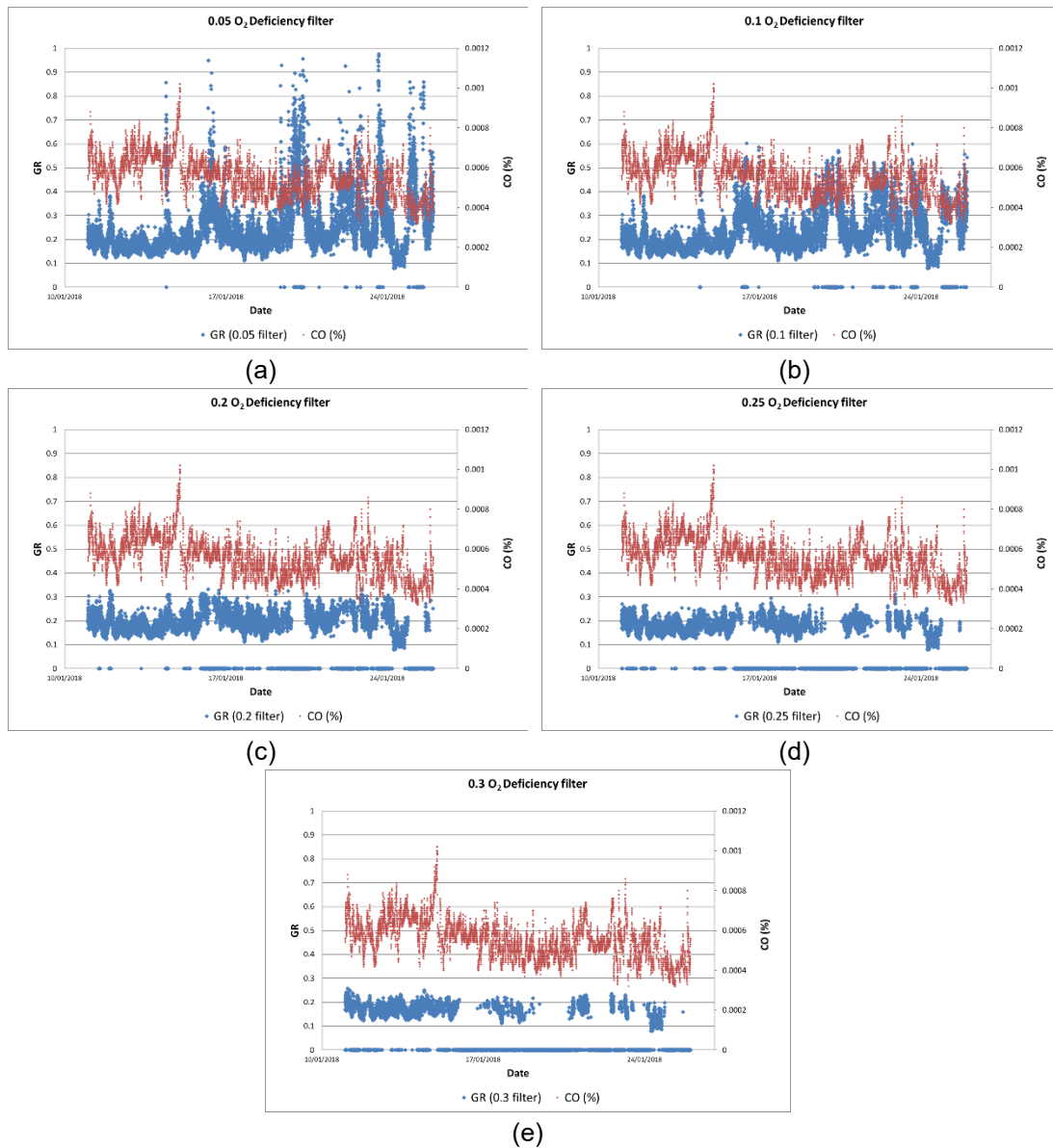


Figure 3: Case study, mine 1, Graham's ratio (applied oxygen deficiency filter (% 0.05 (a), 0.1 (b), 0.2 (c), 0.25 (d) and 0.3 (e)), with CO (%)

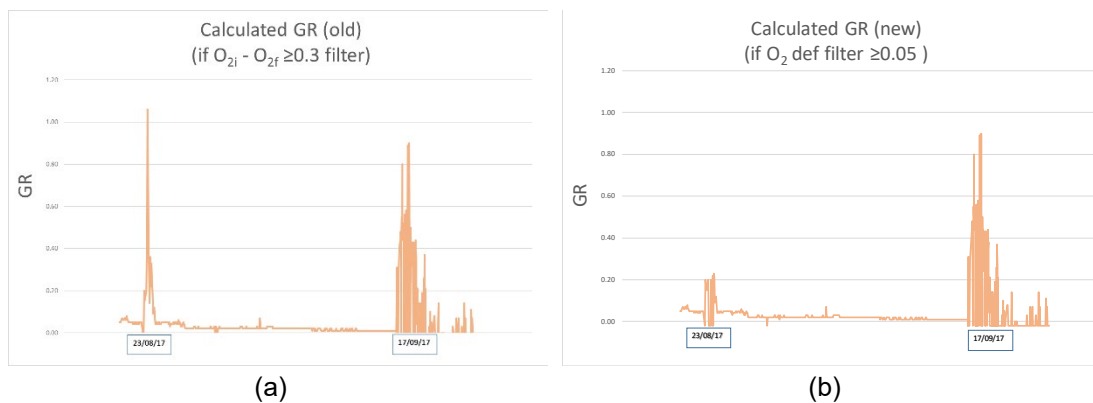


Figure 4: Case study, mine 2, Graham's ratio ((a) O<sub>2i</sub> - O<sub>2f</sub> ≥ 0.3 % filter, (b) oxygen deficiency filter 0.05 %)

There will however remain few false alarms. If higher filters were applied (0.2 % and above) there would be no invalid triggers in the end of June period. The mine investigated this instance and confirmed that GR alarm values were invalid triggers, period around 23<sup>rd</sup> August 2017, and there were no corresponding significant increases in CO or CO Make. The mine then accepted the 0.05 % filter change for this location. Furthermore, in period between 15<sup>th</sup> and 23<sup>rd</sup> of September, over 30 GR alarms were noted. The 0.05 % filter included these values and the mine investigated the situation. In this case there was an increase in CO and CO make, confirming valid triggers in GR ratios. If higher filters were applied in this case there would have been the possibility of valid data loss. Filter 0.1 % would still remove 100 % of invalid data, and retain 89.20 % of valid triggers, while higher filters, 0.2 % and above, would remove 100 % of valid triggers from this period (Figure ). Reduction of suspected triggers “investigate” is optimised with a 0.1 % filter (85.79 %), while a 0.05 % filter only reduces 54.64 % of suspected “investigate” data points.

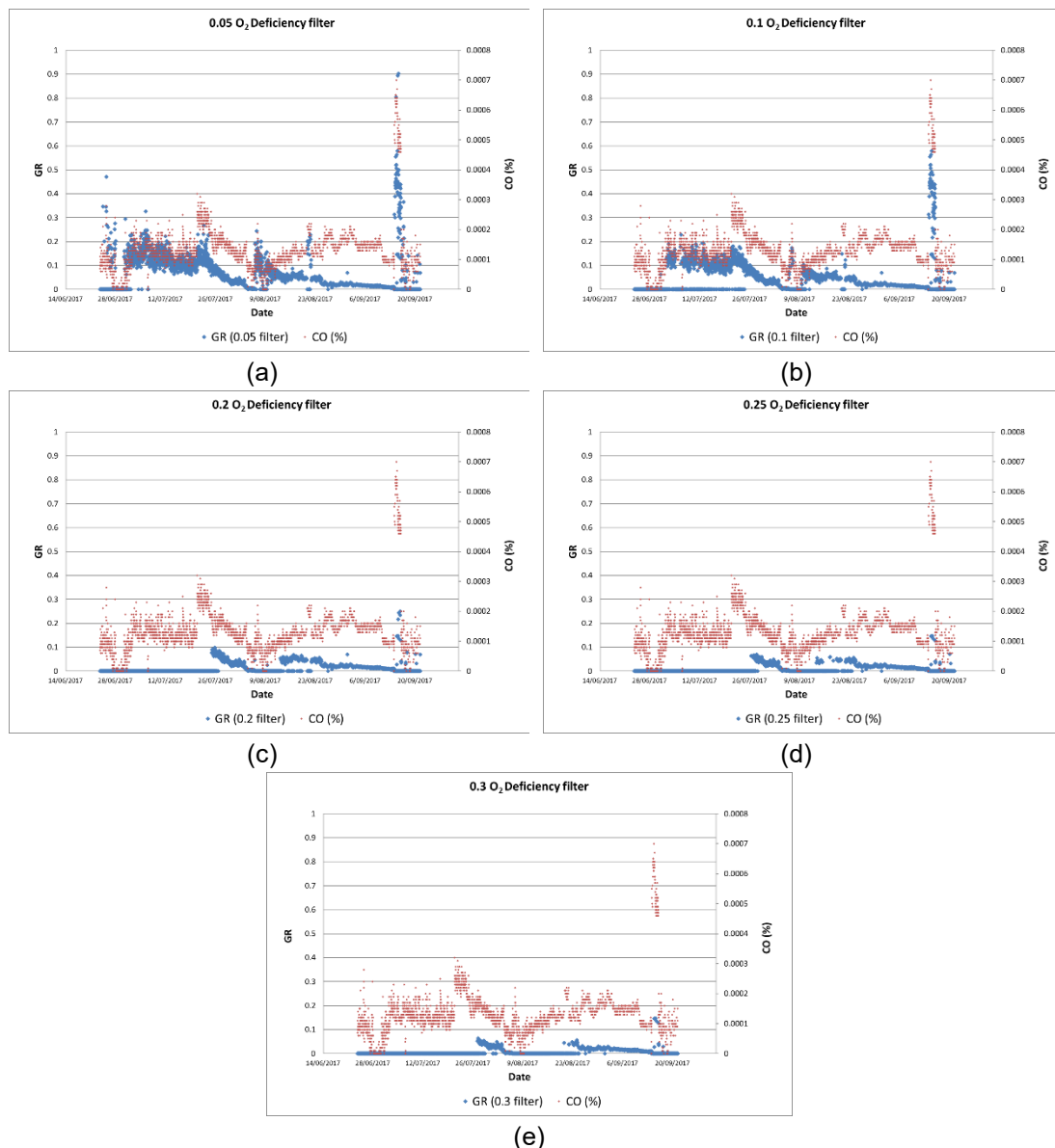


Figure 5: Case study, mine 2, Graham’s ratio (applied oxygen deficiency filter (% 0.05 (a), 0.1 (b), 0.2 (c), 0.25 (d) and 0.3 (e)), with CO (%)

## CONCLUSIONS AND RECOMMENDATIONS

The optimal oxygen deficiency filter is most likely dependant on mine deposit, individual database and measurement technique (instruments). It is possible that different locations may require different filter points. CO and CO Make filter could be considered as addition to oxygen deficiency filter for GR ratio trigger alarm. These parameters could also be included in TARPs together with Graham's ratio. It is clear, based on presented data that different measurement techniques had different optimal filter points. Further testing and investigation is required for optimal alarm threshold points. It is possible that a 0.05 % filter for tube bundle, as suggested previously, is too conservative for this application and that 0.1 % or higher values may be more appropriate. Based on presented data set, the threshold value of 0.05 % did not appear optimal. However, the number of false alarms was considerably reduced and no positive alarms were removed by using a 0.05 % filter.

## ACKNOWLEDGMENTS

Simtars would like to acknowledge mines who agreed to provide data for this research. All data remain confidential and are used for research purposes only.

## REFERENCES

- Brady, Darren 2007. "The Influence Analytical Techniques and Uncertainties in Measurement Have on the Assessment of Underground Coal Mine Atmospheres." Paper presented at the Queensland Mining Industry Health and Safety Conference.
- Cliff, David, Colin Hester and Carmel Bofinger. 1999. *The Interpretation of Mine Atmospheres particularly for Spontaneous Combustion, Mine Fire and Explosions*. Redbank: SIMTARS.
- Cliff, David, Martin Watkinson and Darren Brady. 2018. *Spontaneous Combustion in Australian Coal Mines* edited by Simtars. 2018 ed. Brisbane: Simtars.
- Mines Rescue Gas Detection and Emergency Preparedness*. 2014. edited by Murray Bird.
- Muller, Sean, Larry Ryan, Hollyer Jeremy and Snezana Bajic. 2017. "Review of Oxygen deficiency requirements for Graham's ratio." Paper presented at the Coal 2017, Wollongong
- Strand and MacKenzie-Wood. 1985. "A Manual on Mines Rescue, Sfaety and Gas Detection", edited by CSM Press.

# RECENT CASE STUDIES USING THE REMOTE ROCSIL® FOAM PLUG SYSTEM

Neil Alston<sup>1</sup>, Jean-Luc Schmitter<sup>2</sup>, Andrew Alcott<sup>3</sup>, Russell  
Fry<sup>4</sup>

**ABSTRACT:** ROCSIL® FOAM is a versatile product that has been successfully used to rapidly seal mines or critical areas of the mine directly in-seam or remotely via boreholes or shafts. The product is chemically stable, fire resistant, fast setting, has high expansion and excellent self-supporting characteristics making it an ideal product for these types of applications. It can also be used on sloping ground and with mine services such as conveyor structure or pipes remaining in-situ to form effective plug seals. For remote sealing, special mixing heads are designed to effectively deliver the product into mine roadways or shafts without the need for labour to be deployed underground or when exclusion zones are in place on the surface. This paper will describe the remote head technology, system development and process via a number of case studies where the remote sealing system was successfully used. Each case required novel techniques to meet particular mine constraints. Once the critical mine event is under control, the plug can be easily removed to facilitate safe re-entry of the mine. The remote ROCSIL® FOAM plug seal system is a world-class innovation available to deal with underground explosions, heating or fire events in a safe, cost-effective and rapid way.

## INTRODUCTION

Mine fires are fought indirectly when access to the fire zone is impossible because of safety reasons, blocked underground access, a limited supply of available firefighting materials and a fire zone that is too large for available underground personnel. This approach involves sealing the mine or construction of in-mine temporary seals (ventilation-control structures, hereinafter referred to as mine seals) to isolate the fire area. These in-mine seals can be constructed from within the mine or remotely through boreholes. Sealing the mine or isolating the fire area is designed to control or extinguish the fire by reducing the oxygen concentration in the mine atmosphere to a level that will not support combustion.

## THE BENEFITS OF REMOTE PLUGS IN EMERGENCY SITUATIONS

Preventative applications provide the most favourable option for clients with current mining regulations requiring *in situ* provision of remote sealing of mine operations. This can be achieved by placing a mixing gun and two flexible hoses at an accessible point in the roof of selected roadways. The product can be applied from surface to seam using a high-volume delivery pump attached to the pre-installed hoses. The product pods are connected in the event of a potential incident from a safe location, pumped from the surface until it expands to the roof and ribs forming an airtight barrier as shown in Figure 1.

- 
1. Business Development Manager, Quarry Mining, Email: [neil.alston@quarrymining.com](mailto:neil.alston@quarrymining.com) Tel: +61 409 809 415
  2. Technical Director, Weber Mining Group. Email: [jeanluc.schmitter@weber-mining.com](mailto:jeanluc.schmitter@weber-mining.com) Tel: +33 672 886 909
  3. Sales & Marketing Manager, Mastermyne. Email: [andrew.alcott@mastermyne.com.au](mailto:andrew.alcott@mastermyne.com.au) Tel: +61 437 329 443
  4. Business Development Manager, Mastermyne. Email: [russell.fry@mastermyne.com.au](mailto:russell.fry@mastermyne.com.au) Tel: +61 409 346 692

In certain emergency situations, shuttering is constructed underground by an emergency team and filled with foam to create an airtight barrier. In incidents where this is not possible, the application head can be lowered into the seam via a borehole with the foam being placed remotely without shuttering. Foam consumption is higher as there is no formwork to contain the products' expansion, but it provides a crucial option requiring no personnel underground should an exclusion zone be in place. Remote pumping provides a much safer alternative than emergency crews building formwork and has been the only methodology employed by Wilson Mining (WM) in the installation of these seals in Australia.

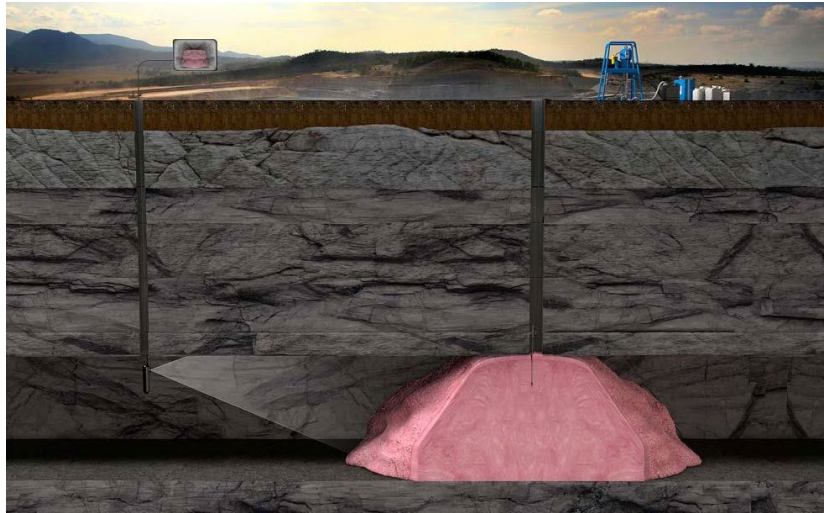
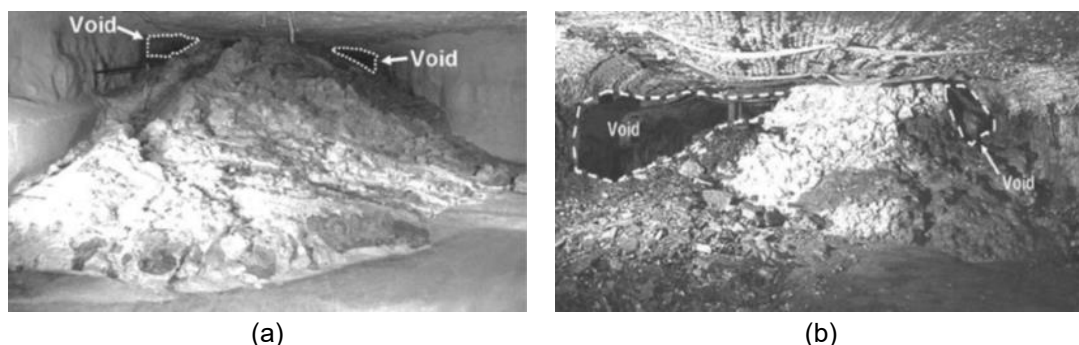


Figure 1: Example of a surface to seam setup

Whichever method of remote sealing is chosen, using ROCSIL® FOAM in this manner provides a fast and simple solution. The seal integrity is maintained during any convergence experienced, with the matrix consolidating on its own due to its expansion properties. (Trevits and McCartney, 2008).

#### WHY ROCSIL® FOAM PHENOLIC FOAM

By design, the chosen seal material is supposed to flow and completely fill the mine roof-rib interface. Depending on the product used, however, this methodology is not always successful. The underground observations of remotely installed cementitious mine seals in Figure 2 (a and b) show that certain materials often do not fully close the mine opening.



Figures 2: Cement-based remotely installed mine seal

If a mine seal does not completely close the opening, then oxygen inflow cannot be stopped, which can lead to growth or further expansion of the fire. Mine seals that do not completely close the mine opening may be used to restrict or control the amount of air or inert gas that passes in or out of a fire area, depending on the size of the remaining open area in the seal.



ROCSIL® Foam is a LOBA (Arnsberg) and Mines Safety and Technology Centre approved phenolic resin introduced into the Australian coal mining industry in 2002. Since its introduction, WM have completed over 1300 successful applications in underground coal mines in Australia and New Zealand. Although ROCSIL® FOAM is most commonly known for the consolidation of longwall and development roof cavities, it has many other applications, including:

- Rapid underground sealing of mine roadways (Vent plug)
- Remote sealing of mine roadways via surface boreholes
- Vent plug installation on longwall faces to restrict ventilation from entering the goaf
- Sealing of underground heating and mine fires

The characteristics that makes ROCSIL® FOAM ideal for remote plugs is that it is chemically stable, fire resistant and has a high expansion rate. It has a fast setting time, excellent self-supporting characteristics with ability to form around complex infrastructure such as conveyors, making it ideal for forming remote plugs. Figure 3 is an illustration of a typical installed seal utilising formwork.

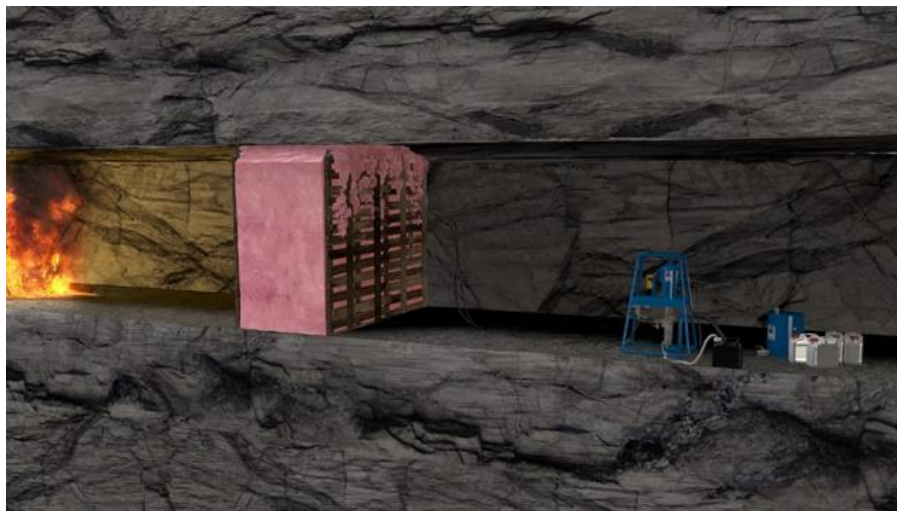


**Figure 3: Example of ROCSIL® FOAM seal with formwork**

### **A LONG HISTORY OF LESSONS – EARLY CASE STUDIES**

The first remote plug seals in Australia were undertaken by WM as early as 2003 at Southlands Mine to provide a plug for their longwall heating event. Previous applications had been undertaken in both France and USA, with Weber Mining playing a crucial role in developing this technology and partnering with WM in developing and improving these systems over the last 16 years.

Since Southlands in 2003, WM have completed remote emergency seal projects at Newlands in 2007, Blakefield South in 2011, Pike River in 2011 and 2019 and a QLD Operation 2019. Over this 16-year period, many refinements and much experience has been learned and developed, with WM offering extensive experience in the safe and effective application of remote and surface to seam plug seals using phenolic foams.

### THE IMPORTANCE OF REMOTE HEAD TECHNOLOGY

The most important consideration in the safe and effective remote installation of ROCSIL® FOAM is maintaining the correct mixing ratio. The correct mixing ratio is essential to provide the appropriate foaming characteristics to appropriately seal the roadway and to ensure the correct mechanical properties as shown in Figure 4.

In many instances, WM have had to 'pump blind'. This is where there has been no provision to lower a camera into adjacent boreholes to monitor the quality of the installed product. WM have invested significant efforts into developing the remote head that provides peace of mind when pumping remotely without visibility on the outcome.

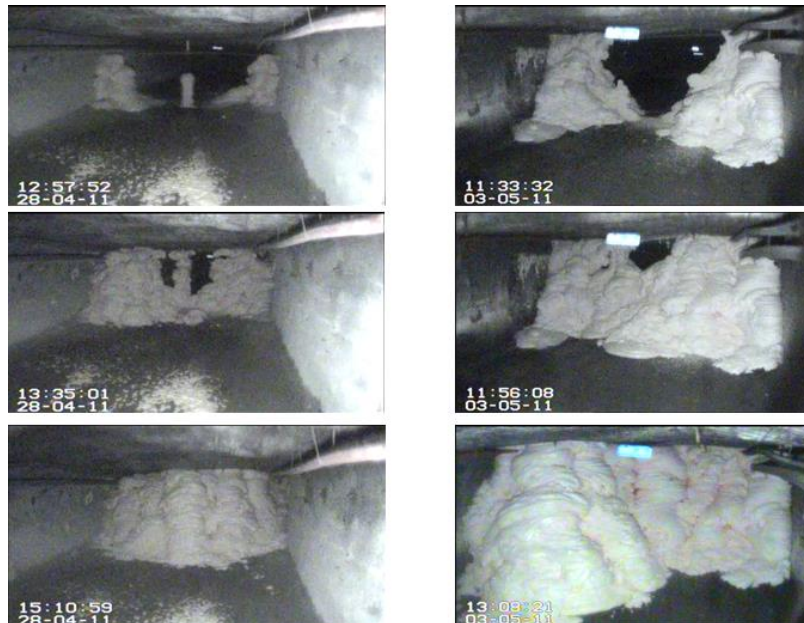


**Figure 4: Remote ROCSIL® FOAM plug seals installed at Blakefield South in 2011**

A considerable amount of pressure is exerted by the product at the mixing head during operations, especially those with a high depth of cover. As the Part A and Part B of the ROCSIL® FOAM has different densities, maintaining correct ratios is critical as this can have significant impacts on the technical properties of the foam. Designing a mixing head (Figures 5 and 6) that controls the back pressure and maintains consistent mixing ratios has been a key development of the WM business.

Product components need to be contained inside the delivery lines while the pump is switched off, therefore valves have to cope with pressure exerted to prevent overflow and clogging of the mixing head. In balance, they have to be sufficiently versatile to open once the pumping commences and product is mixed and delivered through the head.



**Figure 5: Mixing head internal**



Figure 6: Mixing head body 130mm diameter

## RECENT CASE STUDIES

### Case study 1 – Pike River Mine

The Pike River Recovery Agency (PRRA) was tasked with the recovery operation of the Pike River Mine, located 46 kilometres northeast of Greymouth as shown in Figure 7, following the coal mining incident that began on 19 November 2010. At the time of the incident thirty one miners and contractors were present in the mine. Two miners managed to walk from the mine, the remaining sixteen miners and thirteen contractors were believed to be at least 1.5 kilometres from the mine entrance.

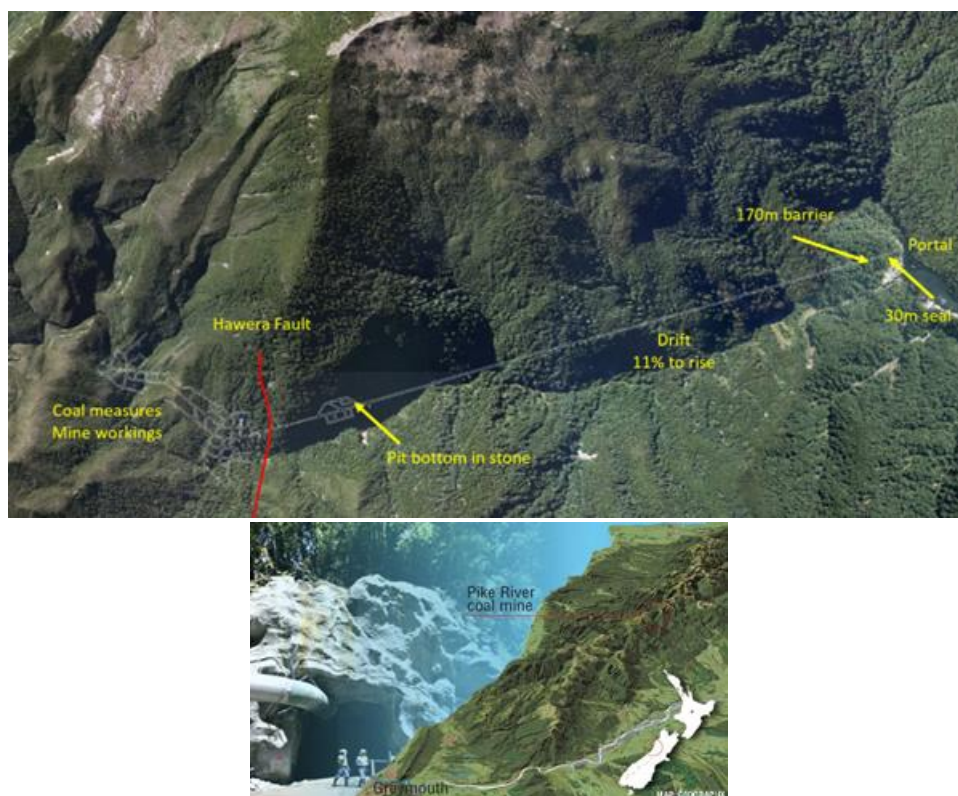
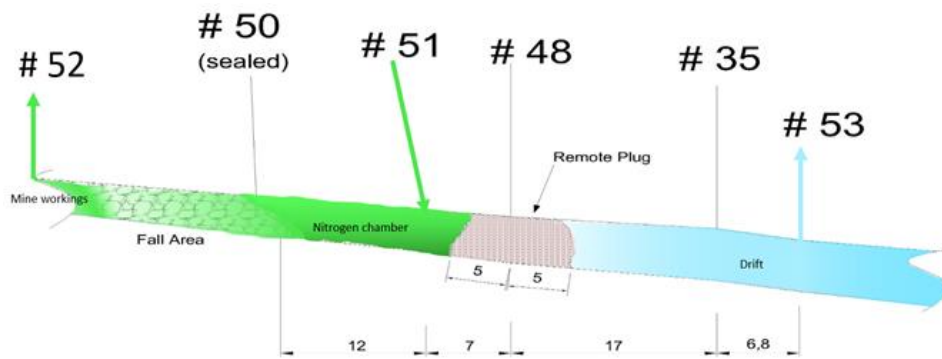


Figure 7: Pike River Mine location (Inset) and aerial image of drift location

WM were contracted to install a remote ventilation plug seal down the 102 m # 48 borehole at the head of the drift as shown in Figure 8. The plug is a key ventilation control measure for the recovery of the mine, allowing forensic teams to recover the bodies of the deceased that remain within the mine. The plug provided a seal between the nitrogen filled mine workings on one side and the fresh air to be pumped through borehole # 53 to allow access back into the drift, (Te Kahui Whakamana Rua Tekau Ma Iwa, 2019 a and b).





**Figure 8: Ventilation Plug in the Drift**

The remote location of the worksite at Pike River Mine required logistics to be well planned both in advance and throughout execution. Aside from equipment, personnel and product being shipped from Australia, the remote work site was accessible by helicopter only (Figure 9).



**Figure 9: Remote worksite helicopter access (inset bundled product and pump pod)**

Weather conditions were challenging with a highly variable climate. The product was being shipped from the warmth of Australia to the extreme cold where it was to be applied. Maintaining temperatures is critical in the safe application of phenolic foams as too low temperatures can affect product mixing at the head and reduce expansion. To ensure the quality of application for such a critical project, WM utilised reverse cycle air-conditioned containers to cool the material down when in Australia and then warm up the product before it was flown to the work front. Once there, a heater was rigged to ensure correct product pumping temperature was maintained.

WM maintain high environmental standards at all times, but in this case the work front was in a National Park, requiring the highest level of controls. Through the entirety of the project, fully bunded equipment was used to contain any possible spill. The installed plug was tested to prove that it had the required resistance to keep the chamber between the plug and the roof fall full of nitrogen with no oxygen ingress. It also provided enough resistance to ensure the

nitrogen could flow out of the chamber and into the old mine workings past the rock fall. Testing proved positive to the required resistance allowing PRRA to continue the recovery operation.

### **Case study 2 – Queensland Mining Heating Event 2018**

In September 2018, WM assisted a mine in Queensland combat an underground heating event. This involved the rapid installation of temporary seals into mine roadways, drifts and mine fan using novel remote application methods. The requirement of the project was initially to isolate the longwall heating event. As the event escalated the requirements changed to mine sealing then progression to segregation of mine workings into zones. The purpose at each stage was essentially to control or extinguish the fire by reducing the oxygen concentration in the mine atmosphere to a level that would no longer support combustion.

Starting at the tailgate chute road in the recently active longwall panel, Zone E, shown in Figure 10, all headings had two ROCSIL® FOAM plugs installed with a cementitious plug in between. Once Zone E was segregated, WM progressed through all headings in the mains with ROCSIL® FOAM plugs to create Zone D, then another line of plugs to create Zone C and so forth through to Zones B and A.

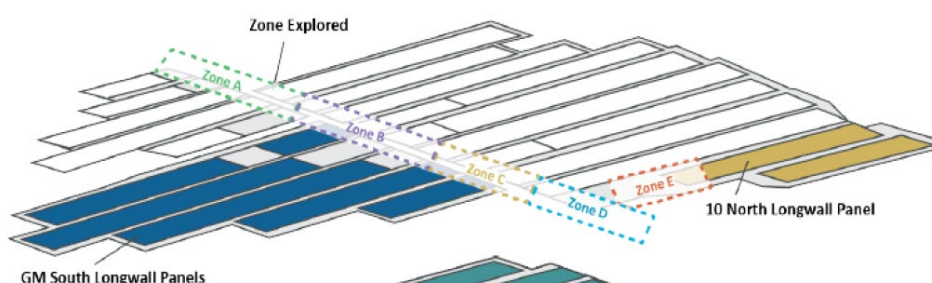


**Figure 10: Underground treated active mine zones**

Given the scale and varying requirements of each plug, the project provided numerous challenges to the WM Operations Team. The project was an active underground heating event, requiring a quick response to minimise damage and maximise recovery. With exclusion zones in effect and no underground access available, WM utilised remote control machinery where possible.

With insufficient time to drill another borehole, only one borehole was available from surface to seam pumping. With no second borehole in proximity for a camera, WM were unable to observe plug construction. As a result, several boreholes were 'pumped blind' using the WM operational expertise from previous projects.

In addition, there was no casing on the lower 15 m of the boreholes as well as mesh and cable bolt obstructions. This prevented the mixing heads being able to be lowered into the roadways at certain boreholes. In these instances, where no suitable boreholes were available nearby they were re-reamed to ensure clear access for the mixing heads. There were also occasions of bore holes being drilled at an angle to contend with power lines in close proximity. For the sealing of the drifts at 1:4 and 1:7 grade decline, ROCSIL® FOAM was pumped building on itself to form a plug with no formwork. The fact that ROCSIL® FOAM fills in, under and around structure was essential to form seals where there was existing infrastructure such as the vent fan above the upcast shaft or around conveyor systems.

The checks performed post construction proved that each seal, even those pumped blind, provided excellent sealing (Figure 11). Many of the seals had been in place for in excess of eight months had minimal deterioration and no leakage. Each seal was subject to different conditions, including a pressure differential of approximately 3000 Pa between zones and

holding 2 m head of water. The plugs have shown to provide a durable and resistant seal over an extended period.



**Figure 11: Example of a ROCSIL® FOAM seal forming around mine infrastructure**

### **THE FUTURE OF SURFACE TO SEAM REMOTE PLUGS**

#### **Overpressure rated ROCSIL® FOAM seals**

WM engaged Burke Engineering Services and Inducta Engineering to complete a theoretical analysis using finite element modelling to determine the required thickness of a mine plug seal utilising ROCSIL® FOAM, to aid in assessing the feasibility of utilising the product for load rated seals in underground mine applications.

The single analysis for given roadway dimensions and imposed loading, was completed to determine the required plug depth. A preliminary seal thickness based on de-bonding shear failure of the interface between the seal mass and the surrounding roadway was calculated. A value of 16.2 kPa for shear adhesion between the seal mass and the perimeter strata, and a load factor of safety of 1.1 was utilised in the design calculations. This resulted in a preliminary plug depth of 17 m measured at the roof line.

A finite element model utilising three dimensional elements was constructed and pressure loading increased incrementally until the select failure mechanism occurred. In this case the failure mechanism was sliding along the contact surfaces with a maximum principal shear stress of 110 kPa. The surface where the pressure was applied initially deformed, sustaining principle shear stresses larger than 70 kPa, which indicated localised failure in the first third of the seal length. Other elements, deep in the seal, had shear less than 70 kPa at this point in the analysis. Subsequent to this, the bond failed along the contact surfaces. It has been assumed that this failure mechanism is stable. Figure 12 shows the conceptual shear failure mechanism development.

The analysis results were as follows:

- Failure criterion: Drucker-Prager (3D general elastic-perfect plastic yield surface) with control of max principal shear stresses  $\tau_{13} = |G1 - G3|/2$ , (stresses  $\tau_{13} > 70$  kPa are denoted by red dots) (see Figure 13)
- End of non-linear P-Delta analysis (failure): 769 steps, 39 PSI = 268.94 kPa = 5083 kN
- Maximum displacement: 0.85 m (sliding)
- Failure type: sliding along the contact surfaces, with max principal shear stresses in the body 110kPa.

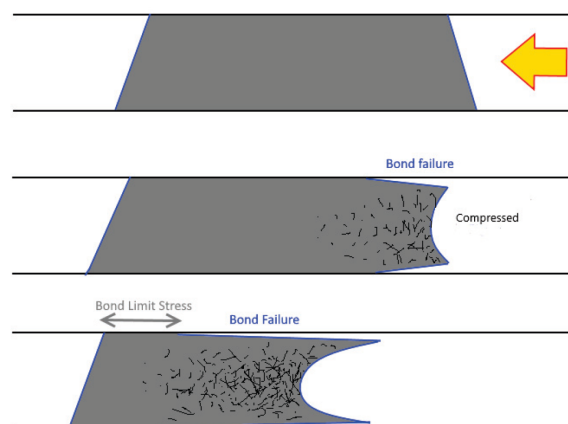


**Figure 12: Conceptual failure mechanism**

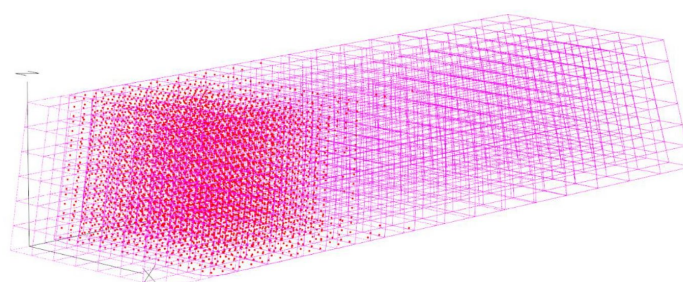


**Figure 13: Principal shear stress failure points (red dots) along length of seal (Loading from LHS)**

The design seal depth of 17m placed into a roadway 5.4m wide x 3.5m high is structurally adequate to resist an imposed pressure load of 35 PSI with a factor of safety of 1.1.

#### **Pre-Installed emergency sealing systems**

In 2019, WM where engaged to provide a permanent remote emergency sealing system in the workings of a coal mine in the Hunter Valley, NSW. This pre-installed system provides a significant time reduction in the event of a mine fire or explosion, allowing remote plug seals to be installed in the best suited location with gas monitoring systems in fixed positions. This installation project is currently in construction phase. The emergency seal system consists of a remote ROCSIL® FOAM head being positioned 30 m inbye of each of the five portal entries. The portal position allows for drone camera technology to monitor the remote plugs whilst pumping is underway.

Each of the remote heads are fed using purpose-built and pre-installed hosing from a single 200mm cased borehole drilled 63.7 m down from the surface. The borehole casing is capped with a customised flanged manifold allowing the hosing to be permanently fixed to the borehole manifold, providing a 120 PSI rating. The borehole is located on the highwall, clear of the expected blast radius in the event of a mine fire or explosion as per mining regulations. The surface and mine infrastructure is designed significantly improve the speed of mobilisation, allowing WM to connect hosing and commence the emergency sealing sequence much quicker in the event of an emergency. Comparative to reactive emergency sealing, pre-installed systems are estimated to reduce plug installation times by 70%. In addition to reducing the speed of installation, pre-installed systems provide numerous additional benefits, including:

- Mine sealing plan designed for optimal outcome
- Remote seal locations in optimum locations



- Pre-installed gas monitoring on inbye side of plug location
- Opportunity to skill workforce in sealing system
- Rocsil quantities known and understood
- Fewer boreholes reduces costs

To further reduce mobilisation time for surface to seam operations or emergency plug sealing, WM are developing a 'Surface to Seam Relocatable Pumping Container' as illustrated in Figure 14. This container has all equipment and consumables ready, and can simply be loaded onto the truck should the requirement for pumping arise. This further reduces the installation timeframe of seals which can be critical during emergency response installations.

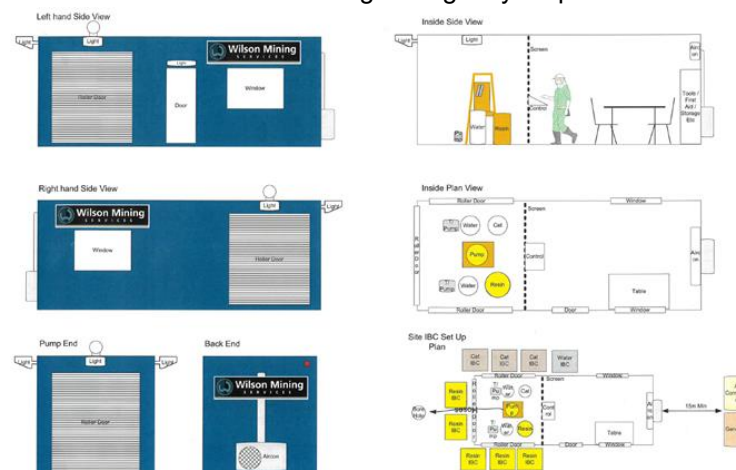


**Figure 14: Surface to seam relocatable pumping container**

### SUMMARY

ROCSIL® FOAM plugs are a proven system for the effective sealing of critical areas of the mine in-seam or remotely via boreholes. The material's rapid setting and high expansion characteristics make it ideal for maximising roof-rib interface and for forming a seal around complex infrastructure. Importantly, WM provide technical expertise and experience to be able to apply the product safely and to a high standard in a wide variety of conditions. They recognise the importance of working with mining operations to provide pre-installed systems to rapidly respond to emergency events as well as the required engineering support in-keeping with legislative requirements.

### ACKNOWLEDGEMENTS

Mastermyne acquired Wilson Mining Services in September 2019 and would like to acknowledge the past and present members of the business who have contributed to the operational and technical expertise that remain at the heart of the business until this day. It would also like to thank those who have contributed to this paper directly and indirectly and for the operations that have agreed for the information to be shared for the benefit of the broader coal industry.

### REFERENCES

- Trevits, M.A. and McCartney, C. (2008). NIOSH-use of ROCSIL® FOAM to remotely construct mine seals p.2, p.5
- Te Kahui Whakamana Rua Tekau Ma Iwa, 2019a. Pike River Recovery Agency, Presentation to "MMAA CPD Seminar Pokolbin" p.13, p.19
- Te Kahui Whakamana Rua Tekau Ma Iwa, 2019b. Pike River Recovery Agency, Remote Ventilation Plug (ROCSIL) p.3

# SELF-HEATING HAZARD INVESTIGATION OF CONVEYOR BELT RUBBER FINES

Basil Beamish<sup>1</sup>, Jan Theiler<sup>2</sup>

**ABSTRACT:** Conveyor belt fires have often been attributed to the heating of accumulated coal fines beneath the belt structure. However, could it be possible that conveyor belt rubber fines produced from friction of the belt in contact with defective rollers or other parts of the belt structure are a self-heating hazard source? The United Kingdom Health and Safety Executive issued a briefing note in December 2012 on the spontaneous heating of piled tyre shred and rubber crumb. This contained information on laboratory experiments that show rubber crumb and tyre shred are more susceptible to self-heating than cellulosic materials (like hay and straw) in conditions of high ambient temperature. No self-heating experiments have been reported for conveyor belt rubber in any form. This paper presents results of adiabatic incubation testing of conveyor belt rubber fines and slack coal fines collected from the immediate vicinity of a recent Queensland underground coal mine conveyor belt heating incident. Incubation test results show that rubber fines generated from conveyor belt friction are able to self-heat from a temperature as low as 84.5 °C. The spongy fibrous form of the rubber fines creates both a high permeability to airflow and a high surface area for oxidation reaction. In addition, the friction mechanism of the conveyor belt rubber fines generation would create an induced temperature required to alter the environmental boundary conditions to the point where self-heating is sustained. When the rubber fines are mixed with slack coal they increase the likelihood of the coal to incubate and create a spontaneous combustion event.

## INTRODUCTION

Clothier and Pritchard (2003) noted that among the materials listed by Bowes (1984) that are susceptible to self-heating and spontaneous ignition, rubber-containing products are conspicuously absent. More recent studies (Chen, Yeh and Chang, 1997; Beyler, 2006) have focussed on the self-heating properties of Styrene-Butadiene Rubber (SBR), which is a major constituent of car and light truck tyre retread compounds. SBR is also used in the manufacture of conveyor belts, brake and clutch pads, hoses, extruded gaskets, moulded rubber goods, cable insulation and jacketing, and food packaging (Beyler, 2006). Production of SBR is often in the form of a crumb, which is then used to form the final product. The crumb can be transported and stored in large quantities at a fine particle size. A detailed study by Eremina, Zhurbinskii and Steblev (1991) on comminuted rubber crumb provides valuable insight to the self-heating characteristics of these rubber fines. However, little is known about the self-heating properties of conveyor belt rubber fines.

The United Kingdom recently issued a briefing note on the spontaneous heating of piled tyre shred and rubber crumb (UKHSE, 2019). The following comments are included in the briefing note:

- “Chopping and grinding of tyres produces a low density, porous material through which air may percolate. The total surface area of tyre chips or crumb particles may also be

---

<sup>1</sup> Managing Director, B3 Mining Services Pty Ltd. Email: [basil@b3miningservices.com](mailto:basil@b3miningservices.com) Tel: +61 7 3375 4100

<sup>2</sup> Senior Mining Engineer, B3 Mining Services Pty Ltd. Email: [jan@b3miningservices.com](mailto:jan@b3miningservices.com) Tel: +61 7 3375 4100

large compared with the volume occupied. The combination of permeability to air-flow and a high surface area means that a combustible material such as rubber is potentially susceptible to spontaneous combustion.

- “Surface symptoms of the onset of spontaneous combustion can be subtle: a slight sulphurous odour, condensation aerosols emerging from vents or evidence of oil contamination of rainwater draining through the tyre shred. The fire may intensify from smouldering to flaming as the combustion wave reaches the surface or if the pile is disturbed – allowing ingress of additional air.”
- “Laboratory experiments show that rubber crumb and tyre shred are more susceptible to self-heating than cellulosic materials (like hay and straw) in conditions of high ambient temperature. Typically a given volume of tyre shred will spontaneously ignite at a lower ambient temperature than an equivalent volume of hay.”

The description of a recent drift belt incident at a New South Wales underground coal mine (NSW Resources Regulator, 2019a) has many similarities to a recent Queensland conveyor belt incident and the symptoms described also fit the UKHSE briefing note, including the detection by the smell of burning rubber. The NSW Resources Regulator weekly incident summary documents the following:

“A fire was detected and extinguished by the workers in an underground coal mine. The workers were inbye of the boot end of the drift belt when they smelled burning rubber. On investigation, they identified a return roller running in fines and reported a ‘light glow’ from the fines. The area was hosed down and cleaned immediately.”

It would appear that the cause of the New South Wales incident is attributed to heating of the coal fines with no consideration given to the possibility of the conveyor rubber as the source of heating. This seems to be the reasoning attached to many previous conveyor belt incidents. The coal in this particular incident is from the Bulli seam, which has an identical intrinsic spontaneous combustion propensity rating to the coal from the Queensland Mine of Low (based on an  $R_{70}$  value  $<0.5$ ). The circumstances of these two incidents would seem to be more than just coincidence.

This paper presents the results of an investigation into the spontaneous combustion likelihood of Conveyor Belt Rubber Fines (CBRF) compared to Slack Coal Fines (SCF) from underground workings, using samples supplied of each material from the Queensland conveyor belt incident.

#### **SAMPLE DESCRIPTION AND ANALYTICAL DATA**

The CRBF is from severe mechanical abrasion of the 4-ply conveyor belt (Figures 1 and 2). It is in the form of a black spongy fibrous mass (Figure 3), which at a distance is visibly indistinguishable from the SCF obtained from the floor of the roadway adjacent to the incident location. At higher magnification the fibrous nature of the material is quite noticeable (Figure 4), with most of the fibres being less than 200  $\mu\text{m}$  across. It is highly porous and permeable.



Figure 1: Sample of used conveyor belt that generated the CBRF



Figure 2: Sample of used conveyor belt that generated the CBRF, showing Polyester Nylon (PN) webbing embedded in rubber layers



Figure 3: Photograph of ROM CBRF mass



Figure 4: Digital microscope image of CBRF

Proximate analysis and calorific value results for the CBRF and SCF samples are contained in Table 1. The analytical values obtained for the SCF are consistent with a medium volatile bituminous coal. The CBRF has a very high volatile matter content that is consistent with a combustible material. This is emphasised by the calorific value of the CBRF being very similar to the SCF.

**Table 1: Analytical data for CBRF and SCF samples**

Analysis (air-dried basis)	CBRF	SCF
Moisture (%)	1.8	0.9
Ash (%)	5.5	12.4
Volatile Matter (%)	51.9	23.4
Fixed Carbon (%)	40.8	63.3
Calorific Value (MJ/kg)	29.12	30.15

Pure SBR is composed of 1.38% moisture, 98.58% combustibles (volatile matter + fixed carbon) and 0.04% ash content (Cheh, Yeh and Chang, 1997). The CBRF sample has a much higher ash content than pure SBR indicating the presence of significant inorganic material. Conveyor belt rubber is manufactured as Fire Resistant Anti-Static (FRAS) by the inclusion of inorganic additives. The most common additives are mineral fillers such as aluminium and magnesium hydroxide or other mixed mineral assemblages (Hull, Witkowski and Hollingbery, 2011). The results of an ash analysis of the CBRF and a cored sample from the conveyor belt shown in Figures 1 and 2 are contained in Table 2. These results are compared in Figure 5. It should be noted that the cored conveyor belt sample had an ash content of 16.5%.

**Table 2: Ash analysis data for CBRF samples**

Inorganic Constituent (wt %)	CBRF	Cored Conveyor Belt
SiO <sub>2</sub>	6.8	5.9
Al <sub>2</sub> O <sub>3</sub>	2.8	69.2
Fe <sub>2</sub> O <sub>3</sub>	45.28	0.51
CaO	4.5	0.20
MgO	12.65	13.79
Na <sub>2</sub> O	4.29	5.49
K <sub>2</sub> O	0.20	0.39
TiO <sub>2</sub>	0.12	<0.01
Mn <sub>3</sub> O <sub>4</sub>	0.427	0.002
SO <sub>3</sub>	7.40	0.35
P <sub>2</sub> O <sub>5</sub>	0.66	0.90
BaO	<0.01	<0.01
SrO	0.03	<0.01
ZnO	16.10	3.17

The cored conveyor belt sample recorded high Aluminium contents, with lesser amounts of Magnesium and Sodium (Figure 5). These elements can be related to the inorganic additives included in the rubber for FRAS purposes. However, the CBRF is noticeably deficient in Aluminium and high in Iron with noticeable Zinc also being present (Figure 5). The most likely source of these elements would be from the friction mechanism with the steel conveyor structure that created the rubber fines, with the Zinc coming from either galvanised structure or paint. A minor amount of Calcium is also present in the CBRF sample, which may be due to a trace of stone dust being present in the sample. The low Aluminium content of the CBRF sample indicates it is deficient in fire retardant and this may be due to the fines being generated from friction of the outer side edge of the conveyor belt, which would also explain the fibrous nature.

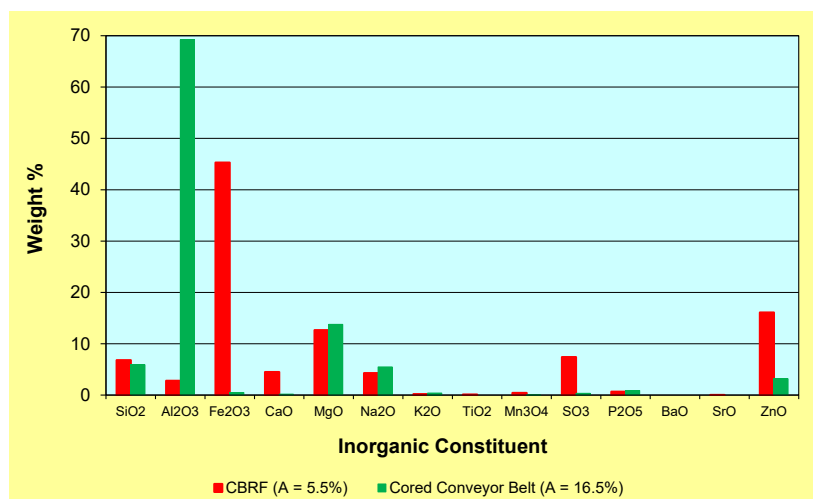


**Figure 5: Trends for inorganic constituents from ash analysis of CBRF and cored conveyor belt samples**

### SELF- HEATING TEST PROCEDURES

#### Adiabatic oven $R_{70}$ self-heating rate

Full details of the adiabatic oven are given in Beamish, Barakat and St George (2000). The sample to be tested is crushed and sieved to  $<212 \mu\text{m}$  in as short a time as possible to minimise the effects of oxidation on fresh surfaces created by the grinding of the coal. A 150 g sample is placed in a 750 mL volumetric flask and a unidirectional flow of nitrogen at 250 mL/min applied to the flask inside a drying oven. Precautions are taken to ensure the exclusion of oxygen from the vessel prior to heating the coal for drying. Hence, the air is flushed from the system at room temperature for a period of one hour. After one hour, the oven is ramped up to 110 °C and the coal is dried under nitrogen for at least 16 h to ensure complete drying of the sample. All  $R_{70}$  tests are performed on a dry basis to standardise the test results.

At the completion of drying, the coal is transferred into the reaction vessel and left to stabilise at 40 °C in the adiabatic oven with nitrogen passing through it. The reaction vessel is a 450 mL thermos flask inner. When the sample temperature has stabilised, the oven is switched to remote monitoring mode. This enables the oven to track and match the coal temperature rise due to oxidation. The gas selection switch is turned to oxygen with a constant flow rate of 50 mL/min. The temperature change of the coal with time is recorded by a datalogging system for later analysis. The oven limit switch is set at 160 °C to cut off the power to the oven, and stop the oxygen flowing when the sample reaches this temperature. When the oven cools down, the sample is removed from the reaction vessel, which is then cleaned in preparation for the next test. The results are used to classify the intrinsic spontaneous combustion propensity of the sample according to the rating scheme published by Beamish and Beamish (2011).

#### Adiabatic oven self-heating incubation

This test is designed to replicate true self-heating behaviour from low ambient temperature. As such, the normal in-mine temperature is used as the starting point for the test. The nature of the test also assumes that in the real operational situation there is a critical pile thickness present that minimises any heat dissipation (represented by the adiabatic oven testing environment) and there is a sufficient supply of oxygen present to maintain the oxidation reaction. A larger sample mass and lower oxygen flow rate is used, compared to the  $R_{70}$  test method, to produce conditions that more closely match reality (Beamish and Beamish, 2011).

The sample either reaches thermal runaway, or begins to lose heat due to insufficient intrinsic reactivity to overcome heat loss from moisture release/evaporation and/or heat sink effects from non-reactive mineral matter. The results are used to characterise the self-heating incubation behaviour of the sample as well as quantify if thermal runaway is possible and if so does this occur in a practical timeframe for the mine site conditions.

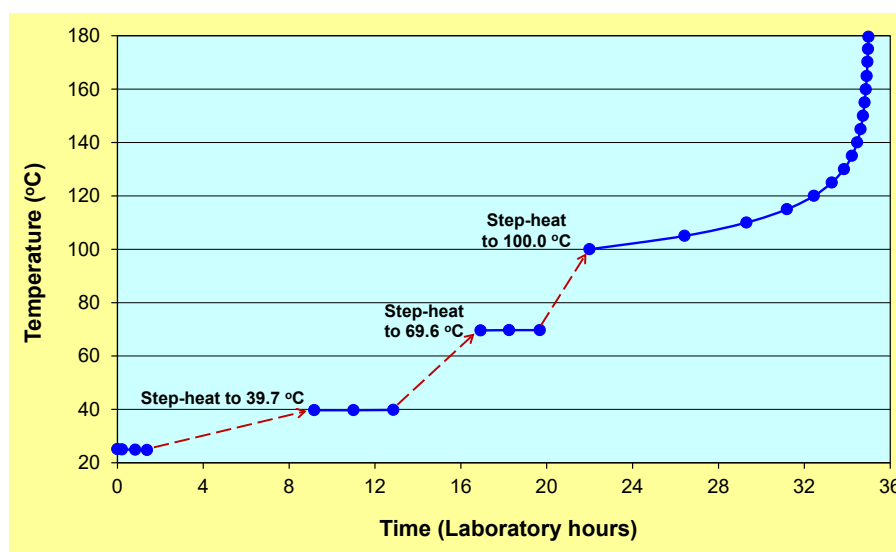
## ADIABATIC SELF-HEATING RESULTS AND DISCUSSION

### Intrinsic spontaneous combustion propensity

The  $R_{70}$  values for the CBRF and the SCF are 0 and 0.18 °C/h respectively. This indicates both samples have a low intrinsic spontaneous combustion propensity. The rating for the SCF is consistent with the rank and type of coal and fits within the range of previous results for the Queensland Mine. An  $R_{70}$  value of 0 obtained for the CBRF is consistent with the self-heating behaviour of rubber at an ambient temperature of 40 °C.

### Self-heating incubation behaviour

Incubation testing of the CBRF from a start temperature of 25.1 °C with a moisture content of 2.0% shows no sign of self-heating from this low mine ambient temperature (Figure 6). After step-heating the sample temperature to 39.7 °C using the oven heaters and returning to adiabatic mode also shows no initiation of self-heating. A further step-heat to 69.6 °C also results in no sustained self-heating. However, a step-heat to 100 °C is able to initiate self-heating of the CBRF followed shortly after by thermal runaway (Figure 6). Consequently, these results suggest that self-heating is possible at a temperature between 69.6 °C and 100 °C.



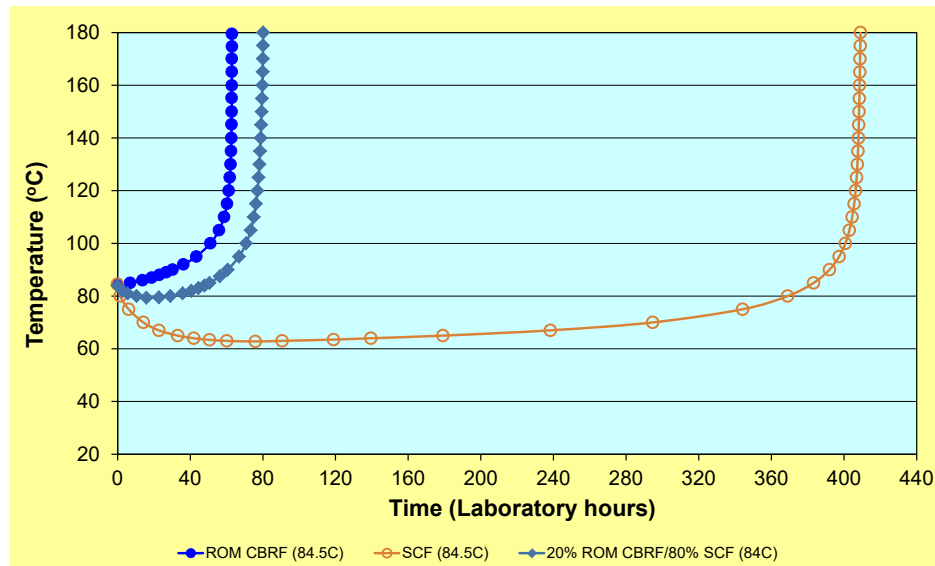
**Figure 6: Adiabatic oven test results for CBRF showing self-heating incubation behaviour at successively elevated temperatures**

Figure 7 shows the results obtained from starting a new incubation test on a duplicate of the CBRF sample at 84.5 °C. The sample initially slowly self-heats and then progresses to thermal runaway in an exponential manner, suggesting the oxidation reaction is following Arrhenius rate behaviour.

Incubation testing of the SCF from a start temperature of 84.5 °C with a moisture content of 3.8% shows an initial decrease in temperature due to moisture evaporative heat loss (Figure 7). After a substantial period of time, the heat balance between moisture evaporative heat loss



and coal oxidation heat production equilibrates and remains balanced for 30 hours. Subsequently, the heat production from coal oxidation takes over resulting in temperature gradually increasing for an extended period of time before eventually accelerating to the point of thermal runaway. In practical terms the time for the SCF to incubate to a spontaneous combustion event is inordinately long and most likely would not occur under normal site conditions.



**Figure 7: Adiabatic oven test results for CBRF, SCF and a 20%/80% blend of the two showing self-heating incubation behaviour to thermal runaway**

The incubation test results for a sample blend containing 20% CBRF and 80% SCF are also shown in Figure 7. This sample blend initially decreases in temperature similar to the SCF, but the heat balance equilibrium point occurs much sooner and the temperature increase to thermal runaway occurs in a much shorter timeframe. This suggests only a minor percentage of the CBRF is needed to increase the likelihood of the SCF to incubate to a spontaneous combustion event in a practical timeframe.

These incubation test results clearly show that the CBRF can more readily self-heat than the SCF. In addition, if the CBRF accumulates with the SCF, this also increases the likelihood of the SCF self-heating. It is highly likely that the friction mechanism that created the CBRF would be capable of elevating the temperature of the material to the point of sustained self-heating. Also the insulating properties of the rubber would enable the development of a hot spot in a relatively thin pile of CBRF. For example, at 100 mm thickness temperatures of approximately 135 °C or higher may lead to spontaneous combustion of comminuted rubber crumb as shown in Figure 8 (Eremina, Zhurbinskii and Steblev, 1991). It should be noted that the particle size of comminuted rubber crumb (0.8-1.2 mm) is much coarser than the CBRF shown in Figure 4. Therefore, at 100 mm thickness the self-ignition temperature of 84.5 °C recorded by the CBRF from incubation testing is realistically consistent with these findings.

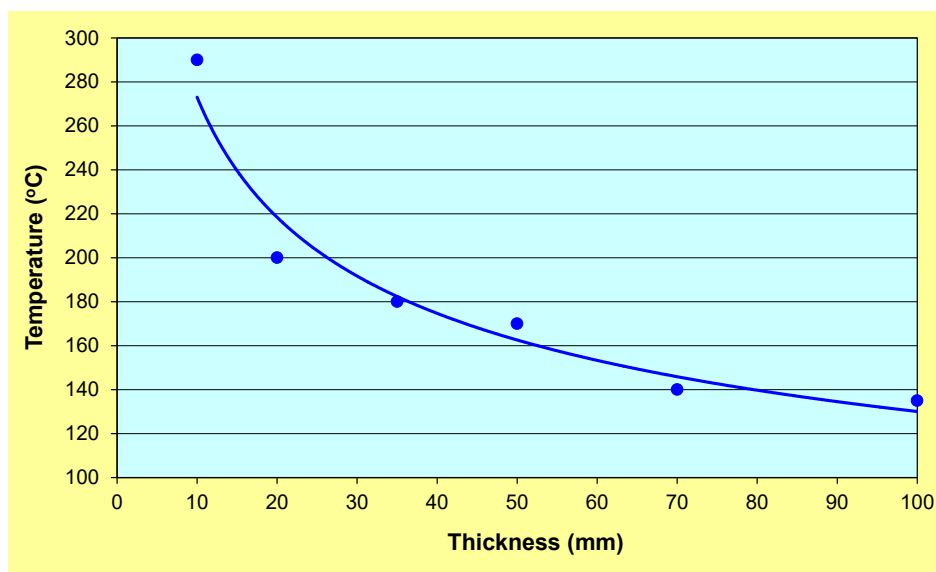


**Figure 8: Dependence of comminuted rubber crumb self-ignition temperature on deposition thickness (modified from Eremina, Zhurbinskii and Steblev, 1991)**

### CONCLUSIONS

This is the first time that adiabatic testing has been conducted on rubber fines from any source. Incubation test results show that rubber fines generated from conveyor belt friction are able to self-heat from a temperature as low as 84.5 °C. The spongy fibrous form of the rubber fines creates both a high permeability to airflow and a high surface area for oxidation reaction. In addition, the friction mechanism of the conveyor belt rubber fines generation would create an induced temperature required to alter the environmental boundary conditions to the point where self-heating is sustained due to the excellent insulating properties of the rubber. When the rubber fines are mixed with slack coal they also increase the likelihood of the coal to incubate and create a spontaneous combustion event.

As a result of these new findings the principal cause of conveyor belt fires needs to be evaluated more closely with a detailed forensic examination of the materials involved. In the meantime a safety bulletin has been issued with the following recommendations (NSW Resources Regulator, 2019b):

- “Review the risk assessment for fires associated with conveyor systems.”
- “Update the conveyor management plan to include the risk of spontaneous combustion of rubber fines.”
- “Update belt inspection training material and procedures to make workers aware of the risk of rubber fines spontaneously combusting.”

### REFERENCES

- Beamish, B and Beamish, R, 2011. Testing and sampling requirements for input to spontaneous combustion risk assessment, in *Proceedings of the Australian Mine Ventilation Conference*, pp 15-21 (The Australasian Institute of Mining and Metallurgy: Melbourne).
- Beyler, C, 2006. Self-heating properties of styrene-butadiene rubber, *Fire Materials*, 30: 215-221.
- Bowes, PC, 1984. Self-heating: evaluating and controlling the hazards, HM Stationery Office (London).

## Coal Opertors' Conference

- Chen, K S, Yeh, R Z and Chang, Y R, 1997. Kinetics of thermal decomposition of styrene-butadiene rubber at low heating rates in nitrogen and oxygen, *Combustion and Flame*, 108: 408-418.
- Clothier, PQE and Pritchard, HO, 2003. Atmospheric oxidation and self-heating in rubber-containing materials, *Combustion and Flame*, 122: 207-210.
- Ermina, L, Zhurbinskii, S and Steblev, A, 1991. Fire and explosion safety of the production of comminuted rubber crumb, *International Polymer Science and Technology*, 18(8):21-23.
- Hull, R, Witkowski, A and Hollingbery, L, 2011. Fire retardant action of mineral fillers, *Polymer Degradation and Stability*, doi: 10.1016/j.polymdegradstab.2011.05.006.
- New South Wales Resources Regulator, 2019a. Weekly incident summary – Week ending Friday 31 May 2019, NSW Government. Available from: [https://www.resourcesregulator.nsw.gov.au/\\_\\_data/assets/pdf\\_file/0004/1137460/Weekly-incident-summary-week-ending-31-May-2019.pdf](https://www.resourcesregulator.nsw.gov.au/__data/assets/pdf_file/0004/1137460/Weekly-incident-summary-week-ending-31-May-2019.pdf) [Accessed: 7 June 2019]
- New South Wales Resources Regulator, 2019b. Safety bulleting – Spontaneous combustion of rubber fines, DOC19/908437, SB19-12.
- United Kingdom Health and Safety Executive, 2019. Spontaneous heating of piled tyre shred and rubber crumb – Briefing note [online]. Available from: <http://www.hse.gov.uk/rubber/spontaneous.htm> [Accessed: 30 May 2019].

# EVALUATION OF THE RECOVERY OF BLOCK CAVE UNDERBREAK BY SUB LEVEL CAVING

Ellie Hawkins<sup>1</sup> and Scott Sheldon<sup>2</sup>

**ABSTRACT:** Northparkes Mines (NPM) is located 27 kilometres north of the township of Parkes in central New South Wales, Australia. The operations consist of underground block cave mines and an ore processing plant which produces high grade copper and gold concentrate. Production is currently sourced from the E48 Lift 1 block cave mine, E26 Sublevel Cave (SLC) and open cut stockpiles. Mining at Northparkes has been underway for over 20 years in various forms. Beginning with open pit mining and later progressing to block cave and sub-level cave mining methods, operations haven't been without their technical challenges.

During mining of E26 Lift 2 block cave, a wedge of high grade material failed to cave, even with the assistance of preconditioning. The unrecovered wedge created the E26 SLC, which commenced mining in 2015, with production following in 2016. The SLC provides 1Mt/a to supplement the lowering grade of the current block cave feed.

The poor ground conditions in close proximity to the cave have proved a challenge. This was particularly noticeable on the first level, 9740L, with half of the firings including more than one ring. The loss of the brow encountered when blasting in ground that had been initially preconditioned for block cave mining created a heavy reliance on redrills in the operation causing poor drawpoint turnovers. Precharging was researched to improve the flow, however due to prevalence of brow loss; concerns were raised over the inability to hook up the charged ring. In 2018, a wireless initiation trial was completed in the E26 SLC over 24 rings. The trial showed that precharging was achievable in this environment and greatly improved the safety of charge up personnel.

## INTRODUCTION

The CMOC Northparkes (NPM) mine is located 27 kilometres north of the township of Parkes in central New South Wales, Australia. NPM is currently operating in production with E48 block cave and E26 Sublevel Cave (SLC), with commencement of development E26 Lift 1 North block cave. NPM is currently producing 6 Mt/a with an expansion project currently in construction to ramp up by 2021 to 7.5 Mt/a. The E26 orebody which is the topic of this paper, shown in Figure 1, is a steeply plunging orebody to the NNE at approximately 80° in a generally upright, pipe-like geometry. It is centred around a tight cluster of quartz monzonite porphyry fingers and an underlying pre-mineral Biotite Quartz Monzonite (BQM).

The E26 orebody hosted the first block cave in Australia, Lift 1, which mined the orebody at a depth of 480 metres below surface. Following its completion, production commenced in E26 Lift 2, 350 metres below Lift 1. During the mining of Lift 2, a wedge of high grade material failed to cave as shown in Figure 2. As a means to recovering the wedge, preconditioning was conducted through a hydro-fracturing program, a Vertical Crater Retreat (VCR) style blasting program with boundary weakening blasts was arranged with the goal to liberate as much ore as possible. From the preconditioning, there were signs of success with finely fragmented ore

---

<sup>1</sup> Ellie Hawkins: Mining Engineer, CMOC Northparkes, Parkes, NSW 2870, Email: [ellie.hawkins@au.cmoc.com](mailto:ellie.hawkins@au.cmoc.com)

<sup>2</sup> Scott Sheldon: Senior Specialist Engineer, Orica, Kurri Kurri, NSW 2327, Tel: 0402506891  
[Email:scott.sheldon@orica.com](mailto:Email:scott.sheldon@orica.com)

presenting to drawpoints in Lift 2, however the possibility of recovering through Lift 2 became unfeasible due to the inundation of clay.

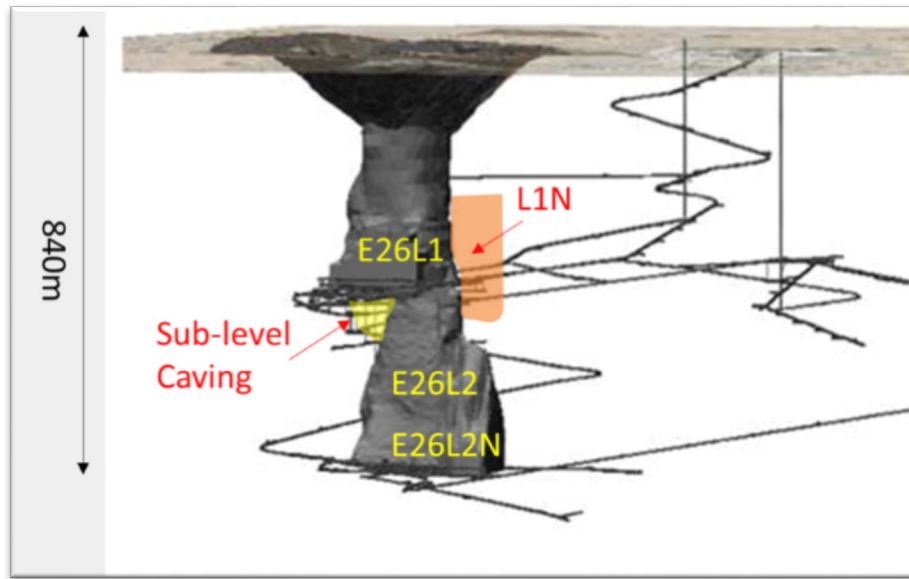


Figure 1: E26 mining activities

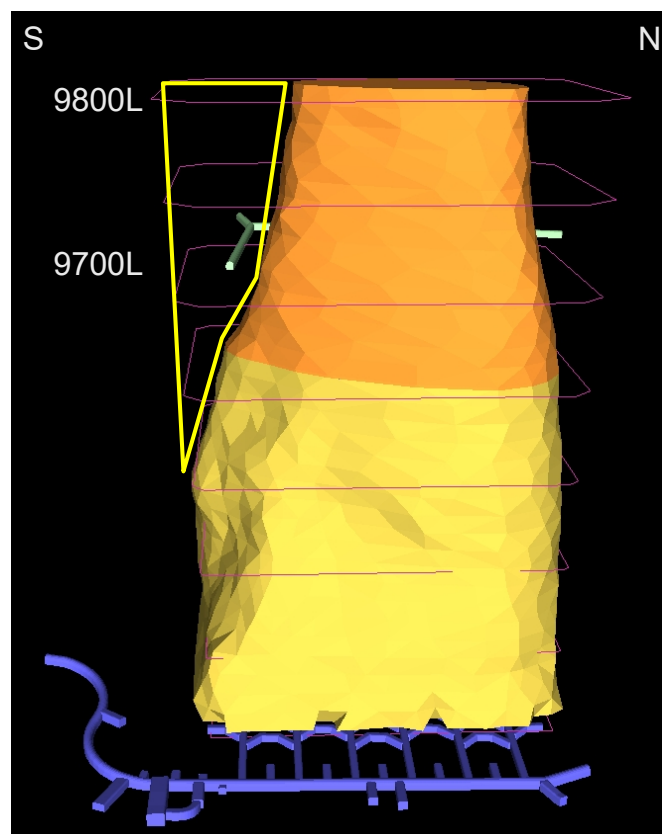


Figure 2: Lift 2 southern wedge (outlined in yellow)

### RECOVERY OF THE SOUTHERN WEDGE METHODOLOGY

As a result of the underbreak of the Lift 2 cave approximately 9 million tonnes of the original Lift 2 reserve were left behind in what is known as the Lift 2 South Wedge between the

9650mRL and the 9800mRL. Table 2 shows the options investigated and the use through the recovery of the wedge. Between 2005 - 2007, a combination of the hydraulic fracturing, blasting operations and extraction level extension to the North of Lift 2 took place, however with the presence of clay and fines migration in Lift 2, full recovery of the resources was not feasible. The migration of clay also made the option of the Undercut extension or an extension to the East of Lift 2 unfeasible.

From all the options, SLC was the preferred option due to the high likelihood of success, stemming from the reliance of drill and blast mining methods, rather than natural caving for primary rock breakage. The SLC option also provided greater control over the infiltration and control of clay and fines to draw points through retreat blasting where required, and a crown pillar between the depleted block cave and the SLC. The greatest advantage, stemming from the method being similar to undercutting for block caving, which the operational and technical teams had previous experience.

**TABLE 1: Options for Southern Wedge Recovery**

Option	Time to complete	Likelihood of Success	Option
Hydraulic Fracturing	3-12 Months	Low/Uncertain	Used
Blasting Options	6 weeks	Low/Moderate	Used
North Extension to Lift 2	12 months	Low/Moderate	Used
East Extension to Lift 2	12 months	Low/Moderate	Not Considered
Panel Cave	2 years	60%	Not Considered
Sublevel Cave	2 years	90%	Final Solution

The recovery of the Southern wedge was postponed due to the development and early production of the E48 block cave. Then, almost a decade later, the lowering head grade of the producing block cave required a supplementary grade enhancer. The Southern Wedge was identified as a potential source of grade, creating the E26 SLC. As shown in Figure 3, the wedge created a four level transversal SLC with complex geometries with the occurrence of as-built in the footprint and unknown ground conditions presented from the preconditioning.

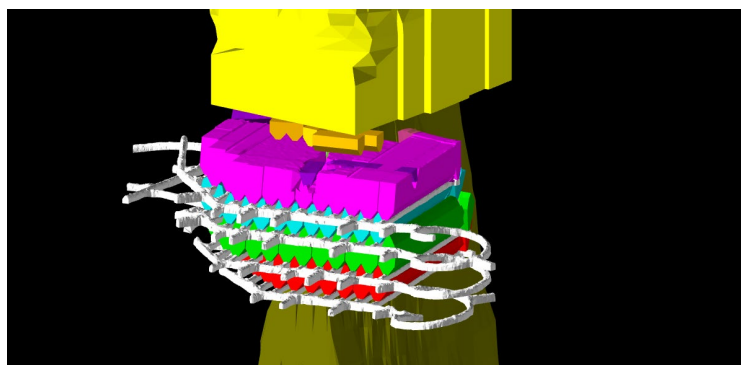


**Figure 3: E26 SLC**

### Sublevel Cave Performance

The preconditioned ground and cave stresses which the mining area had undergone from Lift 2 caving proved complex with the following drill and blast challenges:

- Backbreak of the drawpoint as far as the next ring collars;
- Reluctant material flow to a drawpoint (hang ups);
- Frozen ground, forming sides to the stope that limits material flow to a drawpoint,
- Collar bridging and requirement to re-charge collars,
- Hole dislocations in the next ring to be charged and;
- Firing against clay and fines, causing compaction.

The initial level, 9740 level (Figure 4), exhibited poor outcomes in terms of blasting outcomes when commencing the cave front in the East and Western ore drives. As the cave front was retreating back along the cave front, there were 15 events with full loss of brow within the first six month of production. These events, in addition to the high reliance on redrills from short holes, heighten the risk of traditional wired precharge and the SLC remained to operate under a single ring, charge and fire cycle.

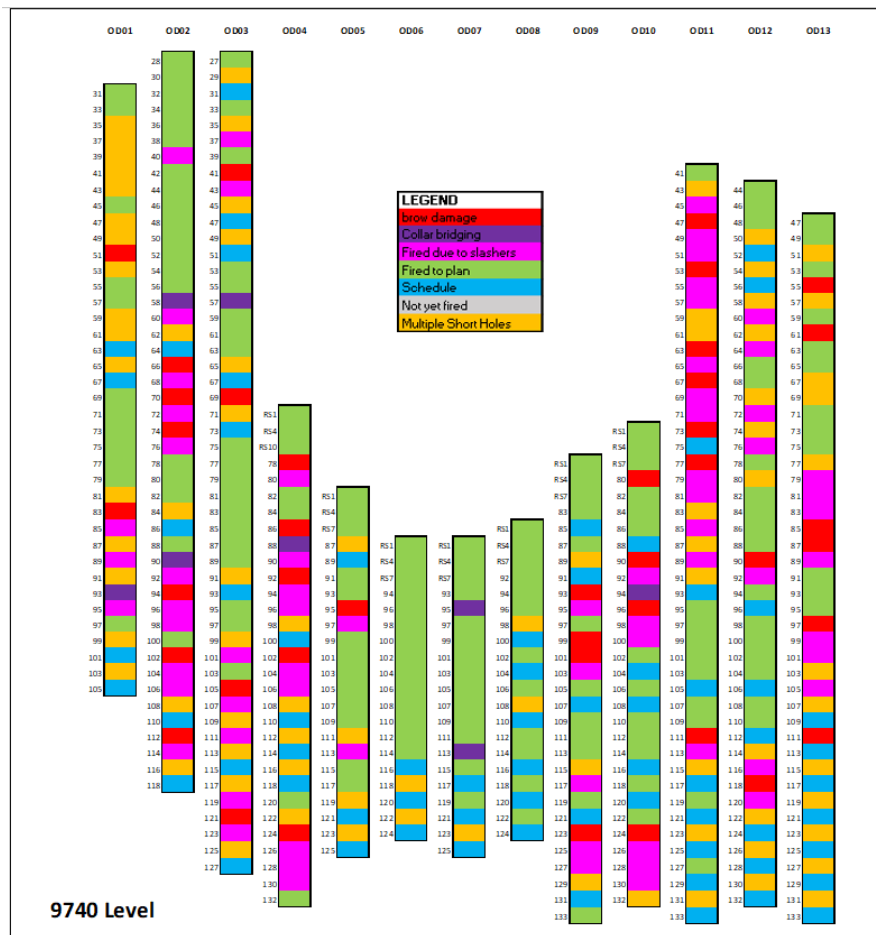


Figure 4: Failure modes of 9740 Level

The initial DB design for the SLC was based off best practises, however were reviewed for the blasting outcomes to ensure more optimal results. The changes included:

- Burden between each ring was increased from 2.6 m to 3 m
- Ring pattern – reduction from 10 to 9 hole rings



Coal Opertors' Conference

- Hole spacing – increased to 3.1 metres with the decrease in holes per ring
- Reduction in powder factor from 0.6 to 0.45

Due to the cave front, these changes were trialled in 9740 OD6, OD7 and OD8. These changes produced 81% of rings fired to plan in the trial drives, compared to 49% for the remaining ore drives, see Figure 5. Due to the improvement shown in the trial drives, the changes were applied to the next level, 9720. The changes did have an impact in terms of reducing entire loss of the brow, from 42 events total on the 9740 to a total of 24 events on the 9720 Level. This result is related directly to the increase in burden between the production rings. The improvement of brow damage and the occurrence of short holes

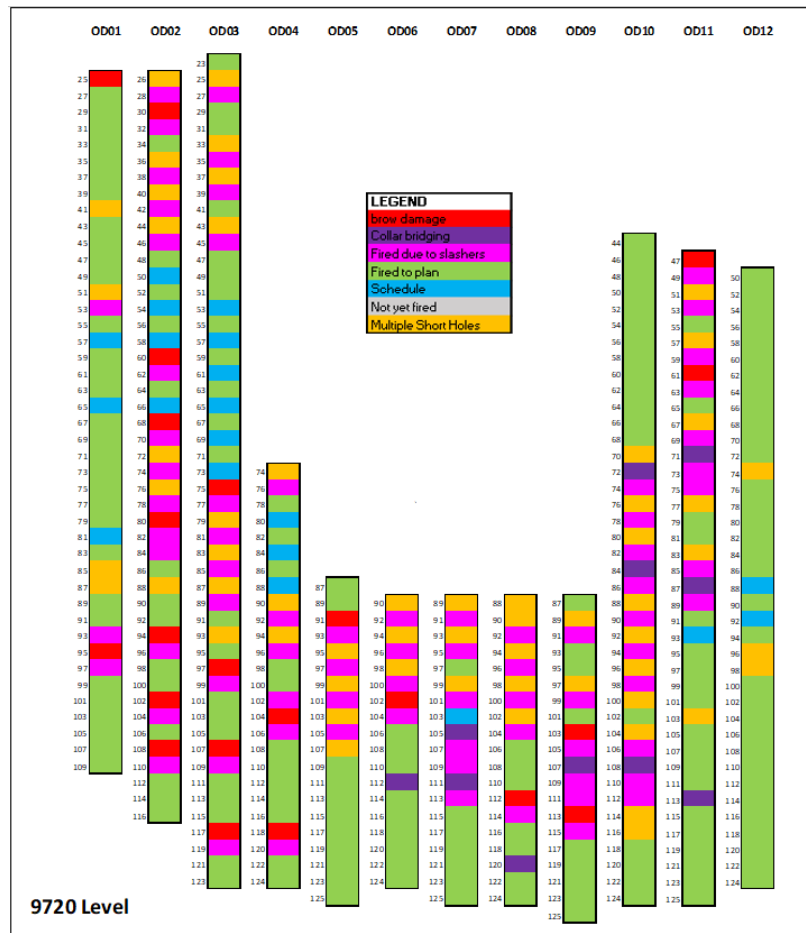


**Figure 5: Failure modes of 9720 Level**

delivered a reduction in the multiple ring firings, improving primary draw. However this was offset by a deterioration in ground conditions and hence an increase in the number of rings requiring re-drill, shown in Table 2.

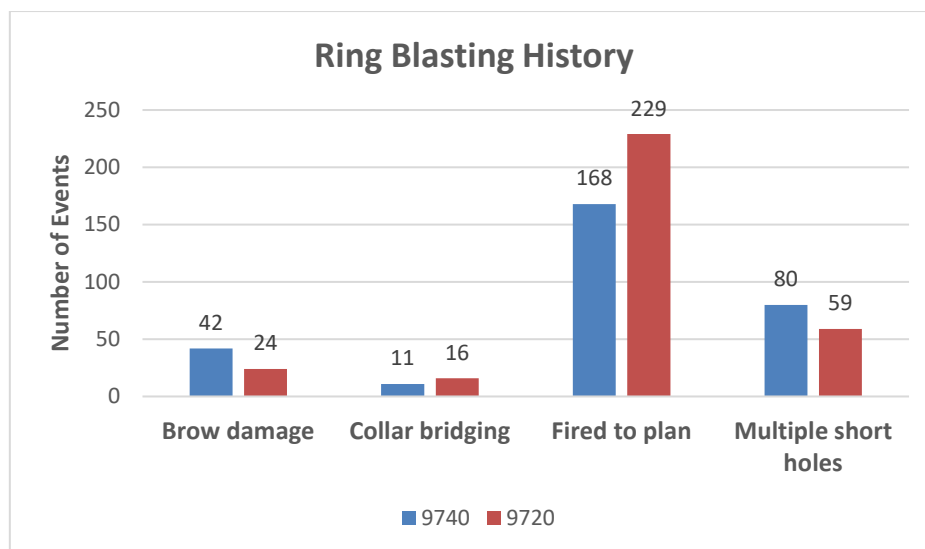


**Figure 6: Ring Blasting History**

To overcome the less than optimal outcomes, high level of remediation was required to ensure cave propagation. The re-work process can include the stand-up of drawpoint rill, application of shotcrete for reinforcement and the drilling of recovery or slasher rings. This caused production delays and also impacted on the ability to maintain an optimum cave front with operational drives advancing ahead of drives requiring remediation. Particularly where recovery or slashing rings were drilled in an attempt to recover multiple production rings to be fired in a drawpoint in one blast event.

Previous studies completed by the Ridgeway SLC found that the influence zone for depth of draw of LHD mucking a production ring is generally less than 2.6 m (Power 2004). With the current burden at 3 m for the 9720 level, the firing of multiple rings caused early dilution into the draw cones, as the production mucking attempted to draw the tonnes from the whole blast.

**TABLE 2: Performance summary of 9740 and 9720 levels**

Measure	9740 Level	9720 Level
% of rings requiring re-drill	23.3%	26.4%
% Re-drills (% of total m drilled)	11.0%	16.4%
Short holes per ring	15.0%	20.0%
Shotcrete usage m3/ring fired	1.42	1.13
% of double ring firings	45.5%	32.0%
% of rings fired to plan	55.8%	66.2%

Across the SLC, due to the complexities of geometries, no production rings are the same length, from the 9740 Level with 30 m high production rings to 20 m high production rings on the 9720 Level. There was no constants in the trialling in terms of the mine design, making a DB best practice across the cave difficult to develop, rather it relies on geological contacts, previously problematic areas of the cave and daily inspections of the drawpoint. The exposure of underground personnel in close proximity to the rill was a concern with the hours shown in Table 3. The aim was to reduce the exposures of personnel in close proximity to the brow, which was achievable with precharging on the lower levels with WebGen100.

**TABLE 3: Labour demand of rework process on 9740 and 9720 levels**

<b>Measure</b>	<b>9740 Level</b>	<b>9720 Level</b>
Re-drill events	98	90
Re-drill man hours	420	491
Rework shotcrete events	173	120
Rework shotcrete man hours	519	360
Average exposure Man-hours per blast event (including charge and fire)	5.94	6.22
Total exposure man hours (rework, charge and fire)	1935	1710

### **Application of pre-charging**

The majority of SLC operations in Australia and internationally conduct precharging to take advantage of the improvement in safety performance, working conditions and production flexibility compared to traditional SLC charging practices. One of the major threats to the introduction of precharging in the E26 SLC was managing brow condition to allow for access to the collar of the blast holes. To abandon a production ring due to the inability to hook-up precharge would impact on the ability to recover caving conditions, as well as impede on the safety of personnel with undetonated primers reporting to the draw on future levels.

Precharging presents opportunity for the business in terms of production flexibility and mine efficiency as the dependency on charge up activities is somewhat reduced with the reduction in rework processes. Ridgeway stated that the implementation of precharging provided a 'realised' direct cost savings in excess of A\$1 million per annum (Wiggin 2002). NPM re-opened the investigation of precharging in the E26 SLC. The steps taken in this investigation were:

- Reviewed the outcomes of a trial conducted by EHM using Orica's WebGen™ 100 wireless initiation system (te Kloot et al. 2017)
- Reviewed the original SLC risk assessment that excluded precharging with context of it could use wireless initiation
- Engaged with Orica to conduct a 24 ring trial using the WebGen™ 100 wireless initiation system.

It was expected that a wireless initiation system would allow precharging to take place in the preconditioned ground of the E26 SLC. If access to the collars of a precharged ring were lost the ring could still be fired off if the initiation system in the precharged hole was wireless. A wireless system would also remove the need to recover lost brows thereby removing the charge crew from having to access damaged brows.

### **Wireless initiation trial**

Before a precharging trial could be commenced the following capabilities needed to be established:

- Extending explosive bulk product sleep times from seven days to at least 28 days
- Confirming the wireless initiation primer could sustain blast induced pressures
- Confirming the strength, range and reliability of the wireless initiation system signal in the E26 SLC ore body

### Extended sleep times

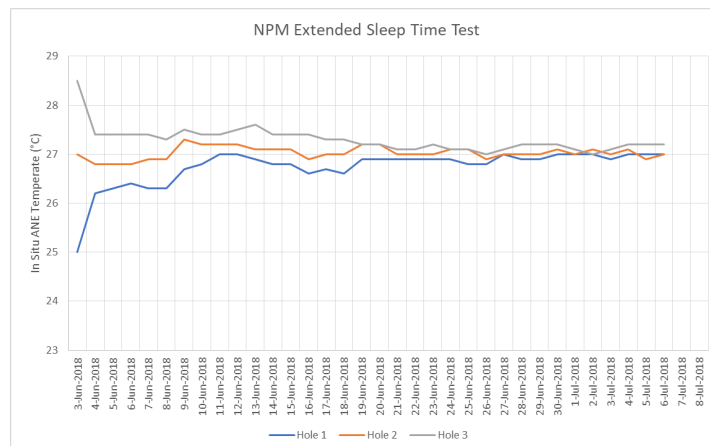
The NPM E26 ore body had previously returned positive samples when testing for reactivity of the ground with Ammonium Nitrate (AN). As a result of the past results, NPM was operating on a maximum 7 day sleep time for any charged hole. With up to 25 drives across two levels in the SLC, the cycle time between ring firings in a single drive was nominally 24 days. In order, to implement a precharging operation across the full SLC, a minimum 28 day sleep time would be required.

Ideally NPM required two precharged rings per drive but it was conservatively estimated that a minimum 40 day sleep time would be required to manage this. So, the plan that was agreed to with Orica was to progressively test and implement extended sleep times until 28 days was reached such that, if the precharging trial was successful, then single ring precharging could be implemented. Once implemented then a program would be put in place to investigate extending sleep times further to a nominal target of 40 days.

Rock samples across the 9720 and 9700 levels were collected focussing on geology that had previously shown to be reactive. These samples were then tested by Orica for reactivity following the guidelines of 2017 *AEISG Code of Practice Elevated Temperature and Reactive Ground*. Of the 17 samples collected, four tested positive to AN. As a result, the four samples were tested in Ammonium Nitrate Emulsion (ANE) at an elevated temperature of 55°C for a period of 116 days in the lab as per the code of practise. These four samples showed no reactivity with ANE and passed the assessment.

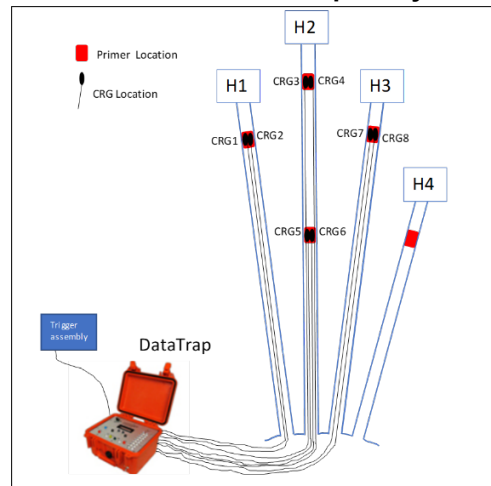
To validate the successful lab results, in situ testing commenced with a program involving three holes were drilled in an area that was defined as being high risk to reactivity (pyrite-anhydrite hydrothermal breccia unit). These holes were loaded with Subtek™ ANE, WebGen™ 100 wireless primers and a thermocouple wire. The thermocouple gauge was located beside the WebGen™ primer to measure the temperature of the emulsion at this point. The holes were inspected daily for indications of reactivity and the temperature reading from the thermocouple was recorded. The procedure in place dictated the frequency of temperature measurement and if a temperature increase beyond 2°C was observed, then shift readings were to be taken. If the temperature reading increased by more than 5°C from ambient ground temperature, the procedure involved E26 blast area excavation and the test holes being fired immediately.

Figure 7 shows the results of the temperature monitoring of these three extended sleep time test holes. The three test holes were successfully slept for the 35 day test period. They showed no indication of reactivity. All three holes were successfully fired at the end of the period via the WebGen™ 100 wireless initiation system.



**Figure 7: In situ extended sleep time results**

### Wireless Primer Capability



**Figure 8: Testing setup for pressure hole testing**

Before the full integration into production blasting with the WebGen100 system, there was a requirement to investigate the effect of blast induced pressure on a precharged ring when firing the production ring in front. The test needed to validate that the wireless unit could withstand the blasting pressure and not be made inoperable when exposed to close field blasting.

The testing was completed in two slashing rings on 9720 OD6 R102A-R102B (shown in Figure 9) after the initial testing area failed at capturing data. The use of the slashing rings provided a higher blast pressure for the wireless units to withstand with a burden of 1.5 m compared to a typical precharged ring fired on a 3.0 m burden. Each hole was charged as per the plan with the only difference being the addition of a Carbon Resistor Gauge (CRG) attached to each of the wireless units as shown in Figure 8. At firing time, the four CRG cables were then connected to a DataTrap™ II monitor to record the pressure gauge readings when the preceding ring in front was fired. Results from this test recorded blast pressures well below the rating for the WebGen™ receiving unit used in the wireless primer.

With the successful results from the pre-work testing, a 24-ring trial using the WebGen™ 100 wireless initiation system was undertaken. The trial commenced in the 9720 level where production on the level was well underway, using a wired initiation system with no precharge. The concept was to phase out the single ring wired initiation charging and introduce precharged rings with wireless initiation across a section of the cave front.

This strategy was proven to be not suitable with the combination of wireless precharged blasting systems with wired blasting systems in non-precharge conditions. It was noted that this combination was unworkable unless it could be immediately adopted across the entire level. The primary reason behind this conclusion was that precharging was not occurring in neighbouring drives and the failures of brow loss and short hole were occurring, requiring remediation. If redrilling was required in remediation, the neighbouring precharged drives would need to be fired off, due to the 20 m exclusion zone applied to charged solids at NPM as shown in Figure 10. No consistency in drives nor across the level was achievable across the 5 rings fired with WebGen100 on the 9720 Level, and hence the trial was moved to the 9700 Level.

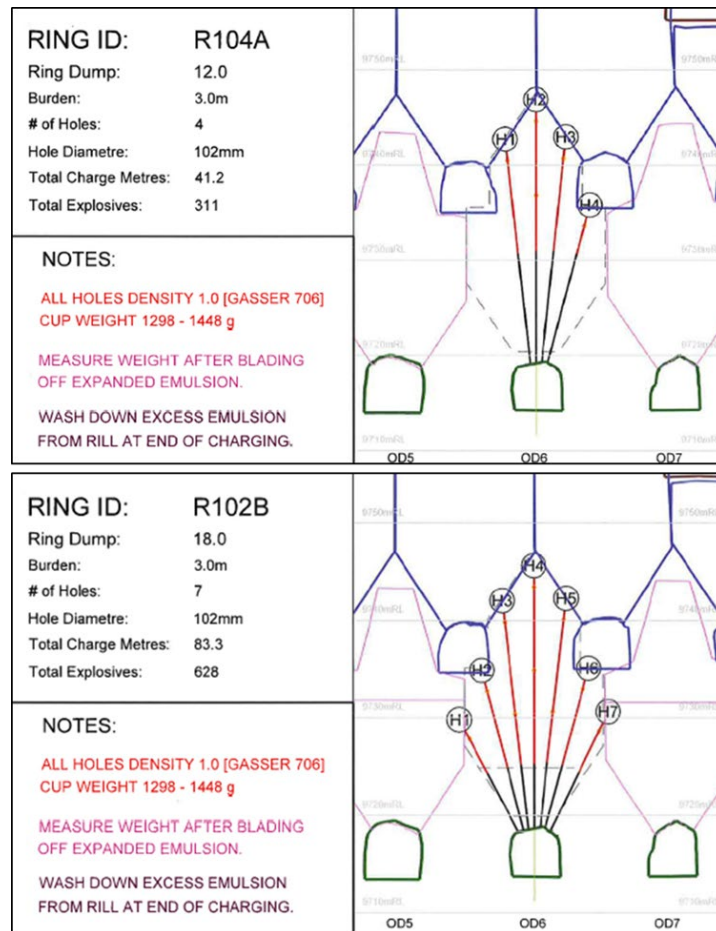


Figure 9: Slashing ring design for the pressure hole testing

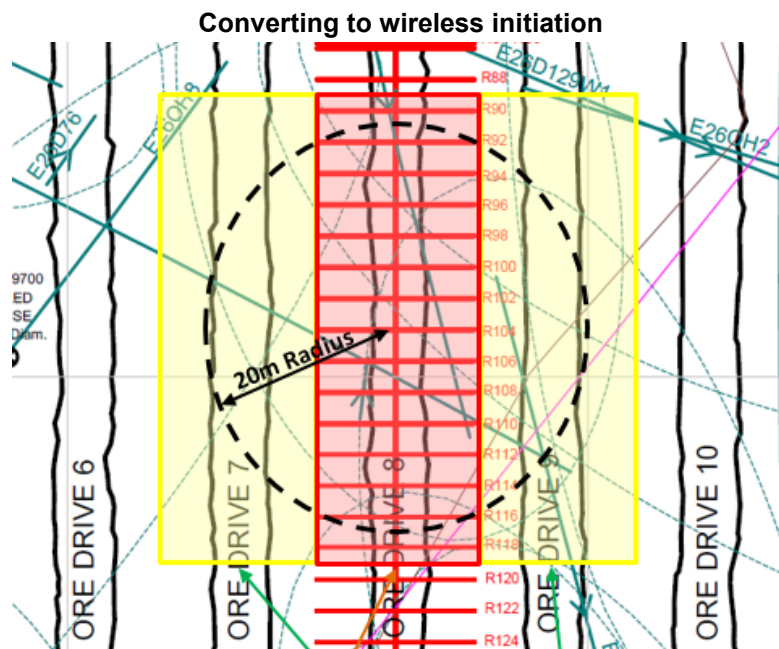


Figure 10: Exclusion zone

The 9700 level was in the initial stages of production and the cave front was yet to be established on the Western portion. The commencement of the level meant that precharging could be rolled sequentially into adjacent drives with the breakthrough to the cave. Of the 24 trial rings, 19 were implemented on the 9700 level. This method when utilised allowed for the first set of slot rings and the final development cut to be initiated with a wired blasting system with the next set of slot rings precharged. The method over the first three drives of the 9700 Level provided the correct conditions for the ability to consistently precharge across the entire cave front with no remediation interruptions.

The main risk involved with the traditional wired detonator and its use in precharging is the loss of access to the collars for firing. Across the trial, a total of four entire brow losses were experienced. Figure 11 shows the backbreak of R59 after firing. The brow damage passed the precharged ring collars (R61) which is evidenced by reflective tag on the left side of the rill. This showed the immediate benefit of wireless initiation, as this loss of brow would require no remediation for access and allow for recovery. Once bogging was completed, the precharge process was applied to the next ring with no further issues.

The wireless initiation system allowed precharging to be undertaken successfully in this preconditioned ground. The result was a complete removal of all the issues faced on the 9740 and 9720 levels by the uninterrupted application of precharging. Precharging, as shown in Table 4, removed all requirements for re-drilling and reduced the requirement of rill reinforcement with shotcrete. Over the trial, all rings were fired to plan, with no multiple ring firings in all precharged rings.



**Figure 11: 9700 OD01 R59 bogging with precharged R61 not visible**



**TABLE 4: Labour demand of rework process on 9740 and 9720 levels**

Measure	9740 Level Wired	9720 Level Wired	9700 Level Wireless
% of rings requiring re-drill	23.3%	26.4%	0%
% Re-drills (% of total m drilled)	11.0%	16.4%	0%
Short holes per ring	15.0%	20.0%	8.7%
Shotcrete usage m <sup>3</sup> /ring fired	1.42	1.13	0.32
% of double ring firings	45.5%	32.0%	0%
% of rings fired to plan	55.8%	66.2%	100%

Moreover, the main aim of the trial was to reduce the exposures of personnel in close proximity to the brow when on foot. Table 5 shows the reduction in exposures from over 6 man hours per blast event, reduced to 2.5 man hours per WebGen100 blast.

**TABLE 5: Exposure hours in close proximity to the brow on foot**

Measure	9740 Level Wired	9720 Level Wired	9700 Level Wireless
Re-drill events	98	90	0
Rework shotcrete events	173	120	2
Average exposure man-hours per blast event(including charge and fire)	5.94	6.22	2.53

Following the successful completion of the trial, NPM assessed the impact on safety for the production crews and the overall improvement in the performance of the cave when precharging. Being first generation technology, the cost per blast is higher, however, this is offset by the remediation works and the primary recovery improvement. Consequently, NPM became the first operation in Australia and the second operation globally to convert to a wireless initiation system for use in production blasting.

### Observations to date

As of date of this paper:

- 105 production rings have been fired with the wireless initiation system. The wireless initiation system has 100% success rate in firing of rings.
- 25 production rings have been slept for 28 days without any sign of reactivity. Embarking on a program to collect more data on in hole performance and to further extend sleep time.
- A second extended sleep time trial was conducted underground in a production ring for 35 day, with no reactivity presented and minimal change in the VOD from 28 day firing data.
- Product ejection has led to changing from red caps to gas bags for stemming. Undertaking a program to assess performance of different stemming modes.

The conversion to the wireless system is an on-going strategy with daily changes in draw points impeding on precharged stocks. Currently, 40% of all blasts in 2019 were initiated utilising WebGen100, with the goal to increase to 90% in 2020.

## CONCLUSIONS

The E26 Sub level cave has enabled the recovery of the Lift 2 Southern Wedge. The complex geometries and poor ground conditions have created challenges in recovery and optimal drill and blast outcomes. The poor outcomes in blasting increased the exposure risk for the production crews, with particular attention to working in close proximity to the rill on foot during remediation. The wireless technology has enabled the near elimination of working in close proximity on foot.

The proved application of WebGen on site has enabled a trial of high lift drawbells in the blasting in the new block cave, E26 L1N. The major challenge has now shifted from the creation of a wireless detonation system to allow for sequential blasting of decked up holes, to a reliable stemming mechanism to deck the up holes and prevent connections. The intent of this trial is to create a functional methodology for all future block caves to remove the need to develop an undercut level.

## ACKNOWLEDGEMENTS

The authors acknowledge the support of the Northparkes management team throughout the wireless initiation program. The long history of innovation at Northparkes has been shown to continue over the 25 years of operation on-site.

Acknowledgement to Orica support personnel and the Northparkes charge-up operators throughout the trial, who provided practical method changes and were receptive to the change.

## REFERENCES

- AEISG Code of Practice Elevated Temperature and Reactive Ground Edition 4 March 2017
- Power, G, 2004. *Modelling Granular Flow in Caving Mines- Large Scale Physical Modelling and Full Scale Experiments*, PhD thesis, The University of Queensland, Brisbane.
- Silveria, A, Cunningham, R and Duniam, P, 2007. Propagation of the Southern Wedge – Drill and Blast, in *Proceedings EXPLOR Conference 2007*, pp 195-203 (The Australasian Institute of Mining and Metallurgy).
- te Kloot, C, Liu, Z, Purvis, T, Thomson, S, Lovitt, M, and Nguyen, T, 2017. Improving safety through technology– Orica wireless electronic blasting system trials at Ernest Henry Mine, in *Proceedings 13<sup>th</sup> Underground Operators' Conference*, The Australasian Institute of Mining and Metallurgy, pp 39-49.
- Wigging, M, Trout, P, Macaulay, B, 2005. Solving the Problems of Precharging Sublevel Caving Rings at Ridgeway Gold Mine, in *Proceedings Ninth Underground Operators' Conference*, Australasian Institute of Mining and Metallurgy, pp 81-89.

# FIBRE REINFORCEMENT SHOTCRETE IN COAL

**Barry Sturgeon<sup>1</sup>**

*ABSTRACT:* Fibrecrete Reinforced Shotcrete (FRS), a cement-based mixture pneumatically applied at a high velocity onto coal surfaces. The material component of shotcrete is essentially cement and fly ash blend in a mixed powder form combined with sand, gravel and water. This wet process of shotcrete application is unique to coal, but has been used in the civil industry and hard rock mines for many years. This process allows a good compaction of applied ground support liner that allows penetration into the strata giving a bonded liner with stability, compared to cast-in-place concrete. The advantages of the shotcrete process are related to the reduction of the installation time for ground support, compared with the traditional mesh and bolts system, with the added advantage being a reduction of labour required to place the same work load. The logistics are advanced with a better safety factor, environmental conditions, improved ventilation and reduction of roadway gases. FRS is considered as a primary and secondary support material particularly suitable and used in underground coal mining. The current use of FRS wet mix, which has significant resistance to segregation and benefits as a ground support system as implemented in Queensland mines particularly within the Bowen Basin.

## **FIBRECRETE REINFORCED SHOTCRETE (FRS) UNDERGROUND COAL**

This paper discusses the development of the FRS and the introduction of a Flameproof Shotcrete Rig (FSR), shown in Figure 1, with improved performance into underground coal mine. Over the past seven years FRS has been considered as the primary and secondary support material particularly suitable in underground coal mining. The current use of FRS wet mix, which has significant resistance to segregation and benefits as a ground support system has been implemented primarily in coal mines in the Bowen Basin area of Queensland. It allows a significant reduction in manual handling and resources in this application as it is applied by robotic spraying. Key benefits associated with FRS ground support systems and the development of the FRS to be used in all areas of the mine as listed below:

- Secondary support to development roadways
- Rehabilitation works
- Ventilation control devices
- Gas Mitigation to strata in old workings
- Underground roadways which interlock into the walls
- Drainage sumps
- M and M drift repair
- Overcasts and underpasses
- Conveyor drifts rehabilitation by hand spraying from a movable conveyor platform
- Works completed via robotic and hand spraying using the FSR

---

<sup>1</sup>Senior Project Manager - Mining CNC; Email, [b.sturgeon@cccivil.com.au](mailto:b.sturgeon@cccivil.com.au), Tel 0417 718 627



**Figure 1: Flameproof Shotcrete Rig (FSR)**

Figure 2 demonstrates FRS used as a wall and intersection support system for ground fretting and sustaining damage from trailing cables and machinery bumping the walls. The FRS is the first custom built underground self-propelled FRS. A stand-alone Diesel-powered unit that is mining compliant to be driven around the mine pumping and effectively placing FRS to the desired result with the robotic and hand held spraying diversity. The FRS is operated remotely, from a hand held control box connected to the FRS by a 10 metre (M) cable with an extendable 9.5 M boom. This ensures operators safety and mining compliance allowing the operator to be safe under supported ground during the FRS placement process. The rig can spray and place 15 cubic metres of FRS per hour depending on the delivery cycles and/or mining environmental variables and factors. This paper explores the current Fibrecreting innovative technology and methodology in addition to the FRS; pumping technology and Drop Hole Technology to allow the shotcrete mix to be dropped from the surface into receiving kettles then into a kibble and transported to shotcrete rig.



**Figure 2: Underground Intersection rib support with FRS**

### **SHOTCRETING FRS INNOVATIVE AND PRACTICAL WAYS**

The industry is yet again facing difficult times with the pressure of low coal prices and reduced tolerances to cost exposures to operations. Yet to survive in this industry it is well known over the years that such cycles do happen and will continue to happen. Mine operators and contractors need to adapt and maintain control to deliver safe coal production and financial

returns back to stakeholders and ensure corporate families continue to have confidence with the company. To achieve this, many successful companies have turned to innovation to assist in finding ways to get critical activities done in a safe, effective low cost method. This requires vision of key decision makers to recognise such things. These decision makers understand every aspect of current costs and future projections for the success for the innovation. As well as understanding the process of risk management in all areas of business and have the ability to articulate the vision of what the innovation will produce. Innovation does not have to be seen as an additional cost, but if done right, a cost reduction system by working collaboratively with clients with such innovation and vision. To recognize all of the above factors and with the expertise and the commitment of the project team and the proactive vendors heavily involved in our projects. One true testament of such innovation being successful is presented in the excellent safety results reported despite the hard financial times, thereby proving that the innovation is real and effective. This then should be used as a good example for the industry, if done right; the FRS innovation must be a priority for any business, particularly in the hard times faced today, while keeping all personnel safe.

### **SHOTCRETING INNOVATIVE SYSTEM (FOUR MOST IMPORTANT STEPS)**

Shotcreting involves four important steps: Raw Materials/ Mix Design/ Batching and testing; delivery/ placement mix and human resources. Shotcrete has the potential to be an easy and pleasurable operation and very cost effective to mine operators, giving long term results if all of the steps are followed.

#### **MIX DESIGNS**

Shotcrete mix design relies on raw materials, their shape and ability to pack, and a good ongoing supply of a constant gradings. The quality of the cement blend and clinker needs to be of a general purpose fly ash blend. To reduce the risk of flotation, potable water must be utilised in conjunction with the correct use of prescribed chemicals and dose rates as directed by the chemical providers. Batching plants are required to meet all of the Australian standards and have a full computerised recording system in conjunction with multi weight bins. Each and every load must meet the required slump, be checked at the batch plant, and leave the batch plant fully mixed.

#### **BATCHING**

The mix needs to be of a high standard following quality assurance and quality control procedures to meet with the Australian Standards. Batching can be altered to meet the individual needs of mine manager's dependant on mix design rules.

#### **DELIVERY MIX**

FRS is delivered by a mixing agitator road truck from a local concrete batch plant to the drop off point in the mine. It needs to be well mixed before the delivery is slumped and dispatched. The mix needs to meets the required slump design, then dispatched into a drop hole or waiting kibble slump retention. It is vital that additional water not be added on site as this will reduce the mix design strength. As shotcrete is used as a ground support system, strength is of high importance in conjunction with flexible-strength and toughness of the FRS mix. Therefore using the drop hole system which does not impact on the mix, design testing is carried out on a weekly basis checking strength on the surface at the batch plant and sampling the FRS at the receiving point in the underground from the same load. Demonstrated results from tests carried out by National Association of testing Australia (NATA) are shown in Tables 1-3.

### DELIVERY AND PLACEMENT OF THE FRS UNDERGROUND

The FRS is delivered to the spray machine via kibble. Depending on the location of the drop hole it may take up to 60 minutes to get into the application area. All loads have been retarded for four hours, giving time for the product to be transported from the batch plant and out to the onsite location. Once the FRS enters the machine, the pumping commences and a hydration activator chemical is injected into the mix whilst spraying. Spraying coverage is managed utilising placement pins arranged in diamond patterns.

### FRS SYSTEM DEVELOPMENT

The system for coal was developed in the 1990's overseas where it was tested to withstand the constant movement and fretting associated with coal mines before being introduced to Australia in 2012. The catalyst for FRS was due to mines experiencing drift and strata failure. It was imperative that a permanent low risk solution be found to mitigate the risk of reoccurrence. With this in mind a full design was completed and evaluated by multiple experts, both internal and external to the company. The implementation and objectives of the project was to increase the safety factor of the support in drifts and life mine system. Figure 3 demonstrates the Round Determined Panel (RDP) size and design sprayed with the same FRS as placed in the underground.



Figure 3: Sprayed RDP

Table 1: RDP testing results (tested by NATA - Mackay)

Sample Date	Concrete Class	Report No.	Location	Joules – Energy at 40mm	
				Joules	Age (days)
25/04/2018	32Fibrecrete - 6kg/m3 fibre	102544	49-52CT D-F Hdg Mains	570.0	28.0
25/04/2018	32Fibrecrete - 6kg/m3 fibre	102545	49-52CT D-F Hdg Mains	448.0	28.0
25/04/2018	32Fibrecrete - 6kg/m3 fibre	102546	49-52CT D-F Hdg Mains	424.0	28.0
25/04/2018	32Fibrecrete - 6kg/m3 fibre	102547	49-52CT D-F Hdg Mains	554.0	28.0
2/05/2018	32Fibrecrete - 6kg/m3 fibre	102976	67-69CT D-F Hdg Mains	373.0	28.0



Figure 4 the 400 mm x 400 mm sprayed sample it is cored where four sample get removed and tested at 7 days 14 days 21 days 28 days



**Figure 42: 400 mm x 400 mm core panel**

**Table 2: Core panel testing results carried out by Nata of Mackay**

Sample Date	Concrete Class	Report No.	Location	Compressive Strength (MPa)				
				7	14	21	28	56
11/06/2019	32 Fibrecrete - 6kg/m3 fibre	5676/R/51996-1	20-21CT C HDG 2nd North Mains	19.5	26.0	29.0	32.5	-
18/06/2019	32 Fibrecrete - 6kg/m3 fibre	5676/R/52194-1	22-23CT C Hdg 2nd North Mains	24.5	26.5	28.0	30.5	-
25/06/2019	32 Fibrecrete - 6kg/m3 fibre	5676/R/51948-1	TG604 X Drive	23.5	26.5	26.0	28.5	-
4/07/2019	32 Fibrecrete - 6kg/m3 fibre	5676/R/52672-1	2-9CT B HDG East Mains	20.5	22.5	26.0	30.0	-
9/07/2019	32 Fibrecrete - 6kg/m3 fibre	5676/R/52823-1	14-18CT HDG East Mains	19.5	21.5	22.5	24.5	-

**Table 3: Record of concrete compressive strength reports (Tested by Nata of Mackay)**

Sample Date	Concrete Class	Report No.	Location	Compressive Strength (Mpa)				
				7	14	21	28	56
19/03/2019	32 Fibrecrete - 6kg/m3 fibre	14892/R/20997-2	66-67CT E Hdg Mains	17.5	23.0		32.5	-
26/03/2019	32 Fibrecrete - 6kg/m3 fibre	14892/R/21032-1	66-67CT E Hdg Mains	25.0	30.5		36.0	-
2/04/2019	32 Fibrecrete - 6kg/m3 fibre	14892/R/21037-2	81CT D-E Hdg Mains	20.0	25.0		30.3	-
9/04/2019	32 Fibrecrete - 6kg/m3 fibre	14892/R/21199-1	14-15CT HDG 2nd N/Mains	16.5	25.0		33.3	-
24/04/2019	32 Fibrecrete - 6kg/m3 fibre	14892/R/21284-1	17-20CT C HDG 2nd N/Mains	26.5	29.5		36.5	-

Figure 5 shows the 400 x 400mm steel core box where the FRS is sprayed into the test box for sampling.





**Figure 43: 400mm x 400mm Core Panel Box**

### **PEOPLE**

In order to achieve quality application, the collaboration of a skilled project team with the commitment of stakeholders with a shared vision of the project outcome is required. Additionally, the operating team members in charge of placing the FRS need to be fully trained in placing FRS on to the coal strata as this differs from hard rock spraying.

The support team helping with the placement FRS needs to be of a high standard in delivering the FRS to the FSR they need to understand the QA-QC requirements as well as being very confident with the pumping process of the FSR

### **SUMMARY**

The innovation of the FRS system was more than just a shotcreting machine and spraying shotcrete for different purposes. There were various additional innovations to support the differing system uses, which have been found for this new innovative material in coal. This system has been heavily used in Hard Rock mining for the past 40 years, initiating in the Mount Isa region before expanding to other areas. Examples of its use include several mines in the Mount Isa Mining District Mine (A) Deep Copper Mine used daily in conjunction with the in cycle mining system Mine (B) development of life of mine roadways Today the Hard Rock mines located in all parts of Australia use FRS on a daily basis as permanent ground support this has allowed them the ability to reduce the bolting patterns and numbers of bolts. Civil Industry use FRS as a ground support under the exposed segments it is used as a sealing process and permeant support within the tunnel system Tunnel (A) located in Queensland going under the Brisbane river is a prime example of the versatility FRS tunnels located in New South wales and Victoria all use FRS as their secondary and primary support. Even the construction industry, use FRS in Dam construction and roadway bank surfacing on major highways ( Dam (A) Roller Compacted Concrete (RCC) dam wall RCC is one of the first to be constructed in Australia using the FRS to enhance the wall surfacing and supporting the RCC process compaction significant advances have been made with this work.

# HEALTH MONITORING OF MINING CONVEYOR BELTS

Shuvashis Dey<sup>1</sup>, Omar Salim<sup>2</sup>, Hossein Masoumi<sup>3</sup>, and Nemai Karmakar<sup>4</sup>

**ABSTRACT:** The paper presents a new methodology for monitoring health conditions of mining conveyor belts using Radio Frequency Identification (RFID) based sensors. The existing monitoring technique is based on simple visual inspections which is quite labor intensive and do not provide accurate health condition of the conveyor belt. The new methodology based on UHF chipped and chipless RFID sensors provides highly sophisticated real-time monitoring schemes for different conveyor belt health parameters such as cracks. When combined with machine learning algorithm-based approach, the proposed technique can detect and predict wear and tear over the entire belt. Simulation results show that the proposed methodology offers high accuracy in detecting cracks with width of 0.5 mm and demonstrates the efficiency of RFID sensors to track the crack orientation in the belt.

## INTRODUCTION

Zipper failure and conveyor belt rips induce a great safety, maintenance and financial concern for the coal mining industry. Many injuries and fatalities in coal mines have been caused by such failures. The conveyor belts carry thousands of tonnes of materials per hour and a stoppage in their operation for a mere minute causes the industry to lose a significant amount of revenue between \$600 and \$1800 Australian dollars per minute (Owen, 1997). To address such issues, many systems for monitoring health of the conveyor belt have been designed in the past to prevent or even reduce the damage of longitudinal belt rips. The first system mentioned in Davis (1987) depends on the mechanically operated devices that use two cables installed under the belt with alarm buttons on each of its sides. Ultrasonic operated devices are also used, which show the differences in the power of received signal if the belt undergoes longitudinal rips. The main problem of using ultrasonic devices is the coupling of the high-frequency waves to the belt materials as well as the impact of air and dust on them. Moreover, the ultrasonic system requires high maintenance and it only works in some special scenarios of the belt. Other systems use electrically operated devices that consist of a stationary transmitter and receiver as well as conductive loops across the width of the belt from edge to edge. The conductive loops must be very large to achieve good coupling between the transmitter and receiver leading to high maintenance cost. Current belt temperature measurement techniques include thermal imaging cameras and non-contact thermal measurement systems. The most recent studies by Yang, et al., (2014) and Li, et al., (2018) investigated the use of machine vision detection for longitudinal rip of conveyor belt. The system based on machine vision is quite expensive and requires high installation and maintenance cost. Moreover, the rip detection based on machine vision is usually influenced by external light sources and electromagnetic noise. In this regard, the passive Radio Frequency Identification

---

<sup>1</sup> Research Fellow, Monash University, Email: Shuvashis.Dey@monash.edu Tel: +61 3 9905 53478

<sup>2</sup> Research Fellow, Monash University, Email: Omar.Salim@monash.edu Tel: +61 3 9905 53478

<sup>3</sup> Senior Lecturer, Monash University, Email: Hossein.Masoumi@monash.edu Tel: +61 3 990 56468

<sup>4</sup> Associate Professor, Monash University, Email: Nemai.Karmakar@monash.edu +61 3 9905 1252

(RFID) technology could offer a simple solution for monitoring the health of conveyor belts and it provides absolute robustness in harsh environments.

## RFID BASED SENSORS

Recent advances in combining sensor and sensing technologies with RFID systems can monitor and share information about the surrounding environment by using sensor-enabled tags. An object that simultaneously provides its own condition and identification simplifies the total infrastructure and enhances the quality of information. Designing appropriate sensors and their associated measurement circuits currently pose a challenge towards developing a low-cost intelligent sensing system; passive RFID sensors shown in Figure 1 can be an excellent solution for this challenge (Subhas, 2013). Passive electromagnetic (EM) transduction based RFID sensors are employed to detect a range of physical parameters to address different sensing parameters relevant to the belt. The sensors are proposed to be integrated into the belts and they are interrogated by RFID reader to obtain their electromagnetic signature which is displayed at operator's dashboard in central database management center.

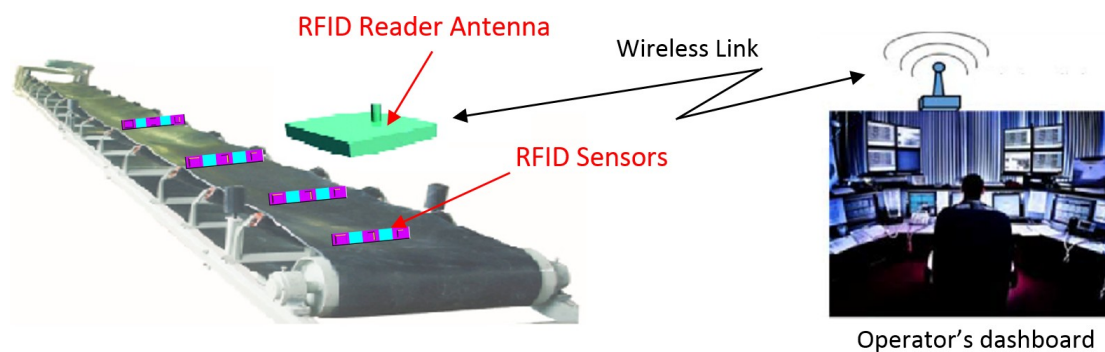


**Figure 1: Generic diagram of a conveyor belt with integrated RFI sensors.**

Such signatures contain information about the belt health and thus enable the detection of any inconsistencies such as a rip in the belt. Here, the detection of cracks using chipless RFID sensors is achieved by observing the resonance frequency shift compared to that of the one in the intact state, while the change of the received signal strength indicator (RSSI) from the UHF RFID sensor is used to detect the cracks in the belt (Dey, et al., 2015). The machine learning technique is also proposed to analyse the RFID sensor extracted data and enable the prediction of any disruptions on the entire conveyor belt such as applied pressure, local temperature, humidity, and gas concentration. Identifying these physical parameters is important in manufacturing, biotechnology, pharmaceuticals, precision agriculture and consumer goods applications (Das, 2015, Dey, et al., 2015). These sensors can also be used in structural-health monitoring systems to detect strains and cracks in aerospace, military, civil or architectural structures as well as mining industry. The tremendous robustness of RFID sensors in harsh environments has been proved recently (Popperl, 2016).

Monash Microwave, Antenna, RFID and Sensor (MMARS) Laboratory within the Monash University has successfully developed RFID sensors for different practical applications such as crack detection and monitoring (e.g. Kalansuriya et al. 2012, Dey, et al., 2014, Dey, et al., 2015), humidity sensing (e.g. Amin et al. 2013, Amin, et al., 2013, Amin, et al., 2014), precision agriculture (Dey, et al., 2016) and multi-parameter sensing (Amin, 2016).

## MACHINE LEARNING

Machine learning is a data analysis technique which can automate analytical model building. In other words, it is the science of enabling computers to perform without being explicitly programmed. It can be used to augment human ability to come up with solutions for different types of problems and make informed decisions on them. Machine learning can be applied to solve a variety of issues starting from diseases diagnosing to even global climate change. This is a specialized branch of artificial intelligence (AI) which lets a system to learn from data, identify patterns and make inferences with least human involvement. Machine learning has iterative characteristics, which allows the system models to independently adapt when they are exposed to new data. It lets the models to learn from preceding computations to generate consistent and repeatable results. As for example, the RFID sensor generated temperature and strain data can be used with the machine learning algorithm to *develop* a failure prediction tool.

## NEW METHODOLOGY USING RFID SENSORS

Figure 1 shows a new methodology for monitoring health conditions of mining conveyor belts using RFID based sensors. As shown in Figure 1, the proposed RFID based wireless sensing system deploys UHF chip based as well as chipless RFID sensors

## SIMULATION RESULTS AND DISCUSSIONS

In this section, a conveyor belt made of a combination of four aramid fiber and three reinforced fabric layers is designed using Computer Simulation Technology (CST) Microwave Studio software, as shown in Figure 2. The RFID sensor based on chipless tag is also designed here using Taconic TLX-8 substrate material. The dielectric constant of this material is 2.55 and the loss tangent is 0.0019. The simulated operating frequency range of the designed tag is 2-3 GHz. The CST simulation is conducted to perform the following analyses as well.

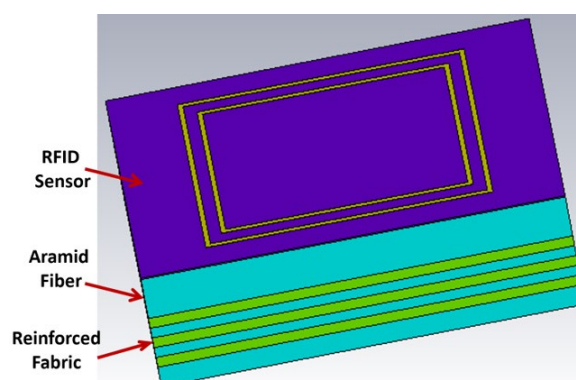
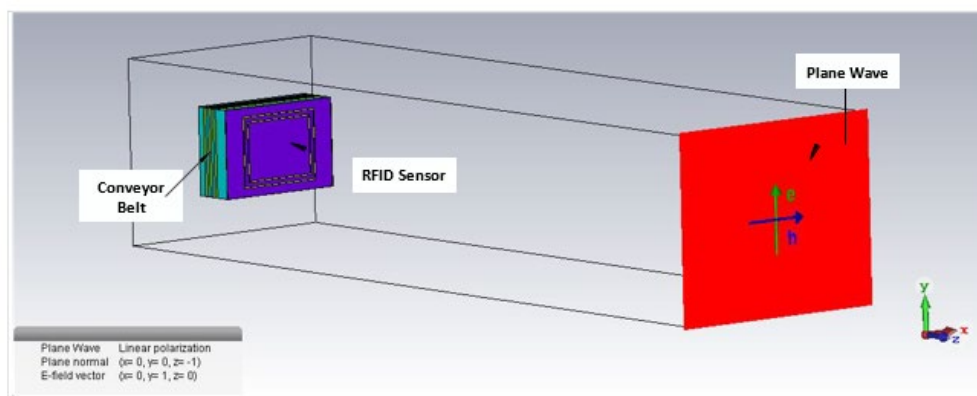


Figure 2: CST Design of conveyor belt along with the RFID sensor

### RCS response

The backscattered radar cross section (RCS) response of the sensor is extracted and analyzed by interrogating it using a vertically polarized plane wave as shown in Figure 3.



**Figure 3: Sensor interrogation using plane wave**

A comparative RCS response of the conveyor belt at the presence and absence of sensing tag is shown in Figure 4. As depicted, the belt alone provides a flat RCS response whereas the sensing tag has a resonating notch of about 20 dB with a resonance frequency at 2.74 GHz. This frequency is used as the reference frequency of the intact (healthy non-cracked) state of the belt to detect and measure the crack variation in the next analytical sections.

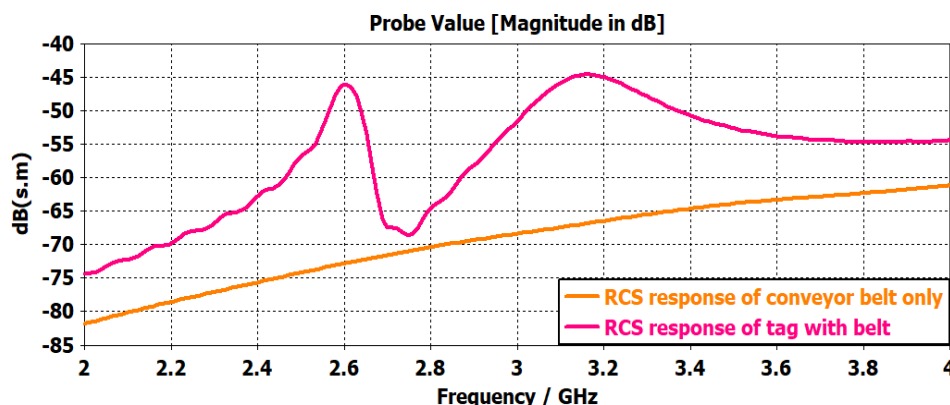


**Figure 4: RCS response of the sensing tag compared to the belt response**

**Crack detection and analysis of its width variation**

In this section, the sensor is used to detect cracks on the belt. Figure 5 shows the sensor with belt having a crack of 0.5 mm width. The comparative RCS response of the sensor for the healthy and cracked condition is shown in Figure 6. The crack introduces an apparent reduction in the dimension of the resonating arms and this in turn interrupts the electrical current path inside the tag's structure. This results in a resonance frequency shift of the sensor by 47.65 MHz from that of the intact state. Such phenomenon clearly indicates that the RFID based sensors have the ability to detect cracks even if their width is very narrow.

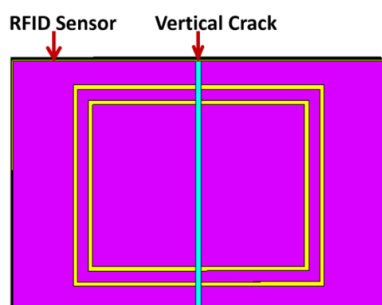


**Figure 5: RFID sensor with crack**

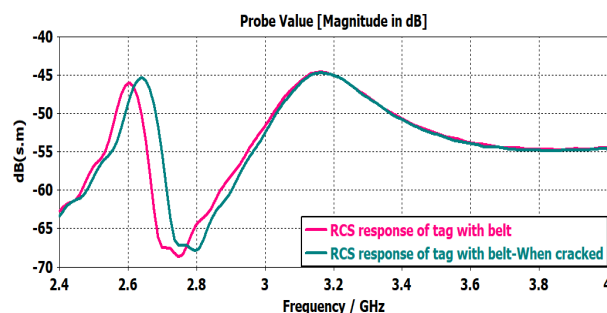


**Figure 6: Comparative RCS**

### Response of sensor

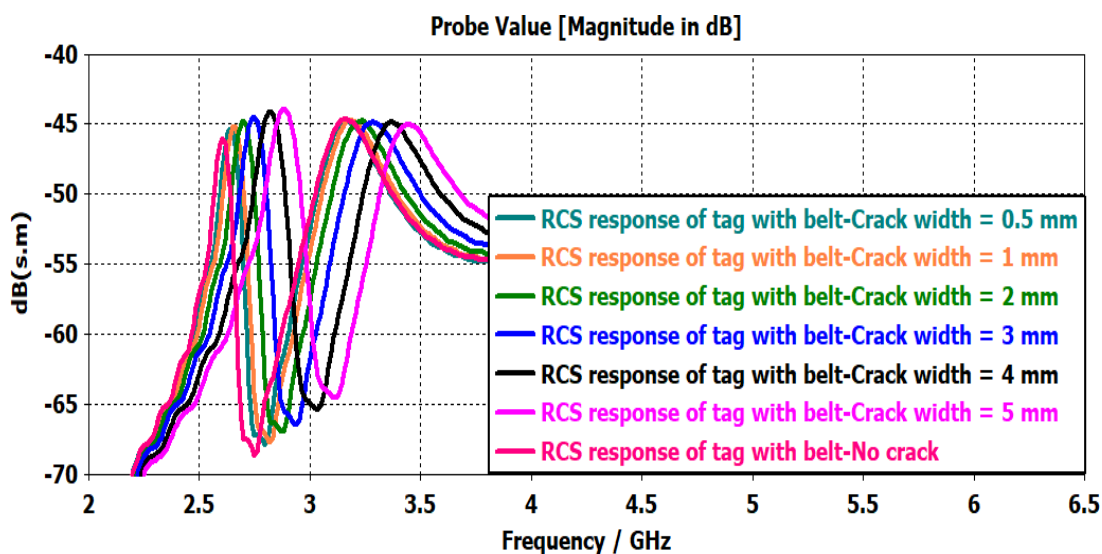


**Figure 7: RCS response of sensing tag at different crack width**

Figure 7 shows the RCS response variation of the sensing tag for different crack width ranging from 0.5-5 mm which corresponds to the resonance frequency shift between 47.65 - 370 MHz. As observed from the figure, the resonance frequency shift can suggest the presence of a crack in the belt whereas the value of the resonance shift can indicate the crack width.

Figure 8 shows the resonance shift of the sensor for different crack width. As illustrated in the figure, the RFID sensor can track the crack variations since the shift of resonance frequency has a linear relationship with the crack width. The result in Figure 8 also clearly shows the ability of the RFID sensor to monitor the health condition of the belt. Such monitoring can help making a decision to manage maintenance actions such as mechanical services, repairing and replacement.

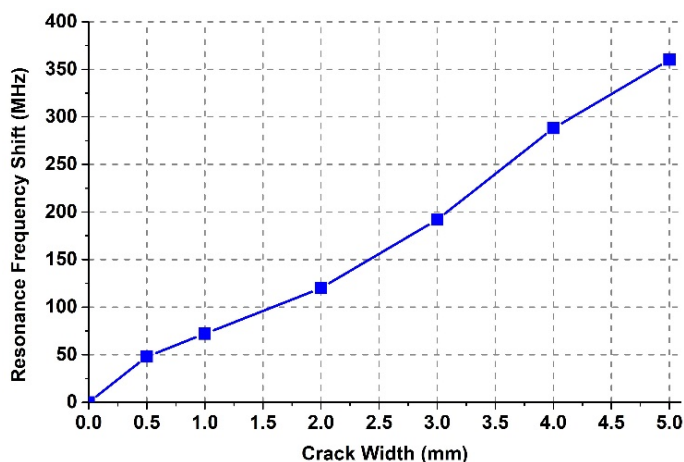


**Figure 8: Resonant frequency shift of sensor for different crack width**

### Crack Orientations

In this section, the RFID sensor is analyzed for different crack orientations such as vertical, horizontal, and angled crack propagation in the belt as shown in Figure 9.

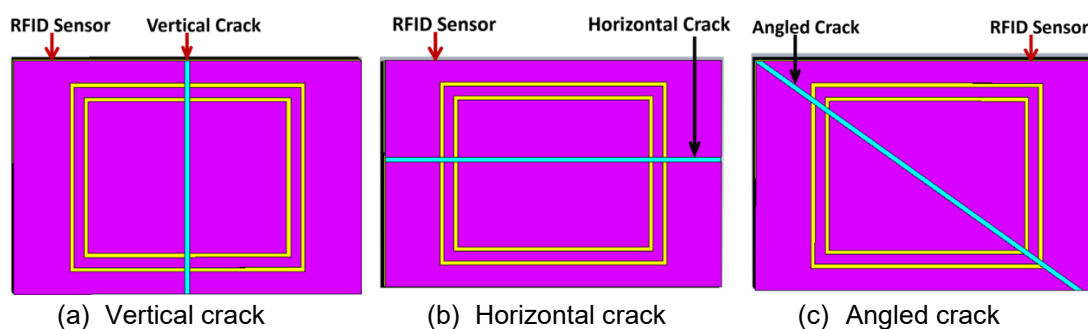


Figure 9: RFID sensor with different crack orientation

The RCS response of the tag at different crack orientations is illustrated in Figure 10. As shown in the figure, the nature of RCS response is varied based on the orientation of crack. When compared to the response of an intact state, the vertical crack incurs a linear shift of resonance (as observed in figure 6, 7 and 8). However, for a horizontal crack, an abrupt shift of 2.29 GHz is encountered as the resonance frequency changes to 5.03 GHz from the intact state resonance of 2.74 GHz.

For the angled crack, the resonance notch appears to get split into two separate notches with a significantly shorter RCS depth. The results depicted in Figure 10 clearly shows that the orientation of crack propagation on the belt can be identified based on the RCS response of the sensor

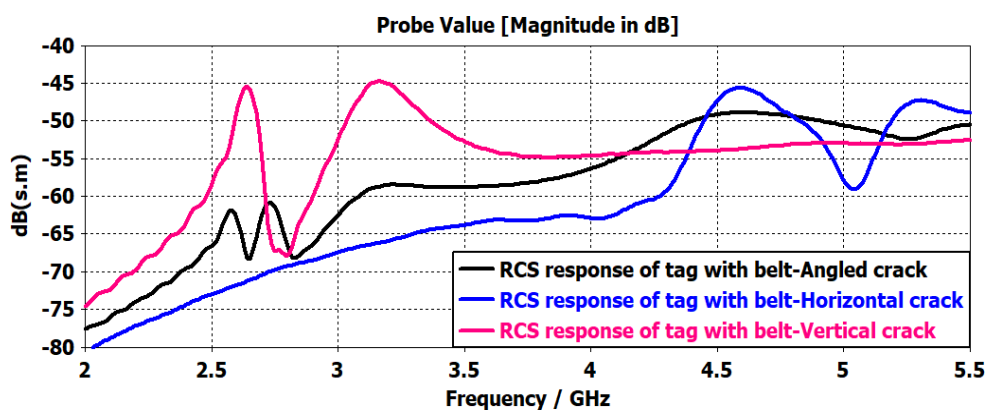
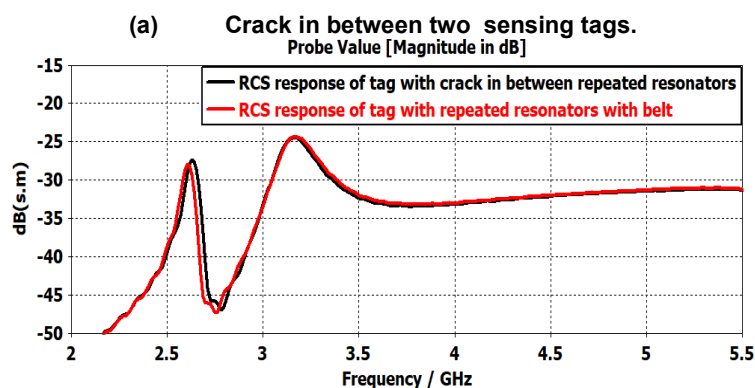
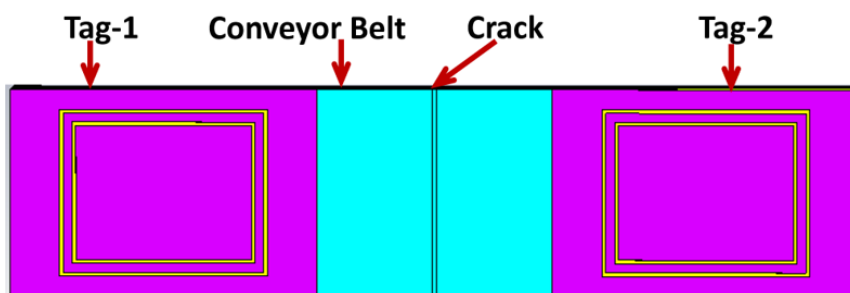


Figure 10: RCS response of tag at different crack orientations

### Crack propagation in between sensing tags

This section describes the RCS response of crack in between the tags (severing the belt only). In this analysis, a crack with the width of 0.5 mm is propagated through the conveyor belt without perturbing any of the tags, as shown in Figure 11 (a). Figure 11 (b) shows the comparative response of the scenarios when a crack is present and absent in between the sensing tags. As observed, the resonance frequency of cracked condition is shifted by 54 MHz compared to that of the intact state.





(b) Comparative RCS response of crack presence and absence between two sensing tags.

**Figure 11: Crack propagation in between sensing tags**

The result in Figure 11 highlights a significant use of RFID sensors to monitor conveyor belts since the crack is detected even if it is not occurred in the sensor structure itself. Therefore, it can be deduced that the RFID sensors can be used to detect the presence and growth of the crack irrespective of whether it propagates through both the belt and the sensor structure or through the belt only.

## CONCLUSIONS

This paper provides a brief overview of the RFID based conveyor belt health monitoring system. A proof of concept of the sensing scheme is provided by using a simple chipless RFID based crack sensor design. The simulated analysis depicted that the sensor is able to detect the presence and growth of a crack on the belt surface. The future analysis of such sensing system would involve the fabrication and field measurement of the sensor. The extracted information from the field test will be used as training data set for machine learning to develop a reference/calibration data set. When the sensors are deployed in a mass scale for sensing operation, such reference data set can be used for analyzing any random sensor response. This will enable an efficient integrity testing of conveyor belts and will eventually reduce the zipper failure by a significant scale and hence make the Australian coal mines a better, secure and safe place for the workers.

## ACKNOWLEDGEMENTS

The authors would like to thank ACARP for their monetary funding of the project.

## REFERENCES

- P. Owen, 1997. Condition monitoring for conveyors, in *Proceedings of the 9th International Materials Handling Conference*.

- C. M. Subhas 2013. Recent advancements in smart sensors and sensing technology,” in *Advanced RFID Systems, Security, and Applications*, K. N. Chandra, Ed. Hershey, PA: IGI Global, pp. 334–353.
- R. Das. (2015, June 14). Chipless RFID—The end game. [Online]. Available: <http://www.idtechex.com/research/articles/chipless-rfid-the-end-game-00000435.asp>
- G.J. Davis, 1987. Modern Concepts in Belt Rip Detection for Steel-Cord Reinforced Conveyor Belts, *4th Int. Materials Handling Conference BELTCON, South Africa*.
- Y. Yang, C. Miao, X. Li, X. Mei, 2014. On-line conveyor belts inspection based on machine vision, *Optik* 125 (19) pp. 5803–5807.
- Xianguo Li, Lifang Shen, Zixu Ming, Can Zhang, Hangqi Jiang, 2018. Laser-based on-line machine vision detection for longitudinal rip of conveyor belt, *Optik* 168 pp. 360–369
- M. Pöpperl, J. Adametz and M. Vossiek, 2016. Polarimetric Radar Barcode: A Novel Chipless RFID Concept With High Data Capacity and Ultimate Tag Robustness, *IEEE Transactions on Microwave Theory and Techniques*, vol. 64, no. 11, pp. 3686-3694, Nov.
- P.Kalansuriya, R. Bhattacharyya, S. Sarma, and N. Karmakar, 2012. Towards chipless RFID-based sensing for pervasive surface crack detection, in *Proc. IEEE Int. Conf. RFID-Technologies Applications*, pp. 46–51.
- S. Dey, P. Kalansuriya, and N. C. Karmakar, 2014. Chipless RFID based high resolution crack sensing through SWB technology, in *Proc. IEEE Int. Microwave RF Conf.*, pp. 330–333.
- S. Dey, J. K. Saha, and N. C. Karmakar, 2015. Smart sensing: Chipless RFID solutions for the Internet of everything, *IEEE Microw. Mag.*, vol. 16, no. 10, Nov., pp. 26–39.
- E. M. Amin, S. Bhuiyan, N. Karmakar, and B. Winther-Jensen, 2013. A novel EM barcode for humidity sensing, in *Proc. IEEE Int. Conf. RFID*, pp. 82–87.
- E. M. Amin, N. C. Karmakar, and B. Winther-Jensen, 2013. Polyvinyl-alcohol (PVA)-based RF humidity sensor in microwave frequency, *Prog. Electromagn. Res. B*, vol. 54, Sept., pp. 149–166.
- E. M. Amin, M. S. Bhuiyan, N. C. Karmakar, and B. Winther-Jensen, 2014. Development of a low cost printable chipless RFID humidity sensor, *IEEE Sensors J.*, vol. 14, no. 1, pp. 140–149.
- S. Dey, P. Kalansuriya, and N. C. Karmakar, 2016. Electromagnetic characterization of soil moisture and salinity for UHF RFID applications in precision agriculture”, in *Proc. IEEE European Microwave Conf. (EuMC)*, pp. 616-619.
- E. M. Amin, N. C. Karmakar, B. W. Jensen, 2016. Fully printable chipless RFID multi-parameter sensor, *Sens. Actuators A Phys.*, vol. 248, pp. 223-232.

# **SAFETY ASPECTS OF DISPOSAL OF A MINE AND ABANDONED UNDERGROUND WORKINGS AND RISKS RESULTING FROM THE MINE DISPOSAL**

**Radovan Kukutsch<sup>1</sup>, Petr Waclawik<sup>2</sup>, Jan Nemcik<sup>3</sup>, Libin  
Gong<sup>4</sup>**

*ABSTRACT:* Since time immemorial, mining has been an inseparable part of human history. Generations of our ancestors drove and excavated mining workings to enable them find and exploit useful minerals from the ground. Shafts, drifts and corridors created in this way, however, had always limited service life; their significance and purpose mostly expired as soon as the available reserves in the deposit were exhausted. Unused workings were then often abandoned without having been disposed and safeguarded properly. For mining companies, namely, these activities represented and still represent spending of substantial financial resources with zero economic effect. This always relied exclusively on the contemporary state of mining legislation at the given place and time as well as executive ability to check and enforce pertinent provisions of the mining law concerning disposal of mining workings. Nevertheless, existence of an insufficiently disposed or unsecured working represents a considerable safety risk for the surroundings, whereas this paper includes reasons for disposal and requirements for proper disposal of the mine.

## **INTRODUCTION**

Decommissioning and disposal of an underground mine is an integral part of the mining capacity implementation cycle, irrespective of the kind of the mineral resource and deposit location (Makarius 1999).

It is caused by natural and technological factors (depletion of usable deposits, technology of mining and treatment of the mineral resource), commercial (loss of strategic characteristic of raw materials) or economic factors related to insufficient level of the production sales or its prices, which does not enable creation of sufficient financial flows to finance the mining entity's business activities.

Technical disposal of permanently terminated operation in mining workings represents a set of works and necessary precautions which must provide for elimination of potential risks for the future in which the underground will not be accessible (Hudeček et al. 2007).

---

1 Dr/Researcher, The Czech Academy of Sciences, Institute of Geonics. kukutsch@ugn.cas.cz +420 596979242

2 Dr/Researcher, The Czech Academy of Sciences, Institute of Geonics. waclawik@ugn.cas.cz +420 596979701

3 Dr/Honorary Senior Fellow, University of Wollongong. jnemcik@uow.edu.au +61 2 4221 44920

4 Ph.D. Graduate, University of Wollongong. lg283@uowmail.edu.au +61 424387896

Technical disposal of an underground mine after completion of early development, preparatory works and mining involves:

- technical disposal of the mine underground;
- technical disposal or safeguarding of the surface (removal of machinery and equipment, disposal of building objects, operating units) if the surface objects are not to be used for other purposes;
- elimination of consequences of mining activities with regard to restoration of the area for other utilisation, including removal of mining damage, redevelopment and reclamation of plots affected by extraction.

### **SAFETY ASPECTS OF DISPOSAL OF THE MAIN MINING WORKINGS, MINE AND ABANDONED UNDERGROUND**

Potential risks during disposal of main mining workings include (Hudeček et al. 2007):

- impaired stability of the working opening (subsidence of the working opening and its incoherent surroundings into the shaft as a result of the backfill material slide or break of the bulkhead);
- sudden surface subsidence (caused by caving of the drift, for instance)
- ascent of mine gases to the surface (with possible accumulation of gases in objects, with subsequent explosion, inflammation or poisoning).

#### **Impaired underground stability of abandoned workings**

*Insufficiently disposed underground workings:* Impaired stability of the shaft opening means slide of the shaft opening and its incoherent surroundings into free spaces in the shaft or adjacent corridors as a result of insufficient disposal of the shaft in the past. The highest imminent risk includes cases of objects built directly above the shaft or in its immediate vicinity. In practice, several types of insufficiently disposed shafts can be found.

- The shaft is only closed by means of a closing pit bank bulkhead. The stability is impaired by breakthrough of the bulkhead (caused by aging of the material used or exceeding of its bearing capacity) or collapse of incoherent rocks into free spaces.
- In some cases, particularly of very old shafts, only the upper part of the shaft was backfilled to the created bulkhead, mostly wooden, which collapsed with subsequent slide of the backfilling material and breakdown of the shaft opening and its incoherent surroundings.
- Another cause of impaired stability of the shaft is slide of unconsolidated backfilling material into unfilled corridors mouthed into the shaft, as a result of insufficient strength or total absence of closing dams at the shaft entrances.

- One of the possibilities of impaired stability of the shaft is slide of backfilling material into free space in the shaft, which developed at the filling time owing to insufficient fragmentation of the material which fills up the free spaces only partly or creates an arch in the shaft.
- Another possible cause of the backfilling material slide and thus the impaired shaft stability is insufficient removal of the shaft accessories and filling of ducts and ventilation pipes.
- Non-observance of specified precautions and procedures during monitoring of the backfill state and its refilling during disposal of main mining workings is another of the possible risks.
- Non-observance of technological procedures during production of consolidated cement-ash mixture and concrete for the pit bank plug, or consolidated plug in the pit shaft can also add certain risks of impaired stability of the main mining workings disposed.
- Backfilling materials of certain types can also slide if the backfilling material is flooded with water, its properties totally change, and it subsequently pours out into the free spaces. Such cases occur, for instances, after heavy rains or partial flooding of the shaft with mine waters.

Water effect on the backfilling material stability: Impaired stability of unconsolidated backfilling material in the shaft may also be caused by water if any of the following cases occurs (Slivka et al. 2007):

- creation of a water column above the impermeable plug in the shaft;
- watering or hydraulisation of the backfilling material above the impermeable plug;
- flooding of mining spaces including the backfill in the shaft.

#### **Water column above impermeable plug in the shaft**

During disposal, a column of water flowing in the shaft may form, either by creation of a watertight plug in the shaft or by filling the shaft with impermeable material. In this case, the water column acts on the backfilling material in the shaft with hydrostatic pressure corresponding to the water column height. This pressure may rise so that the shaft plug cannot resist this pressure or the backfilling material is pushed by the water column out into the free mining spaces.

#### **Watering of the backfilling material above the watertight plug**

The shaft is filled up with unconsolidated backfilling material, whereas a watertight plug is created at a certain depth or this plug is created in the backfilling material by sedimentation of its small fraction, in which way the backfill becomes impermeable. The backfilling material above the plug is saturated by the inflowing water. This material, however, is of such a kind as not to behave as a hydraulic liquid (such as dump material) after watering. In this case, pressure is created equal to the sum total of the backfilling material pressure and water pressure.

### **Hydraulicization of the backfilling material above the watertight plug**

In the shaft, the same case occurs as with the above-mentioned watering of the backfilling material; in contrast, the shaft is filled up with a material behaving like a hydraulic liquid after being flooded with water. Only materials composed primarily of silts and fine sands (0.002–0.2 mm), which are able to be hydraulised, can behave in this way.

### **Flooding of mine spaces including the shaft backfill**

The shaft is filled up with unconsolidated backfilling material; subsequently, *the mine spaces including the shaft are flooded*, partly or up to the surface. In this case, it depends on the type of the backfilling material whether it can or cannot be washed out or even hydraulised.

In the flooded shaft with *water-saturated backfill material*, pressures caused by the water in the shaft and surrounding free spaces equalize and only pressures induced by the backfill material are acting.

If the backfill material in the shaft behaves like a *hydraulic liquid*, this material induces pressure which is approximately twice as high as the pressure induced by water in the surrounding flooded free spaces. Consequently, the backfilling material may slide into these spaces.

Effect of water on the backfilling material stability in the shaft can be expressed by the degree of risk of the backfilling material slide.

### **Degree of risk of the backfilling material slide caused by flooding**

- 1) shafts unaffected by flooding of the backfilling material
- 2) shafts with a negligible risk (consolidated backfilling material; flooding in a short shaft length only; flooding only in the case of the full retention tank; unconsolidated backfilling material, but smaller flooding depth and closing dams at the levels).
- 3) shafts endangered by slide of the backfilling material (unconsolidated backfilling material and higher flooded depth with closing dams at the levels; without any objects in the safety zone (hereinafter SZ); disposal without dams, but with a concrete plug under the pit bank).
- 4) shafts dangerous for slide of the backfilling material caused by flooding (unconsolidated backfilling material, higher flooded depth, without closing dams at the levels and with objects in SZ).

### **Surface subsidence spots**

Another risk and harmful effect of abandoned underground workings is creation of *surface subsidence* caused by caving of old drifts, air-raid shelters or by subsequent settlement of seam stopes at low depth under the surface, particularly of worked-out areas of seams in steep dips. This is a particular risk of shallow-positioned deposits with seeping surface water, which can cause waterlogging of the ground and influence conditions of surface objects. Here one must try to dispose of them by means of adequate additional backfilling. Subsidence places may form on the surface as a result of the sudden surface descend, which can both endanger the safety on the surface and cause loss of stability at the shaft opening.

Dimensions and design of the safety area of the main mining working, drift and inclined shaft is determined by calculation according to the specified methodology (Makarius 2000).

### **Ascent of mine gases to the surface**

After termination of mining activities and disposal of the mine, mine gases, primarily methane, continue escaping from the carboniferous massif. One speaks of the so-called *residual gas-bearing capacity*. Ascent of mine gases to the surface is influenced by a variety of natural, atmospheric and mining-engineering factors. After termination of controlled ventilation of the mine, the mine gases may uncontrollably ascend to the surface by natural and artificial communications. Various exceptional events give evidence of this fact (Žůrek et al. 2012).

The source of an exceptional event is methane accumulated at explosive concentration in the mining workings disposed. A ventilation plant must be in permanent operation in the spaces.

In term of the extent of the area affected by ascent of mine gases to the surface, the following is distinguished:

- **point ascent** (that is, ascent though abandoned underground parts opened to the surface);
- **areal ascent** (that is, ascent from worked-out areas of seams at places of gas-permeable covering formation or through tectonic zones).

During disposal of main mining workings opened to the surface, ascent of mine gases is one of the risk factors, see Fig 1.



**Figure 1: Gas explosion at Hermanice Mine during the liquidation of the He-III shaft**

### **Artificial communication with the surface**



Artificial communications cause the so-called point ascent of mine gases to the surface, which is caused by:

- *Mining and underground workings* (shafts and drifts opened to the surface);
- *Geological workings* (older surface test holes of larger diameters).

In connection with every mine disposal, risks related to the ascent of mine gases must already be assessed within processing of project documentation; to prevent them, technical and safety measures must be specified in a plan, particularly on the basis of:

- evaluation of gas-bearing capacity of the mine at the time of its exploitation, prognosis of residual gas-bearing capacity;
- determination of the ventilation system, or degassing in the disposal process;
- design of the monitoring system.

#### **Issues of interconnection with adjacent mines**

- work at the boundary of the mining area;
- possible impacts of the disposal on the adjacent mining area;
- changes of ventilation in connection with disposal of some of the interconnected mining areas;
- changes of water pumping in connection with disposal of some of the interconnected mining areas;
- transfer of resources.

#### **Principles of treatment of worked-out underground and stopes of the disposed mine**

Disposal of the mine by backfilling its underground spaces is aimed at both long-term safeguarding of the actual mine underground and minimization of impacts of mining activities on the surface as well as, naturally, economic feasibility of the works and environmental friendliness of the entire process of disposal. The basic safety condition of the mine disposal by backfilling is filling up of free spaces of the mine from the deepest level to the surface and from the mining area boundary to the shafts.

The decision on the method and extent of the disposal of the mine or its parts is significantly influenced by these criteria:

- Minimization of subsidence risks and effects on the surface after completion of the mine disposal

- Elimination of potential water migration in the mining area affected by mining after completion of the mine disposal
- Minimization of potential accumulation of mine gases and its effect on the surface after completion of the mine disposal
- Maximum utilization of the available underground yardage (filling coefficient) of the disposed mine
- Maximum utilization of the existing technological equipment of the disposed mine
- Final utilization of the treated territory of the mining area of the disposed mine

Inventory of mining workings to the extent of the mining area of the mine shall delimit mining spaces for implementation of the method of their disposal within the mine disposal. The inventory shall include all accessible and maintained mining workings. Of the closed mining workings, the inventory shall include temporarily closed mining workings, or other workings the disposal of which can be justified by safety or other requirements.

#### **MINIMIZATION OF RISKS OF SUBSIDENCE AND EFFECTS ON THE SURFACE AFTER COMPLETION OF THE MINE DISPOSAL**

One of the most significant factors of the decision on the method and extent of disposal of the mine or its part is the task to ensure minimization of subsidence and slumping risks and other effects resulting from free underground spaces after completion of mining activities. In particular, this is an essential requirement on execution of disposal works in densely populated and built-up mining areas. Therefore, the mine disposal documentation must include a detailed description of possible effects on surface objects in terms of undermining, anticipated course of subsidence, slumping as well as possible dynamic effects with regard to underground vibrations after backfilling in seismic mines or mines with mining methods creating large free spaces (long-wall mining in massive seams with firm top, by chamber working).

Identification of risk localities with regard to stability of accompanying rocks, which represent the abandoned underground mining spaces located near the surface and mining workings opened to the surface (in particular, abandoned and old mining workings) is executed by evaluation of map sources of mining-survey documentation.

With regard to the disposal works – disposal of workings from bottom to top – it must be stated whether the risks also impend during the disposal works and how they are to be eliminated.

#### **Elimination of potential water migration in the mining area affected by mining after completion of the mine disposal**

Filling of all free underground spaces with suitable backfilling eliminates the possibility of water migration in the area of the disposed mine. In the mining practice, numerous cases have been recorded when flooding of a mine resulted in outflow of contaminated mine waters with subsequent menace to surface waters (Oslavany, Rтынě in Podkrkonoší). Therefore, the mine disposal documentation must include a thorough analysis of the underground water state

including its quantity, stability of inflow and chemical status, predicted development and changes, particularly in the chemical status of this water, outflows after prospective flooding of the mine and necessary investments in their cleaning. For mines operated on a long-term basis, it is also necessary to indicate effects of old mining activities in terms of anticipated contamination and outflow of waste waters.

Description of these risks may play a significant role in the phase of deciding on the method of the mine disposal and support of the selected method of disposal by its backfilling, particularly on the part of professional bodies.

### **Minimization of possible accumulation of mine gases and its effect on the surface after completion of the mine disposal**

As mentioned above, after completion of mining activities and artificial ventilation, underground and gaseous mines pose a considerable risk of ascent of explosive mine gases. Again, this must be described in detail in the mine disposal documentation, including the anticipated communication ways, possible amount and concentration of gases as well as the risk of their impossible estimate.

It is also necessary to indicate the time estimate and development of gas ascent, including the risk of accumulation in the flooded underground.

In the built-up area of the disposed mine, this fact may again play a significant role in the phase of decision on the method of disposal and support to the underground disposal by its backfilling. If the mine is to be disposed by backfilling of its free spaces with artificial ventilation for the entire time of disposal works, the risk must be analysed even though it is minimized in this way.

### **Maximum utilization of the available underground yardage (filling coefficient) of the disposed mine**

To fulfil the above-mentioned requirements on this method of disposal during disposal of the mine by backfilling of its underground spaces, it is necessary to achieve the highest possible infilling of the available free yardage, whereas the backfilling properties must ensure that, after decantation of water, its volume does not reduce significantly, it has minimum compressibility, yet maximum elasticity, and, in particular, it can be transported even to the farthest places and least accessible spaces of the mine. For this, it is necessary to choose both backfilling of a suitable type as well as transport technology in the mine and method of backfilling. In the ideal state, the achieved infilling coefficient of free spaces of the disposed mine would be equal to one.

To carry out a check of infilling, it is first necessary to calculate the free underground yardage as precisely as possible in the documentation so that the check can be carried out simultaneously with the process of the mine disposal. This calculation must also consider backfilling of free top excavations and drifts (in particular, by means of blasting operations, with workings through which gob and disturbed rocks passed) as well as unfilled stopes.

Thus the documentation for the mine disposal by backfilling must contain not only calculation of free spaces by parts, levels and the entire mine, but also calculation of the infilling coefficient of the disposed workings and parts of the mine on the basis of the determined transport

technology, backfilling method and procedure and the proposed types of backfilling. The calculation of anticipated yardages is based on mine maps on the scale of 1:1000 and determination of the yardage coefficient, considering the time factor and type of working, properties of accompanying rocks and influence of surrounding mining activities (by action of mining pressures). Its value is determined by expert estimate in the range of 0.25- 0.8. At the same time, control mechanisms must be specified to monitor the real state of infilling.

### **Final utilization of the treated territory of the mining area of the disposed mine**

The documentation shall solve not only the method and actual execution of the disposal of the mine underground, redevelopment and reclamation of the area affected by mining in the disposed mine locality and the entire affected mining space, but also the subsequent utilization of the redeveloped surface. In our case, in contrast to abandoned unfilled underground of the mine, a variant solution of utilization of the mine surface premises can be suggested in the documentation of the disposed mine with underground backfilling, possibly also for other equipment in the mining area, which was formerly used for mining activities. After the underground has been filled up with backfilling of necessary parameters, further utilization of objects can be proposed boldly, for example, for:

- creation of a museum of mining;
- transformation of the premises into an industrial zone;
- combination of the above variants.

### **REQUIREMENTS FOR TECHNICAL DISPOSAL OF UNDERGROUND MINES**

The method of technical disposal of the mine must be based on the mine-geological conditions in the deposit locality, morphology and geology of wider surroundings, hydrogeological and geomechanical relations, situation of the mining capacity in the countryside, particularly in relation to habitation, method of the deposit early development and application of mining methods.

The adopted technical solution of the mine disposal must provide for elimination, or at least minimization, of risks related to abandonment of the locality, particularly those of the safety, health and environmental character, specifically:

- a) ascent of mine gases from underground spaces with the risk of their accumulation in surface and underground building objects;
- b) impaired stability of openings of main mining workings;
- c) sudden surface subsidence through loss of stability of accompanying rocks owing to caving of underground spaces of abandoned mining workings located near the surface;
- d) contamination of mine waters migrating through the mine environment, owing to leaching of substances out of this environment or contaminants left in the underground spaces:

During disposal of the mine, the entity must:

- manage economical utilization of the deposit reserves, safeguard the unused part of the mineral deposit;
- safeguard the adjacent deposits;
- take necessary measures to protect mining workings of the adjacent mines;
- take necessary measures to protect the environment and utilize the area after termination of mining activities;
- implement essential measures to provide for labour and operational safety and prevent risks in the locality.

The disposal plan shall include execution of all necessary works for safe disposal of the mine as an operating unit. Particularly, it shall specify the technical method of disposal, use of technologies, technical equipment, means and precautions to ensure safety and environmental protection.

### CONCLUSIONS

At the present time, Czech mining faces a period of deep downturn. Essentially, classic mining activities in the underground are taking place in OKD only; even there, they are to be terminated within a few years. In the area of elimination of the consequences of past mining activities, however, there is still a huge task to deal with for the Czech state.

It is necessary to perform gradual reconnaissance of most of the registered mining workings, evaluate the state of their safeguarding, the rate of risk which they pose for their surroundings, and subsequently safeguard the selected workings in a proper manner. All organisational units of the state should reach an agreement on the common procedure of these activities so that the financial resources assigned for the given purpose according to law are spent with maximum efficiency. Proper attention to the issue of past mining activities should also be paid by municipalities and pertinent building authorities within production of land-use plans.

### REFERENCES

- Hudeček, V, Žůrek, P, Kukutsch, R 2007. *Concept of liquidation procedure of mining workings and underground mines* [in Czech Návrh metodiky likvidace hlavních důlních děl]. Ostrava: VŠB-TU Ostrava, 66 p.
- Hudeček, V, Žůrek, P, Kukutsch, R 2007. *Guideline for underground mine liquidation filling methods* [in Czech Metodický pokyn k likvidaci hlubinného dolu zakládáním] Ostrava: VŠB-TU Ostrava, 21 p.
- Makarius, R., 1999. *Czech Mining Law, Part I* [in Czech České horní právo, Díl I]. Ostrava: Montanex
- Makarius, R., 2000. *Czech Mining Law, Part I*. [in Czech České horní právo, Díl II] .Ostrava: Montanex
- Slivka, V, Dvořáček, J, Cigánek, F, Hudeček, V, Grmela, A, Žůrek, P, Adamec, Z, Podzemský, K, Daněk, T, Kukutsch, R, Martinec, V, Novotný, K, Rakouš, I 2007. *Underground mine*

*liquidation using filling methods after termination of mining activities for decrease safety and ecological hazards* [in Czech Likvidace hlubinného dolu zakládáním po ukončení báňské činnosti pro snížení bezpečnostních a ekologických rizik]. VŠB-TU Ostrava, 100 p. ISBN 978-80-248-1680-7

Žůrek, P, Hudeček, V, Kukutsch, R 2012. Utilization of old mine workings in the Czech Republic. *Journal of Mines, Metals and Fuels*. No 7-8 (2012), p. 151-155. ISSN 0022-2755

# INDEX

---

## A

Alberto Kamenar · 9  
Alex Remennikov · 146  
Ali Mirzaghobanali · 32, 104, 116, 146,  
162  
Andreas Helwig · 32  
Andrew Alcott · 321  
Antoine Schneiderwind · 155  
Ashkan Rastegarmanesh · 32

---

## B

Barry Sturgeon · 353  
Basil Beamish · 331  
Brendan Scott · 198

---

## C

Chengguo Zhang · 116, 128

---

## D

Danqi Li · 138  
David Cliff · 295  
Dennis Black · 281  
Derek Avalle · 198  
Dihon Tadic · 186  
Duncan Best · 155

---

## E

Edward Steed · 57  
Ellie Hawkins · 340

---

## F

Faham Tahmasebinia · 128  
Frank Hungerford · 207

---

## G

Gaetano Venticinque · 233, 264, 275  
Gelber Taco · 9  
George Klenowski · 175

Guy Reed · 219

---

## H

Hadi Nourizadeh · 116  
Hossein Masoumi · 45, 138, 359

---

## I

Ian Gray · 74  
Isaac Dzakpata · 186  
Ismet Canbulat · 45, 116, 126, 128

---

## J

James Miedecke · 198  
Jan Nemcik · 233, 242, 264, 275, 367  
Jan Theiler · 331  
Jason Emery · 57  
Jean-Luc Schmitter · 321  
Jeff Edgoose · 9  
Joji Quidim · 186  
Joung Oh · 116

---

## K

Kent McTyer · 163  
Kevin McDougall · 32, 116

---

## L

Larry Ryan · 304  
Libin Gong · 233, 264, 367

---

## M

Martin Mackinnon · 219  
Martin Tsai · 304  
Martin Watkinson · 304  
Mehdi Serati · 23  
Mladen Gido · 314  
Mohammad Ataei · 104  
Muhammad Zohaib · 32  
Mutaz El-Amin Mohmoud · 23



---

**N**

Naj Aziz · 32, 104, 116, 146, 155, 162  
Neil Alston · 321  
Nemai Karmakar · 359

---

**O**

Omar Salim · 359  
Onur Vardar · 128

---

**P**

Patrick Booth · 242  
Peter Gregor · 32  
Peter Yee · 45  
Petr Waclawik · 233, 367  
Phil McNamara · 175

---

**R**

Radovan Kukutsch · 233, 367  
Reza Kakaie · 104  
Russell Frith · 219  
Russell Fry · 321

---

**S**

Sadjad Mohammadi · 104  
Saman Khaleghparast · 146, 155  
Scott Sheldon · 340  
Sean Muller · 314  
Serkan Saydam · 45, 128  
Shuvashis Dey · 359  
Sina Anzanpour · 146, 155  
Snezana Bajic · 314  
Sungsoon Mo · 45

---

**T**

Terri O'Sullivan · 45  
Tim Gibbons · 74  
Ting Ren · 242  
Travis Marshall · 155

---

**Z**

Zahra Faraji Rad · 104  
Zhongwei Chen · 23